International Journal of Photoenergy

Photovoltaic Materials and Devices

Guest Editors: Bhushan Sopori, Teh Tan, and Peter Rupnowski

Photovoltaic Materials and Devices

International Journal of Photoenergy

Photovoltaic Materials and Devices

Guest Editors: Bhushan Sopori, Teh Tan, and Peter Rupnowski

Editorial Board

Contents

Contents

Hindawi Publishing Corporation
International Journal of Photoenergy
Volume 2012, Article ID 673975, 1 page
doi:10.1155/2012/673975

Editorial

Photovoltaic Materials and Devices

Bhushan Sopori,[1] Teh Tan,[2] and Peter Rupnowski[3]

[1] *National Renewable Energy Laboratory, 1617 Cole Boulevard, Golden, CO 80401, USA*
[2] *Department of Mechanical Engineering and Materials Science, Duke University, Durham, NC 27706, USA*
[3] *Dow Corning Corporation, 2200 W Salzburg Road, Midland, MI 48686, USA*

Correspondence should be addressed to Bhushan Sopori, bhushan_sopori@nrel.gov

Received 3 April 2012; Accepted 3 April 2012

As the global energy needs grow, there is increasing interest in the generation of electricity by photovoltaics (PVs) devices or solar cells—devices that convert sunlight to electricity. Solar industry has seen an enormous growth during the last decade. The sale of PV modules has exceeded 27 GW in 2011, with significant contributions to the market share from all technologies. While the silicon technology continues to have the dominant share, the other thin film technologies (CdTe, CIGS, a-Si, and organic PV) are experiencing fast growth. Increased production of silicon modules has led to a very rapid reduction in their price and remains as benchmark for other technologies. The PV industry is in full gear to commercialize new automated equipment for solar cell and module production, instrumentation for process monitoring technologies, and for implementation of other cost-reduction approaches, and extensive research continues to be carried out in many laboratories to improve the efficiency of solar cells and modules without increasing the production costs. A large variety of solar cells, which differ in the material systems used, design, PV structure, and even the principle of PV conversion, are designed to date.

This special issue contains peer-reviewed papers in the recent developments in research related to broad spectrum of photovoltaic materials and devices. It contains papers on many aspects of solar cells—the growth and deposition, characterization, and new material development.

Acknowledgment

The editors acknowledge with thanks the contributing authors for the work they have put in participation and reviewers for ensuring good quality and the staff at the Hindawi Publishing Corporation for their helpful assistance and efficient handling of the publication. They are thankful to Dr. Sudhakar Shet, National Renewable Energy Laboratory, for his assistance in preparing this special issue. The support of Mona Mahmoud, Editorial Office, Hindawi Publishing Corporation is gratefully acknowledged.

Bhushan Sopori
Teh Tan
Peter Rupnowski

Hindawi Publishing Corporation
International Journal of Photoenergy
Volume 2012, Article ID 810801, 9 pages
doi:10.1155/2012/810801

Research Article

New Results in Optical Modelling of Quantum Well Solar Cells

Silvian Fara,[1] Paul Sterian,[2] Laurentiu Fara,[2] Mihai Iancu,[1] and Andreea Sterian[2]

[1] *IPA SA, Calea Floreasca 169, 014459 Bucharest, Romania*
[2] *University Politehnica of Bucharest, Splaiul Independentei 313, 060042 Bucharest, Romania*

Correspondence should be addressed to Andreea Sterian, andreea_sterian@physics.pub.ro

Received 6 October 2011; Accepted 24 January 2012

Academic Editor: Bhushan Sopori

This project brought further advancements to the quantum well solar cell concept proposed by Keith Barnham. In this paper, the optical modelling of MQW solar cells was analyzed and we focussed on the following topics: (i) simulation of the refraction index and the reflectance, (ii) simulation of the absorption coefficient, (iii) simulation of the quantum efficiency for the absorption process, (iv) discussion and modelling of the quantum confinement effect, and (v) evaluation of datasheet parameters of the MQW cell.

1. Background

Quantum well (QW) photovoltaic cells, third-generation solar cells, were proposed in 1990 by the research group of Professor Barnham [1] aiming at extending the spectral response and at increasing the photocurrent.

The quantum well solar cell (QW) is a p-i-n structure having quantum wells built in the intrinsic. Doped regions on each side will produce an electric field perpendicular to the layers of quantum wells. It is also possible to have induced electric fields, because of the piezoelectric effects. These fields are induced by the intensities from the semiconductor layers, because of the disparity between network constants [2].

The multiple quantum well (MQW) solar cell is a system that contains a layer in which the carrier assemblies comply quantum rules in connection with layers in which the carrier assemblies are performing classical, and its modelling is conducted on two-dimensional levels [3]:

(1) quantum level in which one computes the energy spectrum of the electron and the absorption coefficient of the MQW;

(2) macroscopic level in which one studies the transport of charge carriers in a similar manner to the conventional p-i-n diode [4]. The reflection of light is brought considering MQW cell a pseudohomogeneous medium. This combination of quantum and classical elements used in modelling of MQW solar cell justifies the name of hybrid given to the model of MQW solar cell. An example of application of this *hybrid model (HM)* [5] is the case of solar cell based on a ternary alloy semiconductor $A_xB_{1-x}C$ ($Al_xGa_{1-x}As$) which has the lowest BC band gap equal with zero and achieve the greatest value ($x = 1$) for the AC semiconductor band gap.

In Figure 1 are graphically represented the transmittances and energetic levels in the MWQ system as a result of the transport matrix algorithm [6]. The proper values from Figure 1(a) and resonances from Figure 1(b) are identical and mutually confirmed. The levels represented in Figure 1(a) are obtained by applying Kramer's rule, while the transmittances represented in Figure 1(b) are calculated via the transfer matrix. It is noted that a large variation of alloy composition x does not determine significant changes in position of the first level from the quantum wells, which means that there is a weak dependence between short-circuit current and the ternary alloy composition. Each curve in Figure 1(b) is calculated in 104 points in less than a minute.

Figure 2 shows the geometry of an MQW solar cell in the HM hybrid model. This model allows determining the configuration that leads to maximum conversion efficiency. This layer configuration can further be designed, by using the transfer matrix method and the properties of the real materials. In other words, starting from a hypothetic layer system, the HM model allows optimization of the cell

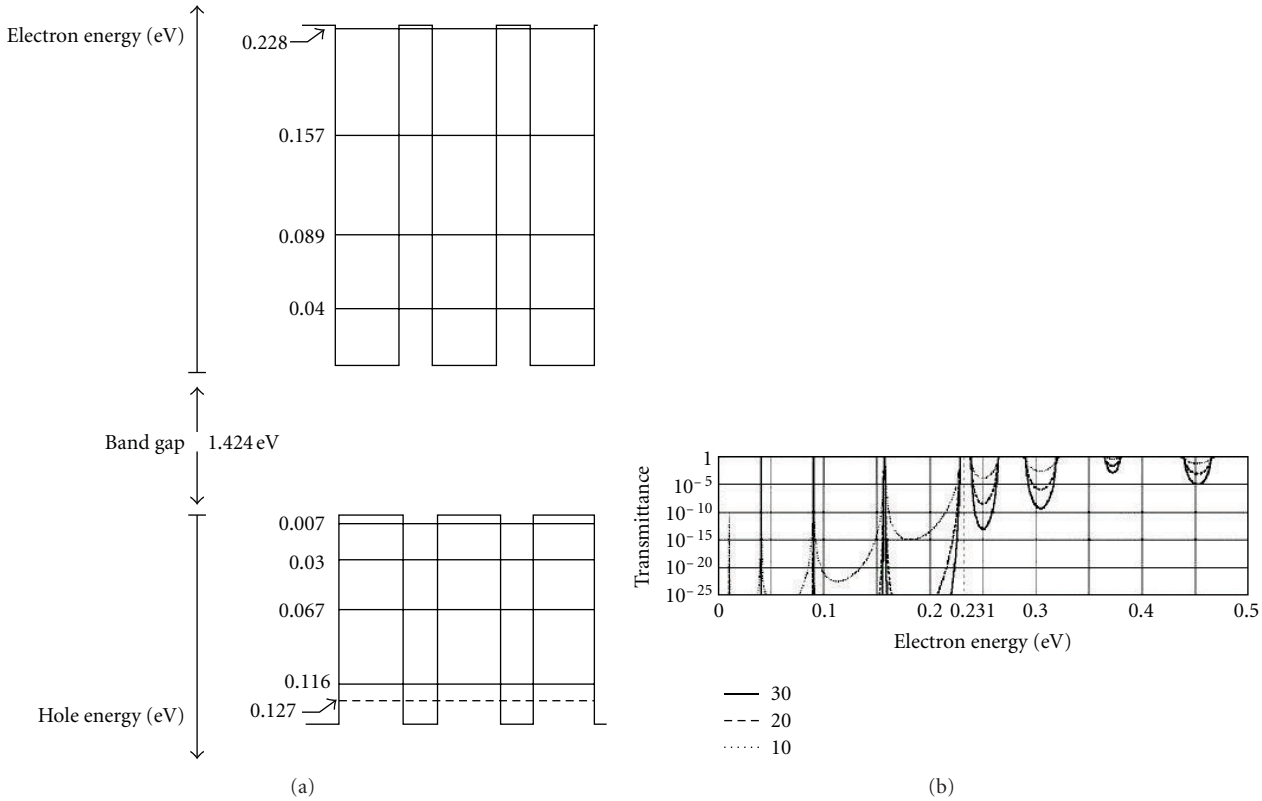

Figure 1: (a) Schematic representation of levels in the valence bands and conduction for the MQW system $Al_{0.3}Ga_{0.7}As/GaAs$ containing 30 quantum wells. The corresponding level for the heavy gaps is shown with dotted line. (b) Transmission coefficient based on the electron energy for the same system. The curves parameter is the number of quantum wells.

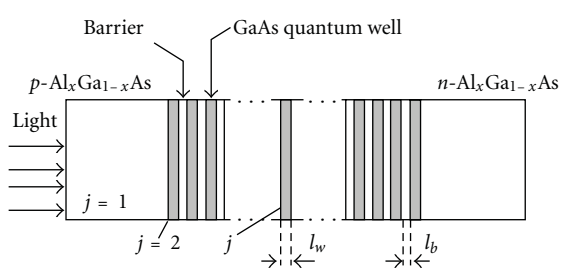

Figure 2: Geometry of a solar cell in the HM hybrid model.

configuration in order to obtain maximum output electrical power, for a certain state of illumination [4].

The HM model may have the capability to evaluate the performances of the MQW cell. These are represented by *the shape factor of cell*

$$F_f = \frac{V_m I_m}{V_{CD} J_{SC}} \text{ and conversion efficiency } \eta = \frac{V_m I_m}{\int G_0(\lambda) d\lambda}, \quad (1)$$

where V_m and I_m are the operation point coordinates when the power supplied in the load is maximum.

2. Modeling and Simulation of Refraction Index and Reflectance

Investigation of electric field effects on the *refraction index* of MQW solar cells can be achieved by calculating the absorption coefficient [7]. In the case of solar cells with quantum wells was introduced the hypothesis of an electrostatic field generated by the load [8]. For this reason, it is expected a nonvarying change in the refraction index. Based on the results obtained by Barnham, it should be noted that the quantum wells from the solar cells of this type are designed to use the spectrum region, with the possibility of generating particles in those quantum wells. For the refraction index of the solar cell with quantum wells it was used the following expression:

$$n_2 = n = \sqrt{1 + \frac{E_d}{E_o} + \frac{E_d}{E_o^3} E^2 + \frac{\eta}{\pi} E^4 \ln\left(\frac{2E_o^2 - E_g^2 - E^2}{E_r^2 - E^2}\right)}. \quad (2)$$

The parameters are $E_g = 1.6729$; $E_r = 1.4235$; $E_o = 2.6 + 0.7E_r$; $E_d = F/E_o$ and $\eta = \pi E_d/(2E_o^3(E_o^2 - E_r^2))$.

The simulation results for the refraction index depending on the photon energy are represented in Figure 3.

The *index of refraction model* can be used to explore the relation between the index of refraction and reflectance. To achieve this, the refraction index model must be combined with the *Fresnel relations,* thus allowing the finding of the

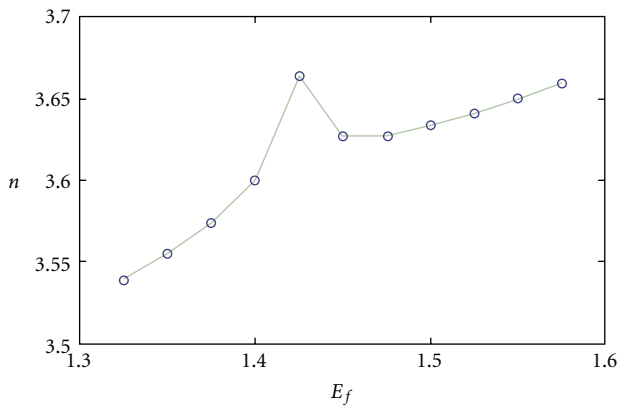

Figure 3: The refraction index of the cells with quantum wells depending on the photon energy.

losses caused by reflection of the quantum wells structure. The R reflectance of the solar cell can be calculated using a Fresnel-type relation [9]

$$R = \frac{r_1^2 + r_2^2 + 2r_1 r_2 \cos 2\theta}{1 + r_1^2 r_2^2 + 2r_1 r_2 \cos 2\theta}, \tag{3}$$

where

$$r_1 = \frac{n_0 - n_1}{n_0 + n_1}; \quad r_2 = \frac{n_1 - n_2}{n_1 + n_2}; \quad \theta = \frac{2\pi\pi_1 d_1}{\lambda}. \tag{4}$$

The following notations were introduced:

(i) n_0 the refraction index of the incident environment; for air $n_0 = 1$;

(ii) n_1 the refraction index of the antireflecting coating;

(iii) n_2 the refraction index of the under layer (the solar cell with quantum wells).

Thickness d_1 of the antireflecting coating can be determined by minimizing the last relation (5). It was noted that this value is approximately 600–650 nm, for the minimum reflection.

It can be evaluated the *effect of the quantum well number* on the index of refraction and on the *reflection losses* so the optimal number of the quantum well for the structure could be calculated [10].

In Figure 4 are the results of the optical simulation of solar cells with quantum well (based on relations (3)-(4)), in the from of dependence on reflectance R, depending on the wavelength for different thicknesses d for the antireflecting coating; were considered two cases of antireflecting coating ($n_1 = 2.4$—TiO_2 and $n_1 = 1.4$—SiO). Results from model are consistent with experimental results obtained. The reflectance model can be used to determine the variation effects of quantum well number on the index of refraction.

The simulation of refraction index and reflectance of the solar cells with quantum wells have been made with the Octave software, version 3.02.

The cell reflectance can be calculated using the refraction indices of GaAs semiconductor and of the $Al_{0.3}Ga_{0.7}As$ alloy (obtained by filtering the experimental data [11].

$$n_{\mathrm{GaAs}} = \begin{cases} \dfrac{3.24123 - (4.8304085/\lambda) + (2.82482/\lambda^2) - (0.769037/\lambda^3) + (0.08198/\lambda^4)}{1 - (1.5308/\lambda) + (0.9123972/\lambda^2) - (0.2508648/\lambda^3) + (0.026769/\lambda^4)}, & \text{if } 0.325 < \lambda \le 4, \\ \dfrac{2.8434068 - (1.8916996/\lambda) + (0.4189801/\lambda^2) - (0.0308637/\lambda^3)}{1 - (0.682372/\lambda) + (0.154593/\lambda^2) - (0.01159/\lambda^3)}, & \text{if } 0.2 \le \lambda \le 0.325. \end{cases} \tag{5}$$

In (5) λ is expressed in μm. The refraction index of ternary alloy $Al_xGa_{1-x}As$ is calculated using the same translation procedure of the axes as in the case of the absorption coefficient:

$$n_{\mathrm{Al}_x\mathrm{Ga}_{1-x}\mathrm{As}}(\lambda) = \left[1.05 - 0.53x + 0.09x^2\right] n_{\mathrm{GaAs}}(\lambda_x) \quad \text{with } \lambda \text{ in } \mu\text{m}. \tag{6}$$

To minimize the reflection losses the solar cells are frequently coated with *antireflecting coating (ARC)*.

In Figure 5(a) are the values calculated for the four refraction indices listed according to the wavelength. The MQW layer was considered to consist of 30 quantum wells of GaAs of 20 nm width separated by barriers $Al_{0.3}Ga_{0.7}As$ with width of 10 nm.

In Figure 5(b) are summarized the results of reflection losses for the various thicknesses of the antireflecting coating. In the absence of ARC, reflection is an important mechanism of losses exceeding 30% on the spectral range in which the cell absorbs. The other curves show that it is possible to reduce losses through reflection by covering with an antireflecting coating of appropriate thickness.

3. Modelling and Simulation of Absorption Coefficient

In applications related to calculating the conversion efficiency of solar cells, but also in other applications, the coefficient of absorption (the absorbance) is practically described by continuous functions. For GaAs, dropping from the experimental data [12] was determined the following function that approximates the acceptable rate of absorption:

$$\alpha_{\mathrm{GaAs}}(\lambda) = \begin{cases} e^{F_1(\lambda)}, & 0.7 < \lambda \le 0.88, \\ e^{F_2(\lambda)}, & 0.24 < \lambda \le 0.7, \\ e^{F_2(0.24)}, & 0 < \lambda \le 0.24, \\ 0, & \text{otherwise}, \end{cases}$$

$$F_1(\lambda) = -0.7863 + 5.3115\left[1 + \mathrm{erf}\left(-\frac{\lambda - 0.84291}{0.038}\right)\right],$$

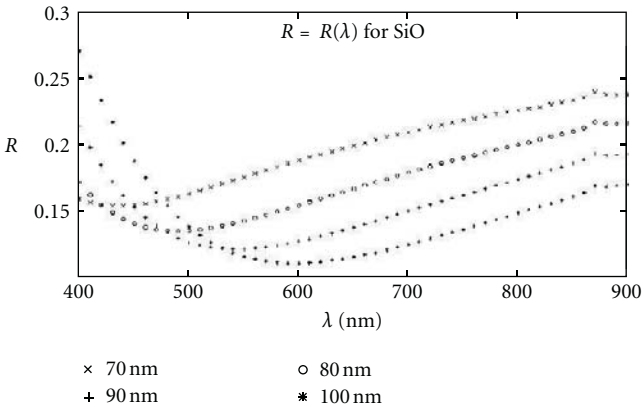

Figure 4: Simulation of the reflectance for a solar cell with QW structure, for a SiO antireflecting coating.

$$F_2(\lambda) = -447.432 + 4201.2\lambda^2 + 6835.128\lambda^2 \ln\lambda - 3781.193\lambda^3 + \frac{3.9049}{\lambda^2}. \quad (7)$$

In Figure 6(a) is graphically represented the absorption coefficient for GaAs calculated with the algorithm from [13] for different compositions of the alloy.

In Figure 6(b) are graphically compared the absorption coefficients for GaAs, $Al_{0.5}Ga_{0.5}As$, and MQW system. It is noted that with increasing energy the absorption coefficient from MQW system increases in steps; this is because of the quantifying of the density of states in confinement of the carriers' direction.

Absorption coefficient $\alpha_x(\lambda)$ of the $Al_xGa_{1-x}As$ alloy is generated from the absorption coefficient of the GaAs: $\alpha_x(\lambda) = \alpha_0(\lambda_x)$ (h is Planck constant, c is the speed of light, $a = 0.62$ and $b = 0.5$ [13])

$$\lambda_x = \frac{hc}{(hc/\lambda) - E_g(x) + E_g(0) + \alpha\left[(hc/\lambda) - E_g(0)\right]^b x}. \quad (8)$$

4. Increasing Quantum Efficiency of the QW Solar Cells

4.1. Simulation of the Quantum Efficiency of QW Solar Cells by Using a Semiquantum Model. The analyzed model uses the transport equation of $Al_xGa_{1-x}As$ quantum well solar cells, where x represents the Aluminium concentration. We considered the results obtaining by Hutchby and Fudurich [14], Connolly in his doctoral thesis [15], and Barnham's research group [16].

The model used the transport equation of $Al_xGa_{1-x}As$ solar cells. The expression of the quantum efficiency is given by

$$\mathrm{QE} \cong \frac{\alpha k(\alpha - S)}{(k^2 - \alpha^2)(S\sinh(kz) - k\cosh(kz))} \cong \frac{\alpha - S}{\alpha^2(S-1)}. \quad (9)$$

It is introduced the parameter S of the boundary condition on the surface. It is resulted $S \approx 2\varepsilon f$, α = spectral absorption coefficient, ε_f = effective electric field due to the minoritary carriers in the band.

The simulated results are presented in the Figures 7(a) and 7(b).

From the analysis of the data obtained, one can draw the following comments:

(i) quantum efficiency increases with any increase in λ, reaching significant values of maximum 90%, in the case of large diffusion wavelength;

(ii) quantum efficiency increases with any increase of z and ε_f, respectively.

4.2. Quantum Confinement Effect. In order to find ways for increasing efficiency through the simulation of nanostructured solar cells (QW), we have used a mathematical model for the quantum efficiency of the transitions between the resonant levels (in GaAs) and another one for the quantum efficiency of the transitions between the confining levels (in $Al_xGa_{1-x}As$) [17].

In the case of resonant levels, quantum efficiency of the absorption process is given as follows [18]:

$$\mathrm{QE}_\lambda = \frac{8\pi^2 e^2}{c\hbar\varepsilon_0\varepsilon_{rw}}\left[\left(1 - \frac{\sin^2 i}{4\varepsilon_{rw}}\right) + \frac{t_w^2}{L^2}\frac{\sin^2 i}{4\varepsilon_{rw}}\right], \quad (10)$$

where α is prism angle, i is incidence angle, ε_r is relative permittivity, and n is confinement level of quantum efficiency.

For transitions between the confining levels, the quantum efficiency is given by

$$\mathrm{QE}_{\lambda_n} = \frac{4096e^2}{\pi^2 c\hbar\varepsilon_0\varepsilon_{rw,b}^2}\frac{t_{w,b}^2}{L^2}\frac{n^2\sin^2 i}{(4n^2-1)^4}. \quad (11)$$

In expressions (10) and (11), index w refers to GaAs, and index b refers to $Al_xGa_{1-x}As$.

For GaAs one obtains the curves of quantum efficiency of the transitions between the resonant levels (see Figures 8(a) and 8(b)) and between the confining levels, depending on the prism refraction index and on the incidence angle of the ray that falls on the prism, for $\alpha = \pi/6$ and $\alpha = 2\pi/3$. Similarly one obtains the quantum efficiency, for $Al_xGa_{1-x}As$, $Np = 1.5$ ($Np = 2$ resp.), $\alpha = \pi/6$ and $\alpha = 2\pi/3$, depending on the quantity of Aluminium.

From the analysis of the results, one can conclude the following.

(i) The quantum efficiency of the absorption process for nanostructured (quantum) solar cells is higher for a larger range of wavelengths, in comparison to the semiquantum solar cells.

(ii) Although the quantum efficiency of the absorption on the confining levels is very low, the appearance of electrons in the gap greatly increases the photocurrent through photoassisted tunnelling.

(iii) Monitoring the operating parameters (processor loading, memory used, network traffic, etc.) of the cluster (which allowed a large volume of computations) was done with the help of the Ganglia application.

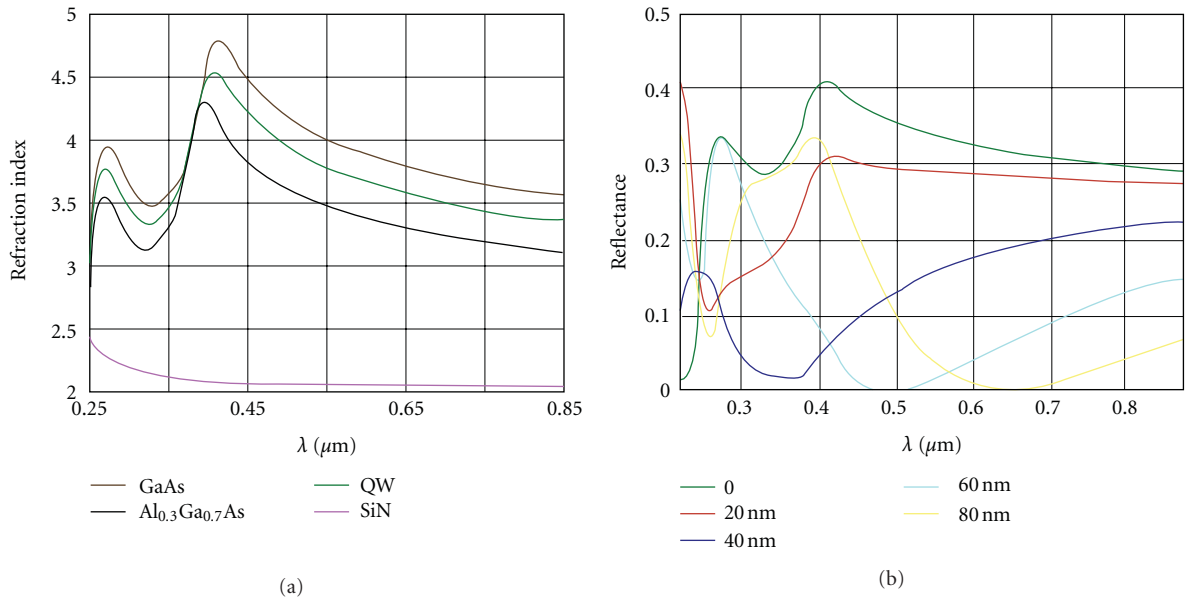

Figure 5: (a) The refraction index for the materials involved in constructing a MQW cell. (b) Spectral reflectance of the MQW cell for different width (nm) of the antireflecting coating. The HM model was run for GaAs/$Al_{0.3}Ga_{0.7}As$ with $N_w = 30$, $l_w = 20$ nm and $l_b = 10$ nm.

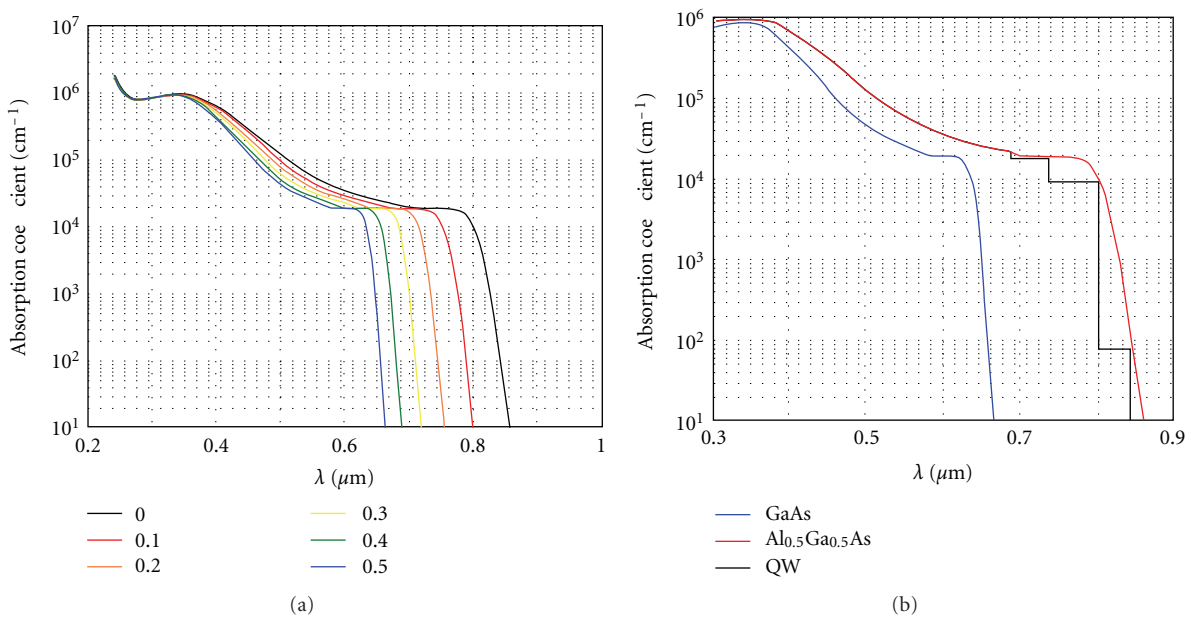

Figure 6: (a) Absorption coefficient of $Al_xGa_{1-x}As$ depending on wavelength; x is the curves parameter. (b) Absorption coefficient in GaAs crystal; the ternary compound $Al_{0.5}Ga_{0.5}As$ is calculated using axes translation in MQW system.

5. The Results Obtained during Simulation of the Cell Parameters

In Figure 9, for the cell parameters $N_w = 30$, $l_w = 20$ nm, and $l_b = 10$ nm are summarized the calculation results of the conversion efficiency. In Figure 9(a) are represented the current-intensity characteristic with the power dissipated by the cell in the external circuit. Hence the main parameters of the cell are $J_{SC} = 48.5\,\text{mA/cm}^2$, $V_{CD} = 0.886$ V, $F_f = 0.86$, and $\eta = 0.371$. The numerical values are closed to those reported in the literature [19, 20]. As for the conventional cell with a p-n junction the maximum possible efficiency is estimated at 34% [3]. The result nor confirms nor invalidates that the insertion of MQW in the space-load region improves the conversion efficiency.

Figure 9(b) shows the conversion efficiency dependence on the antireflecting coating depth. It can be noted that in the ideal case, when the cell reflectance is neglected, the MQW

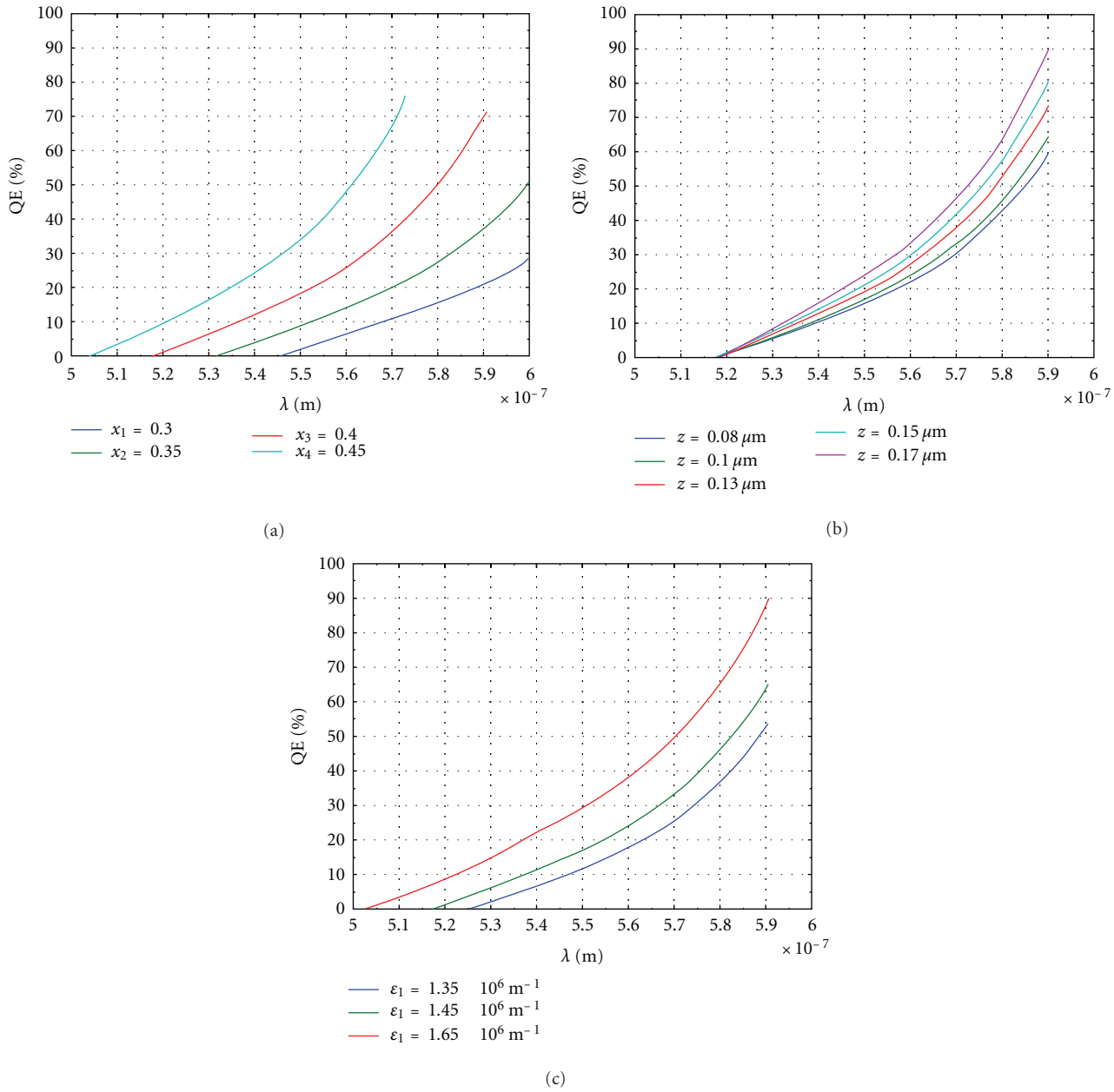

Figure 7: (a) Variation of the quantum efficiency with the wavelength, for different fractions of Al. (b) Variation of the quantum efficiency with the wavelength, for different solar cell thicknesses. (c) Variation of the quantum efficiency with the wavelength, for different effective field.

cell efficiency based on GaAs/$Al_xGa_{1-x}As$ does not exceed 40%.

Unlike the reflectance, in Figure 9(c) it is observed that the conversion efficiency is strongly correlated with the number of quantum wells up to $N_w = 30$; over this value the efficiency is saturated in proportion to N_w. Inside the MQW system the saturation is installed when the road length travelled by light is comparable with the absorption length.

This is a one way to use the HM model. Knowing the materials componence of MQW cell and its optoelectronic properties, for a given geometric configuration the conversion efficiency can be calculated. Obviously the calculation can be repeated varying different geometrical and material parameters in order to determine the optimal configuration, that is, one that maximizes efficiency.

Recently good experimental results were reported in MQW solar cells [21]. The fabricated solar cells based on $In_{0.3}Ga_{0.7}N$/GaN MQWs exhibit an open-circuit voltage of about 2 V, fill factor of about 60%, and an external efficiency of 40%–10% at 420 nm–50 nm.

6. Conclusions

The results were based on the HM hybrid model of the MQW solar cells; after simulation there were highlighted the following conclusions.

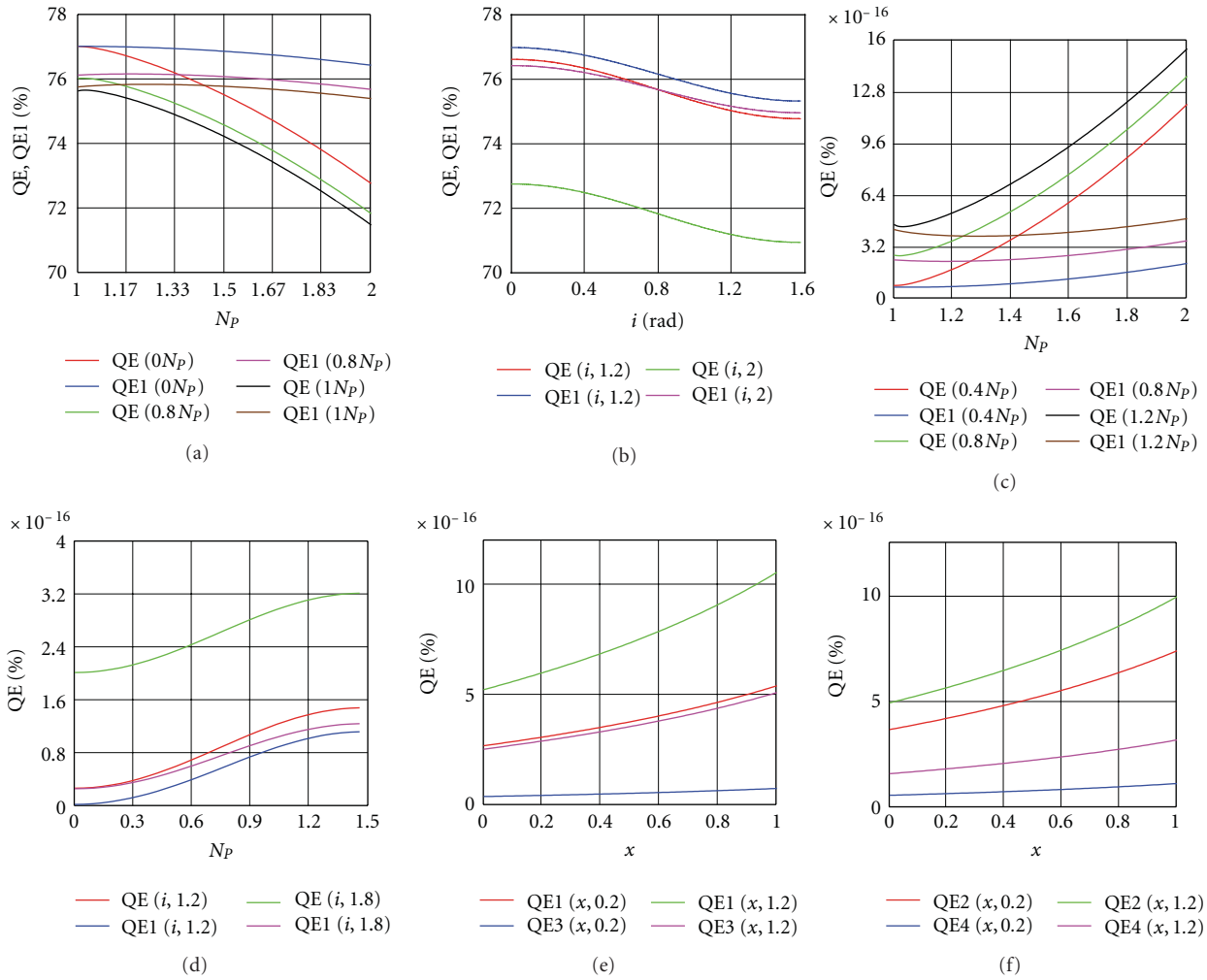

Figure 8: (a) Quantum efficiency of the transitions between resonant levels for GaAs as a function of the prism refraction index. It is considered the following two main cases: (1) prism angle $\alpha = \pi/6$ and incidence angle: $i = 0$ rad (red curve), $i = 0.8$ rad (green curve), $i = 1$ rad (black curve). (2) prism angle $\alpha = 2\pi/3$ incidence angle $i = 0$ rad (blue curve), $i = 0.8$ rad (violet curve), $i = 1$ rad (brown curve). (b) Quantum efficiency of the transitions between resonant levels for GaAs as a function of the incidence angle for the ray falling on the prism. (c) Quantum efficiency of the transitions between confinement levels for $Al_xGa_{1-x}As$ as a function of the prism refraction index. (d) Quantum efficiency of the transitions between confinement levels for AlGaAs as a function of the incidence angle of the ray falling on the prism. (e) Quantum efficiency of the transitions between confinement levels for $Al_xGa_{1-x}As$ as a function of the aluminium quantity; prism refraction index is $Np = 1.5$. (f) Quantum efficiency of the transitions between confinement levels for $Al_xGa_{1-x}As$ as a function of the aluminium quantity; prism refraction index is $Np = 2$.

(i) It could be evaluated the quantum well number effect over the refraction index and reflection losses by evaluation of the quantum well optimal number of the structure.

(ii) The reflectance model proposed by authors could be used to determine variation effect of the quantum well number over the refraction index.

(iii) It was developed an absorption coefficient model which was used for studying the simulation of the MQW solar cells in special weather conditions.

(iv) It was obtained the internal quantum efficiency for the absorption process between the confining levels.

(v) The results generated by the model simulator agree with the experimental ones [22].

There were studied several MQW solar cells configurations for optimized values of the optical parameters (reflectance, refraction index, and absorption), so the conversion efficiency could be improved. Although in our study, we considered only rectangular quantum wells, the HM hybrid model allows computing the levels whatsoever the form of the quantum wells is.

New solar devices could be conceived based on optical properties of nanostructured materials [23, 24].

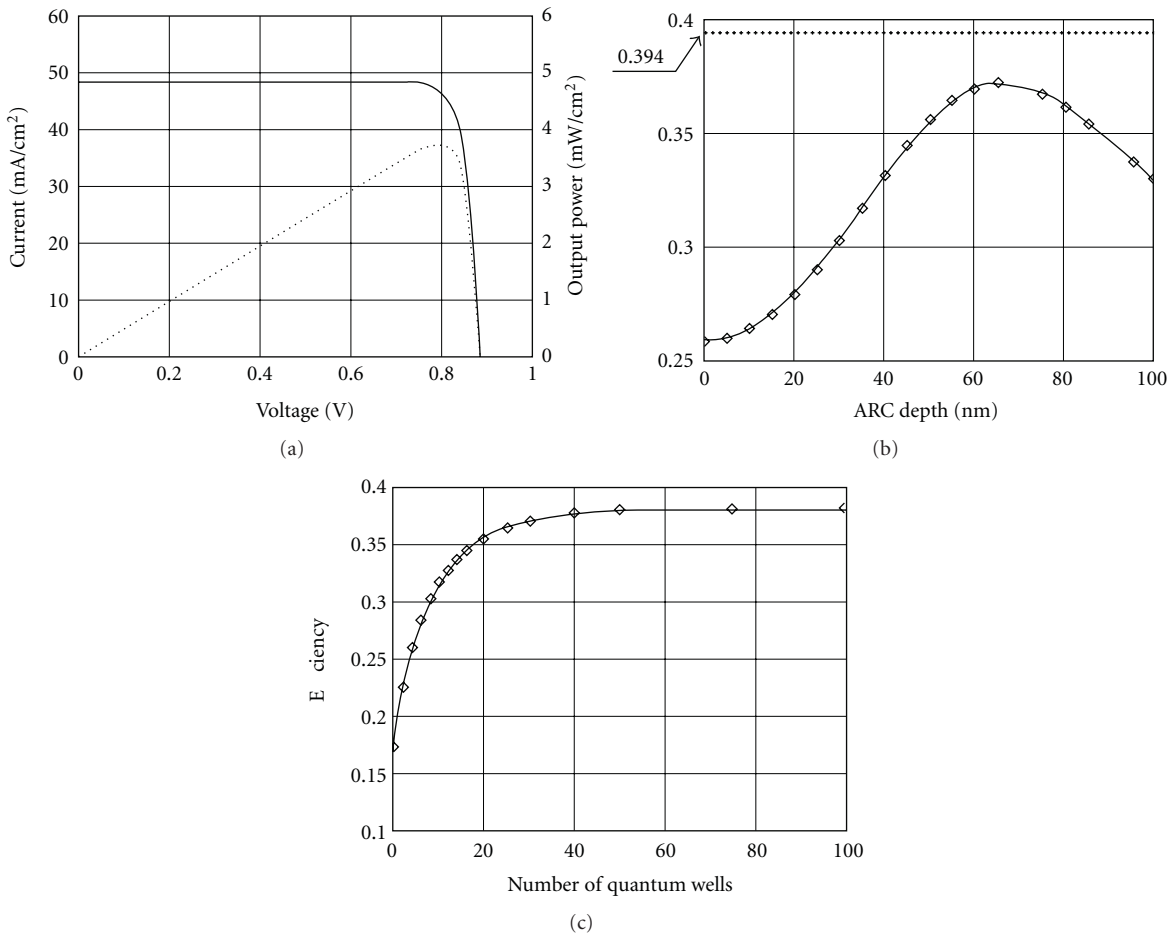

Figure 9: (a) Voltage-current characteristic (line) and the output power (points) of the cell with the following MQW system: GaAs/$Al_{0.3}Ga_{0.7}As$, $N_w = 30$, $l_w = 20$ nm, $l_b = 10$ nm and the antireflecting coating depth $d = 64$ nm. (b) The MQW cell efficiency depending on the antireflecting coating depth. The dotted line indicates the ideal cell efficiency with zero reflectance. (c) The efficiency of MQW cell based on the number of quantum wells.

QuantaSol [25] is a company form UK which developed firstly quantum wells and quantum dots for solar photovoltaics as well as concentrating solar cells for individual requirements.

Acknowledgments

Between 2006 and 2009, the NANO-PV (research concerning increase in the efficiency of nanostructured solar cells) project was run in the framework of the Romanian National Programme of Excellence in Research. The project was developed by the research groups in three universities (Polytechnic University of Bucharest, Timisoara West University, and Polytechnic University of Timisoara) which were coordinated by *IPA SA*. The authors would like to acknowledge and thank their collaborators from the University Politehnica of Bucharest, the West University of Timisoara, and the University Politehnica of Timisoara for the good and fruitful collaboration in developing the NANO-PV project.

References

[1] K. W. J. Barnham and G. Duggan, "A new approach to high-efficiency multi-band-gap solar cells," *Journal of Applied Physics*, vol. 67, no. 7, pp. 3490–3493, 1990.

[2] K. W. J. Barnham, "A novel approach to higher efficiency—the quantum well solar cell," in *Proceedings of the 11th E. C. Photovoltaic Solar Energy Conference*, pp. 146–149, Montreux, Switzerland, 1992.

[3] A. Goetzberger, J. Knobloch, and B. Voss, *Crystalline Silicon Solar Cells*, Wiley, London, UK, 1998.

[4] J. E. Velazquez-Perez and Y. G. Gurevich, "Charge-carrier transport in thin film solar cells: new formulation," *International Journal of Photoenergy*, vol. 2011, Article ID 976063, 5 pages, 2011.

[5] J. Ferber, R. Stangl, and J. Luther, "Electrical model of the dye-sensitized solar cell," *Solar Energy Materials and Solar Cells*, vol. 53, no. 1-2, pp. 29–54, 1998.

[6] T. Oda, S. Tanaka, and S. Hayase, "Differences in characteristics of dye-sensitized solar cells containing acetonitrile and ionic liquid-based electrolytes studied using a novel model,"

Solar Energy Materials and Solar Cells, vol. 90, no. 16, pp. 2696–2709, 2006.

[7] G. Smestad, C. Bignozzi, and R. Argazzi, "Testing of dye sensitized TiO_2 solar cells I: experimental photocurrent output and conversion efficiencies," *Solar Energy Materials and Solar Cells*, vol. 32, no. 3, pp. 259–272, 1994.

[8] A. Jüngel and S. Tang, "Numerical approximation of the viscous quantum hydrodynamic model for semiconductors," *Applied Numerical Mathematics*, vol. 56, no. 7, pp. 899–915, 2006.

[9] W. Shockley and W. T. Read Jr., "Statistics of the recombinations of holes and electrons," *Physical Review*, vol. 87, no. 5, pp. 835–842, 1952.

[10] L. Fara, R. M. Mitroi, V. Iancu, G. Noaje, and G. Milescu, *Modelling and Numerical Simulation of Nanostructured Solar Cells*, Punct Publishing House, Bucharest, Romania, 2008.

[11] M. Paulescu, D. A. Vangheli, E. Tulcan-Paulescu et al., *Nanostructured Photovoltaic Cells*, West University Publishing House, Timisoara, Romania, 2007.

[12] M. Paulescu, P. Gravila, and E. Tulcan-Paulescu, "Optical and electrical modelling of multiple quantum well solar cells," *Scientific Bulletin of the "Politehnica" University of Timisoara*, vol. 53, no. 66, pp. 114–121, 2007.

[13] M. Paulescu and E. Tulcan-Paulescu, "Assessments on the multijunction solar cells photoelectric efficiency related to the semiconductor band gap and outdoor conditions," *Modern Physics Letters B*, vol. 19, no. 9-10, pp. 447–457, 2005.

[14] J. A. Hutchby and R. L. Fudurich, "Theoretical analysis of $Al_xGa_{1-x}As$-GaAs graded band-gap solar cell," *Journal of Applied Physics*, vol. 47, no. 7, pp. 3140–3151, 1976.

[15] J. P. Connolly, *Modelling and optimizing GaAs/$Al_xGa_{1-x}As$ multiple quantum well solar cells*, Ph.D. thesis, Imperial College of Science, Technology and Medicine, University of London, London, UK, 1997.

[16] J. P. Connolly, I. M. Ballard, K. W. J. Barnham, D. B. Bushnell, T. N. D. Tibbits, and J. S. Roberts, "Efficiency limits of quantum well solar cells," in *Proceedings of the 19th European Photovoltaic Solar Energy Conference*, pp. 355–358, 2004.

[17] V. Iancu, L. Fara, and R. M. Mitroi, "Quantum confinement modeling and simulation for quantum well solar cells," *Annals of the Academy of Romanian Scientists*, vol. 1, no. 1, pp. 35–46, 2009.

[18] J. S. Blakemore, "Semiconducting and other major properties of gallium arsenide," *Journal of Applied Physics*, vol. 53, no. 10, article R123, 59 pages, 1982.

[19] K. W. J. Barnham, I. M. Ballard, B. C. Browne et al., "Recent progress in quantum well solar cells," *Nanotechnology for Photovoltaics*, pp. 187–210, 2010.

[20] J. P. Connolly, I. M. Ballard, K. W. J. Barnham, D. B. Bushnell, T. N. D. Tibbits, and J. S. Roberts, "Efficiency limits of quantum well solar cells," in *Proceedings of the 19th European Photovoltaic Solar Energy Conference*, pp. 355–359, Paris, France, June, 2004.

[21] R. Dahal, B. Pantha, J. Li, J. Y. Lin, and H. X. Jiang, "InGaN/GaN multiple quantum well solar cells with long operating wavelengths," *Applied Physics Letters*, vol. 94, no. 6, Article ID 063505, 3 pages, 2009.

[22] K. W. J. Barnham, I. Ballard, J. P. Connolly et al., "Quantum well solar cells," *Physica E*, vol. 14, no. 1-2, pp. 27–36, 2002.

[23] G. E. Jonsson, H. Fredriksson, R. Sellappan, and D. Chakarov, "Nanostructures for enhanced light absorption in solar energy devices," *International Journal of Photoenergy*, vol. 2011, Article ID 939807, 11 pages, 2011.

[24] M. S. A. Abdel-Mottaleb, J. A. Byrne, and D. Chakarov, "Nanotechnology and solar energy," *International Journal of Photoenergy*, vol. 2011, Article ID 194146, 2 pages, 2011.

[25] http://www.quantasol.com/.

Hindawi Publishing Corporation
International Journal of Photoenergy
Volume 2012, Article ID 175610, 7 pages
doi:10.1155/2012/175610

Research Article

Exploring Spray-Coating Techniques for Organic Solar Cell Applications

Wanyi Nie,[1] Robert Coffin,[1] Jiwen Liu,[1] Christopher M. MacNeill,[2] Yuan Li,[1] Ronald E. Noftle,[2] and David L. Carroll[1]

[1] *Center for Nanotechnology and Molecular Materials, Wake Forest University, 501 Deacon Boulevard, Winston-Salem, NC 27105, USA*
[2] *Department of Chemistry, Wake Forest University, 1834 Wake Forest Road, Winston-Salem, NC 27109, USA*

Correspondence should be addressed to David L. Carroll, carroldl@wfu.edu

Received 5 December 2011; Revised 5 March 2012; Accepted 7 March 2012

Academic Editor: Peter Rupnowski

We have investigated spray coating as a novel processing method for organic solar cell fabrication. In this work, spraying parameters and organic solvent influences have been correlated with cell performance. Using airbrush fabrication, bulk heterojunction photovoltaic devices based on a new low band gap donor material: poly[(4,8-bis(1-pentylhexyloxy)benzo[1,2-b:4,5-b′]dithiophene-2,6-diyl-alt-2,1,3-benzoxadiazole-4,7-diyl] with the C60-derivative (6,6)-phenyl C61-butyric acid methyl ester (PCBM) as an acceptor, have achieved power conversion efficiencies over 3%. We show that airbrush fabrication can be carried out with simple solvents such as pristine 1,2-dichlorobenzene. Moreover, the influence of device active area has been studied and the 1 cm^2 device by spray coating maintained an excellent power conversion efficiency of 3.02% on average.

1. Introduction

Worldwide, organic photovoltaics are under development as an inexpensive approach for collecting solar energy. Within the field, much effort has been given to the modification of either the absorber chemistry or its structural order. The chemical approach used by most researchers is to modulate the HOMO-LUMO levels of the donor polymer to obtain a low optical band gap (<1.74 eV) and thereby allow for absorption in a range that best matches the solar spectrum [1]. Recently, significant progress has been achieved following these routes, from a starting efficiency of around 1% in 1995 [2] when the bulk-heterojunction architecture was introduced, to 5% in 2007 for the first low band gap donor polymer [3] and most recently record efficiencies of 6%–8% [4–6]. However, these results are generally limited to the laboratory by the experimental requirement of using ultra-thin layers that typically means employing spin coating. This method of fabrication only allows for devices on a small scale (usually 2.5 cm × 2.5 cm chips) that would neither control the cost nor satisfy the needs of large-scale manufacturing. Because of this, alternative coating technologies for absorbers have been of significant interest, aimed specifically at cheap, large area coating. These have included ink-jet printing [7], roll-to-roll printing [8], brush painting [9], and spray coating [10, 11]. Among these techniques, spray coating began to gain attention when Vak et al. in 2007 [12] showed they could easily fabricate the active layer with a commercially available hand-held airbrush. Up until now, most of the studies on spray coating OPV have been based on the poly(3-hexyl thiophene) (P3HT): the C_{60}-derivative (6,6)-phenyl C61-butyric acid methyl ester (PCBM) bulk-heterojunction (BHJ) material system and the commonly achieved efficiency was 2-3% with a small active area (10 mm^2). Therefore, a natural question is "how will the low band gap polymers with higher efficiencies translate into these scalable techniques?"

Previously we reported a newly designed and synthesized low band gap polymer (~1.69 eV) poly[(4,8-*bis*(1-pentylhexyloxy)benzo[1,2-*b*:4,5-*b*′]dithiophene-2,6-diyl*alt*-2,1,3-benzoxadiazole-4,7-diyl] (**P1**) [13]. When optimized with solvent additives in spin coating fabrication, this polymer easily achieves efficiencies exceeding 6%. Based on a similar donor-acceptor architecture as the record polymers referenced above, this polymer provides an excellent opportunity to

Table 1: Average JV characteristics by spraying coating. P1 : PCBM solutions dissolved by CB, DCB and TCB under room temperature and spin coated from DCB. The maximum value of PCE over 8 devices under each condition is given in the last column as Peak PCE.

	Solvent	Voc (V)	Jsc (mA/cm^2)	FF	PCE	Peak PCE
Spray coating	CB	0.946	5.67	0.455	2.37%	2.53%
	DCB	0.960	6.88	0.404	2.68%	3.00%
	TCB	0.902	3.88	0.377	1.31%	1.40%
Spin coating	CB	0.978	2.58	0.564	1.38%	1.42%
	DCB	0.923	7.61	0.496	3.49%	3.72%
Spray coating P3HT	Un-annealed	0.628	4.59	0.316	0.91%	
	Annealed	0.624	9.39	0.426	2.5%	2.72%

study correlations in such systems, between spray-coating techniques and device performance for potential large scale applications.

2. Experiment

Prepatterned ITO substrates were cleaned in an ultrasonication bath with triton water, DI water, acetone, and isopropyl-alcohol for 20 min respectively and dried in a vacuum oven at 100°C for 1 hour. A 30 min UV-Ozone treatment was performed on the ITO surface afterwards and PEDOT : PSS (CLEVIOS 4083) was spun cast at a spin speed of 4000 rpm. The 100 nm active layer was either spun cast or spray-coated from the blend solution of **P1** and PCBM (the optimized ratio of 1 : 2 by weight was previous determined by experiment and IV curve available in Figure 4 in the appendix) dissolved in 1,2-dichlorobenzene (DCB). The substrates with dried films were transferred to a vacuum chamber, pumped down to 1×10^{-6} torr and LiF (~0.25 nm) as hole blocking layer and aluminum (~100 nm) as cathode were added. The resulting organic photovoltaic (OPV) devices were tested in air with a standard A.M 1.5 G solar simulator for I-V characters and external quantum efficiency (EQE) measurement was carried out by a Newport Cornerstone 260 Monochromator connected with a Newport 300 W Xenon light source.

3. Results and Discussion

3.1. Nozzle to Substrate Distance. Parameter control is the first step in developing this technology for any new polymer. Then, comparisons with standard spin-coating methods can be made between the thin films. From the basic structure of an airbrush in Figure 1, the carrier gas brings the polymer solution from a feed cup, along a needle that leads to the nozzle (dia. 0.18 mm in our case). Once the solution passes through the nozzle, a fine line composed of very small droplets will be generated and deposited on the substrate. In this process, a variety of parameters are correlated with the resulting thin film morphology [12, 13]. These include the needle-nozzle distance which determines the size of the spray spot (and density of droplets), the carrier gas pressure which controls the deposition rate, and the nozzle to substrate distance which determines the droplet drying time during flight. A detailed study on the nozzle to substrate distance was carried out in the first study in spray coating on OPV by Vak et al.

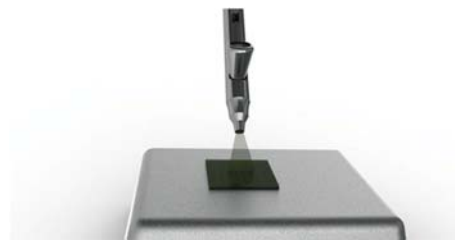

Figure 1: Airbrush spraying polymer on top of a device.

[12]. In that work, they defined the three regions between airbrush nozzle and substrate as "wet", "intermediate," and "dry" and they found the best linear control over thickness as a function of spraying time was in the "intermediate zone." They also suggested that the "intermediate zone" varied with the boiling point of the solvent used.

Initially, as a control, we fabricated devices using P3HT : PCBM as the absorbing layer and the performance was quit close to that reported elsewhere [10] and shown in Table 1 for the spray distance of 15 cm. A detailed study was then carried out for our **P1** polymer [14] and based on this, the "intermediate zone" was found to be very similar to the P3HT system; around 15 cm, using the fixed solution made by dissolving 2.5 mg P1 and 5 mg PCBM in DCB. We note that the DCB solution will dry the film slower than chlorobenzene due to the higher boiling point and therefore gives us a wider window for film thickness control [15].

3.2. Polymer Ink Properties. The properties of the spray solution not only affects the choice of nozzle-substrate distance for thickness optimization, but also plays an important role on film morphology. This is based primarily on the choice of solvent boiling point and vapor pressure. The basic concept is to choose a fast drying solvent to prevent droplets from redissolving sublayers but not so fast so as to allow for a homogenous and pin-hole free film to form. Green et al. [15] found chlorobenzene (CB) to be an excellent choice for a good film quality and achieved efficiencies ~2.36% using P3HT : PCBM as the sprayed active layer. In 2009, Hoth et al. [16] adjusted the polymer solution viscosity by using a solvent mixture combining DCB and 1,3,5-trimethylbenzene in order to prevent the droplets from drying before touching the substrate as pristine CB does. This approach allowed for

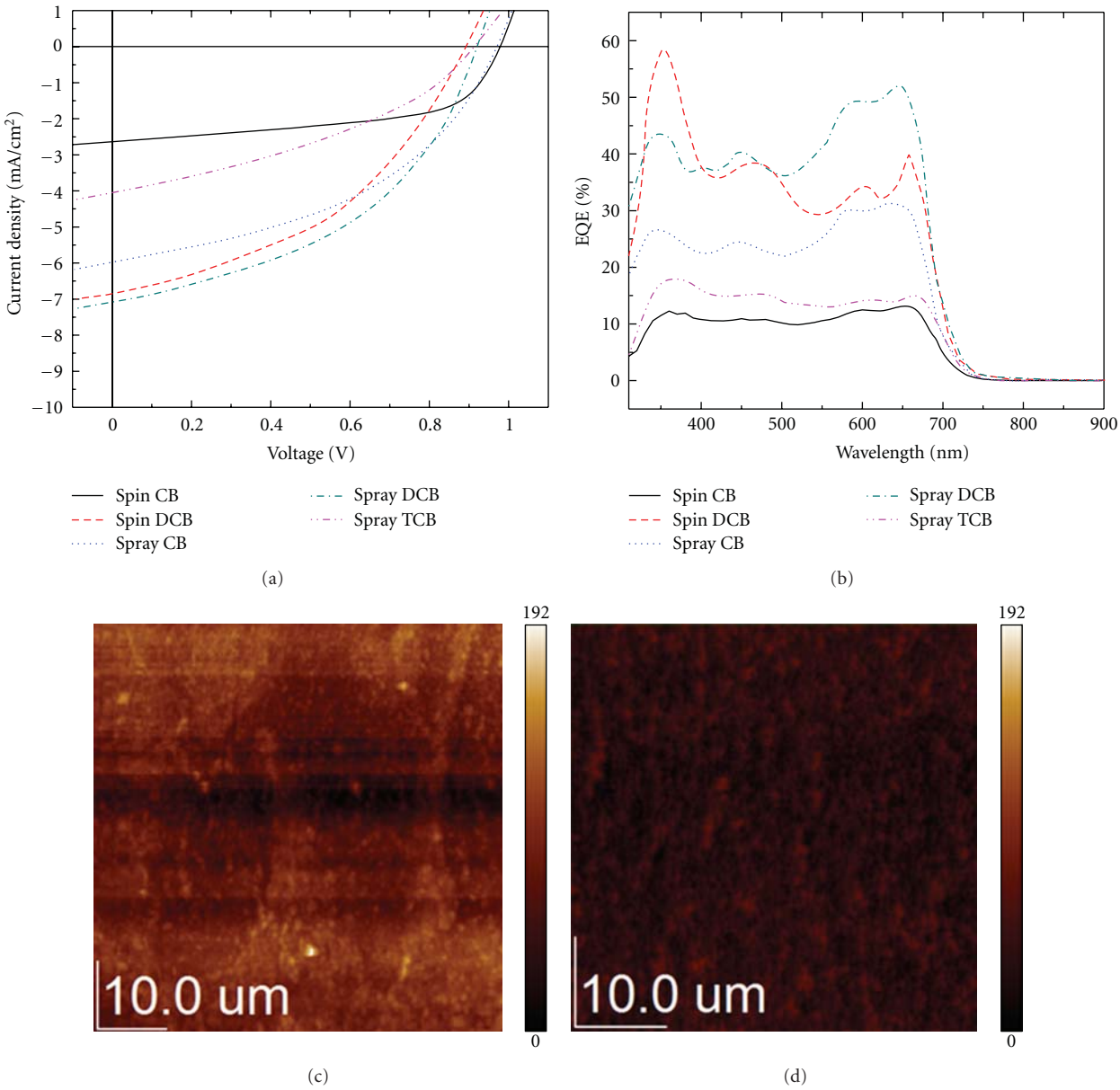

Figure 2: (a) I-V character under illumination and (b) EQE for spin and spray-coated device using difference solvents; AFM images for (c) spray-coated and (d) spin-coated device; the scale bar for AFM is in units of nm.

efficiencies up to 3.1% in the same BHJ material system with the resulting reduced surface tension allowing for the formation of a preferred morphology. Very recently, Susanna et al. used the mixed solvent of DCB and CB to achieve a similar morphology and obtained a PCE ~ 4.2% [13].

However, the choice of solvent varies the solution viscosity, which is then related to the specific material to be sprayed. So it was necessary to determine the best solvent for the blended solution of **P1** and $PC_{61}BM$. Considering both the solubility of the polymer and the boiling point (bp) (related to the drying rate) of the host solvent, we initially investigated three solvents: CB (bp = 131°C), DCB (bp = 180.5°C), and 1,2,4-trichlorobenzene (TCB, bp = 241.4°C). The optimum ratio of **P1** : $PC_{61}BM$ was previously determined to be 1 : 2 and this was held constant for this study. Absorbing layers were sprayed at room temperature (RT) with constant volumes (200 μL) and concentrations (3.00 mg/mL), yielding a film thickness of 90 ± 33.5 nm.

The current density-voltage (JV) characteristics are summarized in Table 1. Active layers sprayed from DCB gave the best results with average power conversion efficiency (PCE) of 2.68%, and a peak value of 3.00%. Comparing to data from the devices sprayed from CB and TCB solution, we find that differences in performance are largely a result of differnces in short-circuit current density, which is 20% and 77% lower for the devices sprayed from CB and TCB, respectively.

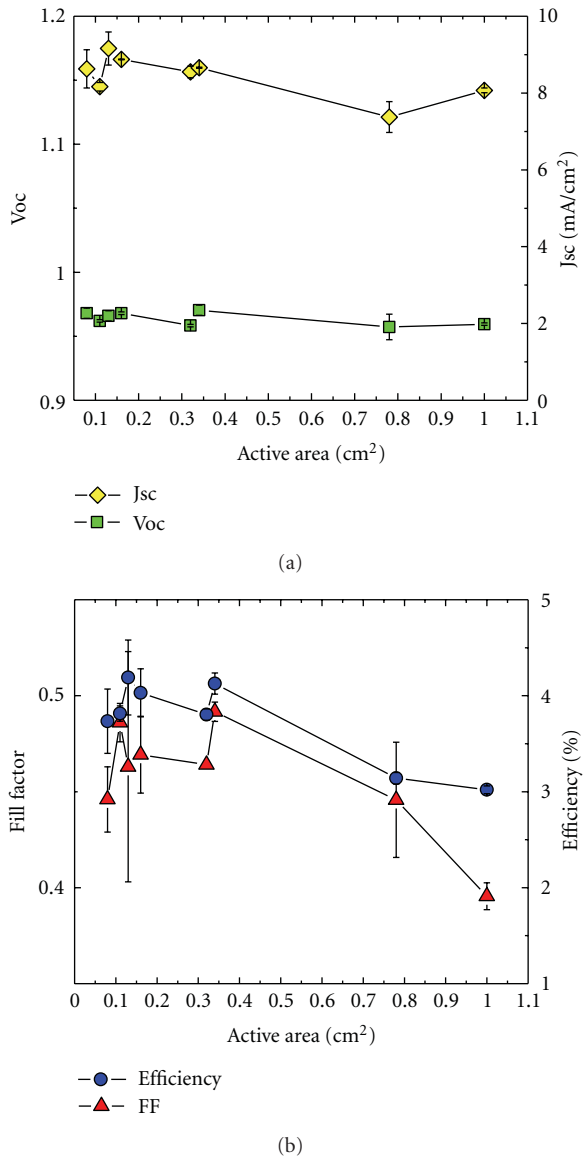

Figure 3: Statistical study with scale bars on (a) open-circuit voltage (Voc square) and short-circuit current (Jsc diamond). (b) Filling factor (triangle) and power conversion efficiency (circle) tested under a standard AM 1.5 solar simulator for sprayed devices as a function of active area.

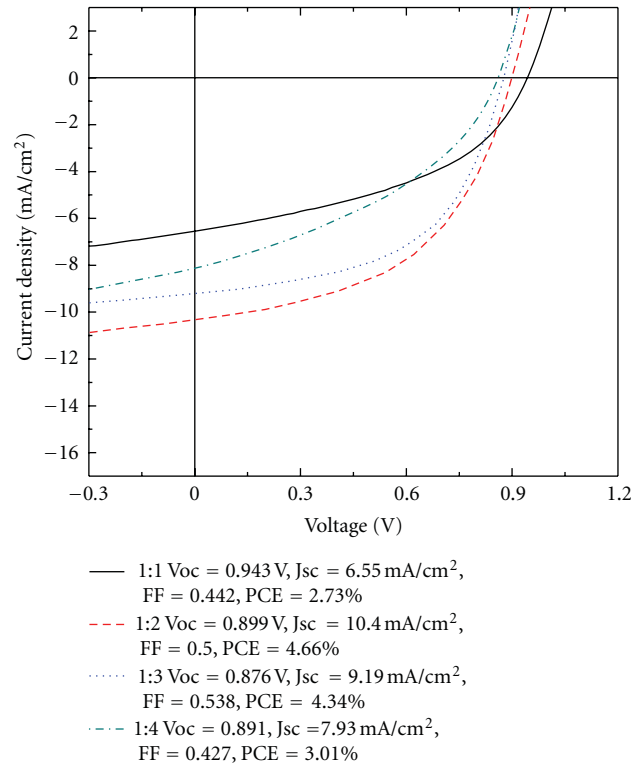

Figure 4: JV characteristics under 100 mW/cm^2 illumination by standard A.M. 1.5 solar simulator with P1 : PCBM ratio at 1 : 1 (black solid), 1 : 2 (red dash), 1 : 3 (blue dot), and 1 : 4 (green dash-dot).

Similar to our previous work with **P1** we find that the fill factor (FF) is higher for the devices sprayed from CB (~0.455) compared with DCB (~0.405), though this difference is not significant enough to offset the Jsc difference.

Figure 2 shows the JV curve under illumination and the corresponding external quantum efficiency and indicating that the performances are quite close between spin cast devices and sprayed devices. The slightly lower fill factor can be explained by observing in the atomic force microscopy (AFM) images of Figures 2(c) and 2(d), which show a similar morphology, but a much higher height variation for spray-coated films (0 ~ 192 nm) than spun cast films (0 ~ 82 nm) (refer to Figure 5 in the appendix). A variation in film thickness and roughness will result in a charge recombination due to the limited charge mobility for conjugated polymers. Therefore, the thicker parts in the spray-casted film will lower the total shunt resistant and affect the device filling factors. However, this confirms that spray coating does present an approach to large-scale fabrication for OPV using this materials system.

3.3. Active Area. Researchers have also begun to focus on the realistic processes for larger area production. Na et al. [17] reported fully spray-coated, ITO-free, solar cells using the anode (PEDOT : PSS) and the active layer (P3HT : PCBM). They were able to achieve PCE ~ 2.17%, thereby moving towards a cost-effective deposition method. At the same time, Girotto et al. [11] have developed a physical model for understanding droplet dynamics. In this work, they were able to spray a uniform PEDOT : PSS followed by a spray-coated absorbing layer with a fill factor over 70%, which is comparable to that achieved experimentally on spun-coated films. Taken together, these suggest that spray-coating can lead the OPV device to market without sacrificing efficiency but morphological considerations may be different from the spun cast approach.

However, we note that most of the studies [11, 12, 15, 18, 19] for spray coating OPV were carried out with an active area of around 10 mm^2 so scalability has not been

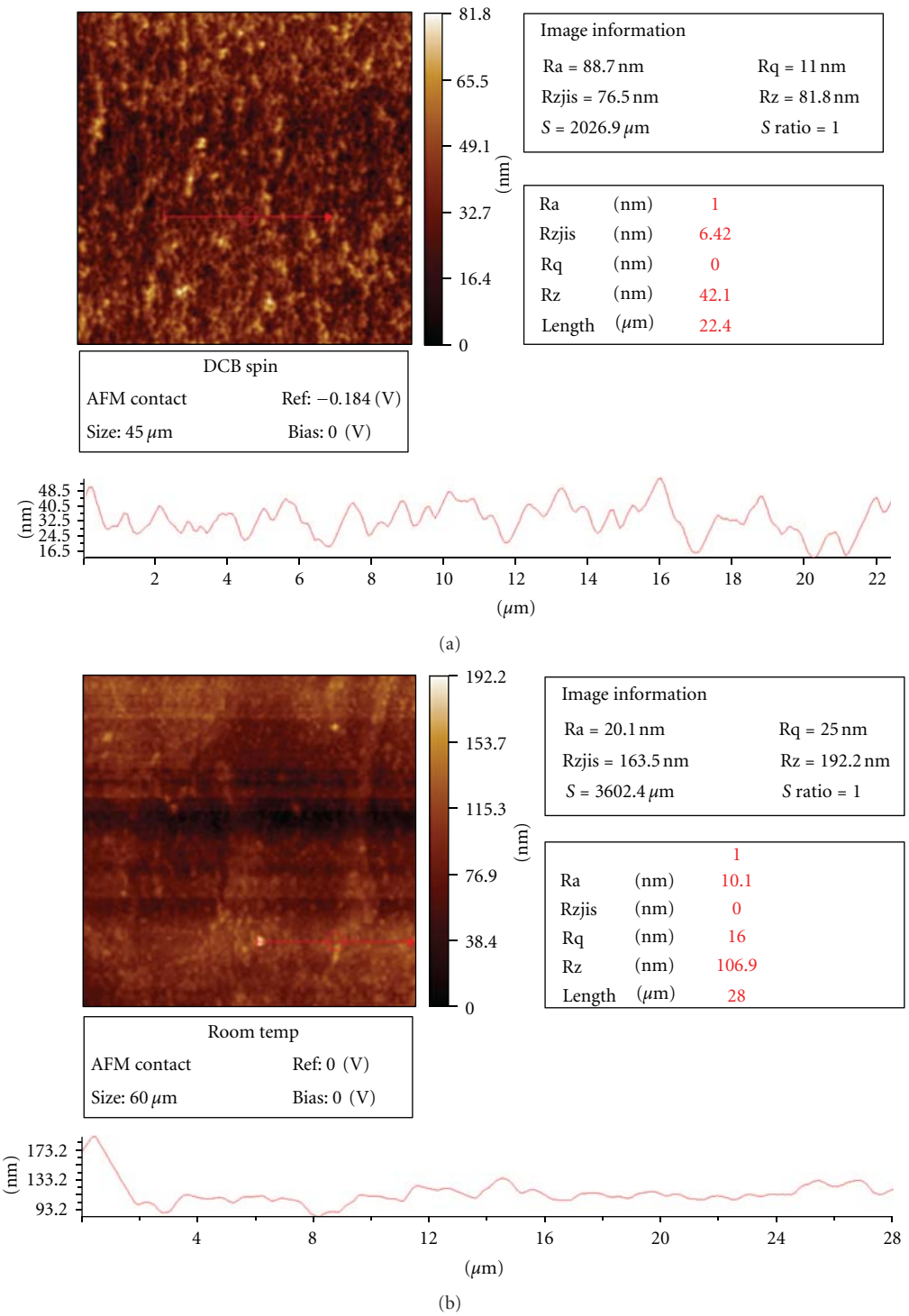

Figure 5: AFM topology analysis of (a) a spun-casted film and (b) a spray-casted film using DCB as carrier solvent.

demonstrated. Importantly, the roughness and thickness of sprayed films may reduce the final performance in large devices due to the increased internal resistance. In fact, it has been demonstrated that a 50% decrease occurs in a very large device (over 12 cm^2) [20], whereas on a 4 cm^2 device very little loss of performance (2.64%) from the smaller devices was observed. In our study, we observed a 1% decrease as well when larger device sizes (to 1 cm^2) were fabricated by spraying. This is due to the rougher surface.

In order to scale up our device by spray coating, we studied the JV performance as a function of active area statistically in Figure 3. Each point in Figure 3 refers to the average

over 8 electrodes (2 chips of 4-electrode devices). Each electrode is an active area of the film. The error was estimated by the difference between the average and maximum. Again, the Voc is not affected by active area as shown in Figure 3 with voltages ranging from 0.957 V to 0.970 V. Jsc is also relatively constant at $8.52 \pm 0.5\,\mathrm{mA/cm^2}$ up to the active area of $34\,\mathrm{mm^2}$. It dropped to $0.45\,\mathrm{mA/cm^2}$ when device sizes were increased to $100\,\mathrm{mm^2}$, which is only a 5% sacrifice in performance. The fill factor also decreased at $100\,\mathrm{mm^2}$ as expected to 0.395 ± 0.007 but the device with an active area of $34\,\mathrm{mm^2}$ still maintains a good fill factor of 0.49 that is comparable to the spun-casted devices. Because of the variation in thickness across the active are, the polymer solar cell can be viewed as a number of devices connected in parallel. When the active area increases, the shunt resistant was reduced from $853\,\mathrm{ohm\cdot cm^2}$ for the $0.3\,\mathrm{cm^2}$ device down to $585\,\mathrm{ohm\cdot cm^2}$ due to this film thickness variation which leads to charge recombination (AFM analysis is available in Figure 5 in the appendix). We suggest that this dominates the change in device filling factor. Surprisingly, the $100\,\mathrm{mm^2}$ devices show an average PCE of 3.02% in spraying coated devices. For such large active area devices this is quite good even though there is a 1.1% drop compared to the peak value of 4.12% for an active area of $34\,\mathrm{mm^2}$.

4. Conclusion

In summary, a review of the recent achievements in large-scale OPVs (mainly based on P3HT : PCBM BHJ structures) by spray coating technology, has identified several important parameters such as nozzle-substrate distance, choice of solvent, mixture of cosolvent that influence morphology optimization. Using these parameters in this work, we have explored the possibility of fabricating solar cell devices by a hand-held airbrush with an active layer composed of a new low band gap copolymer poly[(4,8-*bis*(1-pentylhexyloxy)benzo[1,2-*b*:4,5-*b*′]dithiophene-2,6-diyl-*alt*-2,1,3-benzothiadiazole-4,7-diyl] and phenyl-C_{61}-butyric acid methyl ester ($PC_{61}BM$). 1,2-Dichlorobenzene is shown as an appropriate carrier solvent by comparing the solar cell performance with other two solvents (chlorobenzene, 1,2,4-trichlorobenzene) under identical conditions, and we obtain a promising PCE~ 3.00% on average without any special treatment under room temperature conditions. We believe these results may give some guidance to spray approaches in this class of donor acceptor polymers.

Appendix

See Figures 4 and 5.

References

[1] M. C. Scharber, D. Mühlbacher, M. Koppe et al., "Design rules for donors in bulk-heterojunction solar cells—towards 10 % energy-conversion efficiency," *Advanced Materials*, vol. 18, no. 6, pp. 789–794, 2006.

[2] G. Yu, J. Gao, J. C. Hummelen, F. Wudl, and A. J. Heeger, "Polymer photovoltaic cells: enhanced efficiencies via a network of internal donor-acceptor heterojunctions," *Science*, vol. 270, no. 5243, pp. 1789–1791, 1995.

[3] J. Peet, J. Y. Kim, N. E. Coates et al., "Efficiency enhancement in low-bandgap polymer solar cells by processing with alkane dithiols," *Nature Materials*, vol. 6, no. 7, pp. 497–500, 2007.

[4] Y. Y. Liang, Z. Xu, J. B. Xia et al., "For the bright future—bulk heterojunction polymer solar cells with power conversion efficiency of 7.4%," *Advanced Materials*, vol. 22, no. 20, pp. E135–E138, 2010.

[5] T. Y. Chu, J. Lu, S. Beaupré et al., "Bulk heterojunction solar cells using thieno[3,4- c]pyrrole-4,6-dione and dithieno[3,2-b:2′,3′- d]silole copolymer with a power conversion efficiency of 7.3%," *Journal of the American Chemical Society*, vol. 133, no. 12, pp. 4250–4253, 2011.

[6] S. H. Park, A. Roy, S. Beaupré et al., "Bulk heterojunction solar cells with internal quantum efficiency approaching 100%," *Nature Photonics*, vol. 3, no. 5, pp. 297–303, 2009.

[7] F. C. Krebs, M. Jørgensen, K. Norrman et al., "A complete process for production of flexible large area polymer solar cells entirely using screen printing-first public demonstration," *Solar Energy Materials and Solar Cells*, vol. 93, no. 4, pp. 422–441, 2009.

[8] F. C. Krebs, "Fabrication and processing of polymer solar cells: a review of printing and coating techniques," *Solar Energy Materials and Solar Cells*, vol. 93, no. 4, pp. 394–412, 2009.

[9] S. Kim, S. Na, J. Jo, G. Tae, and D. Kim, "Efficient polymer solar cells fabricated by simple brush painting," *Advanced Materials*, vol. 19, no. 24, pp. 4410–4415, 2007.

[10] L. M. Chen, Z. R. Hong, W. L. Kwan et al., "Multi-source/component spray coating for polymer solar cells," *ACS Nano*, vol. 4, no. 8, pp. 4744–4752, 2010.

[11] C. Girotto, D. Moia, B. P. Rand, and P. Heremans, "High-performance organic solar cells with spray-coated hole-transport and active layers," *Advanced Functional Materials*, vol. 21, no. 1, pp. 64–72, 2011.

[12] D. Vak, S. S. Kim, J. Jo et al., "Fabrication of organic bulk heterojunction solar cells by a spray deposition method for low-cost power generation," *Applied Physics Letters*, vol. 91, Article ID 081102, 3 pages, 2007.

[13] G. Susanna, L. Salamandra, T. M. Brown, A. Di Carlo, F. Brunetti, and A. Reale, "Airbrush spray-coating of polymer bulk-heterojunction solar cells," *Solar Energy Materials and Solar Cells*, vol. 95, no. 7, pp. 1775–1778, 2011.

[14] W. Nie, C. M. MacNeill, Y. Li, R. E. Noftle, D. L. Carroll, and R. C. Coffin, "A soluble high molecular weight copolymer of benzo[1,2-b:4,5-b′] dithiophene and benzoxadiazole for efficient organic photovoltaics," *Macromolecular Rapid Communications*, vol. 32, no. 15, pp. 1163–1168, 2011.

[15] R. Green, A. Morfa, A. J. Ferguson, N. Kopidakis, G. Rumbles, and S. E. Shaheen, "Performance of bulk heterojunction photovoltaic devices prepared by airbrush spray deposition," *Applied Physics Letters*, vol. 92, no. 3, Article ID 033301, 2008.

[16] C. N. Hoth, R. Steim, P. Schilinsky et al., "Topographical and morphological aspects of spray coated organic photovoltaics," *Organic Electronics: Physics, Materials, Applications*, vol. 10, no. 4, pp. 587–593, 2009.

[17] S. I. Na, B. K. Yu, S. S. Kim et al., "Fully spray-coated ITO-free organic solar cells for low-cost power generation," *Solar Energy Materials and Solar Cells*, vol. 94, no. 8, pp. 1333–1337, 2010.

[18] K. Kawano, J. Sakai, M. Yahiro, and C. Adachi, "Effect of solvent on fabrication of active layers in organic solar cells based on poly(3-hexylthiophene) and fullerene derivatives," *Solar Energy Materials and Solar Cells*, vol. 93, no. 4, pp. 514–518, 2009.

[19] C. Girotto, B. P. Rand, J. Genoe, and P. Heremans, "Exploring spray coating as a deposition technique for the fabrication of solution-processed solar cells," *Solar Energy Materials and Solar Cells*, vol. 93, no. 4, pp. 454–458, 2009.

[20] S. Y. Park, Y. J. Kang, S. Lee et al., "Spray-coated organic solar cells with large-area of 12.25 cm^2," *Solar Energy Materials and Solar Cells*, vol. 95, no. 3, pp. 852–855, 2011.

Hindawi Publishing Corporation
International Journal of Photoenergy
Volume 2012, Article ID 396792, 11 pages
doi:10.1155/2012/396792

Research Article

Detection of Degradation Effects in Field-Aged c-Si Solar Cells through IR Thermography and Digital Image Processing

E. Kaplani

Mechanical Engineering Department, T.E.I. of Patras, Megalou Alexandrou 1, 26334 Patra, Greece

Correspondence should be addressed to E. Kaplani, ekaplani@teipat.gr

Received 27 December 2011; Accepted 7 February 2012

Academic Editor: Peter Rupnowski

Due to the vast expansion of photovoltaic (PV) module production nowadays, a great interest is shown in factors affecting PV performance and efficiency under real conditions. Particular attention is being given to degradation effects of PV cells and modules, which during the last decade are seen to be responsible for significant power losses observed in PV systems. This paper presents and analyses degradation effects observed in severely EVA discoloured PV cells from field-aged modules operating already for 18–22 years. Temperature degradation effects are identified through IR thermography in bus bars, contact solder bonds, blisters, hot spots, and hot areas. *I-V* curve analysis results showed an agreement between the source of electrical performance degradation and the degradation effects in the defected cell identified by the IR thermography. Finally, an algorithm was developed to automatically detect EVA discoloration in PV cells through processing of the digital image alone in a way closely imitating human perception of color. This nondestructive and noncostly solution could be applied in the detection of EVA discoloration in existing PV installations and the automatic monitoring and remote inspection of PV systems.

1. Introduction

During the last decade, the integration of photovoltaics (PV) in buildings, telecommunication stations, power plants, and industrial applications has greatly expanded, in an effort to provide cheaper and greener energy production and energy saving. While the c-Si and pc-Si PV module production account together for about 83% of the market share worldwide [1], newer cell technologies such as thin film, a-Si, CdTe, and $CuInSe_2$ [2] are constantly being sought and further investigated in an attempt to provide higher module efficiency and more reliable PV performance. Recent research interest has shifted towards a deeper understanding of factors which affect PV performance and efficiency under real conditions, whereby the PV power output is often largely different from the expected performance under the specified factory rating norms. Temperature, solar irradiance, and spectral effects [3], as well as the degradation of PV cells and modules [4], which often appears after a few years of operation and continues to increase thereafter, are the main factors which attribute to the discrepancy observed. The extent of cell and module natural degradation after 20–25 years performance in silicon module productions can nowadays be observed [5]. Due to the complex manner in which these defects appear and interrelate, a deeper understanding of the nature of these defects and the degree to which they correlate with reduction in PV performance and efficiency is of prime importance both for the early and accurate defect detection in existing technologies and the offering of highly improved PV systems.

PV cell and module degradation has been attributed to the discoloration of the ethylene vinyl acetate (EVA) encapsulant used in PV modules, which is more evident in modules operating at locations of high ambient temperature and high solar irradiation especially at lower UV wavelengths [6]. Studies have reported on the degradation mechanisms of the EVA copolymer induced from UV and high temperatures developed in cells, involving the formation of acetic acid and polyenes, the production of ketone and aldehyde, and the production of acetaldehyde and other gases [4, 6]. EVA discoloration is connected to the formation of polyenes and α,β-unsaturated carbonyl products and, further, to the depletion in the UV stabilizing additives, such as Cyasorb UV 531 and Tinuvin 770 [4, 6]. EVA discoloration in silicon PV cells appears in several degrees and extends from yellow to dark brown. Cell and module degradation is also attributed to the delamination of the encapsulant near the edges of

the cell due to water penetration [7], the formation of high conductivity paths, known as shunts, inside the cell or along its edges as a result of crystal defects and impurities [8], and sometimes to manufacturing microdefects that may be passed through the fabrication process. Furthermore, external factors responsible for cell and module degradation include partial shading, dirt, or dust, which cause cell mismatch and may lead to the formation of hot spots and hot areas [9], or other factors such as cracks or sealant diffusion allowing humidity penetration [7].

Several of these factors are seen to cause a temperature increase at the defected area, which is often several degrees above the temperature of the healthy part of the cell. Depending on the severity of the defect and the extent of the cell area it covers, the temperature increase may be realized through hot spots or large hot areas. The defected cells are shown to produce less current, leading to cell mismatch in the module and result in the defected cell operating under reverse-bias mode, dissipating power in the form of heat [9]. Studies have shown that short-circuit current (I_{sc}) and fill factor (FF) are significantly affected by module aging and cell degradation, leading to considerable maximum power (P_m) losses, with FF decrease mainly attributed to degradation in the cell interconnections causing increase in the series resistance (R_s), and I_{sc} losses mainly due to degradation in the optical properties (EVA discoloration, delamination, etc.) [10]. Furthermore, nonuniform EVA degradation among modules leads to additional power losses due to mismatch [6].

Optical defects including EVA discoloration, delamination, cracks, and humidity ingress along with corrosion defects in the metallic elements of the cell can be easily detected by means of visual inspection. Recently, great interest is shown in the use of IR thermography for nondestructive testing and inspection of PV modules. As defected cell areas exhibit higher or lower localized temperature than that of the remaining cell, the use of an IR camera to capture the temperature distribution on the surface of the cell can easily assist in the detection of these defects. Recent studies have reported on the detection of hot spots and hot areas using conventional IR cameras [11, 12]. The use of IR cameras equipped with spectral filters with IR sensitivity in the midwavelength rather than the conventional long-wave IR detectors was shown to effectively aid in the identification of shunt paths and resistive solder bonds in solar cells [13].

The study presented in this paper analyses aging defects appearing in 18–22-year-old PV modules, identified by means of IR thermography and digital image processing. The defects detected show the extent of optical degradation after several years of module operation in field conditions. *I-V* curves obtained from these PV modules assisted in the determination of the degree of performance degradation and verified the results of IR and digital image processing attributing the source of power and current losses to degradation in the cell interconnections and its optical properties.

2. Experimental Methodology

Experiments were performed during a period of several months on SIEMENS M55 and BP B 1233 c-Si PV modules with 18 and 22 years of field operation, respectively, at the R.E.S. Lab of T.E.I. of Patras, Greece. Both digital images and IR images were obtained from cells exhibiting different degrees and forms of optical degradation. Images of the cell neighborhood were also obtained for relative comparison reasons.

Digital images were obtained using a conventional 7.1 MP digital camera. The digital images were processed and analysed with software developed for the purposes of this study in MATLAB environment. The IR images were obtained using TROTEC IC080LV thermocamera with detector resolution 384 × 288 pixels and accuracy of ±2°C. The detector is an uncooled microbolometer with spectral range 7.5 to 14 μm. For the calibration settings, emissivity was set to 0.83 for the front glass side of the cell and 0.91 for the back side Tedlar surface. The temperature data files extracted using the specialized camera software were then processed and analysed in MATLAB. For the *I-V* curves obtained, an *I-V* curve analyser for photovoltaics, PV-KLA, was used with a silicon irradiance sensor Si-01TCext with active temperature compensation and a PT-100 sensor for measuring module temperature. For each measurement the temperature coefficients of P_m, I_{sc}, and V_{oc} for the PV module were set.

The experiments with the SIEMENS M55 modules were performed during September 2011 on days 13, 17, and 27, while the experiment with the BP B 1233 PV module was performed during April 2011 on day 8. At the time of the experiment, the following parameters were recorded: the ambient temperature via means of an MP101A sensor, the wind speed via means of a 05103 R.M. Young wind sensor and the global solar radiation at horizontal via means of a CM6B pyranometer.

3. Visual Inspection

Several SIEMENS M55 PV panels operating for 18 years in the T.E.I. of Patras, Greece, were visually examined for signs of optical degradation. The panels have been exposed to the rather hot and dry Greek climate, and about 10 years ago lumps of mortar were incidentally shed on the PV array and covered several cells for a prolonged period of several months (see Figure 1).

Although EVA discoloration in panels is known to be heterogeneous, the fact that some cells exhibit a significantly higher degree of browning is highly considered to be because of the shading effect caused by the layer of mortar. This induced shading effect caused the cells covered by this layer of mortar to operate under reverse bias mode, developing higher temperatures within the cell due to Joule effect. These modules exhibit now different types of degradation effects and to a different degree. These include browning due to EVA discoloration, corrosion of contacts and fingers, delamination, and humidity ingress, see Figure 2.

4. IR Thermography

4.1. Junction Box Effects. The IR images of the SIEMENS M55 modules were obtained using the thermocamera. The

Figure 1: SIEMENS M55 PV generator subjected to lumps of mortar during the past.

(a) (b) (c)

Figure 2: Various degradation effects observed in 18-year-old SIEMENS M55 PV cells.

ambient temperature recorded was 31.5°C, the average wind speed was 2 m/sec, and the global solar radiation at horizontal was 680.5 W/m^2.

IR thermography shows the temperature distribution on the PV surface. When taken from a distance only large temperature variations can be observed. Figure 3 shows the front and back of two PV modules. A hot spot area with an increased temperature of about 7°C compared to the temperature of the rest of the module is shown at the cell where the bypass diode box lies. The IR image of the back of the modules shows an even higher temperature at the sealant of the junction box. This temperature increase at the cell where the junction box lies causes a difference in voltage δV_{oc}, resulting in mismatch between the cells equivalent to partial shadowing effects and leads to a δP_m reduction in the power output. As this effect is constant, the cell operating under increased temperature will eventually experience a slow physical degradation leading to permanently reduced power output.

Furthermore, cell temperatures measured at the back of the panel are observed to be higher by about 7–10°C from temperatures measured at the front. This is due to the increase of the thermal resistance added by the tedlar insulation at the back of the module. Based on the heat conduction law, the temperature at the back due to higher insulation is expected to be higher than temperatures at the front of the panel.

4.2. Browning and Bus Bar Degradation Effects. The IR images of cells exhibiting different degree of browning were captured for the determination of any temperature degradation effects. Figures 4(a) and 4(b) show the digital image and the IR image of a c-Si cell neighborhood from a SIEMENS M55 panel, whereby the bottom corner cell with severe EVA discoloration is shown in the IR image to display an average temperature increase by about 25°C compared to the temperature of the nearby cells exhibiting browning to a lesser degree. Furthermore, the IR image reveals the existence of two hot spots reaching 86°C, a relative increase by more than 35°C with respect to the temperature of the nearby cells. Due to the overall conductance of the PV module front cover, heat propagates around the hot spots, while the tedlar insulation at the back of the panel having low conductivity discloses the hot spots more clearly. The IR image at the back side tedlar surface of the cell reveals that these two hot spots are located on the bus bars of the cell, see Figure 5(b). The larger one appears at the soldering bond where the contact is corroded (see Figure 4(a)). The temperature of these hot spots at the back side of the cell reaches 96°C,

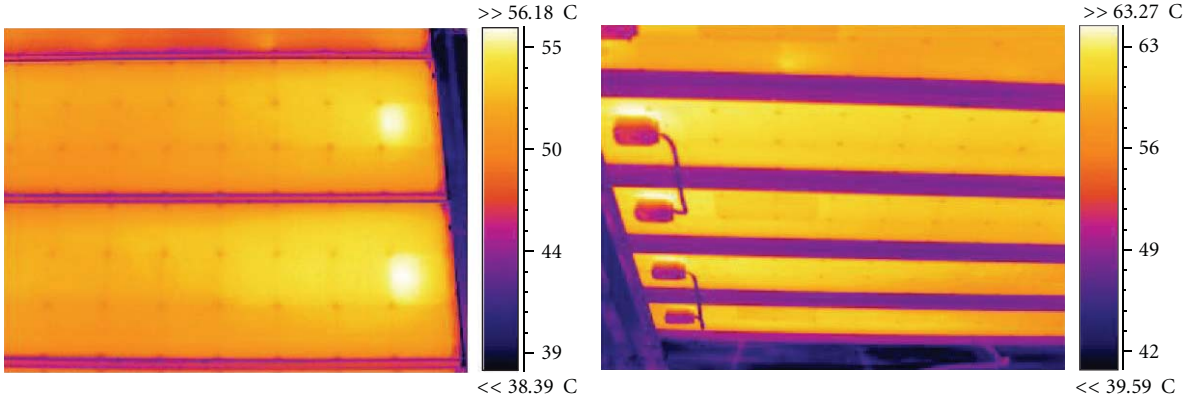

(a) (b)

Figure 3: IR image of PV modules showing hot area at the junction box, (a) at the front of the panels, and (b) at the back of the panels.

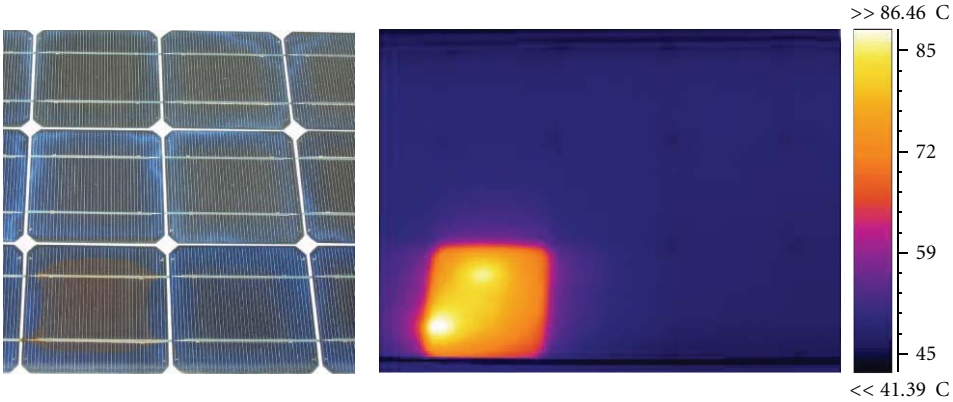

(a) (b)

Figure 4: (a) Digital and (b) IR image, of browned cell and neighboring cells. IR image reveals two hot spots at the severely browned cell.

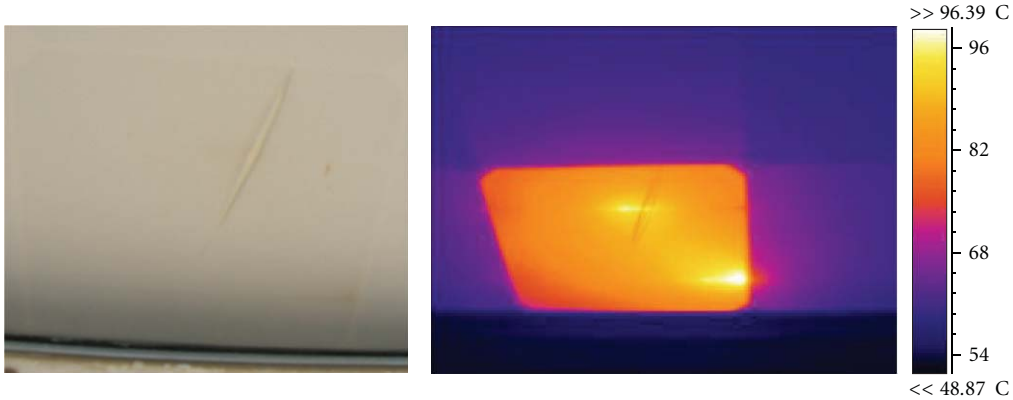

(a) (b)

Figure 5: (a) Digital and (b) IR image, of the back of the severely browned cell of Figure 4. IR images reveals the two hot spots are located on the two bus bars. The tear of the tedlar sheet also appears in the IR image.

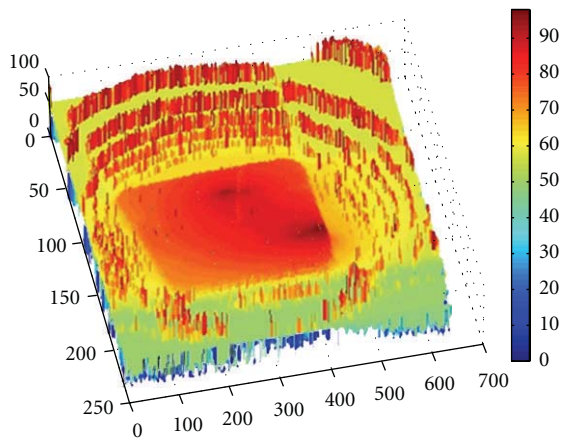

Figure 6: 3D temperature plot of IR data extracted from the back of the cell of Figure 5(b).

which is detrimental to the operational lifetime of the cell. At the time of the experiment, the ambient temperature was 32.2°C, the wind speed was 2.2 m/sec, and the global solar radiation at horizontal was 607.1 W/m^2. During summer higher temperatures have been recorded, with the hot spot reaching temperatures above 100°C.

Figure 5(a) also shows a tear in the tedlar sheet, which also appears in the IR image crossing through the bus bar at the hot spot and displaying slightly lower temperature at the edges of the tear (see Figure 5(b)). The temperature data extracted from the back side of the cell of Figure 5(b) were also analysed in MATLAB. The data were filtered with a 3×3 median filter. The 3D temperature plot is shown in Figure 6. The two hot spots appear clearly and the small temperature decrease at the place of the tear is now obvious. A temperature pattern appears, due to heat propagation, between the two hot spots which replicates the exact temperature pattern observed at the front side of the cell.

4.3. Blister Effects. Another SIEMENS M55 c-Si cell exhibiting severe browning discoloration, particularly evident at the bus bar contacts and solder bond, is displayed in Figure 7(a). The image of the back of the cell (Figure 7(b)) exhibits a large blister at the bottom bus bar and a smaller blister at the top bus bar. The browning at the bus bar and solder bond is also visible at the back of the cell. The IR image at the front and back side of the cell are displayed in Figures 8(a) and 8(b), respectively. The ambient temperature recorded was 36.5°C, the wind speed was 1.7 m/sec, and the global solar radiation at horizontal was 717.1 W/m^2.

A large hot spot area is visible in the front IR image, while the IR image at the back displays more information. A hot spot appears on the bus bar with its temperature reaching nearly 99°C, extremely detrimental for the operational health of the cell, which is higher by about 30°C from the remaining part of the cell. An extended part of the bus bar around the hot spot appears with also an increased temperature by 15–25°C compared to the temperature of the remaining part of the cell. An effect of this extreme temperature of the bus bar is a blister which has formed at the tedlar backsheet cover located on the bus bar at the edges of this hot area. The blister exhibits lower temperature 63°C, about 6-7°C below the temperature of the remaining part of the cell.

4.4. Natural Discoloration, Hot Spots and Hot Areas. A 22-year-old c-Si BP B 1233 PV module examined revealed natural EVA discoloration on all of its cells covering about 90% of the cell area. The EVA discoloration appears not only on the surface of the cell but also on the street surface between the cells. The digital image of the lower part of the panel is displayed in Figure 9(a). The IR image of the back of the panel reveals one of the cells to exhibit higher temperature than the others (see Figure 9(b)).

The temperature data extracted from the back of the panel were further analysed in MATLAB, and the 3D temperature plot is displayed in Figure 10(a). A temperature pattern with a hot area reaching 53°C appears on the cell indicated by the arrow. Temperature data extracted from the IR images capturing this cell from the front glass side are plotted in Figure 10(b) together with neighbouring cells and in Figure 10(c) the temperature pattern of this cell alone. The temperature data of the cell neighborhood identify the defected cell having about 10°C higher temperature than the nearby cells. The temperature distribution of the defected cell alone (Figure 10(c)) reveals the existence of a large hot spot and hot area in the middle of the cell area. The highest temperature at the hot spot was 47°C due to the low irradiation 550 W/m^2 at the time of the experiment, while ambient temperature was 17°C. The relative temperature differences compared to the remaining part of the cell can be observed.

5. *I-V* Curve Analysis

In order to investigate whether the thermographic information identifying the source of degradation in a PV module correlates with its electrical performance, a series of *I-V* experiments were carried out with the SIEMENS M55 module of Figure 4(a). The *I-V* curve of the PV module was obtained using the *I-V* curve analyser. The *I-V* curve was obtained for a series of shading configurations: with all cells of the module unshaded; with the severely browned cell shaded by 100% using a black carton; with each one of the three strings of the module successively shaded (all 12 cells) by 100%. This was done in order to determine which string of cells contributed to the deterioration observed in PV performance. It should be noted that each string has 12 cells and the three strings are connected in series. The module has two bypass diodes connected so that the first diode bypasses the first and second strings and the second diode bypasses the second and third strings. Thus, the second string is bypassed by both diodes. When the second string is shaded, the circuit configuration changes so that the first and third strings are now connected in parallel and the total current at the panel output is higher than the current output when all cells are unshaded [14, 15]. Figure 11 shows the *I-V* curves obtained under the various configurations.

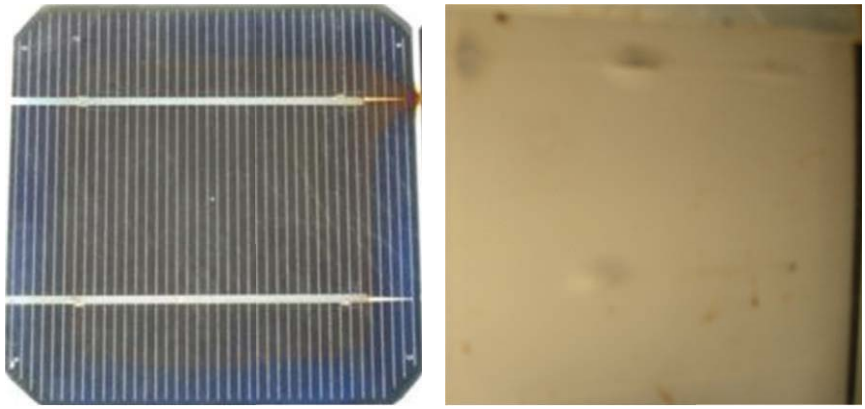

(a) (b)

Figure 7: Digital image (a) front and (b) back, of a SIEMENS M55 c-Si cell exhibiting browning, degradation at bus bars and solder bond, and the appearance of blisters at the back sheet tedlar cover.

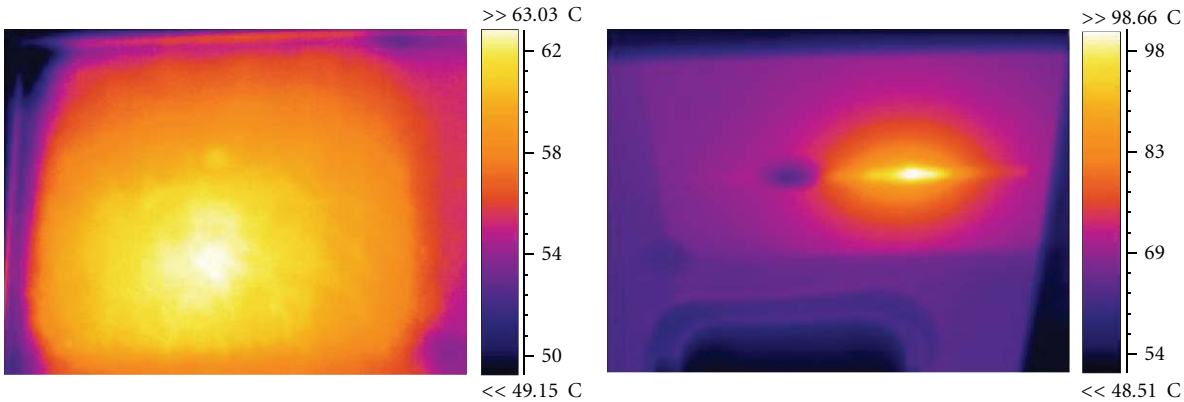

(a) (b)

Figure 8: IR image (a) front and (b) back, of the cell displayed in Figure 7, exhibiting a large hot spot area at the front and increased temperature on the bus bar and blister at the back.

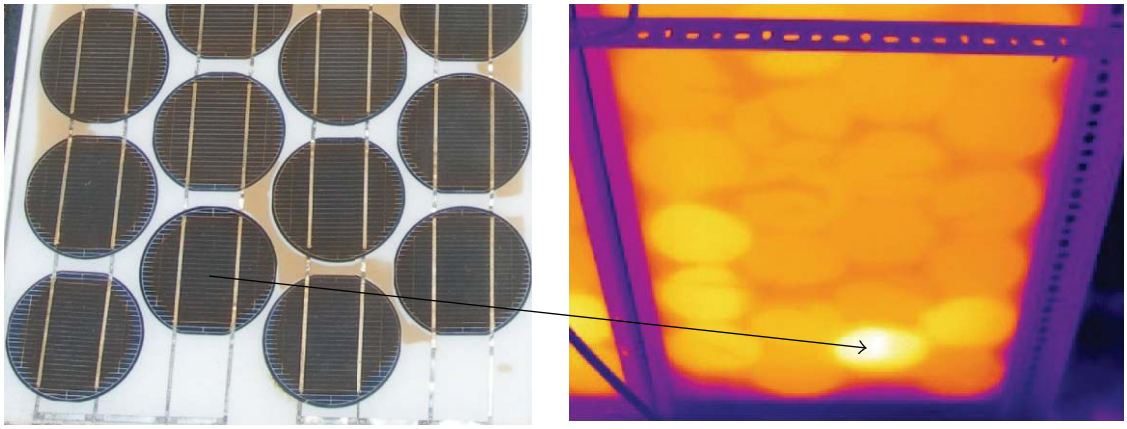

(a) (b)

Figure 9: (a) Digital image of the lower part of a BP B 1233 c-Si PV panel; (b) IR image of the back of the panel revealing a hot cell in reverse order as illustrated by the arrow.

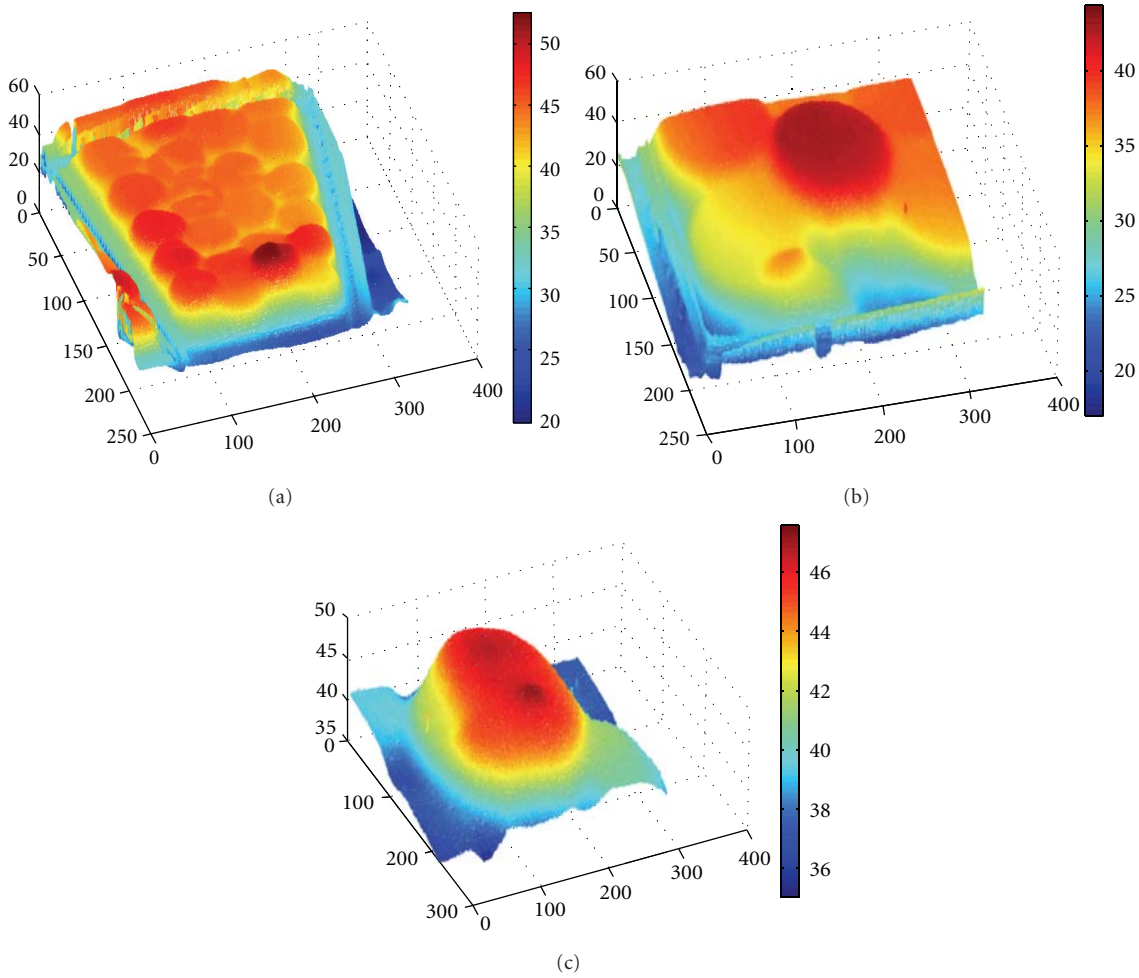

Figure 10: 3D temperature plot of defected cell and neighboring cells as seen in clockwise order (a) from the back of the panel (in reverse order), (b) the front side lower corner of the panel, and (c) the temperature plot of the defected cell alone revealing a hot spot and hot area.

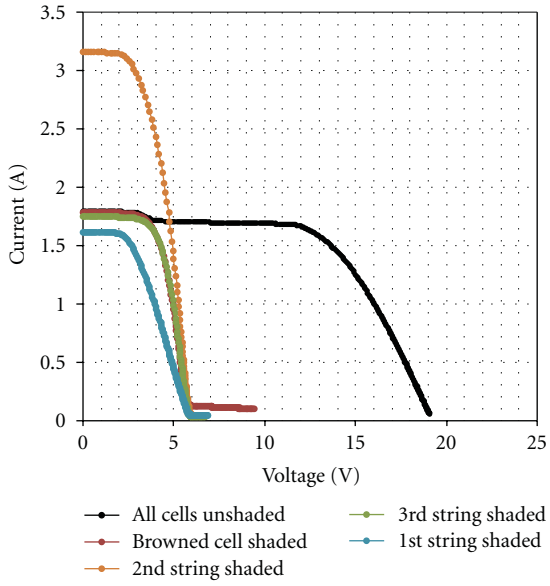

Figure 11: *I-V* curves obtained from the aged SIEMENS M55 PV module under the various configurations.

The slope of the I-V curve at V_{oc} indicates the series resistance R_s, while the slope of the I-V curve at I_{sc} indicates the shunt resistance R_{sh} [5]:

$$\left.\frac{dV}{dI}\right|_{V=V_{oc}} \longrightarrow -R_s, \tag{1a}$$

$$\left.\frac{dI}{dV}\right|_{I=I_{sc}} \longrightarrow -\frac{1}{R_{sh}}. \tag{1b}$$

The I-V curve of a healthy panel would be rather horizontal at I_{sc} and steep at V_{oc}, indicating high R_{sh} and low R_s.

The I-V curve of the PV module in Figure 11, when all cells are unshaded, displays a step-wise decrease, which reveals the existence of deteriorated cell(s). The decreased slope at V_{oc} proves the existence of a high parasitic series resistance R_s. On the other hand, the small slope at I_{sc} indicates high R_{sh} and therefore a small parasitic shunt resistance. Parasitic shunt resistances arise from high conductivity paths (shunts) in or at the edges of the cell [8], while series resistances arise from contact resistance, bus bar resistance, and fingers [14]. Thus, the I-V curve of the PV module shows that the deterioration in PV performance is mainly due to high resistance at the cell bus bars and contacts.

Due to the connection of the diodes earlier explained, when the first string was entirely shaded, the PV module operated through the cells of the third string. The I-V curve obtained under this configuration (see Figure 11) displays an increased R_s illustrated by the decreased slope at V_{oc}. This indicates the existence of a high parasitic resistance in the third string. On the other hand, for the configurations whereby the browned cell was shaded or the third string was entirely shaded, which means that the PV module operated through the cells of the first string, the I_{sc} remains as high as the initial I-V of the module and the slope at V_{oc} is now steep indicating a significantly smaller series resistance. Thus, the location of the increased parasitic series resistance is the browned cell located in the third string, as identified by the thermography, which detected in this severely browned cell an increased bus bar resistance due to the high temperature observed at the hot spots located on both bus bars (see Figures 4 and 5).

An indication of the overall PV module performance degradation may be shown through the reduced $P_m = 47.7$ W and FF $= 61.7\%$ when converted to standard test conditions (STC). The reduction of P_m from the nominal 53 W value, $\delta P_m/P_m$, is 10%. It should be noted that a small deviation in the measured power losses may be observed due to spectral variations and sky conditions. While the reduction is obvious and significant, considering the 18 years of field operation of the PV panel, the technology used at the time of production, the optical and electrical degradation which it exhibits, it may be said that the degradation is smaller than expected.

6. Digital Image Processing

Visual inspection of PV cells and modules may reveal many optical and electrical defects. As a correlation has been observed between optical degradation and current loss [4, 7], which was also shown in this paper, the ability to automatically detect optical degradation through EVA discoloration would bring major improvements in the remote monitoring of the operational health of PV systems and the identification of early signs of degradation. The human eye can easily detect EVA discoloration in PV cells and generally distinguish between largely different degrees of discoloration. An algorithm has been developed in this study to automatically detect optical degradation in PV cells through processing of the digital image alone, in a way closely related to human perception.

The algorithm developed first converts the RGB image of the cell to the HSV (hue, saturation, value) color space. The HSV color model belongs to a group of similar hue-oriented color models (HSI, HSV, HSL) which correspond more closely to the human perception and interpretation of color. These models share the same attribute for hue and differ in terms of their definition of saturation and of intensity/value/lightness. The HSV coordinate system is cylindrical, and the H, S, and V components can be derived from the R, G, and B components through the following equations [16]. Note that in the equations RGB values are normalized to the range [0, 1], and H needs to be normalized to the range [0, 1] by dividing by 360:

$$\mathrm{H} = \begin{cases} \theta & \text{if } \mathrm{B} \le \mathrm{G}, \\ 360 - \theta & \text{if } \mathrm{B} > G, \end{cases} \tag{2a}$$

$$\text{with} \quad \theta = \cos^{-1} \frac{1/2(\mathrm{R}-\mathrm{G}) + (\mathrm{R}-\mathrm{B})}{\sqrt{(\mathrm{R}-\mathrm{G})^2 + (\mathrm{R}-\mathrm{B})(\mathrm{G}-\mathrm{B})}}, \tag{2b}$$

$$S = \frac{\max(\mathrm{R},\mathrm{G},\mathrm{B}) - \min(\mathrm{R},\mathrm{G},\mathrm{B})}{\max(\mathrm{R},\mathrm{G},\mathrm{B})}, \tag{3}$$

$$V = \max(\mathrm{R},\mathrm{G},\mathrm{B}). \tag{4}$$

Segmentation is then carried out in HSV color space based primarily on hue, which is the only component carrying color information. The saturation component is used to mask out regions for which hue is undefined, and the value component is used to further detect different tones of color in regions specified by hue—in order to detect different strengths of browning effect. The segmentation results are presented via a pseudocolor image produced based on the following. Hue in the range of [180°, 300°) corresponds to blue colors and is represented with a blue color in the pseudocolor image, identifying the unaffected area of the cell. Hue in the range of [300°, 360°] and [0°, 60°] corresponds to red and golden colors and is represented by red in the pseudocolor image, which identifies the yellowing and browning in discolored cell areas. Depending on the value component and with respect to different hues, a greater value of V is represented in brighter color (red or blue) in the pseudocolor image while a smaller value of V in darker color,

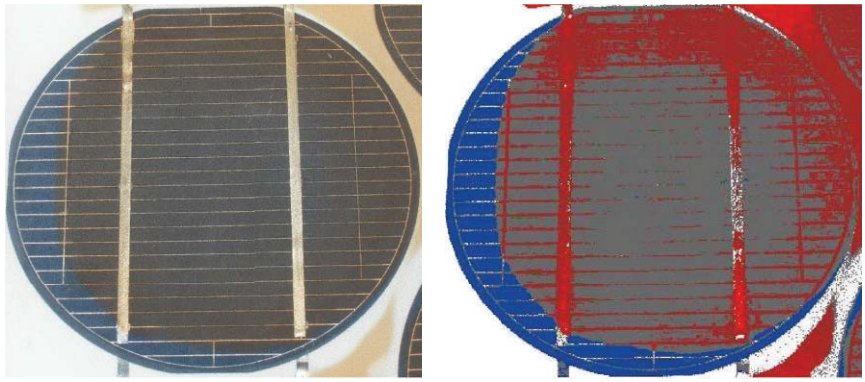

(a) (b)

Figure 12: (a) Original digital image of a c-Si BP B1233 cell, (b) respective pseudocolour image provided by the proposed segmentation algorithm.

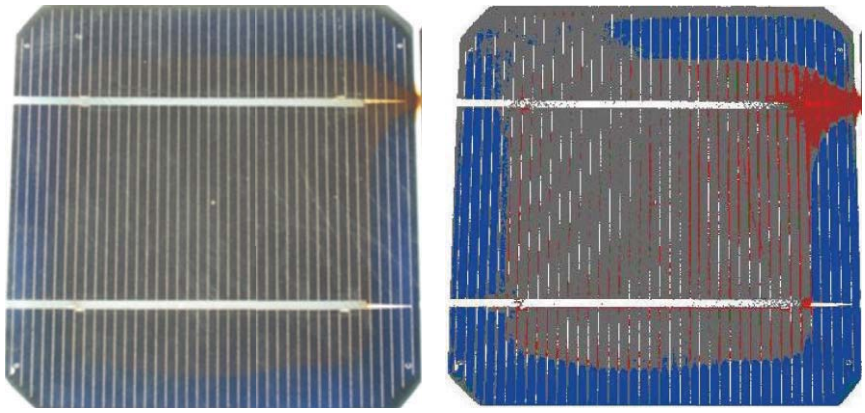

(a) (b)

Figure 13: (a) Original digital image of a c-Si SIEMENS M55 cell, (b) respective pseudocolour image provided by the proposed segmentation algorithm.

signifying different levels of brightness in the color. Values of V near 0 are represented with black. Values of S near 0 and V near 1 are represented with white in the pseudocolor image and distinguish the street regions between the cells. For saturation 0 the value of hue is irrelevant. Saturation near 0, signifying ambiguous grey-ish colors, often evident in discolored parts of the cell, is represented in gray color in the pseudocolor image.

Figures 12(a) and 12(b) show, respectively, the original digital image of an aged c-Si cell from the BP B 1233 PV module, and the pseudocolor image produced by the segmentation algorithm. It may be observed in the pseudocolor image that the undamaged part of the cell has been accurately detected, and the nonbrowned part of the street surface around the cell. Furthermore, the browning has been accurately detected on all affected areas, which is shown in red and dark red color in the pseudocolor image. Also, areas exhibiting different severity of browning appear in grey color in the pseudocolor image. The browning which appears on the bus bars and fingers has also been accurately detected. Figure 13(b) displays the resulting pseudocolor image for a browned c-Si cell from a SIEMENS M55 module (Figure 13(a)). It is evident that the pseudocolor image produced has accurately detected the undamaged and damaged parts of the cell. The browning which appears on both bus bars and soldering bond is clearly detected and appears in red in the pseudocolor image. The small browning at the lower bus bar, which could have been passed unnoticed during a visual inspection, has been correctly identified and appears in red in the pseudocolor image.

The identified discoloured part of the cell is also measured in terms of percentage area of coverage with respect to the true area of the cell, and in terms of the different tones of colour in order to identify the severity of browning detected. An extended analysis of this algorithm will be presented in a separate study.

7. Discussion

Optical and electrical defects in field-aged PV modules of 18–22 years of operation have been identified and analysed through visual inspection, digital image processing, IR thermography, and I-V curve analysis. The SIEMENS M55

modules exhibited in certain cells severe optical degradation which was induced by external field factors in the past, while the BP B 1233 module exhibited severe natural EVA discolouration. PV cells exhibiting severe EVA discoloration were identified through visual inspection, and the IR image of the PV panels also confirmed temperature degradation defects in these discolored cells. Severely discolored cells of the M55 module exhibited degradation defects mainly on the bus bars of the cell, increasing cell temperature and, further, increasing the series resistance of the cell. This in turn causes mismatch effects and reduces the power output of the module as seen in the *I-V* curve analysis performed. The temperature measured at the hot spots reached temperatures above 95°C for the experiments carried out during September 2011, which is detrimental for the operational health of the cell. In the most severe cases examined, hot spots experienced temperature increase $\delta T_c/T_c$ by 50%–80% compared to the temperature of the nearby cells. Cells including these hot spots experienced an average temperature increase in the entire cell by 20–50% compared to the temperatures of the nearby cells. Milder hot areas due to junction box effects exhibited temperature increase by about 15% compared to the temperature of the nearby cells. Hot spots in the IR image of the BP cell captured during April exhibited also a temperature increase by about 18% compared to the temperature of nearby cells. For measurements under higher ambient temperature and higher solar radiation, this relative temperature increase at the hot spots and within the cell is expected to be higher mainly due to the Joule effect I^2R_s.

Due to the overall conductance of the PV module front cover, temperature propagation appears around the area of the hot spot. It was shown that the IR image at the back of the panel exhibited more precisely the temperature topography assisting in the identification of the exact location of the hot spots. In addition, higher temperatures by about 10°C were measured at the back side of the panels compared to temperatures measured at the front.

IR images were captured at different seasons, and the identification of the hot spots was possible even for cases when solar radiation was much lower than the maximum range observed during summer. This highlights the appropriateness and flexibility of the IR thermography as a method for defect detection. Nevertheless, the severity of the defect needs to be considered also under the high solar radiation conditions that prevail at the site of the PV installation for an indication of the maximum temperatures that may be observed and may be accounted responsible for permanently increasing deterioration of the operational health of the cells and modules. On the other hand, identification of discolored cells, hot spots, and defected areas can be reliably performed even during colder months of the year.

Via means of an *I-V* curve analyser, the *I-V* curves obtained through a series of experiments on one of the modules led to a correlation between the results of the visual inspection, thermography, and the *I-V* curve characteristics. The hot spots on the bus bars and solder bond identified through the IR thermography was verified by the *I-V* curve characteristics showing increased parasitic series resistance when operating with the severely discolored cell, identifying this cell as the source of electrical performance degradation for the module.

The algorithm developed for the automatic detection of EVA discoloration in PV cells via digital image processing gave reliable results identifying correctly the discolored cell area and the healthy part of the cell. The percentage area of coverage of the discoloration with respect to the true area of the cell and the identification of different tones of color gives estimates of the severity of browning detected. The ability to easily detect optical degradation is of high importance for the inspection and monitoring of the operational health of PV modules. This could be applied in the detection of EVA discoloration in existing PV installations via means of a single digital picture, or in the automatic monitoring and remote inspection of PV systems.

8. Conclusions

This paper has presented and analysed optical and electrical degradation effects in modules operating under field conditions already for 18–22 years. Certain modules or cells had experienced heavily induced degradation by external field factors, while others exhibited signs of severe EVA discoloration due to natural aging. The degree of EVA discoloration observed differed between cells and modules with some cells exhibiting severe signs of discoloration which affected the bus bars and contacts of the cells. The type of optical degradation also differed among modules, with most experiencing EVA discoloration and a few exhibiting a higher degree of delamination of the encapsulant. The naturally aged BP module did not exhibit the severe degradation of bus bars and contacts, which was observed in the cells of the M55 modules subjected to the induced aging by the external factors.

The optical degradation was detected through visual inspection and through IR thermography, which reliably identified hot spots and hot areas, leading to increased series resistance in the cells and causing mismatch effects. Results of the IR thermography were also verified by the *I-V* curve characteristics showing increased parasitic series resistance when operating with the severely discolored cell, identifying this cell as the source of electrical performance degradation for the module. The IR thermography proved a reliable and accurate tool for the diagnosis of degradation defects, both optical and electrical, in PV cells and, furthermore, for the identification of the precise location and the severity of these faults. The relative temperature differences measured within the cell or between neighboring cells may further assist in the diagnosis of early signs of degradation. This is important as degradation is observed to advance in an increasing rate.

Finally, an algorithm was developed to automatically detect EVA discoloration in cells through digital image processing in a way closely imitating human perception of color. The algorithm gives an accurate identification of the healthy and discolored part of the cell and presents the result in pseudocolor image. Furthermore, it identifies different degrees of severity of discoloration and gives an estimate of the percentage area coverage of the discoloration. This novel

approach brings several advantages in the area of automatic defect diagnosis for remote inspection and monitoring of PV cell and module condition. The latter is particularly important for the early diagnosis of faults, assisting in prolonging the operational lifetime of the system.

Acknowledgments

The project is cofunded by the European Union–European Regional Development Fund and National Resources (NSRF 2007–2013). The author would like to express her appreciation for the funding received. The author would also like to express her gratitude to Professor S. Kaplanis, Head of the R.E.S. Laboratory of T.E.I. of Patras and project coordinator, for his valuable input.

References

[1] A. Goetzberger, C. Hebling, and H. W. Schock, "Photovoltaic materials, history, status and outlook," *Materials Science and Engineering R*, vol. 40, no. 1, pp. 1–46, 2003.

[2] R. W. Birkmire, "Compound polycrystalline solar cells: recent progress and Y2K perspective," *Solar Energy Materials and Solar Cells*, vol. 65, no. 1, pp. 17–28, 2001.

[3] S. Nann and K. Emery, "Spectral effects on PV-device rating," *Solar Energy Materials and Solar Cells*, vol. 27, no. 3, pp. 189–216, 1992.

[4] A. Parretta, M. Bombace, G. Graditi, and R. Schioppo, "Optical degradation of long-term, field-aged c-Si photovoltaic modules," *Solar Energy Materials and Solar Cells*, vol. 86, no. 3, pp. 349–364, 2005.

[5] S. Kaplanis and E. Kaplani, "Energy performance and degradation over 20 years performance of bp c-Si PV modules," *Simulation Modelling Practice and Theory*, vol. 19, no. 4, pp. 1201–1211, 2011.

[6] A. W. Czanderna and F. J. Pern, "Encapsulation of PV modules using ethylene vinyl acetate copolymer as a pottant: a critical review," *Solar Energy Materials and Solar Cells*, vol. 43, no. 2, pp. 101–181, 1996.

[7] D. Chianese, A. Realini, N. Cereghetti et al., "Analysis of weathered c-si pv modules," in *Proceddings of the 3rd World Conference on Photovoltaic Energy Conversion*, pp. 2922–2926, Osaka, Japan, May 2003.

[8] C. Radue and E. E. van Dyk, "A comparison of degradation in three amorphous silicon PV module technologies," *Solar Energy Materials and Solar Cells*, vol. 94, no. 3, pp. 617–622, 2010.

[9] M. Simon and E. L. Meyer, "Detection and analysis of hot-spot formation in solar cells," *Solar Energy Materials and Solar Cells*, vol. 94, no. 2, pp. 106–113, 2010.

[10] A. Skoczek, T. Sample, and E. D. Dunlop, "The results of performance measurements of field-aged crystalline silicon photovoltaic modules," *Progress in Photovoltaics: Research and Applications*, vol. 17, no. 4, pp. 227–240, 2009.

[11] S. Vergura and O. Falcone, "Filtering and processing IR images of PV modules," in *Proceedings of the International Conference on Renewable Energies and Power Quality (ICREPQ' 11)*, Las Palmas, Spain, April 2011.

[12] P. N. Botsaris and J. A. Tsanakas, "Infrared thermography as an estimator technique of a photovoltaic module performance via operating temperature measurements," in *Proceedings of the 10th ECNDT Conference*, Moscow, Russia, June 2010.

[13] D. L. King, J. A. Kratochvil, and M. A. Quintana, "Applications for infrared imaging equipment in photovoltaic cell, module, and system testing," in *Proceedings of the 28th IEEE Conference Record of the Photovoltaic Specialists Conference*, pp. 1487–1490, Anchorage, Alaska, USA, September 2000.

[14] S. Silvestre, A. Boronat, and A. Chouder, "Study of bypass diodes configuration on PV modules," *Applied Energy*, vol. 86, no. 9, pp. 1632–1640, 2009.

[15] Y. J. Wang and P. C. Hsu, "Analysis of partially shaded pv modules using piecewise linear parallel branches model," *Proceedings of World Academy of Science, Engineering and Technology*, vol. 60, pp. 783–789, 2009.

[16] K. N. Plataniotis and A. N. Venetsanopoulos, *Color Image Processing and Applications*, Springer, 2000.

Hindawi Publishing Corporation
International Journal of Photoenergy
Volume 2012, Article ID 910256, 8 pages
doi:10.1155/2012/910256

Research Article

Simulation of Nonpolar p-GaN/i-$In_xGa_{1-x}N$/n-GaN Solar Cells

Ming-Jer Jeng

Department of Electronic Engineering and Green Technology Research Center, Chang-Gung University, 259 WenHwa 1st Road, Kweishan, Taoyuan 333, Taiwan

Correspondence should be addressed to Ming-Jer Jeng, mjjeng@mail.cgu.edu.tw

Received 1 November 2011; Revised 15 February 2012; Accepted 20 February 2012

Academic Editor: Peter Rupnowski

It is well known that nitride-based devices suffer the polarization effects. A promising way to overcome the polarization effects is growth in a direction perpendicular to the *c*-axis (nonpolar direction). Nonpolar devices do not suffer polarization charge, and then they have a chance to achieve the high solar efficiency. The understanding of the solar performance of non-polar InGaN-based solar cells will be interesting. For a pin non-polar solar cell with GaN p- and n-cladding layers, the conduction band offset (or barrier height, ΔE) between an intrinsic layer and n-GaN layer is an important issue correlating to the efficiency and fill factor. The efficiency and fill factor will be seriously degraded due to sufficiently high barrier height. To reduce a high barrier height, some graded layers with an energy bandgap between the energy bandgap of n-GaN and $In_xGa_{1-x}N$ intrinsic layer can be inserted to the interface of n-GaN and $In_xGa_{1-x}N$ layers. From simulation, it indicates that the insertion of graded layer is an effective method to lower energy barrier when there exists a high energy band offset in non-polar nitride devices.

1. Introduction

Nitride-based materials such as $In_xGa_{1-x}N$ have become important in fabricating photovoltaic devices due to their energy band gaps lying between 0.7 and 3.4 eV [1–5]. It can absorb the full solar spectrum by a single material of $In_xGa_{1-x}N$ with different indium contents. Many theoretical calculations on the performance evaluation of InGaN-based solar cells have been performed [1, 4, 5]. They demonstrated that a very high solar efficiency could be achieved. The direct bandgap properties and high absorption coefficients make it have great potential in photovoltaic application. Further, the GaN-based materials have a high resistant to high energy irradiation and temperature variations [6, 7]. Thus, it is suitable for space applications or high concentrator solar cell systems. However, a good-quality InGaN film with high indium composition cannot be obtained due to the low miscibility of InN in GaN. It also suffers polarization effects that degrade the device performance seriously [8–11]. Although the current nitride devices suffer the polarization effects, a promising way to overcome the polarization effects is growth in a direction perpendicular to the c-axis (nonpolar direction) [12–14]. In the heterojunction of p-GaN/i-$In_xGa_{1-x}N$/n-GaN structure on r-plane sapphire (nonpolar a-plane GaN), the nitride devices do not suffer polarization charge, and then they have a chance to achieve a high solar efficiency. The understanding of solar performance on non-polar InGaN-based solar cells will be interesting. In this work, the solar performance of non-polar p-GaN/i-$In_xGa_{1-x}N$/n-GaN solar cells with different $In_xGa_{1-x}N$ energy bandgaps from 1.1 to 3.2 eV has been simulated. It is observed that the conduction band offset between $In_xGa_{1-x}N$ and n-GaN layer will be an important issue for the efficiency of pin solar cells. Although a pn junction device is the most common structure in solar cells, a pin structure will be the best choice for high-defect materials due to drift field assistant properties. It is known that an intrinsic layer with low energy bandgap in pin solar cells has higher solar efficiency than that with high energy bandgap. But, one has to pay attention to the effects of the conduction band offset on the efficiency of solar cells. The photogenerated carriers cannot tunnel through the energy barrier if the ΔE is too high. To reduce the barrier height, some graded layers with an energy bandgap between the energy bandgap of n-GaN and $In_xGa_{1-x}N$ intrinsic layer can be inserted to the interface of n-GaN and $In_xGa_{1-x}N$ layers.

Table 1: The simulation parameters for $In_xGa_{1-x}N$ materials at 300 K [1].

Parameters	Expression	References
Energy bandgap (eV)	$E_g(In_xGa_{1-x}N) = 0.7x + 3.4(1-x) - 1.43x(1-x)$	[15]
Electron mobility ($cm^2\,eV^{-1}\,s^{-1}$)	Linear fitting: 170 at $P = 4 \times 10^{18}\,cm^{-3}$ and 100 at $P = 1 \times 10^{19}\,cm^{-3}$	[16, 17]
Hole mobility ($cm^2\,eV^{-1}\,s^{-1}$)	Linear fitting: 22 at $n = 3 \times 10^{17}\,cm^{-3}$ and 13 at $n = 1 \times 10^{18}\,cm^{-3}$	[16, 18]
Relative permittivity ε	$\varepsilon(In_xGa_{1-x}N) = x \cdot \varepsilon_{InN} + (1-x) \cdot \varepsilon_{GaN}$	[19, 20]
Electron affinity χ (eV)	$\chi_{GaN} + 0.7 \cdot (3.4 - E_g)$	[19, 21]
Effective density of states in the conduction band N_c (cm^{-3})	$N_c(In_xGa_{1-x}N) = xN_c^{InN} + (1-x)N_c^{GaN}$	[19]
Effective density of states in the valence band N_v (cm^{-3})	$N_v(In_xGa_{1-x}N) = xN_v^{InN} + (1-x)N_v^{GaN}$	[19]
Absorption coefficient α (cm^{-1})	$\alpha(\lambda) = 2.2 \times 10^5 \quad (1.24/\lambda) - E_g$	[19]
Carrier lifetime τ (ns)	1 ns	[22]
Surface recombination velocities S_{p0}, S_{pL}, S_{n0}, S_{nL} (cms^{-1})	1000	[23]

It can assist the photogenerated carriers to tunnel through the energy barrier and result in a higher solar efficiency. Thus, a graded GaN/$In_xGa_{1-x}N$/GaN solar cell grown on a nonpolar epilayer is simulated.

2. Simulation Parameters

The simulation parameters for $In_xGa_{1-x}N$ materials at 300 K are listed in Table 1 [1, 15–23]. The In composition dependence of $In_xGa_{1-x}N$ energy bandgap at 300 K is calculated by Wu's fitting equation [15]. The doping level dependence of the carrier mobility in $In_xGa_{1-x}N$ materials at 300 K is based on the fitting data [16–18], and the other related calculation parameters are assumed to be the same as GaN [22]. The simulation software of AMPS-1D is used to simulate the characteristics of $In_xGa_{1-x}N$ pin solar cells. The parameter of the front contact reflectivity is set to 0.1 in order to reflect general condition, and the back contact reflectivity is set to zero. It is noted that the series and shunt resistance of solar cells will degrade the solar performance. The series resistance mainly consists of contact and film resistance, and the shunt resistance results from the bulk and surface leakage current. It is known that the film quality of the p-type GaN is not good for a very high concentration. In addition, it is difficult to form a good ohmic contact when the concentration of the p-type GaN is lower than $1 \times 10^{17}\,cm^{-3}$. So, a concentration of $5 \times 10^{17}\,cm^{-3}$ is used as the doping concentration of p-type GaN region and a concentration of $1 \times 10^{18}\,cm^{-3}$ is assumed in the n-type GaN region. The concentration of the intrinsic layer is assumed as $5 \times 10^{16}\,cm^{-3}$ due to unintentionally high background concentration of donors. A quite good ohmic contact to p-GaN with a concentration of $5 \times 10^{17}\,cm^{-3}$ was obtained by semitransparent ohmic contact formation and metal grid deposition [3]. Thus, an ideal contact is assumed in this simulation. No attempt is made to find the optimum condition for the layer thickness and doping concentration. It just wants to demonstrate the needed layer structure of pin solar cells for a small energy bandgap of the intrinsic layer due to a high conduction band energy barrier at the interface of $In_xGa_{1-x}N$ and n-GaN layers.

3. Results and Discussions

Figures 1(a) and 1(b) show the efficiency and short circuit current (J_{sc}) as well as open circuit voltage (V_{oc}) and fill factor of $In_xGa_{1-x}N$ pn junction solar cells, respectively, with an In composition from $x = 0$ ($E_g = 3.4$ eV) to $x = 0.75$ ($E_g = 1.11$ eV) under AM1.5G illumination. The inset of Figures 1(a) and 1(b) shows the structure of $In_xGa_{1-x}N$ pn junction solar cells. By doing the simulation, the thickness of n-type region doped with $1 \times 10^{18}\,cm^{-3}$ is fixed at 250 nm and the thickness of p-type region doped with $5 \times 10^{17}\,cm^{-3}$ is optimized to obtain the highest efficiency at each In composition. A small optimum thickness range of 180 to 310 nm in p-type region is observed. It is noted that the efficiency reaches the maximum of 18.4% ($V_{oc} = 0.9$ V, $J_{sc} = 26.1\,mA/cm^2$) at an In composition of $x = 0.6$ ($E_g = 1.44$ eV) and then decreases with further increase in In composition. The higher the In composition of $In_xGa_{1-x}N$ is, the higher the J_{sc}, the lower the FF, and the lower the V_{oc} are. With the increase of In composition from $x = 0$ to 0.75, the V_{oc} linearly decreases from 2.64 to 0.59 V, the J_{sc} monotonously increases from 0.38 to 37.2 mA/cm^2, and the fill factor decreases from 0.89 to 0.72.

It is noted that a pn junction device has the best performance in solar cells for good-quality material. However, a pin structure will be the best choice for high-defect materials. In this paper, it is assumed that the carrier lifetime is 1 ns that is obtained from a more real quality GaN film [22]. So, the efficiency of the pn junction solar cells is better than that of the pin solar cells. One can demonstrate the clear advantages of the pin solar cells over pn junction if the carrier lifetime is shorter than 0.3 ns. (i.e., high-defect $In_{0.6}Ga_{0.4}N$ film) The carrier lifetime is strongly correlated to the film quality. The longer the carrier lifetime is, the better the film quality is. Figure 2 presents the comparison of the efficiency in $In_{0.6}Ga_{0.4}N$ pn and pin solar cells versus the carrier lifetime. Clearly, the pin solar cells exhibit better

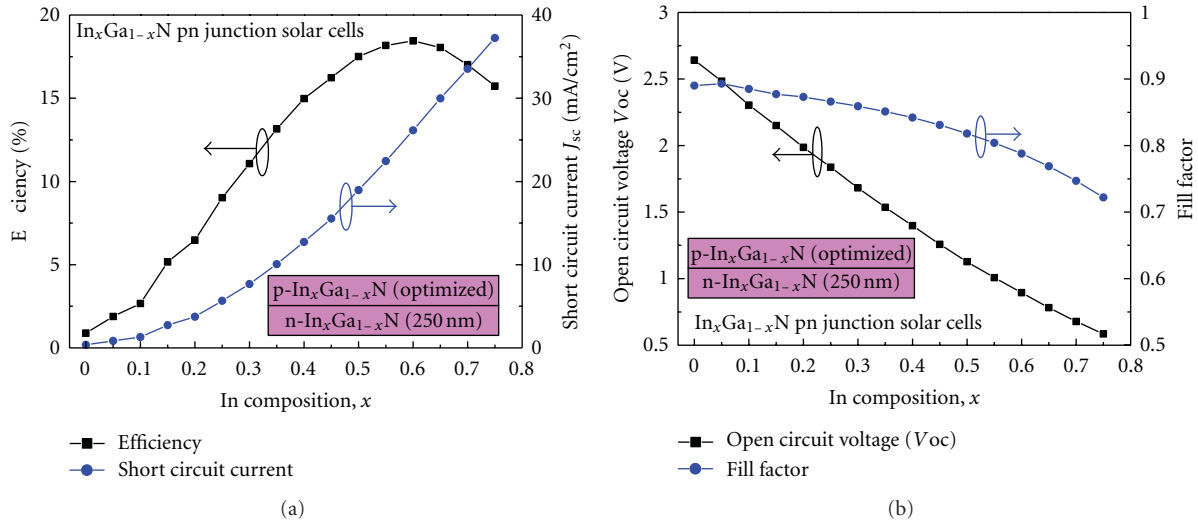

FIGURE 1: (a) The efficiency and short circuit current (J_{sc}) as well as (b) open circuit voltage (V_{oc}) and fill factor of $In_xGa_{1-x}N$ pn junction solar cells, respectively, with an In composition from $x = 0$ ($E_g = 3.4$ eV) to $x = 0.75$ ($E_g = 1.11$ eV) under AM1.5 illumination. The inset shows the structure of $In_xGa_{1-x}N$ pn junction solar cells.

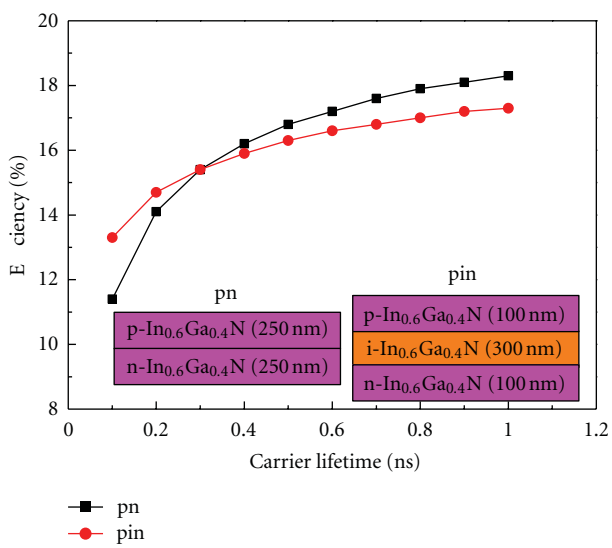

FIGURE 2: The efficiency of $In_{0.6}Ga_{0.4}N$ solar cells with a pn junction and a pin structure as a function of carrier lifetime.

efficiency than the pn solar cells when the carrier lifetime is shorter than 0.3 ns.

It is difficult to grow good-quality film especially in a thick $In_xGa_{1-x}N$ film with high In composition due to InN segregation problems. Presently, the film quality for a thin $In_xGa_{1-x}N$ film (several tenth nanometers) is good, but it is not good for a thick $In_xGa_{1-x}N$ film (several hundred nanometers). Generally, the acceptable film quality of $In_xGa_{1-x}N$ film is less than 100 nm for higher In composition ($x > 0.3$). However, the thickness of an $In_xGa_{1-x}N$ solar cell with enough light absorption is larger than 400 nm, which is mainly determined by the carrier lifetime and the material light absorption coefficients. The good solar cell performance of $In_xGa_{1-x}N$(p)/$In_xGa_{1-x}N$(n) or $In_xGa_{1-x}N$(p)/$In_xGa_{1-x}N$(i)/$In_xGa_{1-x}N$(n) structures with high In composition cannot be achieved due to poor $In_xGa_{1-x}N$ quality film with high In composition. An alternate structure of GaN(p)/$In_xGa_{1-x}N$(i)/GaN(n) is more easy to be achieved, like the recent published papers with relative high quantum efficiency [2, 3]. Thus, for more practical realization consideration, both of p-GaN and n-cladding layers are used in this simulation although the 17.3% efficiency of the $In_{0.6}Ga_{0.4}N$(p)/$In_{0.6}Ga_{0.4}N$(i)/$In_{0.6}Ga_{0.4}N$(n) solar cells is slightly better than the 16.8% efficiency of the GaN(p)/$In_{0.6}Ga_{0.4}N$(i)/GaN(n) with three graded-layer insertions at the carrier lifetime of 1 ns. The efficiency of p-GaN (100 nm)/i-$In_xGa_{1-x}N$ (200~500 nm)/n-GaN (100 nm) solar cells with an In composition of $x = 0.05$–0.3 is shown in Figure 3(a). Clearly, the higher the thickness of intrinsic layer, the higher the efficiency of the solar cell, but the increment is small due to high absorption in $In_xGa_{1-x}N$ layer. It is noted that the efficiency reaches the maximum of 9.2% at an In composition of $x = 0.26$ and then drops dramatically with the further increase of In composition. However, it is well known that an intrinsic layer with low energy bandgap in pin solar cells has higher solar efficiency than that with high energy bandgap under the same illumination. What reason causes the efficiency drop after the increase of In composition to higher than 0.26? It is possibly due to that a large conduction band energy barrier, ΔE, exists between $In_xGa_{1-x}N$ intrinsic layer and n-type GaN region. It is noted that high energy barrier in pin solar cells will seriously degrade the solar efficiency and the fill factor.

Figure 3(b) shows the fill factor of pin solar cells with various intrinsic layer thicknesses and In compositions. The fill factor begins to reduce dramatically when the In composition of $In_xGa_{1-x}N$ intrinsic layer is higher than

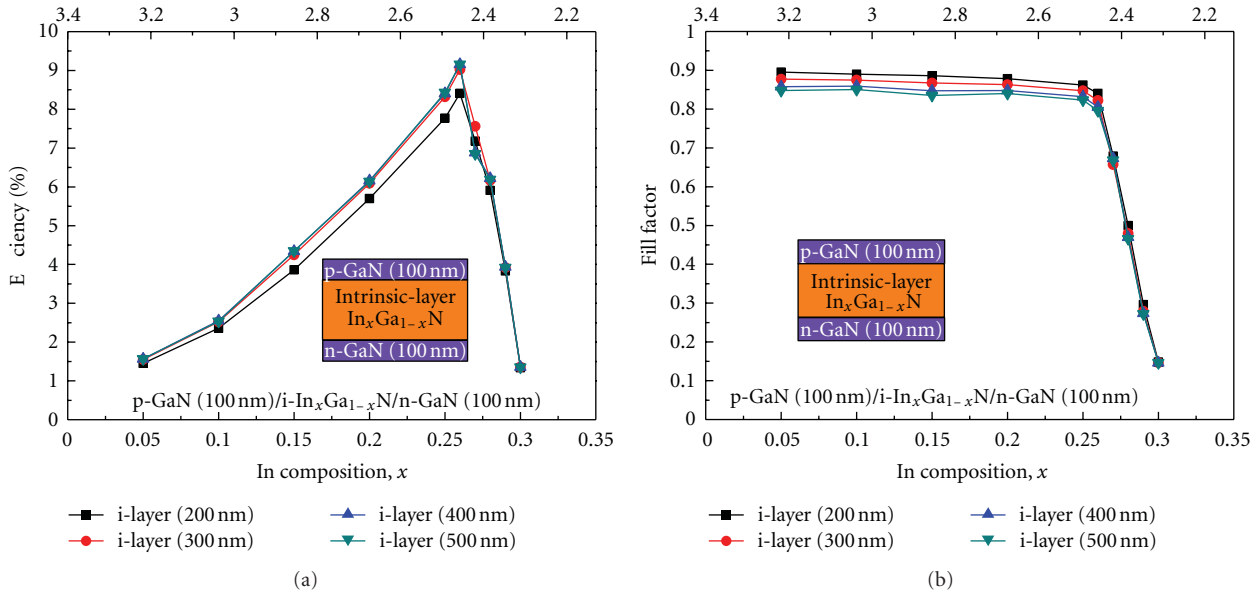

FIGURE 3: The efficiency (a) and the fill factor (b) of a p-GaN (100 nm)/i-$In_xGa_{1-x}N$ (200∼500 nm)/n-GaN (100 nm) solar cells with an In composition of $x = 0.05$–0.3.

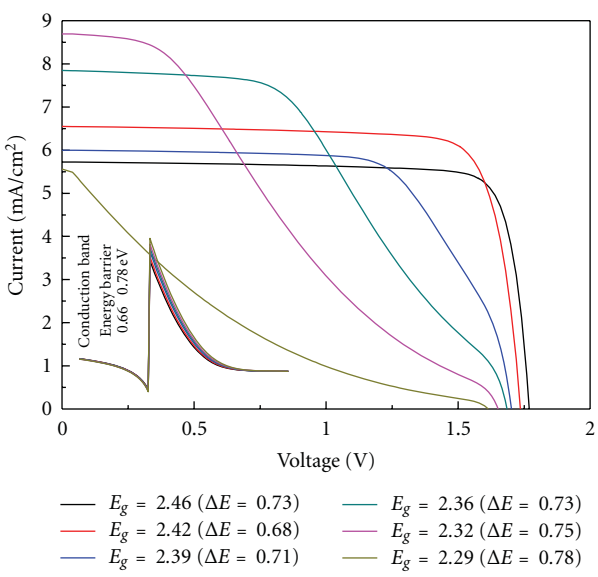

FIGURE 4: The current-voltage (I-V) curve of pin solar cells with various $In_xGa_{1-x}N$ energy bandgaps (corresponding to an In composition of 0.25–0.3 in Figure 2).

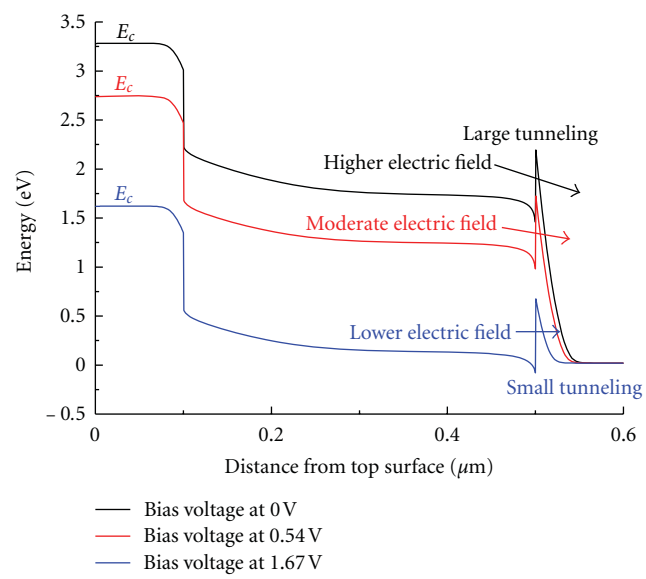

FIGURE 5: The conduction band energy diagram of $In_{0.3}Ga_{0.7}N$ pin solar cells at the voltage bias of 0, 0.54 and 1.67 V.

0.26, which is corresponding to an energy barrier of 0.68 eV. The photogenerated carriers cannot tunnel through the energy barrier if the ΔE is higher than 0.68 eV or if an existing electric field is small. It will seriously reduce the electric current and then result in a very low fill factor. It is noted that the diffusion current is dominated in the pn junction solar cells. However, the drift current is dominated in pin solar cells especially for high-defect materials. In the $In_xGa_{1-x}N$ pn junction structures, the diffusion current is dominated. In the $In_xGa_{1-x}N$(p)/$In_xGa_{1-x}N$(i)/$In_xGa_{1-x}N$(n) structures, the diffusion current is still dominated when the carrier lifetime is longer than 0.3 ns and the drift current will be dominated when the carrier lifetime is shorter than 0.3 ns (a lot of diffusion currents will be recombined by defects and cannot be effectively collected by the contact). In the GaN(p)/$In_xGa_{1-x}N$/GaN(n) structures, the drift current is dominated due to less current contribution in GaN, which generates less photocurrent by its high bandgap. More

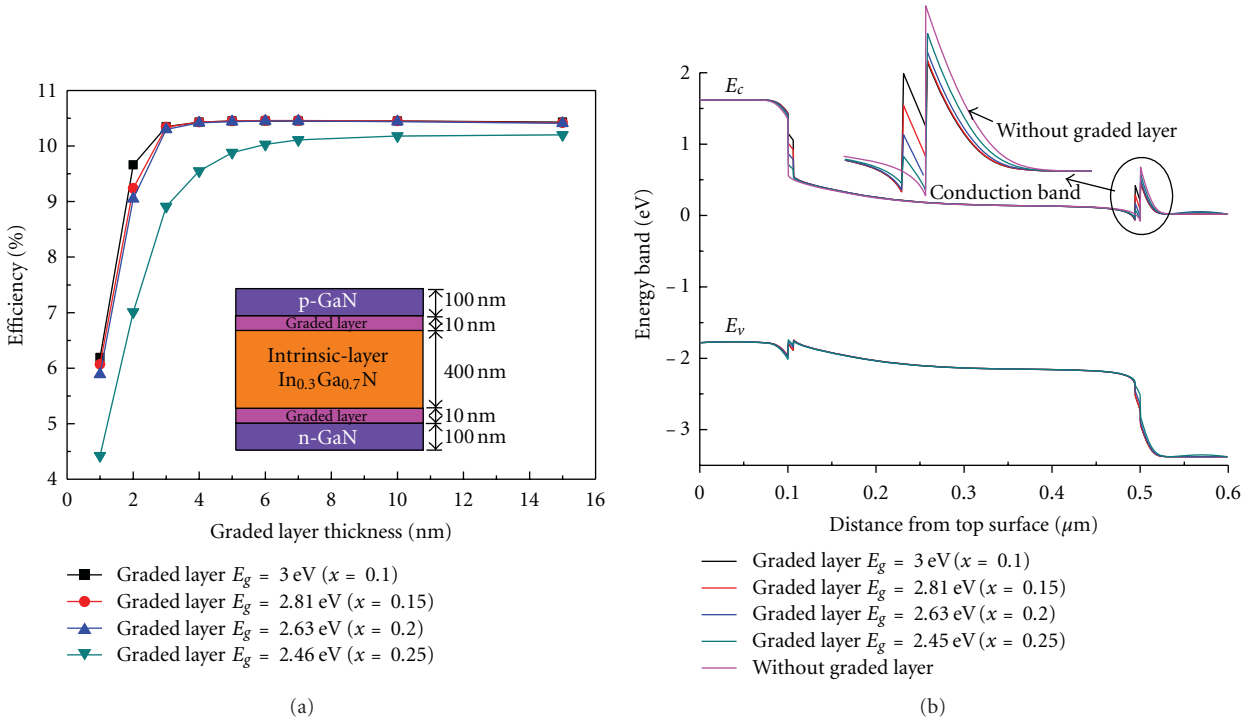

Figure 6: (a) The efficiency of one graded-layer $In_{0.3}Ga_{0.7}N$ pin solar cells with four different graded energy bandgap of 3.01, 2.81, 2.63, and 2.46 eV as a function of the graded layer thickness. (b) The energy band diagram of one graded-layer $In_{0.3}Ga_{0.7}N$ pin solar cells with four different graded energy bandgap of 3.01, 2.81, 2.63, and 2.46 eV.

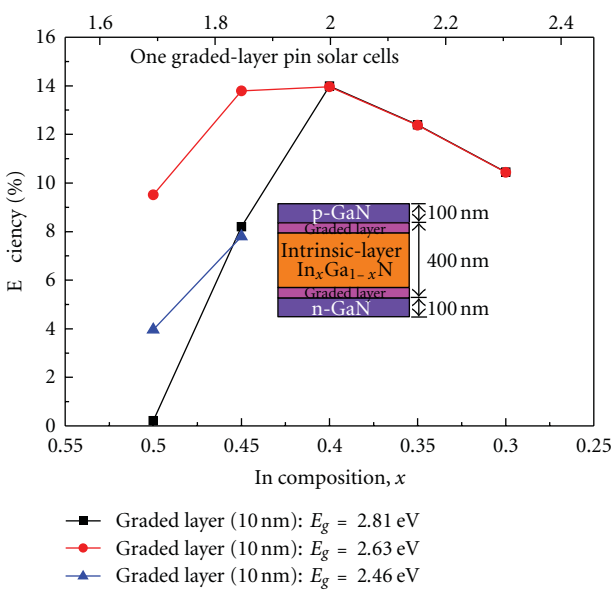

Figure 7: The efficiency of one graded-layer pin solar cells as a function of In composition from 0.3 to 0.5.

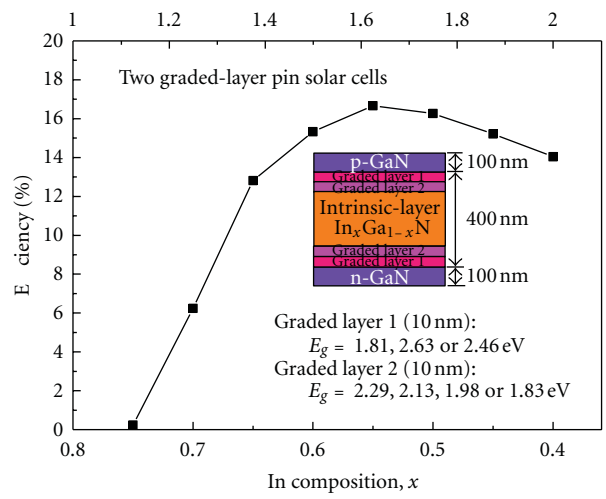

Figure 8: The efficiency of two graded-layer pin solar cells as a function of In composition from 0.4 to 0.75.

photogenerated currents will be contributed in GaN by the $In_xGa_{1-x}N$ intrinsic layer.

The current-voltage (I-V) curve of pin solar cells with various $In_xGa_{1-x}N$ energy bandgaps (corresponding to an In composition of 0.25–0.3 in Figure 3) is shown in Figure 4. Clearly, the I-V curve begins to deform with increase of voltage bias when the $In_xGa_{1-x}N$ energy bandgap is lower than 2.42 eV (x = 0.26). The deformation of I-V curve will gradually worsen with the decrease of $In_xGa_{1-x}N$ energy bandgap (increasing In composition). It means that the fill factor will become smaller. A completely deformed curve is observed in the $In_xGa_{1-x}N$ energy bandgap of 2.29 eV (x = 0.3), which has a very low fill factor of 0.13. The inset

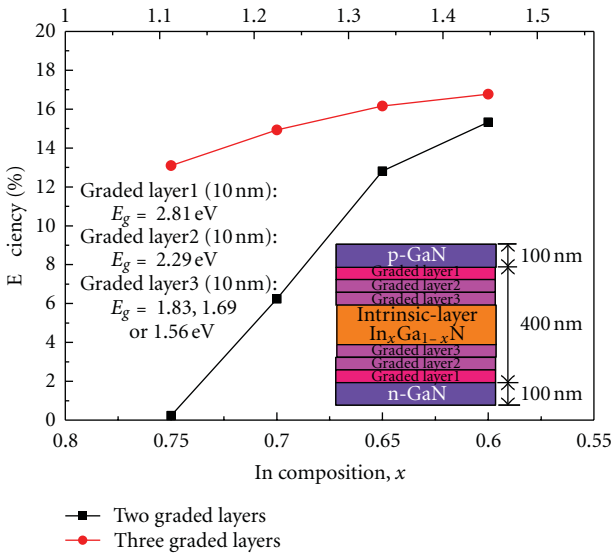

Figure 9: The efficiency of three graded-layer pin solar cells as a function of the In composition from 0.6 to 0.75.

of Figure 4 shows the conduction band energy barrier in pin solar cells with an In composition of 0.25–0.3. The $In_xGa_{1-x}N$ intrinsic layer with an In composition of 0.3 exhibits the highest energy barrier at the interface. Therefore, it has the lowest fill factor. Figure 5 shows the conduction band energy diagram of $In_{0.3}Ga_{0.7}N$ pin solar cells at the voltage bias of 0, 0.54 and 1.67 V, respectively. It can clearly explain why a large reduction of fill factor is in a high energy barrier of pin solar cells. At lower voltage bias (around 0V), there exists a high electric field in intrinsic layer. Most of the photogenerated carriers can tunnel through the energy barrier due to high field-assisted tunneling and then be collected by electrode contact; hence, a high J_{sc} is observed. However, the electric field will gradually reduce with the increase of voltage bias. At a higher voltage bias, most of the photogenerated carriers cannot tunnel through the energy barrier due to low field-assisted tunneling or high energy barriers, existing at the interface between $In_xGa_{1-x}N$ intrinsic layer and n-GaN region. Few photogenerated carriers are collected in the electrode contact and result in a small electric current. It is noted that a reduction of the electric current will begin to occur at moderate voltage bias if the energy barrier at the interface is too high, for example, in the case of In composition with 0.27–0.3 it will seriously degrade the fill factor of solar cells due to poor current shape gradually changing from a seemingly rectangular shape to a triangular shape with an increasing energy barrier, which is consistent with the I-V observations in Figure 4. Recently, both $In_{0.2}Ga_{0.8}N$/GaN and $In_{0.28}Ga_{0.72}N$/GaN multiple quantum well solar cells (MQWSCs) are experimentally fabricated and compared. The I-V curve behavior of $In_{0.2}Ga_{0.8}N$/GaN and $In_{0.28}Ga_{0.72}N$/GaN MQWSCs is similar to the simulation observation in Figure 4 [24]. The higher the energy barrier height is, the lower the fill factor is. The $In_{0.28}Ga_{0.72}N$/GaN MQWSCs with the higher energy barrier between well and barrier materials exhibit more deformed I-V curve and lower fill factor than the $In_{0.2}Ga_{0.8}N$/GaN MQWSCs. It is believed that this behavior is possibly related to the energy barrier height (or conduction band offset).

To reduce the high energy barrier height, one can insert a graded layer of 10 nm with an energy bandgap between the energy bandgap of GaN and $In_xGa_{1-x}N$ intrinsic layer to the interface of GaN and $In_xGa_{1-x}N$. Figure 6(a) presents the efficiency of one graded-layer $In_{0.3}Ga_{0.7}N$ pin solar cells with four different graded energy bandgaps of 3.01, 2.81, 2.63, and 2.46 eV as a function of the graded layer thickness. The pin solar cells with a graded layer having an energy bandgap of 2.81 eV exhibit the highest efficiency, when the energy barrier is closely to a half of bandgap difference between GaN (3.4 eV) and $In_{0.3}Ga_{0.7}N$ (2.29 eV). A graded layer with an energy bandgap of 2.46 eV has the worst efficiency due to poor fill factor (large energy barrier). To achieve high efficiency, the optimized thickness of the graded layer is observed at 6 nm and the efficiency drops dramatically at 2 nm. The energy band diagram of one graded-layer $In_{0.3}Ga_{0.7}N$ pin solar cells with four different graded energy bandgap of 3.01, 2.81, 2.63, and 2.46 eV is shown in Figure 6(b). Clearly, an $In_{0.3}Ga_{0.7}N$ pin solar cell with a graded-layer insertion exhibits an energy barrier lower than that without a graded layer insertion. Especially for a graded layer with an energy bandgap of 2.81 eV, it has the lowest energy barrier. This indicates that the barrier height (ΔE) between an intrinsic layer and n-GaN is an important issue correlating to the efficiency and fill factor. The higher the barrier height is, the poorer the efficiency and fill factor are, as shown in Figure 4.

As mentioned above, it is known that the efficiency and fill factor will seriously degrade when an In composition of $In_xGa_{1-x}N$ intrinsic layer is larger than 0.26. In order to improve the solar efficiency, a graded layer is needed to lower the energy barrier height. Figure 7 shows the efficiency of one graded-layer pin solar cells as a function of In composition from 0.3 to 0.5. The efficiency of $In_{0.3}Ga_{0.7}N$ pin solar cells can be improved from 1.4% (as shown in Figure 3(a)) to 10.5% with a graded-layer insertion due to a great improvement of the fill factor from 0.15 to 0.87 (due to a lower barrier height ΔE). It is interesting to note that one graded-layer insertion has an effective improvement of efficiency only in the In composition range of 0.3–0.45. The efficiency begins to drop when an In composition of $In_xGa_{1-x}N$ intrinsic layer is larger than 0.45. The graded layer with an In composition of 0.2 has better efficiency than those with the In composition of 0.15 or 0.25 in higher In composition of $In_xGa_{1-x}N$ intrinsic layer ($x = 0.4$ or 0.45). One simple rule that can be used to determine the In composition of a graded layer is a half value of In composition of $In_xGa_{1-x}N$ intrinsic layer. For example, a pin solar cell with an In composition of 0.3 in $In_xGa_{1-x}N$ intrinsic layer optimally needs a graded layer with an In composition of 0.15, while that with an In composition of 0.4 or 0.45 needs a graded layer with an In composition of 0.2. In addition, the energy barrier height of $In_xGa_{1-x}N$ pin solar cells with an In composition of 0.5 is still too high and results in a poor efficiency although a graded layer has been inserted. That is to say, more graded layers are needed for high In composition $In_xGa_{1-x}N$ intrinsic layer ($x > 0.45$).

Table 2: The optimum In-composited combination of two graded layers for each In composition of $In_xGa_{1-x}N$ pin solar cells.

The In composition of $In_xGa_{1-x}N$ intrinsic layer (corresponding energy bandgap eV)	0.4 (1.98)	0.45 (1.83)	0.5 (1.69)	0.55 (1.56)	0.6 (1.44)	0.65 (1.32)	0.7 (1.21)	0.75 (1.11)
The In composition of the 1st graded layer	0.15 (2.81)	0.15 (2.81)	0.15 (2.81)	0.15 (2.81)	0.2 (2.63)	0.2 (2.63)	0.2 (2.63)	0.25 (2.46)
The In composition of the 2nd graded layer	0.3 (2.29)	0.3 (2.29)	0.3 (2.29)	0.35 (2.13)	0.4 (1.98)	0.4 (1.98)	0.45 (1.83)	0.5 (1.69)

Table 3: The optimum In-composited combination of three graded layers for each In composition of $In_xGa_{1-x}N$ pin solar cells.

The In composition of $In_xGa_{1-x}N$ intrinsic layer (corresponding energy bandgap eV)	0.6 (1.44)	0.65 (1.32)	0.7 (1.21)	0.75 (1.11)
The In composition of the 1st graded layer	0.15 (2.81)	0.15 (2.81)	0.15 (2.81)	0.15 (2.81)
The In composition of the 2nd graded layer	0.3 (2.29)	0.3 (2.29)	0.3 (2.29)	0.35 (2.13)
The In composition of the 3rd graded layer	0.45 (1.83)	0.5 (1.69)	0.5 (1.69)	0.55 (1.56)

The efficiency of two graded-layer pin solar cells as a function of In composition from 0.4 to 0.75 is shown in Figure 8. Clearly, an $In_{0.6}Ga_{0.4}N$ pin solar cell with two graded-layer insertion exhibits the highest efficiency of 15.3%. The efficiency of $In_xGa_{1-x}N$ pin solar cells dramatically drops when an In composition of pin solar cell is at 0.75. It means that three graded-layer insertions are needed to lower the energy barrier height in such high In composition. Table 2 lists the optimum In composite combination of two graded layers for each In composition of $In_xGa_{1-x}N$ pin solar cells. An equally spacing interval of In composition is observed to achieve high efficiency. It is reasonable due to that it can equally minimize the energy barrier height.

Figure 9 shows the efficiency of three graded-layer pin solar cells as a function of the In composition from 0.6 to 0.75. The efficiency of two graded-layer pin solar cells is also shown for comparison. A great improvement of efficiency from 0.23% to 13.1% can be seen at an In composition of 0.75 by three graded-layer insertion. The three graded-layer pin solar cells exhibits a little increase of efficiency at an In composition lower than 0.7 in comparison with two graded-layer pin solar cells. The $In_{0.6}Ga_{0.4}N$ pin solar cells with three graded-layer insertions exhibit the highest efficiency of 16.8% ($V_{oc} = 0.83$ V and $J_{sc} = 26.2$ mA/cm^2). The optimum In composite combination of three graded layers for each In composition of $In_xGa_{1-x}N$ pin solar cells is listed in Table 3. For the In composition range of 0.6 to 0.75, the first graded layer with an In composition of 0.15 and the second graded layer with an In composition of 0.3 or 0.35 are the best choices. The selection rule of In composition of the third graded layer is that the In composition differences are no more than 0.2 between $In_xGa_{1-x}N$ intrinsic layer and the second graded layer.

4. Conclusions

The non-polar $In_xGa_{1-x}N$ pn and pin junction solar cells with different In compositions have been simulated. It is observed that an $In_{0.6}Ga_{0.4}N$ ($E_g = 1.44$ eV) pn junction solar cell exhibits the highest efficiency of 18.4% ($V_{oc} = 0.9$ V and $J_{sc} = 26.1$ mA/cm^2). For the pin solar cells with a GaN/$In_xGa_{1-x}N$/GaN structure, a graded layer is needed at the interface of $In_xGa_{1-x}N$ intrinsic layer and n-GaN region when the energy barrier height is too high. In order to obtain higher efficiency, one graded layer is necessary when the In composition of $In_xGa_{1-x}N$ intrinsic layer is larger than 0.26, while two graded layers are necessary when the In composition of $In_xGa_{1-x}N$ intrinsic layer is larger than 0.45. Finally, three graded layers are needed when the In composition of $In_xGa_{1-x}N$ intrinsic layer is larger than 0.7. It is interesting to note that one graded-layer insertion has an effective improvement of efficiency only in the In composition range of 0.3–0.45. Two and three graded-layer insertions are needed to improve the efficiency and fill factor when the In composition of the intrinsic layer is larger than 0.45 and 0.7, respectively. The GaN/$In_{0.6}Ga_{0.4}N$/GaN pin solar cells with two and three graded-layer insertions exhibit the highest efficiency of 15.3% and 16.8%, respectively ($V_{oc} = 0.82$ V and $J_{sc} = 26.2$ mA/cm^2). This simulation work indicates that the insertion of graded layer is an effective method to lower energy barrier when there exists a high energy band offset in non-polar nitride devices.

Acknowledgments

This work was supported by the National Science Council of Taiwan, (Project no. NSC98-2221-E-182-006). The author acknowledges the use of AMPS-1D developed by Professor Fonash of the Pennsylvania State University.

References

[1] X. Zhang, X. Wang, H. Xiao et al., "Simulation of In0.65Ga0.35 N single-junction solar cell," *Journal of Physics D*, vol. 40, no. 23, pp. 7335–7338, 2007.

[2] O. Jani, I. Ferguson, C. Honsberg, and S. Kurtz, "Design and characterization of GaNInGaN solar cells," *Applied Physics Letters*, vol. 91, no. 13, Article ID 132117, 2007.

[3] C. J. Neufeld, N. G. Toledo, S. C. Cruz, M. Iza, S. P. DenBaars, and U. K. Mishra, "High quantum efficiency InGaN/GaN solar cells with 2.95 eV band gap," *Applied Physics Letters*, vol. 93, no. 14, Article ID 143502, 2008.

[4] H. Hamzaoui, A. S. Bouazzi, and B. Rezig, "Theoretical possibilities of InxGa1-xN tandem PV structures," *Solar Energy Materials and Solar Cells*, vol. 87, no. 1–4, pp. 595–603, 2005.

[5] O. Jani, C. Honsberg, A. Asghar et al., "Characterization and analysis of InGaN photovoltaic devices," in *Proceedings of the 31st IEEE Photovoltaic Specialists Conference*, pp. 37–42, Lake Buena Vista, Fla, USA, January 2005.

[6] J. F. Muth, J. H. Lee, I. K. Shmagin et al., "Absorption coefficient, energy gap, exciton binding energy, and recombination lifetime of GaN obtained from transmission measurements," *Applied Physics Letters*, vol. 71, no. 18, pp. 2572–2574, 1997.

[7] J. Wu, W. Walukiewicz, K. M. Yu et al., "Superior radiation resistance of $In_{1-x}Ga_xN$ alloys: full-solar-spectrum photovoltaic material system," *Journal of Applied Physics*, vol. 94, no. 10, pp. 6477–6482, 2003.

[8] M. Mehta, O. Jani, C. Honsberg, B. Jampana, I. Ferguson, and A Doolittle, "Modifying PC1D to model spontaneous and piezoelectric polarization in III-V nitride solar cells," in *Proceedings of the 22nd European Photovoltaic Solar Energy Conference*, p. 409, Milan, Italy, 2007.

[9] O. Jani, B. Jampana, and M. Mehta, "Optimization of GaN window layer for InGaN solar cells using polarization effect," in *Proceedings of the 33rd IEEE Photovoltaic Specialists Conference*, pp. 1–4, San Diego, Calif, USA, May 2008.

[10] M. J. Jeng, "Influence of Polarization on the Efficiency of $In_xGa_{1-x}N$/GaN p–i–n Solar Cells," *Japanese Journal of Applied Physics*, vol. 49, Article ID 128001, 2 pages, 2010.

[11] Z. Q. Li, M. Lestradet, Y. G. Xiao, and S. Li, "Effects of polarization charge on the photovoltaic properties of InGaN solar cells," *Physica Status Solidi A*, vol. 208, no. 4, pp. 928–931, 2011.

[12] C. Q. Chen, M. E. Gaevski, W. H. Sun et al., "GaN homoepitaxy on freestanding $(1\bar{1}00)$ oriented GaN substrates," *Applied Physics Letters*, vol. 81, no. 17, pp. 3194–3196, 2002.

[13] H. M. Ng, "Molecular-beam epitaxy of GaN/$Al_xGa_{1-x}N$ multiple quantum wells on R-plane $(10\bar{1}2)$ sapphire substrates," *Applied Physics Letters*, vol. 80, no. 23, pp. 4369–4371, 2002.

[14] A. Chitnis, C. Chen, V. Adivarahan et al., "Visible light-emitting diodes using a-plane GaN-InGaN multiple quantum wells over r-plane sapphire," *Applied Physics Letters*, vol. 84, no. 18, pp. 3663–3665, 2004.

[15] J. Wu, W. Walukiewicz, K. M. Yu et al., "Small band gap bowing in In1-xGaxN alloys," *Applied Physics Letters*, vol. 80, no. 25, p. 4741, 2002.

[16] K. Kumakura, T. Makimoto, N. Kobayashi, T. Hashizume, T. Fukui, and H. Hasegawa, "Minority carrier diffusion length in GaN: dislocation density and doping concentration dependence," *Applied Physics Letters*, vol. 86, no. 5, Article ID 052105, pp. 1–3, 2005.

[17] P. Kozodoy, H. Xing, S. P. DenBaars et al., "Heavy doping effects in Mg-doped GaN," *Journal of Applied Physics*, vol. 87, no. 4, pp. 1832–1835, 2000.

[18] H. M. Ng, D. Doppalapudi, T. D. Moustakas, N. G. Weimann, and L. F. Eastman, "The role of dislocation scattering in n-type GaN films," *Applied Physics Letters*, vol. 73, no. 6, pp. 821–823, 1998.

[19] M. E. Levinshtein, S. L. Rumyantsev, and M. S. Shu, *Properties of Advanced Semiconductor Materials*, John Wiley & Sons, New York, NY, USA, 2001.

[20] A. S. Barker and M. Ilegems, "Infrared lattice vibrations and free-electron dispersion in GaN," *Physical Review B*, vol. 7, no. 2, pp. 743–750, 1973.

[21] N. Li, *Simulation and analysis of GaN-based photoelectronic devices*, Dissertation, Institute of Semiconductor, Chinese Academy of Sciences, Beijing, China, 2005.

[22] G. F. Brown, J. W. Ager, W. Walukiewicz, and J. Wu, "Finite element simulations of compositionally graded InGaN solar cells," *Solar Energy Materials and Solar Cells*, vol. 94, no. 3, pp. 478–483, 2010.

[23] R. Aleksiejunas, M. Sudzius, V. Gudelis et al., "Carrier transport and recombination in InGaN/GaN heterostructures, studied by optical four-wave mixing technique," *Physica Status Solidi*, vol. 0, no. 7, pp. 2686–2690, 2003.

[24] M.-J. Jeng, Y.-L. Lee, and L.-B. Chang, "Temperature dependences of $In_xGa_{1-x}N$ multiple quantum well solar cells," *Journal of Physics D*, vol. 42, no. 10, Article ID 105101, 2009.

Hindawi Publishing Corporation
International Journal of Photoenergy
Volume 2012, Article ID 527820, 9 pages
doi:10.1155/2012/527820

Research Article

Construction of Tungsten Halogen, Pulsed LED, and Combined Tungsten Halogen-LED Solar Simulators for Solar Cell I-V Characterization and Electrical Parameters Determination

Anon Namin,[1] Chaya Jivacate,[2] Dhirayut Chenvidhya,[2] Krissanapong Kirtikara,[2] and Jutturit Thongpron[3]

[1] *Division of Energy Technology, School of Energy, Environment and Materials, King Mongkut's University of Technology Thonburi, 126 Pracha-uthit Road, Bangmod, Thungkhru, Bangkok 10140, Thailand*
[2] *CES Solar Cell Testing Centre, Pilot Plant Development and Training Institute (PDTI), Thailand*
[3] *Faculty of Engineering, Rajamangala University of Technology Lanna, 128 Huaykaew Road, Muang, Chiangmai 50300, Thailand*

Correspondence should be addressed to Jutturit Thongpron, t_jutturit@yahoo.com

Received 14 December 2011; Revised 14 February 2012; Accepted 15 February 2012

Academic Editor: Peter Rupnowski

I-V characterization of solar cells is generally done under natural sunlight or solar simulators operating in either a continuous mode or a pulse mode. Simulators are classified on three features of irradiance, namely, spectral match with respect to air mass 1.5, spatial uniformity, and temporal stability. Commercial solar simulators use Xenon lamps and halogen lamps, whereas LED-based solar simulators are being developed. In this work, we build and test seven simulators for solar cell characterization, namely, one tungsten halogen simulator, four monochromatic (red, green, blue, and white) LED simulators, one multicolor LED simulator, and one tungsten halogen-blue LED simulator. The seven simulators provide testing at nonstandard test condition. High irradiance from simulators is obtained by employing elevated supply voltage to tungsten halogen lamps and high pulsing voltages to LEDs. This new approach leads to higher irradiance not previously obtained from tungsten halogen lamps and LEDs. From *I-V* curves, electrical parameters of solar cell are made and corrected based on methods recommended in the IEC 60891 Standards. Corrected values obtained from non-STC measurements are in good agreement with those obtained from Class AAA solar simulator.

1. Introduction

Solar simulators for solar cell testing can be broadly classified into 3 groups, namely, AM 1.5 G terrestrial system solar simulators, AM 1.5 D concentrating PV solar simulators, and AM 0 space system solar simulators. Major building blocks of solar simulators, are light sources and light quality control components, such as filters and lenses, rendering AM 1.5 spectrum as specified in the IEC 60904-3 Standards and ASTM G173-03 Standards or AM 0 specified in ASTM E490-00a [1–3]. The IEC 60904-9 and ASTM E927-10 classify solar simulators in terms of spectral match, uniformity and temporal stability into simulator classes [4, 5].

Solar simulators have been continuously developed for nearly five decades, with differing approaches on lamp selection, combined light sources and filtering. Xenon arc lamps and metal halide arc lamps are employed in commercial solar simulators. Research solar simulator works during the last two decades are reported on light emitting diodes (LED) as they are inexpensive, consume small power and can be combined to produce required spectrum outputs, and promising a new approach to low cost. Current-voltage characterizations of solar cells are done at standard test condition (STC) (1,000 $W \cdot m^2$, 1.5 AM spectrum, cell at 25°C) as specified in IEC 60904-1 Standards [6]. As there are simulators not conforming to AM 1.5 G, notably simulators based on metal halide lamps and LEDs, the IEC 60891 Standards provide correction methods to convert the non-STC test results to the STC [7]. During the present decade the major research trend in solar simulators for terrestrial solar cells is on low cost and high intensity LED solar simulators and translation of non-STC results. This paper focuses on construction and

characteristics of simulators not conforming to AM 1.5 G, with emphasis on LED-based simulators, and applications of the IEC 60891 Standards on non-STC results.

Solar simulators using Xenon lamps and metal halide sources were reported over forty years ago, initially for space radiation simulation and afterwards for terrestrial solar cell characterization. An excellent review on early works is undertaken by Emery [8]. Compact source iodide (CSI) lamps were introduced in 1980s, as reported by Beeson [9]. After that multi-CSI solar simulators for large scale testing have become commercially available. On pioneering LED-based solar simulators, Kohraku and Kurokawa measure spectral responses of solar cells using 4-color and 6-color LED simulators [10]. Potential low cost and simplicity of LED-based simulators are pointed out. During the past decade, numbers of research work are published on LED simulators, all showing low intensity limitations of LED-based simulators. Bliss et al. develop an LED-based solar similar prototype producing light at variable flash speeds and pulse shapes [11]. Color and UV LEDs and halogen light sources are employed.

This paper is on construction and testing of seven solar simulators for solar cell characterization using tungsten halogen lamps and monochromatic red, green, blue, and white LEDs. High irradiance is achieved by operating lamps at elevated supply voltage above rated voltage, and in LEDs by applying voltage high pulses. This approach leads to higher irradiance that has not been previously obtained. Solar cell electrical parameters are derived and corrected according to the IEC 60891 Standards for I-V characterization at non-STC obtained under the seven simulators.

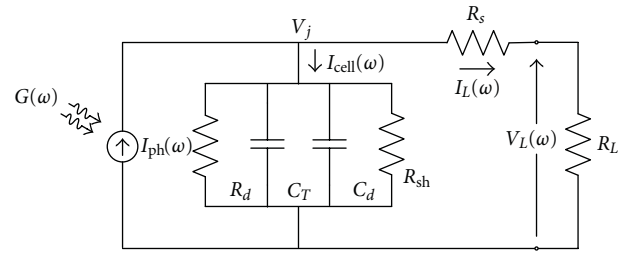

Figure 1: AC equivalent circuit of a solar cell.

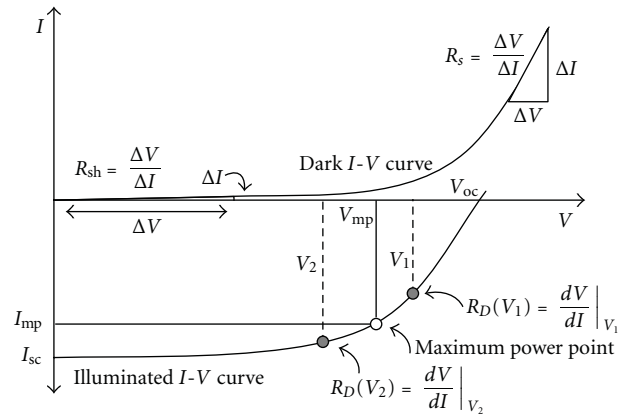

Figure 2: Dark and illuminated I-V curves of a solar cell.

2. Electrical Parameters of Solar Cells

In representing solar cells (and modules) one uses a DC equivalent circuit or an AC equivalent circuit. The DC circuit consists of three resistances, namely, series resistance (R_S), shunt resistance (R_{sh}), and internal dynamic resistance (R_d). The AC equivalent circuit has two additional parameters, that is, junction capacitance (C_T) and diffusion capacitance (C_D). C_T is voltage dependent whereas C_D is voltage and frequency dependent. Figure 1 shows an AC equivalent circuit.

Series and shunt resistances are determined from dark I-V characteristics or dark IV curves. Dark or illuminated IV curves are employed to determine internal dynamic resistance. The IEC 60904-1 Standards provide guidelines on performing I-V characteristics measurements under natural sunlight, steady-state simulated sunlight, and pulsed simulated sunlight [6].

Impedance spectroscopic techniques, not covered in this paper, are employed to determine dynamic parameters. Spectroscopic measurements can be done by expensive impedance spectroscopy equipment, reported by Kumar et al. [12]. Alternatively, Chenvidhya et al. has determined dynamic parameters utilizing laboratory equipment, with small periodic signals superimposing on AC signal as inputs to solar cells and FFT analysis of output signals [13].

From a dark I-V curve as showen in Figure 2, R_S is a slope in the first quadrant and depends on resistances of bulk semiconductors and contacts. R_{sh} can be derived from a slope at near-zero voltage, and depends on defects and traps in semiconductors. For each solar cell, R_S and R_{sh} are constant at all operating conditions. On the other hand, R_d is operating point dependent and is a slope at of an I-V curve (under dark or illumination) at a particular operating point.

In comparing performance of solar cells, apart from series and shunt resistance, other electrical parameters are also required. These are open circuit voltage (V_{OC}), short circuit current (I_{SC}), maximum power (P_{pm}) (and corresponding current and voltage), solar cell efficiency (η), and fill factor (FF).

3. Equipment

For characterization of solar cell under Class AAA simulator according to IEC 60904-9 Standards [4], natural sunlight and seven solar simulators fabricated in this study, we use a solar cell obtained from a local module manufacturer. It is a monocrystalline silicon solar cell with a dimension of $12.5 \times 12.5\,\text{cm}^2$. The solar cell is encapsulated with EVA and has a Tedlar backsheet.

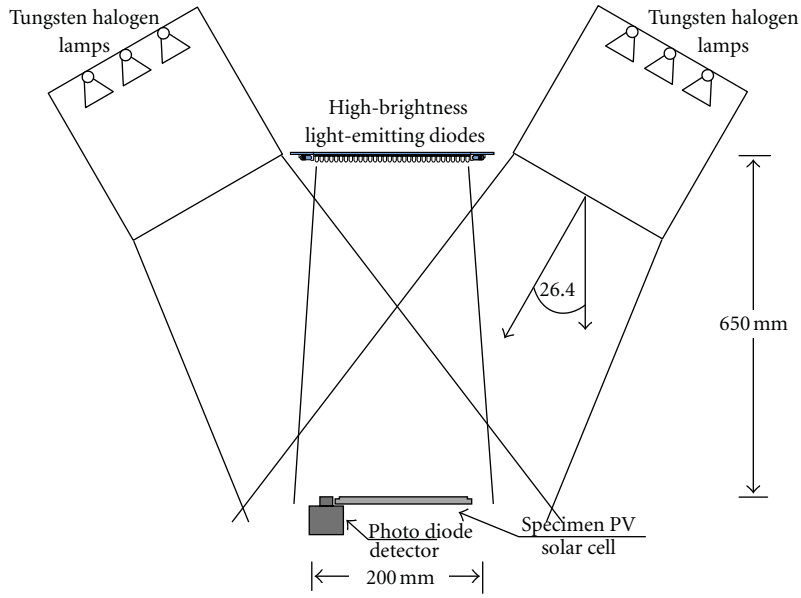

Figure 3: A schematic structure of combined tungsten halogen and blue LED solar simulator.

3.1. Solar Simulators

3.1.1. Tungsten Halogen Solar Simulator. The basic lamp array consists of 3×3 Philips tungsten halogen lamps, each rated at 12 V and 50 W. The array is naturally ventilated. Supply voltages can be varied from 100%, 120%, and 140% of rated voltage to increase lamp light outputs. This, however, affects color temperature of lamps, and resultant spectra.

As lamp supply voltage increases, lamp light outputs increase and the spectra are blueshifted. To maintain a constant irradiance of $1{,}000\,\mathrm{W \cdot m^{-2}}$ on a test plane, spacing distances between the array and the test plane are adjusted. For supply voltages at 100%, 120%, and 140% of rated voltage, the spacing distances are 42 cm, 62 cm, and 78 cm, respectively.

3.1.2. LED Solar Simulators. Study on five LED simulators, four monochromatic LED arrays, and one combined color LED array, used in this work, has been reported by Namin et al. [14]. Four monochromatic LEDs are red-R at 632 nm, green-G at 525 nm, blue-B at 468 nm and white-W. Each array has 1,024 LEDs and is 227.5 mm $\times$ 227.5 mm. The LED array is 3 mm above a glass diffuser, under which is a test plan. Supply voltages to LEDs are pulse signals whose amplitudes are increased above rated voltages to raise light outputs. Amplitudes of pulse signals can be continuously varied from 0–150 V with a pulse width of 10 ms and a period of 1 s. Heat from LEDs is removed with LED heat sinks and forced air cooling. This helps maintain steady temperature of heat sink at 25°C.

3.1.3. Combined Tungsten Halogen-Blue LED Solar Simulator. Tungsten halogen lamp light outputs are deficient in the blue part of the spectrum. To augment the blue part, we incorporate a blue LED array with tungsten halogen lamps as shown in Figure 3. The simulator combined light sources consisting of two 3×3 tungsten halogen lamp arrays and one blue LED array, similar to the one described above. The blue LED array is located directly 65 cm above the test plane. Two tungsten halogen lamp arrays are placed along opposite sides of the blue LED array, and at an inclined angle of 26 degrees with respect to the horizon.

3.1.4. Class AAA Solar Simulator. PASAN Class AAA Sun Simulator IIIc is used as a reference solar simulator. It is a commercial short-pulse solar simulator employing 4 flash Xenon lamps. Light pulses can be varied between 2–10 ms. Up to 2×2 m solar cells modules can be tested.

4. Measurements and Analysis

4.1. Measurements on Solar Simulator Characteristics. The following measurements are made.

Tungsten Halogen Solar Simulator. Spectral characteristics, irradiance spatial uniformity, and temporal stability are maintained when lamps are supplied at 100%, 120%, and 140% of rated voltage.

LED Solar Simulators. The above-mentioned study of Namin et al. covers

(i) thermal characteristics of LED arrays under continuous and pulsed operations. This is to compare temperature profiles of arrays under the two operating conditions. Infrared pictures of LED heat sinks are taken and used to determine corresponding temperature,

(ii) continuous and pulsed operations of LEDs at different amplitudes, pulse widths, and pulse periods. The

Table 1: Irradiance uniformity and temporal instability of seven solar simulators.

Light sources	Average irradiance (Wm^{-2})	Uniformity		Temporal instability	
		% Uniformity	Uniformity class	% Temporal instability	Temporal instability class
Tungsten halogen lamps					
Supply voltage and separation distance					
100% rated voltage, 42 cm	1004	9.8	C	1.25	A
120% rated voltage, 62 cm	1006	4.85	B	1.25	A
140% rated voltage, 78 cm	1005	2.60	B	1.25	A
Tungsten halogen lamps with blue LEDs					
120% rated voltage, 62 cm	1,040	3.60	B	0.47	A
Light emitting diodes					
Blue LED	1,015	2.68	B	1.40	A
Red LED	1010	2.60	B	1.50	A
Green LED	410	3.92	B	2.50	B
White LED	415	2.92	B	2.75	B
Combined R-G-B LED	810	3.84	B	3.10	B

shortest pulse duration that can be used would be governed by the sweeping time from the short circuit condition to the open circuit condition in I-V curve measurement,

(iii) spatial uniformity and temporal stability of irradiance are examined.

Table 1 shows irradiance levels, uniformity, and temporal stability of the seven solar simulators. Averaged irradiance levels are calculated from measured irradiance at 64 locations on the test plane.

4.2. Determination of IV Curves. The seven solar simulators used to measure I-V curves are (i) one tungsten halogen simulator, (ii) four monochromatic LED solar simulators, (iii) one combined RGB LED solar simulator, and (iv) one combined tungsten halogen-blue LED solar simulator. IV curves of a solar cell are made under STC condition PASAN Class AAA solar simulator, non-STC conditions (seven simulators) and under natural sunlight. The I-V characterization method follows the IEC 60904-1 Standards [6].

4.3. Analysis of Electrical Parameters

STC Condition. Calculations are made on solar cell electrical parameters (I_{SC}, V_{OC}, P_{mp}, efficiency, fill factor) and resistances (R_S, R_{sh}, R_d).

Non-STC Conditions. At present, there are correction methods based on the IEC 60891 Standards for measurements at non-STC conditions. I-V curves at different irradiances and temperatures were characterized by Class AAA solar simulator. The R_S and temperature coefficients of current (α) and voltage (β) and curve correction factor (κ) are determined.

The equations to translate or correct the non-STC results are as follows:

$$I_2 = I_1 + I_{SC}\left[\frac{I_{SR}}{I_{MR}} - 1\right] + \alpha(T_2 - T_1),$$
$$V_2 = V_1 - R_s(I_2 - I_1) - \kappa I_2(T_2 - T_1) + \beta(T_2 - T_1). \quad (1)$$

In the above equations, I_1, V_1 are measured current and voltage at non-STC; I_2, V_2 are corrected current and voltage; I_{SC} is the short circuit current of the test solar cell; I_{MR} is the short circuit current of the reference cell; I_{SR} is the short circuit current of the reference cell under standard light intensity; T_1 is the measured temperature of the test solar cell; T_2 is the standard temperature or other specified temperatures; α and β are temperature coefficients of current and voltage, respectively; κ is the curve correction factor.

Based on the equations outlined above, we correct results obtained from seven solar simulators using the IEC 60891 Standards and compared with the STC results. Figure 4 is a flowchart on solar simulator construction and corrections of electrical parameters using the IEC 60891 Standards.

5. Results and Discussions

5.1. Spectral Irradiance of Tungsten Halogen and Combined Tungsten Halogen-Blue LED Solar Simulators. For simplicity, we herein will use the term "spectral irradiance" of solar

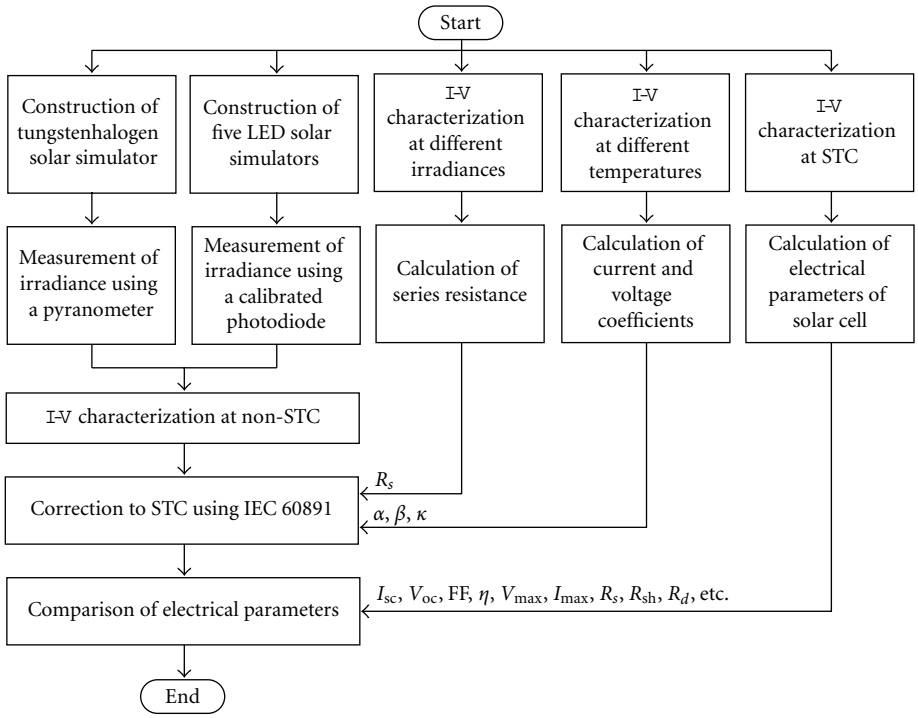

Figure 4: Flowchart of solar simulator construction and corrections of electrical parameters using IEC 60891 Standards.

simulator instead of spectral intensity. It can be seen from Figure 5 that spectra of the tungsten halogen simulator are different from the reference spectral irradiance [1]. The spectra are more "red" in contents. As the supply voltages are increased, the lamps get hotter and the output light spectra shift towards shorter wavelengths—blue-shifting. As a consequence, better spectrum matching with the AM 1.5 spectrum can be expected at elevated supply voltages. Thus, one can improve the spectral match of tungsten halogen solar simulators by raising supply voltages. The disadvantages would be higher power consumption and shorter lamp life. Adopting pulsed supply voltages would reduce such disadvantages, permit even higher supply voltages, and improve spectral match. We do not pursue such idea with tungsten halogen lamps, but carrying this out with LED simulators. The results are reported in later parts of the paper.

The spectral irradiance and intensity of a combined tungsten halogen-blue LED solar simulator is shown in Figure 6. The spectral match is improved by adding a blue irradiance component in the range of 400–500 micron. Temporal stability of irradiance of tungsten halogen solar simulators, obtained from an ordinary power supply with simple rectifier and a high quality power supply, shown in Figure 7, are compared and evaluated. It is seen that a Class A temporal stability is achieved using a high quality power supply.

Tables 2 and 3 compare spectral matches obtained from the tungsten halogen solar simulators using three supply voltages, and a combined tungsten halogen-blue LED solar simulator.

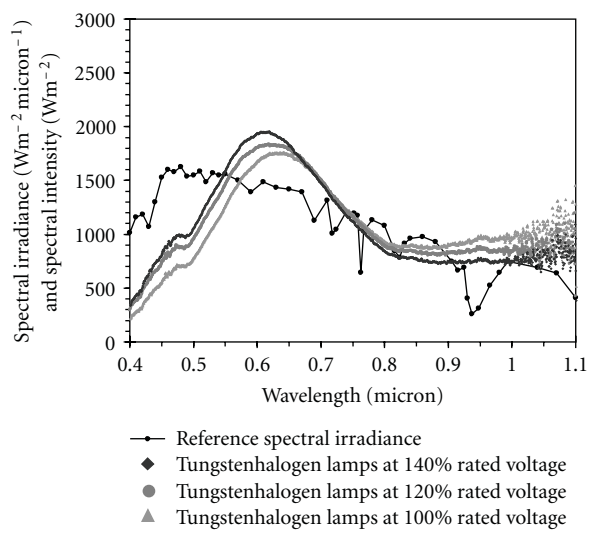

Figure 5: Reference spectral irradiance [1] and spectral intensity of tungsten halogen simulator under various supply voltage.

It is clearly seen form Tables 2 and 3 that combining blue LEDs with tungsten halogen lamps produce a better spectral match. Better I-V characterization and more accurate electrical parameters can be expected. This opens new avenues for low cost solar simulator construction.

5.2. LED Array Characterization. Followings are salient features on LED array characterization undertaken by Namin et al.

Table 2: Spectral match of tungsten halogen solar simulator at three different supply voltages.

Wavelength range (nm)	Supply voltage at 100% of rated voltage		Supply voltage at 120% of rated voltage		Supply voltage at 140% of rated voltage	
	Spectral match	Class	Spectral match	Class	Spectral match	Class
400–500	0.40	C	0.49	C	0.55	C
500–600	0.84	A	0.95	A	1.04	A
600–700	1.21	A	1.25	A	1.28	B
700–800	1.05	A	1.04	A	1.00	A
800–900	0.94	A	0.88	A	0.82	A
900–1100	1.65	C	1.38	B	1.29	B
Classification	1,010 $W \cdot m^{-2}$	C	1,009 $W \cdot m^{-2}$	C	1,010 $W \cdot m^{-2}$	C

Note: In the IEC 60904-9 Standards, six wavelength ranges are used to determine a spectral match with standard AM 1.5 G [9].

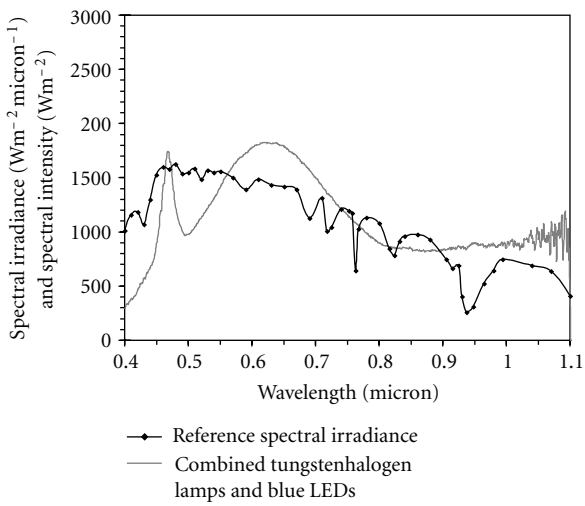

Figure 6: Reference spectral irradiance [1] and spectral intensity of combine tungsten halogen operated at 120% rated voltage and blue LEDs.

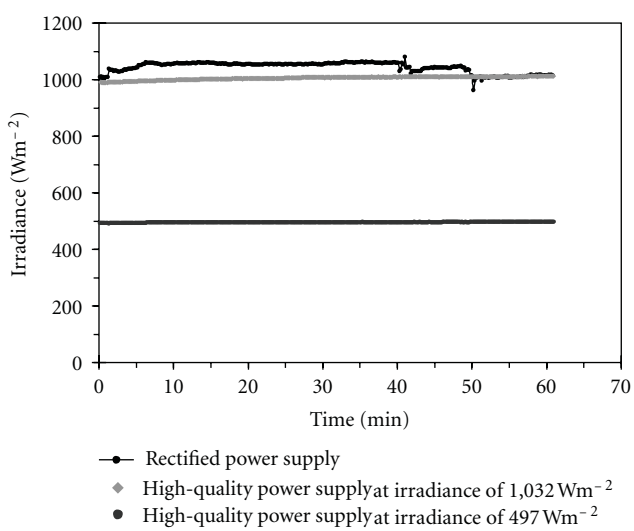

Figure 7: Temporal stability of irradiance of tungsten halogen solar simulator under different supply voltages.

Table 3: Classification of tungsten halogen solar simulator and combined tungsten-halogen blue LED solar simulator.

Classification	Light sources at irradiance of 1,000 Wm^{-2}	
	Tungsten halogen lamps at 140% rated voltage	Combined tungsten halogen lamps (120% rated voltage) and blue LEDs
Spectral match class	C	B
Nonuniformity class	B	B
Temporal instability class	A	A
Standard classification	CBA	BBA

Thermal Characteristics of LED Arrays. Under continuous voltage, heat sink temperature rises substantially (63°C). However, under pulse operation mode the array remains cool at room temperature (27°C). The merit of the pulse operation mode is evident.

Stability of Irradiance from LED Arrays under Pulse Operations. Irradiance stability of the R, G, B, and W LED arrays and the RGB array under 10 ms pulse operations is studied. Pulse amplitudes at one, two, and three times LED-rated voltages are applied, and irradiance stability is recorded. It is found that amplitudes of pulses can be increased to at least twice the rated voltage, and the array still provides a stable light output. Temporal stability is under 5%, and, the 5 simulators are Class B.

Spatial Uniformity of Irradiance. On the test plane, the spatial uniformity is better than 5%. The 5 simulators are Class B.

Relationship between the LED Current and Irradiance. LED light outputs and irradiance levels initially increase with increasing LED current but level off, due to temperature rises. Among the four monochromatic R, G, B, and W arrays and the combined RGB array, only R and G arrays provide irradiance higher than 1000 Wm^{-2}. Less than 1000 $W \cdot m^{-2}$ is available from G, W, and RGB arrays. Blue and white LEDs

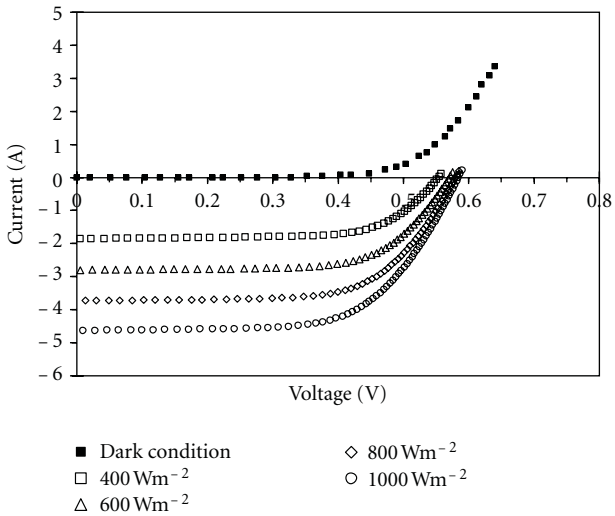

Figure 8: Dark and illuminated I-V curves of an X-Si solar cell obtained from Class AAA solar simulator.

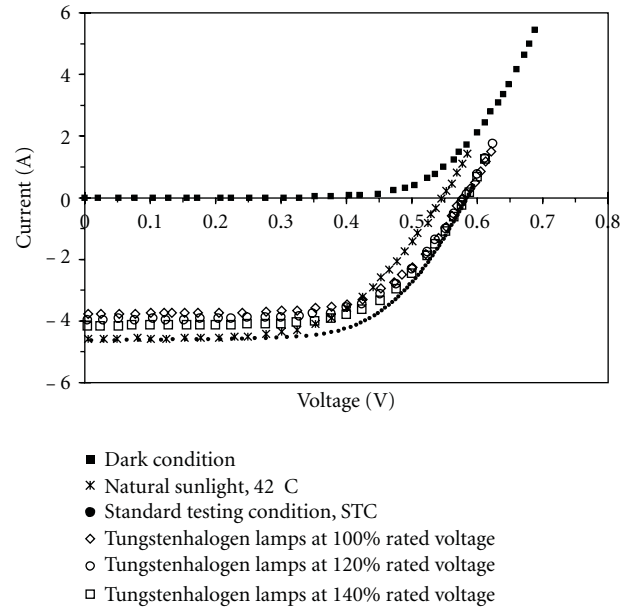

Figure 9: Uncorrected I-V curves obtained from tungsten halogen simulator under three supplied voltages, natural lighting, and Class AAA solar simulator at irradiance of 1,000 W·m^{-2}.

are more temperature dependent and are less efficient as their light outputs rapidly fall with increasing supply current.

In principle we can further increase LED light outputs by using higher pulse amplitudes while keeping LED temperature down. Chilled air, instead of room temperature air, could possibly be used in the cooling. But LED array structures would be complex and more expensive.

5.3. I-V Characteristics Obtained from the Seven Solar Simulators

5.3.1. Uncorrected I-V Curves Obtained from the Non-STC Simulators. We compare I-V curves obtained from seven non-STC solar simulators with I-V curves from a reference STC solar simulator (PASAN Class AAA Sun Simulator IIIc). Results are plotted in Figures 10 and 11.

From the Figures 8, 9, and 10, we note the following.

(a) PASAN Sun Simulator can be adjusted to provide an irradiance over 400–1,000 W·m^{-2}, Figure 8.

(b) Tungsten halogen simulator supply voltage can be adjusted to 140% of rated voltage, resulting in changes in irradiance and spectrum shift.

(c) For all 5 LED simulators, voltages and current can varied to provide irradiance in the range of 400–1,000 W·m^{-2}, and light spectra being different from AM 1.5. Out of the 5 simulators, only the red and blue LED simulators provide an irradiance of 1,000 W·m^{-2}. Results are previously reported and not shown here [14].

For the tungsten halogen simulator, at the irradiance level of 1,000 W·m^{-2}, Figure 10, uncorrected I-V curves measured with the three supply voltages are of the same shape as the I-V curve of the Class AAA simulator, with some deviations. The curve of the simulator operated at 140% rated

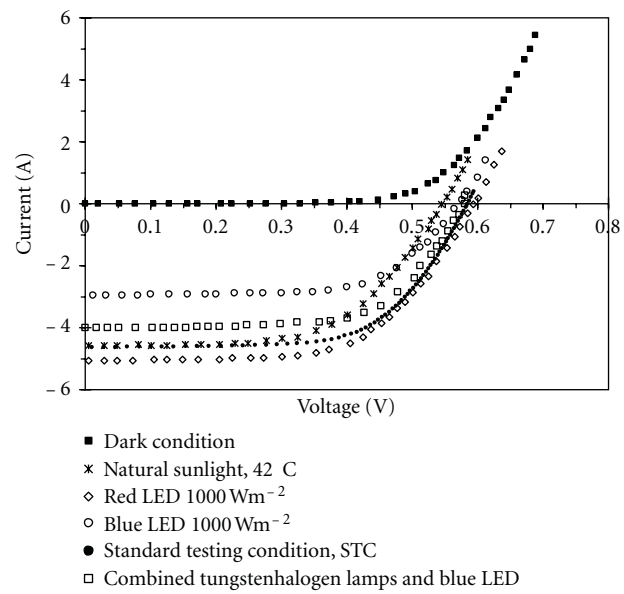

Figure 10: Uncorrected I-V curves from natural sunlight, Class AAA solar simulator, red LED, blue LED, and combined tungsten halogen-blue LED simulators at irradiance of 1,000 W·m^{-2}·

voltage is the best fit. This is understandable as at elevated voltages, the lamp temperature increases with accompanying spectrum shift towards the short wavelength. On the other hand, I-V curves of the red and blue LED simulators are significantly different from that of the Class AAA simulator, Figure 11. Red LED simulator results in higher current than blue LED simulator. This could be explained partly by the fact that at the same irradiance there are more red photons

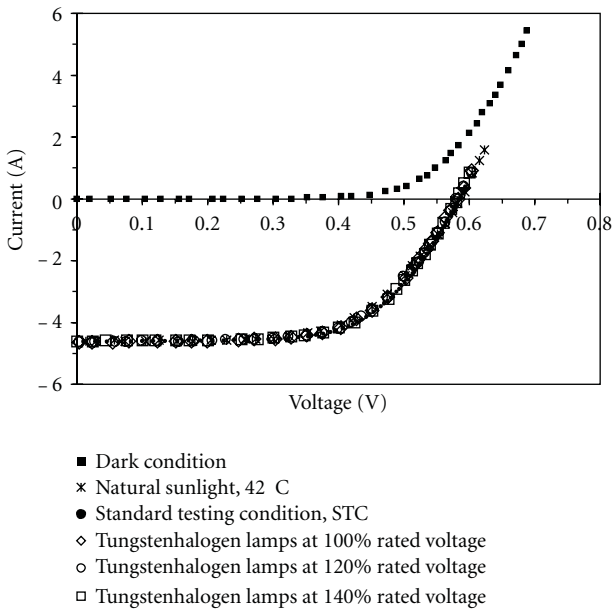

Figure 11: Corrected I-V curves measured under natural sunlight, Class AAA solar simulator, and tungsten halogen simulator (at 100%, 120%, and 140% rated voltage) after IEC 60891 Standards correction.

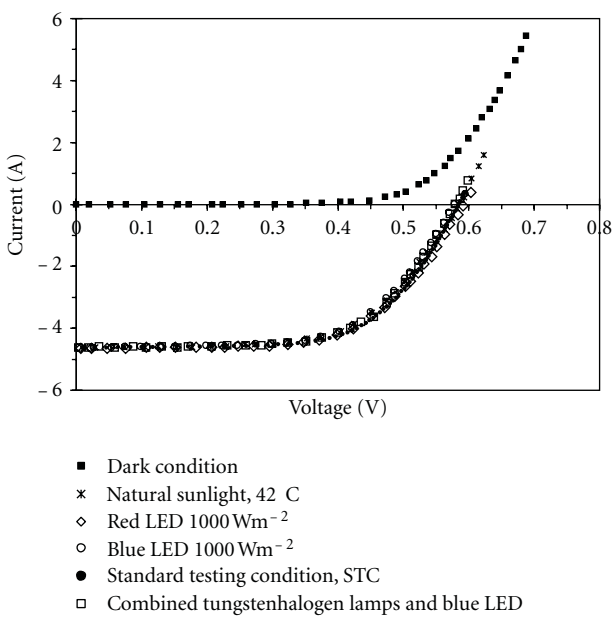

Figure 12: Corrected I-V curves measured under natural sunlight, Class AAA solar simulator, red LED simulator, blue LED simulator, and combined tungsten halogen-blue LED simulator after IEC 60891 Standards correction.

(at lesser energy) than blue photons. Hence, photocurrent due to red photons is greater.

5.3.2. Corrected I-V Curves at STC Based on the IEC 60891 Standards. We undertake corrections of the non-STC measurements of the seven non-STC simulators using the IEC 60891 Standards, outlined in Section 4.3, and plot results as Figures 11 and 12.

The corrected I-V curves and that of the Class AAA simulator are quite similar. We wish to point out that this is the first instance that the IEC 60891 correction method is applied for tungsten halogen, LED and tungsten halogen-LED simulators. Kohraku and Kurokawa have proposed a different correction method, called the Two-curve method.

5.3.3. Electrical Parameters of Solar Cell at STC. From the corrected I-V curves of the tungsten halogen simulator, the red and blue simulators, and the tungsten halogen-blue LED simulator at 1,000 W·m^{-2}, we derive electrical parameters (I_{SC}, V_{OC}, P_{mp}, efficiency, fill factor) at the STC. The results are shown in Table 4.

Comparing electrical parameters obtained from the seven non-STC simulators after corrections based on the IEC 60891 Standards and those obtained from Class AAA simulator, very good agreement is seen. Differences in values of electrical parameters are about 2% or less. This level of result accuracy is essential in adopting tungsten halogen lamps, LED and combined tungsten halogen-LED simulators in solar cell characterization. Less expensive but yet excellent-performance solar simulators can be constructed from these light sources.

6. Conclusions

We construct and test seven solar simulators with tungsten halogen lamps and LEDs as light sources for solar cell characterization. The seven simulators are one simulator using tungsten halogen lamps, four simulators using monochromatic red, green, blue, and white LEDs, one with combined red-green-blue LEDs and one tungsten halogen lamps—blue LEDs. Higher irradiance are achieved with tungsten halogen lamps and LEDs, by operating lamps at elevated supply voltage above rated voltage and pulsing LEDs by at voltage, respectively. Irradiance uniformity and instability qualify the seven simulators as Class B. Their spectral match with air mass 1.5 is varied. Using these simulators, I-V curves of solar cell are measured under non-STC conditions. Solar cell electrical parameters are derived. Applying correction methods recommended in the IEC 60891 Standards, for I-V characterization at non-STC, results on electrical parameters obtained with the tungsten halogen simulator, the combined tungsten halogen-blue LED simulator, and the monochromatic red and blue LED simulators are in good agreement with Class AAA simulator. Less expensive and excellent performance solar simulators can be fabricated with tungsten halogen lamps and LEDs as light sources.

Acknowledgments

The authors wish to acknowledge supports from their two universities for research facilities and research funds. They wish to acknowledge supports from the CSSC for excellent research facilities. Valuable advices have been given by

Table 4: Electrical parameters of solar cell measured under natural sunlight, Class AAA solar simulator, and non-STC solar simulators after IEC 60891 Standards correction.

Parameters	Light sources							
	Tungsten halogen lamps under three supply voltages			Red LED	Blue LED	Combined tungsten halogen and LEDs	Natural sunlight	Class AAA (STC)
	100% rated voltage	120% rated voltage	140% rated voltage					
G (W·m^{-2})	1000	1000	1000	1000	1000	1000	1000	1002
T (C)	25	25	25	25	25	25	25	25
V_{oc} (V)	0.58	0.58	0.58	0.59	0.57	0.58	0.58	0.58
I_{sc} (A)	4.63	4.63	4.63	4.63	4.63	4.63	4.59	4.63
P_{max} (W)	1.65	1.68	1.67	1.69	1.65	1.68	1.66	1.72
V_{mp} (V)	0.41	0.42	0.41	0.41	0.41	0.42	0.41	0.42
I_{mp} (A)	4.07	4.04	4.07	4.11	4.03	4.04	4.07	4.06
FF (%)	61.8	62.7	62.8	61.9	62.1	62.7	62.2	63.5
η (%)	11.3	11.5	11.4	11.5	11.1	11.5	11.4	11.7
R_s (Ω)	0.03	0.03	0.03	0.03	0.03	0.03	0.03	0.03
R_{sh} (Ω)	5.20	5.20	5.20	5.20	5.20	5.20	5.20	5.08
R_d @ V_{mp} (Ω)	0.08	0.08	0.08	0.08	0.08	0.08	0.08	0.08

Assistant Professor Proapran Plienpoo, Associate Professor Dr. Koarakot Wattanavichean, and Dr. Veerapon Monyakul.

References

[1] IEC Standards, "IEC 60904-3 Photovoltaic devices—Part 3: Measurement principles for terrestrial photovoltaic (PV) solar devices with reference spectral irradiance data," edition 2.0, 2008.

[2] ASTM Standards, "ASTM G173-03," Standard tables for reference solar spectral irradiance: Direct normal and hemispherical on 37° tilted surface, 2008.

[3] ASTM Standards, "ASTM E490-00a," Standard solar constant and zero air mass solar spectral irradiance tables, 2006.

[4] IEC Standards, "IEC 60904-9 Photovoltaic devices—Part 9: Solar Simulator Performance requirements," edition 2.0, 2007.

[5] ASTM Standards, "ASTM E927-10 Standard specification for solar simulator for terrestrial photovoltaic testing".

[6] IEC Standards, "IEC 60904-1 Part 1: Measurement of photovoltaic current-voltage characteristics," 2nd edition, 2006.

[7] IEC, "IEC 60891 Photovoltaic devices—procedures for temperature and irradiance corrections to measured I-V characteristics," 2.0 edition 2.0, 2009.

[8] K. A. Emery, "Solar simulators and I-V measurement methods," *Solar Cells*, vol. 18, no. 3-4, pp. 251–260, 1986.

[9] E. J. G. Beeson, "The CSI lamp as a source of radiation for solar simulation," *Lighting Research and Technology*, vol. 10, no. 3, pp. 164–166, 1978.

[10] S. Kohraku and K. Kurokawa, "New methods for solar cells measurement by LED solar simulator," in *Proceddings of the 3rd World Conference on Photovoltaic Energy Conversion*, pp. 1977–1980, May 2003.

[11] M. Bliss, T. R. Betts, and R. Gottschalg, "An LED-based photovoltaic measurement system with variable spectrum and flash speed," *Solar Energy Materials and Solar Cells*, vol. 93, no. 6-7, pp. 825–830, 2009.

[12] R. A. Kumar, M. S. Suresh, and J. Nagaraju, "GaAs/Ge solar cell AC parameters under illumination," *Solar Energy*, vol. 76, no. 4, pp. 417–421, 2004.

[13] D. Chenvidhya, K. Kirtikara, and C. Jivacate, "A new characterization method for solar cell dynamic impedance," *Solar Energy Materials and Solar Cells*, vol. 80, no. 4, pp. 459–464, 2003.

[14] A. Namin, C. Jivacate, D. Chenvidhya, K. Kirtikara, and J. Thongpron, "Determination of solar cell electrical parameter and resistances using color and white LED-based solar simulators with high amplitude pulse input voltage," in *Proceedings of the 1st Asia-Pacific Forum on Renewable Energy*, pp. 16–19, Busan, Republic of Korea, November 2011.

Hindawi Publishing Corporation
International Journal of Photoenergy
Volume 2012, Article ID 732647, 4 pages
doi:10.1155/2012/732647

Research Article

Quinhydrone Chemical Passivation of a Silicon Surface for Minority Carrier Bulk-Lifetime Measurements

M. Solcansky,[1,2] J. Vanek,[1] and A. Poruba[2]

[1] *Faculty of Electrical Engineering and Communication, Brno University of Technology, Technicka 10, 61600 Brno, Czech Republic*
[2] *Technology division, Solartec s.r.o., Televizni 2618, 756 61 Rožnov pod Radhoštěm, Czech Republic*

Correspondence should be addressed to M. Solcansky, solcansky@phd.feec.vutbr.cz

Received 19 June 2011; Accepted 23 January 2012

Academic Editor: Bhushan Sopori

For the measurement of the minority carrier bulk-lifetime the characterization method MW-PCD is used, where the result of measurement is the effective carrier lifetime, which is very dependent on the surface recombination velocity and therefore on the quality of a silicon surface passivation. This work deals with an examination of a different solution types for the chemical passivation of a silicon surface. Various solutions are tested on silicon wafers for their consequent comparison. The main purpose is to find optimal solution, which suits the requirements of a time stability and start-up velocity of passivation, reproducibility of the measurements and a possibility of a perfect cleaning of a passivating solution remains from a silicon surface, so that the parameters of a measured silicon wafer will not worsen and there will not be any contamination of the other wafers series in the production after a repetitive return of the measured wafer into the production process. The cleaning process itself is also a subject of a development.

1. Introduction

The main objective of this work is to propose a solution, which would meet a few key parameters. It has to exhibit an immediate startup of passivation properties as well as long-time stability (few hours for an appropriate high-resolution scan or degradation study). Last but not least the reproducibility of the lifetime measurement is very important, which means that a repeating of measurement-cleaning process will not lead to extreme lifetime degradation due to passivation solution residues on a silicon surface of the tested wafer. Therefore perfect cleaning of the wafer surface must be possible. If a contaminated wafer is returned back to the production process, the whole wafer series may be contaminated (mainly during the high-temperature processes). The carrier lifetime is measured by the WT-2000 machine using the MW PCD method [1]. Wafers with a resistivity of 20 $\cdot$cm and 4″ in size used for the measurements went through saw damage removal (etching in 60% KOH at a temperature of 80–90°C for 1–5 min + washing 3×2 min in demineralized water). Some wafers were textured by an anisotropic texturing process in 3% NaOH + IPA. Excellent passivation properties of a solution are needed to gain the maximum average lifetime values. This means that there is nearly no surface recombination, which is the main objective of chemical passivation for experimental purposes [2].

2. Chemical Passivation in Iodine/Ethanol Solution

Testing of the standard passivation solution of 1% iodine/ethanol (see Figure 1) exhibits quite remarkable time instability. On the other hand, the immediate startup of the passivating ability is the big advantage of this solution. The measured average lifetime values are at their maxima from the beginning, and then they decrease by about 25% per hour. This may influence the final results (measurement of high-quality wafers even with a resolution of 1 mm takes up to 30 minutes).

The disadvantage of this solution is the somewhat problematic reproducibility of measurement, as a significant decrease of the average lifetime (more than 10%) was recorded after each rinsing. The main reason is that there are residues

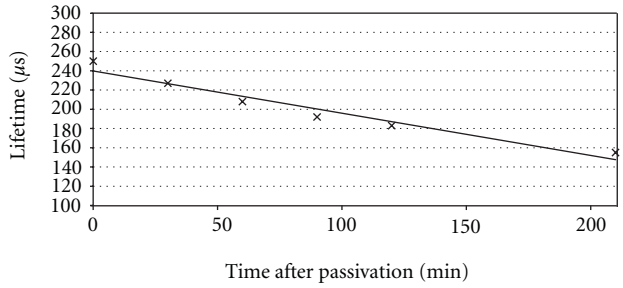

Figure 1: Time stability of iodine passivation.

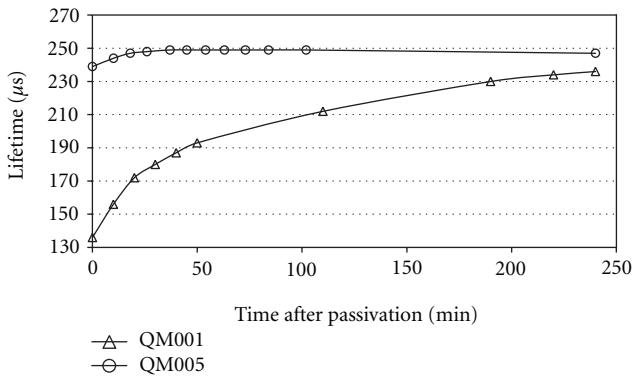

Figure 2: Comparison of the passivation startup between QM001 and QM005.

of the solution left on the surface thus degrading it, and therefore it is not possible to achieve equal or similar results. Next problem may be caused by ethanol, which can decrease surface tension and hinder the texture creating process after the postpassivation cleaning. There are areas without any texture on the surface after the alkaline texturing in 3% NaOH solution. For other solutions which contained methanol instead of ethanol, this phenomenon did not exist and the process of texturation was completed in the standard way.

3. Chemical Passivation in Quinhydrone/Methanol Solution

3.1. Comparison between QM001 and QM005. The quinhydrone/methanol solution shows a very good time stability [3, 4]. There is nearly no decrease in average lifetime values observed approximately after 2 hours after their stabilization at reached maxima, and even later the measured values decreased by only about 10% within 10 hours. The solution with the concentration of 0.01 mol/dm^3 marked QM001 (218 mg of quinhydrone in 100 mL of methanol) cannot be used for practical purposes, because the start-up of passivation abilities in this case is about 3 hours (see Figure 2).

This solution can be used to measure the efficiency of rinsing after the chemical passivation. Quinhydrone residues which remain on the surface increase the concentration of the solution near the surface and thus decrease the startup time of the passivating abilities. This can be recognized from

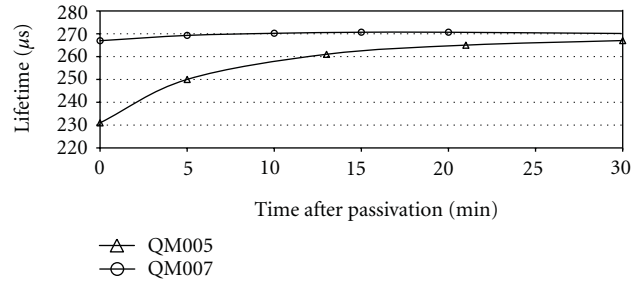

Figure 3: Comparison of the passivation startup between QM005, and QM007.

a graph, and it can be estimated how much quinhydrone remains on the surface of the rinsed wafer.

The solution marked as QM005 (the solution with concentration of 0.05 mol/dm^3) has a significantly lower passivation ability start-up time (20 minutes for polished wafers and 40 minutes for textured wafers). However, it is not yet sufficient enough for practical lifetime measurement for industrial use.

3.2. Quinhydrone/Methanol Solution QM007. It is possible to meet all the initial requirements with concentration of 0.07 mol/dm^3, marked QM007. The startup is nearly immediate (see Figure 3). This solution passivates immediately after the wafer diving for polished wafers and within 10 minutes for textured wafers. The solution also meets the time stability requirement (minimally 1 hour and then a decrease of 15% in 10 hours). This solution also exhibits a high reproducibility of the measurement with the possibility to texture Si wafers after effective rinsing.

3.3. Influence of Quinhydrone Concentration on the Temporal Stability of the Passivation Layer

Hypothesis H1. The increasing of quinhydrone concentration in the solution causes rapid degradation of the passivation layer. The reason for this hypothesis is to demonstrate zero impact on the temporal stability of passivation layer. The concentration has to be specified exactly, the high concentrated solutions do not have any importance.

Graphs for both concentrations are parallel (see Figure 4), which means that the velocity of decline is the same and therefore the time degradation of the passivation layer does not depend on the quinhydrone concentration in the solution, hypothesis H1 was rejected.

3.4. Quinhydrone/Methanol Solution with High Concentration for Textured Wafers

Hypothesis H2. The increasing of quinhydrone concentration in methanol will result in the an acceleration of start-up passivation ability for textured silicon wafers.

As the increasing quinhydrone concentration over 0.07 mol/dm^3 produces no effect for textured Si wafers, it is not desirable to increase the concentration (see Figure 5).

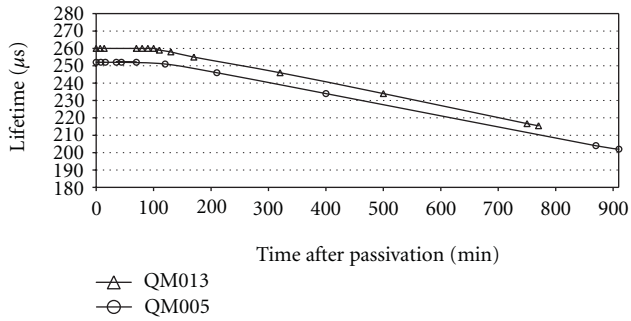

Figure 4: Comparison of the temporal stability of chemical passivation between QM005 and QM013.

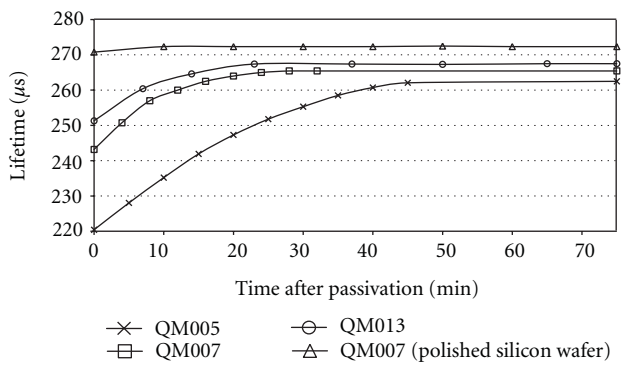

Figure 5: Comparison of the passivation startup between QM005, QM007, and QM013 for textured wafers.

With the concentration of 0.07 mol/dm^3, velocity saturation occurs for textured wafers and further concentration increasing has no effect on the startup of passivation. The solution with a concentration of 0.13 mol/dm^3 is useless for practical purposes, because there is a problem with dissolving of quinhydrone (the solution is "saturated") and quinhydrone crystallisation from the solution produces a large amount of quinhydrone waste. Another problem with the rinse is where the quinhydrone waste quickly pollutes methanol in the rinse cascade.

4. Postpassivation Cleaning

Postpassivation cleaning is important if the wafer should be returned back to the production process, and it is desirable that the silicon surface remains clean, without any remains of the passivation solution that could damage the final solar cell structure or even contaminate the whole series of wafers in next production operations (especially high-temperature operations). The cleaning in pure methanol (see Figure 6) requires an improved rinsing technique, because some surface degradation can be observed after multiple testing. The degradation of 3–5% after each testing is insignificant and caused by scratches and crystal-lattice defects during manipulation.

A possible modification of the cleaning process is based on adding another cleaning step—washing of the wafer in DEMI (demineralized) water with a temperature of 80°C

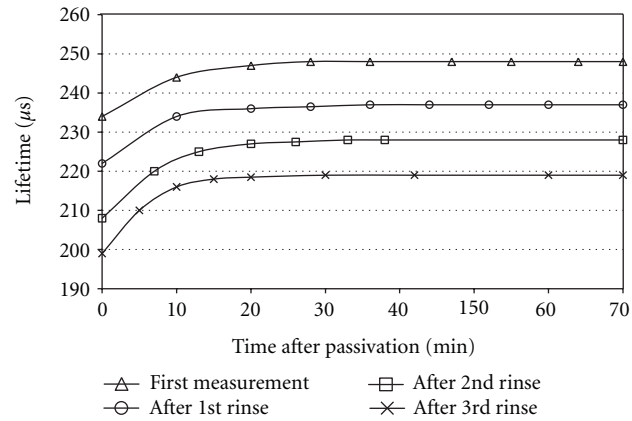

Figure 6: Three cycles of passivation-cleaning process (passivated in QM005).

after the cleaning in pure methanol. But since this rather time-consuming technique is not particularly efficient, the multiple-cleaning process in pure methanol seems to be more acceptable. As quinhydrone is more difficult to resolve and easy to catch at a silicon surface, a methanol cascade was designed. The cascade consists of three small baths filled with methanol. The cleaned wafer goes to the first bath, then it is rinsed by DEMI water (to get rid of most quinhydrone remains). After that comes the second and subsequently the third bath to ensure that the wafer is perfectly clean. After multiple tests the methanol in the last two baths is clean.

5. Conclusions

This work confirms the drawbacks of the commonly used iodine/ethanol passivation, where this solution shows the time instability of the passivation abilities, problems with the reproducibility of the measurement and mainly with cleaning of the solution residues from the surface after the passivation. As a consequence there is a problem in the texturing process after iodine passivation, which may be also caused by decreased surface tension (ethanol).

The quinhydrone/methanol solution, for which the ideal concentration of 0.07 mol/dm^3 was determined, has nearly ideal parameters of the silicon surface chemical passivation. This solution marked as QM007 exhibits a high time stability of the passivation abilities (at least 2 hours without average lifetime decrease and then only a slow decrease of about 10% in 10 hours), immediate startup of passivation abilities (for the polished wafers, and less than 10 minutes for the textured wafers: enlargement of the total surface and its different orientation, where the initial measured lifetime τ is 80% of the maximum), good reproducibility of the measurement (decrease of the average lifetime values by 3–5% after each cleaning, the degradation only due to scratches and crystal-lattice defects during manipulation), and possibility of perfect surface cleaning with the subsequent successful texturing process.

The influence of quinhydrone concentration on the degradation of passivation layer was verified. With increasing

concentration, there was no degradation; therefore hypothesis H1 was rejected. When increasing quinhydrone concentration in methanol concentration over 0.07 mol/dm^3, a faster start-up passivation ability for textured wafers was not achieved and hypothesis H2 was rejected.

For practical use of chemical passivation of silicon surfaces for minority carrier bulk-lifetime measurements, the ideal solution is QM007 which overtops the commonly used chemical passivation in iodine/ethanol solution. Postpassivation cleaning in a methanol cascade is a sufficient rinsing technique.

Acknowledgments

This research was supported by R&D Project FEKT-S-11-7 at the Brno University of Technology and supported by "Centre for Research and Utilization of Renewable Energy" CVVOZE CZ.1.05/2.1.00/01.0014.

References

[1] A. Cuevas and D. Macdonald, "Measuring and interpreting the lifetime of silicon wafers," *Solar Energy*, vol. 76, no. 1–3, pp. 255–262, 2004.

[2] H. Hasegawa, T. Sato, S. Kasai, B. Adamowicz, and T. Hashizume, "Dynamics and control of recombination process at semiconductor surfaces, interfaces and nano-structures," *Solar Energy*, vol. 80, no. 6, pp. 629–644, 2006.

[3] H. Takato, I. Sakata, and R. Shimokawa, "Quinhydrone/Methanol treatment for the measurement of carrier lifetime in silicon substrates," *Japanese Journal Of Applied Physic*, vol. 40, pp. 1003–1004, 2001.

[4] H. Takato, I. Sakata, and R. Shimokawa, "Surface passivation effect of silicon substrates due to quinhydrone/methanol treatment," *Japanese Journal Of Applied Physics*, vol. 41, pp. 870–872, 2002.

Hindawi Publishing Corporation
International Journal of Photoenergy
Volume 2012, Article ID 418924, 5 pages
doi:10.1155/2012/418924

Research Article

Photothermal Deflection Spectroscopy Study of Nanocrystalline Si (nc-Si) Thin Films Deposited on Porous Aluminum with PECVD

S. Ktifa,[1] M. Ghrib,[2] F. Saadallah,[1] H. Ezzaouia,[2] and N. Yacoubi[1]

[1] *Photothermal Laboratory, Nabeul, Tunisia*
[2] *Photovoltaic Laboratory, Research and Technology Centre of Energy, Borj-Cedria Science and Technology Park, BP 95, 2050 Hammam-Lif, Tunisia*

Correspondence should be addressed to F. Saadallah, faycel1@yahoo.fr

Received 15 December 2011; Revised 12 February 2012; Accepted 13 February 2012

Academic Editor: Bhushan Sopori

We have studied the optical properties of nanocrystalline silicon (nc-Si) film deposited by plasma enhancement chemical vapor deposition (PECVD) on porous aluminum structure using, respectively, the Photothermal Deflection Spectroscopy (PDS) and Photoluminescence (PL). The aim of this work is to investigate the influence of anodisation current on the optical properties of the porous aluminum silicon layers (PASL). The morphology characterization studied by atomic force microscopy (AFM) technique has shown that the grain size of (nc-Si) increases with the anodisation current. However, a band gap shift of the energy gap was observed.

1. Introduction

Porous anodic alumina films are an interesting material [1] for nanotechnology applications because of their unusual properties compared to the bulk counterparts [2]. Many works have been published relative to the deposition of porous aluminum films [3, 4]. Different methods of film growth on the surface of the porous matrix layer were used, as for example reactive sputtering [5] and low pressure metal-organic chemical vapor deposition [6].

In this work we demonstrate the capability to grow porous aluminum layers (PAL) by a simple electrochemical anodisation method. The anodizing process was done by varying the anodizing voltage between 200 to 400 mV. Crystalline silicon films are deposited on the PAL by a PECVD technique. Photothermal deflection spectroscopy (PDS) is used to determine the optical absorption spectrum and gap energy by comparing the experimental amplitude of the photothermal signal to the corresponding theoretical one. PL and PDS are used in order to study the influence of anodic current on optical properties of our samples. For this purpose, absorption spectrum, gap energies are measured. The optical properties of the deposited films are correlated to the porous aluminum and nc-Si films morphologie.

2. Film Preparation

High-purity aluminum foil (99.997%), 0.25 mm thick, was used as a starting material. The cleaned samples were anodized during 25 min in a solution of diluted sulfuric acid with 66.66% H_2SO_4 and 33.33% H_2O_2 at room temperature and with five different anodization currents (200 mA, 250 mA, 300 mA, 350 mA, and 400 mA). On the surface, nc-Si films were deposited by PECVD technique [7] at 50°C using a gas mixture of silane and H_2 at a total pressure of 0.5 mTorr.

3. AFM Characterization

The surface morphology of the films was examined by atomic force microscopies. Figure 1 shows AFM images of porous Al filled of nc-Si and obtained with different anodisation currents varying from 200 mA to 400 mA. The surface shows

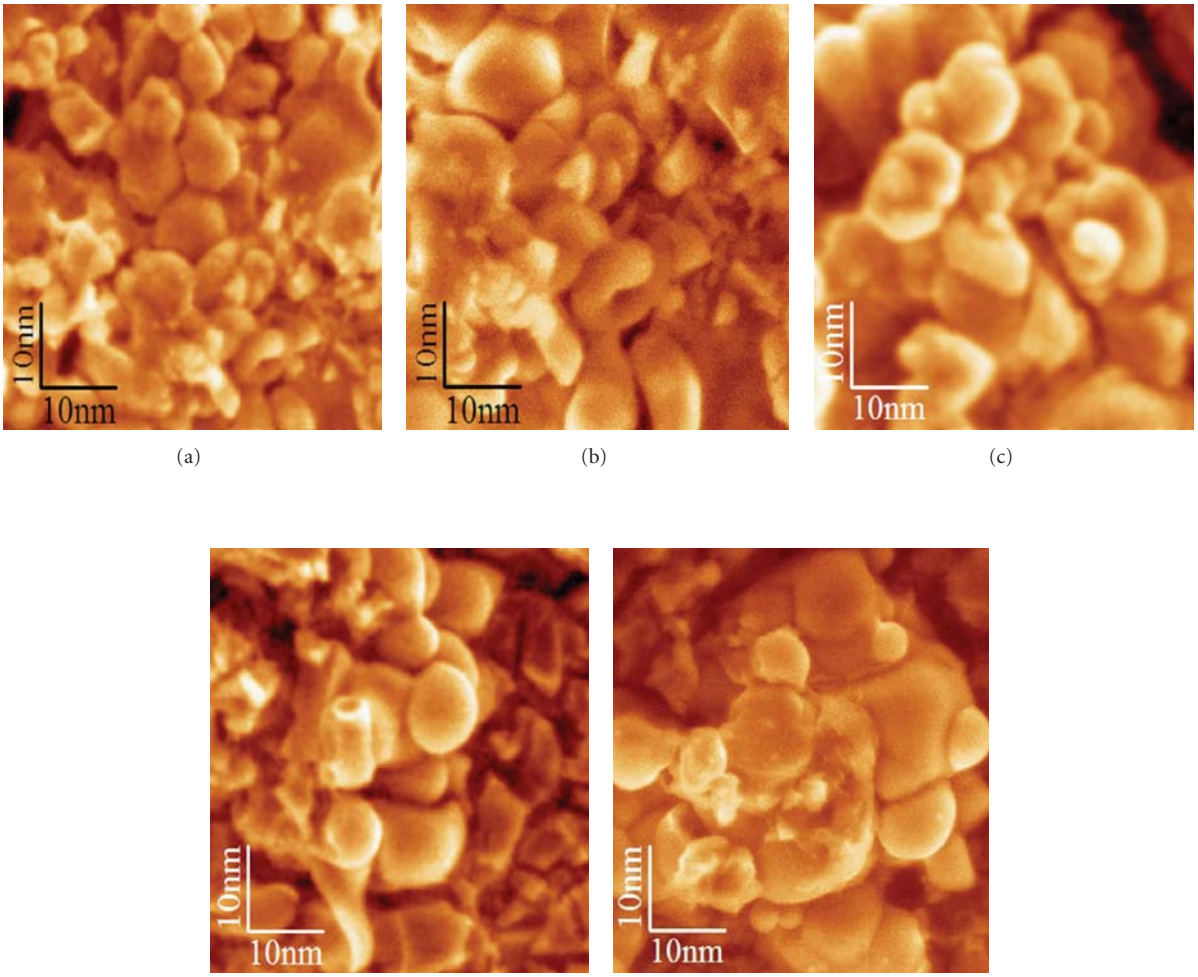

Figure 1: AFM images of silicon deposited on porous aluminum layer (PAL) as a function the anodisation current.

spherical domes with an average size (as estimated from the AFM images), varying approximately from 12 to 15 nm as a function of the anodisation current.

4. Optical Characterization

4.1. Photoluminescence. The PL properties were measured using an Ar laser ($\lambda = 364$ nm) and detected by a cooled GaInAs detector with a standard technique using a lock-in.

Figure 2(a) shows the PL spectrum of the nc-Si layer. The PL emission lies in the orange region of the visible spectral range. The PL band peak position varies from 616 nm to 624 nm (2 and 1.98 eV, resp.) as I_a increases from 200 to 400 mA. This observed PL does not seem to have its origin only from silicon nanocrystals embedded in the porous aluminum matrix, as proposed by Ong and Zhu [8] but it is due to the contributions of the two materials (Si incorporated in PAL). To assure that these peaks come from the nc-Si films, we have measured the PL of porous Al (without nc-Si). As shown in Figure 2(b), the PL peak originates from the PAL that is located at 430 nm (2.8 eV) far from the nc-Si ones. The PL peak position represents a blue shift as the nc-Si size decrease. This effect could be explained by the increase of Si–O/Si–H surface bond ratio [9].

4.2. Photothermal Measurements. The photothermal deflection spectral measurements have been used for investigating optical properties of semiconductors. The great advantage of the PDS is that it is a direct monitor of the nonradiative recombination processes of photo-excited electrons in a semiconductor.

The experimental setup has been described in detail in [10]. When a sample (Figure 1) is irradiated with modulated and monochromatic beam radiation, the absorbed energy is converted into heat through different relaxation processes. The generated thermal wave diffuses in the material and in the surrounding fluid (CCl_4). The temperature variations in the fluid lead to a refractive index gradient causing the deflection of a probe laser beam (He–Ne 4 mW) skimming the sample surface. This deflection is detected by a position photosensor linked to a lock in amplifier. The obtained photothermal signal has two compounds: amplitude and phase.

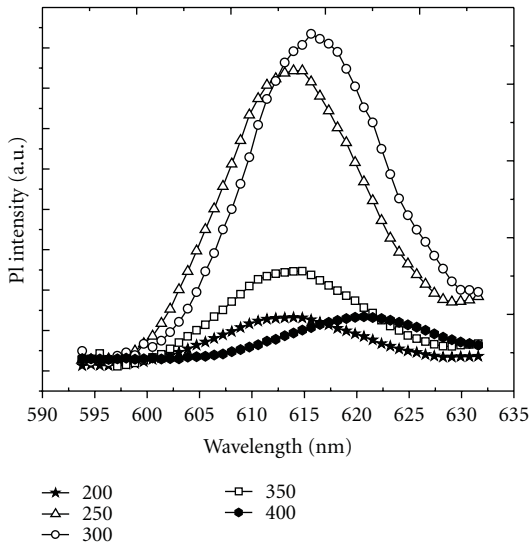

(a)

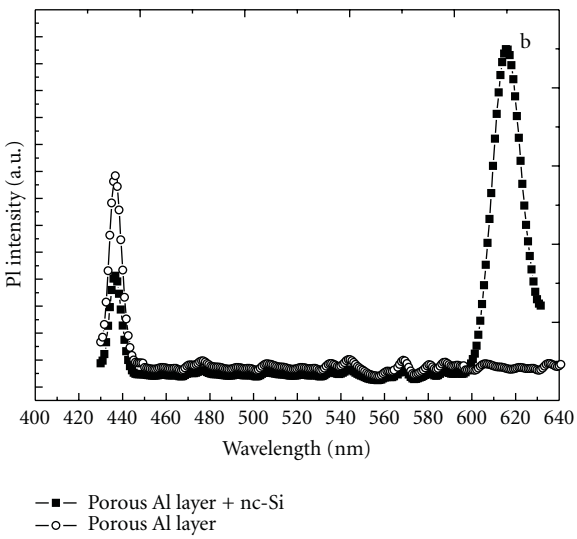

(b)

Figure 2: (a) PL spectra of the nc-Si layer as a function of I_a and (b) typical PL spectrum of nc-Si films compared to PL response of the porous Al layer.

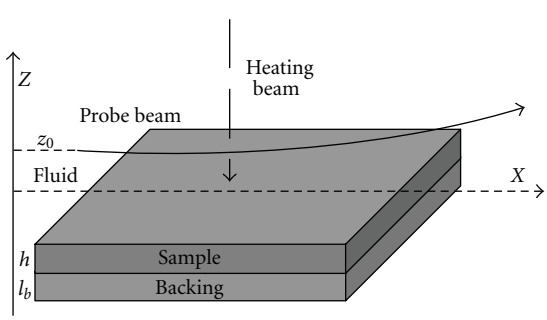

Figure 3: Schema of photothermal deflection principle.

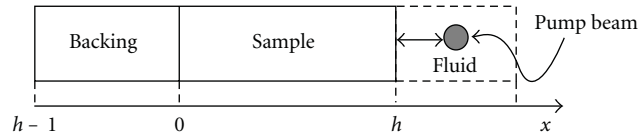

Figure 4: Schema of the PASL sample.

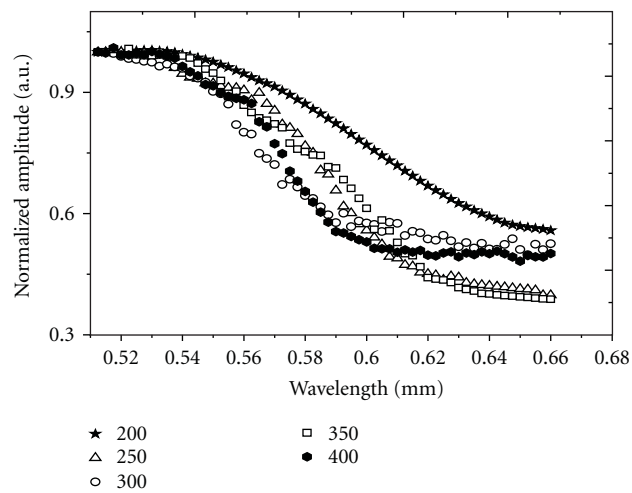

Figure 5: Normalized amplitude obtained with different PASL samples.

The principle of this technique is shown in Figure 3. The probe beam deflection is given by [11]: $= L/n(dn/dT)\sigma_f T_0$ where n is the fluid refractive index, x_0 is the distance between probe beam axis and the sample surface, and L is the sample length. $\sigma_f = (1+j)/\mu_f$, $\mu_f = \sqrt{D_f/\pi F}$ is thermal diffusion length in the fluid, D_f the thermal diffusivity, and F is the modulation frequency of the heating beam. We notice that the deflection is proportional to the complex temperature expression T_0 at the sample surface. This temperature T_0 is calculated by solving the one-dimensional heat equation in the different media sample, backing, and the surrounding fluid (Figure 4):

$$\begin{aligned}
\frac{\partial T_f}{\partial x^2} &= \frac{1}{D_f}\frac{\partial T_f}{\partial t} \quad \text{for } x > 0,\\
\frac{\partial T_e}{\partial x^2} &= \frac{1}{D_e}\frac{\partial T_b}{\partial t} - A\exp(\alpha x)\ \ 1+\exp\ \ jwt\ \ , \\
&\qquad\qquad \text{for } -h < x < 0,\\
\frac{\partial T_b}{\partial x^2} &= \frac{1}{D_b}\frac{\partial T_b}{\partial t}, \quad \text{for } -h-l_b\ < x < -h.
\end{aligned} \tag{1}$$

These equations are solved while taking into account of the boundary conditions at different interfaces. The obtained surface temperature T_0 is given by

$$T_0 = \frac{\alpha I_0}{2K_e(\alpha^2-\sigma^2)}\ \ \frac{(r-1)(b+1)\exp(\sigma_e h) - (r+1)(b-1)\exp(-\sigma_e h) + 2(b-r)\exp(-\alpha h)}{g+1\ \ (b+1)\exp(\sigma_e h) -\ \ g-1\ \ (b-1)\exp(-\sigma_e h)}\ . \tag{2}$$

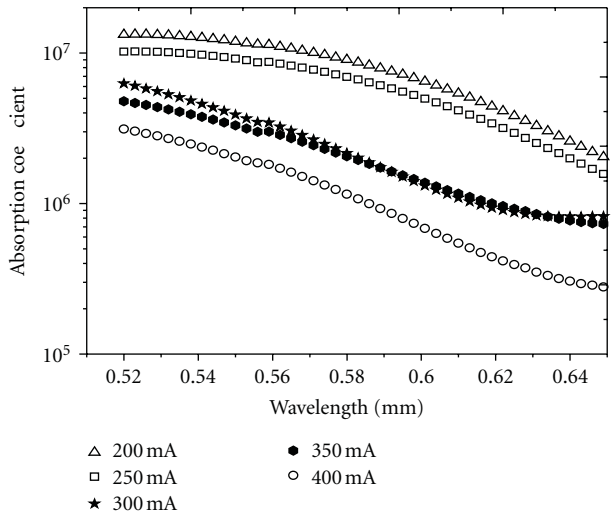

Figure 6: Optical absorption spectra of PASL samples.

Table 1: Evolution of the bandgap energies.

PASL Sample	Anodisation current I_a (mA)	E_g (eV) PDS	E_g (eV) PL
A	200	2.2	2.2
B	250	2	1.99
C	300	2.01	1.9
D	350	1.95	1.98
E	400	1.93	1.97

Thermal and optical parameters that appear in the above expression are given in [12].

4.2.1. Near Gap Absorption Spectrum. Figure 5 shows the obtained experimental curves of the normalized amplitude for the studied samples: nanocrystalline Si (nc-Si) thin films deposited on porous aluminum by plasma-enhanced chemical vapor deposition as a function the anodisation current. 200, 250, 300, 350, and 400 mA. The amplitude shows two saturations zones corresponding, respectively, to high and low optical absorption coefficient. For energy higher than the gap energy, the sample is optically opaque (maximum amplitude) and became more and more transparent when the energy decreases (minimum amplitude). We notice that in the subband gap region, the amplitude saturates at different minimum values for each sample.

The comparison of experimental curves of amplitude versus wavelength to theoretical amplitude versus absorption coefficient permits to obtain the optical absorption spectrum for the samples shown on Figure 6. We remark that the less-anodized sample has a relative higher absorption coefficient in the transparency zone.

4.2.2. Determination of the Gap Energies. In order to obtain the gap energy E_g from optical spectra, we have used the Tauc method [13, 14]. For energies $E = h$ higher than E_g, the quantity $(\alpha E)^n$ should have linear variations with E,

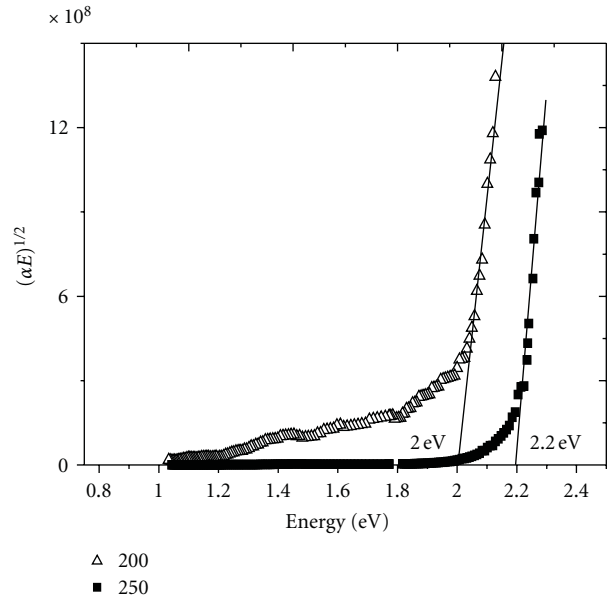

(a)

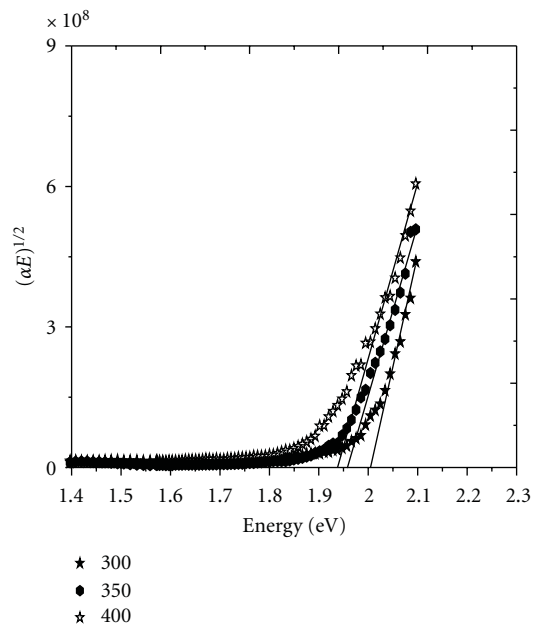

(b)

Figure 7: $(\alpha E)^{1/2}$ versus energy E near the bandgap for the PASL samples.

following the Tauc law: $(\alpha E)^n = \beta(E - E_g)$ where α is the absorption coefficient and β is the slope of the curve. For indirect bandgap semiconductor such as nanocrystalline Si (nc-Si) thin films deposited on porous aluminum: $n = 1/2$. The curves of $(\alpha E)^{1/2}$ versus E are shown in Figures 7(a) and 7(b). The obtained gap energy E_g values are reported in Table 1. We notice a bandgap shift of about 24 mev. The energy bandgap decreases with anodisation current and varies from 2.2 to 1.9 eV as I_a varies from 200 to 400 mA,

respectively (Table 1). The obtained value of E_g agrees with gap energies measured by other authors [15].

Comparison between the various bandgap shows that the optical absorption properties are significantly affected by particle size of the nc-Si films. The fact that these energies are high than the expected ones (for nanosized Si crystal) could be explained by the contribution of alumina in the absorption spectra. Alumina has in fact a high band gap energy ($\approx$3.2 eV) [16] compared to silicon. The effect could be also attributed to the presence of particles with very small size (quantum confinement). In Table 1, the gap energies measured with photoluminescence spectra and photothermal deflection has been compared for different anodized levels. We notice that the E_g is slightly higher than the real gap energy determined by photothermal deflection, because it corresponds to the radiative transition.

5. Conclusion

In this work, nanocrystal silicon thin films were deposited by PECVD technique on a porous aluminum substrate prepared with different anodizations currents. Optical absorption spectrum, and gap energy are measured and analyzed using the PL and PDS techniques. A bandgap shift induced by the anodisation current is detected. We found a correlation between the particle size and the gap energy.

References

[1] L. F. Marsal, L. Vojkuvka, P. Formentin, J. Pallarés, and J. Ferré-Borrull, "Fabrication and optical characterization of nanoporous alumina films annealed at different temperatures," *Optical Materials*, vol. 31, no. 6, pp. 860–864, 2009.

[2] F. Wang, H. Huang, and S. Yang, "Synthesis of ceramic nanotubes using AAO templates," *Journal of the European Ceramic Society*, vol. 29, no. 8, pp. 1387–1391, 2009.

[3] D. Auvergne, J. Camassel, and H. Mathieu, "Band-gap shrinkage of semiconductors," *Physical Review B*, vol. 11, no. 6, pp. 2251–2259, 1975.

[4] G. E. Thompson, "Porous anodic alumina: fabrication, characterization and applications," *Thin Solid Films*, vol. 297, no. 1-2, pp. 192–201, 1997.

[5] Y. Zhao, Y. Qian, W. Yu, and Z. Chen, "Surface roughness of alumina films deposited by reactive r.f. sputtering," *Thin Solid Films*, vol. 286, no. 1-2, pp. 45–48, 1996.

[6] W. Koh, S. J. Ku, and Y. Kim, "Chemical vapor deposition of Al2O3 films using highly volatile single sources," *Thin Solid Films*, vol. 304, no. 1-2, pp. 222–224, 1997.

[7] J. J. Simonne, "State of the art in InP MIS technology," in *Proceedings of the International Conference (INFOS '83)*, pp. 63–70, Eindhoven, The Netherlands, 1983.

[8] P. P. Ong and Y. Zhu, "Strong photoluminescence with fine structures from sandwich-structured films of silicon nanoparticles embedded in Al_2O_3 matrices," *Physica E*, vol. 15, no. 3, pp. 118–123, 2002.

[9] H. C. Chen, W. Wang, K. N. Manjularni, L. C. Snyder, and X. L. Zheng, "Heating laser irradiation and passivation study on the light-emitting porous silicon," *Materials Research Society Symposium Proceedings*, vol. 256, pp. 197–202, 1992.

[10] F. Saadallah, N. Yacoubi, F. Genty, and C. Alibert, "Investigation of thermal and optical properties of distributed Bragg reflectors by photothermal deflection spectroscopy," *Applied Optics*, vol. 41, no. 36, pp. 7561–7568, 2002.

[11] S. Abroug, F. Saadallah, and N. Yacoubi, "Determination of doping effects on Si and GaAs bulk samples properties by photothermal investigations," *Physica B*, vol. 400, no. 1-2, pp. 163–167, 2007.

[12] "Photothermal and photoacoustic spectroscopy measurement," in *Handbook of Optical Constants*, vol. 3, p. 88, 1998.

[13] S. E. Aw, H. S. Tan, and C. K. Ong, "Optical absorption measurements of band-gap shrinkage in moderately and heavily doped silicon," *Journal of Physics: Condensed Matter*, vol. 3, no. 42, article no. 016, pp. 8213–8223, 1991.

[14] A. Chandola, R. Pino, and P. S. Dutta, "Below bandgap optical absorption in tellurium-doped GaSb," *Semiconductor Science and Technology*, vol. 20, no. 8, pp. 886–893, 2005.

[15] M. Ghrib, M. Gaidi, T. Ghrib, N. Khedher, M. Ben Salam, and H. Ezzaouia, "Morphological and optical properties changes in nanocrystalline Si (nc-Si) deposited on porous aluminum nanostructures by plasma enhanced chemical vapor deposition for Solar energy applications," *Applied Surface Science*, vol. 257, no. 21, pp. 9129–9134, 2011.

[16] I. Costina and R. Franchy, "Band gap of amorphous and well-ordered Al2O3 on Ni3Al(100)," *Applied Physics Letters*, vol. 78, no. 26, pp. 4139–4141, 2001.

Hindawi Publishing Corporation
International Journal of Photoenergy
Volume 2012, Article ID 857567, 5 pages
doi:10.1155/2012/857567

Research Article

Layer-by-Layer CdS-Modified TiO_2 Film Electrodes for Enhancing the Absorption and Energy Conversion Efficiency of Solar Cells

Ming Li,[1,2] Yong Liu,[1] Hai Wang,[1,2] Wenxia Zhao,[2] Hong Huang,[2] Chaolun Liang,[3] Youjun Deng,[1] and Hui Shen[1]

[1] *School of Physics and Engineering and State Key Laboratory of Optoelectronic Materials and Technologies and Institute for Solar Energy Systems, Sun Yat-sen University, Guangzhou 510275, China*
[2] *School of Chemical and Biologic Engineering, Guilin University of Technology, Guilin 541004, China*
[3] *Instrumental Analysis and Research Center, Sun Yat-sen University, Guangzhou 510275, China*

Correspondence should be addressed to Yong Liu, liuyong7@mail.sysu.edu.cn

Received 14 November 2011; Accepted 31 January 2012

Academic Editor: Peter Rupnowski

A layer-by-layer assemble method was used to fabricate CdS quantum dots (QDs) sensitized electrodes. Scanning electron microscopy (SEM), energy-dispersive X-ray spectroscopy (EDS), and transmission electron microscopy (TEM) have been utilized to characterize the samples. The absorption spectra and photovoltaic measurement confirmed that much more effective deposition of QDs in TiO_2 matrix and much better power conversion performance were achieved for these multilayer electrodes compared with the ones fabricated by traditional single-layer assembly method.

1. Introduction

In recent years, dye-sensitized solar cells (DSSCs) have attracted a lot of scientific and technological interests owing to their high energy conversion efficiency, low production cost, and a facile fabrication process [1–3]. Besides conventional ruthenium dyes, inorganic short-band-gap semiconductor quantum dots, such as CdS, CdSe, CdTe, PbS and others, have been researched as the good candidate sensitizers in the so-called quantum-dot-sensitized solar cell (QD-SSC) [4–7]. The advantage of inorganic QDs over conventional ruthenium dyes is that QDs can generate multiple electron-hole pairs per proton and improve the efficiency of the solar cells [8]. In addition, QDs' optic and electronic properties can be adjusted to match the solar spectrum much better by changing their shape and size [9–11]. However, the difficulty of penetrating QDs into the mesoporous TiO_2 matrix hindered QD-SSCs from achieving higher energy conversion efficiency. The QDs assembly difficulty can mainly be attributed to the two following reasons: (1) QDs are generally not bound effectively to the TiO_2 crystalline surface to form a firmly anchoring QDs monolayer on TiO_2 nanoparticles [12]. (2) It is relatively difficult for nanoscale QDs to penetrate deep into the TiO_2 mesoporous films and deposit in the underlayer of TiO_2 film. To solve the first problem, the various bifunctional surface modifiers are adopted as linker molecules to anchor the QDs on TiO_2 surface, which indeed enhance assembly of QDs [13–15]. But little attention focused on the second problem. It is still unachievable to obtain an entire coverage of QDs on the surface of TiO_2 crystal throughout the mesoporous films.

In this work, we used multilayered quantum dots assembly method to fabricate CdS QDs sensitized solar cells. The increased coverage ratio, incorporation amount of QDs, and effective deposition of QDs in underlayer of TiO_2 mesoporous films were expected for these multilayer CdS quantum-dots-sensitized solar cells.

2. Experimental Details

8 g TiO_2 powder (P25, Degussa) was thoroughly mixed with 100 mL distilled water by vigorous stirring and ultrasonic. The slurry was then sprayed on transparent conductive oxide (TCO) glass (14 Ω/squ, Nippon Sheet Glass) and the films were dried at 120°C for 10 min. For CdS quantum dot

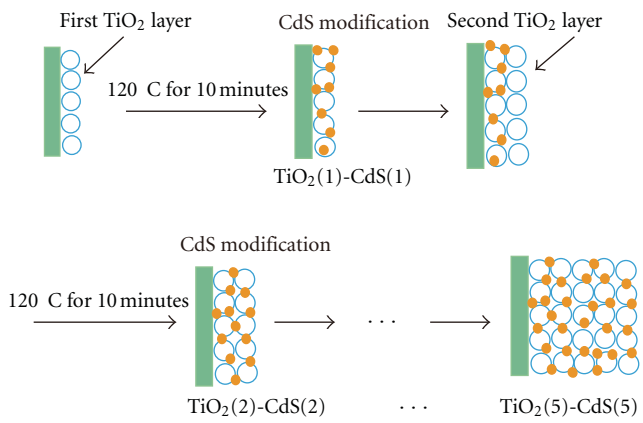

Figure 1: The preparation process of multilayer CdS-sensitized TiO_2 electrodes.

deposition, the TiO_2 films were immersed in 20 mL solution containing 0.002 mmol $Cd(NO_3)_2$, 1 mmol thiourea, and 0.02 mol $NH_3 \cdot H_2O$ and heated up to 60°C for two hours. The as-prepared samples were cleaned sequentially with distilled water. The spraying-drying-depositing procedure was termed as one SDD cycle. One to five cycles were applied to fabricate the $TiO_2(n)$-$CdS(n)$ electrodes ($n = 1$–5). The process used for the preparation of the $TiO_2(n)$-$CdS(n)$ electrodes was displayed in Figure 1. For comparison, one-step (abbr. OS) preparation of TiO_2 film (TiO_2(OS)) with almost same thickness as $TiO_2(5)$ was also fabricated. CdS deposition process was similar to the procedure ascribed above except the longer CdS bath time of 10 h. TiO_2(OS)-CdS and multilayer $TiO_2(n)$-$CdS(n)$ ($n = 1$–5) electrodes were all annealed at 400°C for 30 min in nitrogen.

A surlyn spacer (30 μm thick, DuPont) was sandwiched between the CdS quantum-dot-sensitized electrode and the Pt-coated counterelectrode. The space between the electrodes was filled with the polysulphide electrolyte which consisted of Na_2S (0.5 M), S (0.125 M), and KCl (0.2 M), using water/methanol (7 : 3 by volume) solution as co-solvent. A 0.25 cm^2 active area was defined by a hole punched through the surlyn frame and was additionally masked from illumination by black electrical tape to the same size.

The morphology and chemical composition of photoanode were examined by field-emission scanning electron microscopy (FESEM, JSM-6330F) equipped with an energy-dispersive X-ray spectrometer (EDS) analyzer. The detailed microscopic characterization of CdS QDs was analyzed using transmission electron microscope (TEM, JEM-2010HR). Absorption spectra of samples were recorded using a spectrophotometer (Hitachi U-4100). The photocurrent-voltage (I-V) curve of each cell was measured by Keithley 2400 source meter under an illumination of a solar simulator (Newport Oriel 91192) at 100 mW cm^{-2}. Electron impedance spectroscopy (EIS) measurements were carried out by applying a 10 mV AC signal over the frequency range of 10^{-2}–10^5 Hz under 100 mW cm^{-2} illumination at open circuit voltage by using an electrochemical workstation (CHI760C).

3. Results and Discussion

Figures 2(a) and 2(b) are the SEM images of TiO_2 film before and after CdS quantum dots deposition, respectively. The bare nanocrystalline TiO_2 film was exhibited in Figure 2(a). After CdS modification, there was a coating assembled on the surface of TiO_2 nanoparticles (Figure 2(b)). The EDS analysis (Figure 2(c)) confirmed that this coating consist of CdS. Figure 2(d) shows the TEM image of the CdS nanocrystal. The distance of 0.337 and 0.245 nm between the adjacent lattice fringes can be assigned to the interplanar distance of hexagon CdS (002) and (102) face, respectively. The diameter of QDs was about in the range of 5∼10 nm.

Figure 3 shows the comparison of the absorption spectrum of multilayer electrodes. The absorbance intensities of electrodes increased with SDD cycles. The absorption peaks of CdS-modified electrodes with different cycles were almost at same position of 450 nm, which was consistent to the value reported in the literature [16]. For $TiO_2(5)$-$CdS(5)$, the absorption edge was approximately 510 nm, which was obtained from the intersection of the sharply decreasing region of a spectrum with its baseline. Corresponding to this absorption edge, the band gap was calculated to be 2.43 eV. That was higher than 2.25 eV, the value reported for CdS in bulk [16]. It indicated that the size of the CdS particles deposited on the TiO_2 films were still within the scale of quantum dots. The size of CdS particles was possible to be estimated from the excitonic peaks of the absorption spectra based on the empirical equations proposed by Yu et al. [17]. Then the mean diameter of CdS particles deposited on the TiO_2 films was calculated to be ca. 8.23 nm. The size of CdS calculated based on empirical equations was consistent with that observed in TEM image. For comparison, the UV-Vis absorption spectra of TiO_2(OS)-CdS was also showed in Figure 3. The absorbance of TiO_2(OS)-CdS was lower than that of $TiO_2(5)$-$CdS(5)$ although their film thickness were almost the same, which displayed the superiority of multilayered electrodes in depositing quantum dots. The absorption edge of TiO_2(OS)-CdS was also at ca. 510 nm, indicating that the size of CdS particles on TiO_2(OS) was the same as that on multilayered electrodes.

The effect of SDD cycles on the device performance has also been studied. The photocurrent-voltage (I-V) curves of the QD-SSCs using $TiO_2(n)$-$CdS(n)$ ($n = 1$–5) and TiO_2(OS)-CdS as photoelectrodes were showed in Figure 4. It was considered that the absorption spectrum of photoelectrodes played an important role in determining the energy conversion efficiency of DSSCs. Inferred from Figures 3 and 4, the I-V properties of $TiO_2(n)$-$CdS(n)$ QD-SSCs ($n = 1$–5) were consistent to the absorbance of $TiO_2(n)$-$CdS(n)$ electrodes ($n = 1$–5). Table 1 summarizes the open circuit potential (V_{OC}), short circuit current density (J_{SC}), fill factor (FF), and overall energy conversion efficiency (η) of these cells. The V_{OC}, J_{SC} and η increased with cycles and the QD-SSC using $TiO_2(5)$-$CdS(5)$ photoelectrode exhibited the best performance due to the most incorporated amount of CdS on electrode. The V_{OC}, J_{SC}, and η of TiO_2(OS)-CdS QD-SSC were only 0.31 V, 0.91 mA cm^{-2}, and 0.11%, respectively, which were much lower than those of $TiO_2(5)$-$CdS(5)$

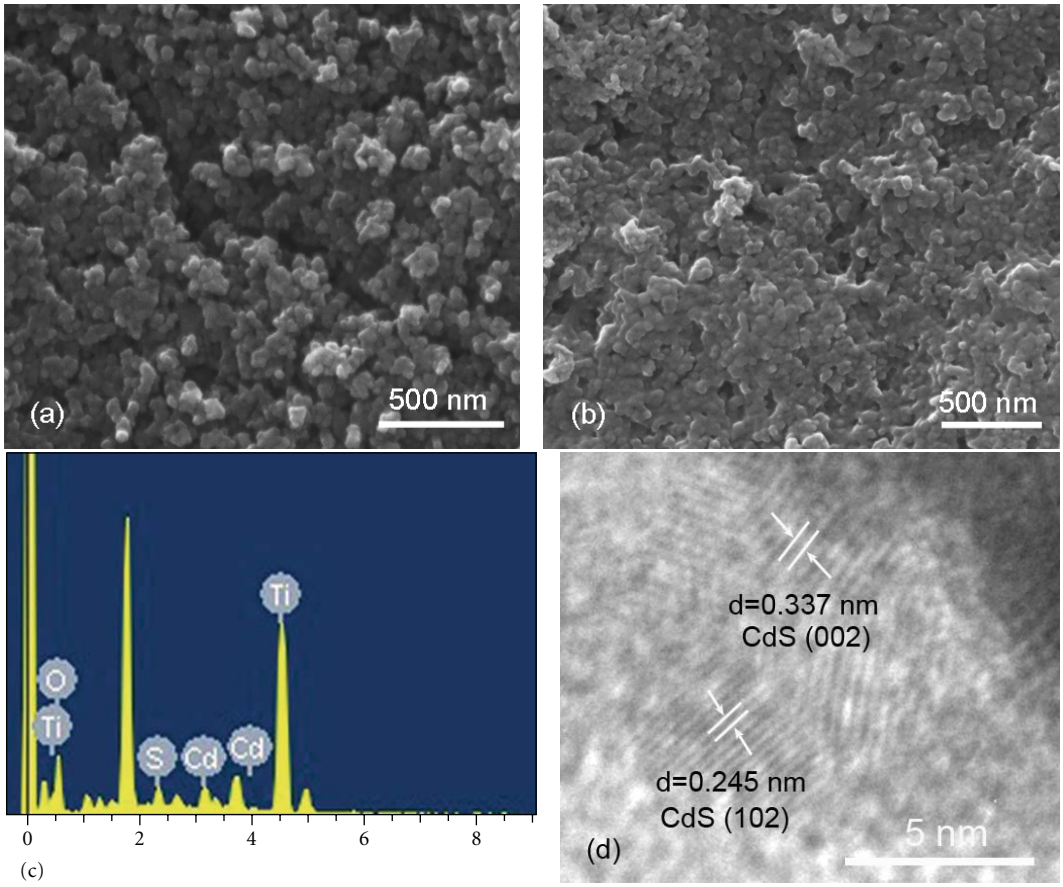

Figure 2: SEM images of TiO_2 nanocrystalline film (a) before and (b) after CdS quantum dots deposition. (c) EDS spectra of CdS-modified TiO_2. (d) TEM image of CdS quantum dots.

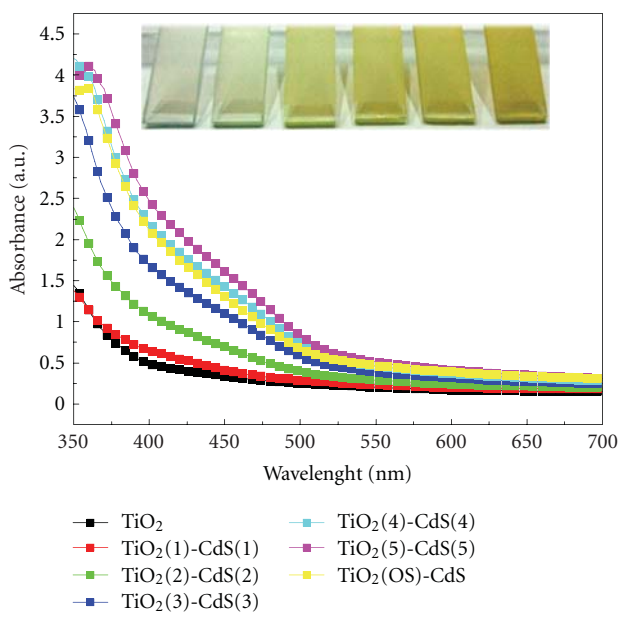

Figure 3: UV-vis absorption spectra of bare TiO_2 nanocrystalline film, $TiO_2(n)$-CdS(n) (n = 1–5) and TiO_2(OS)-CdS electrodes. Photographs of bare TiO_2 and $TiO_2(n)$-CdS(n) (n = 1–5), electrodes were presented in turn as inset.

QD-SSC (0.44 V, 7.12 mA cm^{-2}, and 1.06%), although its absorbance was little lower than that of TiO_2(5)-CdS(5). It may be due to the difficulty for CdS QDs diffusing and depositing in the underlayer of TiO_2 mesoporous film, which resulted in overloading of CdS QDs in the surface of TiO_2 film. Overloading of QDs was reported to be disadvantageous to the cell performance because mesopores were blocked by extra loading of CdS QDs and the electrolyte diffusion was also hindered [18]. So the advantage of multilayer TiO_2 films in cell performance over the traditional TiO_2 films was evident. The sealed multilayer CdS QDSSCs displayed good stability still retaining over 90% of their initial efficiency after 720 h of storage in ambient conditions. Here we used only CdS QDs as multilayer sensitizer in this work. It is very promising to deposit different kinds of QDs, such as CdSe, CdTe, and PbSe and the others in multilayers of electrodes. The extending of absorption range, the increase of absorbance, and improvements in the cell efficiency could be possible for solar cell fabricated by multilayer TiO_2 film sensitized by multiple QDs with different absorption spectra range.

Electron impedance spectroscopy of multilayer QD-SSCs, shown in Figure 5, were measured to investigate the kinetics of charge transfer and recombination. An equivalent

Table 1: A summary of photovoltaic and photoelectron transport properties of CdS QD-SSCs under AM1.5 condition.

Sample	V_{OC} (V)	J_{SC} (mA cm^{-2})	FF (%)	η (%)	R_k (Ω)	k_{eff} (s^{-1})	τ_{eff} (s)	$D_{eff} \times 10^8$ (cm^2/s)	Film thickness (μm)
TiO_2(1)-CdS(1)	0.16	0.91	35.2	0.05	308.75	8.291	0.121	3.770	1.2
TiO_2(2)-CdS(2)	0.33	1.71	30.5	0.17	254.86	6.876	0.145	5.331	2.8
TiO_2(3)-CdS(3)	0.42	3.58	29.4	0.44	228.15	3.167	0.316	8.251	3.9
TiO_2(4)-CdS(4)	0.42	5.40	29.9	0.66	197.18	4.663	0.214	24.193	4.9
TiO_2(5)-CdS(5)	0.44	7.12	33.7	1.06	157.33	5.638	0.177	43.264	5.6
TiO_2(OS)-CdS	0.31	0.91	37.9	0.11	312.71	6.876	0.145	38.763	5.8

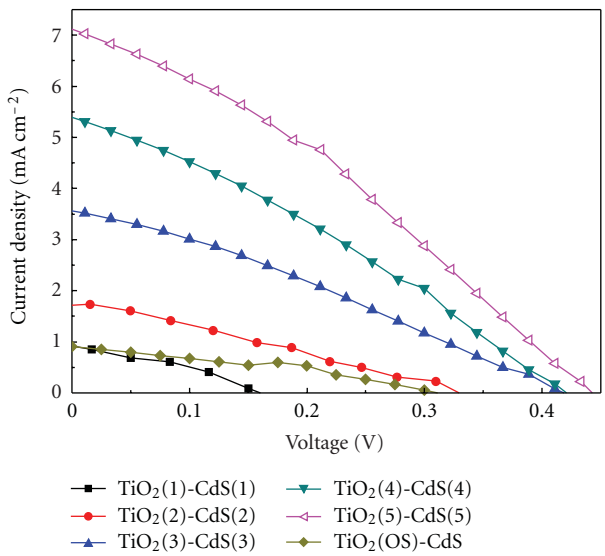

Figure 4: Photocurrent-voltage curves of CdS QD-SSCs measured under AM1.5 condition. The active surface area was 0.25 cm^2.

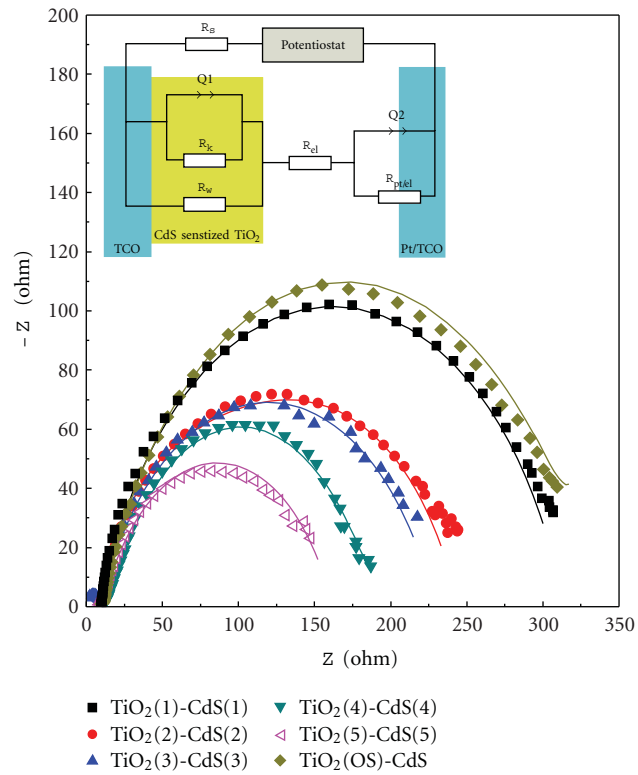

Figure 5: Experimental (dots) and fitted (solid curve) Nyquist plots of CdS QD-SSCs under AM1.5 condition. The equivalent circuit used to fit the experimental data was shown as inset.

circuit used to fit the experimental data was shown as inset in Figure 5. By modeling and fitting the Nyquist plots, the electron transport parameters such as charge transfer resistance related to recombination of electrons at the TiO_2/electrolyte interface (R_k), the first-order reaction rate constant for loss of electrons (k_{eff}), electron life time (τ_{eff}) and effective diffusion coefficient (D_{eff}) were extracted and also presented in Table 1. It was clear that R_k decreased with the SDD cycles, for which there are two possible reasons: (1) an increase in film thickness and (2) an increase in the electron density owing to the increasing current density. k_{eff} decreased with cycles varying from 1 to 3. Thus, the recombination rate decreased with cycles when cycle was below 3. This showed the reason the value of J_{SC} and η increases greatly when cycles were within 3. But k_{eff} increased when cycle was more than 3. The increasing recombination rate means that electrons were lost rapidly by recombination. Inferred from Table 1, although FF decreased with cycle changing from 1 to 3 and then increased when cycle was above 3, the growth rate of η for cells with cycle above 3 decreased comparing with that for ones with cycle below 3 under considering the rate of increase for film thickness. It was deduced that the increase of electron recombination rate may contribute to the decreasing growth rate of η above 3 SDD cycles. D_{eff} increased with the increasing film thickness, which was consistent with the result reported by Adachi et al. [19]. As for TiO_2(OS)-CdS, the R_k value was similar with that of TiO_2(1)-CdS(1), which should due to similar current density of these two cells.

4. Conclusion

We have demonstrated a layer-by-layer assembling method to improve the coverage of QDs on the surface of TiO_2 crystal throughout the mesoporous films effectively and its application in QD sensitized solar cells. The multilayer electrodes showed much more effective deposition of QDs in TiO_2 matrix and better power conversion performance, compared with the ones fabricated by traditional method.

The open circuit voltage, short circuit current, and overall power conversion efficiencies of multilayer CdS QD-SSCs increased with the layers and reached maximum value, 0.44 V, 7.12 mA cm^{-2}, and 1.06%, respectively, for 5 layers.

Acknowledgments

The authors gratefully acknowledge financial support from National Basic Research Program of China (973 Program) (no. 2012CB933704), the Fundamental Research Funds for the Central Universities (no. 10lgpy17), the Research Fund of State Key Laboratory of Optoelectronic Materials and Technologies, China (no. 2010-RC-3-3), and the Production and Research Project of Guangdong Province and Ministry of Education, China (no. 2010B090400020).

References

[1] B. O'Regan and M. Grätzel, "A low-cost, high-efficiency solar cell based on dye-sensitized colloidal TiO_2 films," *Nature*, vol. 353, no. 6346, pp. 737–740, 1991.

[2] M. Grätzel, "Photoelectrochemical cells," *Nature*, vol. 414, no. 6861, pp. 338–344, 2001.

[3] M. Grätzel, "Solar energy conversion by dye-sensitized photovoltaic cells," *Inorganic Chemistry*, vol. 44, no. 20, pp. 6841–6851, 2005.

[4] Y. Zhang, T. Xie, T. Jiang et al., "Surface photovoltage characterization of a ZnO nanowire array/CdS quantum dot heterogeneous film and its application for photovoltaic devices," *Nanotechnology*, vol. 20, no. 15, Article ID 155707, 2009.

[5] K. S. Leschkies, R. Divakar, J. Basu et al., "Photosensitization of ZnO nanowires with CdSe quantum dots for photovoltaic devices," *Nano Letters*, vol. 7, no. 6, pp. 1793–1798, 2007.

[6] C. Ratanatawanate, C. Xiong, and K. J. Balkus, "Fabrication of PbS quantum dot doped TiO_2 nanotubes," *ACS Nano*, vol. 2, no. 8, pp. 1682–1688, 2008.

[7] X. Cao, P. Chen, and Y. Guo, "Decoration of textured ZnO nanowires array with CdTe quantum dots: enhanced light-trapping effect and photogenerated charge separation," *Journal of Physical Chemistry C*, vol. 112, no. 51, pp. 20560–20566, 2008.

[8] A. J. Nozik, "Exciton multiplication and relaxation dynamics in quantum dots: applications to ultrahigh-efficiency solar photon conversion," *Inorganic Chemistry*, vol. 44, no. 20, pp. 6893–6899, 2005.

[9] L. Bakueva, I. Gorelikov, S. Musikhin, X. S. Zhao, E. H. Sargent, and E. Kumacheva, "PbS quantum dots with stable efficient luminescence in the near-IR spectral range," *Advanced Materials*, vol. 16, no. 11, pp. 926–929, 2004.

[10] C. Ghosh, S. Pal, P. Sarkar, and T. Frauenheim, "Size and composition dependent electronic and optical properties of $Ga_xAl_{1-x}As$ and $Al_xGa_{1-x}As$ alloyed nanocrystals," *Applied Physics Letters*, vol. 94, no. 12, Article ID 123105, 3 pages, 2009.

[11] D. More, C. Rajesh, A. D. Lad, G. R. Kumar, and S. Mahamuni, "Two photon absorption in Mn^{2+}-doped ZnSe quantum dots," *Optics Communications*, vol. 283, no. 10, pp. 2150–2154, 2010.

[12] G. Y. Lan, Z. Yang, Y. W. Lin, Z. H. G. Lin, H. Y. Liao, and H. T. Chang, "A simple strategy for improving the energy conversion of multilayered CdTe quantum dot-sensitized solar cells," *Journal of Materials Chemistry*, vol. 19, no. 16, pp. 2349–2355, 2009.

[13] Y. J. Shen and Y. L. Lee, "Assembly of CdS quantum dots onto mesoscopic TiO_2 films for quantum dot-sensitized solar cell applications," *Nanotechnology*, vol. 19, no. 4, Article ID 045602, 2008.

[14] I. Mora-Seró, S. Giménez, T. Moehl et al., "Factors determining the photovoltaic performance of a CdSe quantum dot sensitized solar cell: the role of the linker molecule and of the counter electrode," *Nanotechnology*, vol. 19, no. 42, Article ID 424007, 2008.

[15] N. Guijarro, T. Lana-Villarreal, I. Mora-Seró, J. Bisquert, and R. Gómez, "CdSe quantum dot-sensitized TiO_2 electrodes: effect of quantum dot coverage and mode of attachment," *Journal of Physical Chemistry C*, vol. 113, no. 10, pp. 4208–4214, 2009.

[16] Y. L. Lee and Y. S. Lo, "Highly efficient quantum-dot-sensitized solar cell based on co-sensitization of CdS/CdSe," *Advanced Functional Materials*, vol. 19, no. 4, pp. 604–609, 2009.

[17] W. W. Yu, L. Qu, W. Guo, and X. Peng, "Experimental determination of the extinction coefficient of CdTe, CdSe, and CdS nanocrystals," *Chemistry of Materials*, vol. 15, no. 14, pp. 2854–2860, 2003.

[18] P. Sudhagar, J. H. Jung, S. Park et al., "The performance of coupled (CdS:CdSe) quantum dot-sensitized TiO_2 nanofibrous solar cells," *Electrochemistry Communications*, vol. 11, no. 11, pp. 2220–2224, 2009.

[19] M. Adachi, M. Sakamoto, J. Jiu, Y. Ogata, and S. Isoda, "Determination of parameters of electron transport in dye-sensitized solar cells using electrochemical impedance spectroscopy," *Journal of Physical Chemistry B*, vol. 110, no. 28, pp. 13872–13880, 2006.

Hindawi Publishing Corporation
International Journal of Photoenergy
Volume 2012, Article ID 723714, 7 pages
doi:10.1155/2012/723714

Research Article

In Situ and *Ex Situ* Studies of Molybdenum Thin Films Deposited by rf and dc Magnetron Sputtering as a Back Contact for CIGS Solar Cells

K. Aryal,[1] H. Khatri,[2] R. W. Collins,[2] and S. Marsillac[1]

[1] *Department of Electrical and Computer Engineering, Old Dominion University, Norfolk, VA 23529, USA*
[2] *Wright Center for Photovoltaic Innovation and Commercialization, University of Toledo, Toledo, OH 43606, USA*

Correspondence should be addressed to S. Marsillac, smarsill@odu.edu

Received 16 December 2011; Accepted 31 January 2012

Academic Editor: Bhushan Sopori

Molybdenum thin films were deposited by rf and dc magnetron sputtering and their properties analyzed with regards to their potential application as a back contact for CIGS solar cells. It is shown that both types of films tend to transition from tensile to compressive strain when the deposition pressure increases, while the conductivity and the grain size decreas. The nucleation of the films characterized by *in situ* and real time spectroscopic ellipsometry shows that both films follow a Volmer-Weber growth, with a higher surface roughness and lower deposition rate for the rf deposited films. The electronic relaxation time was then extracted as a function of bulk layer thickness for rf and dc films by fitting each dielectric function to a Drude free-electron model combined with a broad Lorentz oscillator. The values were fitted to a conical growth mode and demonstrated that the rf-deposited films have already smaller grains than the dc films when the bulk layer thickness is 30 nm.

1. Introduction

With 20.3% efficiency, $Cu(In,Ga)Se_2$ (CIGS) solar cells are the most efficient polycrystalline thin films solar cells today [1]. Part of the success of this technology comes from the underlying molybdenum layer. It fulfills most requirements for an effective back contact, notably chemical and mechanical compatibility with the other deposition processes, high conductivity, low contact resistance with the CIGS layer, and commensurate thermal expansion coefficient [2]. The deposition of a molybdenum film as a back contact is not by itself, however, an assurance of a high efficiency solar cell. The deposition process and parameters play a key role in obtaining a layer with the appropriate properties. Extensive research has been done on the deposition of molybdenum thin films by direct-current (dc) sputtering [2–6]. As the potential portfolio of CIGS applications expand, different Mo film properties may be required to adapt to new requirements. In this paper, therefore, we have described the use of dc magnetron sputtering to deposit Mo thin films on soda-lime glass and the comparison of such films with those deposited by radio frequency (rf) magnetron sputtering. To our knowledge, much less research has been performed on Mo thin films deposited by this latter method [7–16]. To assess the potential of this process, the physical, electrical, and optical properties of rf and dc sputtered films were studied as a function of argon pressure via *ex situ* and *in situ* measurements.

2. Experimental Details

Molybdenum thin films were fabricated using rf and dc magnetron sputtering onto soda-lime glass (SLG) substrates. The deposition was carried out in high purity (99.999%) argon ambient using a 2 inch diameter Mo sputtering target. The argon flow was metered with a mass flow controller and fixed at 10 sccm. The required argon pressure for sputtering was achieved by throttling a high vacuum gate valve. The thickness for all depositions was kept constant at 0.7 μm. There was no intentional heating, but it should be noted that the substrate temperature increased to 310 K during the rf depositions. Uniform film thickness ($\pm$5% error)

was achieved using a rotatable substrate holder fixed 6 cm from the target. The argon pressure was varied between 4 and 20 mTorr while keeping a constant sputtering power of 100 W.

The structural, physical, electrical and optical properties of the films were studied as a function of deposition argon pressure. The influence of pressure on the crystallographic properties and the mechanical properties of the films were studied by X-ray diffraction (XRD) using a XPERT-PRO diffractometer. The X-ray scans were performed using CuK_α radiation ($\lambda_{CuK\alpha} = 0.154$ nm) in a scanning 2θ mode with 0.01° step size over a 2θ range of 20° to 90°. The adhesion of the films to the substrates was examined using an adhesive tape test. The samples were mechanically scribed to a rectangular shape, adhesive tape strips of the same length were attached to the scribed films, and the tape was stripped with approximately equal amounts of force. Failure of the test is evidence by any film's residue on the tape. The film resistivity was calculated from the sheet resistance by four-point probe and the film thickness by DekTak^{3}ST Surface Profiler. An atomic force microscope (AFM) operated in noncontact AC mode (320 KHz tip) was used for the topographical images of the films. The acquired AFM images were used to determine the root-mean square roughness (rms) of the films. Spectroscopic ellipsometry measurements were performed *in situ* with a rotating-compensator multichannel instrument in the energy range of 0.75 to 6.5 eV. In ellipsometry, two quantities, ψ and Δ, are measured in reflection; these represent, respectively, the relative amplitude ratio and the phase difference shift between the parallel and perpendicular field components as measured with respect to the plane of incidence in the reflection of polarized light. Pairs of (ψ, Δ) spectra were collected within a time of 1.5 sec. Analyses of the spectra involved numerical inversion and least-squares regression algorithms. The angle of incidence was at 65° [17, 18].

3. Results and Discussion

3.1. Physical Properties. The influence of pressure and deposition process on the crystallographic properties and the mechanical properties of the films was studied by XRD. As shown in Figure 1 (for $p = 10$ mTorr), the rf films tend to have a lower degree of crystallization compared to the dc films, as indicated by their broader and smaller peaks. It was also found that the films deposited with lower pressure had a higher degree of crystallinity as shown in Figure 2. This can be explained by the fact that at lower deposition pressures adatoms have impacted the surface with sufficient energy to enhance their mobility, leading to increased diffusion of atoms, atomic rearrangements, and atomic displacements, which in turn are conducive to the growth of more stable, larger crystalline grains. In the case of the rf films, since a longer deposition is required to achieve the same thickness, there may be an additional reduction of the mobility due to the introduction of contaminant species such as oxygen, which suppresses the diffusion of Mo adatoms and lead to lattice defects.

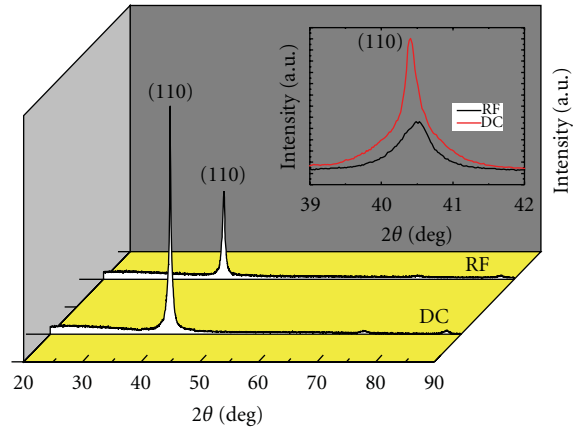

Figure 1: Typical XRD spectra of dc and rf magnetron sputtered molybdenum thin films at 10 mTorr. (Inset: closeup of the (110) peak).

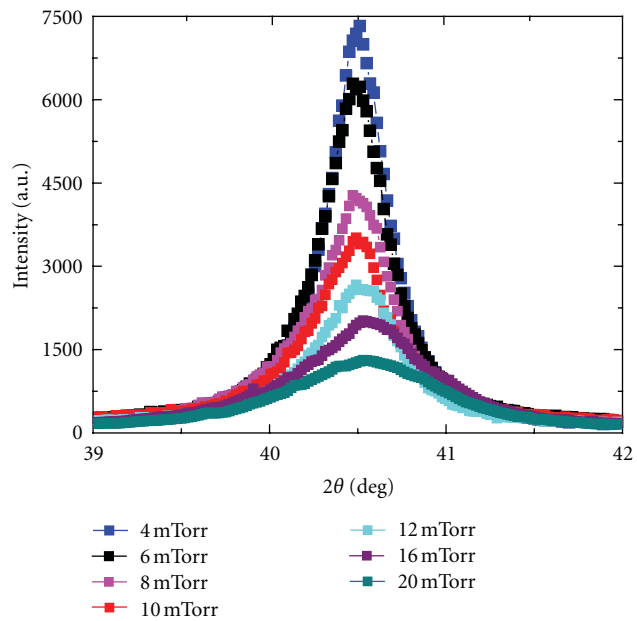

Figure 2: XRD pattern of the (110) peak for rf sputtered molybdenum thin film as a function of argon pressure.

The observed (110) peak distortion can be directly related to the strain in the films, which can be either compressive or tensile. The Bragg law was used to calculate the lattice spacing, $d_{(110)}$, and hence the lattice parameter a. The strain of the film was then calculated using the formula:

$$\text{Strain}(\%) = \frac{\Delta a}{a} \times 100, \tag{1}$$

where Δa is the change in lattice parameter in the film compared to a Mo sheet.

The change in strain with pressure for rf and dc films is shown in Figure 3. In both cases the tensile strain dominates

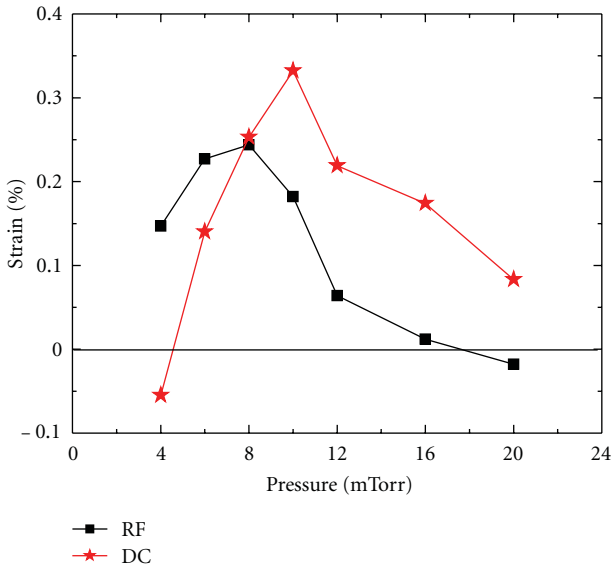

Figure 3: Strain variation in rf and dc films as a function of pressure; (the curves are a guide to the eye).

over compressive strain. These strain versus pressure curves can be split into low and high pressure domains. At low pressure, the films are under either low tensile or compressive strain. With increasing pressure, the tensile strain increases until it reaches a maximum. For the rf films, the maximum is about 0.24% at 8 mTorr, whereas for the dc films it is 0.33% at 10 mTorr. At high pressure, the tensile strain gradually decreases with further increasing pressure, leading toward or reaching compressive strain once again at pressures higher than 16 mTorr. The observed compressive strain at low pressures can be explained by an effect called "atomic peening" in which the high momentum sputtered ions impinge onto the growing film surface [19, 20]. In striking the surface with high momentum, the incident atoms drive the near-surface atoms of the film closer together. As a result, both incident and impacted atoms become embedded deeper into the film surface thus generating the film's compressive stress and concomitantly a denser film microstructure.

Conversely, the absence of energetic particle bombardment at high pressure leads to a tensile stress and to a more porous film microstructure. The compressive stress at the higher pressures is most probably influenced by lattice distortion due to one of the following: (i) incorporation of foreign atoms into the film, (ii) reaction at grain boundaries that produce a phase with a different molar volume, or (iii) surface energy reduction at void surfaces. It is important to notice that the nature and degree of the strain in the Mo films can potentially alter the chemical activity of selenium during the formation of the CIGS layer.

To assess the effect of strain, we measured the adhesion of the films on the substrate by using an adhesive tape test as described in Section 2. We found that all rf and dc films passed the test except for the dc films prepared at 4 mTorr. The failure of the test of the dc films at this pressure may be due to high compressive strain in the films, as observed in Figure 3.

The degree of orientation of the films along the (110) direction, $P(110)$, was calculated using:

$$P(110) = \frac{I(110)/I_0(110) + I(220)/I_0(220)}{\sum_{hkl} I(hkl)/I_0(hkl)}, \quad (2)$$

where $I(hkl)$ is the measured intensity of the (hkl) peak and $I_0(hkl)$ is the relative molybdenum powder diffraction intensity. The rf films did not show any correlation of $P(110)$ with pressure ($P(110) \sim 0.8$-0.9); however, $P(110)$ for the dc films was observed to decrease linearly from 0.96 to 0.87 for films of increasing pressure from 4 to 20 mTorr. The fact that the crystallites have a strong preferential orientation along the (110) plane can be explained by the lowest surface potential energy for these planes.

The variation of the full width at half maximum (FWHM) of the (110) peak with pressure for rf and dc films was also measured. The average grain size of the films was then determined using Scherrer formula [21]:

$$L = \frac{K\lambda}{\beta \cos(\theta)}, \quad (3)$$

where L is the crystallite size, K is the Scherrer constant (considered 0.90 for spherical particles), λ is the X-ray wavelength, β is the FWHM of the peak, corrected for instrument broadening (i.e., $\beta^2 = B^2 - b^2$ where B = experimental, b = instrumental), and θ is the Bragg angle. For both type of films, a decrease in grain size with increasing sputtering pressure was observed, followed by saturation above 12 mTorr (Figure 4). For all pressures, the dc films tend to have larger grain size than the rf films, which may be related to the higher deposition rate of the dc films and therefore the potential for lower foreign atom incorporation.

Film morphology measured by atomic force microscopy (AFM) is shown Figures 5(a) and 5(b) for 4 mTorr. The dc films show relatively smooth surface with uniform grain distribution, whereas the rf films have a wider range of grain sizes, a fibrous or columnar morphology and rougher surfaces. The rms roughness of the dc and rf films were found to increase from 2 nm to 6 nm and from 3 nm to 9 nm, respectively, as pressure increased from 4 mTorr to 20 mTorr. Furthermore, the films deposited at high sputtering pressures showed dendritic-like morphologies, and thus may incorporate high void volume fraction in the films. With an increasing concentration of small void structures with increasing pressure, the film volume may expand slightly into the void regions, leading to tensile stress. As the voids increase in size and their surfaces have a dominating influence, high internal surface tension can then force the film volume toward compression, as observed at the highest pressures in Figure 3.

For optimal CIGS device performance, the desirable Mo films display a fibrous morphology closer to that of the rf sputtered films that allows diffusion pathways for the migration of sodium (Na) atoms from the underlying soda lime glass (SLG) substrate to the CIGS layer during its deposition [5].

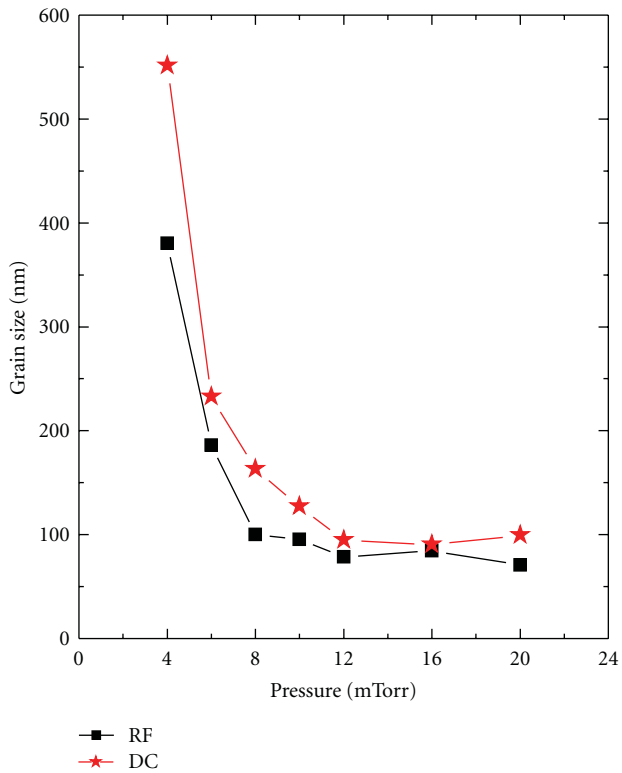

Figure 4: Variation of average grain size of rf and dc films as a function of pressure. The lines connect data points as guides to the eye.

3.2. Electrical Properties. The resistivity of the rf and dc films was found to increase with increasing pressure (Figure 6). The rf films were found to be more resistive compared to the dc films under otherwise identical deposition conditions. The higher conductivity at low pressure is consistent with a dense microstructure, whereas the low conductivity at high pressure correlates well with porous microstructure associated with tensile strain in the films. Low conductivity at higher pressure is also consistent with decreasing grain size.

3.3. Optical Properties. During the deposition of the molybdenum films, real time *in situ* spectroscopic ellipsometry (RTSE) was used over a wide spectral range (0.75–6.5 eV) in order to characterize the growth process and the dielectric functions. We chose 10 mTorr as a characteristic pressure, where high tensile strain is observed for both rf and dc films.

Figure 7 shows the surface roughness and the bulk layer thickness as a function of deposition time extracted from RTSE as the film is deposited. During the initial stage of growth, the incident Mo atoms nucleate forming separate islands which is evidenced by a sharp increase in the surface roughness thickness [22]. The Mo island size for the rf films relative to the dc films is slightly greater, as measured normal to the film surface at the onset of coalescence. Island coalescence is characterized by a subsequent decrease in surface roughness simultaneously with the onset of bulk layer growth. A linear extrapolation of the bulk growth in the uniform growth regime allows calculation of the deposition rates and the final thickness. These thicknesses are found to be in excellent agreement with *ex situ* surface profilometry measurements. After complete coalescence of the islands, the surface roughness thickness increases slightly before saturating to a value of 3.9 nm (dc films) and 5 nm (rf films) which correlates well with the *ex situ* AFM measurements of 2.9 nm and 3.8 nm. Both rf and dc sputtered Mo thin films follow a similar trend of surface roughness and bulk layer thickness variation, but smoother film morphology and higher deposition rates are obtained for the dc films compared with the rf films.

Figures 8 and 9 show the complex dielectric function components $(\varepsilon_1, \varepsilon_2)$ of the Mo films at two bulk layer thicknesses (3.3 nm and 100 nm), as determined by exact inversion of spectra collected in real time during the growth process. The bulk layer thickness used in the inversion was determined through a global fit to spectra collected over a narrow time range [23]. The surface roughness in this comparison was neglected as it was relatively thin. Clear differences in $(\varepsilon_1, \varepsilon_2)$ are observed for rf and dc films at the two thicknesses. At the beginning of the growth (3.3 nm), the overall amplitude of ε_2 for the dc films is larger, indicating less void volume fraction in the dc films. This is an indication of greater coalescence in the dc film at a given thin-layer thickness. Furthermore as the thickness increases from 3.3 nm to 100 nm, the amplitude of ε_1 at the minimum photon energy of 0.75 eV sharply decreases from 9 to -22 and from -6 to -54, for the rf and dc films respectively. This is an indication of an increase in Drude free-electron relaxation time (τ) most likely due to larger grain sizes and reduced grain boundary scattering as the films increase in thickness.

From the full set of dielectric function spectra, collected every 1.5 s during the film growth, an electronic relaxation time was extracted as a function of bulk layer thickness for rf and dc films. This was done by fitting each dielectric function to a Drude free-electron model combined with a broad Lorentz oscillator [24]. The Drude model serves to extract information from the low energy portion of the spectra while the broad Lorentz oscillator serves to represent all background contributions to the dielectric function from higher energy. The Lorentz oscillator component of the model is too broad and weak in the case of our Mo films, so no information can be reliably extracted from it. The Drude model on the other hand allows for a determination of the broadening parameter, Γ, which is inversely proportional to the free electron relaxation time, that is, $\tau \sim \hbar/\Gamma$, where $\hbar$ is Planck's constant. The Drude free-electron equation is given by:

$$\varepsilon(E) = \varepsilon_\infty - \frac{E_p^2}{E(E + i\Gamma)}, \tag{4}$$

where E_p is the free-electron plasma energy and ε_∞ is the contribution to the dielectric function due to higher energy oscillators, that is, the contribution from the interband transitions (excluding the Lorentz oscillator used to obtain a suitable fit). The resulting best-fit relaxation time (τ) as a

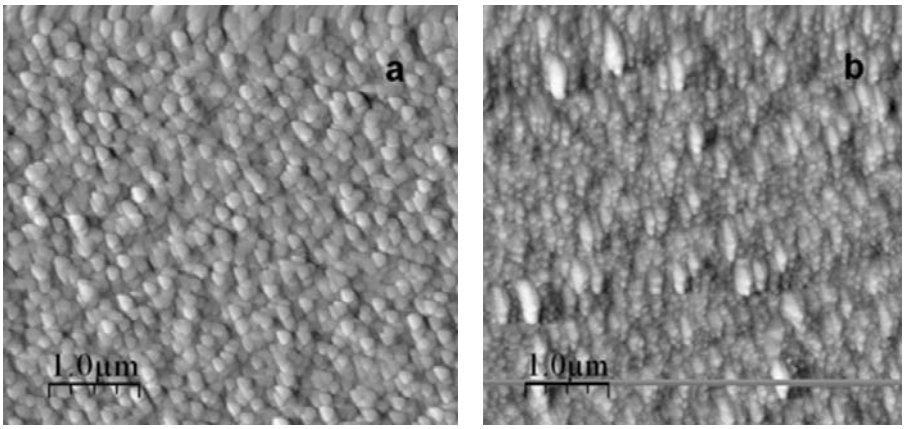

(a) (b)

Figure 5: Topographical images (5 μm × 5 μm) of dc (a) and rf (b) sputtered Mo deposited at 4 mTorr Ar pressure.

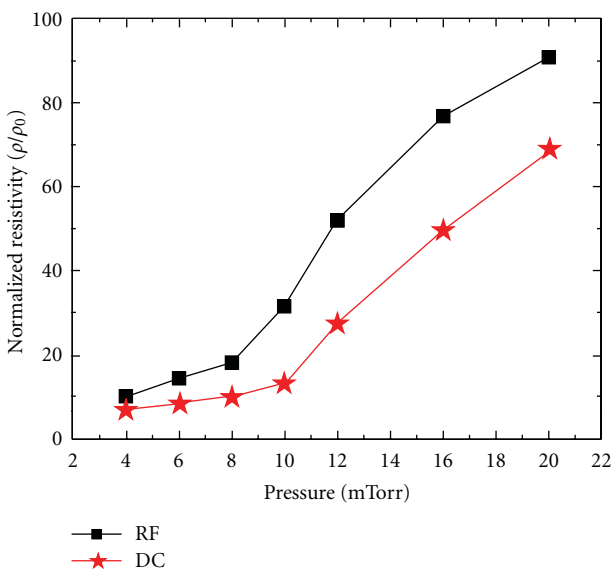

Figure 6: Normalized resistivity as a function of pressure for Mo thin films.

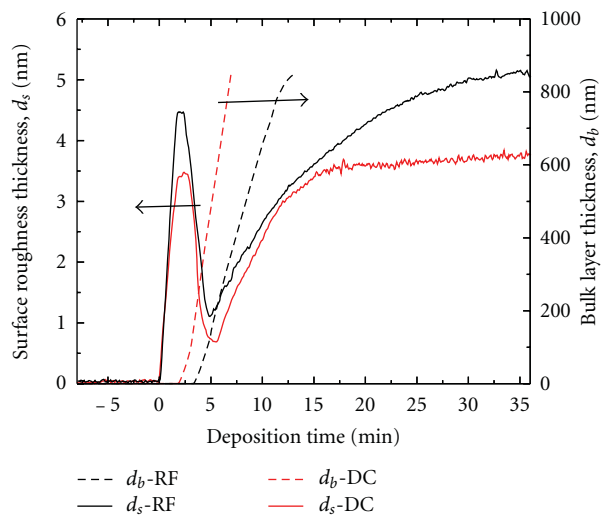

Figure 7: Evolution of surface roughness (solid line) and bulk layer thicknesses (dashed line) obtained by RTSE for Mo deposition using dc and rf sputtering at 10 mTorr. The bulk layer becomes fully opaque at large thickness values and, as a result, its thickness cannot be determined.

function of bulk layer thickness, d_b, is shown in Figure 10. It shows that both rf and dc films have a similar trend for τ, that is, initial increase with increase in d_b and saturation toward the end, most likely when the grain grows with diameter comparable to the bulk thickness. It is important to note that the relaxation time for the rf films is systematically lower than that for the dc films.

The particular functional electronic relaxation time observed in Figure 10 can be attributed to grain boundary scattering. To model this behavior, we use the model proposed by Kasap [25], following (5):

$$\tau^{-1} = \tau_b^{-1} + \frac{3\Re v_F}{\left[2(1-\Re)\lambda_g\right]}, \tag{5}$$

where τ_b is the relaxation time in the limit of a single crystal, $v_F = 1.7 \times 10^6$ m/s is the Fermi velocity for Mo, λ_g is the electron mean free path, and $\Re$ is the grain boundary reflection coefficient, taken to be 0.5 as a first approximation [15]. Reasonable fits to the data for τ in Figure 10 are obtained if one assumes that the mean free path λ_g is proportional to the grain radius and that the crystallite evolution follows a conical growth mode in accordance the relationship $\lambda_g = xd_b$. Values of $x = 0.33$ (rf films) and $x = 0.45$ (dc films) were extracted. This higher value of the grain size for the dc films compared to the rf films is consistent with the XRD results.

4. Conclusion

Molybdenum thin films were deposited onto soda-lime glass substrates, using rf and dc magnetron sputtering. We have

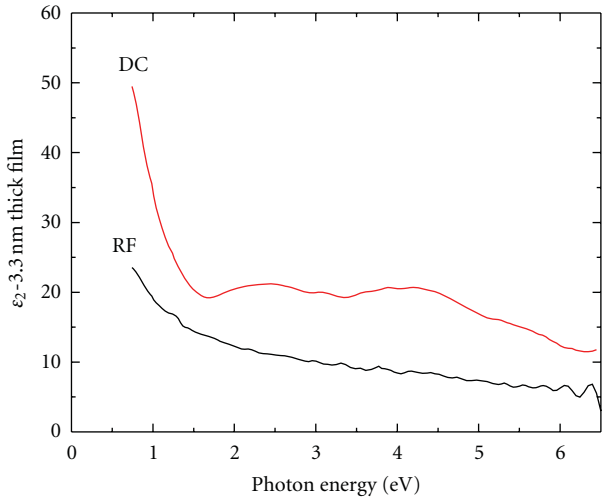

Figure 8: A comparison of the imaginary parts of the dielectric function for 3.3 nm thick Mo films deposited by rf and dc sputtering at 10 mTorr.

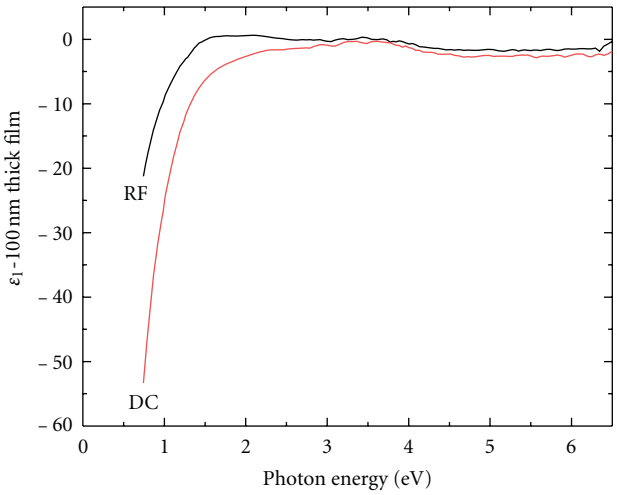

Figure 9: A comparison of the real parts of the dielectric function for 100 nm thick Mo films deposited by rf and dc sputtering at 10 mTorr.

shown that critical sputtering parameters which control the mechanisms and kinetics of film growth are not only pressure and power but also the deposition mode (rf versus dc). Both rf and dc deposited films show similar trends in microstructural evolution, characterized by a Volmer-Weber island growth-coalescence process followed by a continuous increase of the grain size according to a cone-growth model. The strain in the film also varied similarly for both films, transitioning from compressive through tensile and back to compressive again. Interestingly, this has little effect on the adhesion of the films, which was good for all films except those deposited by dc sputtering at low pressure. It is important to note, however, that these films have not been exposed to the CIGS deposition process at 550°C under Se atmosphere, and therefore could still delaminate during solar cell fabrication. Another parameter to take into

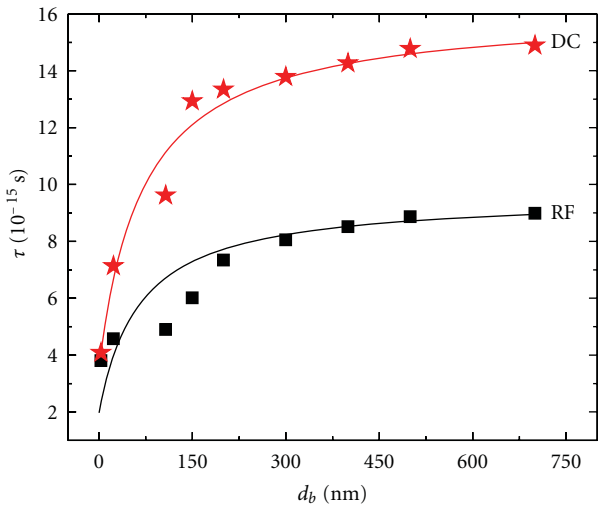

Figure 10: Relaxation time τ for free electrons in Mo as a function of the bulk layer thickness for both dc and rf mode sputtering. Also shown are the results of fits using a simple conical grain growth model.

account, depending on the CIGS deposition process, is the ability of the molybdenum to serve as a conduit for sodium diffusion from the glass. Here, our experiments have shown that the dc films have larger grains from the beginning to the end of the growth, which may be less advantageous for sodium diffusion through grain boundaries. Finally, the lower conductivity of the rf films can be seen as a problem since this may increase the solar cell series resistance. The lower conductivity may also be an indicator of the presence of foreign atoms (such as oxygen), which in turn may allow for more flexibility of the film and less delamination when deposition is performed on flexible substrates [26].

References

[1] P. Jackson, D. Hariskos, E. Lotter et al., "New world record efficiency for Cu(In,Ga)Se_2 thin-film solar cells beyond 20%," *Progress in Photovoltaics: Research and Applications*, vol. 19, no. 7, pp. 894–897, 2011.

[2] K. Orgassa, H. W. Schock, and J. H. Werner, "Alternative back contact materials for thin film Cu(In,Ga)Se_2 solar cells," *Thin Solid Films*, vol. 431-432, pp. 387–391, 2003.

[3] J. H. Scofield, A. Duda, D. Albin, B. L. Ballard, and P. K. Predecki, "Sputtered molybdenum bilayer back contact for copper indium diselenide-based polycrystalline thin-film solar cells," *Thin Solid Films*, vol. 260, no. 1, pp. 26–31, 1995.

[4] A. A. Kadam, A. H. Jahagirdar, and N. G. Dhere, "Effect of stresses in molybdenum back contact film on properties of CIGSS absorber layer," in *Proceedings of the Materials Research Society Spring Meeting*, pp. 423–429, April 2005.

[5] H. A. Al-Thani, F. S. Hasoon, M. Young et al., "The effect of Mo back contact on Na out-diffusion and device performance of Mo/Cu(In,Ga)Se_2/CdS/ZnO solar cells," in *Proceedings of the 29th IEEE Photovoltaic Specialists Conference*, pp. 720–723, New Orleans, La, USA, May 2002.

[6] G. Gordillo, M. Grizález, and L. C. Hernandez, "Structural and electrical properties of DC sputtered molybdenum films,"

Solar Energy Materials and Solar Cells, vol. 51, no. 3-4, pp. 327–337, 1998.

[7] M. C. K. Tinone, T. Haga, and H. Kinoshita, "Multilayer sputter deposition stress control," *Journal of Electron Spectroscopy and Related Phenomena*, vol. 80, pp. 461–464, 1996.

[8] L. Assmann, J. C. Bernède, A. Drici, C. Amory, E. Halgand, and M. Morsli, "Study of the Mo thin films and Mo/CIGS interface properties," *Applied Surface Science*, vol. 246, no. 1–3, pp. 159–166, 2005.

[9] N. Miyata and S. Akiyoshi, "Preparation and electrochromic properties of rf-sputtered molybdenum oxide films," *Journal of Applied Physics*, vol. 58, no. 4, pp. 1651–1655, 1985.

[10] M. A. Martínez and C. Guillén, "Effect of r.f.-sputtered Mo substrate on the microstructure of electrodeposited $CuInSe_2$ thin films," *Surface and Coatings Technology*, vol. 110, no. 1-2, pp. 62–67, 1998.

[11] C. Dicov, M. Marinov, H. Maciel, K. Grigorov, I. Nedkov, and G. Beshkov, "Properties of Cr and Mo thin films deposited by RF sputtering," *Journal of Optoelectronics and Advanced Materials*, vol. 7, no. 1, pp. 385–387, 2005.

[12] T. Wada, "Microstructural characterization of high-efficiency $Cu(In,Ga)Se_2$ solar cells," *Solar Energy Materials and Solar Cells*, vol. 49, no. 1–4, pp. 249–260, 1997.

[13] J. Nagano, "Electrical resistivity of sputtered molybdenum films," *Thin Solid Films*, vol. 67, no. 1, pp. 1–8, 1980.

[14] H. Khatri and S. Marsillac, "The effect of deposition parameters on radiofrequency sputtered molybdenum thin films," *Journal of Physics Condensed Matter*, vol. 20, no. 5, Article ID 055206, 2008.

[15] S. Marsillac, N. Barreau, H. Khatri et al., "Spectroscopic ellipsometry studies of In_2S_3 top window and Mo back contacts in chalcopyrite photovoltaics technology," *Physica Status Solidi C*, vol. 5, no. 5, pp. 1244–1248, 2008.

[16] J. D. Walker, H. Khatri, V. Ranjan, J. Li, R. W. Collins, and S. Marsillac, "Electronic and structural properties of molybdenum thin films as determined by real-time spectroscopic ellipsometry," *Applied Physics Letters*, vol. 94, no. 14, Article ID 141908, 2009.

[17] J. Lee, P. I. Rovira, I. An, and R. W. Collins, "Rotating-compensator multichannel ellipsometry: applications for real time Stokes vector spectroscopy of thin film growth," *Review of Scientific Instruments*, vol. 69, no. 4, pp. 1800–1810, 1998.

[18] B. Johs, J.A. Woollam, C.M. Herzinger, J.N. Hilfiker, R. Synowicki, and C. Bungay, "Overview of variable angle spectroscopic ellipsometry (VASE), Part II: advanced applications," in *Proceedings of the Society of Photo-Optical Instrumentation Engineers*, vol. 72, pp. 29–58, 1999.

[19] H. Windischmann, "Intrinsic stress in sputter-deposited thin films," *Critical Reviews in Solid State and Materials Sciences*, vol. 17, no. 6, pp. 547–596, 1992.

[20] T. Yamaguchi and R. Miyagawa, "Effects of oxygen on the properties of sputtered molybdenum thin films," *Japanese Journal of Applied Physics, Part 1*, vol. 30, no. 9, pp. 2069–2073, 1991.

[21] N. Kasai and M. Kakudo, "Springer series in chemical physics: preface," *Springer Series in Chemical Physics*, vol. 80, pp. 364–365, 2005.

[22] H. V. Nguyen, I. An, and R. W. Collins, "Evolution of the optical functions of thin-film aluminum: a real-time spectroscopic ellipsometry study," *Physical Review B*, vol. 47, no. 7, pp. 3947–3965, 1993.

[23] I. An, Y. M. Li, C. R. Wronski, H. V. Nguyen, and R. W. Collins, "*In situ* determination of dielectric functions and optical gap of ultrathin amorphous silicon by real time spectroscopic ellipsometry," *Applied Physics Letters*, vol. 59, no. 20, pp. 2543–2545, 1991.

[24] F. Wooten, *Optical Properties of Solids*, chapter 3, Academic Press, San Diego, Calif, USA, 1972.

[25] S. O. Kasap, *Principles of Electronic Materials and Devices*, McGraw Hill, New York, NY, USA, 3rd edition, 2006.

[26] E. Eser, S. Fields, G. Hanket, R. W. Birkmire, and J. Doody, "Critical issues in vapor deposition of $Cu(InGa)Se_2$ on polymer web: source spitting and back contact cracking," in *Proceedings of the 31st IEEE Photovoltaic Specialists Conference*, pp. 515–518, January 2005.

Hindawi Publishing Corporation
International Journal of Photoenergy
Volume 2012, Article ID 872324, 6 pages
doi:10.1155/2012/872324

Methodology Report

Investigation on *I-V* for Different Heating Temperatures of Nanocomposited MEH-PPV:CNTs Organic Solar Cells

M. S. P. Sarah, F. S. S. Zahid, and M. Rusop

NANO-ElecTronic Centre, Faculty of Electrical Engineering, Universiti Teknologi MARA Shah Alam, 40450 Selangor, Malaysia

Correspondence should be addressed to M. S. P. Sarah, puteri_ajip@yahoo.com and M. Rusop, nanouitm@gmail.com

Received 27 September 2011; Accepted 16 January 2012

Academic Editor: Bhushan Sopori

This paper discussed the effect of different thermal evaporation treatments for nanocomposited MEH-PPV:CNTs thin films towards the performance of organic solar cells. The configuration of the organic solar cells is ITO/MEH-PPV:CNTs/Au. The heating temperature was varied from, as deposited, 50°C, 75°C, and 100°C. From the results, we observed that the efficiency increase slightly before decreasing back at 100°C. The highest efficiency was solar cells heated at 75°C with efficiency 0.001% which is supported by the *I-V* characteristics and also by the absorption spectra.

1. Introduction

Organic solar cells are gaining much interest in this energy-saving era, due to their simple and low cost fabrication process. However, the efficiency of organic solar cells is still low. Even though much research is done on blending organic material with a nonorganic material, very rare is done on blending polymer with carbon nanotubes (CNTs) because of the dispersity problem.

Even if CNTs have dispersion problems, it still has gained a lot of attention due to its unique properties. The uniqueness of the nanotube arises from its structure, which is the helicity in the arrangement of the carbon atoms in hexagonal arrays on their surface honeycomb lattices [1]. CNTs have high surface area ($\sim 1600\,\mathrm{m}^2/\mathrm{g}$) that offers tremendous opportunity for exciton dissociation [2]. CNTs can be metallic or semiconducting which is determined by the chirality of the nanotube. The diameter of the CNTs is an important property as it has a direct correlation with the optical band gap. The optical absorbance of CNTs is affected by both structure and dimension of the nanotube [3].

CNTs properties like high electron conductivity, high thermal conductivity, and robustness are flexible by nature and are assumed to improve the properties of a conjugated polymer. Basically, conjugated polymer has high absorption coefficient in the visible region ($\sim 10^{-5}\,\mathrm{cm}^{-1}$), charge generation under illumination, and easy deposition on substrates even at room temperature [4], which makes them well-liked in recent research. Poly[2-methoxy-5-(2′-ethylhexloxy-p-phenylene vinylene] (MEH-PPV) is a commonly used conjugated polymer due to its solubility and absorption in the visible range [5]. The structure of electronic states of conjugated polymers is such that several types of excited states (singlet and triplet excitons) and charges (e.g., polarons) can be easily created by visible light excitation [6]. MEH-PPV is a conjugated polymer which is known as a novel class of material that combine the optical and electronic properties of semiconducting with the processing advantages and mechanical properties of plastics. It is found that the corresponding property of the matrices could be enhanced in the presence of homogeneously dispersed CNTs [7].

In order to solve the issue of undispersity of CNTs, the increase percentage of the composition is presented in this work. However, so far the agglomeration of the undisperse CNTs still exists and they are still unevenly scattered. Photoconductivity of MEH-PPV is often limited by low absorption. Therefore, in this paper we fabricate organic cells as shown in Figure 2 and discuss on the heating

Table 1: Description of samples.

Name of sample	Description
S_0	As deposited sample
S_{50}	Sample heated for 5 minutes at 50°C
S_{75}	Sample heated for 5 minutes at 75°C
S_{100}	Sample heated for 5 minutes at 100°C

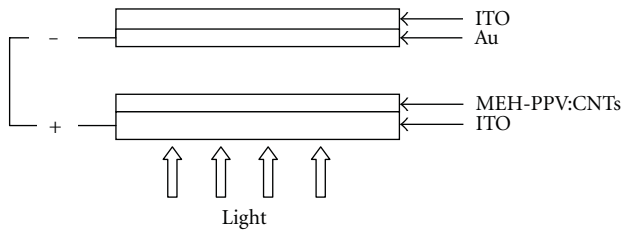

Figure 1: Structure of organic solar cell.

temperature when the concentration of CNTs is high. This is due to heating temperature that also plays vital role in determining the performance of organic solar cells due to removal of moisture in the nanocomposite [8].

2. Methodology

The compositions of CNTs are fixed at 60 wt%. The CNTs used are commercially available with purification >95%. Before adding the CNTs to the polymer solution, it was annealed at 450°C for 30 minutes to ensure that all of the impurities in the CNTs are totally removed. The solvent used for dissolving the MEH-PPV powder is tetrahydrofuran (THF).

A thin layer of nanocomposited MEH-PPV blend CNTs was spin-coated with 2000 rpm for 1 minute on indium tin oxide (ITO) size 2 cm × 2 cm. The deposition was done at room temperature under normal pressure. After the deposition is done, the nanocomposited on the ITO was heated on a hot plate stirrer for 5 minutes to vaporize the solvent at 50°C, 75°C, and 100°C. The detailed descriptions of the samples are shown in Table 1. To compare the performance of the devices, as deposited, and undergo heat treatment, one device is fabricated without undergoing the treatment process. The thickness of the blended device was in the range of 50 to 90 nm. Film thickness is important in determining the efficiency of organic solar cells due to the face that it has short diffusion length which leads to recombination. Therefore, it will yield low photocurrent and gives less energy conversion efficiency. The thickness of the nanocomposited MEH-PPV:CNTs is measured using surface profiler Veeco Dektak 750. A schematic diagram of the present solar cells is shown in Figure 1. The Au was deposited on another ITO using sputter coater so that the blended thin film was sandwiched between Au and ITO electrode.

The current density-voltage (J-V) characteristics of the solar cells were measured both in dark and under illumination at 100 mW/cm^2 by using an AM 1.5 solar simulator CEP 2000 Spectral Sensitivity Analyzing System. The solar cells were illuminated through the side of ITO substrates, and the illuminated areas were 0.01 cm^2.

UV-visible absorption spectra were obtained by using Perkin Elmer Lambda 750 UV/Visible Spectrometer to analyze the absorbance and transmittance.

3. Results and Discussions

3.1. Electrical Properties. The measured current-voltage (I-V) characteristics of a MEH-PPV:CNTs organic solar cells in dark and under illumination are shown in Figures 2(a), 2(b), 2(c), and, 2(d), respectively, where else Figure 2(e) shown the comparison for I-V characteristic under illumination for different thermal evaporation temperature. It can be seen that the I-V curve form Schottky contact when Au was used as the metal contact. The metal-semiconductor (M-S) contact in which $_M > _S$ is called a Schottky barrier diode where there is nonlinear current flow in the device. Because the current flows easily in one direction but not in the other, it is a rectifying contact. The explanation concerning this issue is that Au has work function value higher than the organic-inorganic blend. We also assumed that the Schottky formation is based on solvent used to dissolve the MEH-PPV. Naturally, MEH-PPV is a p-type material but in this paper, MEH-PPV acts as electron acceptor (n-type) and CNTs act as electron donor (p-type). The type of MEH-PPV depends on the solvent used to dissolve the polymer [9]. The Schottky formation can also be regarded as the CNTs being the metallic material and the MEH-PPV is the semiconducting part. Metallic CNTs conduct electricity easily because many electrons have easy access to adjacent conduction states.

It can be seen in Figures 2(a), 2(b), 2(c), and 2(d) that the I-V curve showed insignificant changes under illumination condition as compared to in dark due to the samples are sensitive to light. There is only a slight change for both conditions in dark and under illumination due to CNTs structure that is not compatible with the MEH-PPV polymer chain [10]. However, devices consisting MEH-PPV only show a shorter lifetime compared to organic solar cells fabricated with MEH-PPV blend CNTs [11]. Even though the current shows not much different but the MEH-PPV:CNTs nanocomposite behaves like a photoamplifier, that produce a very large current and more electrons for each photon absorbed by the polymer [12].

Figure 2(e) shows the I-V characteristics at room temperature in treated and as deposited samples. Figure 2 is the same as in Figures 2(a) to 2(d) but in Figure 2(e), we can see that S_{75} shows the highest current. It can be seen that the current tend to increase from as deposited samples to treated samples from S_{50} to S_{75} but it started to decrease at S_{100}. S_{75} showed the highest current under illumination condition compared to the as deposited solar cell. This is due to its high absorbance which is shown in Figure 5, later. The increment from as S_0 to S_{75} implies that as the temperature is increased, more charge carriers overcome the activation energy barrier and participate in the electron movement [13].

The measured current density-voltage (J-V) characteristic of a nanocomposited MEH-PPV:CNTs structure

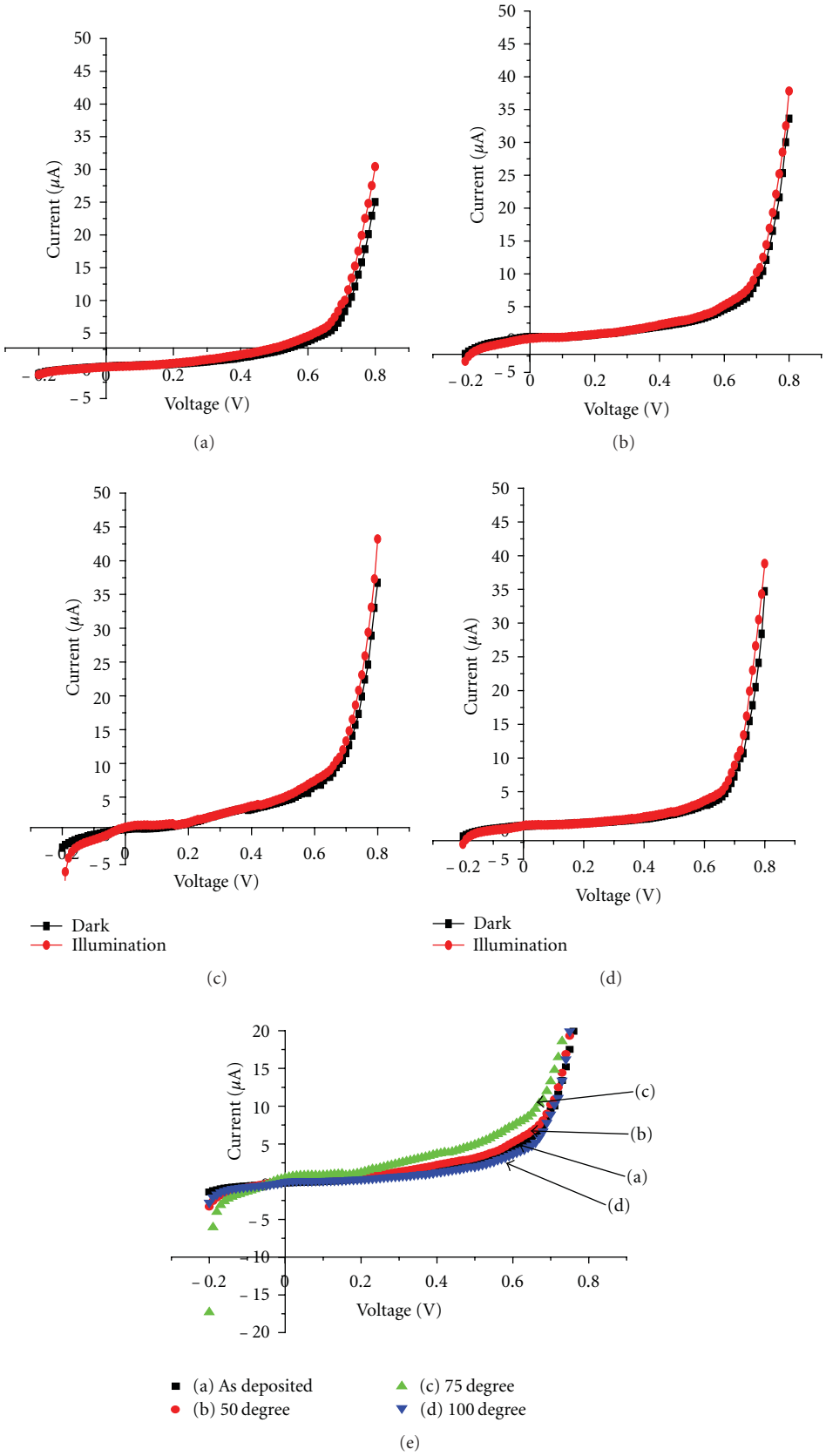

Figure 2: *I-V* for organic solar cells with different thermal treatment: (a) S_0, (b) S_{50}, (c) S_{75}, (d) S_{100}, and (e) comparison for *I-V* under illumination for (nanocomposited MEH-PPV:CNTs as deposited, 50°C, 75°C, and 100°C.

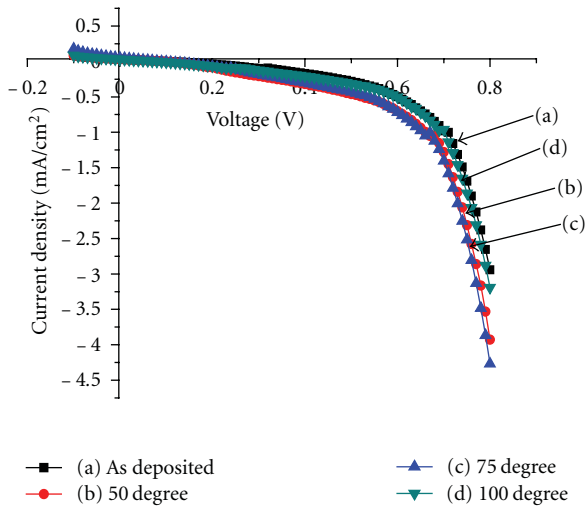

Figure 3: Measured current density-voltage (J-V) characteristics for nanocomposited MEH-PPV:CNTs at different heating temperature.

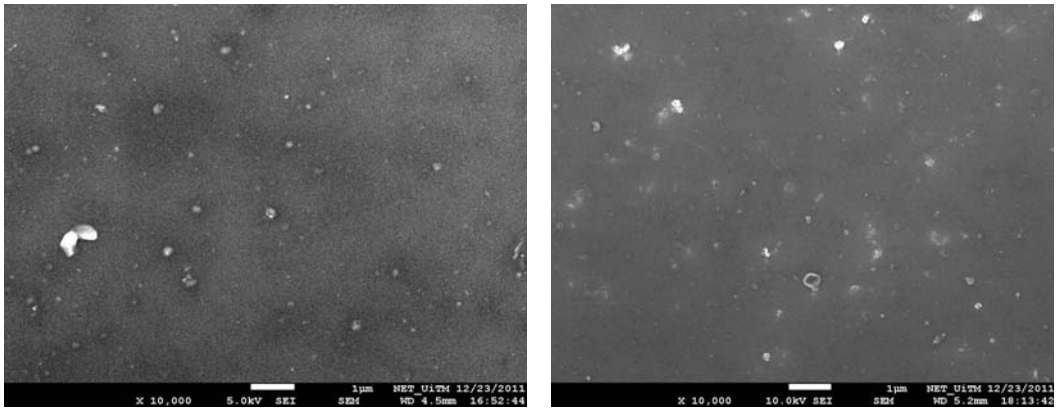

(a) (b)

Figure 4: FESEM images of nanocomposited MEH-PPV:CNTs for (a) untreated, (b) treated.

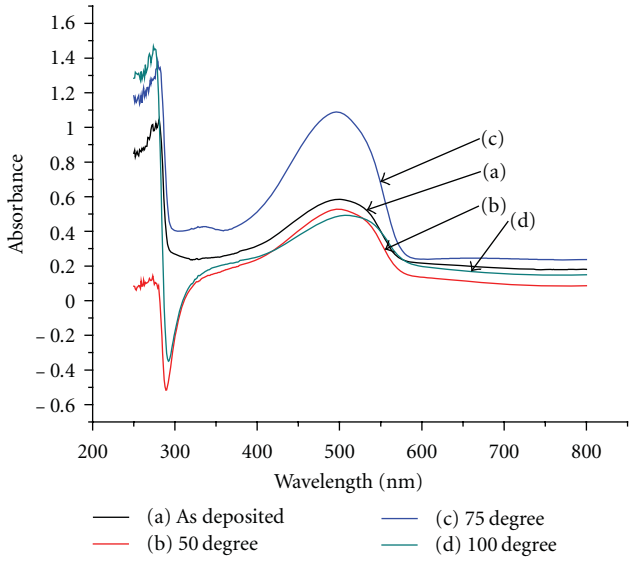

Figure 5: Absorbance spectra for nanocomposited MEH-PPV:CNTs for different heating temperature.

Table 2: Measured parameters of the solar cells.

	As deposited	50°C	75°C	100°C
V_{oc} (V)	0.097	0.094	0.091	0.079
J_{sc} (mA/cm^2)	0.033	0.031	0.052	0.029
FF	0.243	0.269	0.229	0.255
η (%)	0.0007	0.0008	0.001	0.0006

under illumination are shown in Figure 3. Photocurrent of 0.052 mA/cm^2 is observed under illumination for S_{75} which is the highest as compared to the other solar cell. This support the assumption where absorption of light in the MEH-PPV:CNTs, followed by the separation of carriers at the interface. Where else the lowest photocurrent is shown for S_{100} with 0.029 mA/cm^2. This occurred due to the degradation of the MEH-PPV emission properties [14]. Measured parameters of these solar cells are summarized in Table 2. S_{75} showed the highest efficiency which is 0.001% but it has the lowest fill factor (FF) compared to the other solar cell and it has lower open circuit voltage (V_{oc}) compared to the S_0 solar cell.

3.2. Surface Morphology. As can be seen in Figures 4(a) and 4(b) above, no difference can be seen in the morphology of the samples. The dispersion of CNTs in the MEH-PPV still occurs and was unevenly scattered. This is because of the bonding of the CNTs that is not easy to break in order to robust in the polymer matrix. Therefore, we supposed that by adding more CNTs to get well scattered CNTs are not doing well. Another reason of the undispersity was because of the solvent effect [14]. Formation of large CNTs agglomerates is observed because of using nonaromatic solvents instead of aromatic solvents [9].

3.3. Optical Properties. The absorption spectra of MEH-PPV blend CNTs are presented in Figure 5 for various heating temperature of MEH-PPV:CNTs with samples as deposited, S_{50}, S_{75}, and S_{100}, respectively. The maximum absorption occurred at wavelength around 500 nm. The peak did not show any shift either to red or blue light. There is no noticeable wavelength shift observed in the absorption maximum in MEH-PPV:CNTs nanocomposite films, but there is a substantial drop in the magnitudes due to reflectance of light when it heat the undisperse CNTs. As the heating treatment increase, the peak of absorption spectra decrease with respect to the sample as deposited, while sample S_{75} showed the highest absorbance with the value more than 1. We assume that at 75°C the solvent was completely vaporized. This is directly related to the *I-V* characteristic where the same sample showed the highest current. S_{75} absorbed the most light when it is illuminated. Therefore, the excess carriers were excited the most at this sample, where else at 100°C, the polymer was not capable to perform due to reaching its maximum temperature at 75°C where at this temperature, it can be demonstrated that the solvents are completely vaporized. However, the changes cannot be seen from the surface morphology analysis.

4. Conclusion

It can be concluded that MEH-PPV:CNTs nanocomposite shows a Schottky contact when Au is used as the metal contact. There is a slight change for *I-V* in dark and under illumination condition which shows that CNTs influence the behaviour of the conjugated polymer. The highest *I-V* is shown for sample undergoes heat treatment at 75°C. This is supported by the highest absorbance also occurred at 75°C. At 100°C, the nanocomposited MEH-PPV:CNTs was not capable to perform due to its decrement in its photoamplifier properties. From the surface morphology images, the dispersion of CNTs in the polymer matrix also does not show remarkable results that will influence the overall results.

Acknowledgments

The authors would like express their deepest appreciation to Research Management Institute UiTM (600-RMI/ST/DANA 5/3/Dst (399/2011), MOSTI E-Science Grant (06-01-01-SF0328) and MOHE for the financial support. Special thanks to staff of NANO-ElecTronic Centre, Faculty of Electrical Engineering, UiTM Shah Alam.

References

[1] P. M. Ajayan, C. Information, and O. Z. Zhou, "Applications of carbon nanotubes," *Springer Link*, vol. 80, pp. 391–425, 2001.

[2] M. Cinke, J. Li, B. Chen et al., "Pore structure of raw and purified HiPco single-walled carbon nanotubes," *Chemical Physics Letters*, vol. 365, no. 1-2, pp. 69–74, 2002.

[3] B. R. Priya and H. J. Byrne, "Investigation of sodium dodecyl benzene sulfonate assisted dispersion and debundling of single-wall carbon nanotubes," *Journal of Physical Chemistry C*, vol. 112, no. 2, pp. 332–337, 2008.

[4] P. M. Sirimanne, T. Shirata, L. Damodare, Y. Hayashi, T. Soga, and T. Jimbo, "An approach for utilization of organic polymer as a sensitizer in solid-state cells," *Solar Energy Materials and Solar Cells*, vol. 77, no. 1, pp. 15–24, 2003.

[5] J. Hui, Y. B. Hou, X. G. Meng, and Feng Teng, "Charge photogeneration and recombination in poly[2-methoxy-5-(2′-ethyl-hexoxy-p-phenylene vinylene]:fullerene composite films studied by photocurrent response," *Thin Solid Films*, vol. 516, no. 6, pp. 1142–1146, 2008.

[6] O. Mirzov, F. Cichos, C. Von Borczyskowski, and I. G. Scheblykin, "Direct exciton quenching in single molecules of MEH-PPV at 77 K," *Chemical Physics Letters*, vol. 386, no. 4–6, pp. 286–290, 2004.

[7] Z. Chan, F. Miao, Z. Xiao, H. Juan, and Z. Hongbing, "Effect of doping levels on the pore structure of carbon nanotube/silica xerogel composites," *Materials Letters*, vol. 61, no. 3, pp. 644–647, 2007.

[8] E. W. Okraku, M. C. Gupta, and K. D. Wright, "Pulsed laser annealing of P3HT/PCBM organic solar cells," *Solar Energy Materials and Solar Cells*, vol. 94, no. 12, pp. 2013–2017, 2010.

[9] B. Kang, Y. Yang, L. Wang, and Y. Qiu, "Solvent induced semiconductor type conversion of MEH-PPV investigated by surface photovoltage spectra," *Displays*, vol. 25, no. 2-3, pp. 57–60, 2004.

[10] J. P. Ferrance, K. E. Meissner, and J. W. Pettit, "Solvent effects on the electrical and optical properties of composite carbon

nanotube/MEH-PPV films," *Journal of Nanoparticle Research*, vol. 12, no. 2, pp. 405–415, 2010.

[11] C. Wang, Z. X. Guo, S. Fu, W. Wu, and D. Zhu, "Polymers containing fullerene or carbon nanotube structures," *Progress in Polymer Science*, vol. 29, no. 11, pp. 1079–1141, 2004.

[12] Z. Wang, C. Liu, Z. Liu, H. Xiang, Z. Li, and Q. Gong, "π-π interaction enhancement on the ultrafast third-order optical nonlinearity of carbon nanotubes/polymer composites," *Chemical Physics Letters*, vol. 407, no. 1–3, pp. 35–39, 2005.

[13] Y. Li, Y. Hou, H. Jin, Q. Shi, Y. Wang, and Z. Feng, "Photovoltaic properties of MEH-PPV/TiO_2 nanocomposites," *Chinese Science Bulletin*, vol. 53, no. 18, pp. 2743–2747, 2008.

[14] S. Quan, F. Teng, Z. Xu et al., "Solvent and concentration effects on fluorescence emission in MEH-PPV solution," *European Polymer Journal*, vol. 42, no. 1, pp. 228–233, 2006.

Hindawi Publishing Corporation
International Journal of Photoenergy
Volume 2012, Article ID 915352, 6 pages
doi:10.1155/2012/915352

Research Article

Fabrication of Monolithic Dye-Sensitized Solar Cell Using Ionic Liquid Electrolyte

Seigo Ito and Kaoru Takahashi

Department of Electrical Engineering and Computer Sciences, Graduate School of Engineering, University of Hyogo, 2167 Shosha, Himeji, Hyogo 671-2280, Japan

Correspondence should be addressed to Seigo Ito, itou@eng.u-hyogo.ac.jp

Received 15 November 2011; Accepted 6 February 2012

Academic Editor: Peter Rupnowski

To improve the durability of dye-sensitized solar cells (DSCs), monolithic DSCs with ionic liquid electrolyte were studied. Deposited by screen printing, a carbon layer was successfully fabricated that did not crack or peel when annealing was employed beforehand. Optimized electrodes exhibited photovoltaic characteristics of 0.608 V open-circuit voltage, 6.90 cm^{-2} mA short-circuit current, and 0.491 fill factor, yielding 2.06% power conversion efficiency. The monolithic DSC using ionic liquid electrolyte was thermally durable and operated stably for 1000 h at 80°C.

1. Introduction

To meet the demand for renewable cost-effective energy sources, dye-sensitized solar cells (DSCs), which can be fabricated from low-cost materials (TiO_2, dye, etc.) by nonvacuum printing, have attracted attention in academic and industrial research [1–4]. DSCs are normally fabricated by sandwiching TiO_2 and Pt counter electrodes. F-doped tin oxide (FTO) glass substrates for these electrodes account for 80% of DSC-fabrication cost. Additionally, Pt used in the counter electrode is also expensive. Hence, to realize further cost reductions, the use of FTO glass and Pt should be minimized. Toward this end, monolithic DSCs have been fabricated on a single FTO glass substrate with a porous carbon counter electrode (Figure 1) [5–12]. A porous carbon layer and a porous ZrO_2 layer are set on dyed porous TiO_2 layer for the monolithic DSC. The porous ZrO_2 layer has two functions: a function as transportation of electrolyte to dyed porous TiO_2 layer and a function as spacing insulator to separate dyed TiO_2 layer and carbon layer electrically. There are three roles in the porous carbon layer: (1) the catalyst to reduce I_3^- to I^- for the photocurrent flow; (2) the electrical current corrector to external circuits; (3) the transportation of electrolyte to dyed-porous TiO_2 and porous ZrO_2. By means of capillary force within nanoholes, monolithic porous electrodes prevent electrolyte leakage. Through the use of such porous electrodes, highly durable DSCs are expected.

In research on durable DSCs, industrial applications are now being emphasized. Volatility of the DSC electrolyte has been a major problem because the interface temperature of the cell rises considerably in sunlight. To address the problem of thermal instability, the electrolyte should be nonvolatile and solvent-free, which are notable properties of ionic liquids. Accordingly, ionic liquids have been investigated for use as the electrolyte in DSCs in order to enhance their durability [13–15].

In this paper, we report a screen-printing method for fabricating porous carbon electrodes that do not crack or peel off in monolithic DSCs. In particular, we focused on carbon-paste preparation. Finally, ionic liquid electrolyte was used to prepare thermally durable monolithic DSCs that operated stably for 1000 h at 80°C.

2. Experiments

The process for fabricating carbon paste is presented in Figure 2. Carbon powder and TiO_2 powder (P25; Degussa,

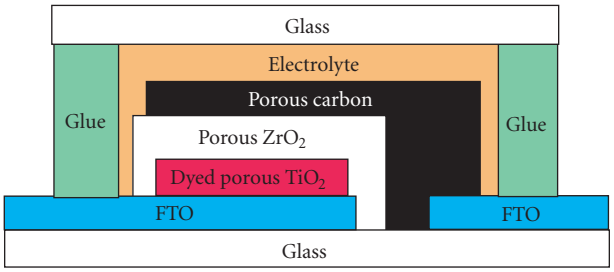

Figure 1: Structure of monolithic DSC.

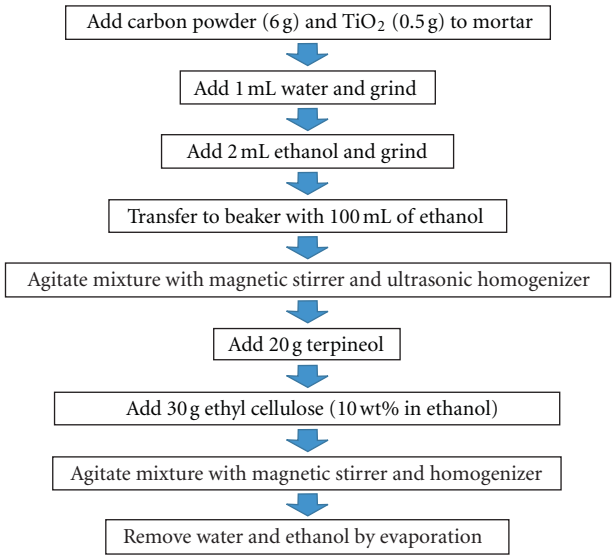

Figure 2: Process for preparing carbon paste for porous carbon electrode in DSCs.

Germany) were ground in a mortar. The carbon powder was a mixture of Printex L (Degussa) and graphite (Aldrich, Germany) or a mixture of Printex L and active carbon (Degussa, Germany). The total weight of carbon powder was 6 g. Water (10 mL) and ethanol (20 mL) were added to the mortar containing the powder mixture, which was further ground. This mixture was transferred from the mortar to a beaker with an additional 100 mL portion of ethanol. Then, the mixture was agitated with a magnetic stir bar for 1 min and an ultrasonic homogenizer (Vibra Cell 72408 Bioblock Scientific, USA) for 2 min. α-Terpineol (20 g, Tokyo Chemical Industry Co., Ltd., Japan) was added to the carbon dispersion and agitated with a magnetic stir bar for 1 min and an ultrasonic homogenizer for 2 min. Ethyl cellulose solution in ethanol (10 wt%, 30 g) was added to the carbon solution and agitated with a magnetic stir bar for 1 min and an ultrasonic homogenizer for 2 min. The ethyl cellulose solution was prepared beforehand by adding equivalent amounts of two ethyl cellulose powders in ethanol (5 wt% of ethyl cellulose no. 46080 and 5 wt% of ethyl cellulose no. 86480, Tokyo Chemical Industries, Co., Ltd., Japan). Removal of water and ethanol by evaporation at 40°C and 125 m bar afforded the carbon paste.

To fabricate monolithic electrodes, FTO glass plates (TEC-15, Nippon Sheet Glass Co., Ltd., Japan) were utilized. The FTO layer was divided into two parts by etching with Zn and HCl (see Figure 1). The etched FTO glass plates were washed with glass-cleaning detergent in an ultrasonic bath for 15 min. The substrates were then rinsed with water and ethanol. Subsequently, the surface of substrate was cleaned in a UV-O_3 system for 18 min. Two types of TiO_2 pastes—PST-30NRD and PST-400C (JGC-CCIC Co., Ltd., Japan)—were deposited by screen printing on one of the FTO layers (Figure 1) as a transparent nanocrystalline—TiO_2 layer (10 μm thick) and a light-scattering layer (4 μm thick), respectively. The resulting TiO_2 electrodes had a double-layered structure [16]. The substrate was sintered on a hotplate at 500°C for 2 h. When the substrate was cooled, ZrO_2 paste was printed on the TiO_2 layer to be 30 μm thick and to cover the porous TiO_2 layer. The ZrO_2 paste was dried on the hotplate at 125°C. The ZrO_2 paste was prepared according to a published procedure [17] using ZrO_2 nanoparticles (d = 40–50 nm; Fulka, USA). The substrate was heated on the hotplate at 200°C at 1 h. When the substrate cooled, carbon paste was printed on the ZrO_2 layer to form a layer with thickness of 130 μm. At the same time, the carbon layer was connected to the other FTO layer and sintered at 400°C (Figure 1). The fabricated electrodes were immersed in dye solution (0.3 mM in acetonitrile and t-butyl alcohol; Z907 Ru-dye, Solaronix SA) and kept at room temperature for 12 h [18].

The dye-coated electrodes were rinsed with acetonitrile and combined with glass plates by heating a hot-melt glue film at 250°C for 1 min (150 μm thick; Bynel 4164, DuPont, USA). A drop of the electrolyte solution was placed into a hole drilled into the glass of the assembled cell and driven into the cell by vacuum backfilling. Finally, the hole was sealed using additional Bynel film and a glass cover slip (0.1 mm thick). The electrolyte was composed of 0.2 M I_2, 0.5 M N-methylbenzimidazole, and 0.1 M guanidinium thiocyanate in PMII and $EMIB(CN)_4$ (13 : 7 v/v), which has been used in highly durability DSCs [18, 19].

Photovoltaic measurements employed an AM 1.5 solar simulator. The power of the simulated light was calibrated to be 100 mW cm^{-2} by using a reference Si photodiode equipped with an IR-cutoff filter (BS-520, Bunkou-Keiki Co., Ltd., Japan) to limit mismatch in the region of 350–750 nm between the simulated light and AM1.5 to less than 2% [20, 21]. I-V curves were obtained by applying an external bias to the cell and measuring the generated photocurrent with a digital source meter (6240A, ADCMT, Japan). The thermal durability test was performed by keeping DSCs in oven at 80°C. The sheet resistances (four-point probe method), the X-day diffraction patterns, and the electrical impedance spectra were measured using Loresta-EP MCP-T360 (Mitsubishi Chemical Analytech Co., Ltd., Japan), MiniFlex II (Rigaku Co., Ltd., Japan), and SP-150 (Bio-Logic, France), respectively. The impedance spectra were analyzed using software (Z-view 2).

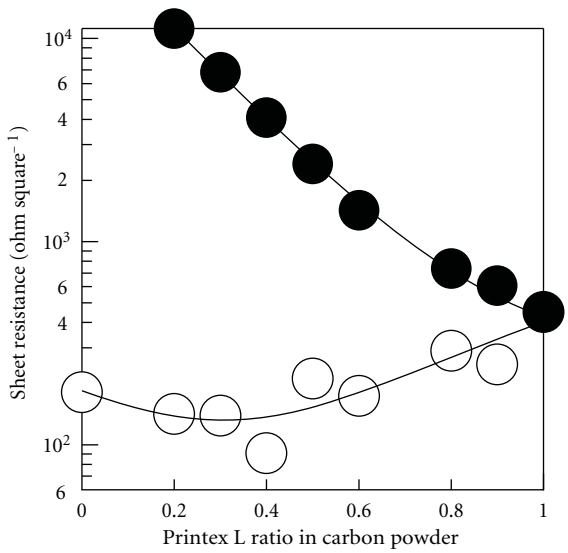

Figure 3: Relation between the carbon powder ratio (the ratio of Printex L in carbon powder) and sheet resistance of carbon electrode: amorphous nanocarbon (Printex L) and graphite (○); amorphous nanocarbon (Printex L) and active carbon (•).

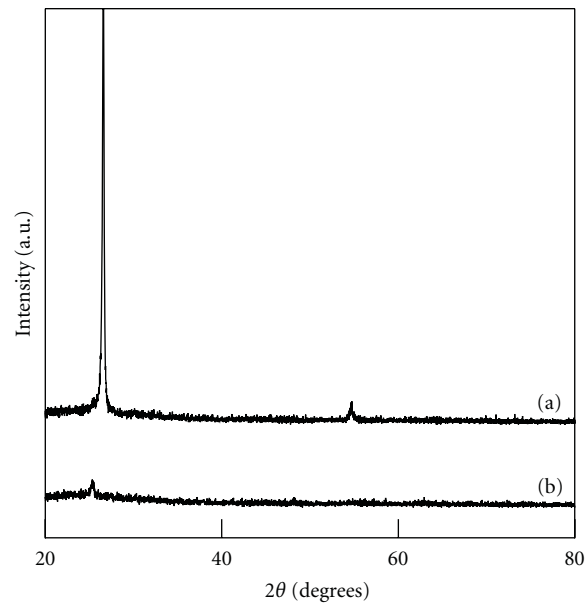

Figure 4: X-ray diffraction patterns of prepared carbon pastes: amorphous nanocarbon (Printex L) and graphite (a); amorphous nanocarbon (Printex L) and active carbon (b).

3. Results and Discussion

In past work, to prepare porous carbon counter electrodes for DSCs, colloidal amorphous TiO_2 particles have been added as a binder for carbon particles [22]. In the present study, however, gas-synthesized TiO_2 nanopowder (80% anatase/20% rutile, P25; Degussa) was added to carbon pastes instead of colloidal amorphous TiO_2. When we used colloidal amorphous TiO_2 nanoparticles to fabricate thicker porous carbon layers for monolithic DSCs, the annealed carbon layer easily cracked and peeled off the substrate, likely caused by crystallization and shrinkage of the amorphous TiO_2 nanoparticles. On the other hand, the gas-synthesized TiO_2 nanopowder gave a thicker (>100 μm), more stable porous carbon layer that did not crack or peel, because the gas-synthesized TiO_2 nanopowder does not undergo further crystallization and shrinkage.

To optimize the conductivity of the porous carbon layer, the ratio of amorphous nanocarbon (Printex L) to graphite or the ratio of amorphous nanocarbon (Printex L) to active carbon was varied. A carbon layer of 13-14 μm in thickness was fabricated on the glass plate by the doctor blade method. The sheet resistance was measured by four-point probe method (Figure 3). The sheet resistance of amorphous nanocarbon (Printex L) layer was increased by adding the active carbon. In contrast, the sheet resistance of amorphous nanocarbon (Printex L) layer was decreased by adding the graphite, reaching a minimum of 90 Ω/ at 40% amorphous nanocarbon in graphite (2.4 g amorphous nanocarbon (Printex L) and 3 g graphite). For the experiments below, carbon paste with this mixing ratio was used.

Figure 4 shows X-ray diffraction spectra of carbon pastes. The carbon paste containing graphite shows an intense peak attributed to the graphite structure, which is not seen in the paste using active carbon. Although the graphite can give high conductivity due to the high crystallinity, the graphite particle was so large that the connection between the graphite particles was not enough to achieve the high conductivity. On the other hand, since the amorphous nanocarbon (Printex L) was very small, the connection between the particles can be very strong. However, because of the low crystallinity of amorphous nanocarbon (Printex L), the pure amorphous nanocarbon layer was not able to improve the conductivity. Hence, the addition of amorphous carbon improved the connection between the graphite particles, resulting in the improvement of conductivity. These are the reasons why the minimum sheet resistance was obtained with 40% amorphous nanocarbon (Printex L) and 60% graphite as shown in Figure 3.

To fabricate porous carbon layers on porous TiO_2/ZrO_2 layers, the annealing process should be optimized. Under simple heating at 400°C for 30 min, the carbon layer cracked and peeled (Figure 5(a)). This cracking and peeling was found to occur on the ZrO_2 layer, but not on the FTO glass plate. Therefore, peeling of the carbon layer was likely attributable to shrinkage of ZrO_2. To prevent ZrO_2 shrinkage from damaging the carbon layer, ZrO_2 was pre-annealed at 200°C for 20 min. Thereafter, carbon paste was printed on the surface of the porous ZrO_2 layer, resulting in a crack-free porous carbon layer (Figure 5(b)).

Figure 6 shows the current-voltage curve of monolithic and standard sandwich-type DSCs. The Monolithic cell

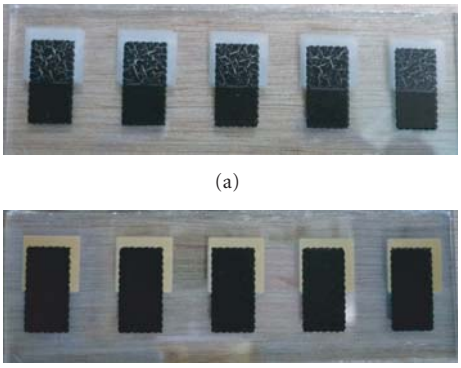

(a)

(b)

Figure 5: Photos of annealed carbon electrodes in monolithic DSCs: (a) without preannealing and (b) with preannealing.

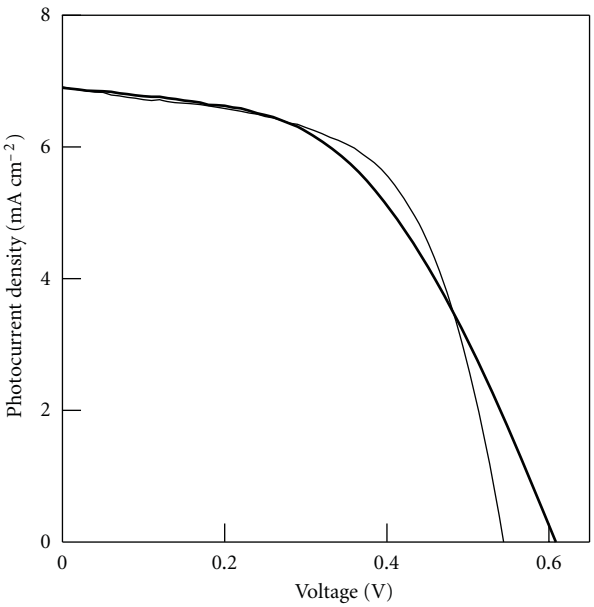

Figure 6: *I-V* curves of DSCs: monolithic structure with carbon electrode (thick line); sandwich structure with Pt/FTO electrode (thin line). Dye (Z907), nanocrystalline-TiO_2 electrodes, photoanode FTO, and ionic liquid electrolyte were the same in the two types of electrodes.

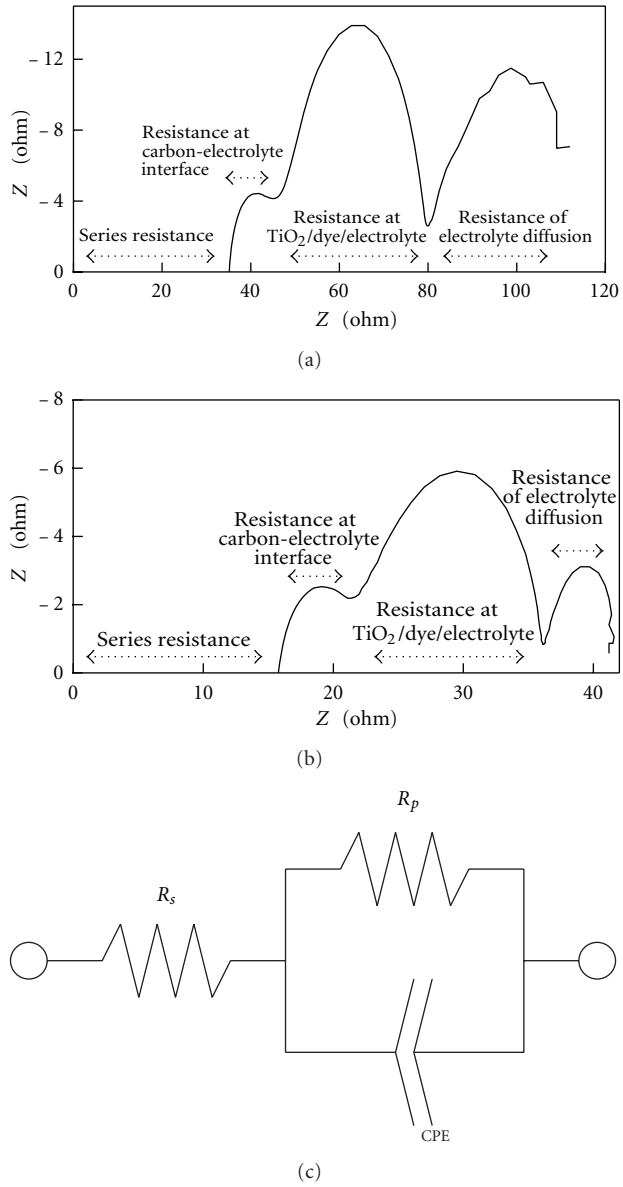

Figure 7: Impedance spectra (Cole-Cole plot) of monolithic- (a) and sandwich- (b) structured DSCs, which was analyzed using an equivalent circuit (c), where R_s, R_p, and CPE are series resistance, parallel resistance and constant-phase element (imperfect capacitance), respectively.

exhibited a short-circuit photocurrent density of 6.90 mA cm^{-2}, open-circuit photovoltage of 0.608 V, and fill factor of 0.491, yielding a power conversion efficiency of 2.06% under AM1.5 irradiation. This photovoltaic performance was comparable to that of standard sandwich-type DSCs using Pt and FTO as counter electrodes (short-circuit photocurrent density, 6.91 mA cm^{-2}; open-circuit photovoltage, 0.544 V; fill factor, 0.592; power conversion efficiency, 2.22%). The prepared monolithic DSCs performed similarly to standard sandwich-structured DSCs in terms of short-circuit photocurrent density. However, the fill factor of the monolithic cells was slight lower than that of standard sandwich-structured DSCs, because the resistance of the carbon layer was higher than that of the FTO layer.

Figures 7(a) and 7(b) show the impedance spectra of monolithic and sandwich-structured DSCs, respectively. The structure of a sandwich DSC was a standard one: <glass/FTO/porous TiO_2/dye/electrolyte/Pt/FTO/glass> [16]. The spacer between FTO-glass substrates was 35 μm, where the electrolyte was filled without porous-ZrO_2 layer. These spectra were analyzed using an equivalent circuit (Figure 7(c)), resulting in a series resistance (R_s), parallel resistances (R_p), and constant-phase elements (CPE,

Table 1: Impedance elements (resistance and constant-phase element) in monolithic- and sandwich-structured DSCs under photoirradiated open-circuit conditions.

DSC structure	Series resistance	Interface of electrolyte/counter electrode		Interface of TiO_2/ dye/electrolyte		Electrolyte diffusion	
	R_s/Ω	R_p/Ω	CPE/F	R_p/Ω	CPE/F	R_p/Ω	CPE/F
Monolithic	35.3	10.5	4.25×10^{-6}	33.8	2.13×10^{-4}	33.1	0.136
Sandwich	16.0	6.24	7.77×10^{-6}	15.2	3.29×10^{-4}	7.04	0.226

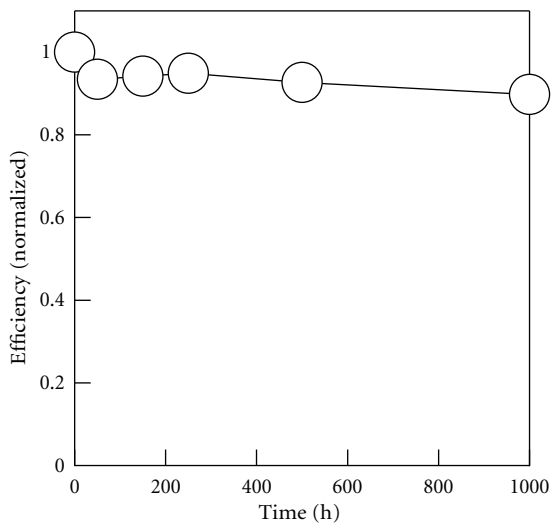

Figure 8: Stability test of monolithic DSC using ionic liquid electrolyte at 80°C in the dark.

imperfect capacitance). Each element was summarized in Table 1. The *CPE* is a kind of capacitance which indicates the depressed semicircles to fit the experimental spectra. In monolithic DSC, the series resistance and interface resistance between the carbon electrode and electrolyte were 35.3 Ω and 10.5 Ω, respectively. For Pt/FTO counter electrodes, these values were 16.0 Ω and 6.24 Ω, respectively. In addition, the diffusion resistance in the electrolyte was increased from sandwich-structured DSC (7.04 Ω) to monolithic-structured DSC (33.1 Ω) due to the addition of the ZrO_2 layer (30 μm). Thus, the deterioration of fill factor was due to the incensement of resistivity by the carbon counter electrode layer and the ZrO_2 layer. Further optimization is needed to improve the photovoltaic characteristic of the carbon electrode and ZrO_2 layer. Figure 8 shows stability test results for an ionic liquid monolithic DSC at 80°C in the dark. Although the efficiency varied slightly at first, it was relatively stable in a 1000 h thermal test at 80°C [18].

In conclusion, we have reported a method using TiO_2 nanopowder, instead of TiO_2 colloid (P25), to prepare carbon paste that does not crack and peel. In addition, cracking due to shrinkage of the ZrO_2 layer was prevented by preannealing the electrode at 200°C for 30 min before printing the carbon layer. As a result, thermally durable monolithic DSCs using ionic liquid electrolyte were prepared that operated stably at 80°C for 1000 h.

References

[1] B. O'Regan and M. Grätzel, "A low-cost, high-efficiency solar cell based on dye-sensitized colloidal TiO_2 films," *Nature*, vol. 353, no. 6346, pp. 737–740, 1991.

[2] M. Grätzel, "Photoelectrochemical cells," *Nature*, vol. 414, no. 6861, pp. 338–344, 2001.

[3] Y. Bai, Y. Cao, J. Zhang et al., "High-performance dye-sensitized solar cells based on solvent-free electrolytes produced from eutectic melts," *Nature Materials*, vol. 7, no. 8, pp. 626–630, 2008.

[4] S. Ito, S. M. Zakeeruddin, P. Comte, P. Liska, D. Kuang, and M. Grätzel, "Bifacial dye-sensitized solar cells based on an ionic liquid electrolyte," *Nature Photonics*, vol. 2, no. 11, pp. 693–698, 2008.

[5] H. Pettersson, T. Gruszecki, R. Bernhard et al., "The monolithic multicell: a tool for testing material components in dye-sensitized solar cells," *Progress in Photovoltaics*, vol. 15, no. 2, pp. 113–121, 2007.

[6] A. Kay and M. Grätzel, "Low cost photovoltaic modules based on dye sensitized nanocrystalline titanium dioxide and carbon powder," *Solar Energy Materials and Solar Cells*, vol. 44, no. 1, pp. 99–117, 1996.

[7] N. Papageorgiou, P. Liska, A. Kay, and M. Grätzel, "Mediator transport in multilayer nanocrystalline photoelectrochemical cell configurations," *Journal of the Electrochemical Society*, vol. 146, no. 3, pp. 898–907, 1999.

[8] S. Burnside, S. Winkel, K. Brooks et al., "Deposition and characterization of screen-printed porous multi-layer thick film structures from semiconducting and conducting nanomaterials for use in photovoltaic devices," *Journal of Materials Science*, vol. 11, no. 4, pp. 355–362, 2000.

[9] H. Pettersson and T. Gruszecki, "Long-term stability of low-power dye-sensitised solar cells prepared by industrial methods," *Solar Energy Materials and Solar Cells*, vol. 70, no. 2, pp. 203–212, 2001.

[10] H. Pettersson, T. Gruszecki, L.-H. Johansson, and P. Johander, "Manufacturing method for monolithic dye-sensitised solar cells permitting long-term stable low-power modules," *Solar Energy Materials and Solar Cells*, vol. 77, no. 4, pp. 405–413, 2003.

[11] N. Kato, K. Higuchi, H. Tanaka, J. Nakajima, T. Sano, and T. Toyoda, "Improvement in long-term stability of dye-sensitized solar cell for outdoor use," *Solar Energy Materials and Solar Cells*, vol. 95, no. 1, pp. 301–305, 2011.

[12] H. Tanaka, A. Takeichi, K. Higuchi et al., "Long-term durability and degradation mechanism of dye-sensitized solar cells

sensitized with indoline dyes," *Solar Energy Materials and Solar Cells*, vol. 93, no. 6-7, pp. 1143–1148, 2009.

[13] D. Kuang, P. Wang, S. Ito, S. M. Zakeeruddin, and M. Grätzel, "Stable mesoscopic dye-sensitized solar cells based on tetracyanoborate ionic liquid electrolyte," *Journal of the American Chemical Society*, vol. 128, no. 24, pp. 7732–7733, 2006.

[14] Y. Bai, Y. Cao, J. Zhang et al., "High-performance dye-sensitized solar cells based on solvent-free electrolytes produced from eutectic melts," *Nature Materials*, vol. 7, no. 8, pp. 626–630, 2008.

[15] H. Matsui, K. Okada, T. Kitamura, and N. Tanabe, "Thermal stability of dye-sensitized solar cells with current collecting grid," *Solar Energy Materials and Solar Cells*, vol. 93, no. 6-7, pp. 1110–1115, 2009.

[16] S. Ito, T. N. Murakami, P. Comte et al., "Fabrication of thin film dye sensitized solar cells with solar to electric power conversion efficiency over 10%," *Thin Solid Films*, vol. 516, no. 14, pp. 4613–4619, 2008.

[17] S. Ito, P. Chen, P. Comte et al., "Fabrication of screen-printing pastes from TiO_2 powders for dye-sensitised solar cells," *Progress in Photovoltaics*, vol. 15, no. 7, pp. 603–612, 2007.

[18] D. Kuang, P. Wang, S. Ito, S. M. Zakeeruddin, and M. Grätzel, "Stable mesoscopic dye-sensitized solar cells based on tetracyanoborate ionic liquid electrolyte," *Journal of the American Chemical Society*, vol. 128, no. 24, pp. 7732–7733, 2006.

[19] D. Kuang, S. Ito, B. Wenger et al., "High molar extinction coefficient heteroleptic ruthenium complexes for thin film dye-sensitized solar cells," *Journal of the American Chemical Society*, vol. 128, no. 12, pp. 4146–4154, 2006.

[20] M. K. Nazeeruddin, P. Péchy, T. Renouard et al., "Engineering of efficient panchromatic sensitizers for nanocrystalline TiO_2-based solar cells," *Journal of the American Chemical Society*, vol. 123, no. 8, pp. 1613–1624, 2001.

[21] S. Ito, H. Matsui, K. I. Okada et al., "Calibration of solar simulator for evaluation of dye-sensitized solar cells," *Solar Energy Materials and Solar Cells*, vol. 82, no. 3, pp. 421–429, 2004.

[22] S. Ito and Y. Mikami, "Porous carbon layers for counter electrodes in dye-sensitized solar cells: recent advances and a new screen-printing method," *Pure and Applied Chemistry*, vol. 83, no. 11, pp. 2089–2106, 2011.

Hindawi Publishing Corporation
International Journal of Photoenergy
Volume 2012, Article ID 385185, 6 pages
doi:10.1155/2012/385185

Research Article

Properties of $Cu(In,Ga)Se_2$ Thin Films and Solar Cells Deposited by Hybrid Process

S. Marsillac,[1] H. Khatri,[2] K. Aryal,[1] and R.W. Collins[2]

[1] *Department of Electrical and Computer Engineering, Old Dominion University, Norfolk, VA 23529, USA*
[2] *Wright Center for Photovoltaics Innovation and Commercialization, University of Toledo, Toledo, OH 43606, USA*

Correspondence should be addressed to S. Marsillac, smarsill@odu.edu

Received 16 December 2011; Accepted 6 February 2012

Academic Editor: Peter Rupnowski

$Cu(In,Ga)Se_2$ solar cells were fabricated using a hybrid cosputtering/evaporation process, and efficiencies as high as 12.4% were achieved. The films were characterized by energy-dispersive X-ray spectroscopy, glancing incidence X-ray diffraction, scanning electron microscopy, auger electron spectroscopy, and transmittance and reflectance spectroscopy, and their properties were compared to the ones of films deposited by coevaporation. Even though the films were relatively similar, the ones deposited by the hybrid process tend to have smaller grains with a slightly preferred orientation along the (112) axis and a rougher surface. Both types of films have uniform composition through the depth. Characterization of these films by variable angle of incidence spectroscopic ellipsometry allowed for the calculation of the position of the critical points, via calculation of the second derivative of the dielectric function and fit with critical points parabolic band oscillators. The solar cells were then characterized by current-voltage and quantum efficiency measurements. An analysis of the diode parameters indicates that the cells are mostly limited by a low fill factor, associated mostly with a high diode quality factor ($A - 1.8$) and high series resistance ($R_s \sim 1.1\,\Omega\text{-cm}^2$) .

1. Introduction

Many technology options exist nowadays to harvest the power of the sun, a sustainable energy source, and generate electricity directly from this source via the photovoltaic effect. Among them, $Cu(In,Ga)Se_2$ has gained significant momentum as a possible high-efficiency and low-cost thin film solar cell material. Results for high-performance $Cu(In,Ga)Se_2$ solar cells have been reported with absorber material prepared either by multisource coevaporation of the elements (Cu, In, Ga, and Se) at temperatures between 550–600°C or by selenization of Cu, In, and Ga films in the presence of H_2Se gas [1–7]. These techniques are currently implemented in companies such as Wurth Solar, Global Solar, or Solar Frontier. The objective of this work is to fabricate device quality $Cu(In,Ga)Se_2$ solar cells using a process that may have greater potential for large-scale production. For the production of this thin film solar cell technology, the implementation of an easily scalable deposition process is effectively as important as the achievement of high efficiencies. One means to accomplish this goal is by introduction of a hybrid process for the deposition of the $Cu(In,Ga)Se_2$ layer using both cosputtering of the metals and evaporation of the selenium. To the best of our knowledge, device fabrication using a similar hybrid process has not been actively pursued since 1995, having achieved an efficiency near 10% on a small area device [8]. In this study, we will present results on the hybrid deposition and characterization of $Cu(In,Ga)Se_2$ thin films and solar cells and will compare these results with those from solar cells in which the $Cu(In,Ga)Se_2$ is purely coevaporated.

2. Experimental

$Cu(In,Ga)Se_2$ thin films were deposited onto molybdenum (Mo) coated soda-lime glass by a hybrid process using dc magnetron cosputtering of elemental copper (Cu), indium (In), and copper-gallium alloy (Cu-Ga: 75–25 at. %) targets along with simultaneous evaporation of selenium (Se). This is a modification of the previous process used for these films [8] with the addition of the copper source, allowing for greater flexibility in the process. Film depositions were

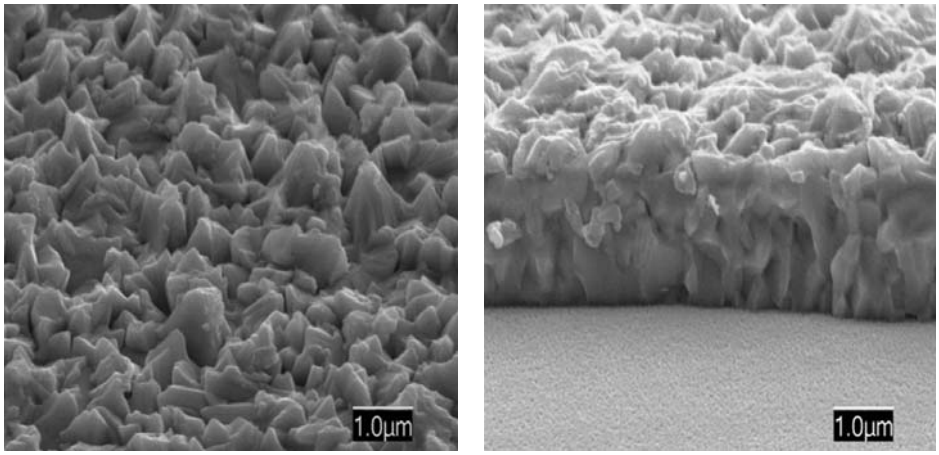

(a) (b)

Figure 1: Surface (a) and cross-sectional (b) scanning electron microscopy (SEM) images of $Cu(In,Ga)Se_2$ films deposited by a hybrid process.

performed at an Ar pressure of 2 mTorr with constant rates for the metal fluxes and the selenium. The $Cu(In,Ga)Se_2$ film thicknesses ranged from 2 μm for the devices down to 60 nm for specialized optical analysis. The substrate temperature was set at 550°C. Good uniformity of the films' elemental composition (∼2%) and its thickness (∼5%) were both obtained by rotating the substrate holder (15 rev/min). Coevaporated $Cu(In,Ga)Se_2$ films were also deposited and characterized for this study using a process described elsewhere [9].

3. Results and Discussions

The elemental composition of the films was determined by energy dispersive X-ray spectroscopy (EDS). The ratios x ≡ Ga/(In +Ga) and y ≡ Cu/(In +Ga) were found to be 0.30 and 0.93, respectively, which results in an energy band-gap, E_g, of 1.16 eV. Figure 1 shows representative surface and cross-sectional images of the 2 μm thick $Cu(In,Ga)Se_2$ film by scanning electron microscopy (SEM). The images reveal that the hybrid-sputtered $Cu(In,Ga)Se_2$ films have well-defined columnar grains with an average grain size of ∼300 nm. This size is smaller than that of the films grown by the coevaporation process for the same composition.

Glancing incidence X-ray diffraction (GIXRD) measurements were performed using CuKα-radiation (λ = 0.15418 nm) with a 0.01° step size and various incidence angles ranging from 0.5° to 10°. The $Cu(In,Ga)Se_2$ films form a single-phase tetragonal crystal structure. The relative crystal orientations of the films prepared by hybrid sputtering and by coevaporation were 0.8 and 0.6, respectively, as measured by the ratio of the area under the (112) and (220)/(204) peaks. This indicates a slightly preferred orientation along the (112) axis for the hybrid-deposited films versus a random orientation for the coevaporated films. The average crystallite size, as determined by the full width at half maximum using Scherrer formula [10], was 393 nm for the hybrid films, which is consistent with the SEM images. The coevaporated films show a larger grain size, above the sensitivity range of this method. Little variation of the peaks was observed as a function of incidence angle indicating a constant compositional profile with depth into the film. This was corroborated by Auger electron spectroscopy measurements, which did not show any variation in composition as a function of depth.

The dielectric functions ($\varepsilon_1, \varepsilon_2$) of $Cu(In,Ga)Se_2$ thin films (60 nm) deposited by the hybrid and coevaporation processes were obtained by variable angle of incidence spectroscopic ellipsometry over the photon energy range from 0.74 eV to 6.6 eV. Thinner films were selected due to their relatively smooth surfaces, which provide higher accuracy results. It should be emphasized, however, that the thinner films may exhibit a smaller grain size and a different preferential grain orientation, factors that may lead to a difference in these dielectric functions relative to those of the thick films used in solar cells.

Given the uniaxial optical nature of the tetragonal chalcopyrite crystal structure, small differences exist between the ordinary and extraordinary dielectric function components of the single crystal. For (112) oriented films as well as for random orientation, the dielectric function is a weighted superposition of ordinary and extraordinary components [11]. In this study, an isotropic model for the dielectric function of the films was assumed. The optical model consists of (i) the soda-lime glass substrate (SLG); (ii) an interface roughness or modulation layer (thickness: d_i) between the SLG and $Cu(In,Ga)Se_2$, whose dielectric function is determined from an effective medium theory as a 0.5/0.5 volume fraction mixture of glass and the overlying bulk layer $Cu(In,Ga)Se_2$; (iii) the bulk layer $Cu(In,Ga)Se_2$ (thickness: d_b); (iv) a surface roughness layer (thickness: d_s), whose dielectric function is determined similarly to that of the interface—now as a 0.5/0.5 volume fraction mixture of the bulk layer material and void.

Figure 2 shows the results of an analysis of *ex-situ* spectroscopic ellipsometry data for the $Cu(In,Ga)Se_2$ films,

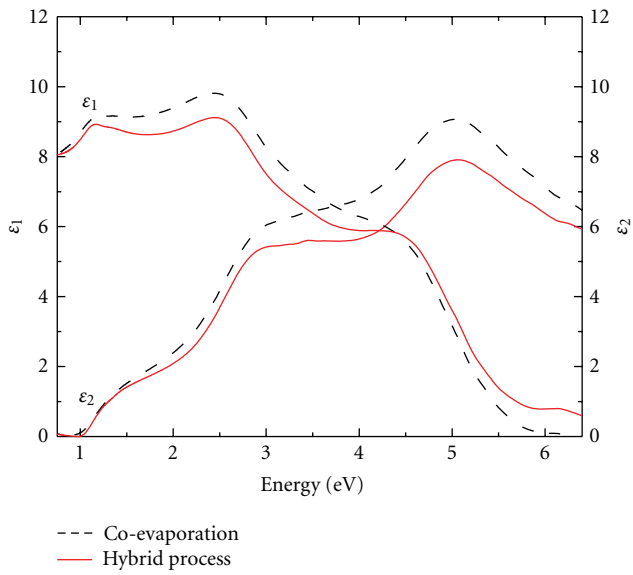

Figure 2: Optical dielectric functions for $Cu(In,Ga)Se_2$ films deposited by the hybrid process (solid line) and coevaporation process (dotted line).

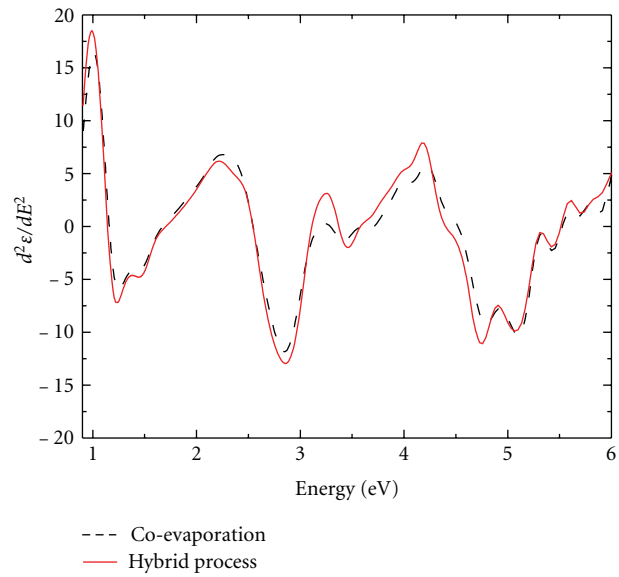

Figure 3: Second derivatives of the imaginary parts of the dielectric functions (ε_2) of 60 nm $Cu(In,Ga)Se_2$ films obtained by hybrid (solid line) and coevaporation processes (dotted line).

applying the optical model of the previous paragraph along with exact inversion. The photon-energy-independent parameters are obtained via the artifact-minimization/semiconductor criterion. In this procedure, bulk, surface, and interface layer thicknesses are chosen to ensure that the imaginary part of the dielectric function ε_2 is constantly below the absorption onset and as close as possible to zero. Such analysis led to the following numerical values for the films by the hybrid process: bulk layer thickness $d_b = 60 \pm 0.6$ nm; surface roughness layer thickness $d_s = 8 \pm 0.3$ nm; interface layer thickness $d_i = 1.4 \pm 0.2$ nm. Similarly, the corresponding parameters for the coevaporated $Cu(In,Ga)Se_2$ film were $d_b = 61 \pm 0.5$ nm, $d_s = 6 \pm 0.6$ nm, and an interface layer thickness $d_i = 1.7 \pm 0.3$ nm. The surface roughness was also measured by noncontact mode atomic force microscopy (AFM) and correlated well with the values obtained by ellipsometry analysis. Values of 6 nm and 4 nm were obtained for the hybrid and coevaporation processes, respectively, indicating a slightly rougher surface for the hybrid process as mentioned earlier.

The dielectric functions (ε_1, ε_2) for the hybrid deposited and coevaporated films are obtained as shown in Figure 2 simultaneously with the identification of the correct (d_b, d_s, d_i) by the artifact-minimization/semiconductor criterion.

The observed features in (ε_1, ε_2) are associated with interband transitions that appear at the van Hove singularities or critical points (CPs) of the joint density of states. These features were fitted assuming parabolic bands (PBs), yielding CP-PB oscillators each given by

$$\varepsilon_j(\omega) = \left[A_j \exp\left(i\phi_j\right)\right]\left(\omega - E_j + i\Gamma_j\right)_j^n, \tag{1a}$$

$$\varepsilon_j(\omega) = \left[A_j \exp\left(i\phi_j\right)\right]\ln\left(\omega - E_j + i\Gamma_j\right), \tag{1b}$$

where A_j is the amplitude, E_j is the energy, Γ_j is the broadening, and ϕ_j is the phase, all for the jth critical point. The exponent n_j is -1, $-1/2$, 0 (i.e., the "ln" function in (1b)), or $+1/2$ for excitonic, 1-dimensional, 2-dimensional, or 3-dimensional CPs, respectively. Here the fundamental transitions were fitted with excitonic CPs, and the higher transition points were fitted with 2-dimensional CPs. Because some CPs were not easily resolved, the second derivatives of the dielectric functions were used in fitting the CP-PB oscillators, as follows [12–15]:

$$\frac{d^2\varepsilon}{dE^2} = \left[A'_j \exp\left(i\phi_j\right)\right]\left(E - E_j + i\Gamma_j\right)_j^{n-2}, \tag{2}$$

where $E = \omega$ is the photon energy. The remaining four parameters for each CP were obtained in fits to the second derivatives of the dielectric functions obtained as described elsewhere [13]. The polynomial order and number of grouped data points used in this differentiation procedure were chosen to smooth the second-order derivatives without excessive line-shape distortion. The derivatives of the imaginary parts (ε_2) of the dielectric functions are shown in Figure 3 for both types of films. A sum of up to twelve resonances of the form of (2) was used to simulate the convolved ordinary and extraordinary dielectric functions of the polycrystalline $Cu(In,Ga)Se_2$ thin films.

The second derivatives of the imaginary parts dielectric functions of $Cu(In,Ga)Se_2$ thin films deposited by both processes in Figure 3 show similar positions for the CP energies. The following electronic transition assignments for the hybrid process are based on a comparison with those of a single crystal [15]. The E_0 transition energies are as follows: $E_0(A) = 1.15$ eV, $E_0(B) = 1.23$ eV, $E_0(C) = 1.46$ eV. The value for $E_0(A)$, the fundamental energy band-gap, when applied to extract composition, yields results in excellent agreement

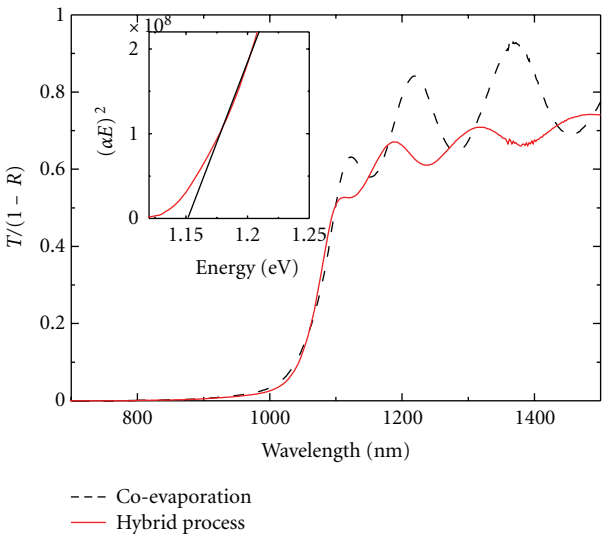

Figure 4: Room temperature $T/(1-R)$ spectra of 2 μm thick $Cu(In,Ga)Se_2$ films; the inset is a plot of $(\alpha E)^2$ versus E for the hybrid deposited sample.

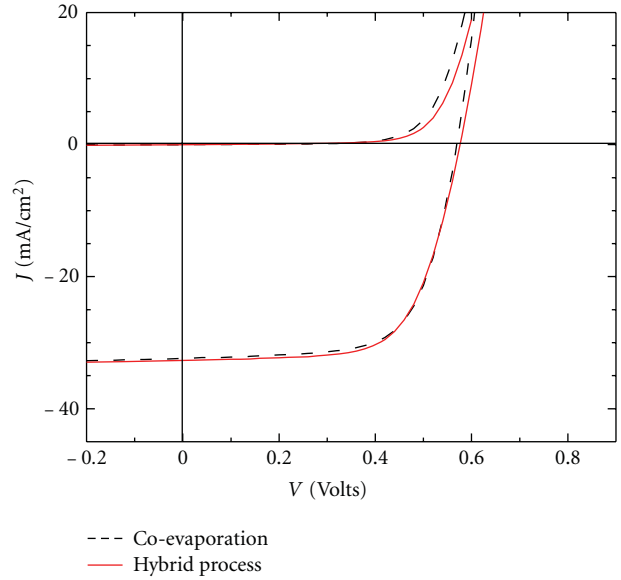

Figure 5: Current density-Voltage (J-V) characteristics of $Cu(In,Ga)Se_2$ solar cells deposited by hybrid and coevaporation processes.

with those obtained by EDS and XRD measurements. Three high energy transitions, namely, E_3–E_5 were also identified; however, assignments to specific electronic transitions in the band-structure are not yet possible. The following describes the higher energy CPs obtained in this analysis: $E_1(A)$ = 2.95 eV, $E(X\Gamma)$ = 3.31 eV, $E_1(B)$ = 3.75 eV, $E(\Delta X)$ = 4.19 eV, $E'(\Gamma X)$ = 4.23 eV, $E_2(A)$ = 4.61 eV, $E_2(B)$ = 4.86 eV, E_3 = 5.14 eV, E_4 = 5.47 eV, and E_5 = 5.94 eV. The CPs are not only directly useful for determining the band gap, which is a critical parameter for the solar cell, but also potentially useful for distinguishing between two materials with different properties that may lead to different device performance parameters. For example, the broadening parameters can provide information on the grain size.

Since $Cu(In,Ga)Se_2$ is a direct gap semiconductor [16], the absorption coefficient α is predicted to follow the well-known relationship $(\alpha n E)^2 = A(E - E_g)$ for $E > E_g$, where E_g is the energy band-gap and n is the refractive index. Thus, to determine the band-gap, it is usual to measure α by transmittance and reflectance (T and R) spectroscopy and then to extrapolate linear plots of $(\alpha E)^2$ versus E to zero ordinate as shown in Figure 4. This is based on the assumption that n is weakly varying with respect to energy in the range of interest. As one can see, a value of E_g = 1.16 eV was obtained for the hybrid process, consistent with the critical point energy $E_0(A)$ obtained by analysis of the dielectric function. It is also interesting to note that the interference fringe amplitude for the coevaporated film is larger, indicating a smoother surface since the film thicknesses are essentially identical.

After the films were fully characterized using the methods described, solar cells were fabricated by the two processes. This requires depositing a thin n-CdS buffer layer (~50 nm) by chemical bath deposition (CBD) and two rf magnetron-sputtered window layers that consist of a highly resistive intrinsic zinc oxide (80 nm) and a conductive and transparent indium tin oxide (180 nm). To enhance current collection, the device was completed by the thermal evaporation of Ni/Al/Ni metal grids with thicknesses of 50 nm/2 μm/50 nm. Finally, a MgF_2 antireflection coating (130 nm) was deposited by thermal evaporation. The cell area of 0.5 cm^2 was defined by mechanical scribing.

The current density-voltage (J-V) measurements of the completed devices were performed under standard test conditions (AM 1.5 global spectrum at 25°C, 100 mW/cm^2). We observed uniform cell performance, with efficiencies greater than 11%, for 1 inch by 3 inch substrates incorporating 26 small area devices (0.50 cm^2). The best cell exhibited an efficiency of 12.4%, with the following critical cell parameters: open circuit voltage V_{oc} = 576 mV, short-circuit current density J_{sc} = 32.7 mA/cm^2 and fill factor FF = 66%. In Figure 5, the J-V curve for the best device by the hybrid process is compared with a similar device deposited by single-stage coevaporation.

Quantum efficiency (QE) measurements were also performed on the best hybrid cell and on a coevaporated cell (Figure 6). The two QE cells are nearly indistinguishable in agreement with their similar current and band gap. The calculation of the current from the QE curve by integrating the data over the entire spectrum leads to value identical to the ones obtained via the J-V curves and confirmed the proper calibration of our system and correct area of the cells. The QE onset in the near infrared (~1070 nm) is consistent with the energy band-gap obtained from the EDS, XRD, and optical measurements.

In the near-infrared region >900 nm, the slight drop in QE for the hybrid cell may be explained by a higher recombination rate for electrons generated by photons absorbed

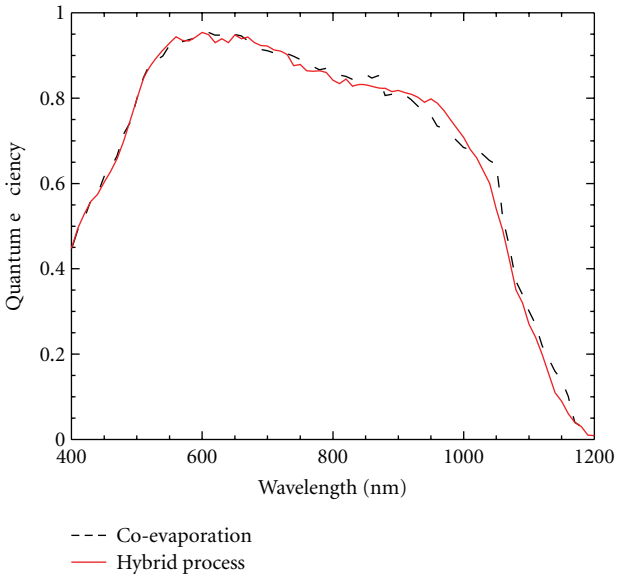

Figure 6: Normalized quantum efficiency (QE) characteristics for $Cu(In,Ga)Se_2$ solar cells deposited by hybrid and coevaporation processes.

deep within the $Cu(In,Ga)Se_2$ layer (i.e., towards the Mo back electrode) and/or by photon absorption by a larger concentration of free carriers in the ITO of the hybrid cell.

The J-V data were then analyzed using the standard diode equation considering that the forward diode current is limited by Shockley-Read-Hall (SRH) recombination through the states within the Space Charge Region (SCR) of the $Cu(In,Ga)Se_2$. The diode equation is given by

$$J = J_0 \exp\left(\frac{q(V - R_s J)}{AkT}\right) - J_0 - J_L + GV, \quad (3)$$

where J_0 is the forward current, A the diode quality factor, R_s the series resistance, J_L the light generated current, and G the shunt conductance. The shunt conductance, calculated from the J-V characteristics in the dark was found to be small for both types of devices and is, therefore, neglected in our device analysis. Differentiation of (3) with $J_L = J_{sc}$ leads to

$$\frac{dV}{dJ} = R_s + \frac{AkT}{q}(J + J_{sc})^{-1}. \quad (4)$$

For the $Cu(In,Ga)Se_2$ films deposited by hybrid sputtering, we found that $R_s \sim 1.1\,\Omega\text{-cm}^2$ and $A \sim 1.8$, whereas for the films deposited by coevaporation, $R_s \sim 0.8\,\Omega\text{-cm}^2$ and $A \sim 1.6$. These data were derived from the slope and intercept, respectively, in a linear fit to dV/dJ plotted versus $(J + J_{sc})^{-1}$. Classically, the value of A is between 1 and 2. The higher value for the diode quality factor in the case of the hybrid process appears to indicate that the main recombination mechanism is more closely related to interface recombination than to space charge region recombination. The higher value of the series resistance for the hybrid process might also be correlated to its higher surface roughness. Further characterization of the devices, as a function of temperature, for example, would be necessary to investigate further this difference.

4. Conclusion

The fabrication and characterization of $Cu(In,Ga)Se_2$ thin films deposited by a hybrid process were performed, and solar cells with efficiencies as high as 12.4% were achieved. Chemical, structural, and optical characterization indicates that the properties of films deposited by the hybrid process are very close to those deposited by a standard coevaporation process. The primary differences include a smaller grain size and thicker surface roughness for the hybrid process. The device performance characteristics are also found to be very similar in this study. Two aspects of this study should be emphasized, however. First, we are currently achieving higher efficiencies by coevaporation using a 3-step process; our modified hybrid process will allow us to do similar multistep deposition in the future. Second, the hybrid device performance is primarily limited by a low fill factor, which may be due to parameters other than those associated with $Cu(In,Ga)Se_2$ material limitations. As a result, further improvement in the hybrid process is expected, and the performance achieved here is not the ultimate limit of the optimization process. Overall, this new hybrid co-sputtering/evaporation process has demonstrated the capability of fabricating devices with reasonable efficiency and high uniformity and, therefore, is a promising process for potential scale up in the future.

References

[1] P. Jackson, D. Hariskos, E. Lotter et al., "New world record efficiency for $Cu(In,Ga)Se_2$ thin-film solar cells beyond 20%," *Progress in Photovoltaics*, vol. 19, no. 7, pp. 894–897, 2011.

[2] I. Repins, M. A. Contreras, B. Egaas et al., "19.9% efficient $ZnO/CdS/CuInGaSe_2$ solar cell with 81.2% fill factor," *Progress in Photovoltaics*, vol. 16, no. 3, pp. 235–239, 2008.

[3] S. Marsillac, P. D. Paulson, M. W. Haimbodi et al., "High-efficiency solar cells based on $Cu(InAl)Se_2$ thin films," *Applied Physics Letters*, vol. 81, no. 7, pp. 1350–1352, 2002.

[4] L. Eldada, "Thin film CIGS photovoltaic modules: monolithic integration and advanced packaging for high performance, high reliability and low cost," in *Proceedings of The International Society for Optical Engineering*, vol. 7942 of *Proceedings of SPIE*, 2011.

[5] A. Meeder, P. Schmidt-Weber, U. Hornauer et al., "High voltage $Cu(In,Ga)S_2$ solar modules," *Thin Solid Films*, vol. 519, no. 21, pp. 7534–7536, 2011.

[6] D. Schmid, I. Koetschau, A. Kampmann et al., "Centrotherm's high end CIGS thin film turnkey solution," in *Proceedings of the International Society for Optical Engineering*, Wuhan, China, August 2009.

[7] Y. Chiba, S. Kijima, H. Sugimoto et al., "Achievement of 16% milestone with 30 cm × 30 cm-sized CIS-based thin-film submodules," in *Proceedings of the IEEE Photovoltaic Specialists Conference*, pp. 164–168, Honolulu, Hawaii, USA, June 2010.

[8] L. C. Yang and A. Rockett, "Cu-Mo contacts to $CuInSe_2$ for improved adhesion in photovoltaic devices," *Journal of Applied Physics*, vol. 75, no. 2, pp. 1185–1189, 1994.

[9] P. D. Paulson, M. W. Haimbodi, S. Marsillac, W. N. Shafarman, and R. W. Birkmire, "$CuIn_{1-x}Al_xSe_2$ thin films and solar cells,"

Journal of Applied Physics, vol. 91, no. 12, pp. 10153–10156, 2002.

[10] N. Kasai and M. Kakudo, *X-Ray Di raction by Macromolecules*, vol. 80 of *Springer Series in Chemical Physics*, Kodansha Scientific, Tokyo, Japan, 2005.

[11] M. I. Alonso, M. Garriga, C. A. Durante Rincon, and M. Leon, "Optical properties of chalcopyrite $CuAl_xIn_{1-x}Se_2$ alloys," *Journal of Applied Physics*, vol. 88, no. 10, pp. 5796–5801, 2000.

[12] M. I. Alonso, M. Garriga, C. A. Durante Rincón, E. Hernández, and M. León, "Optical functions of chalcopyrite $CuGa_xIn_{1-x}Se_2$ alloys," *Applied Physics A*, vol. 74, no. 5, pp. 659–664, 2002.

[13] P. Lautenschlager, M. Garriga, and M. Cardona, "Temperature dependence of the interband critical-point parameters of InP," *Physical Review B*, vol. 36, no. 9, pp. 4813–4820, 1987.

[14] D. E. Aspnes, *Handbook on Semiconductors*, vol. 2, North-Holland Publishing Company, Amsterdam, The Netherlands, 1980.

[15] M. I. Alonso, K. Wakita, J. Pascual, M. Garriga, and N. Yamamoto, "Optical functions and electronic structure of $CuInSe_2$, $CuGaSe_2$, $CuInS_2$, and $CuGaS_2$," *Physical Review B*, vol. 63, no. 7, Article ID 75203, 13 pages, 2001.

[16] R. H. Bube, *Photovoltaic Materials*, Imperial College Press, London, UK, 1998.

Hindawi Publishing Corporation
International Journal of Photoenergy
Volume 2012, Article ID 357218, 5 pages
doi:10.1155/2012/357218

Research Article

Investigation of the Relationship between Reverse Current of Crystalline Silicon Solar Cells and Conduction of Bypass Diode

Hong Yang, He Wang, and Minqiang Wang

Institute of Solar Energy MOE Key Laboratory for Nonequilibrium Synthesis and Modulation of Condensed Matter, Department of Physics, Xi'an Jiaotong University, Xi'an 710049, China

Correspondence should be addressed to He Wang, hw69cn@126.com

Received 9 December 2011; Accepted 31 January 2012

Academic Editor: Bhushan Sopori

In the process of crystalline silicon solar cells production, there exist some solar cells whose reverse current is larger than 1.0 A because of silicon materials and process. If such solar cells are encapsulated into solar modules, hot-spot phenomenon will emerge in use. In this paper, the effect of reverse current on reliability of crystalline silicon solar modules was investigated. Based on the experiments, considering the different shaded rate of cells, the relation between reverse current of crystalline silicon solar cells and conduction of bypass diode was investigated for the first time. To avoid formation of hot spots and failure of solar modules, the reverse current should be smaller than 1.0 A for 125 mm × 125 mm monocrystalline silicon solar cells when the bias voltage is at −12 V.

1. Introduction

More and more people are convinced that solar cell technology is the solution for our future energy supply. The crystalline silicon solar cells have been a workhorse of photovoltaic industry for a long time. Although the hot-spot endurance tests for extreme outdoor conditions are used for qualification tests procedures, and the bypass diodes are also built in crystalline silicon solar module, hot-spot phenomenon still emerges in solar power plant frequently. This is very detrimental to young photovoltaic industry.

Hot-spot heating in crystalline silicon solar modules occurs when the modules' operating current exceeds the short circuit current of a low-current-producing cell. The reduced short circuit current of cells becomes reverse biased, which leads to power dissipation resulting in the increase in surface temperature [1–3].

In order to avoid hot-spot phenomenon in solar power plant, one of the technical requirements of crystalline silicon solar modules is a fulfilment of the pass criteria of the hot-spot endurance test [4]. But in practice, it is found by infrared camera that the hot-spot heating occurs in some modules even if bypass diodes are built-in. One reason for the hot-spot phenomenon is that some cells have large reverse current in crystalline silicon solar modules. Although some photovoltaic experts have investigated reverse current of crystalline silicon solar cells [5–8], nobody gives a standard that rules magnitude of reverse current in the process of solar modules production from theoretical study or experiments. This question is still under discussion in the photovoltaic area. In this paper, the origin of reverse current is analyzed. Considering the different shaded rate of cells, the relation between reverse current of crystalline silicon solar cells and conduction of bypass diode was investigated for the first time. To avoid formation of hot spots and failure of solar modules, the reverse current should be smaller than 1.0 A for 125 mm × 125 mm monocrystalline silicon solar cells when the bias voltage is at −12 V.

2. The Origin of Reverse Current for Crystalline Silicon Solar Cells

Figure 1 shows the reverse bias model and the reverse characteristic of crystalline silicon solar cells.

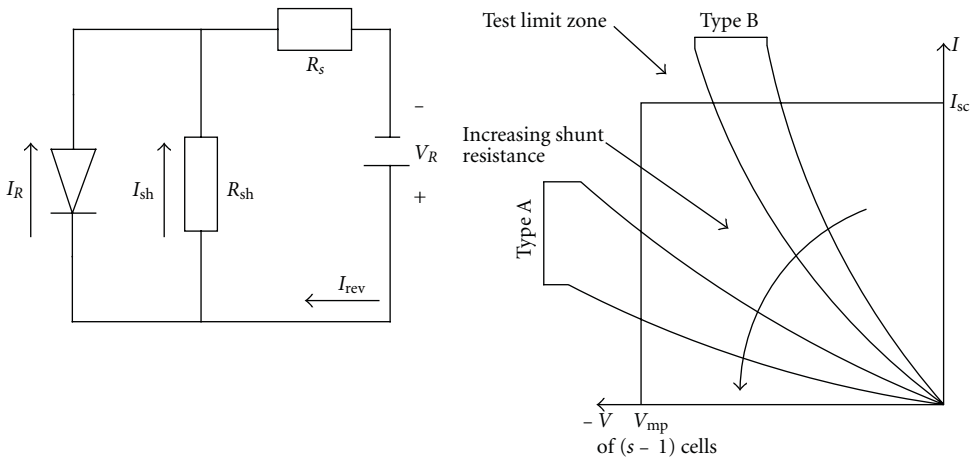

(a) The reverse bias model (b) The reverse characteristics

Figure 1: The reverse bias model and the reverse characteristic of crystalline silicon solar cells.

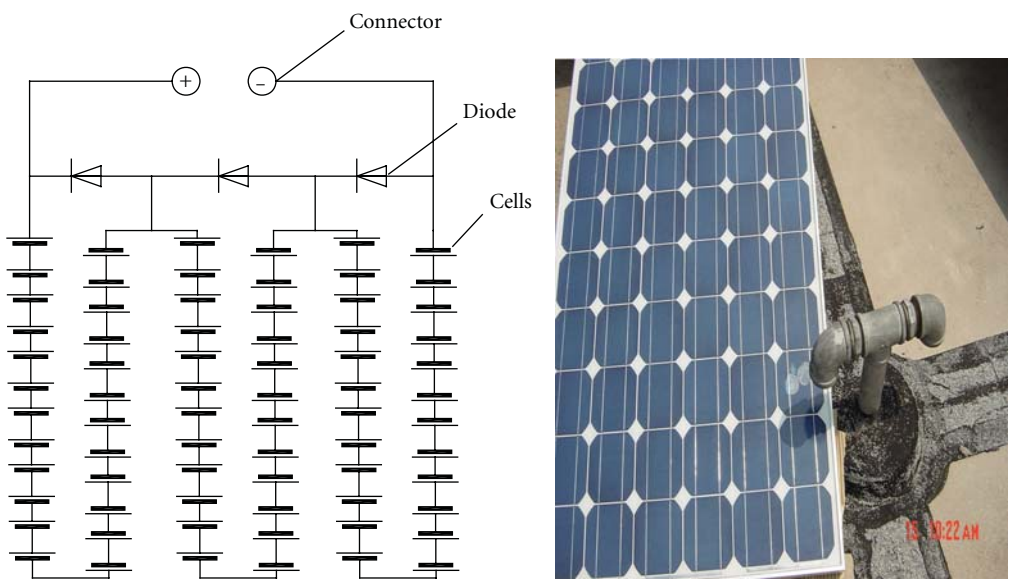

(a) Circuit of solar module (b) Hot-spot phenomena

Figure 2: Hot-spot phenomena of the partially shaded cells.

Figure 1(a), the current flows through the solar cell can be expressed as

$$I_{rev} = I_R + I_{sh} = I_R + \frac{V_R - I_{rev}R_S}{R_{sh}},$$
$$I_{rev} = I_0 + \frac{V_R - I_{rev}R_S}{R_{sh}}, \quad (1)$$
$$I_{rev} = \frac{I_0 R_{sh}}{R_{sh} + R_S} + \frac{V_R}{R_{sh} + R_S},$$

where I_{rev} is the reverse current of crystalline silicone solar cell under reverse bias voltage V_R which is below the breakdown voltage of the silicone diode, I_R is the reverse leakage current of diode, and R_{sh} is the shunt resistance.

The P-N junction leakage current I_R under reverse bias includes the contributions of diffusion current, space charge generation current; band-to-band tunneling current and thermionic emission current. These shunt types are processed-induced, caused by grown-in defects of the material. The process-induced shunts are due to strong recombination sites at grown-in defects and inversion layers caused by microscopic (SiC) precipitates on grain boundaries [9]. As the reverse bias voltage V_R is small, the leakage current I_R can be expressed as the function of saturation current of silicon diode I_0 and shunt resistance R_{sh}. Either the I_0 increase or R_{sh}

Table 1: The terminal voltage of the bypass diode.

The reverse current of cells at bias voltage −12 V	Terminal voltage when the cell is unshaded (V)	Terminal voltage when the cell is half shaded (V)	Terminal voltage when the cell is completely shaded (V)
0.8 A	−5.83	0.23	0.25
0.9 A	−5.83	0.18	0.25
1.0 A	−5.83	0.15	0.25
1.1 A	−5.83	0.09	0.14
1.2 A	−5.84	−0.08	0.05
1.3 A	−5.82	−0.09	−0.24
1.4 A	−5.83	−0.21	−0.34
1.5 A	−5.83	−0.43	−0.59
1.6 A	−5.84	−0.58	−0.83
1.8 A	−5.83	−0.79	−1.12
2.0 A	−5.82	−1.03	−1.25
2.2 A	−5.84	−1.18	−1.47
2.4 A	−5.85	−1.36	−1.79
2.6 A	−5.83	−2.63	−1.83
2.8 A	−5.82	−3.53	−1.99
3.0 A	−5.83	−3.67	−2.56

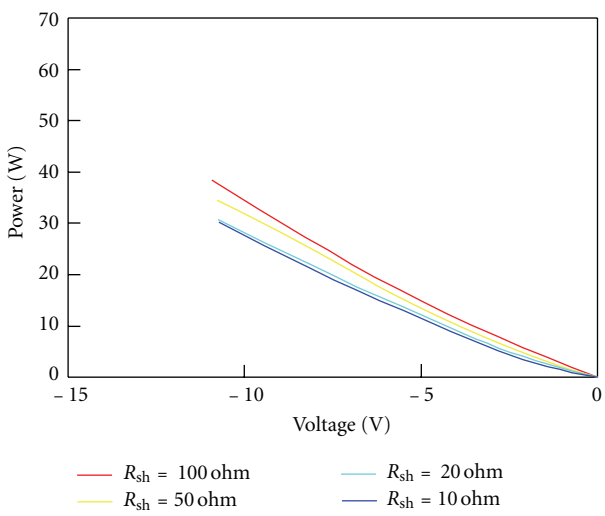

Figure 3: The dissipated power at different shunt resistance.

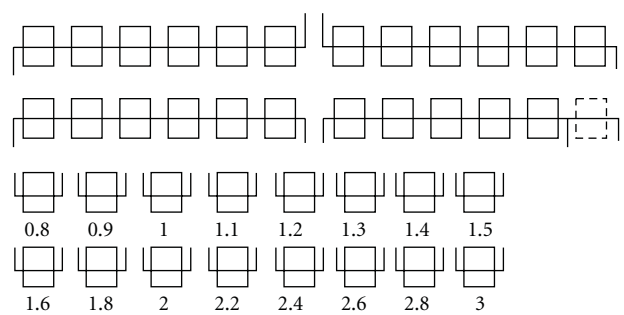

Figure 4: The makeup of module before lamination.

decrease, the reverse current I_{rev} increases with the variable, and these two parameters determine the solar cell type.

Spirito and Abergamo made a distinction between A-type cells, dominated in reverse bias by avalanche multiplication, and B-type cells, dominated by shunt resistance effects in reverse bias [1]. Reverse bias equation for A-type cells is

$$I = I_{SC} - I_0 \exp\frac{V}{mV_t} - 1 \quad M(V),$$
$$M = \frac{1}{1 - (|V|/V_b)^n}, \tag{2}$$

where I_{SC}, I_0, m and V_t have their usual meaning, V_b is breakdown voltage, and n is the Miller exponent.

In the case of B-type cells, the equation used by the authors is

$$I = I_{SC} - I_0 \exp\frac{V}{mV_t} - 1 \quad - \frac{V}{R_{sh}}. \tag{3}$$

The characteristics of different types of solar cells are described in Figure 1(b). The reverse I-V characteristics of the individual cells mainly determine the power dissipated within a single cell under reverse bias.

3. The Effect of Reverse Current on the Reliability of Crystalline Silicon Solar Modules

In a general way, the reverse current of crystalline silicon solar cells originates in cell defects and impurity centers in the materials and can be represented by a shunt resistance. We chose 71 cells (125 mm × 125 mm) whose reverse current is smaller than 1.0 A at $V = -12$ V and the shunt resistance is larger than 20 Ω. And one cell has a 2.008 A of reverse

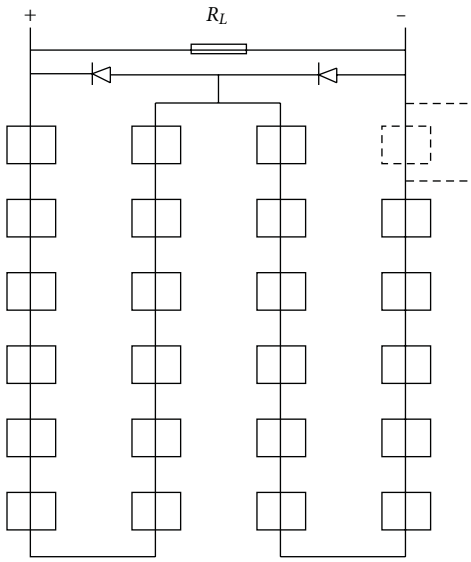

Figure 5: The method of the experiment.

current and 12.88 Ω of shunt resistance. These 72 single silicon solar cells are laminated one module in series that three Schottky diodes are built-in. 24 cells were serially connected with a bypass diode across each string. The modules were short-circuited for several days under natural sunlight; the cell which has a 2.008 A of reverse current at −12 V is partially shaded, and after about 20 k Wh/m^2·day of solar irradiation, there was a hot spot in this module, as can be seen from Figure 2.

From Figure 2, this clearly indicates that focal point heating at the hot-spot sites causes irreversible destruction of the crystalline silicon solar module structure, even if bypass diodes were used in this solar module; this is because the shaded cell dissipated power in the form of heat and led to deterioration of the encapsulation.

Figure 3 shows the dissipated power of the shaded cell in a solar module described by Figure 2(a).

As shown in Figure 3, the smaller the shunt resistance is, the more power the shaded cell dissipates.

4. Investigation of the Threshold of Reverse Current about Bypass Diode Conduction

In order to study the threshold of reverse current that can avoid hot spot, the experiment designed by us is presented in Figure 4. The cells used in this experiment are 125 mm × 125 mm (154.8 cm^2) single crystalline silicon solar cells, and the reverse current of the above two rows of cells is less than 1.0 A at bias voltage −12 V. The reverse current of the rest cells is shown in Figure 4.

In Figure 5, the dashed part represents one cell that has different reverse current (0.8 A–3.0 A) and is connected, respectively.

Table 1 gives out the terminal voltage of the bypass diode under different shaded rate.

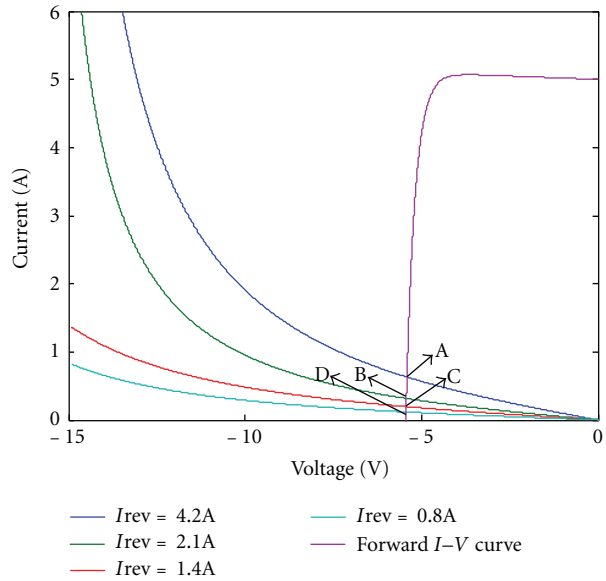

(a) I-V of a cell shaded 75%

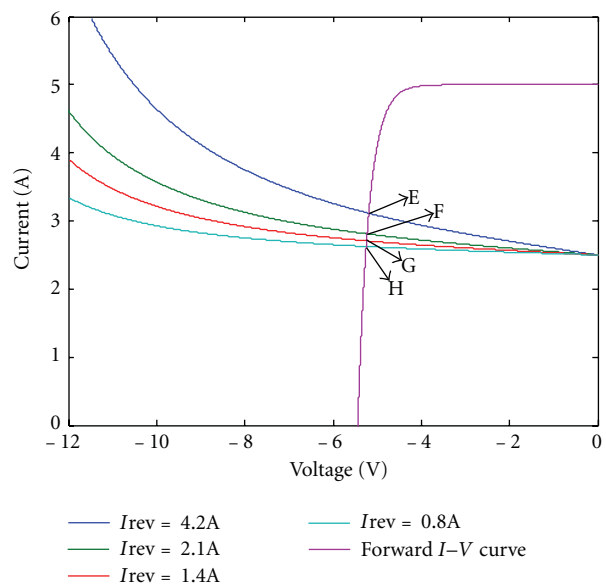

(b) I-V of a cell shaded 25%

Figure 6: The I-V characteristics of module with a shaded cell.

From Table 1, it can be concluded that the bypass diode becomes conductive easily when the reverse current of solar cells is less than 1.0 A at bias voltage −12 V, so we can explain why the bypass diode did not function in Figure 2.

By comparing Table 1 with our former experimental results [10], we find that conduction of the bypass diode is also relevant to the area of crystalline silicon solar cell.

Figure 6 gives out the I-V characteristics of shaded photovoltaic module; the current of module is decided by the points of intersection between the reverse I-V of the shaded cells and the forward I-V of the rest cells.

From this experiment, we find that the larger the reverse current is, the larger the reverse-biased cell dissipates, and it is not more conducive to the bypass diode conduction. The slope of the I-V curve in the reverse bias mode gives information regarding the cell's pn junction properties in shunt resistance and has an effect on the I-V slope of a cell in the reverse bias, resulting in high power dissipation.

For the cells with a large reverse current, in addition to the level of irradiance and reverse current, the dissipated power at a shaded crystalline silicon solar cell is strongly influenced by the shaded rate.

5. Conclusions

In general, to avoid of the formation hot spots for crystalline silicon solar modules, substrings of cells inside the interconnection circuit of modules are bridged by bypass diodes, but conduction of bypass diode is determined by the reverse current and the shading rate of the shaded cell.

When the reverse current is larger than 1.0 A at bias voltage −12 V for 125 mm × 125 mm monocrystalline silicon solar cells, the shaded cell does not become reverse biased and the bypass diode does not conduct; this will lead to irreversible hot-spot damage of cells.

By experiments, we recommended that the reverse current should be smaller than 1.0 A for 125 mm × 125 mm monocrystalline silicon solar cells when the bias voltage is at −12 V.

Acknowledgments

The authors would like to thank the support of Bureau of Science and Technology under the Project no. CXY 1123 and the fund of Applied Materials Co. of USA under the Project no. 201005. This study was also supported by the Fundamental Research Funds for the Central Universities.

References

[1] P. Spirito and V. Abergamo, "Reverse bias power dissipation of shadowed or faulty cells in different array configurations," in *Proceedings of the 4th European Photovoltaic Solar Energy Conference*, pp. 296–300, 1982.

[2] J. Wohlgemuth and W. Herrmann, "Reliability testing for PV modules," in *Proceedings of the 26th IEEE Photovoltaic Specialists Conference (PVSC '82)*, pp. 889–892, 1982.

[3] W. Herrmann, W. Wiesner, and W. Vaassen, "Hot spot investigations on PV modules—new concepts for a test standard and consequences for module design with respect to bypass diodes," in *Proceedings of the 26th IEEE Photovoltaic Specialists Conference*, pp. 1129–1132, Anaheim, Calif, USA, October 1997.

[4] International Standard IEC-61215:2005, "Crystalline silicon terrestrial photovoltaic (PV) modules design qualification and type approval".

[5] M. C. Alonso-García and J. M. Ruíz, "Analysis and modelling the reverse characteristic of photovoltaic cells," *Solar Energy Materials and Solar Cells*, vol. 90, no. 7-8, pp. 1105–1120, 2006.

[6] M. C. Alonso-García, W. Herrmann, W. Böhmer, and B. Proisy, "Thermal and electrical effects caused by outdoor hot-spot testing in associations of photovoltaic cells," *Progress in Photovoltaics: Research and Applications*, vol. 11, no. 5, pp. 293–307, 2003.

[7] M. Simon and E. L. Meyer, "Detection and analysis of hot-spot formation in solar cells," *Solar Energy Materials and Solar Cells*, vol. 94, no. 2, pp. 106–113, 2010.

[8] M. Danner and K. Buecher, "Reverse characteristics of commercial silicon solar cells - impact on hot spot temperatures and module integrity," in *Proceedings of the 26th IEEE Photovoltaic Specialists Conference*, pp. 1137–1140, Anaheim, Calif, USA, October 1997.

[9] O. Breitenstein, J. P. Rakotoniaina, M. H. Al Rifai, and M. Werner, "Shunt types in crystalline silicon solar cells," *Progress in Photovoltaics: Research and Applications*, vol. 12, no. 7, pp. 529–538, 2004.

[10] H. Yang, W. Xu, H. Wang, and M. Narayanan, "Investigation of reverse current for crystalline silicon solar cells-new concept for a test standard about the reverse current," in *35th IEEE Photovoltaic Specialists Conference (PVSC '10)*, pp. 2806–2810, June 2010.

Hindawi Publishing Corporation
International Journal of Photoenergy
Volume 2012, Article ID 834347, 11 pages
doi:10.1155/2012/834347

Research Article

A Study on a Solar Simulator for Dye Sensitized Solar Cells

Kyoung-Jun Lee,[1] Jeong-Hoon Kim,[1] Ho-Sung Kim,[1] Dongsul Shin,[1] Dong-Wook Yoo,[2] and Hee-Je Kim[1]

[1] *Department of Electrical Engineering, Pusan National University, Jangjeon, Geumjeong, Busan 609-735, Republic of Korea*
[2] *Power Conversion Center, HVDC Division, KERI, Changwon, Republic of Korea*

Correspondence should be addressed to Hee-Je Kim, heeje@pusan.ac.kr

Received 27 October 2011; Accepted 27 December 2011

Academic Editor: Bhushan Sopori

Dye-sensitized solar cells (DSSC) are emerging low-cost, simple alternatives to conventional solar cells. While there has been considerable study on improving the efficiency of DSSCs, there has not been sufficient research on a photovoltaic power conditioning system adaptable to DSSCs or on a solar simulator for DSSCs. When DSSCs are commercialized in the near future, the DSSC modules must be connected to an adaptable power conditioning system in order to manage the energy produced and provide a suitable interface to the load. In the process of developing a power conditioning system, a solar simulator with the characteristics of DSSCs is essential to show the performance of the maximum power point tracking. In this paper, a virtual DSSC is designed and simulated in PSIM. Irradiation factors, temperature and shadow effects are considered in dynamic link library block in PSIM which is linked to the external C routine. A 100 W converter is built to show the performance of a DSSC as the solar simulator controlled by a digital signal processor.

1. Introduction

Solar energy has emerged as a solution for problems such as depletion of fossil energy resources and environmental pollution. Solar energy is a clean and permanent energy source. In addition, solar power systems have many benefits such as very low maintenance, long life, and easy installation. That is why the solar power industry is rapidly developing [1]. Most solar panels on the photovoltaic market are crystalline or multicrystalline silicon solar cells. However, in spite of their high efficiency, these are difficult to commercialize due to shortage of raw materials, high manufacturing costs, and complicated fabrication processes. DSSCs based on a photochemical mechanism are in the limelight as a promising alternative to silicon solar cells because of various advantages such as low manufacturing costs, simple fabrication process, flexibility, and transparency [2–4]. However, to commercialize DSSCs, there are still many shortages to overcome [5]. In particular, their low efficiency limits their practical application. Much DSSC research is currently focused on this problem. In addition, research on the installation of large-scale DSSC modules is important [6].

To develop a solar controller for DSSCs, researchers need to consider the output characteristics and conduct an experiment with DSSC modules. However, the output characteristics of DSSCs depend on the weather conditions. Therefore, an assistant power system that simulates the characteristics of DSSCs and that can be controlled arbitrarily by the researcher is required in the development process for reliable experimental data.

To solve these problems, in this paper, a simple and low-cost DSSC solar simulation of discontinuous conduction mode (DCM) boost converter is suggested, showing the performance versus such factors as irradiance, temperature, shading, and connection method. The algorithm is first simulated by the DLL block linked with the external C routine, referring to the extracted data from lab-made DSSCs. The simulation program shows the I-V and P-V curves versus conditions. The proposed solar simulator consists of

the power supply, DC-DC boost converter, electronic load, and digital signal processor (DSP). That system generates the output power to 100 W level of DSSCs controlled by DSP with the SS algorithm. The SS is designed for trial experiments of large scale, and the reliability of the SS is verified in this paper.

2. Dye-Sensitized Solar Cell

2.1. An Equivalent Circuit of DSSCs. The simple equivalent circuit consists of the current source, diode, capacitances, and the resistances. The current source generates the I_{PH} (photoelectric current) in proportion to the irradiation of sunlight. Figure 1 shows the equivalent circuit of a DSSC. The C_{Pt} and R_{Pt} are the impedance through carrier transport on the surface of the counter electrode. The C_{ELEC} and R_{ELEC} are the impedance with regard to carrier transport through the ions in the electrolyte, and those are worked as the diode with regard to electron transfer of TiO_2/dye/electrolyte facing surface. R_{TCO} is the resistance through the surface resistance. R_{SH} is shunt resistance through the back electron transfer. The capacitance elements can be ignored because the values of the capacitances are fairly large. That is why the circuit will be simplified such as current source, diode, one of parallel resistance, and three of series resistances. The Equation (1) represents the I_D which is the current flowing through a diode:

$$I_D = I_O\left\{\exp\left(q\frac{V + IR_S}{nkT}\right) - 1\right\}. \quad (1)$$

Equation (2) represents the I_{SH} which is current flowing through R_{SH}. The R_{TCO}, R_{ELEC}, and R_{Pt} are incorporated as R_S:

$$I_{SH} = \frac{V + IR_S}{R_{SH}}. \quad (2)$$

The output current I_O can be explained like (3). The output current is same as all current excluding I_D and I_{SH} [7–9]:

$$I_O = I_{PH} - I_D - I_{SH} = I_{PH} - I_D\left\{\exp\left(q\frac{V + IR_S}{nkT}\right) - 1\right\} - \frac{V + IR_S}{R_{SH}}. \quad (3)$$

2.2. The Characteristics of DSSCs. The characteristics of DSSCs are changed according to the factors such as irradiation, temperature, shadowing effect, and connecting style. In this paper, the characteristics of a $1 \times 1\,\text{cm}^2$ size DSSC unit cell are explained according to some factors. Figure 2 shows $1 \times 1\,\text{cm}^2$ size lab-made DSSC unit cell.

2.2.1. The Shadowing E ect. The shadowing effects affect the characteristics of a DSSC. When the DSSC is under the shadow, power loss is generated as heat because of reverse current flows [10–12]. But a DSSC is less sensitive to partial shade compared with the Si solar cells.

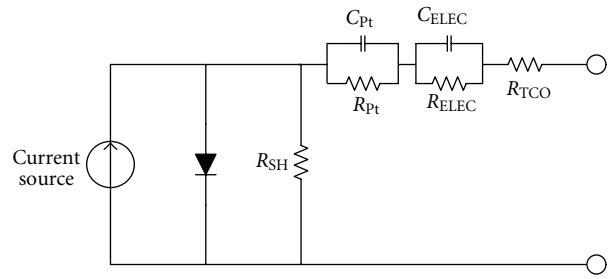

Figure 1: An equivalent circuit of a DSSC.

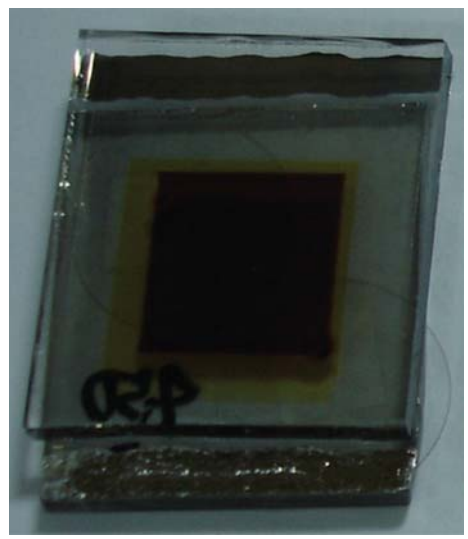

Figure 2: A $1 \times 1\,\text{cm}^2$ size DSSC unit cell.

A $1 \times 1\,\text{cm}^2$ DSSC was prepared for experiments on the shadowing effect. The metal-coated foil was also prepared to create a shadow. The shadowing effects were given to 0, 25, 50, and 75% in order. The photovoltaic performances of the cell were evaluated by a source meter unit (Model 2400, Keithley Instruments Inc.) under the standard test conditions (STC), which is the temperature of 25°C and irradiation of $1000\,\text{W/m}^2$, using a solar simulator (Sun 2000, Abet Technologies Inc., USA). Table 1 shows the characteristics of the unit cell according to the shadowing effects such as open-circuit voltage (V_{oc}), short-circuit current (I_{sc}), fill factor (FF), efficiency, and maximum power. The current is greatly reduced by increasing the shadowing rate. But the voltage is a little reduced. The power is reduced according to the shading rate. The V_{oc} and I_{sc} of each shading condition are considered in SS algorithm.

2.2.2. The Temperature and Irradiation E ect. The DSSCs in the field operate under the variable STC due to the irradiation and temperature changes throughout the day.

Table 1: The characteristics of the unit cell according to the shadowing effect.

Shading rate	Parameter				
	V_{oc} (V)	I_{sc} (mA)	FF	η (%)	P_{max} (mW)
0%	0.734	8.186	0.643	3.863	3.863
25%	0.722	5.932	0.664	2.843	2.843
50%	0.716	4.026	0.707	2.039	2.093
75%	0.702	2.631	0.738	1.363	1.363

The change of temperature and irradiation affects the efficiency and performance of a DSSC. Figure 3(a) shows the I-V characteristics of a DSSC according to the change of the temperature. At this time, the irradiation is constant at 1000 W/m^2. The current is almost constant, and the voltage is changed by the change of the temperature. The voltage decreases by approximately 2.84 mV when the temperature increases by 1°C [13]. The maximum power point is also changed by the alternation of the value of voltage. Figure 3(b) shows the I-V characteristics of a DSSC according to the change of the irradiation. At this time, the temperature is constant as 25°C. The voltage is almost constant, but the current is linearly changed according to the irradiation. The maximum power point is also changed by the value of irradiation.

2.2.3. The Series-Parallel Connection. We assumed that there is no loss in series-parallel connection. The value of the voltage increases in proportion to the number of DSSCs in the series connection. At this time, the current is constant. And the value of the current increased in the parallel connection. At this time, the voltage is constant. Therefore, the I-V and P-V characteristics of DSSCs according to the connection method can be simply obtained by multiplying N_s (Number of series connections) and N_P (Number of parallel connections) to STC data.

3. Simulation Program

3.1. The Design of the Simulation Program. The SP (simulation program) model is designed with DLL block in the PSIM and Microsoft Visual C++. The DLL block is the virtual circuit of the $1 \times 1\,\text{cm}^2$ DSSC unit cell. The DLL block is the linked external C routine which is made from Microsoft Visual C++. The results of the simulation are represented as I-V and P-V curves according to the input conditions such as irradiation, temperature, connection style, and shadow effect. Figure 4 shows PSIM circuit with a DLL block and the window for conditions input.

Since characteristic equations of DSSC are of nonlinear form, the implementation using equivalent equations take lots of data memory size and calculation time in microcontroller unit (MCU). So, the proposed method uses only extracted data from lab-made DSSC according to the factors and interpolation method to obtain the new reference curve in any conditions [14].

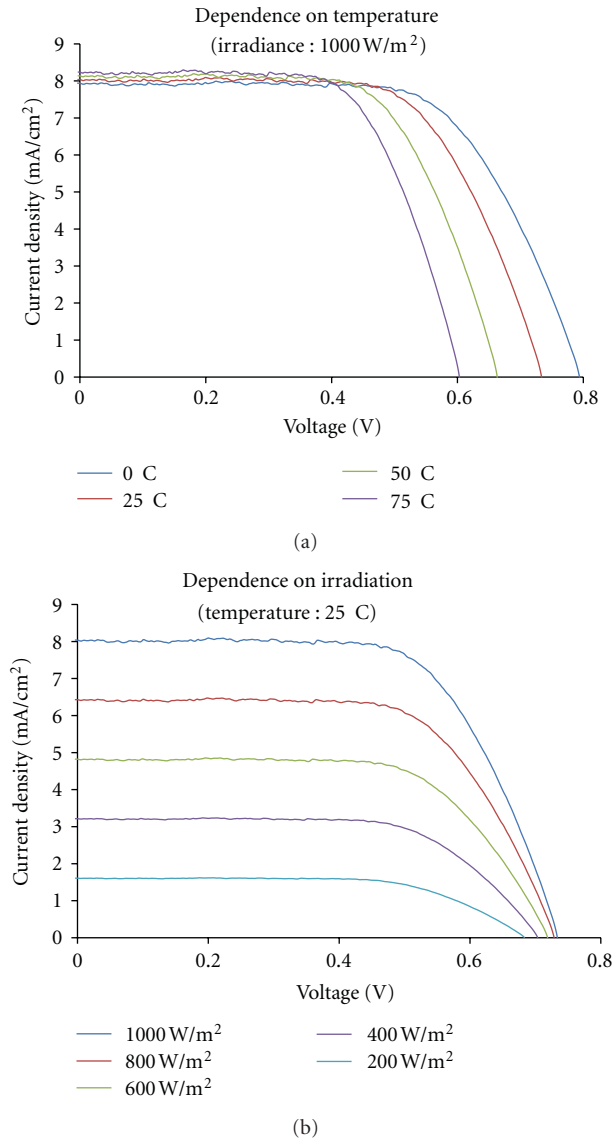

Figure 3: (a) The I-V characteristic curves of DSSCs according to the temperature. (b) The I-V characteristic curves of DSSCs according to the irradiation.

To simplify the process of getting I-V curve in selected new conditions, relationship variables are calculated from Figure 5:

$$V_{\text{Irr}_N} = V_{\text{Irr}_L} - \frac{\text{Irr} - \text{Irr}_L}{\text{Irr}_H - \text{Irr}_L}\left(V_{\text{Irr}_L} - V_{\text{Irr}_H}\right), \tag{4}$$

$$V_{T_N} = V_{T_L} - \frac{T - T_L}{T_H - T_L}\left(V_{T_L} - V_{T_H}\right), \tag{5}$$

$$V_{\text{SH}_N} = V_{\text{SH}_L} - \frac{\text{SH} - \text{SH}_L}{\text{SH}_H - \text{SH}_L}\left(V_{\text{SH}_L} - V_{\text{SH}_H}\right), \tag{6}$$

$$\beta_{\text{Irr}} = \frac{V_{\text{Irr}_N}}{V_{\text{STC}}}, \qquad \beta_T = \frac{V_{T_N}}{V_{\text{STC}}}, \qquad \beta_{\text{SH}} = \frac{V_{\text{SH}_N}}{V_{\text{STC}}}, \tag{7}$$

where V_{Irr_L} is the voltage of the lower range according to the selected irradiation, V_{Irr_H} is the voltage of the higher

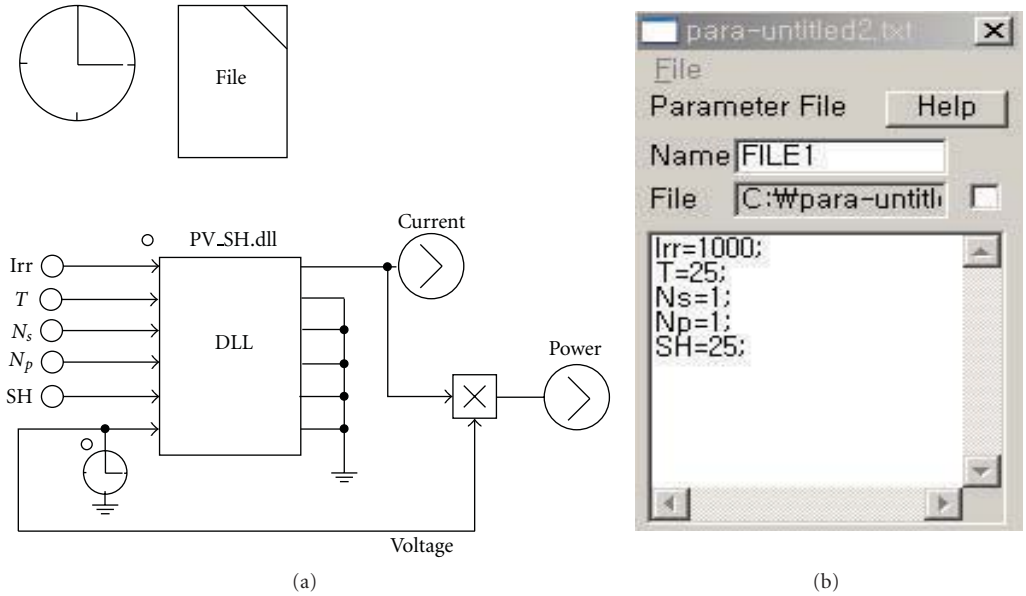

Figure 4: (a) The SP model with DLL block. (b) The window for conditions input.

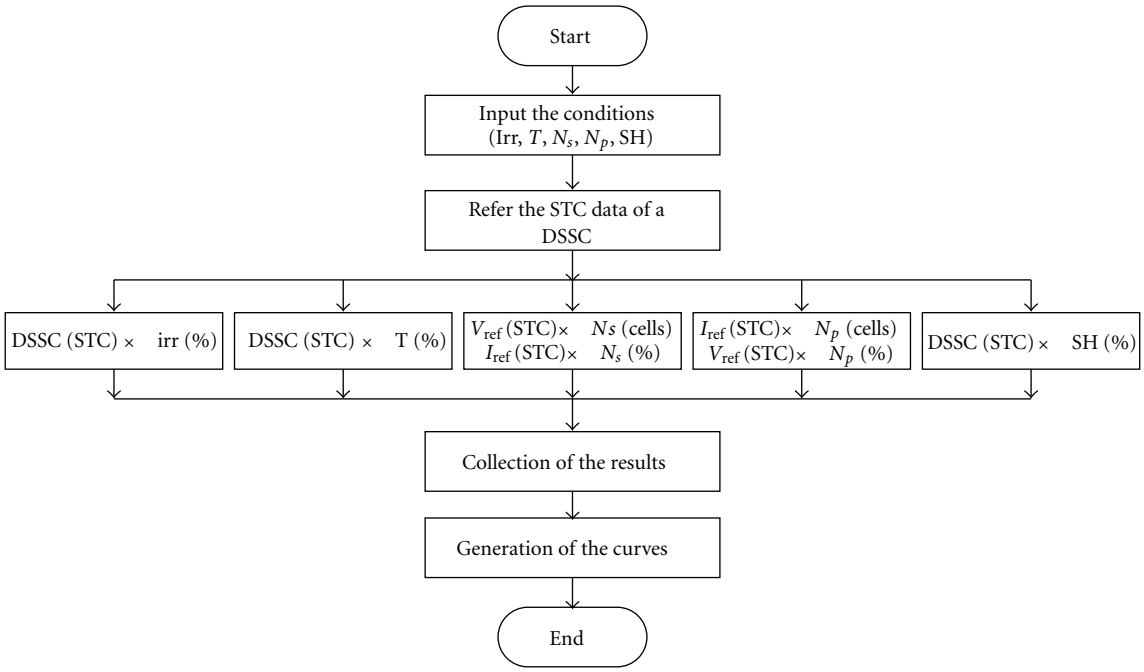

Figure 5: Proposed SS algorithm flow chart.

range according to the selected irradiation, V_{Irr_N} is the new reference voltage according to the selected irradiation, Irr is the selected value of irradiation, V_{T_L} is the voltage of the lower range according to the selected temperature, V_{T_H} is the voltage of the higher range according to the selected temperature, V_{T_N} is the new reference voltage according to the selected temperature, T is the selected value of temperature, V_{SH_L} is the voltage of the lower range according to the selected shadowing rate, V_{SH_H} is the voltage of the higher range according to the selected shadowing rate,

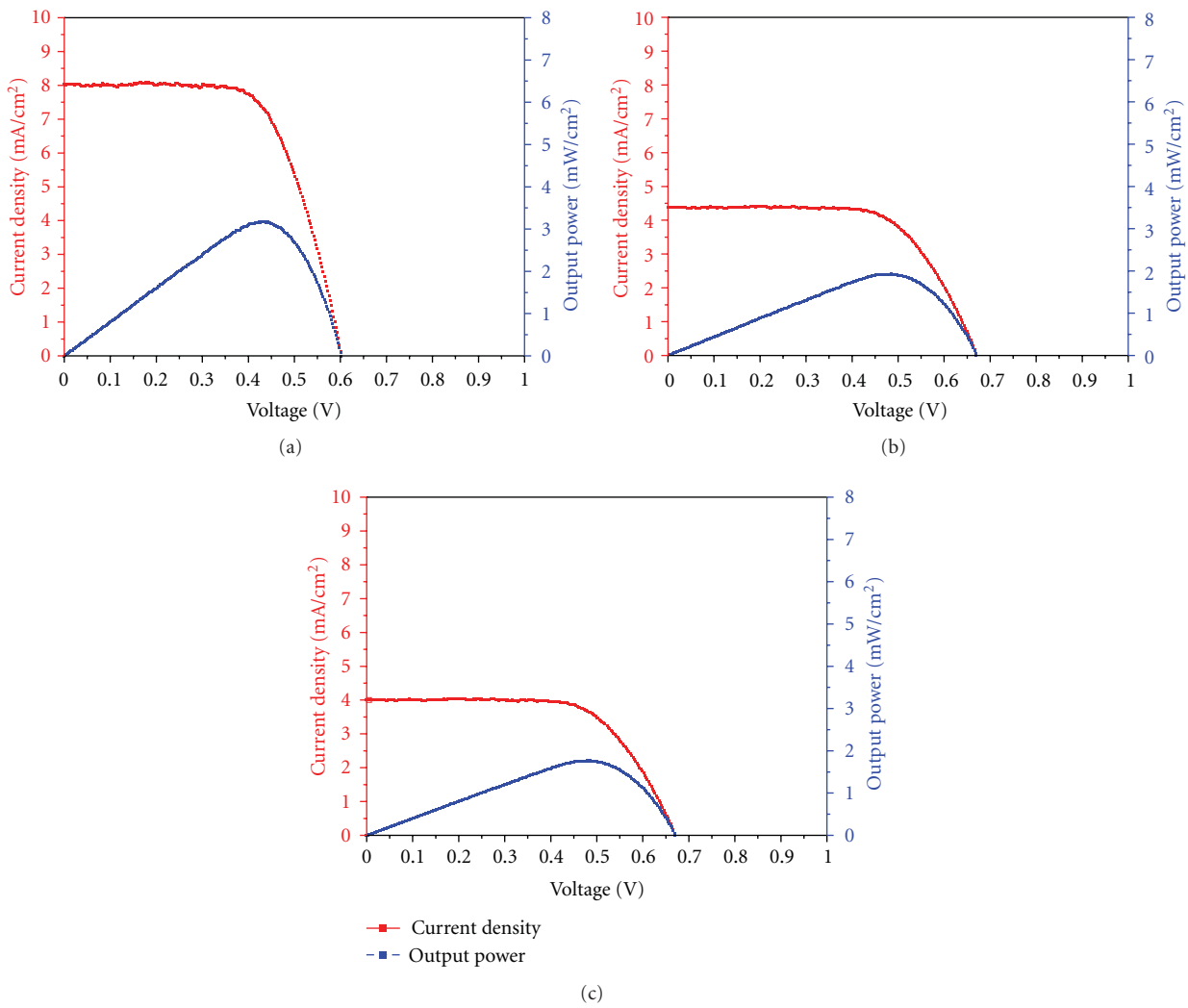

Figure 6: (a) Simulation results at 75°C, 1000 W/m^2, 0% shadowing rate. (b) Simulation results at 25°C, 600 W/m^2, 0% shadowing rate. (c) Simulation results at 25°C, 1000 W/m^2, 50% shadowing rate.

V_{SH_N} is the new reference voltage according to the selected shadowing rate, SH is the selected value of shadowing rate, β_{Irr} is the relationship variable of irradiation, β_T is the relationship variable of temperature, β_{SH} is the relationship variable of shadowing rate, and V_{STC} is the voltage at STC. For example, if the irradiation is selected to 700 W/m^2, the higher range and lower range are each 800 W/m^2 and 600 W/m^2.

Finally, the new reference voltage (V_{REF}) is calculated by

$$V_{REF} = V_{STC} \times (\beta_{Irr} \times \beta_T \times \beta_{SH}) \times N_s. \quad (8)$$

Similarly, the new reference current (I_{REF}) is obtained through the same procedure like (4) ~ (8):

$$I_{REF} = I_{STC} \times (\alpha_{Irr} \times \alpha_T \times \alpha_{SH}) \times N_P, \quad (9)$$

where α_{Irr} is the relationship variable of irradiation, α_T is the relationship variable of temperature, α_{SH} is the relationship variable of shadowing rate, and I_{STC} is the current at STC.

After the calculation is finished according to the conditions, the collection of the results will be made. After the collection is finished, the results of simulation will be displayed at the Simview of the PSIM.

3.2. The Result of the Simulation Program. The output of DSSCs is changed according to some factors. The SP model represents the output of DSSCs in the PSIM. The results of simulation are displayed at the Simview of the PSIM according to some factors. Figure 6 shows the I-V and P-V curves of the simulation for DSSCs. The user can obtain any output curves according to any value of the factors from SP.

4. Solar Simulator

4.1. The Design of the Solar Simulator. Figure 7 shows the block diagram of the SS. The SS consists of the power supply

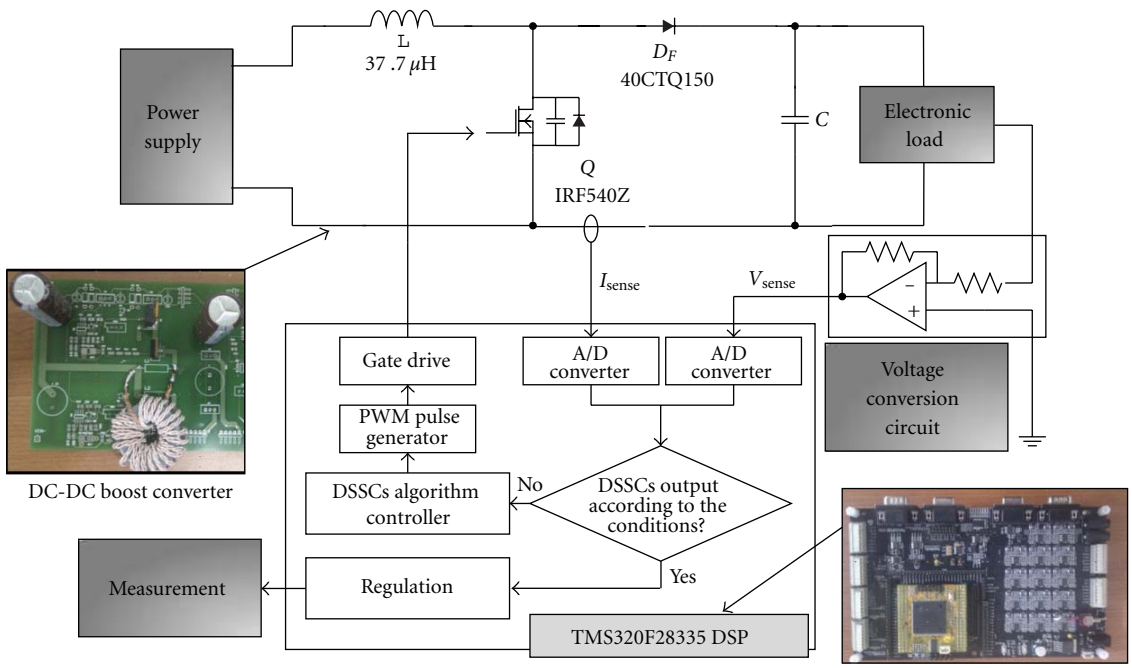

Figure 7: The block diagram of the SS.

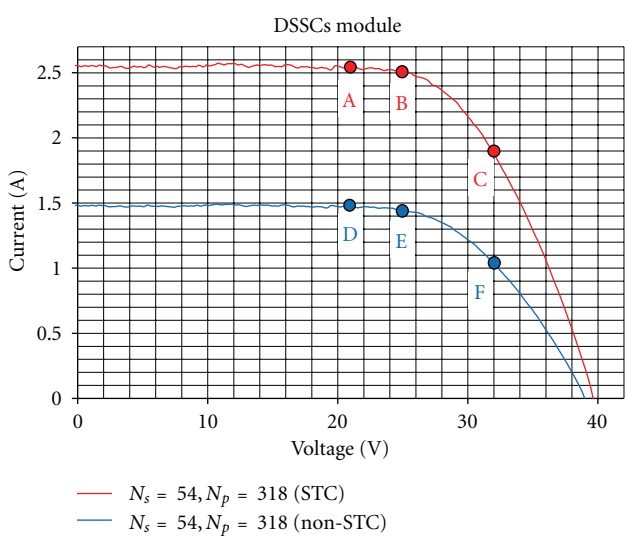

Figure 8: The I-V characteristic curves of DSSCs module (N_S = 54, N_P = 318).

device, DC-DC boost converter, electronic load, voltage conversion circuit, and DSP.

The power supply device supplies the power to the entire system. The DC-DC boost converter in DCM is used to obtain the power of the DSSCs. The basic converter usually uses the hard switching which causes the switching loss and diode recovery loss when the switch is turned on and off [15]. The DCM is not perfect soft switching. However, it is simple to control, only need output voltage to feedback, and is sometimes the best topology given the capacity and switching loss. That is why the DC-DC boost converter in DCM is applied in this paper [16].

The inductor of DCM boost converter was designed:

$$L = \frac{0.64 R_O V_i^2 (V_O - V_i)}{2 f V_O^3}, \tag{10}$$

where L is the value of inductor in DCM, R_O is the output load, V_i is the input voltage, V_O is the output voltage with maximum value of 40 V, and f is the switching frequency of the converter with the value of 30 kHz.

A converter was implemented on lab-made PCB. The electronics load is used to change the output load condition. In this paper, that DSP (TMS320F28335 EVM) is used to control the current and voltage of the converter. The voltage is measured to the ADC of the DSP through the voltage interface board. A DSP compares the voltage with the reference curve of DSSCs according to the conditions such as the irradiance, temperature, connection method, and shadowing effects and generates the PWM signal to control the reference current in boost converter through the simple PI control. Finally, the converter makes the output of DSSCs and then the measurement is implemented. The output of

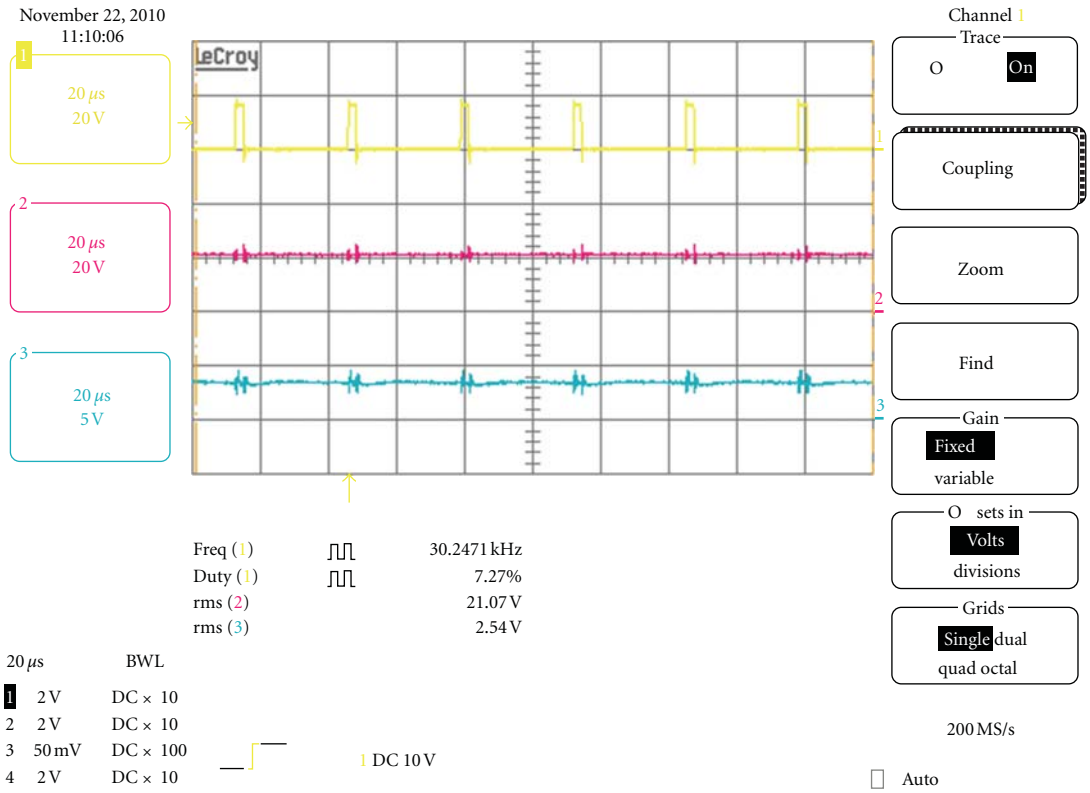

(a)

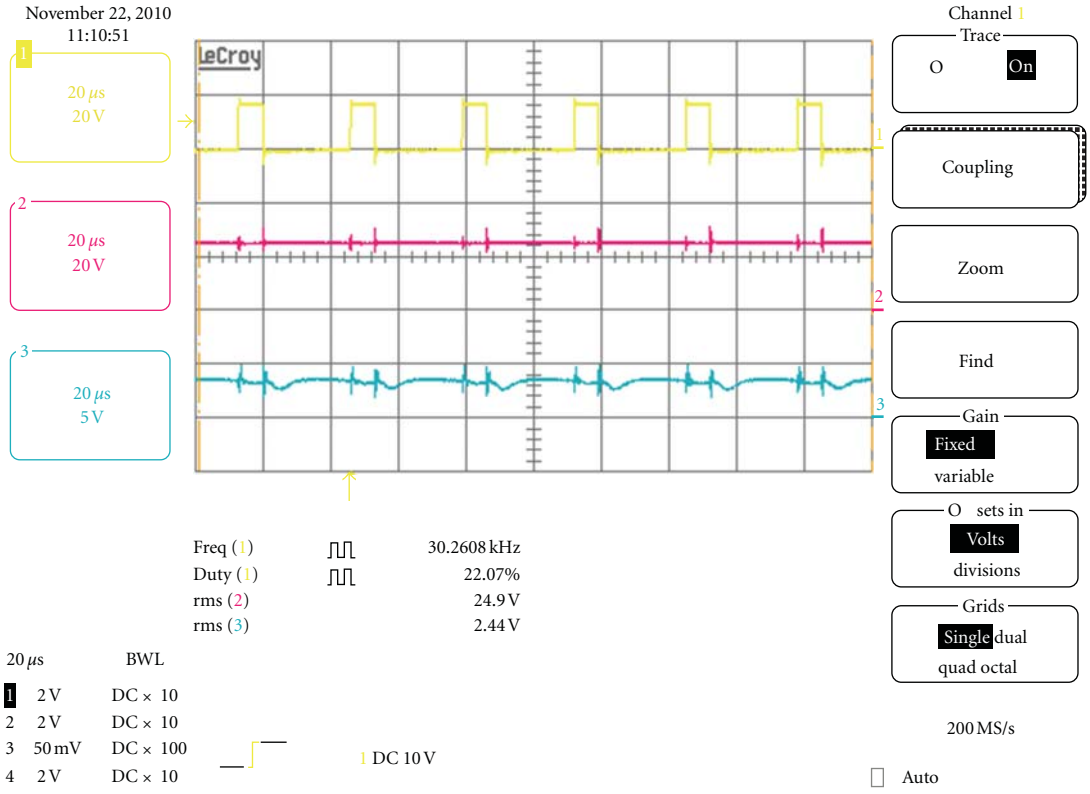

(b)

Figure 9: Continued.

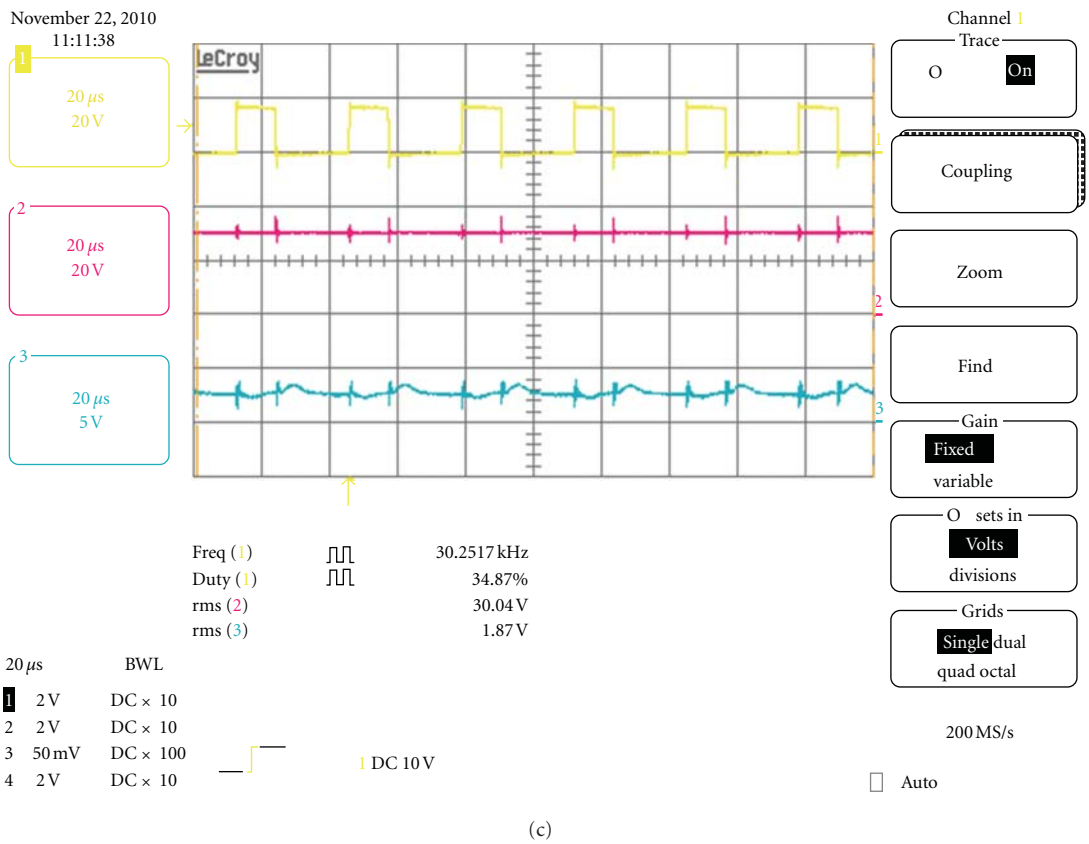

(c)

Figure 9: (a) The wave forms of 21 V and 2.54 A at Point A. (b) The wave forms of 25 V and 2.44 A at Point B. (c) The wave forms of 30 V and 1.87 A at Point C.

DSSCs can be changed according to change of the value of the electronics load as explained previously.

4.2. Experimental Results. Figure 8 shows the I-V curve (red line) of DSSCs module under STC and the I-V curve (blue line) of DSSCs module under non-STC. The module consists of 54 series-318 parallel connection without shadowing effects. Six points from A to F are marked on Figure 8, which is the experiment target.

As shown in Figure 9, there are three different wave forms. The first wave form shows the wave form of the gate (V_{gs}). The second and third wave forms show the wave forms of the output voltage and current. Figure 9(a) shows the wave forms of 21 V and 2.54 A, which is in Point A. Figure 9(b) shows the wave forms of 25 V and 2.44 A, which is in Point B. Figure 9(c) shows the wave forms of 30 V and 1.87 A, which is in Point C. The outputs of DSSCs are confirmed according to the DSP control with the proposed algorithm.

Figure 10 shows the wave forms of the results according to selected irradiation, temperature, and shadowing effect. This module is also DSSCs of the 54 series-318 parallel connected module. At this time, the irradiation is 800 W/m^2, the temperature is 25°C, and the shadowing rate is 25%. Figure 10(a) shows the wave forms of 21 V and 1.47 A, which is in Point D. Figure 10(b) shows the wave forms of 25 V and 1.43 A, which is in Point E. Figure 10(c) shows the wave forms of 30 V and 1.17 A, which is in Point F. The outputs of DSSCs under non-STC are also confirmed with the proposed SS system.

5. Conclusion

In this paper, the simple and low-cost SS is suggested for trial test of the DSSCs for developing adaptable power conditioning system. For the first time, the simulation program is designed to simulate the DSSCs. That consists of the DLL block which is linked with the external C routine in the PSIM. The proposed method is based on the actual data from lab-made DSSC unit cell and simple calculation using interpolation method. The SS consists of the power supply, DC-DC boost converter in DCM, electronics load, and DSP. The performance of SS for DSSC modules was verified through the 100 W level of DCM boost converter according to the factors of irradiation, temperature, and shadow effects.

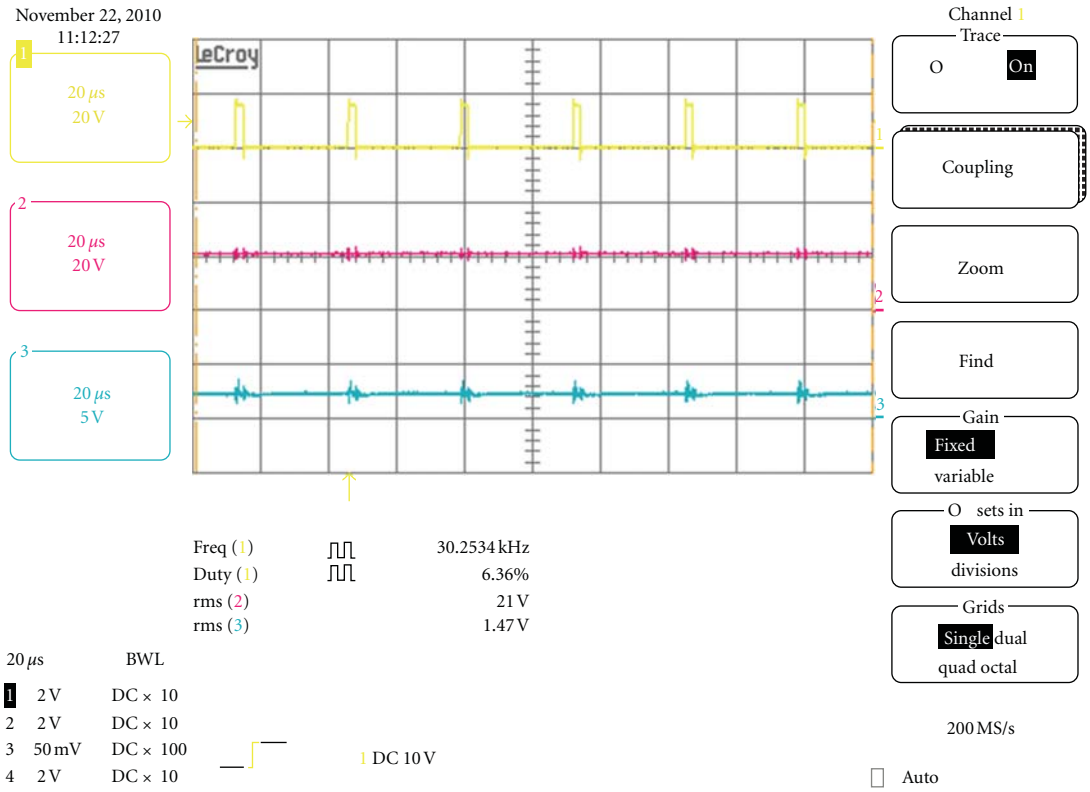

(a)

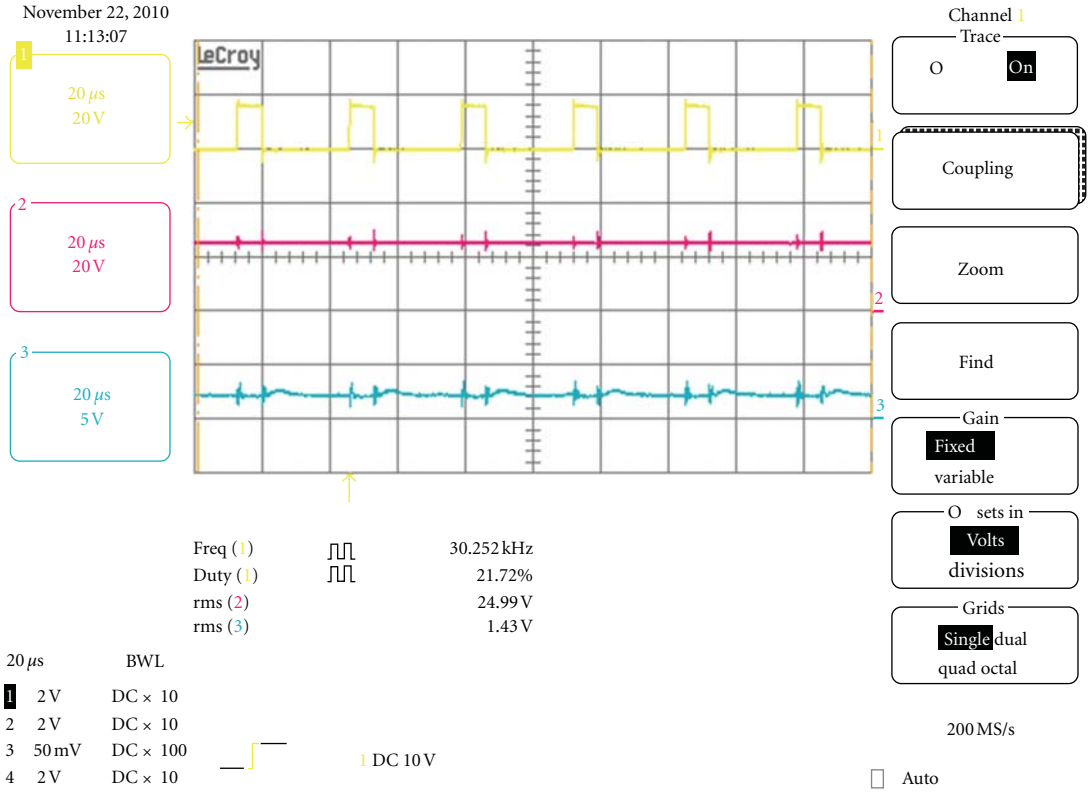

(b)

Figure 10: Continued.

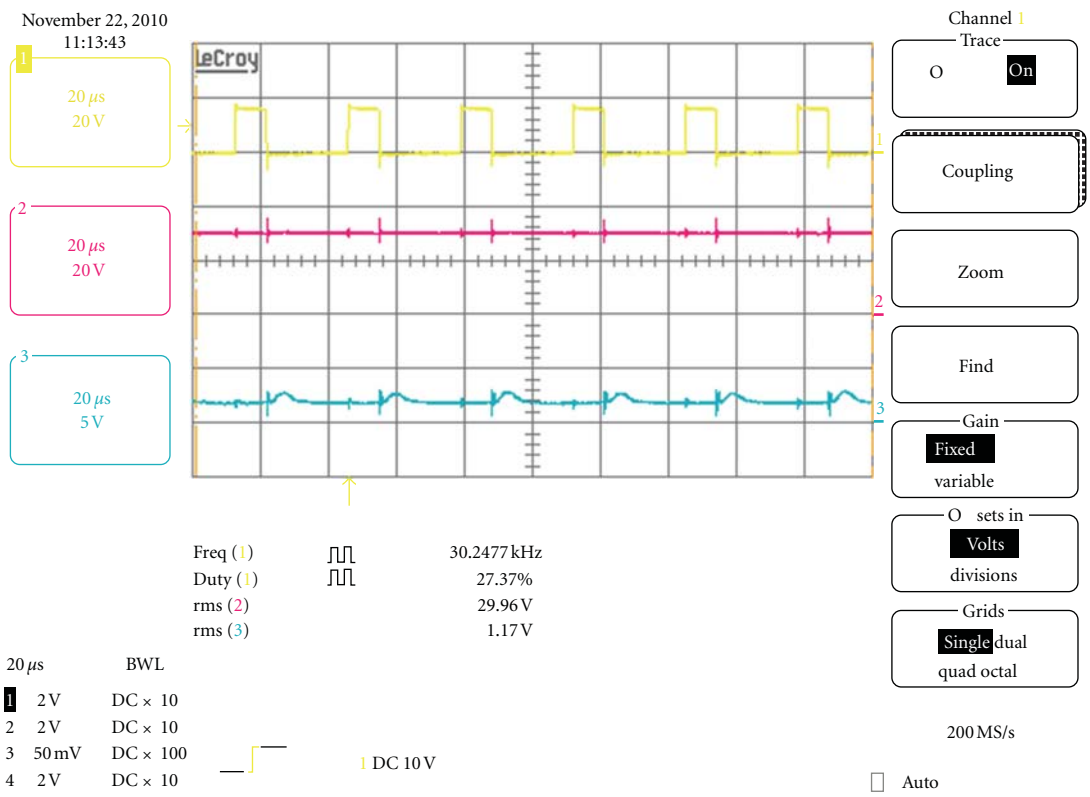

(c)

Figure 10: (a) The wave forms of 21 V and 1.47 A at Point D. (b) The wave forms of 25 V and 1.43 A at Point E. (c) The wave forms of 30 V and 1.17 A at Point F.

Acknowledgment

This work no. 20110001295 was supported by Mid-career Researcher Program through NRF grant funded by the MEST.

References

[1] M. Jung Park, "Optimization for Multi array photovoltaic system," *Theories and Applications of Chemical Engineering*, vol. 12, no. 2, pp. 1528–1531, 2006.

[2] B. O'Regan and M. Grätzel, "A low-cost, high-efficiency solar cell based on dye-sensitized colloidal TiO_2 films," *Nature*, vol. 353, no. 6346, pp. 737–740, 1991.

[3] M. Grätzel, "Conversion of sunlight to electric power by nanocrystalline dye-sensitized solar cells," *Journal of Photochemistry and Photobiology A*, vol. 164, no. 1–3, pp. 3–14, 2004.

[4] M. Grätzel, "Solar energy conversion by dye-sensitized photovoltaic cells," *Inorganic Chemistry*, vol. 44, no. 20, pp. 6841–6851, 2005.

[5] H. Wang, Y. Liu, H. Xu et al., "An investigation on the novel structure of dye-sensitized solar cell with integrated photoanode," *Renewable Energy*, vol. 34, no. 6, pp. 1635–1638, 2009.

[6] S. K. Dhungel and J. G. Park, "Optimization of paste formulation for TiO_2 nanoparticles with wide range of size distribution for its application in dye sensitized solar cells," *Renewable Energy*, vol. 35, no. 12, pp. 2776–2780, 2010.

[7] L. Han, N. Koide, Y. Chiba, A. Islam, and T. Mitate, "Modeling of an equivalent circuit for dye-sensitized solar cells: improvement of efficiency of dye-sensitized solar cells by reducing internal resistance," *Comptes Rendus Chimie*, vol. 9, no. 5-6, pp. 645–651, 2006.

[8] H. Seo, M. K. Son, K. J. Lee, J. Kim, J. T. Hong, and H. J. Kim, "A study on the improvement of the efficiency of dye-sensitized solar cell using the laser scribing and the grid electrode," *Transactions of the Korean Institute of Electrical Engineers*, vol. 57, no. 10, pp. 1802–1806, 2008.

[9] T. O. Saetre, O. -M. Midtgård, and G. H. Yordanov, "A new analytical solar cell I-V curve model," *Renewable Energy*, vol. 36, no. 8, pp. 2171–2176, 2011.

[10] A. Catani, *Shading Losses of Building Intergrated Photovoltaic Systems*, Centre of Applied Research Sustainable Energy Technologies, 2007.

[11] S. Silvestre, A. Boronat, and A. Chouder, "Study of bypass diodes configuration on PV modules," *Applied Energy*, vol. 86, no. 9, pp. 1632–1640, 2009.

[12] A. K. Sharma, R. Dwivedi, S. K. Srivastava, and C. M. Pathak, "Performance analysis of a modified solar array under shadow conditions," *Renewable Energy*, vol. 4, no. 2, pp. 257–260, 1994.

[13] A. Usami, S. Seki, Y. Mita, H. Kobayashi, H. Miyashiro, and N. Terada, "Temperature dependence of open-circuit voltage in dye-sensitized solar cells," *Solar Energy Materials and Solar Cells*, vol. 93, no. 6-7, pp. 840–842, 2009.

[14] J.-J. Kim, B.-D. Min, J.-P. Lee, T.-J. Kim, D.-W. Yoo, and E.-H. Song, "A novel method of simulation of PV characteristic

curves for PV simulator," in *Proceedings of the Korean Institute of Power Electronics Conference (KIPE '07)*, pp. 181–183, 2007.

[15] E.-S. Kim, "High frequency soft switching forward DC/DC converter," in *Proceedings of the Power Electronics Conference*, pp. 19–25, 1999.

[16] D.-K. Kwak and C. S. Kim, "A study on high efficiency boost DC-DC converter of discontinuous current mode control," *The Korean Institute of Electrical Engineers*, vol. 54, no. 9, pp. 431–436, 2005.

Hindawi Publishing Corporation
International Journal of Photoenergy
Volume 2012, Article ID 893962, 5 pages
doi:10.1155/2012/893962

Research Article

High-Temperature Photovoltaic Effect in $La_{0.4}Ca_{0.6}MnO_3/SiO_x/Si$ Heterojunction

Hao Ni,[1,2] Kun Zhao,[2,3,4] Xiaojin Liu,[2] Wenfeng Xiang,[2] Songqing Zhao,[2] Yu-Chau Kong,[3] and Hong-Kuen Wong[3]

[1] *State Key Laboratory of Heavy Oil Processing, China University of Petroleum, Beijing 102249, China*
[2] *College of Science, China University of Petroleum, Beijing 102249, China*
[3] *Department of Physics, The Chinese University of Hong Kong, Hong Kong*
[4] *International Center for Materials Physics, Chinese Academy of Sciences, Shenyang 110016, China*

Correspondence should be addressed to Kun Zhao, zhk@cup.edu.cn

Received 25 November 2011; Accepted 16 January 2012

Academic Editor: Bhushan Sopori

We fabricated a heterojunction of $La_{0.4}Ca_{0.6}MnO_3/SiO_x/n$-Si and investigated its electronic transport and ultraviolet photovoltaic properties at higher temperature up to 673 K. The rectifying behaviors vanished with the energy-band structure evolvement from 300 to 673 K. Under irradiation of a 248 nm pulse laser, the peak values of open-circuit photovoltage and short-circuit photocurrent decreased drastically. This understanding of the temperature-related current-voltage behavior and ultraviolet photodetection of oxide heterostructures should open a route for devising future microelectronic devices working at high temperature. PACS: 73.40.Lq, 71.27.+ a, 73.50.Pz.

1. Introduction

Ultraviolet (UV) sensors have several applications, including flame detection, radiation analysis, drug detection, and environment monitoring. In some cases such as the optical electron sensor for oil and gas optics and the flame detection for a hot engine, thermally stable detectors with high performance are required. Perovskite manganite is a typical system that shows multifunctional properties due to strong electron correlation and magnetic state dependence of the band structure with a chemical stability, which is insensitive to harsh physical environment such as fluctuations of temperature and pressure. Many researchers have devoted time to study the nature of carrier transport in the photoelectric process and explore photoresponse characteristics of devices based on doped manganite thin films and heterostructures [1–8].

Recently, there has been an active study of th photovoltaic properties of the perovskite manganite thin films [9, 10]. Among the different types of detectors, silicon-based photodiode has a great potential for high-temperature detection owing to combine the functional properties of oxides with that of Si electronics [11–13]. In this paper, we aim to develop an UV photodiode for high-temperature applications, which was fabricated by depositing the $La_{0.4}Ca_{0.6}MnO_3$ (LCMO) thin film on the n-type Si (001) wafer. The transport characteristics and UV photodetection were systematically studied in a wide temperature range of 300 to 673 K. The carrier transport and photoresponse properties are discussed with regard to the evolution of band structure by the variation of temperature across the interfaces.

2. Experimental

We fabricated the LCMO/SiO_x/Si heterojunction by depositing the 100 nm thick LCMO thin film on a native n-type Si (001) wafer using facing-target sputtering technique from stoichiometry targets [14]. The two sputtering targets with a nominal composition of LCMO, were prepared using standard ceramic technique. The Si wafer has the carrier concentration of 1×10^{16} cm^{-3}, and a 3 nm thick native silicon oxide layer located on its surface was confirmed by the cross-sectional transmission electron microscopy (TEM) image. During deposition, the substrate temperature was kept

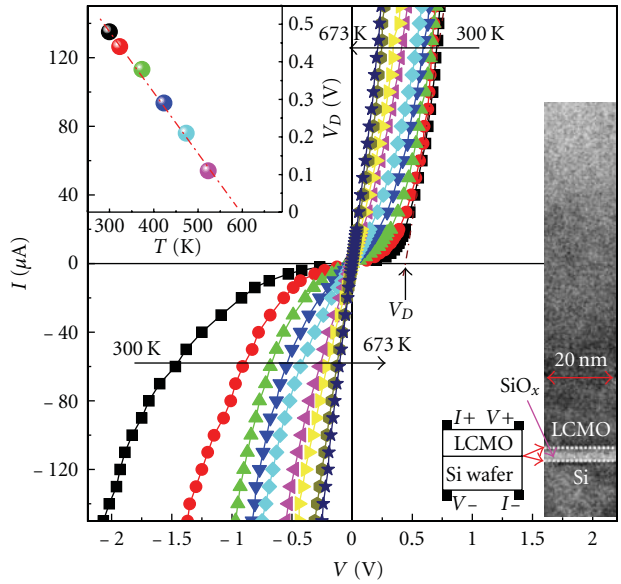

Figure 1: The I-V curves of LCMO/SiO_x/Si heterojunction measuring in a wide temperature range from 300 to 673 K. The right inset is the schematic structure of the electrode settings and the cross-sectional TEM image. The left inset shows the diffusion potential V_D as a function of temperature.

at 680°C. The sputtering gas pressure of Ar and O_2 was 60 mTorr with 1 : 1 gas flow-rate ratio of Ar and O_2. The film thickness was controlled by sputtering time with the deposition rate (~0.03 nm/s). After deposition, the vacuum chamber was immediately back-filled with 1 atm oxygen gas to improve the oxygen stoichiometry. And the sample was then cooled to room temperature with the substrate heater power cut-off.

The LCMO/SiO_x/Si sample was 5 mm × 5 mm in-plane dimension. Before experiments, we carefully cleaned sample using alcohol and acetone. Colloidal silver electrodes of 1 mm × 5 mm area were printed on the LCMO film and Si substrate. Current-voltage (I-V) characteristics of the junction at different temperatures from 300 to 673 K were measured in a four-probe arrangement using a Keithley 2400. The voltage polarity and the layout of the device are illustrated in the lower inset of Figure 1. A 248 nm KrF pulse laser (20 ns pulse width, 0.15 mJ mm^{-2} energy density, and 2 Hz repetition rate) was used to irradiate the LCMO film surface perpendicularly with sample pulse energy of 2.25 mJ. Photovoltaic signals of the sample at different temperatures were recorded with a sampling oscilloscope terminated into 1 MΩ, 50 Ω, and 3 Ω, respectively, as shown in the insets of Figures 2 and 3.

3. Results and Discussion

Figure 1 shows the dark I-V characteristics of the LCMO/SiO_x/Si heterojunction at different temperatures from 300 to 673 K. Electrode settings and the voltage polarity are illustrated schematically in the lower right inset of Figure 1. As can be seen, the heterostructure at room temperature presents a typical rectifying characteristic of a junction diode, which was ascribed to the presence of interfacial potential obtained from carrier diffusion. The diffusion potential V_D of built-in field in junction can be measured by the voltage at which a current rush occurs in positive bias, and its variation with temperature is presented in the left inset of Figure 1. With the temperature elevating to 673 K, the I-V curves become more and more linear and steeper, and it is nearly linear when temperature was over 523 K. The V_D decreased monotonically with increasing temperature, indicating that accompanied by elevating temperature, the built-in field gradually reduced.

The UV detective property in LCMO/SiO_x/Si heterojunction was measured at different temperatures from 300 to 673 K under a 248 nm laser pulse irradiation. The open-circuit photovoltages (PVs) across the 1 MΩ input impedance of oscilloscope are displayed in Figure 2(a). The PV peak value V_{p1} decreases drastically from 215 to 36.4 mV with increasing temperature from 300 to 673 K as evident shown in the inset of Figure 2(b), and the 10–90% rising time τ_1 of the waveforms decreased from 175 to 25 ns with increasing temperature from 300 to 673 K (inset in Figure 2(b)). We note that the photoresponse is composed of a fast rise time and much slower decay. The RC constant in the circuit should be responsible for the slow decay phenomenon. For the impedance matching, a 50 Ω resistance was connected in parallel with the detector. From the temporal profile of photoresponse waveforms (Figure 2(c)), the PV peak value V_{P2} shows similar tendency as V_{P1} and decreases from 71.7 mV at 300 K to 12.4 mV at 673 K, while the rising time τ_2 drop dramatically and maintains around ~17 ns for different temperatures.

For further studying the temperature-dependent photocurrent responses of the LCMO/SiO_x/Si junction, a 3 Ω resistance was connected in parallel with the sample (see the lower left inset of Figure 3). A typical temporal profile of

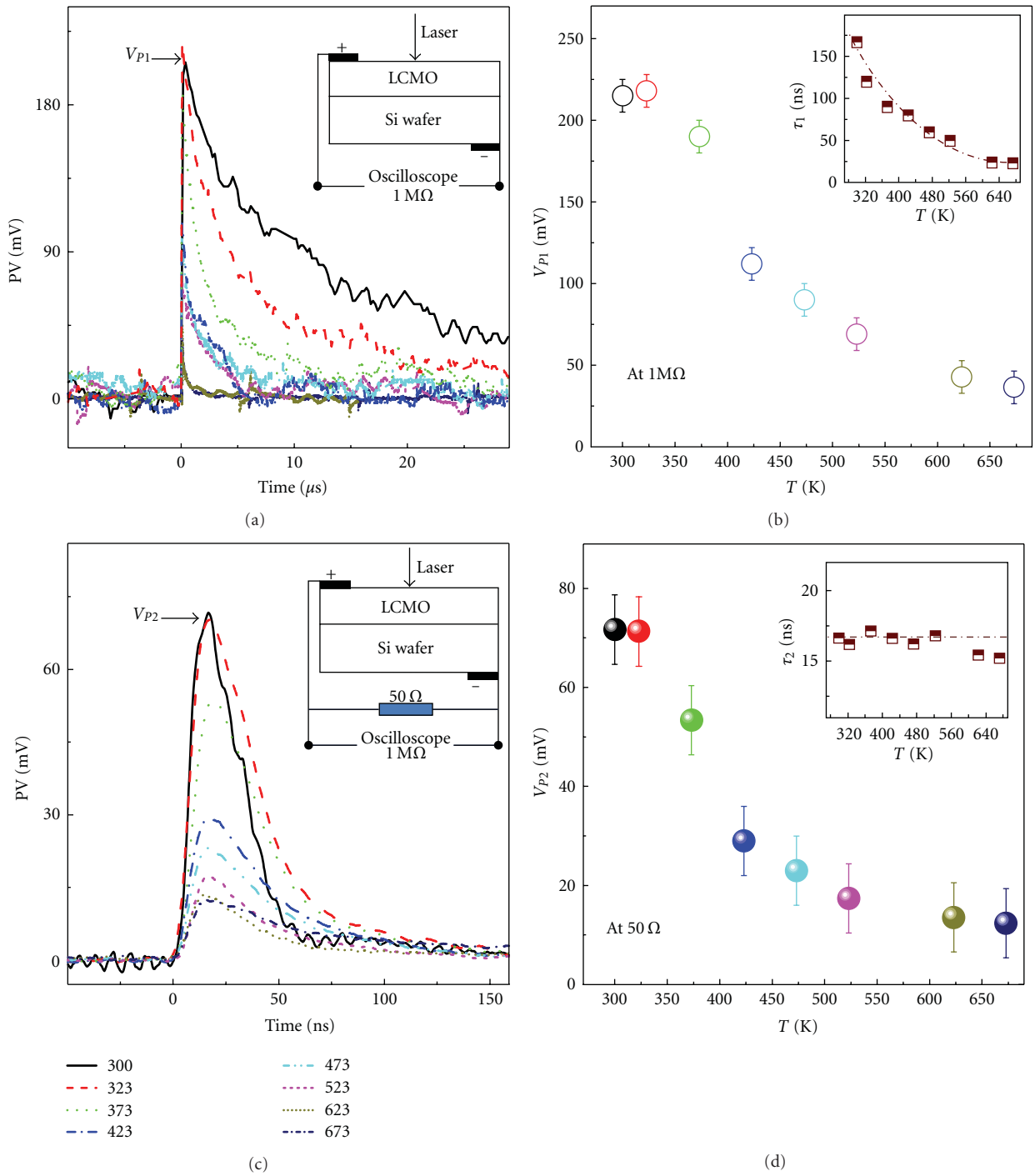

Figure 2: Photovoltaic responses for LCMO/SiO_x/Si heterojunction at different temperature from 300 to 673 K under the 248 nm laser illumination recorded by an oscilloscope terminated into (a) 1 MΩ and (c) 50 Ω. The insets of (a) and (c) display the schematic measurement circuits. (b) and (d) present the dependence of PV peak values V_{p1} and V_{p2} on the temperature, respectively. The insets display the temperature dependence of rising time τ_1 and τ_2 of PV pulses shown in (a) and (c).

photoresponse waveforms measured at 523 K is shown in the upper right inset of Figure 3. The peak value V_p and full width at the half maximum (FWHM) are reduced to about 4.3 mV and 7.6 ns, respectively. The peak photocurrent I_p is calculated approximately by $I_p \cong V_p/3\,\Omega$ where V_p is the peak voltage across the connected resistance 3 Ω. I_P decreases monotonically to 1.16 mA at 673 K, which is 1.88 times smaller than 3.35 mA at room temperature.

The photon energy of 248 nm wavelength (~5.0 eV) is larger than the bandgap (~1.2 eV) of LCMO and Si

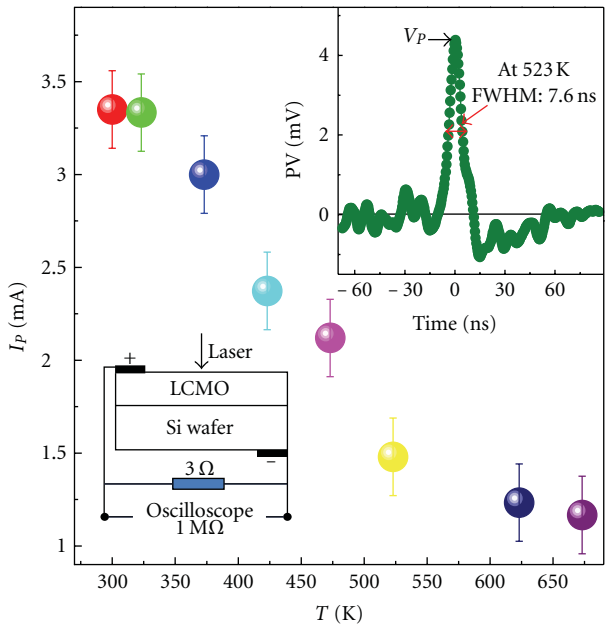

FIGURE 3: The photocurrent peak value I_P as the measurement temperature. The upper inset shows PV pulse at 523 K under 248 nm pulse laser irradiation. The lower inset displays the schematic measurement circuits with a 3 Ω resistance connected in parallel with the detector.

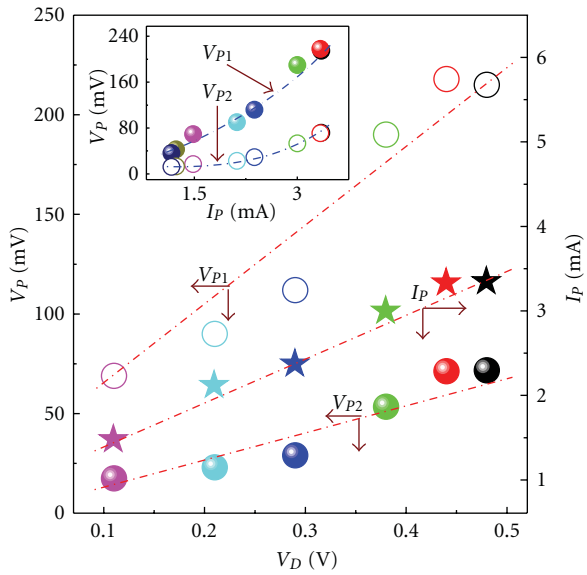

FIGURE 4: Diffusion potential V_D dependences of V_p, V_{p2}, and I_p. The inset shows the relations between V_{p1}, V_{p2}, and I_p.

(~1.12 eV). Valence electrons absorb the photons and transit to conduction band, resulting in the photogeneration process of electron-hole pairs. The internal electric field separates the photogenerated electron-hole pairs, leading to photovoltaic responses between two sides of the junction. Based on this understanding, photovoltaic responses would deeply dependent on the built-in field across the junction. The V_p and I_p dependences of diffusion potential V_D are summarized in Figure 4 and V_p increase monotonically with the I_P (inset of Figure 4). We note that the V_p and I_p almost linearly increase with increasing V_D from 0.11 V at 523 K to 0.48 V at 300 K, indicating that photovoltaic effect due to the built-in field makes the main contribution to the PV signals when the temperature is lower than a certain value (~523 K).

At room temperature, the conductivity of LCMO and Si is mainly due to the n-type doping. With increasing temperature, intrinsic excitation gradually becomes the main role in both LCMO and Si, which makes the Fermi level drop down to the middle of band gap. Consequently, the decrease of the built-in field leads to the decrease of the V_D shown in the inset of Figure 1. When the temperature rises to a certain value, the conduction and valence bands in LCMO flush,

respectively, with that in Si, due to near-identical value of band gap in LCMO and Si. The positive bias, driving the intrinsic carriers across the interface potential barrier, has the same value as the negative one. Thus, the I-V curves show symmetry on positive and negative biases at the temperature over 523 K as shown in Figure 1. Meanwhile, due to the higher temperature, hot carriers carry more energy and can be driven over the interface potential barrier induced by SiO_x even by small applied voltage due to Richardson effect. As the temperature continues to rise, hot carriers that carry more energy can freely cross over the potential barrier. Thus, the I-V curves become linear. The experiment results in Figure 1 reflect the evolution of band structure with the increasing temperature.

As mentioned above the 248 nm photons irradiation produces a photovoltage perpendicular to the LCMO/SiO_x/Si interface because of photovoltaic effect. At room temperature, photoinduced nonequilibrium carriers drift under the built-in electric field within the junction. However, with the increasing temperature, the built-in field becomes weaker and weaker and consequently the diffusion effect plays the main role. So we can see that the peak PVs become smaller with the increasing temperature and then get stabilized.

4. Summary

In conclusion, we fabricated the $La_{0.4}Ca_{0.6}MnO_3$/SiO_x/Si heterojunction and investigated the electronic transport and UV photodetection properties at higher temperature up to 673 K. The I-V curves of the junction change with increasing temperature, which has been explained by considering the energy-band structure evolvement at different temperatures. The open-circuit photovoltage and short-circuit photocurrent peak values decreased drastically from 215 to 36.4 mV and 3.35 to 1.16 mA with increasing temperature from 300 to 673 K. The temperature-related UV photodetection properties of oxide heterostructures should open a route for devising future microelectronic devices working at high temperature.

Acknowledgments

This work has been supported by NCET, RFDP, Direct Grant from the Research Grants Council of the Hong Kong Special Administrative Region (Grant no. C001-2060295), and Foresight Fund Program from China University of Petroleum (QZDX-2010-01).

References

[1] R. Cauro, A. Gilabert, J. P. Contour et al., "Persistent and transient photoconductivity in oxygen-deficient $La_{2/3}Sr_{1/3}MnO_{3-\delta}$ thin films," *Physical Review B*, vol. 63, no. 17, Article ID 174423, 6 pages, 2001.

[2] H. Katsu, H. Tanaka, and T. Kawai, "Photocarrier injection effect on double exchange ferromagnetism in (La,Sr)MnO_3/$SrTiO_3$ heterostructure," *Applied Physics Letters*, vol. 76, no. 22, pp. 3245–3247, 2000.

[3] M. Rajeswari, C. H. Chen, A. Goyal et al., "Low-frequency optical response in epitaxial thin films of $La_{0.67}Ca_{0.33}MnO_3$ exhibiting colossal magnetoresistance," *Applied Physics Letters*, vol. 68, no. 25, pp. 3555–3557, 1996.

[4] L. Méchin, J. M. Routoure, B. Guillet et al., "Uncooled bolometer response of a low noise $La_{2/3}Sr_{1/3}MnO_3$ thin film," *Applied Physics Letters*, vol. 87, no. 20, Article ID 204103, pp. 1–3, 2005.

[5] Y. G. Zhao, J. J. Li, R. Shreekala et al., "Ultrafast laser induced conductive and resistive transients in $La_{0.7}Ca_{0.3}MnO_3$: charge transfer and relaxation dynamics," *Physical Review Letters*, vol. 81, no. 6, pp. 1310–1313, 1998.

[6] R. D. Averitt, A. I. Lobad, C. Kwon, S. A. Trugman, V. K. Thorsmølle, and A. J. Taylor, "Ultrafast conductivity dynamics in colossal magnetoresistance manganites," *Physical Review Letters*, vol. 87, no. 1, Article ID 017401, 4 pages, 2001.

[7] N. Takubo, I. Onishi, K. Takubo, T. Mizokawa, and K. Miyano, "Photoinduced metal-to-insulator transition in a manganite thin film," *Physical Review Letters*, vol. 101, no. 17, Article ID 177403, 2008.

[8] H. Ichikawa, S. Nozawa, T. Sato et al., "Transient photoinduced "hidden" phase in a manganite," *Nature Materials*, vol. 10, no. 2, pp. 101–105, 2011.

[9] K. Zhao, K. J. Jin, Y. H. Huang et al., "Laser-induced ultrafast photovoltaic effect in $La_{0.67}Ca_{0.33}MnO_3$ films at room temperature," *Physica B*, vol. 373, no. 1, pp. 72–75, 2006.

[10] X. M. Li, K. Zhao, H. Ni et al., "Voltage tunable photodetecting properties of $La_{0.4}Ca_{0.6}MnO_3$ films grown on miscut $LaSrAlO_4$ substrates," *Applied Physics Letters*, vol. 97, no. 4, Article ID 044104, 2010.

[11] H. B. Lu, K. J. Jin, Y. H. Huang et al., "Picosecond photoelectric characteristic in $La_{0.7}Sr_{0.3}MnO_3$ Si p-n junctions," *Applied Physics Letters*, vol. 86, no. 24, Article ID 241915, pp. 1–3, 2005.

[12] H. Liu, K. Zhao, N. Zhou et al., "Photovoltaic effect in micrometer-thick perovskite-type oxide multilayers on Si substrates," *Applied Physics Letters*, vol. 93, no. 17, Article ID 171911, 2008.

[13] K. Zhao, K. J. Jin, H. Lu et al., "Transient lateral photovoltaic effect in p-n heterojunctions of $La_{0.7}Sr_{0.3}MnO_3$ and Si," *Applied Physics Letters*, vol. 88, no. 14, Article ID 141914, 2006.

[14] X. T. Zeng and H. K. Wong, "Epitaxial growth of single-crystal (La,Ca)MnO_3 thin films," *Applied Physics Letters*, vol. 66, no. 3371, 1995.

Hindawi Publishing Corporation
International Journal of Photoenergy
Volume 2012, Article ID 169829, 16 pages
doi:10.1155/2012/169829

Review Article

Crystal Growth Behaviors of Silicon during Melt Growth Processes

Kozo Fujiwara

Institute for Materials Research (IMR), Tohoku University, Katahira 2-1-1, Aoba-ku, Sendai 980-8577, Japan

Correspondence should be addressed to Kozo Fujiwara, kozo@imr.tohoku.ac.jp

Received 31 August 2011; Accepted 29 December 2011

Academic Editor: Teh Tan

It is imperative to improve the crystal quality of Si multicrystal ingots grown by casting because they are widely used for solar cells in the present and will probably expand their use in the future. Fine control of macro- and microstructures, grain size, grain orientation, grain boundaries, dislocation/subgrain boundaries, and impurities, in a Si multicrystal ingot, is therefore necessary. Understanding crystal growth mechanisms in melt growth processes is thus crucial for developing a good technology for producing high-quality Si multicrystal ingots for solar cells. In this review, crystal growth mechanisms involving the morphological transformation of the crystal-melt interface, grain boundary formation, parallel-twin formation, and faceted dendrite growth are discussed on the basis of the experimental results of in situ observations.

1. Introduction

The expectations for solar cells have been increasing yearly toward solving energy and environmental problems worldwide. The Si multicrystal (mc-Si) is one of the most important materials along with the Si single crystal (sc-Si) for the substrate of solar cells in the future although other materials are being developed. The crystal structure of an mc-Si ingot obtained by casting based on a unidirectional growth technique is markedly different from that of sc-Si, as illustrated by the formation of grain boundaries and the distribution of crystallographic orientations, which prevent the realization of high-efficiency solar cells. Various types of defect included in an mc-Si ingot, such as grain boundaries, dislocations, sub-grain boundaries, and metallic impurities, affect the properties of solar cells. Therefore, there is increasing importance to control the macro- and microstructures of mc-Si ingots. In recent years, various new methods for controlling the macro- and microstructures have been presented, which focus on controlling the nucleation or crystal growth mechanism in the earlier stage of casting. Dendritic casting is a method in which seed crystals are created from the melt during crystallization by inducing dendrite growth at the bottom of the crucible [1–3]. Seeded casting is a method in which prearranged seed crystals are set at the bottom of a crucible before crystallization, which initiates from seed crystals [4–6]. Other methods have been proposed, in which the nucleation site is controlled by controlling the cooling area in the initial stage of casting [7–9]. Many studies to establish such technologies for obtaining high-quality mc-Si ingots have been continuously performed on all these methods. In this review, such technologies for mc-Si ingot growth will not be discussed; only the melt growth mechanisms of Si will be discussed because fundamental understanding of crystal growth mechanisms is crucial to developing all such technologies. The crystal growth phenomena during melt growth processes including the morphological transformation of crystal-melt interfaces, grain boundary formation, parallel-twin formation, and faceted dendrite growth will be discussed by providing a review of our recent studies.

2. Morphological Transformation of Crystal-Melt Interface

2.1. Crystal-Melt Interface during Unidirectional Growth. To control the morphology of the crystal-melt interface during unidirectional growth processes is crucial to obtaining high-quality crystals because it affects the macro- and microstructures and eventually the mechanical, optical, and electrical

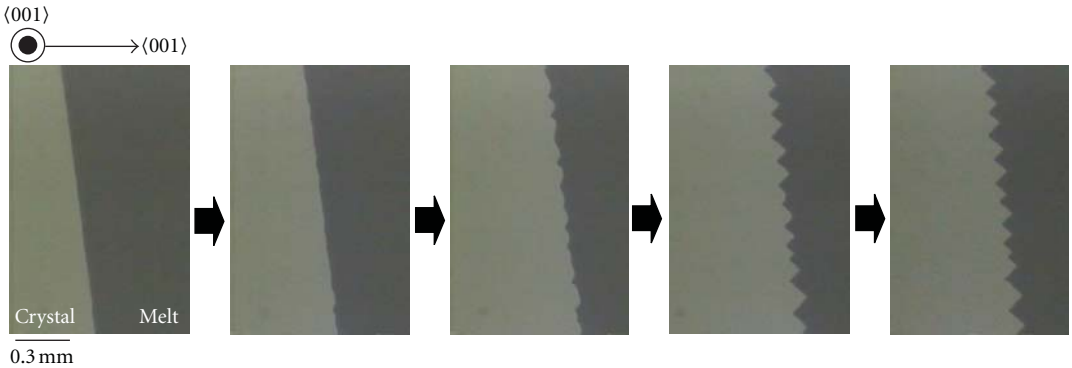

Figure 1: Morphological transformation of Si (100) crystal-melt interface moving at 162 μm/s [10].

properties of materials. It has been suggested that the generation of crystal defects, such as dislocations and twin boundaries, is related to the morphology of the crystal-melt interface [12–14]. The segregation of impurities is also dependent on the interfacial morphology [15]. According to Jackson's theory [16, 17], only the crystal-melt interfaces of Si {111} planes, called facet planes, are atomically smooth; other crystallographic planes are atomically rough. Because the {111} planes have the lowest surface energy [18], a zigzag-faceted interface bounded by {111} planes is expected to form at the crystal-melt interface of rough planes. The crystal-melt interface was observed in recrystallization processes in Si thin films [19–28], and micron-sized zigzag facets at the Si (100) crystal-melt interface were observed. Molecular dynamics simulation showed the existence of atomic-scale zigzag facets at the Si (100) crystal-melt interface [29, 30]. Such a zigzag-faceted interface at the Si (100) crystal-melt interface was also observed in bulk samples [31, 32]. Therefore, as one possible formation mechanism of a zigzag-faceted interface, it was considered that atomic-scale facets are initially formed, which gradually enlarge to macroscopic facets during crystallization [26]. On the other hand, recently, the zigzag-facet formation at the Si (100), (112), (110), and (111) crystal-melt interfaces has been investigated by in situ observation [10, 11].

Figure 1 shows the Si (100) crystal-melt interface whose growth velocity was 162 μm/s [10]. In this experiment, a piece of Si (100) wafer was set between quartz plates inside the furnace to keep the surface of the Si melt flat during crystal growth. The morphology of the interface transformed from planar to zigzag facets during the growth. It was shown that a wavelike perturbation is introduced into a planar interface, the perturbation is amplified, and the zigzag facets are formed finally. A similar morphological transformation from planar to zigzag facets of the moving interface was observed at the Si (112) and (110) crystal-melt interfaces at higher growth velocities, as shown in Figure 2 [11]. On the other hand, when the growth velocity was lower, the planar interfaces were maintained throughout the crystallization, as shown in Figure 3. The critical growth velocity for the morphological transformation, V_c, was found to be 123 μm/s $< V_c <$ 147 μm/s, 107 μm/s $< V_c <$ 124 μm/s, and 102 μm/s $< V_c <$ 129 μm/s at the Si (100), Si (110), and Si (112) crystal-melt interfaces, respectively [10, 11]. In those experiments, the temperature gradient along the growth direction in the furnace was about 8 K/mm. It was found that the critical growth velocity was dependent on the temperature gradient in the furnace. When the temperature gradient was about 4 K/mm, the critical growth velocity of the Si (100) interface was 36 μm/s $< V_c <$ 100 μm/s [33]. Figure 4 shows isochrones of the interface of Si (100) and Si (110) when the planar interface transformed to a zigzag-faceted interface. It was shown that the wavelength of the wavy interface completely agreed with that of the zigzag-faceted interface. The perturbation was amplified with time, and one perturbation peak formed one zigzag facet peak. Here, it should be determined why the perturbation is amplified when the growth velocity is high, using stability arguments [34]. Tokairin et al. calculated the thermal field in the Si crystal and melt during crystallization along the growth direction at a constant growth velocity, before the zigzag facet formation [10]. Generally, a crystal-melt interface becomes unstable, leading to the amplification of the perturbation, when the temperature gradient at the interface is negative along the growth direction [35]. However, the temperature gradient in the furnace was positive in Figures 1–4. Therefore, it was considered that the latent heat of crystallization increases the temperature at the crystal-melt interface, and that the temperature gradient in the Si melt at the interface becomes negative when growth velocity is high, because the amount of generated latent heat per unit time increases with growth velocity. The thermal field of the Si crystal and melt, $T_{c,m}$, is governed by the partial differential equation [36]

$$\begin{aligned}\rho_{c,m}C_{\mathrm{P}c,m}\frac{\partial T_{c,m}}{\partial t} &= -\rho_{c,m}C_{\mathrm{P}c,m}V\frac{\partial T_{c,m}}{\partial X}\\ &= K_{c,m}\frac{\partial^2 T_{c,m}}{\partial X^2}+\frac{2K_q}{l_q l_{\mathrm{Si}}}(Gx+T_i-T_{c,m}),\end{aligned} \tag{1}$$

where $\rho_{c,m}C_{\mathrm{P}c,m}$, $k_{c,m}$, k_q, l_q, and l_{Si} are the heat capacity of the Si crystal and melt, the thermal conductivity of the Si crystal and melt, the thermal conductivity of the quartz plate, the thickness of the quartz plate, and the thickness

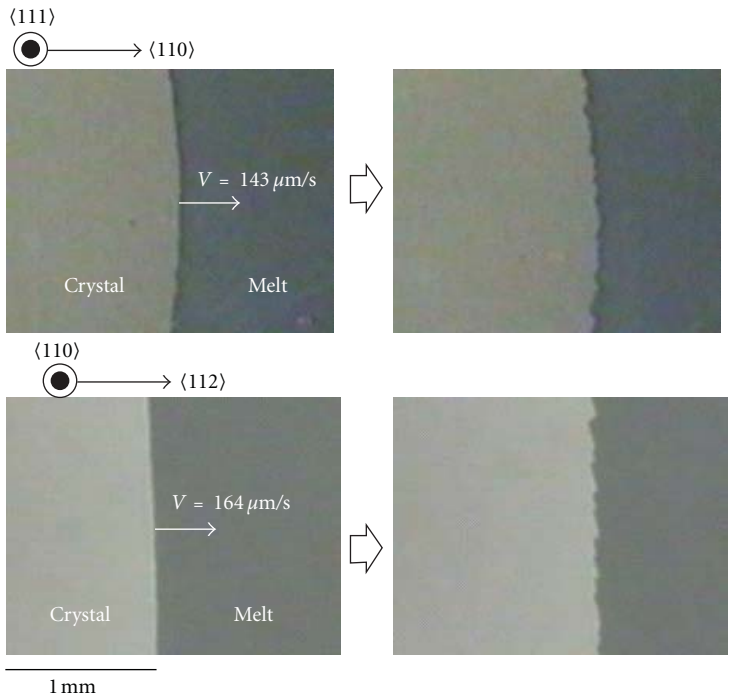

Figure 2: Morphological transformation of Si (110) and (112) crystal-melt interfaces at high growth velocities [11].

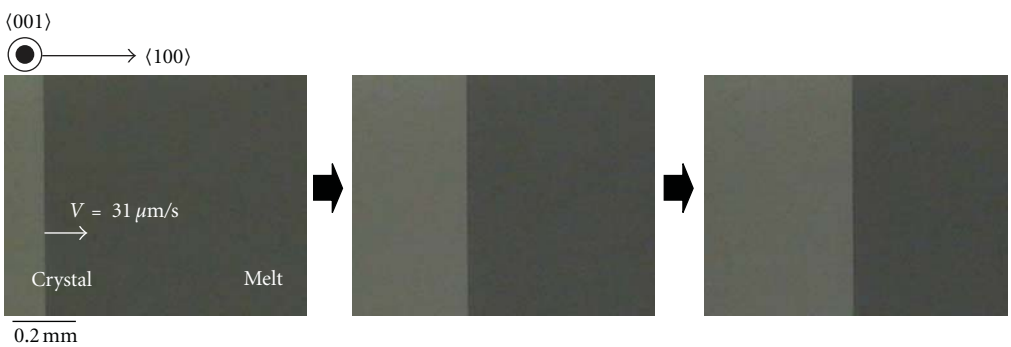

Figure 3: Morphology of Si (100) crystal-melt interface at low growth velocity [10].

of the Si, respectively. The origin of the coordinate is the crystal-melt interface, which moves with the growth velocity V. $Gx + T_i$ is the furnace temperature, where G is the temperature gradient in the furnace, and T_i is the furnace temperature at the interface. The first and second terms on the right-hand side of (1) come from the heat diffusion along the growth direction and the heat conduction between the Si crystal or melt and the furnace through the quartz plates, respectively. From the solution of (1), the thermal fields of the Si crystal and melt during crystal growth for various growth velocities were obtained, as shown in Figure 5 [10]. The physical properties of Si used were based on those indicated in [37], and l_q, l_{Si}, and G were based on experimental values. The temperature gradient in the Si melt at the interface changes from positive to negative as growth velocity increases. When the growth velocity is low, the temperature gradient is positive, and this means that the interface is stable and the planar interface is maintained. On the other hand, when the growth velocity exceeds its critical value, the temperature gradient in the Si melt at the interface changes from positive to negative, and thus the perturbation introduced into the planar interface is amplified, forming zigzag facets at high growth velocities.

Figure 6 shows the crystal-melt interface of the Si (111) plane growing at a high growth velocity of 200 μm/s. The Si (111) interface maintained a planar shape even at a high growth velocity although a negative temperature gradient should have been formed at the interface at such a high growth velocity. The difference in interface morphology between the (111) plane and the other planes could be explained by considering the anisotropy of growth velocity. The growth velocity along the ⟨111⟩ direction is the lowest. Moreover, the growth velocity on the Si (111) plane was more than 2 orders lower than that on the Si (100) plane at a given undercooling [38]. Thus, even though perturbation is introduced into the (111) planar interface, the morphology

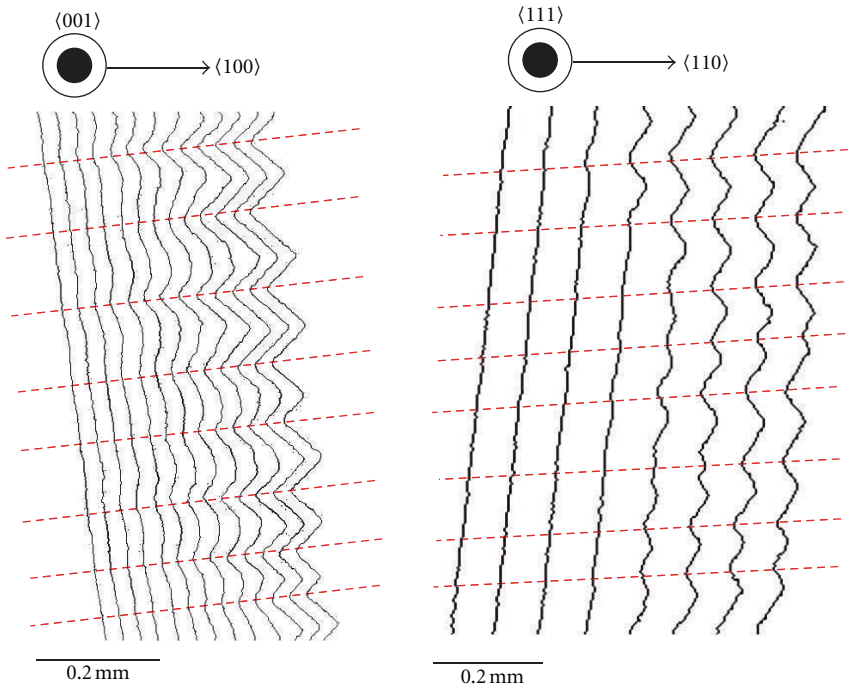

Figure 4: Isochrones of Si (100) and Si (110) interfaces when planar interface transformed to zigzag faceted interface [10].

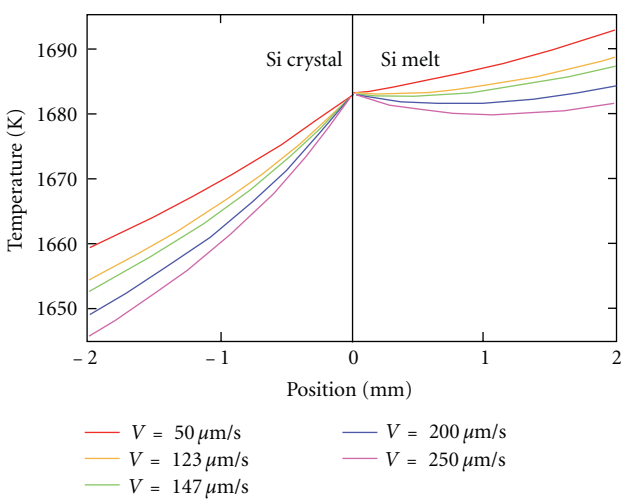

Figure 5: Calculated thermal fields of Si crystal and melt during crystallization for V = 50, 123, 147, 200, and 250 μm/s. $\rho_c C_{Pc}$ = 2.29×10^{-3} J/mm^3 K, $\rho_m C_{Pm}$ = 2.53×10^{-3} J/mm^3 K, k_c = 2.2×10^{-2} W/mm K, k_m = 5.4×10^{-2} W/mm K, k_q = 4.3×10^{-3} W/mm K, l_q = 1.0 mm, l_{Si} = 0.5 mm, G = 8 K/mm, ΔH = 4.122 J/mm^3, and T_{mp} = 1683 K. l_q, l_{Si}, and G are based on the experimental values, and the physical properties of Si used are based on those mentioned in [37]. The temperature gradient in the Si melt at the crystal-melt interface changed from positive to negative as V increased [10].

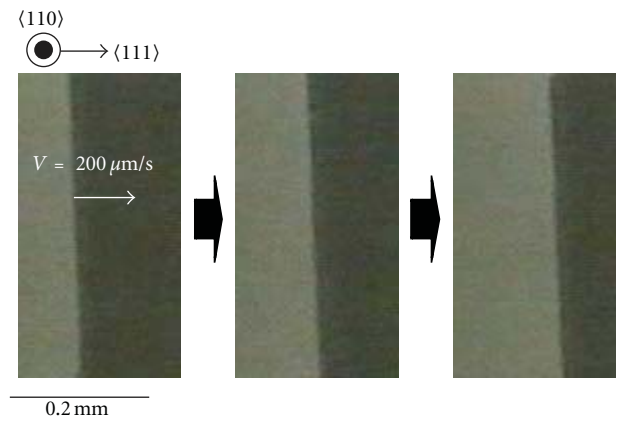

Figure 6: Typical image of the Si (111) crystal-melt interface during crystal growth [11].

of the interface remains planar owing to the faster growth in the lateral direction than in the ⟨111⟩ direction. For added consideration regarding the growth of the Si (111) interface, it was reported that the step-flow mode is stable up to an undercooling of 40 K by molecular dynamics simulation [39]. The step velocity at the (111) interface was found to be quite high because of the large step kinetic coefficients, that is, 0.29–0.79 m/sK. Such a high step velocity makes the interface planar in this growth mode.

It has been shown that the interface morphology is controlled by temperature gradient and growth velocity. When the zigzag facets are formed at the crystal-melt interface of rough planes during a unidirectional growth process of an mc-Si ingot by casting, the growth velocity difference between the rough planes and {111} facet planes becomes larger [32, 40]. When two crystal grains, the one has (100) interface and the other one has (111) interface, exist

side by side, the (100) grain with zigzag facets interface grows much faster than (111) grain with planar interface, and the (100) grain gradually occupies the space and becomes larger than (111) grain during the unidirectional growth. In such competitive growth process between the two crystal grains, the shape of the grain boundary between two crystal grains is also changing during the growth [32, 40]. The stress given to the grain boundary maybe increased with the shape change, which leads to increasing the defect generation, such as dislocations or twin boundaries, at the grain boundary. Moreover, when the zigzag facets are formed at the crystal-melt interface of rough planes during a unidirectional growth process, the impurities segregate at the valleys of zigzag facets, which lead to in-plane inhomogeneity in an ingot. Those phenomena seem to affect the quality of an mc-Si ingot in an adverse way. On the other hand, Si-faceted dendrites easily grow from a zigzag facets interface [12]. In the dendritic casting, faceted dendrites are promoted to grow along the bottom of the crucible in the earlier stage of casting [1]. In this method, the growth condition to form the zigzag facets interface should be selected to initiate the dendrite growth in the initial stage of casting, which leads to the formation of large-size grains at the bottom of the ingot. Thus, we should carefully control the growth mechanism during casting for obtaining high-quality mc-Si ingots.

2.2. Growth Kinetics in Melt Growth of Silicon. In the previous section, the morphological transformation of crystal-melt interfaces for different orientations was shown. Those phenomena observed at crystal-melt interface depend on the anisotropy of crystal-melt interfacial energy, which governs the growth kinetics and growth modes. It is well known that Si (111) is a facet plane, which means that the surface of crystal-melt interface is atomically smooth, and other planes are atomically rough. Therefore, the growth kinetics in melt growth processes seems to be different between the (111) plane and other planes. In general, the growth on the (111) facet plane is discussed by a 2D nucleation mode, and that of rough planes are discussed by a normal growth mode [38]. The normal growth velocity, V_n, on Si rough plane is expressed as $V_n = \beta_{\text{rough}}\,\Delta T$, where β_{rough} and ΔT are the kinetic coefficient for rough plane and undercooling at the crystal-melt interface, respectively. The value of the kinetic coefficient for Si (100) rough plane has been derived by computations as approximately 0.1 m/(sK) [38, 39]. Thus, the growth velocity on Si (100) rough plane linearly increases with increasing the amount of undercooling. On the other hand, the growth velocity on a Si (111) facet plane increases exponentially with undercooling in a 2D nucleation growth mode [38, 42]. Therefore, the growth velocity on a facet plane seems to be much smaller than that of the rough plane at a low undercooling. However, direct evidences by experiments for the growth kinetics in melt growth processes have been very limited comparing with those in the solution growth or the vapor growth. Thus, a more detailed discussion of the growth mode should be reserved for future works. The growth mode on a Si (111) facet plane has been well summarized in [42].

2.3. Crystal-Melt Interface at the Grain Boundary Formation. In mc-Si grown by a casting, grain boundaries are one of the main factors governing the mechanical, optical, and electrical properties. For instance, some of the grain boundaries inhibit the increase in the energy conversion efficiency of solar cells because they act as recombination centers of photocarriers. Therefore, the relationships between grain boundary properties and electrical activity have been extensively investigated [44–51]. Moreover, a $\{111\}\sum 3$ grain boundary, which is usually straight, is electrically inactive, but other CSL (coincidence site lattice) boundaries or random grain boundaries, which are straight, wavy or curved, are electrically active. Grain boundary structures are also investigated by transmission electron microscopy [52–54] or computer simulation [55–57]. Almost all studies of grain boundaries in Si have been performed after crystallization. Here, the crystal growth behaviors in grain boundary formation during crystallization from Si melt are shown.

Figure 7(a) shows the crystal growth behavior when two crystals converge during the crystallization process [41]. Most of the crystal-melt interface between the two crystals is linear, which suggests that the growth direction vertical to those interfaces is $\langle 111\rangle$. In the underlying crystal, a sharp triangular corner is observed at the right edge of the interface when there is sufficient distance between the two growing crystals. This difference in interfacial shape is due to the difference in the growth direction owing to the existence of a grain boundary at the location marked by a red arrow in Figure 7(a). The sharp corner gradually flattens as the two crystals become approach each other. Figure 7(b) shows the result of crystallographic orientation analysis after crystallization determined by the electron backscattering diffraction pattern (EBSP) method [41]. The directions vertical to the grain boundary are shown in color using the inverse pole figure triangle. A linear grain boundary was formed corresponding to the shape of crystal-melt interfaces just before grain boundary formation. It is found that the growth directions vertical to the linear growing interfaces were $\langle 111\rangle$ (shown in blue), and that the growth direction with a sharp-cornered interface in the underlying crystal was $\langle 100\rangle$ (shown in red). Grain boundary characteristics are also indicated by colored lines in Figure 7(b). The grain boundary characteristic differs depending on location. A (111) $\sum 3$ grain boundary, shown by a red line, is formed where $\{111\}$ facet planes impinge on each other. On the other hand, a random grain boundary, shown by a black line, is formed at a location where the shape transition of the growing interface occurs just before grain boundary formation. Figure 8(a) shows isochrones of the position of the growing interfaces at 1/3 s intervals for the sample shown in Figure 7, and Figure 8(b) shows the *t*-*x* plot of the growing interface at the two parts marked by the red and blue lines on the isochrones [41]. The color of dots in Figure 8(b) corresponds to the line color in Figure 8(a). The initial point of the shape transition of the interface is indicated in Figure 8(b). It is shown that the growth velocity of the growing interfaces, the gradient of the *t*-*x* curve, decreases from this point. This means that the amount of undercooling in front of the growing interface decreased and the melt temperature in

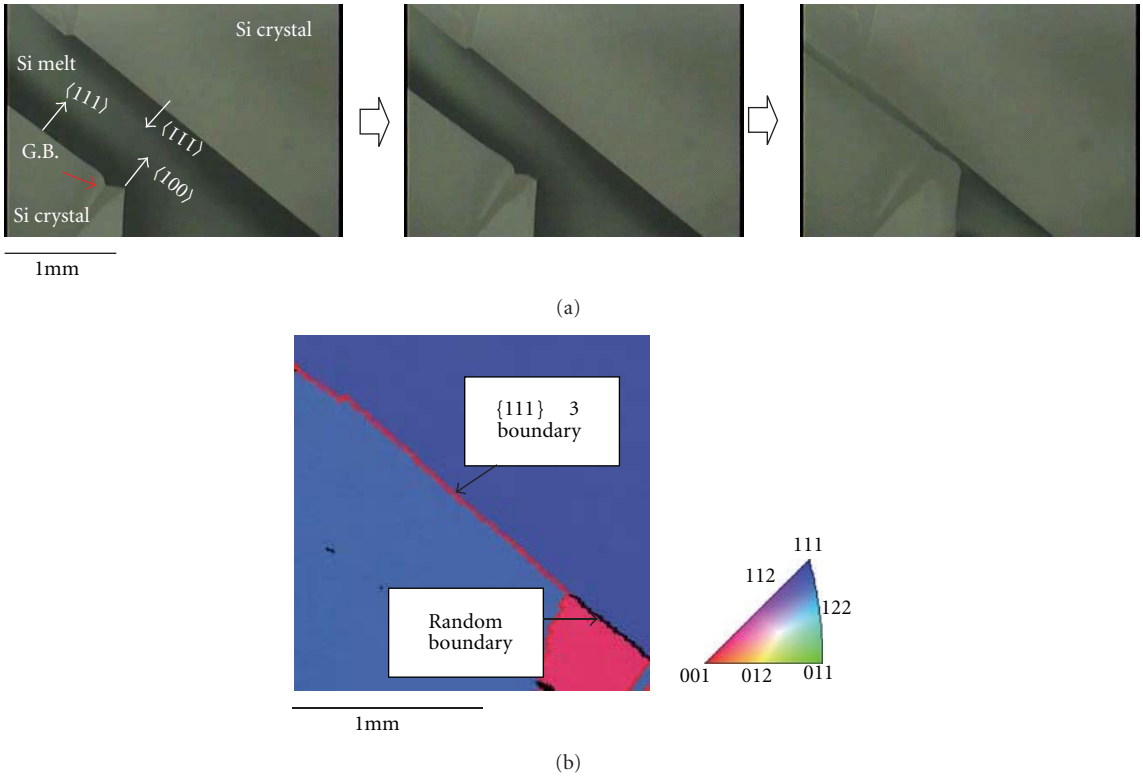

Figure 7: (a) Growth behavior of two Si crystals when they meet during crystallization. In the underlying crystal, the shapes of the growing interface are different on both sides of the grain boundary indicated by the arrow [41]. (b) Result of EBSP analysis of region observed in (a). The orientation vertical to the grain boundary is shown in color using the inverse pole figure triangle. The grain boundary is also shown in color in accordance with the grain boundary characteristics [41].

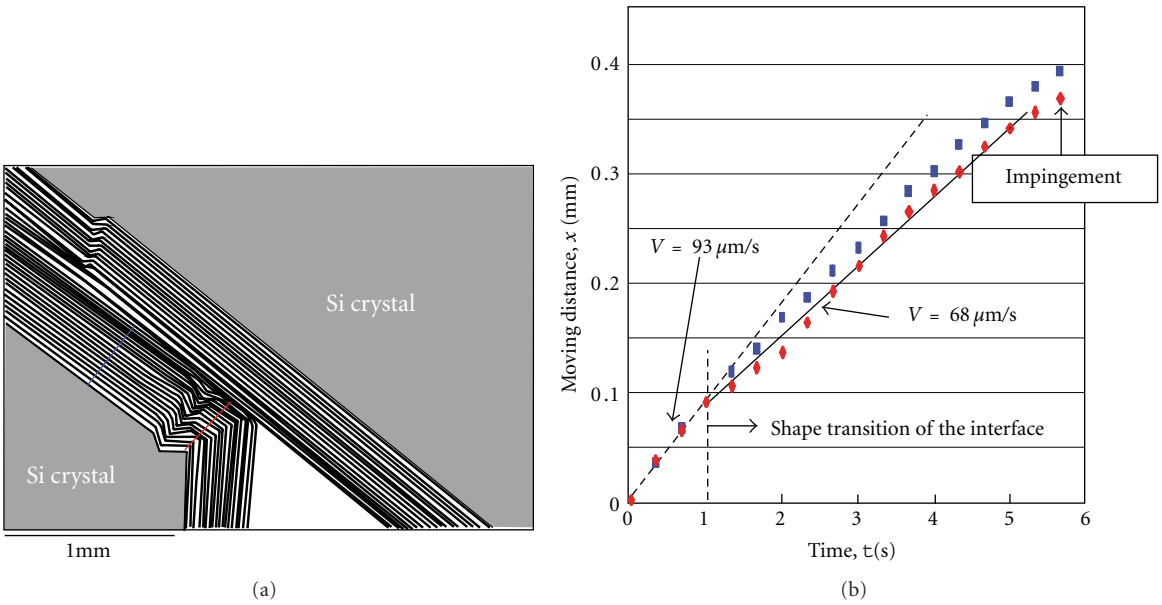

Figure 8: (a) Isochrones of positions of growing interface at 1/3 s intervals for sample shown in Figure 7 [41]. (b) *t*-*x* plot of moving interface for two parts shown by red and blue lines across isochrones in (a). The color of dots corresponds to the color of the lines in (a). The moving velocity of the interface is lower from the initiation point of the interface shape transition [41].

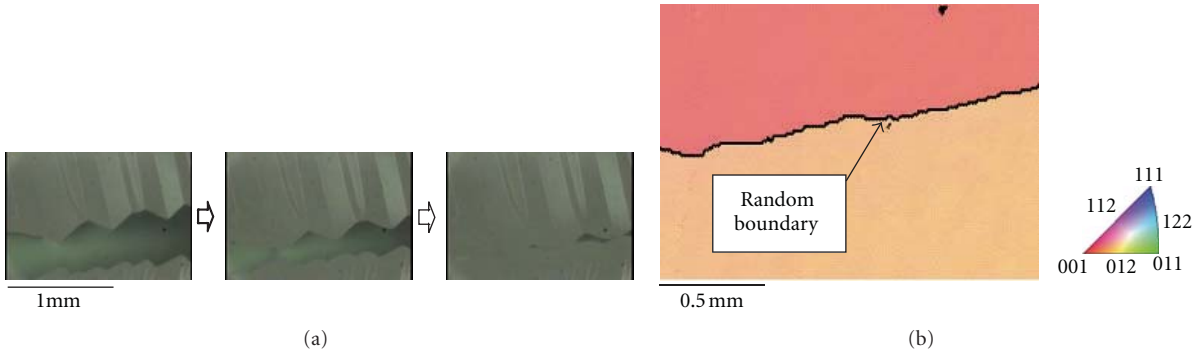

Figure 9: (a) Growth behavior of two Si crystals with zigzag-faceted interfaces [41]. It is observed that the sharp corners on the faceted interfaces gradually disappear as the crystals grow. (b) Result of EBSP analysis of the sample shown in (a) [41]. The growth direction vertical to the line indicated in (b) is shown in color.

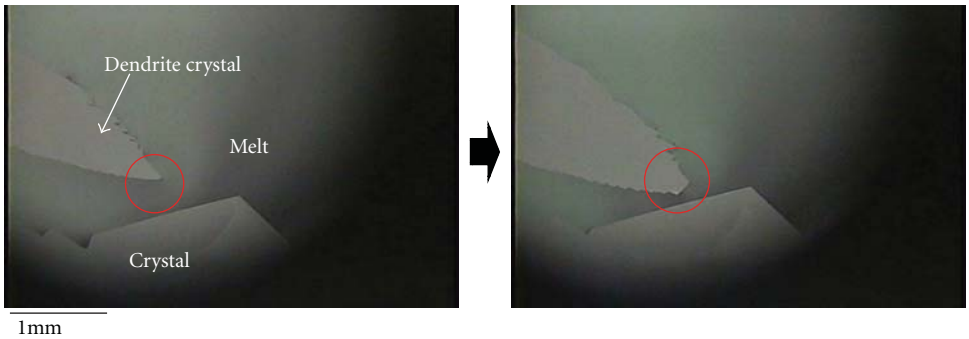

Figure 10: Growth behavior of faceted dendrite at grain boundary formation. The tip of the dendrite becomes flat during growth.

front of the growing interface increased. We explained this phenomenon by considering the thermal fields in front of the growing interface. When a crystal is growing from the melt, the heat of crystallization is released. The heat of crystallization can be taken away through the melt and/or crystal [58] when the two crystals are sufficiently separated. However, as the distance between two crystals becomes smaller, thermal fields in front of the two growing crystals overlap and the heat of crystallization cannot be taken away; then the temperature between the two crystals increases. This leads to the reduction in the growth velocity at the tip of the corner on the growing interface, and, as a result, the shape of the interface becomes flat. Figure 9(a) shows the growth behavior of the two crystals with zigzag-faceted interfaces [41]. Although the distance between the two crystals is large, well-developed {111} facet planes appear on the growth surfaces, and, thus, sharp corners are formed. As the distance between the two crystals becomes smaller, the shape transition of the growing interface is observed. The sharp corners on the interfaces gradually disappear, and wavy interfaces are formed. Just at impingement, the shape of the interfaces becomes more linear. This behavior of the growing interface is similar to that observed in Figure 7. Figure 9(b) shows the result of orientation analysis. The grain boundary was wavy owing to the shape transition of the growing interface, and a random grain boundary was formed [41]. The results in Figure 7 to Figure 9 show that the grain boundary shape and grain boundary characteristics are dependent on the behavior of the growing interface before impingement, which, in turn, strongly depends on the shape of the faceted interface. Figure 10 shows the growth behavior of the dendrite at the grain boundary formation. The tip of the dendrite is narrow and sharp when the distance between the two crystals is large. As the distance between the two crystals becomes smaller, the tip of the dendrite becomes wider and flatter. To continue the dendrite growth, sufficient undercooling, that is, more than 10 K, is necessary [12]. When the distance between the two crystals becomes smaller, melt temperature seems to increase owing to the overlapping thermal fields in front of the crystal-melt interfaces, as explained before, and then the dendrite growth cannot continue; thus, the tip of the dendrite is flattened.

3. Parallel-Twin Formation

In mc-Si ingots, twin boundaries are often observed at a high density [59]. The twin boundary formation energy is very low [60, 61], and some origins of twin boundary formation have been reported [16, 62–64]. Figure 11 shows an mc-Si wafer (left) and a faceted dendrite crystal examined by EBSP analysis (right). Most straight lines observed in the mc-Si wafer and the red lines at the center of the dendrite by EBSP analysis are twin boundaries. It is observed that at least two twin boundaries often exist parallel to each other, with a

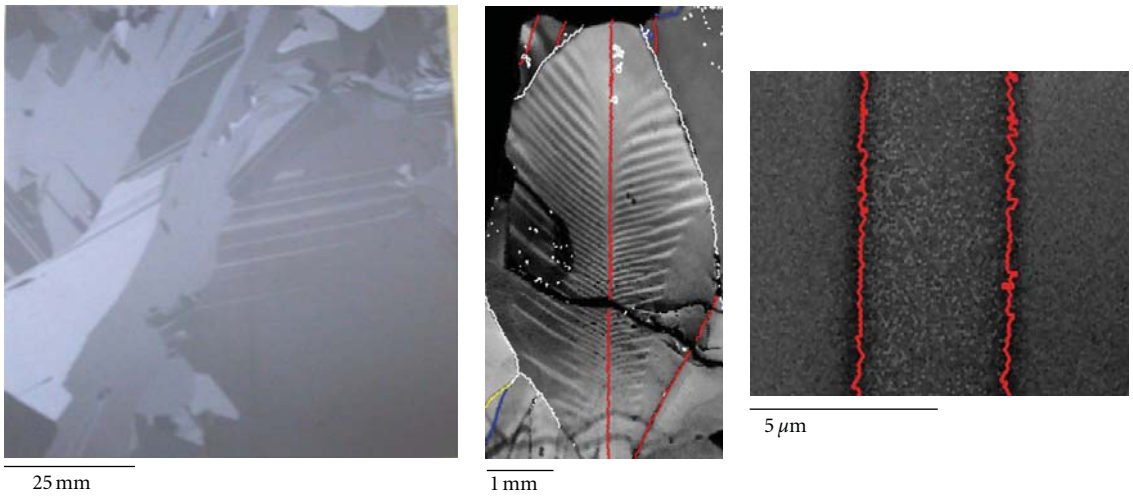

Figure 11: Mc-Si wafer (left) and faceted dendrite crystal examined by EBSP analysis (right) [43].

narrow spacing. Here, the parallel-twin formation, which is related to the faceted dendrite growth, is discussed.

The fundamental study of faceted dendrite growth has had a long history since the first report by Billig [65]. It has been shown that more than two parallel twins exist at the center of a faceted dendrite [65–69]. There have been some discussions concerning when and/or where a twin boundary is formed, that is, whether a nucleus originally contains a twin boundary [70] or whether a twin is formed after nucleation [71]. There was a report that twin boundaries are generated from a normal grain boundary during directional growth [72]. It has also been reported that parallel twins can form at (111) microfacets at a crystal-melt interface [43]. Pohl et al. studied this issue by classical molecular dynamics simulation [13]. In their simulations, parallel twin formation at the normal grain boundary was observed, but that at microfacets on a crystal-melt interface was not observed.

Figure 12 shows the growth behavior of a faceted dendrite grown from a crystal-melt interface. In this experiment, the crystal growth was initiated from a Si single-crystal seed. A faceted dendrite always appears following the zigzag facet formation on a crystal-melt interface during unidirectional growth. Figure 13 shows the result of the EBSP analysis of the faceted dendrite after crystallization. The EBSP analysis was performed at the origin of the dendrite growth. The direction along the dendrite growth was colored using the inverse pole figure triangle. $\sum 3$ grain boundaries were indicated by red lines, and other grain boundaries were labeled by black lines if they existed in the crystal. It was found that no grain boundaries without twin boundaries related to the dendrite growth existed in the crystal. This suggests that the grain boundary is not always necessary for twin boundary formation. To explain the experimental result, it should be considered that the twin boundary is formed on microfacets at the crystal-melt interface. Figure 14 schematically shows a model for generating parallel twins at the crystal-melt interface

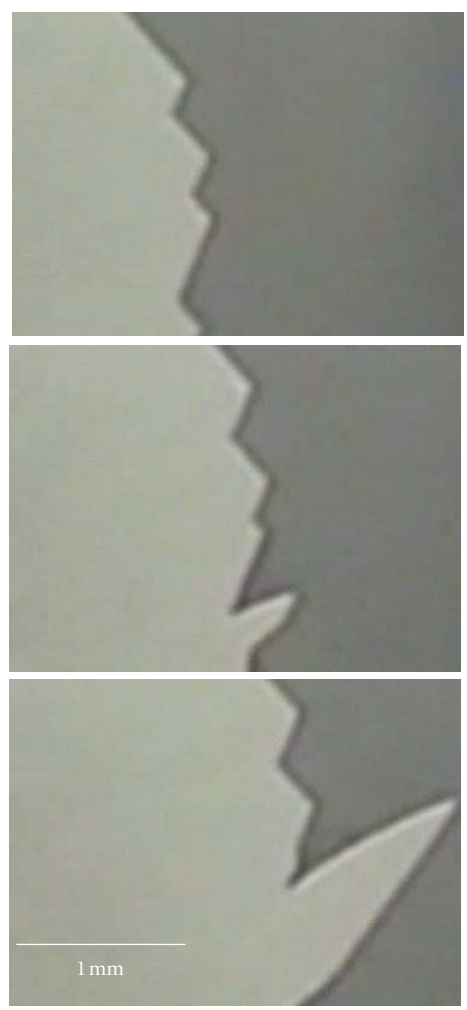

Figure 12: Growth behavior of faceted dendrite grown from crystal-melt interface.

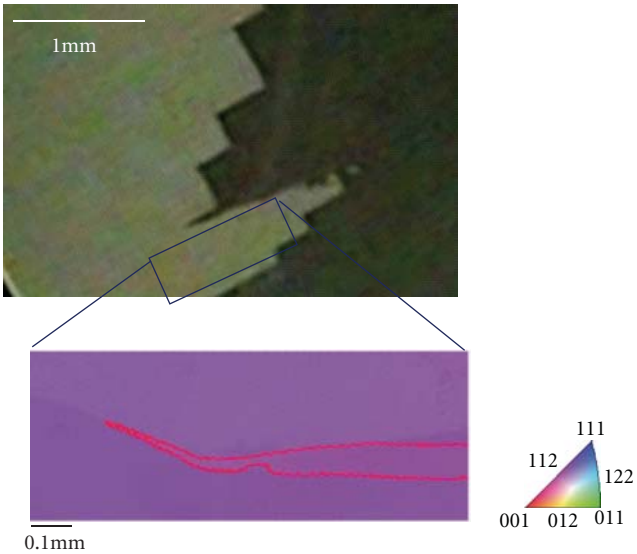

Figure 13: Result of EBSP analysis of faceted dendrite after crystallization. The EBSP analysis was performed at the origin of dendrite growth. The direction along the dendrite growth was shown in color using the inverse pole figure triangle. $\sum 3$ grain boundaries were indicated by red lines, and other grain boundaries were indicated by black lines when they existed in the crystal.

[43]. The formation of a zigzag-faceted interface bounded by {111} planes was discussed in Section 2.1. The shape of the faceted interface is dependent on crystal growth orientation, and crystal growth is always promoted on {111} facet planes at the zigzag-faceted interface. When an atom attaches to a facet plane with a twin relationship, a layer that maintains the twin relationship is formed on the facet plane after lateral growth, and then one twin boundary is generated on the layer, as shown in Figure 14(b). The crystal continuously grows in the lateral-growth mode on the {111} plane (Figure 14(c)), and then another twin boundary forms parallel to the previous twin boundary, as shown in Figure 14(d). In this model, the formation of parallel twin boundaries is ensured when one twin boundary is formed on a facet plane at the zigzag-faceted interface. When the undercooling of the melt is sufficient, a faceted dendrite grows from the parallel twin boundaries.

4. Faceted Dendrite Growth

Dendritic growth is a widespread phenomenon that appears during crystallization from a liquid or vapor phase in almost all types of materials containing metals, semiconductors, oxides, and organic materials. Dendrites of faceted materials, so-called "faceted dendrites," which are distinguished from those of nonfaceted materials in metals and alloys, were discovered in the 1950s [65]. It is known that the surface of a dendrite is bounded by {111} habit planes, and at least two parallel twin boundaries exist at the center of the dendrite [65–69]. Moreover, the preferential growth directions of Si-faceted dendrites are ⟨112⟩ and ⟨110⟩ [69], and the growth rate of faceted dendrites is higher than that of equiaxed grains. Such features can be applied in technologies for growing thin Si ribbon crystals [76, 77] and mc-Si ingots [1–3] for solar cells. The growth model of faceted dendrites preferentially grown in the ⟨112⟩ direction, hereafter referred to as ⟨112⟩ dendrites, was first proposed in 1960 by Hamilton and Seidensticker [67]. Recently, the growth model has been modified to apply to an actual growth based on experimental evidence by in situ observation of the growth behavior of ⟨112⟩ dendrites [74]. It was also shown that the modified model is adequate to explain the growth behavior of ⟨110⟩ dendrites [73].

Figure 15 shows a ⟨110⟩ dendrite and a ⟨112⟩ dendrite growing from a portion of a faceted crystal-melt interface. In both dendrites, parallel twins exist parallel to the {111} surface. The shape of the tip of the growing dendrite is markedly different between the ⟨110⟩ and ⟨112⟩ dendrites. Although the tip of the ⟨112⟩ dendrite becomes wider during growth, that of the ⟨110⟩ dendrite remains narrow during growth. Figure 16 shows the growth process of the ⟨112⟩ dendrite. It was found that triangular corners with an angle of 60° were formed at the tip of the dendrite and that the direction of the corners alternately changed from outward to forward in the direction of growth [74].

The modified growth model of the ⟨112⟩ dendrite based on experimental evidence is shown in Figure 17 [74]. Figure 17(a) shows the equilibrium form of the Si crystal with two parallel twins. The crystal is bounded by {111} habit planes, and parallel twin planes exist parallel to the ⟨111⟩ upper surface. In the explanation, the twins are distinguished by labeling them twin_1 and twin_2. A reentrant corner with an external angle of 141° (type I) appears at the growth surface only at twin_1 when the dendrite is growing in one direction. Nucleation more readily occurs at the reentrant corner than at {111} flat surfaces [69, 73, 74, 78–80], and thus the rapid growth occurs there. In this mechanism, it is considered that a triangular corner with an angle of 60° is formed at the growth tip of a dendrite owing to the rapid growth at the reentrant type I corner, as shown in Figure 17(b). This is the major difference from the previous growth mechanism of the ⟨112⟩ dendrite presented by Hamilton and Seidensticker [67]. In their explanation, it was considered that the formation of a triangular corner disturbs the continuous growth of a dendrite because the reentrant type I corner disappears. However, the formation of a triangular corner at the tip of the ⟨112⟩ dendrite is observed in Figure 16 by in situ observation [74]. Crystal growth can continue on the {111} flat surface although the rapid growth is inhibited owing to the disappearance of the type I corner (Figures 17(b)-17(c)). After the propagation of the crystal, two new type I corners are formed on the growth surface at twin_2 (Figure 17(c)). Thus, rapid growth occurs there again, and triangular corners with an angle of 60° are formed in the same manner as before (Figure 17(d)). Crystal growth is promoted on the {111} flat surface, leading to the formation of a new reentrant type I corner at twin_1 (Figure 17(e)), and the rapid growth occurs again (Figure 17(f)). A faceted dendrite continues to grow by the repetition of the same processes. In this

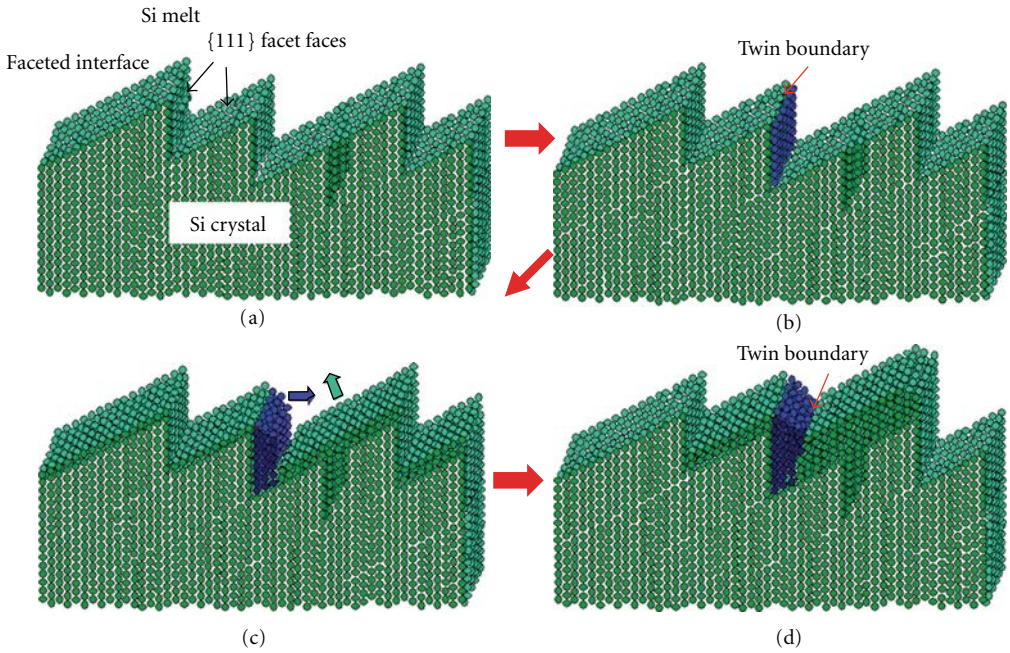

Figure 14: Model of parallel-twin formation at crystal-melt interface during crystal growth from Si melt. When a twin boundary is accidentally formed on a {111} facet plane, another twin boundary is formed parallel to the first twin after lateral growth is promoted [43].

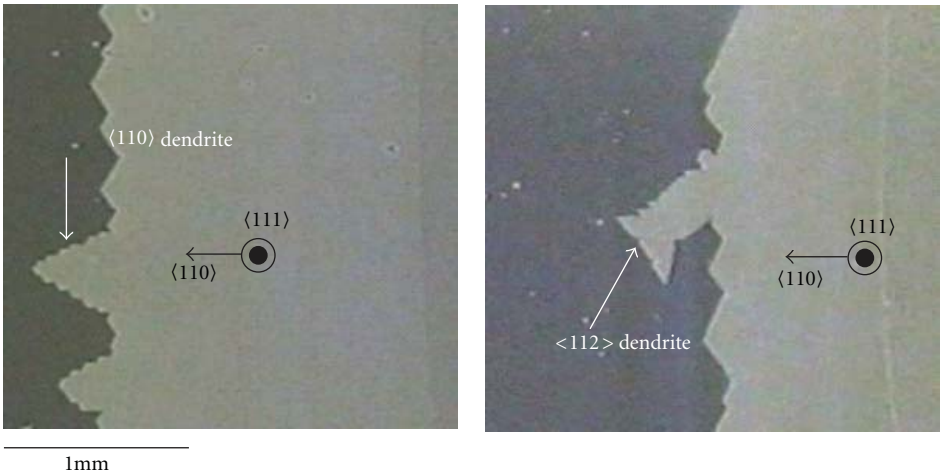

Figure 15: Growth shape of Si ⟨112⟩ and ⟨110⟩ faceted dendrites [73].

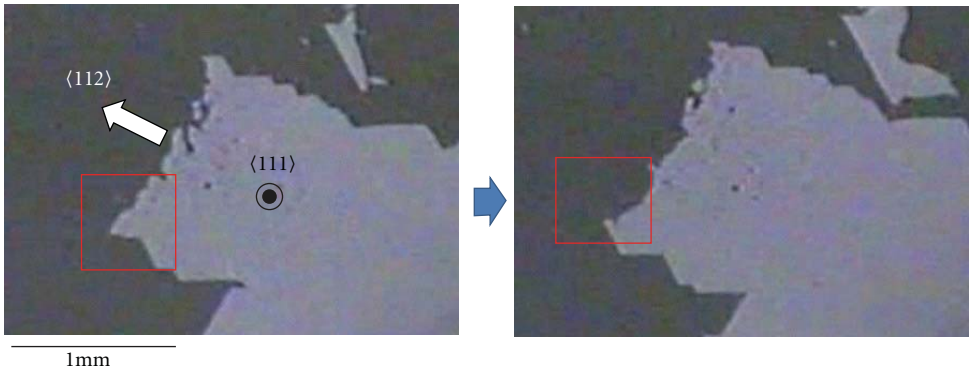

Figure 16: Growth behavior of Si ⟨112⟩ faceted dendrite observed perpendicular to {111} twins. Triangular corners of angle 60° are formed at the growth, tip and the direction of the corner changes with growth [74].

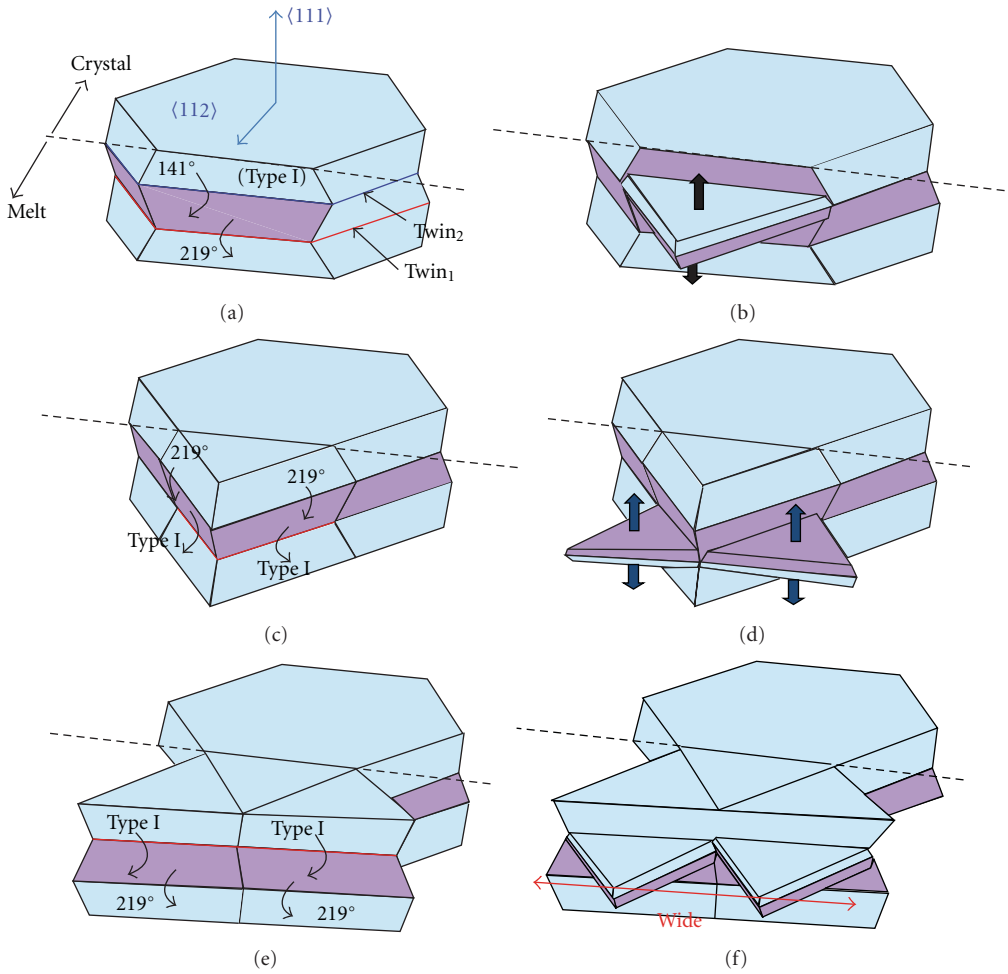

Figure 17: Schematic images of growth of Si ⟨112⟩ dendrite [73, 74]. (a) Equilibrium form of a crystal with two twins, which is bounded by {111} habit planes. It is considered that the crystal grows only in the ⟨112⟩ direction for simplicity. A reentrant corner of 141° angle (type I) appears at the growth surface only at twin$_1$. (b) A triangular corner is formed owing to the rapid growth at the type I corner at twin$_1$. (c) Crystal growth can continue on the {111} flat surface although the rapid growth is inhibited because of the disappearance of the type I corner. When the triangular crystal propagates across twin$_2$, two new type I corners are formed at twin$_2$. (d) Rapid growth occurs at the two type I corners again, and a triangular corner is formed. (e) After the propagation of the crystal, a type I corner is formed at twin$_1$. (f) Rapid growth occurs at a type I corner. A faceted dendrite continues to grow along the ⟨112⟩ direction by repeating the process from (b) to (f). The tip of the ⟨112⟩ dendrite becomes wider with crystal growth.

model, the tip of the ⟨112⟩ dendrite becomes wider during the growth.

Figure 18 shows the growth mechanism of a ⟨110⟩ dendrite [73]. Two parallel twins are also contained in this dendrite, and thus the initial shape of the crystal should be the same as that shown in Figure 17(a). This means that the elemental process for the growth of the ⟨110⟩ dendrite is the same as that of the ⟨112⟩ dendrite. It is found that type I corners exist at both twin$_1$ and twin$_2$ on the growth surface (Figure 18(a)). This is the major difference from the case of the ⟨112⟩ dendrite, in which type I corners alternately appear at each twin. Rapid growth occurs at these type I corners (Figure 18(b)), leading to the formation of triangular corners. Although the rapid growth is inhibited after the formation of triangular corners, the crystal continuously grows on the {111} flat surface (Figures 18(b)-18(c)). When triangular crystals propagate across the other twin, two type I corners appear, and rapid growth occurs there again (Figures 18(c)-18(d)). When triangular crystals propagate across the other twin, two type I corners appear (Figure 18(e)). The tip of the dendrite remains narrow during crystal growth. Thus, the shapes of the ⟨112⟩ and ⟨110⟩ dendrites during growth are explained by the models shown in Figures 17 and 18.

The equation for the growth velocity of a ⟨112⟩ dendrite and a ⟨110⟩ dendrite is derived on the basis of the growth model shown in Figures 17 and 18 [75]. The growth velocities of both dendrites are, respectively, described as

$$V_{\langle 112\rangle} = \frac{h}{2\,(h/V_1 + d/V_2)} + V_2,$$
$$V_{\langle 110\rangle} = \frac{h}{\sqrt{3}\,(h/V_1 + d/V_2)} + V_2, \quad (2)$$

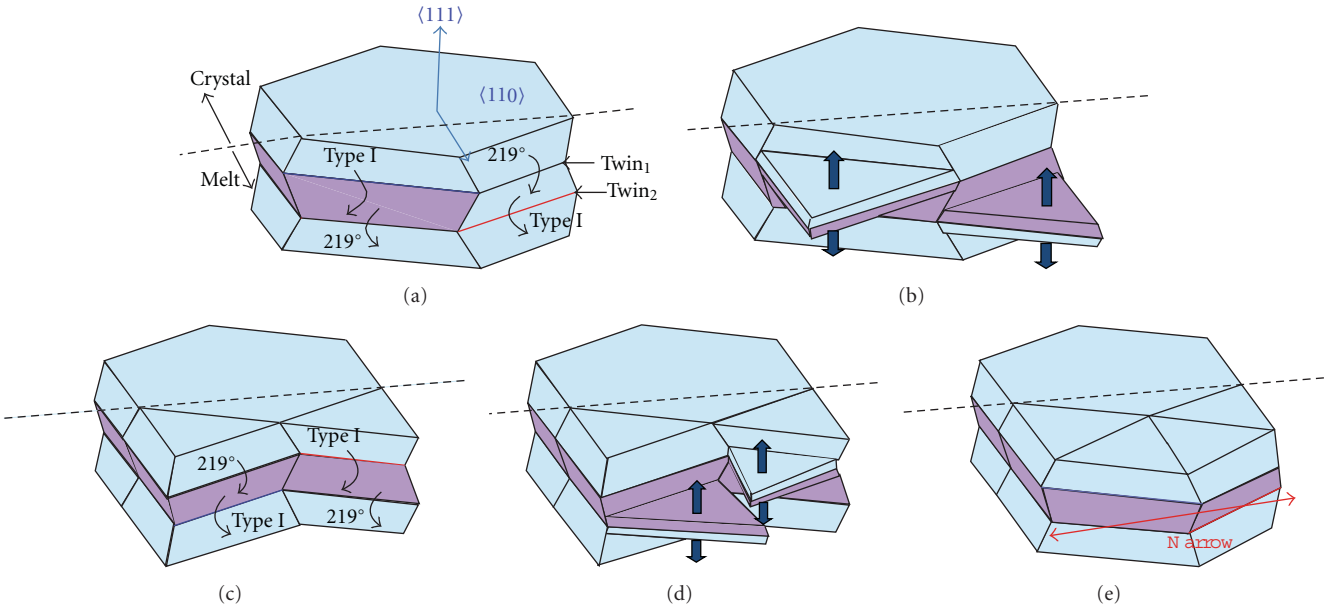

Figure 18: Schematic images of growth of Si ⟨110⟩ dendrite [73]. (a) Equilibrium form of crystal with two twins, which is similar to that shown in Figure 17(a). It is considered that the crystal grows only in the ⟨110⟩ direction. Reentrant type I corners appear at both twin_1 and twin_2. This is markedly different from the growth of the ⟨112⟩ dendrite. (b) Triangular corners are formed owing to the rapid growth at both twins. (c) Crystal growth can continue on the {111} flat surface. When triangular crystals propagate across another twin, two new type I corners are formed at both twins. (d) Rapid growth occurs at the two type I corners again, and a triangular corner is formed. (e) After the propagation of the triangular crystals, type I corners are formed at both twins. A faceted dendrite continues to grow along the ⟨110⟩ direction by repeating the process from (b) to (e). The tip of the ⟨110⟩ dendrite remains narrow during crystal growth.

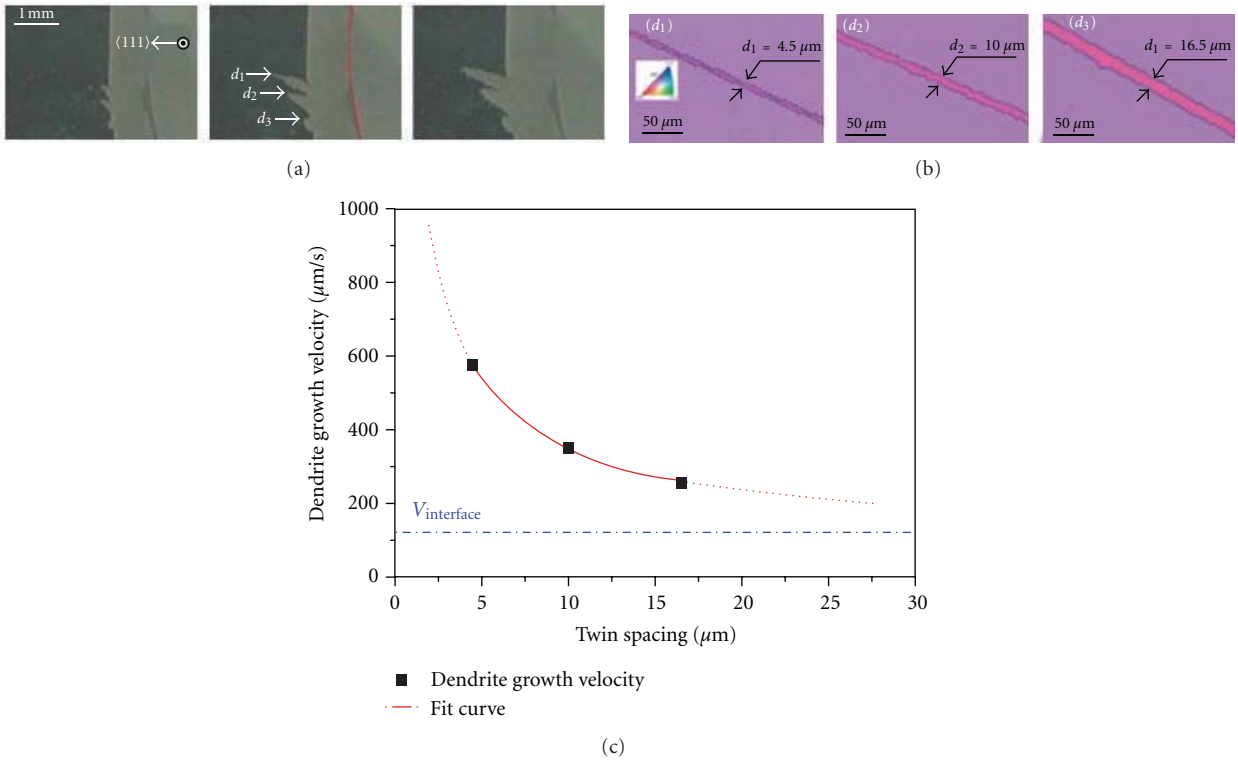

Figure 19: (a) Growth process of three dendrites (d1, d2, and d3) grown from same crystal-melt interface at same time [75]. (b) Parallel twins observed at center of d1, d2, and d3 by EBSP measurement. The average twin spacings in d1, d2, and d3 are 4.5 μm, 10 μm, and 16.5 μm, respectively [75]. (c) Dendrite growth velocity as function of twin spacing [75].

where h is the height of a triangular corner, d is the twin spacing, V_1 is the growth velocity at a type I corner, and V_2 is the growth velocity on the {111} plane. It is found that the growth velocity of a dendrite is inversely proportional to twin spacing. Figure 19(a) shows the growth of three dendrites (d1, d2, and d3) from the same crystal-melt interface at the same time [75]. The preferential growth direction of these three dendrites is ⟨110⟩. The growth velocities are clearly different among the three dendrites. Figure 19(b) shows the parallel twins observed at the center of d1, d2, and d3 by EBSP measurement. The average twin spacings in d1, d2, and d3 are 4.5 μm, 10 μm, and 16.5 μm, respectively. Dendrite growth velocity as a function of twin spacing is plotted in Figure 19(c). As twin spacing decreases, dendrite growth velocity nonlinearly increases. The equation above was used to fit the experimental results, as shown by the red line in Figure 19(c). It is found that the growth velocity of a dendrite eventually approaches a certain value as twin spacing increases to infinity. The dependence of the growth velocity of faceted dendrites on undercooling was also investigated [81]. Dendrite growth velocity increased linearly with increasing undercooling. It was also found that the relationship between dendrite growth velocity and undercooling is most sensitive to twin spacing [81].

5. Summary

Some crystal growth behaviors observed in melt growth processes were reviewed in this paper. Other significant issues not treated in this review include the dislocation/sub-grain-boundary formation [82–87] and impurity behavior [88–93] in crystal growth processes. For the complete understanding of crystal growth mechanisms and the control of the macro- and microstructures of mc-Si ingots, further data accumulation is required. It is expected that such ongoing studies will lead to the establishment of a technology for producing high-quality mc-Si ingots in the near future.

Acknowledgment

The author would like to acknowledge S. Uda and K. Nakajima for their fruitful discussions. This work was partially funded by the JST PRESTO Program and the Cabinet Office, Government of Japan through its "Funding Program for Next Generation World-Leading Researchers."

References

[1] K. Fujiwara, W. Pan, N. Usami et al., "Growth of structure-controlled polycrystalline silicon ingots for solar cells by casting," *Acta Materialia*, vol. 54, no. 12, pp. 3191–3197, 2006.

[2] K. Fujiwara, W. Pan, K. Sawada et al., "Directional growth method to obtain high quality polycrystalline silicon from its melt," *Journal of Crystal Growth*, vol. 292, no. 2, pp. 282–285, 2006.

[3] K. Nakajima, K. Kutsukake, K. Fujiwara, K. Morishita, and S. Ono, "Arrangement of dendrite crystals grown along the bottom of Si ingots using the dendritic casting method by controlling thermal conductivity under crucibles," *Journal of Crystal Growth*, vol. 319, no. 1, pp. 13–18, 2011.

[4] N. Stoddard, B. Wu, I. Witting et al., "Casting single crystal silicon: novel defect profiles from BP solar's mono2 wafers," *Diffusion and Defect Data Part B*, vol. 131–133, pp. 1–8, 2008.

[5] B. Wu and R. Clark, "Influence of inclusion on nucleation of silicon casting for photovoltaic (PV) application," *Journal of Crystal Growth*, vol. 318, no. 1, pp. 200–207, 2011.

[6] H. Zhang, L. Zheng, X. Ma, B. Zhao, C. Wang, and F. Xu, "Nucleation and bulk growth control for high efficiency silicon ingot casting," *Journal of Crystal Growth*, vol. 318, no. 1, pp. 283–287, 2011.

[7] T. Y. Wang, S. L. Hsu, C. C. Fei, K. M. Yei, W. C. Hsu, and C. W. Lan, "Grain control using spot cooling in multi-crystalline silicon crystal growth," *Journal of Crystal Growth*, vol. 311, no. 2, pp. 263–267, 2009.

[8] Y. Nose, I. Takahashi, W. Pan, N. Usami, K. Fujiwara, and K. Nakajima, "Floating cast method to realize high-quality Si bulk multicrystals for solar cells," *Journal of Crystal Growth*, vol. 311, no. 2, pp. 228–231, 2009.

[9] K. M. Yeh, C. K. Hseih, W. C. Hsu, and C. W. Lan, "High-quality multi-crystalline silicon growth for solar cells by grain-controlled directional solidification," *Progress in Photovoltaics: Research and Applications*, vol. 18, no. 4, pp. 265–271, 2010.

[10] M. Tokairin, K. Fujiwara, K. Kutsukake, N. Usami, and K. Nakajima, "Formation mechanism of a faceted interface: in situ observation of the Si(100) crystal-melt interface during crystal growth," *Physical Review B*, vol. 80, no. 17, Article ID 174108, 2009.

[11] K. Fujiwara, R. Gotoh, X. B. Yang, H. Koizumi, J. Nozawa, and S. Uda, "Morphological transformation of a crystal-melt interface during unidirectional growth of silicon," *Acta Materialia*, vol. 59, no. 11, pp. 4700–4708, 2011.

[12] K. Fujiwara, K. Maeda, N. Usami et al., "In situ observation of Si faceted dendrite growth from low-degree-of-undercooling melts," *Acta Materialia*, vol. 56, no. 11, pp. 2663–2668, 2008.

[13] J. Pohl, M. Müller, A. Seidl, and K. Albe, "Formation of parallel (1 1 1) twin boundaries in silicon growth from the melt explained by molecular dynamics simulations," *Journal of Crystal Growth*, vol. 312, no. 8, pp. 1411–1415, 2010.

[14] T. Duffar and A. Nadri, "On the twinning occurrence in bulk semiconductor crystal growth," *Scripta Materialia*, vol. 62, no. 12, pp. 955–960, 2010.

[15] K. A. Jackson, K. M. Beatty, and K. A. Gudgel, "An analytical model for non-equilibrium segregation during crystallization," *Journal of Crystal Growth*, vol. 271, no. 3-4, pp. 481–494, 2004.

[16] K. A. Jackson, *Liquid Metal and Solidification*, American Society for Metals, Cleveland, Ohio, USA, 1958.

[17] K. A. Jackson, "On the twinning occurrence in bulk semiconductor crystal growth," *Materials Science and Engineering*, vol. 65, no. 1, pp. 7–13, 1984.

[18] D. J. Eaglesham, A. E. White, L. C. Feldman, N. Moriya, and D. C. Jacobson, "Equilibrium shape of Si," *Physical Review Letters*, vol. 70, no. 11, pp. 1643–1646, 1993.

[19] M. W. Geis, H. I. Smith, B. Y. Tsaur, J. C. C. Fan, D. J. Silversmith, and R. W. Mountain, "Zone-melting recrystallization of Si films with a moveable-strip-heater oven," *Journal of the Electrochemical Society*, vol. 129, no. 12, pp. 2812–2818, 1982.

[20] M. W. Geis, H. I. Smith, D. J. Silversmith, R. W. Mountain, and C. V. Thomson, "Solidification-front modulation to entrain

subboundaries in zone-melting recrystallization of Si on SiO_2," *Journal of the Electrochemical Society*, vol. 130, no. 5, pp. 1178–1183, 1983.

[21] J. C. C. Fan, B. Y. Tsaur, and M. W. Geis, "Graphite-strip-heater zone-melting recrystallization of Si films," *Journal of Crystal Growth*, vol. 63, no. 3, pp. 453–483, 1983.

[22] E. H. Lee and G. A. Rozgonyi, "Modes of growth stability breakdown in the seeded crystallization of microzone-melted silicon on insulator," *Journal of Crystal Growth*, vol. 70, no. 1-2, pp. 223–229, 1984.

[23] L. Pfeiffer, S. Paine, G. H. Gilmer, W. van Saarloos, and K. W. West, "Pattern formation resulting from faceted growth in zone-melted thin films," *Physical Review Letters*, vol. 54, no. 17, pp. 1944–1947, 1985.

[24] D. Dutartre, M. Haond, and D. Bensahel, "Study of the solidification front of Si films in lamp zone melting controlled by patterning the underlying SiO_2," *Journal of Applied Physics*, vol. 59, no. 2, pp. 632–635, 1986.

[25] J. S. Im, H. Tomita, and C. V. Thompson, "Cellular and dendritic morphologies on stationary and moving liquid-solid interfaces in zone-melting recrystallization," *Applied Physics Letters*, vol. 51, no. 9, pp. 685–687, 1987.

[26] L. Pfeiffer, A. E. Gelman, K. A. Jackson, K. W. West, and J. L. Batstone, "Subboundary-free zone-melt recrystallization of thin-film silicon," *Applied Physics Letters*, vol. 51, no. 16, pp. 1256–1258, 1987.

[27] D. A. Williams, R. A. McMahon, and H. Ahmed, "Dynamic morphology of the nonequilibrium solid-melt interface in silicon," *Physical Review B*, vol. 39, no. 14, pp. 10467–10469, 1989.

[28] D. K. Shangguan and J. D. Hunt, "Dynamical study of the pattern formation of faceted cellular array growth," *Journal of Crystal Growth*, vol. 96, no. 4, pp. 856–870, 1989.

[29] U. Landman, W. D. Luedtke, R. N. Barnett et al., "Faceting at the silicon (100) crystal-melt interface: theory and experiment," *Physical Review Letters*, vol. 56, no. 2, pp. 155–158, 1986.

[30] U. Landman, W. D. Luedtke, M. W. Ribarsky, R. N. Barnett, and C. L. Cleveland, "Molecular-dynamics simulations of epitaxial crystal growth from the melt. I. Si(100)," *Physical Review B*, vol. 37, no. 9, pp. 4637–4646, 1988.

[31] K. Fujiwara, K. Nakajima, T. Ujihara et al., "In situ observations of crystal growth behavior of silicon melt," *Journal of Crystal Growth*, vol. 243, no. 2, pp. 275–282, 2002.

[32] K. Fujiwara, Y. Obinata, T. Ujihara, N. Usami, G. Sazaki, and K. Nakajima, "Grain growth behaviors of polycrystalline silicon during melt growth processes," *Journal of Crystal Growth*, vol. 266, no. 4, pp. 441–448, 2004.

[33] M. Tokairin, K. Fujiwara, K. Kutsukake, N. Usami, and K. Nakajima, "Formation mechanism of a faceted interface: in situ observation of the Si (100) crystal-melt interface during crystal growth," *Physical Review B*, vol. 80, no. 17, Article ID 174108, 2009.

[34] W. W. Mullins and R. F. Sekerka, "Stability of a planar interface during solidification of a dilute binary alloy," *Journal of Applied Physics*, vol. 35, no. 2, pp. 444–451, 1964.

[35] W. Kurz and D. J. Fisher, *Fundamentals of Solidification*, Trans Tech Publications, Dürnten, Switzerland, 4th revised edition, 1998.

[36] W. M. Rohsenow, J. P. Hartnett, and E. N. Ganic, *Handbook of Heat Transfer Fundamentals*, chapter 1, McGraw-Hill, New York, NY, USA, 2nd edition, 1985.

[37] K. W. Yi, H. T. Chung, H. W. Lee, and J. K. Yoon, "The effects of pulling rates on the shape of crystal/melt interface in Si single crystal growth by the Czochralski method," *Journal of Crystal Growth*, vol. 132, no. 3-4, pp. 451–460, 1993.

[38] K. M. Beatty and K. A. Jackson, "Monte Carlo modeling of silicon crystal growth," *Journal of Crystal Growth*, vol. 211, no. 1–4, pp. 13–17, 2000.

[39] D. Buta, M. Asta, and J. J. Hoyt, "Kinetic coefficient of steps at the Si(111) crystal-melt interface from molecular dynamics simulations," *Journal of Chemical Physics*, vol. 127, no. 7, Article ID 074703, 2007.

[40] P. Chen, Y. L. Tsai, and C. W. Lan, "Phase field modeling of growth competition of silicon grains," *Acta Materialia*, vol. 56, no. 15, pp. 4114–4122, 2008.

[41] K. Fujiwara, S. Tsumura, M. Tokairin et al., "Growth behavior of faceted Si crystals at grain boundary formation," *Journal of Crystal Growth*, vol. 312, no. 1, pp. 19–23, 2009.

[42] W. Miller, "Some remarks on the undercooling of the Si (1 1 1) facet and the "monte Carlo modeling of silicon crystal growth" by Kirk M. Beatty & Kenneth A. Jackson, J. Crystal Growth 211 (2000) 13," *Journal of Crystal Growth*, vol. 325, no. 1, pp. 101–103, 2011.

[43] K. Fujiwara, K. Maeda, N. Usami, G. Sazaki, Y. Nose, and K. Nakajima, "Formation mechanism of parallel twins related to Si-facetted dendrite growth," *Scripta Materialia*, vol. 57, no. 2, pp. 81–84, 2007.

[44] H. F. Mataré, "Carrier transport at grain boundaries in semiconductors," *Journal of Applied Physics*, vol. 56, no. 10, pp. 2605–2631, 1984.

[45] C. R. M. Grovenor, "Grain-boundaries in semiconductors," *Journal of Physics C*, vol. 18, no. 21, pp. 4079–4119, 1985.

[46] K. Yang, G. H. Schwuttke, and T. F. Ciszek, "Structural and electrical characterization of crystallographic defects in silicon ribbons," *Journal of Crystal Growth*, vol. 50, no. 1, pp. 301–310, 1980.

[47] A. Bary and G. Nouet, "Electrical activity of the first- and second-order twins and grain boundaries in silicon," *Journal of Applied Physics*, vol. 63, no. 2, pp. 435–438, 1988.

[48] R. Rizk, A. Ihlal, and X. Portier, "Evolution of electrical activity and structure of nickel precipitates with the treatment temperature of a Σ=25 silicon bicrystal," *Journal of Applied Physics*, vol. 77, no. 5, pp. 1875–1880, 1995.

[49] Z. J. Wang, S. Tsurekawa, K. Ikeda, T. Sekiguchi, and T. Watanabe, "Relationship between electrical activity and grain boundary structural configuration in polycrystalline silicon," *Interface Science*, vol. 7, no. 2, pp. 197–205, 1999.

[50] J. Chen, T. Sekiguchi, D. Yang, F. Yin, K. Kido, and S. Tsurekawa, "Electron-beam-induced c1urrent study of grain boundaries in multlcrystalline silicon," *Journal of Applied Physics*, vol. 96, no. 10, pp. 5490–5495, 2004.

[51] J. Chen and T. Sekiguchi, "Carrier recombination activity and structural properties of small-angle grain boundaries in multicrystalline silicon," *Japanese Journal of Applied Physics, Part 1*, vol. 46, no. 10, pp. 6489–6497, 2007.

[52] H. Sawada and H. Ichinose, "Structure of {112}Σ3 boundary in silicon and diamond," *Scripta Materialia*, vol. 44, no. 8-9, pp. 2327–2330, 2001.

[53] N. Sakaguchi, H. Ichinose, and S. Watanabe, "Atomic structure of faceted Σ3 CSL grain boundary in silicon: HRTEM and Ab-initio calculation," *Materials Transactions*, vol. 48, no. 10, pp. 2585–2589, 2007.

[54] N. Sakaguchi, M. Miyake, S. Watanabe, and H. Takahashi, "EELS and Ab-Initio study of faceted CSL boundary in

silicon," *Materials Transactions*, vol. 52, no. 3, pp. 276–279, 2011.

[55] P. Keblinski, S. R. Phillpot, D. Wolf, and H. Gleiter, "Thermodynamic criterion for the stability of amorphous intergranular films in covalent materials," *Physical Review Letters*, vol. 77, no. 14, pp. 2965–2968, 1996.

[56] M. Kohyama and R. Yamamoto, "Tight-binding study of grain boundaries in Si: energies and atomic structures of twist grain boundaries," *Physical Review B*, vol. 49, no. 24, pp. 17102–17117, 1994.

[57] S. Von Alfthan, P. D. Haynes, K. Kaski, and A. P. Sutton, "Are the structures of twist grain boundaries in silicon ordered at 0 K?" *Physical Review Letters*, vol. 96, no. 5, Article ID 055505, 2006.

[58] I. V. Markov, *Crystal Growth for Beginners*, World Scientific, Singapore, 1995.

[59] A. Voigt, E. Wolf, and H. P. Strunk, "Grain orientation and grain boundaries in cast multicrystalline silicon," *Materials Science and Engineering B*, vol. 54, no. 3, pp. 202–206, 1998.

[60] H. P. Iwata, U. Lindefelt, S. Öberg, and P. R. Briddon, "Energies and electronic properties of isolated and interacting twin boundaries in 3C-SiC, Si, and diamond," *Physical Review B*, vol. 68, no. 11, Article ID 113202, 2003.

[61] C. Raffy, J. Furthmüller, and F. Bechstedt, "Properties of hexagonal polytypes of group-IV elements from first-principles calculations," *Physical Review B*, vol. 66, no. 7, Article ID 075201, 2002.

[62] V. V. Voronkov, "Growth of a silicon crystal with one dislocation," *Kristallografiya*, vol. 20, no. 6, pp. 1145–1151, 1975.

[63] D. T. J. Hurle, "A mechanism for twin formation during Czochralski and encapsulated vertical Bridgman growth of III-V compound semiconductors," *Journal of Crystal Growth*, vol. 147, no. 3-4, pp. 239–250, 1995.

[64] K. Kutsukake, T. Abe, N. Usami, K. Fujiwara, K. Morishita, and K. Nakajima, "Formation mechanism of twin boundaries during crystal growth of silicon," *Scripta Materialia*, vol. 65, no. 6, pp. 556–559, 2011.

[65] E. Billig, "Growth of monocrystals of germanium from an undercooled melt," *Proceedings of the Royal Society of London Series A*, vol. 229, no. 1178, pp. 346–363, 1955.

[66] R. S. Wagner, "On the growth of germanium dendrites," *Acta Metallurgica*, vol. 8, no. 1, pp. 57–60, 1960.

[67] D. R. Hamilton and R. G. Seidensticker, "Propagation mechanism of germanium dendrites," *Journal of Applied Physics*, vol. 31, no. 7, pp. 1165–1168, 1960.

[68] K. K. Leung and H. W. Kui, "Microstructures of undercooled Si," *Journal of Applied Physics*, vol. 75, no. 2, pp. 1216–1218, 1994.

[69] K. Nagashio and K. Kuribayashi, "Growth mechanism of twin-related and twin-free facet Si dendrites," *Acta Materialia*, vol. 53, no. 10, pp. 3021–3029, 2005.

[70] R. Y. Wang, W. H. LI, and L. M. Hogan, "Faceted growth of silicon crystals in Al-Si alloys," *Metallurgical and Materials Transactions A*, vol. 28, no. 5, pp. 1233–1243, 1997.

[71] R. W. Cahn, "Twinned crystals," *Advances in Physics*, vol. 3, no. 12, pp. 363–445, 1954.

[72] M. Kitamura, N. Usami, T. Sugawara et al., "Growth of multicrystalline Si with controlled grain boundary configuration by the floating zone technique," *Journal of Crystal Growth*, vol. 280, no. 3-4, pp. 419–424, 2005.

[73] K. Fujiwara, H. Fukuda, N. Usami, K. Nakajima, and S. Uda, "Growth mechanism of the Si 110 faceted dendrite," *Physical Review B*, vol. 81, no. 22, Article ID 224106, 2010.

[74] K. Fujiwara, K. Maeda, N. Usami, and K. Nakajima, "Growth mechanism of Si-faceted dendrites," *Physical Review Letters*, vol. 101, no. 5, Article ID 055503, 2008.

[75] X. Yang, K. Fujiwara, R. Gotoh et al., "Effect of twin spacing on the growth velocity of Si faceted dendrites," *Applied Physics Letters*, vol. 97, no. 17, Article ID 172104, 2010.

[76] S. O'Hara and A. I. Bennett, "Web growth of semiconductors," *Journal of Applied Physics*, vol. 35, no. 3, pp. 686–693, 1964.

[77] D. L. Barrett, E. H. Myers, D.R. Hamilton, and A. I. Bennett, "Growth of wide, flat crystals of silicon web," *Journal of the Electrochemical Society*, vol. 118, no. 6, pp. 952–957, 1971.

[78] C. F. Lau and H. W. Kui, "Microstructures of undercooled germanium," *Acta Metallurgica Et Materialia*, vol. 39, no. 3, pp. 323–327, 1991.

[79] D. Li and D. M. Herlach, "Direct measurements of free crystal growth in deeply undercooled melts of semiconducting materials," *Physical Review Letters*, vol. 77, no. 9, pp. 1801–1804, 1996.

[80] T. Aoyama, Y. Takamura, and K. Kuribayashi, "Dendrite growth processes of silicon and germanium from highly undercooled melts," *Metallurgical and Materials Transactions A*, vol. 30, no. 5, pp. 1333–1339, 1999.

[81] X. Yang, K. Fujiwara, K. Maeda, J. Nozawa, H. Koizumi, and S. Uda, "Dependence of Si faceted dendrite growth velocity on undercooling," *Applied Physics Letters*, vol. 98, no. 1, Article ID 012113, 2011.

[82] I. Takahashi, N. Usami, K. Kutsukake, G. Stokkan, K. Morishita, and K. Nakajima, "Generation mechanism of dislocations during directional solidification of multicrystalline silicon using artificially designed seed," *Journal of Crystal Growth*, vol. 312, no. 7, pp. 897–901, 2010.

[83] N. Usami, R. Yokoyama, I. Takahashi, K. Kutsukake, K. Fujiwara, and K. Nakajima, "Relationship between grain boundary structures in Si multicrystals and generation of dislocations during crystal growth," *Journal of Applied Physics*, vol. 107, no. 1, Article ID 013511, 2010.

[84] V. Ganapati, S. Schoenfelder, S. Castellanos et al., "Infrared birefringence imaging of residual stress and bulk defects in multicrystalline silicon," *Journal of Applied Physics*, vol. 108, no. 6, Article ID 063528, 2010.

[85] G. Sarau, S. Christiansen, M. Holla, and W. Seifert, "Correlating internal stresses, electrical activity and defect structure on the micrometer scale in EFG silicon ribbons," *Solar Energy Materials and Solar Cells*, vol. 95, no. 8, pp. 2264–2271, 2011.

[86] S. Nakano, X. J. Chen, B. Gao, and K. Kakimoto, "Numerical analysis of cooling rate dependence on dislocation density in multicrystalline silicon for solar cells," *Journal of Crystal Growth*, vol. 318, no. 1, pp. 280–282, 2011.

[87] G. Stokkan, "Relationship between dislocation density and nucleation of multicrystalline silicon," *Acta Materialia*, vol. 58, no. 9, pp. 3223–3229, 2010.

[88] A. A. Istratov, T. Buonassisi, R. J. McDonald et al., "Metal content of multicrystalline silicon for solar cells and its impact on minority carrier diffusion length," *Journal of Applied Physics*, vol. 94, no. 10, pp. 6552–6559, 2003.

[89] B. Gao, S. Nakano, and K. Kakimoto, "Effect of crucible cover material on impurities of multicrystalline silicon in a unidirectional solidification furnace," *Journal of Crystal Growth*, vol. 318, no. 1, pp. 255–258, 2011.

[90] T. Buonassisi, A. A. Istratov, M. A. Marcus et al., "Engineering metal-impurity nanodefects for low-cost solar cells," *Nature Materials*, vol. 4, no. 9, pp. 676–679, 2005.

[91] G. Coletti, P. C.P. Bronsveld, G. Hahn et al., "Impact of metal contamination in silicon solar cells," *Advanced Functional Materials*, vol. 21, no. 5, pp. 879–890, 2011.

[92] P. Gundel, M. C. Schubert, W. Kwapil et al., "Micro-photoluminescence spectroscopy on metal precipitates in silicon," *Physica Status Solidi—Rapid Research Letters*, vol. 3, no. 7-8, pp. 230–232, 2009.

[93] T. Buonassisi, A. A. Istratov, M. D. Pickett et al., "Micro-photoluminescence spectroscopy on metal precipitates in silicon," *Progress in Photovoltaics*, vol. 14, no. 6, pp. 513–531, 2006.

Hindawi Publishing Corporation
International Journal of Photoenergy
Volume 2012, Article ID 753456, 5 pages
doi:10.1155/2012/753456

Research Article

Ultrathin Oxide Passivation Layer by Rapid Thermal Oxidation for the Silicon Heterojunction Solar Cell Applications

Youngseok Lee,[1] Woongkyo Oh,[2] Vinh Ai Dao,[2,3] Shahzada Qamar Hussain,[1] and Junsin Yi[1,2]

[1] *Department of Energy Science, Sungkyunkwan University, Suwon 440-746, Republic of Korea*
[2] *School of Information and Communication Engineering, Sungkyunkwan University, Suwon 440-746, Suwon, Republic of Korea*
[3] *College of Science, Faculty of Material Science, Vietnam National University, 227 Nguyen Van Cu, Hochiminh, Vietnam*

Correspondence should be addressed to Junsin Yi, yi@yurim.skku.ac.kr

Received 16 November 2011; Accepted 27 December 2011

Academic Editor: Bhushan Sopori

It is difficult to deposit extremely thin a-Si:H layer in heterojunction with intrinsic thin layer (HIT) solar cell due to thermal damage and tough process control. This study aims to understand oxide passivation mechanism of silicon surface using rapid thermal oxidation (RTO) process by examining surface effective lifetime and surface recombination velocity. The presence of thin insulating a-Si:H layer is the key to get high V_{oc} by lowering the leakage current (I_0) which improves the efficiency of HIT solar cell. The ultrathin thermal passivation silicon oxide (SiO_2) layer was deposited by RTO system in the temperature range 500–950°C for 2 to 6 minutes. The thickness of the silicon oxide layer was affected by RTO annealing temperature and treatment time. The best value of surface recombination velocity was recorded for the sample treated at a temperature of 850°C for 6 minutes at O_2 flow rate of 3 Lpm. A surface recombination velocity below 25 cm/s was obtained for the silicon oxide layer of 4 nm thickness. This ultrathin SiO_2 layer was employed for the fabrication of HIT solar cell structure instead of a-Si:H, (i) layer and the passivation and tunneling effects of the silicon oxide layer were exploited. The photocurrent was decreased with the increase of illumination intensity and SiO_2 thickness.

1. Introduction

The surface passivation effect is one of the most important characteristics in the fabrication of solar cells [1, 2]. The decrease in quality of surface passivation limits the efficiency of solar cell due to increase of surface recombination velocity (S_{eff}). An increase in surface recombination reduces the generation of electron hole pair (EHP). The quality of the silicon wafer is also a decisive factor to get high-efficiency solar cell. One of the typical features that decide the quality of a wafer is its diffusion length. The diffusion length of a wafer can be correlated with its diffusivity and surface passivation. The typical passivation layers used are SiO_2 and silicon nitride (SiN_x) thin films. The passivated emitter, rear locally diffused (PERL) cell and heterojunction with intrinsic thin layer (HIT) solar cell recorded an efficiency of 23% and 24.7%, respectively [1, 2]. The PERL cell utilized SiO_2 as the passivation layer whereas a-Si:H(i) is used as passivated layer in HIT solar cell to obtain an efficiency of over 20%. S. De Wolf et al. [3] indicated that a-Si:H layer is thermally unstable. However, SiO_2 will be an appropriate passivation layer for the solar cell fabrication due to its thermal stability and low interface defect density (D_{it}) [4]. The oxidized n-type silicon has a much better surface passivation properties than p-type silicon due to the small hall capture cross-section ($\sigma_n/\sigma_p \approx 1000$ at mid gap) [5] and optimized thermal oxide interface state densities of the order of 10^9 to 10^{10} $\text{cm}^{-2}\,\text{eV}^{-1}$ range [5, 6]. Two different mechanisms leading to good passivation are (i) the reduction of interface defect states and (ii) the field effect passivation, that is, the high reduction of one type of carrier by the incorporation of fixed charges Q_f in the passivation layer [7]. A reduction of interface state together with the field effect passivation is more effectively expected to attain for thermally grown SiO_2 layers [8, 9].

This thermal oxide growth could be achieved by two different methods. One is by the normal conventional furnace process (CFO) and the other is by the rapid thermal oxidation (RTO) process. The CFO process has

few disadvantages such as low throughput, high process cost, and high thermal budget. On the other hand RTO process is driven by the necessity to reduce the overall thermal budget associated with device fabrication and in particular to maintain the desired device electrical properties [10].

In this study, we used a thermal oxide process (RTO process) for the growth of the SiO_2 as a passivation layer for the HIT solar cell application and discussed SiO_2 layer's passivation property.

2. Experimental Method

2.1. Thermal Oxide Passivation Process. The n-type polished crystalline (100) silicon substrates having a resistivity of 2-3 -cm were used for this study. The resistivity of the silicon substrate has a decisive effect on the growth rate of SiO_2. The substrates were cut into 20 cm^2 pieces and were ultrasonically cleaned in sequence by dipping in acetone, isopropyl alcohol, and deionized (DI) water for 10 minutes. The native oxide layer was removed by dipping the substrate in 2% HF for 2 minutes. Rapid thermal oxidation technique using infrared (IR) lamp was utilized to oxidize the silicon substrates. The oxygen flow rate and temperature were varied in the range of 1–8 Lpm and 500–950°C, respectively. Firstly, the chamber was filled with nitrogen gas. At the steady state temperature, only oxygen was passed through the chamber. Lifetime was measured by photoconductive decay (PCD, WCT-1200) model. We confirmed the surface passivation effect of SiO_2 layer and estimated the surface recombination velocity (SRV) using PCD. The thickness of the SiO_2 layer formed by RTO process was measured by Ellipsometry (VB-250, J. A. Woollam) system. The metal-oxide-semiconductor (MOS) structure was fabricated to measure the interface trap density (D_{it}). The D_{it} value of the MOS structure was calculated by C-V measurement (HP-4129A) at 1 MHz.

2.2. Heterojunction Fabrication Process. The HIT solar cell structure was fabricated after growing an ultrathin SiO_2 layer on the silicon substrate by the RTO process. A p-type hydrogenated amorphous silicon (a-Si:H(p)) layer was deposited as an emitter on the polished side of the n-type Czochralski (CZ) silicon substrate and n-type hydrogenated amorphous silicon (a-Si:H(n)) layer was deposited as back surface field (BSF) layer on the rear side of the n-type CZ wafer. The thickness of the SiO_2 layer was around 3 nm. The thickness of the a-Si:H(p^+) and a-Si:H(n^+) layers was kept fixed at 7 nm and 10 nm, respectively. The deposition of ITO was performed by magnetron sputtering using a metal mask that was directly placed on the a-Si:H(p) surface. The evaporation method was used to deposit Ag/Al electrodes (200 nm) on the ITO and rear side to enable a good ohmic contact. The reactive ion etching (RIE) was carried out using SF_6 gas on the top side for mesa-etching. Finally, the above sample was annealed in air, and the solar cell characteristics have been measured.

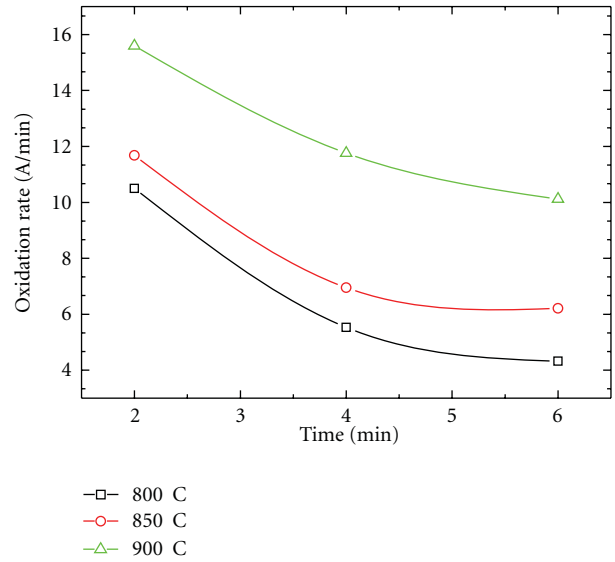

Figure 1: Oxidation rate of silicon substrate during rapid thermal annealing process at 800, 850, and 900°C with time.

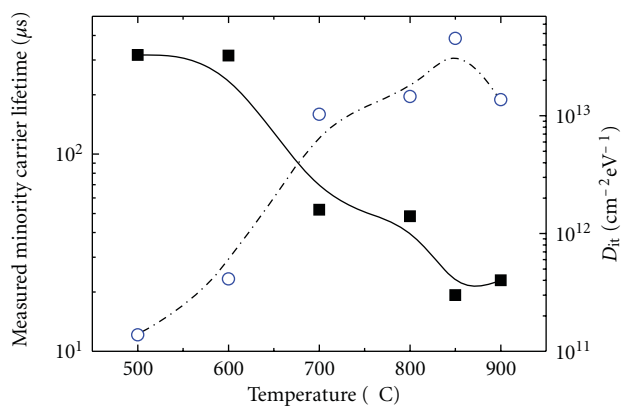

Figure 2: Variation of effective lifetime and interface trap density (D_{it}) as a function of rapid thermal annealing temperature.

3. Results and Discussion

Figure 1 depicts variations in the oxidation rate of silicon substrate during the rapid thermal annealing process at 800, 850, and 900°C as a function of time. The variation of the oxidation rate as a function of time can be explained by modifying the Deal-Grove model, which is accurate for very thin layer up to 1 nm, and proposed by Watanabe et al. [11]. Based on the Watanabe formulas, the thickness of the film as function of time can be expressed in the following form:

$$\frac{d}{dx_0}\frac{dt}{dx_0} = \frac{N_1}{D_0 C^*} - \frac{N_1}{2D_0^2 C^*}(A + 2x_0)\frac{dD_0}{dx_0}, \quad (1)$$

where the second term on the right side corresponds to the deviation from the linear kinetics of dt/dx_0. If $dD/dx_0 > 0$; that is, D_0 is decreased as x_0 decreases, the slope of dt/dx_0 decreases. In this case, the plot bends upward at the thin oxide region (short annealing time), as shown in our

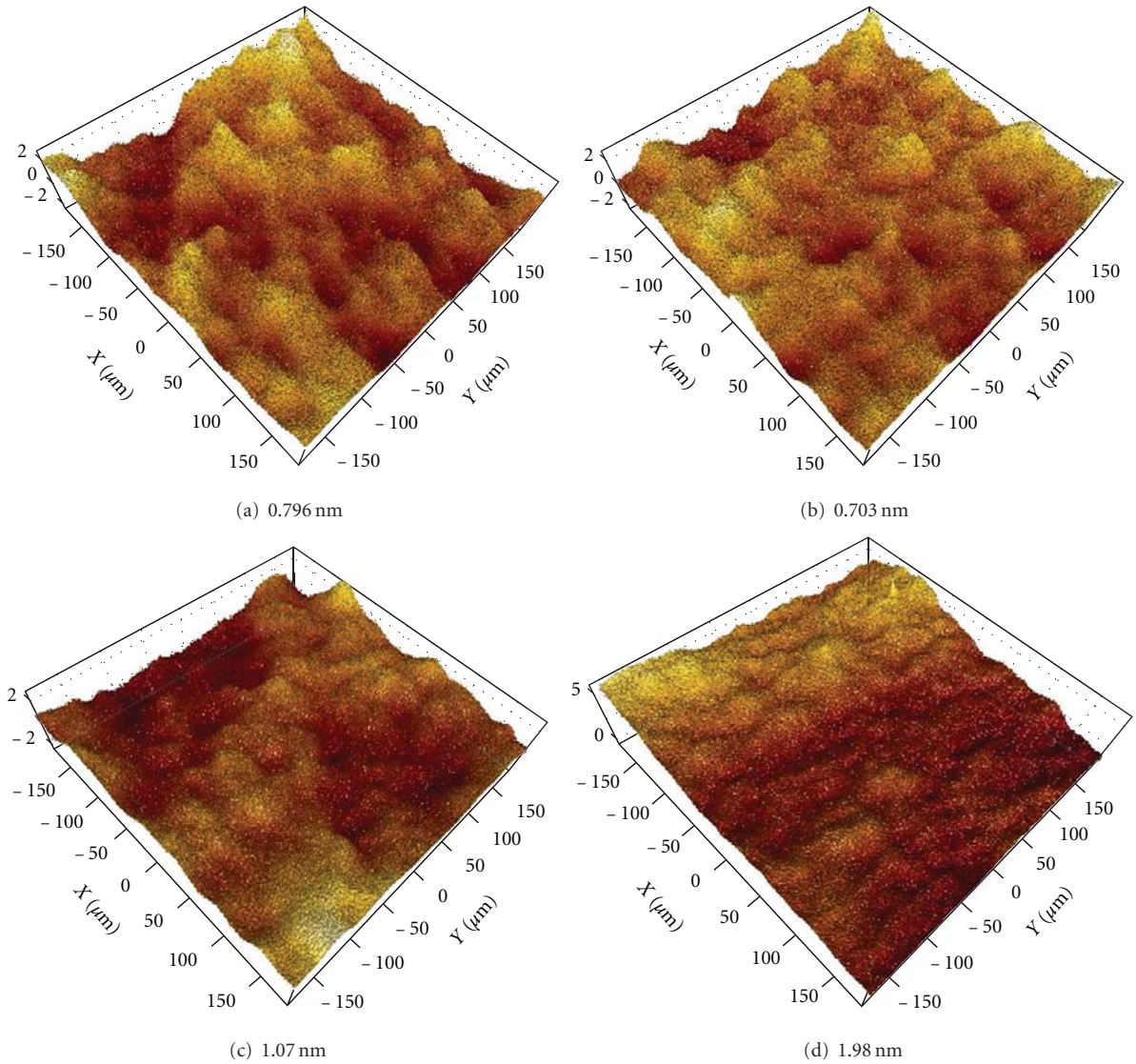

(a) 0.796 nm (b) 0.703 nm

(c) 1.07 nm (d) 1.98 nm

Figure 3: RMS as a function of rapid thermal annealing temperature: (a) 750, (b) 850, (c) 900, and (d) 950°C.

experiment results. Thus, it can be seen from the figure that the oxidation rate depends on the rapid thermal annealing temperature and shows a similar trend in the variation irrespective of RTO temperature. However, as the RTO temperature increased from 800 to 900°C, the SiO_2 layer formation rate was higher, as expected.

Figure 2 shows the variation in the effective lifetime and interface trap density (D_{it}) of the HIT solar cell as a function of RTA temperature. According to (1), an increase in effective life time would reduce the surface recombination velocity of the structure. When the thermal annealing temperature increased, the defect content of the surface may decrease that would reduce the surface recombination of carriers and result in an increase of effective carrier life time. The figure also shows that the effective lifetime increased when the temperature was increased from 500 to 850°C, maximum being at 850°C. As expected, the interface trap density (D_{it}) decreased with an increase of RTO annealing temperature, implying that the surface passivation quality is enhanced with an increase of temperature. The D_{it} gives a measure of the defects at the interface between Si substrate and SiO_2 layers. In order to explain the tendency of D_{it}, the surface roughness of the SiO_2/c-Si was estimated at different annealing temperatures, that is, 750, 850, 900 and 950°C, as shown in Figure 3. From Figure 3, we can deduce the average interface nanoroughness affects the interface condition (D_{it}). As the average interface nanoroughness gets bigger, however, the τ_{eff} decreased. It is also revealed that the lowest D_{it} as well as nanoroughness simultaneously can be observed. This is considered because the carriers are scattered by nanoroughness of the Si/SiO_2 interface [12]. Therefore it will become of more importance to improve the smoothness of Si/SiO_2 interface.

The illuminated current-voltage (I-V) characteristics of the device at different light intensity sources are shown in Figure 4 along with the dark I-V characteristics measured at

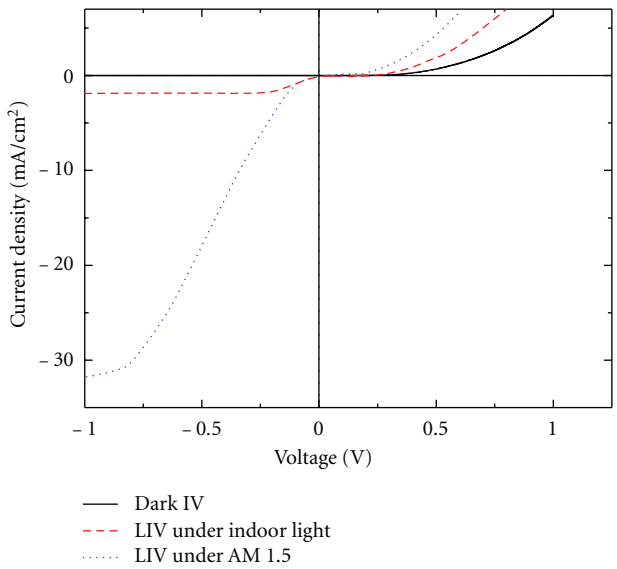

Figure 4: The illuminated current-voltage (I-V) characteristics of the device at different light intensity sources.

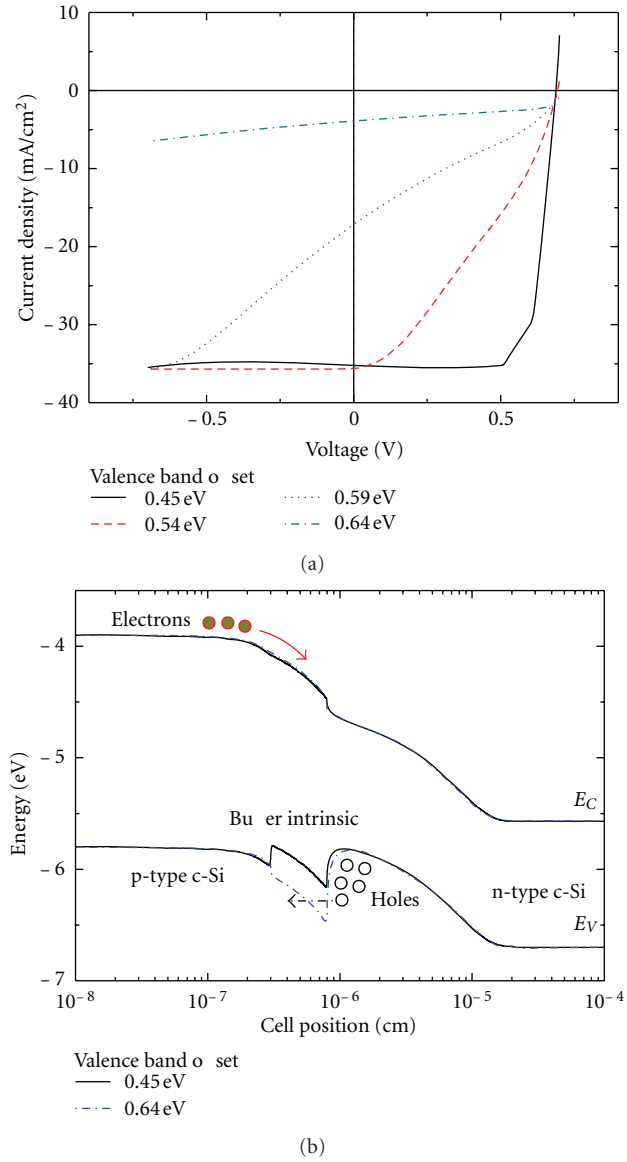

Figure 5: (a) Simulated I-V curve with different energy band gap of passivation layer, (b) schematic of the band diagram depend on energy band gap of passivation layer.

room temperature. It is observed from the figure that the illuminated I-V curve has been distorted (S-shaped) and the dark I-V curve retain in its original form. A change in light intensity results in changing of output current density, but does not change the shape of the photo I-V curve. We performed numerical simulation using AFORS-HET to determine the probable cause of the S-shaped I-V curve. The simulation results are shown in Figures 5(a) and 5(b). Figure 5(a) shows the change in illuminated I-V curve with increasing energy bandgap. When we increased the energy bandgap from 1.72 to 1.89 eV, the illuminated I-V shape changed toward our experimental results. Figure 5(b) shows the band diagram of the device having different valence band offset. From band diagram we may assume that higher bandgap of the buffer intrinsic oxide results in higher band offset, lowering electron affinity, and opposes the flow of the photocurrent in the device.

In order to remove the S-shaped curve in the I-V characteristics, both our simulation and van Cleef's experiment [13] suggested that (1) the energy band gap is either lower than 1.72 eV or (2) enhances the tunneling mechanism at the interface which mitigate the blocking of photo-generated free holes by a high valence band discontinuity. It is well known that SiO_2 is a wide-band-gap material (>4.0 eV) if it is grown by RTO method. Figure 6 shows the I-V characteristics of our device as a function of the intrinsic SiO_2 thickness in range of 1.0–3.4 nm. The S-shaped curve in I-V characteristics can be significantly reduced or even completely removed with the reduction of thickness. It is clear that the decrease thickness of the SiO_2 in the results in a narrow valence band spike. Then photogenerated holes are able to tunneling through the SiO_2 layer. Consequently a high accumulation of holes at the interface is prevented, and, also depletion region is prevented from spreading too much inside the emitter. At the same time, the SiO_2 layer's band gap is too high for the photoelectrons to cross the tunneling layer. When we apply wide-band-gap material to passivation layer in HIT solar cell structure, we should consider compromising condition between band gap and thickness.

4. Conclusion

The surface passivation is very important issue in amorphous and crystalline silicon solar cell applications as it highly influenced the performance of the device. Here we used ultrathin thermal passivation SiO_2 layer deposited by RTO system as a function of temperature and time for the fabrication of HIT solar cell. The high RTO annealing temperature can decrease the surface defects and reduce the

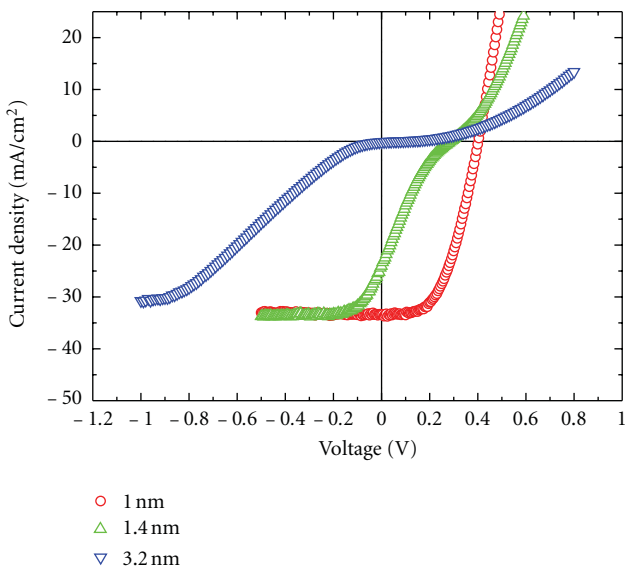

Figure 6: Variation of current density as a function of voltage of silicon oxide layer with thicknesses 1, 1.4, and 3.2 nm formed by rapid thermal annealing process.

surface recombination which caused an increase in effective life time. The SiO_2 layer deposited at a temperature of 850°C for 6 minutes gives the best values of S_{eff}, although the performance of our fabricated HIT solar cell using SiO_2 passivation layer is not better than the conventional HIT solar cell using a-Si:H(i) as a passivation layer. The bandgap is also a key factor to use SiO_2 as a passivation layer, which is yet to be tried to achieve for the upcoming experiments. The SiO_2 passivation layer can be employed in HIT solar cell by proper control of bandgap and tunnelling mechanism.

Acknowledgments

This research was supported by WCU (World Class University) program through the National Research Foundation of Korea funded by the Ministry of Education, Science and Technology (R31-2008-000-10029-0).

References

[1] J. Zhao, A. Wang, and M. A. Green, "24.5% efficiency silicon PERT cells on MCZ substrates and 24.7% efficiency PERL cells on FZ substrates," *Progress in Photovoltaics*, vol. 7, no. 6, pp. 471–474, 1999.

[2] T. Mishima, M. Taguchi, H. Sakata, and E. Maruyama, "Development status of high-efficiency HIT solar cells," *Solar Energy Materials and Solar Cells*, vol. 95, no. 1, pp. 18–21, 2011.

[3] S. De Wolf and M. Kondo, "Boron-doped a-Si:Hc-Si interface passivation: degradation mechanism," *Applied Physics Letters*, vol. 91, no. 11, Article ID 112109, 3 pages, 2007.

[4] S. W. Glunz, "High-efficiency crystalline silicon solar cells," *Advances in Optoelectronics*, vol. 2007, Article ID 97370, pp. 1–15, 2007.

[5] A. G. Aberle, "Surface passivation of crystalline silicon solar cells: a review," *Progress in Photovoltaics*, vol. 8, no. 5, pp. 473–487, 2000.

[6] S. R. Wenham, J. Zhao, X. Dai, A. Wang, and M. A. Green, "Surface passivation in high efficiency silicon solar cells," *Solar Energy Materials and Solar Cells*, vol. 65, no. 1, pp. 377–384, 2001.

[7] A. G. Aberle, S. Glunz, and W. Warta, "Field effect passivation of high efficiency silicon solar cells," *Solar Energy Materials and Solar Cells*, vol. 29, no. 2, pp. 175–182, 1993.

[8] A. G. Aberle, S. W. Glunz, A. W. Stephens, and M. A. Green, "High-efficiency silicon solar cells: Si/SiO2 interface parameters and their impact on device performance," *Progress in Photovoltaics*, vol. 2, no. 4, pp. 265–273, 1994.

[9] W. D. Eades and R. M. Swanson, "Calculation of surface generation and recombination velocities at the Si-SiO2 interface," *Journal of Applied Physics*, vol. 58, no. 11, pp. 4267–4276, 1985.

[10] B. J. O'Sullivan, P. K. Hurley, C. Leveugle, and J. H. Das, "Si(100)-SiO_2 interface properties following rapid thermal processing," *Journal of Applied Physics*, vol. 89, no. 7, pp. 3811–3820, 2001.

[11] T. Watanabe, K. Tatsumura, and I. Ohdomari, "New linear-parabolic rate equation for thermal oxidation of silicon," *Physical Review Letters*, vol. 96, Article ID 196102, p. 4, 2006.

[12] S. De Wolf, G. Agostinelli, G. Beaucarne, and P. Vitanov, "Influence of stoichiometry of direct plasma-enhanced chemical vapor deposited SiN films and silicon substrate surface roughness on surface passivation," *Journal of Applied Physics*, vol. 97, no. 6, Article ID 063303, pp. 1–8, 2005.

[13] M. W. M. van Cleef, F. A. Rubinelli, R. Rizzoli, R. Pinghini, R. E. I. Schropp, and W. F. van der Weg, "Amorphous silicon carbide/crystalline silicon heterojunction solar cells: a comprehensive study of the photocarrier collection," *Japanese Journal of Applied Physics*, vol. 37, no. 7, pp. 3926–3932, 1998.

Hindawi Publishing Corporation
International Journal of Photoenergy
Volume 2012, Article ID 879261, 6 pages
doi:10.1155/2012/879261

Research Article

Effect of Sheet Resistance and Morphology of ITO Thin Films on Polymer Solar Cell Characteristics

Ram Narayan Chauhan,[1] C. Singh,[2] R. S. Anand,[2] and Jitendra Kumar[1]

[1] *Materials Science Programme, Indian Institute of Technology Kanpur, Kanpur 208016, India*
[2] *Department of Electrical Engineering, Indian Institute of Technology Kanpur, Kanpur 208016, India*

Correspondence should be addressed to Ram Narayan Chauhan, chauhanramnarayan@gmail.com

Received 8 October 2011; Accepted 21 December 2011

Academic Editor: Bhushan Sopori

Solar cell fabrication on flexible thin plastic sheets needs deposition of transparent conducting anode layers at low temperatures. ITO thin films are deposited on glass by RF sputtering at substrate temperature of 70°C and compare their phase, morphology, optical, and electrical properties with commercial ITO. The films contain smaller nanocrystallites in (222) preferred orientation and exhibit comparable optical transmittance (∼95%) in the wavelength range of 550–650 nm, but high sheet resistance of ∼ 103 Ω/□ (the value being ∼36 Ω/□ for commercial ITO).The polymer solar cells with PEDOT: PSS and P3HT: PCBM layers realized on RF sputtered vis-a-vis commercial ITO thin films are shown to display a marginal difference in power conversion efficiency, low fill factor, and low open-circuit voltage but increased short-circuit current density. The decrease in fill factor, open-circuit voltage is compensated by increased short-circuit current. Detailed study is made of increased short-circuit current density.

1. Introduction

Indium tin oxide (ITO) is n-type degenerate semiconductor with a wide band gap (E_g = 3.5–4.2 eV). It has excellent photoelectrolytic properties, namely, electrical conductivity (10^3–10^4 ohm^{-1} cm^{-1}), transparency (80–95%) in the visible range and reflectance better than 80% in the infrared region [1–5]. It has found numerous applications in transparent electrode, antireflection coating, heat reflecting mirror, transparent electromagnetic shield, display, optoelectronic and photovoltaic devices, and so forth [6]. ITO is of particular interest to high efficiency heterojunction solar cells [7] and organic light-emitting diode (OLED) [8, 9]. Its thin films can be prepared by a variety of techniques like plasma-enhanced metal organic chemical vapour deposition (PEMOCVD) [10], ion-assisted deposition (ISD) [11], pulsed laser deposition (PLD) [12–14], dip coating [15], ion beam sputtering [16], RF magnetron sputtering [17, 18], and reactive thermal evaporation [19]. However, majority of the methods require elevated substrate temperatures to obtain thin films of reasonably high conductivity and good optical transmittance. But the amorphous silicon photovoltaic and flexible electrooptical devices demand the deposition of ITO at low temperatures (<200°C). RF sputtering allows preparation at low temperatures and on large areas [20]. Therefore, an attempt has been made here to fabricate solar cells using (i) ITO thin films deposited by RF sputtering and (ii) commercial low sheet resistance ITO and undertake comparative study of their characteristics.

2. Experimental Details

ITO thin films of thickness t ∼120 nm were deposited on a glass plate (size 30 mm × 30 mm) through shadow mask with 8 mm wide × 30 mm long slits at substrate temperature of 70°C in pure argon by radiofrequency (RF) sputtering using $In_2O_3 : SnO_2$ (90 : 10 wt%) target of 99.99% purity. The system was evacuated upto ∼10^{-6} mbar prior to deposition. The film thickness, sheet resistance, and optical transmittance were measured by surface Profilometer (Tencoralpha-step X-100), four probe sheet resistance measurement system, and a fiber optic spectrometer (Ocean optic model USB 2000), respectively. The crystalline phase was determined by X-ray diffraction (Thermo Electron ARL X'TRA X-ray

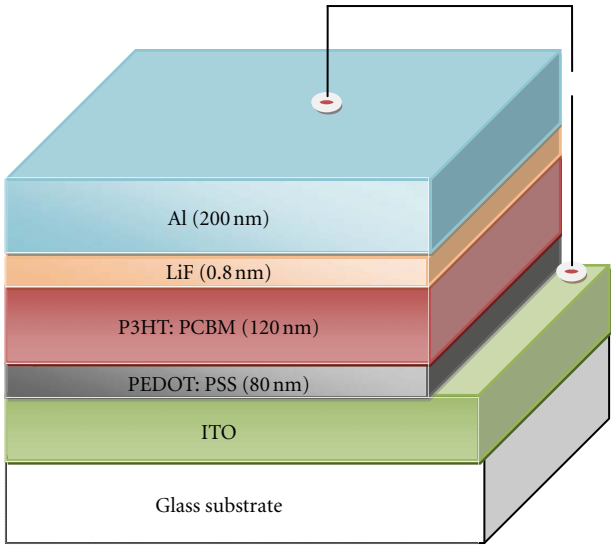

Figure 1: Schematic diagram of solar cell device.

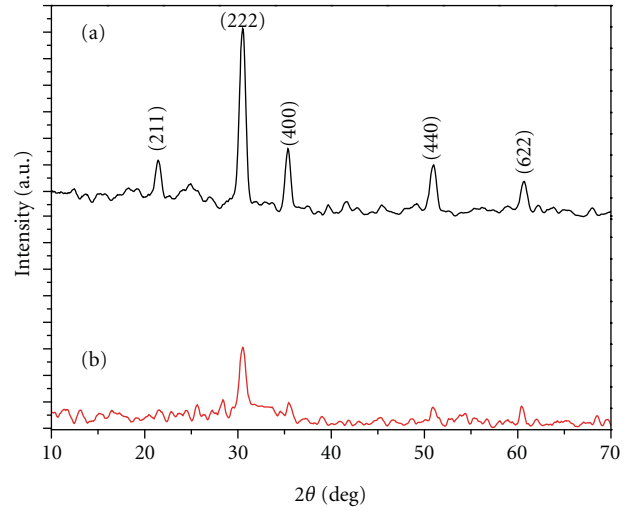

Figure 2: XRD patterns of (a) commercial and (b) RF-sputtered ITO thin films.

diffractometer), whereas the morphology was observed in scanning electron microscopes FEI, (Quanta 200, and carl zeiss SUPRA 40 VP). Further, the work function of RF sputtered and commercial ITO films was measured by Kelvin probe model 7.

For solar cell fabrication, polyethylenedioxythiophene : polystyrenesulfonic acid (PEDOT : PSS) was spin-coated at 2500 rpm on the patterned ITO-glass substrate and annealed at 120°C for 1 h in vacuum $\sim$ 1-2 $\times 10^{-5}$ mbar. A polymer active layer was then spin-coated at 1100 rpm over the dried PEDOT : PSS layers using the solutions of P3HT (poly 3-hexylthiophene) and PCBM ([6,6]-phenyl-C61-butyric acid methyl ester) 20 mg/cc each in an organic solvent mixed in volume ration 1 : 1 and annealed at 110°C for 20 min in vacuum. Finally, bilayer metal cathode of LiF and Al (thickness 0.8 nm and 200 nm, resp.) was realized on the active layer by thermal evaporation method. The device structure glass/ITO/PEDOT : PSS/P3HT : PCBM/LiF/Al thus fabricated is shown schematically in Figure 1. Similar devices were also made in the same batch on the commercial (36 ohm/sq, 150 nm thickness) ITO coated glass substrates. The J-V characteristics of solar cells were obtained by Keithley source measure unit (SMU) model 236 and a data acquisition system.

3. Results and Discussion

The XRD patterns of the commercial and RF-sputtered ITO thin films are shown in Figure 2. The commercial ITO sample exhibits five peaks of indices 211, 222, 400, 440, and 622, which match well with the bixbyite tin substituted In_2O_3 structure having lattice parameter $a = 10.124$ Å [21]. The thermalized sputtered species are known to orient as (222) plane while the species with higher energies prefer growth planes as (400) and (440) [22]. However, RF-sputtered ITO thin films exhibit (222) preferred orientation (Figure 2(b)). Obviously, the glass substrate is either placed in thermalized region or the above observation does not conform to the cited findings [22]. The grain size (δ) has been deduced with the 222 diffraction peak data and using the Scherrer relation

$$\delta = \frac{0.9\lambda}{\beta \cos\theta}, \tag{1}$$

where β is the corrected full width at half maxima (FWHM) at Bragg angle θ and λ is the X-ray wavelength [23–25]. The values of (δ) for the RF-sputtered and commercial ITO samples are $\sim$7 and $\sim$12 nm, respectively.

The morphologies of the thin films are shown in Figure 3. These reveal granular structure with smaller average grain size ($\sim$7 nm) for RF-sputtered ITO thin films vis-a-vis commercial sample. This is observation consistent with the XRD data and results due to low deposition rate (0.7 Ås^{-1}) used [26, 27]. The optical transmittance spectra of ITO thin films in the wavelength range of 300–800 nm are shown in Figure 4. Accordingly, the RF sputtered thin films display somewhat poor transmittance than the commercial ITO below 550 nm and above 650 nm, possibly because of substantial scattering from the grain boundary regions. Nevertheless, transmittance level of ITO thin films prepared by RF sputtering is as high as 95% in the wavelength range of 550–650 nm.

The sheet resistance (R_s) values of RF sputtered and commercial ITO thin films are 103 and 36 Ω/□, respectively. The values of electrical conductivity (σ) of RF and com ITO thin films, obtained from their sheet resistance ($R_s = 1/\sigma t$) are 8.1×10^2 and 1.9×10^3 ohm^{-1}-cm^{-1}, respectively. Slater theory tells that smaller grain size will have a higher energy barrier. The carriers have to cross the grain boundary, when they travel from one grain to the other. They need additional energy to surmount the grain boundary barrier [28]. The lower electrical conductivity in RF-sputtered ITO thin film is associated with larger barrier height $\phi \propto (X - f\delta)^2$, formed by the smaller grain size (δ). Here, X is the barrier width

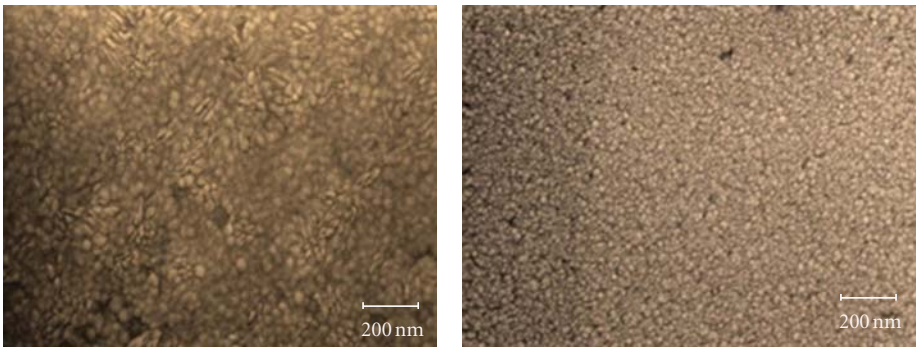

(a) (b)

Figure 3: Scanning electron micrographs of (a) commercial and (b) RF-sputtered ITO thin films.

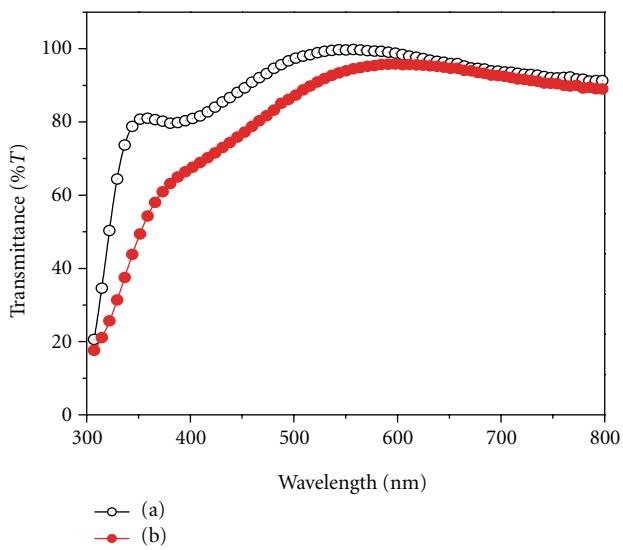

Figure 4: Transmission spectra of (a) commercial and (b) RF-sputtered ITO thin films.

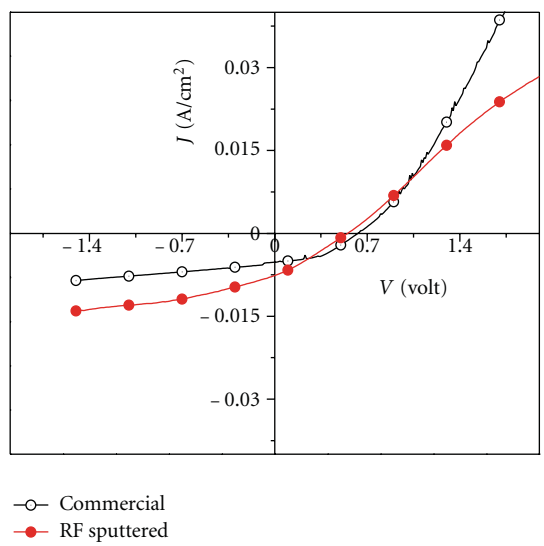

Figure 5: Current density (J)-voltage (V) characteristics of solar cells on commercial ITO and RF sputtered ITO thin films.

related to the number of disorder atom layers, and f is a fraction of the order of 1/15 to 1/50.

The solar cells fabricated on the commercial and RF-sputtered ITO thin films had areas of 0.05 and 0.08 cm^2, respectively. Their J-V characteristics are presented in Figure 5. The fill factor (FF) and conversion efficiency (η) are deduced from [29–31]

$$\mathrm{FF} = \frac{(JV)_{\max}}{J_{\mathrm{sc}} V_{\mathrm{oc}}} = \frac{P_{\max}}{J_{\mathrm{sc}} V_{\mathrm{oc}}}, \tag{2}$$

$$\%\eta = \frac{P_{\max}}{P_{\mathrm{in}}} \times 100 = \frac{\mathrm{FF} \times J_{\mathrm{sc}} V_{\mathrm{oc}}}{P_{\mathrm{in}}} \times 100, \tag{3}$$

where $(JV)_{\max}$ represents the maximum power that can be extracted from the cell and J_{sc}, V_{oc}, and P_{in} stand for the short-circuit current density (A cm^{-2}), open-circuit voltage (V) and incident photon flux (W cm^{-2}), respectively. Clearly, solar cell based on RF-sputtered ITO generates more current density ($J_{\mathrm{sc}} \sim 7.6$ mA cm^{-2}) due to more light absorption (Figure 6). More light is scattered from the grain boundaries of RF-sputtered ITO, leading to better absorption. The scattering light intensity (I_g) from the grain boundaries is expressed as [32]

$$I_g = I_0 - (1 - R_L)e^{-\gamma_g t}, \tag{4}$$

where I_0 is the intensity of incident light, R_L is reflection loss, t is the thickness of film, and γ_g is the grain boundary scattering coefficient. Here, the light scattering from the pore has been neglected because of film being compact. The scattering coefficient (γ_g) depends on the wavelength (λ) of incident light, grain density (N_g), grain size (δ), absolute refractive index difference ($\Delta n \sim$ refractive index difference of ITO and glass) and is given by

$$\gamma_g = N_g \left(\frac{\pi^3}{2\lambda}\right) \delta^4 (\Delta n)^2. \tag{5}$$

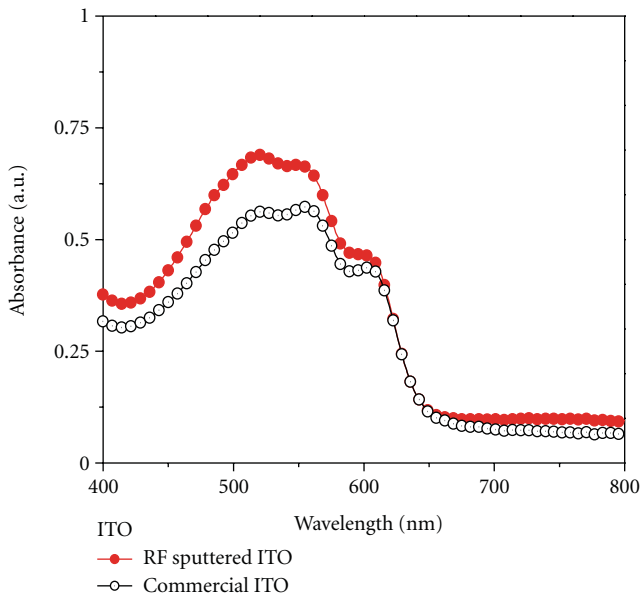

Figure 6: Absorption spectra of the devices fabricated on commercial and RF-sputtered ITO thin films.

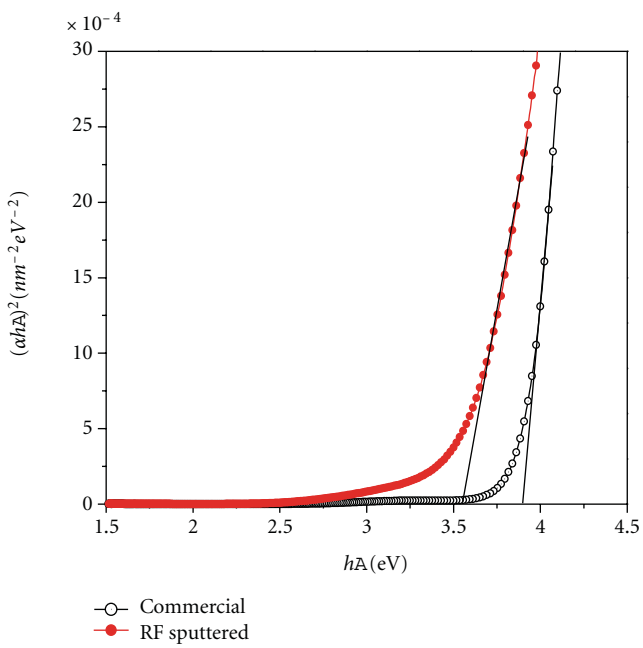

Figure 7: $(\alpha h\ )^2$ versus $h\ $ plots for commercial and RF-sputtered ITO thin films.

The linear refractive index (n) of thin films can be deduced from [33]

$$\frac{n^2-1}{n^2+2} = 1 - \sqrt{\frac{E_g}{20}}, \tag{6}$$

where E_g is the energy band gap of the film. The E_g of a direct band gap semiconductor can be estimated from the relation [5]

$$(\alpha h\ )^2 = A\left(h\ - E_g\right), \tag{7}$$

where A is a constant, α represents the absorption coefficient, and $h\ $ stand for photon energy. The values of the energy band gap of the RF-sputtered and commercial ITO thin films have been determined from the plot $(\alpha h\ )^2$ versus photon energy ($h\ $) by extrapolating linear portion of the spectrum to the abscissa ($h\ $-axis) as shown in Figure 7; the values obtained are 3.56 and 3.91 eV for RF sputtered and commercial ITO thin films, respectively. Their refractive index values obtained from (6) are 2.26 and 2.19, respectively. The corresponding absolute refractive index difference (Δn) values turn out to 0.76 and 0.69, respectively, by taking the "n" value of glass substrate as 1.5. Since the RF-sputtered films have small grain size, their number density (N_g) will be larger than the commercial ITO samples. So, RF-sputtered ITO films should exhibit larger grain boundary regions hence the more scattered light towards the active layer for enhancing the short-circuit current density.

The values of the open-circuit voltage achieved in devices on commercial and RF-sputtered ITO glass substrate are 0.63 and 0.55 V, respectively. The open-circuit voltage is mainly governed by the junction between two organic materials [34]. The open-circuit voltage (V_{oc}) is given by energy difference between the LUMO of acceptor and HOMO of the donor with a reduction of 0.2 V arising due to band bending at contact following accumulation of charges when the contact is ohmic in nature. However, in case of a nonohmic contact, V_{oc} is given by the difference of the work functions [35, 36]. The values of work function for the RF-sputtered and commercial ITO measured with Kelvin Probe are 4.76 ± 0.02 eV and 4.84 ± 0.02 eV, respectively. The difference in work function may arise due to size effects and additional defects present in RF-sputtered films vis-a-vis commercial ITO. These features may trap/accumulate charges at the anode interface and cause reduction in the work function. Incidentally, the V_{oc} of RF-sputtered ITO device is lower than that of commercial ITO-based device by about 0.08 V, which is exactly the difference in work functions. This corresponds to situation mentioned above.

The fill factor (FF) of the solar cells fabricated on commercial and RF-sputtered ITO thin films are 0.44 and 0.28, respectively at a light intensity of 95 mW/cm^2 under AM 1.5 illumination at room temperature. Since FF is totally dependent on the quality of J-V characteristics. For this, it is crucial to have high carrier mobility, low trap density, and negligible space charge effect. In other ways, effective collection of free charge carriers results better output power [37]. The conversion efficiencies of the above solar cell devices are 1.5 and 1.2%, respectively, that is, lower for the RF-sputtered ITO case. The inferior fill factor and lower conversion efficiency of the solar cell fabricated on the RF-sputtered ITO films is due to higher sheet resistance, that is, poor conductivity ($\sigma = 8.1 \times 10^2\ \Omega^{-1}\ \text{cm}^{-1}$). The parasitic resistive power loss also causes reduction in FF and depends mainly on series and shunt resistances. For an efficient solar cell, series resistance should be low whereas shunt resistance should be high. The series resistance (R_s) originates from the bulk of organic layer (P3HT : PCBM blends and PEDOT : PSS), electrodes (anode ITO and cathode metals), and the contact resistance between

the active layer and the electrode. On the other hand, the shunt or parallel resistance (R_{sh}) arises from the charge recombination at the donor/acceptor interface, through the cell and around the edges of the device [38, 39]. The R_s and R_{sh} have been determined from the inverse slopes of J-V curve at bias voltage of over V_{oc} (i.e., $J_{sc} \geq 0$), and zero, respectively [40]. The series resistance of identical device on commercial and RF-sputtered ITO are 55.7 and 64.3 Ω-cm^2, respectively. The corresponding shunt resistance values are 325.4 and 110 Ω-cm^2, respectively. The higher value of shunt resistance in commercial ITO results in negligible leakage current and so leads to higher conductivity. It may be pointed out that the commercial ITO is normally annealed at a high temperature for attaining low sheet resistance value, that is, high conductivity. The present experiment is directed towards RF sputtered ITO films for solar cells and OLED on polythene sheets, high temperature annealing is intentionally avoided.

4. Conclusions

The ITO thin films can be prepared by RF sputtering at a substrate temperature of 70°C on glass with (222) preferred orientation, grain size of 7 nm, high optical transparency of 95% in the wavelength range of 550–650 nm, and sheet resistance of 103 Ω/□ (higher than 36 Ω/□ of commercial ITO). The short-circuit current density (J_{sc}) and open-circuit voltage (V_{oc}) of the device fabricated on the RF sputtered are 7.6 mA-cm^{-2} and 0.55 V, respectively. The corresponding values of J_{sc} and V_{oc} are 5.2 mA-cm^{-2} and 0.63 V for solar cells based on commercial ITO. The fill factor (0.28) and conversion efficiency (1.2%) of the solar cell with RF-sputtered ITO layer are smaller than those fabricated with commercial ITO (values being 0.44 and 1.5%, resp.). The substantial increase in short-circuit current density of the solar cell can be attributed to smaller nanocrystallites which cause dominant light scattering at the grain boundaries towards the active layer for better light absorption. The open-circuit voltage is limited by the size effects as well as defects, responsible for trapping/accumulation of charge carriers at the anode interface, of ITO. This emphasizes the importance of the anode (ITO) surface morphology in polymer solar cells.

Acknowledgment

The financial support from DRDO and DST is duly acknowledged.

References

[1] B. Ren, X. Liu, M. Wang, and Y. Xu, "Preparation and characteristics of indium tin oxide (ITO) thin films at low temperature by r.f. magnetron sputtering," *Rare Metals*, vol. 25, no. 6, pp. 137–140, 2006.

[2] D. Kalhor, S. A. Ketabi, A. Ebrahimzad, and M. M. Rezaei, "Annealing effects on opto-electronic properties of thermally-evaporated ITO/Ag/ITO multilayered films for use in color filter electrodes," *World Applied Sciences Journal*, vol. 6, pp. 83–87, 2009.

[3] A. Sharma, P. J. Hotchkiss, S. R. Marder, and B. Kippelen, "Tailoring the work function of indium tin oxide electrodes in electrophosphorescent organic light-emitting diodes," *Journal of Applied Physics*, vol. 105, no. 8, Article ID 084507, 6 pages, 2009.

[4] J. G. Yoon, S. W. Cho, E. Lee, and J. S. Chung, "Characteristics of indium-tin-oxide Schottky contacts to ZnMgO/ZnO heterojunctions with band gap grading," *Applied Physics Letters*, vol. 95, no. 22, Article ID 222102, 3 pages, 2009.

[5] V. S. Reddy, K. Das, A. Dhar, and S. K. Ray, "The effect of substrate temperature on the properties of ITO thin films for OLED applications," *Semiconductor Science and Technology*, vol. 21, no. 12, pp. 1747–1752, 2006.

[6] R. G. Gordon, "Criteria for choosing transparent conductors," *MRS Bulletin*, vol. 25, no. 8, pp. 52–57, 2000.

[7] S. E. Shaheen, R. Radspinner, N. Peyghambarian, and G. E. Jabbour, "Fabrication of bulk heterojunction plastic solar cells by screen printing," *Applied Physics Letters*, vol. 79, no. 18, pp. 2996–2998, 2001.

[8] Y. Yang, Q. Huang, A. W. Metz et al., "High-performance organic light-emitting diodes using ITO anodes grown on plastic by room-temperature ion-assisted deposition," *Advanced Materials*, vol. 16, no. 4, pp. 321–324, 2004.

[9] Y. Hong, Z. He, N. S. Lennhoff, D. A. Banach, and J. Kanicki, "Transparent flexible plastic substrates for organic light-emitting devices," *Journal of Electronic Materials*, vol. 33, no. 4, pp. 312–320, 2004.

[10] Y. C. Park, Y. S. Kim, H. K. Seo, S. G. Ansari, and H. S. Shin, "ITO thin films deposited at different oxygen flow rates on Si(100) using the PEMOCVD method," *Surface and Coatings Technology*, vol. 161, no. 1, pp. 62–69, 2002.

[11] J. Matsuo, H. Katsumata, E. Minami, and I. Yamada, "O_2 cluster ion-assisted deposition for tin-doped indium oxide films," *Nuclear Instruments and Methods in Physics Research, Section B*, vol. 161, pp. 952–957, 2000.

[12] J. Olivier, B. Servet, M. Vergnolle, M. Mosca, and G. Garry, "Stability/instability of conductivity and work function changes of ITO thin films, UV-irradiated in air or vacuum. Measurements by the four-probe method and by Kelvin force microscopy," *Synthetic Metals*, vol. 122, no. 1, pp. 87–89, 2001.

[13] E. Holmelund, B. Thestrup, J. Schou et al., "Deposition and characterization of ITO films produced by laser ablation at 355 nm," *Applied Physics A*, vol. 74, no. 2, pp. 147–152, 2002.

[14] V. Craciun, D. Craciun, X. Wang, T. J. Anderson, and R. K. Singh, "Transparent and conducting indium tin oxide thin films grown by pulsed laser deposition at low temperatures," *Journal of Optoelectronics and Advanced Materials*, vol. 5, no. 2, pp. 401–408, 2003.

[15] K. Nishio, T. Sei, and T. Tsuchiya, "Preparation and electrical properties of ITO thin films by dip-coating process," *Journal of Materials Science*, vol. 31, no. 7, pp. 1761–1766, 1996.

[16] D. Kim, Y. Han, J.-S. Cho, and S.-K. Koh, "Low temperature deposition of ITO thin films by ion beam sputtering," *Thin Solid Films*, vol. 377-378, pp. 81–86, 2000.

[17] K. H. Kim, K. Choi, E. S. Choi, J. H. Hwang, and J. T. Hwang, "Indium tin oxide thin films deposited by RF-magnetron sputtering for organic electro-luminescence devices," *Journal of Ceramic Processing Research*, vol. 4, no. 2, pp. 96–100, 2003.

[18] I. Baía, M. Quintela, L. Mendes, P. Nunes, and R. Martins, "Performances exhibited by large area ITO layers produced by r.f. magnetron sputtering," *Thin Solid Films*, vol. 337, no. 1-2, pp. 171–175, 1999.

[19] A. Subrahmanyam and N. Balasubramanian, "Studies of the photovoltaic behaviour of indium tin oxide (ITO)/silicon junctions prepared by the reactive thermal evaporation technique," *Semiconductor Science and Technology*, vol. 7, no. 3, article 07, pp. 324–327, 1992.

[20] M. Nisha, S. Anusha, A. Antony, R. Manoj, and M. K. Jayaraj, "Effect of substrate temperature on the growth of ITO thin films," *Applied Surface Science*, vol. 252, no. 5, pp. 1430–1435, 2005.

[21] N. Manavizadeh, F. A. Boroumand, E. Asl-Soleimani et al., "Influence of substrates on the structural and morphological properties of RF sputtered ITO thin films for photovoltaic application," *Thin Solid Films*, vol. 517, no. 7, pp. 2324–2327, 2009.

[22] C. V. R. Vasant Kumar and A. Mansingh, "Effect of target-substrate distance on the growth and properties of rf-sputtered indium tin oxide films," *Journal of Applied Physics*, vol. 65, no. 3, pp. 1270–1280, 1989.

[23] B. D. Cullity, *Elements of X-Ray Di ractions*, Addison-Wesley, Reading, Mass, USA, 1959.

[24] T. S. Sathiaraj, "Effect of annealing on the structural, optical and electrical properties of ITO films by RF sputtering under low vacuum level," *Microelectronics Journal*, vol. 39, no. 12, pp. 1444–1451, 2008.

[25] R. Vinodkumar, K. J. Lethy, D. Beena et al., "Effect of ITO buffer layers on the structural, optical and electrical properties of ZnO multilayer thin films prepared by pulsed laser deposition technique," *Solar Energy Materials and Solar Cells*, vol. 94, no. 1, pp. 68–74, 2010.

[26] A. K. Kulkarni, K. H. Schulz, T. S. Lim, and M. Khan, "Dependence of the sheet resistance of indium-tin-oxide thin films on grain size and grain orientation determined from X-ray diffraction techniques," *Thin Solid Films*, vol. 345, no. 2, pp. 273–277, 1999.

[27] P. Thilakan, C. Minarini, S. Loreti, and E. Terzini, "Investigations on the crystallisation properties of RF magnetron sputtered indium tin oxide thin films," *Thin Solid Films*, vol. 388, no. 1-2, pp. 34–40, 2001.

[28] J. C. Slater, "Barrier theory of the photoconductivity of lead sulfide," *Physical Review*, vol. 103, no. 6, pp. 1631–1644, 1956.

[29] T. L. Benanti and D. Venkataraman, "Organic solar cells: an overview focusing on active layer morphology," *Photosynthesis Research*, vol. 87, no. 1, pp. 73–81, 2006.

[30] L. A. Dobrzanski, L. Wosinska, B. Dolzanska, and A. Drygała, "Comparison of electrical characteristics of silicon solar cells," *Journal of Achievements in Materials and Manufacturing Engineering*, vol. 18, pp. 215–218, 2006.

[31] J. D. Servaites, M. A. Ratner, and T. J. Marks, "Practical efficiency limits in organic photovoltaic cells: functional dependence of fill factor and external quantum efficiency," *Applied Physics Letters*, vol. 95, no. 16, Article ID 163302, 3 pages, 2009.

[32] R. Apetz and M. P. B. Van Bruggen, "Transparent alumina: a light-scattering model," *Journal of the American Ceramic Society*, vol. 86, no. 3, pp. 480–486, 2003.

[33] V. Dimitrov and S. Sakka, "Linear and nonlinear optical properties of simple oxides. II," *Journal of Applied Physics*, vol. 79, no. 3, pp. 1741–1745, 1996.

[34] C. Y. Kwong, A. B. Djurišić, P. C. Chui, and W. K. Chan, "CuPc/C60 solar cells—influence of the indium tin oxide substrate and device architecture on the solar cell performance," *Japanese Journal of Applied Physics, Part 1*, vol. 43, no. 4, pp. 1305–1311, 2004.

[35] V. D. Mihailetchi, P. W. M. Blom, J. C. Hummelen, and M. T. Rispens, "Cathode dependence of the open-circuit voltage of polymer:fullerene bulk heterojunction solar cells," *Journal of Applied Physics*, vol. 94, no. 10, pp. 6849–6854, 2003.

[36] C. J. Brabec, N. S. Sariciftci, and J. C. Hummelen, "Plastic solar cells," *Advanced Funtional Materials*, vol. 11, no. 1, pp. 15–26, 2001.

[37] A. Gadisa, F. Zhang, D. Sharma, M. Svensson, M. R. Andersson, and O. Inganäs, "Improvements of fill factor in solar cells based on blends of polyfluorene copolymers as electron donors," *Thin Solid Films*, vol. 515, no. 5, pp. 3126–3131, 2007.

[38] B. Muhsin, J. Renz, K. H. Drüe, G. Gobsch, and H. Hoppe, "Influence of polymer solar cell geometry on series resistance and device efficiency," *Physica Status Solidi (A)*, vol. 206, no. 12, pp. 2771–2774, 2009.

[39] J. Nelson, *The Physics of Solar Cell*, Imperial College Press, London, UK, 2003.

[40] M. Chegaar, Z. Ouennoughi, F. Guechi, and H. Langueur, "Determination of solar cells parameters under illuminated conditions," *The Journal of Electron Device*, vol. 2, pp. 17–21, 2003.

Hindawi Publishing Corporation
International Journal of Photoenergy
Volume 2012, Article ID 743947, 7 pages
doi:10.1155/2012/743947

Research Article

A New Ruthenium Sensitizer Containing Benzo[1,9]quinolizino(acridin-2-yl)vinyl-2,2′-bipyridine Ligand for Effective Nanocrystalline Dye-Sensitized Solar Cells

Jeum-Jong Kim,[1] Jeonghun Yoon,[1] Eun Jung Kim,[2] Bo Ram Kim,[2] Yong-Jin Yoon,[2] and Mangu Kang[1]

[1] *Advanced Solar Technology Research Department, Electronics and Telecommunications Research Institute, Daejeon 305-700, Republic of Korea*
[2] *Department of Chemistry and Research Institute of Natural Science, Gyeongsang National University, Chinju 660701, Republic of Korea*

Correspondence should be addressed to Mangu Kang, 10009kang@etri.re.kr

Received 10 June 2011; Accepted 13 December 2011

Academic Editor: Peter Rupnowski

Novel ruthenium bipyridyl sensitizer incorporating conjugated benzo[1,9]quinolizino-(acridin-2-yl)vinyl-2,2′-bipyridine ligand [**JJ-12**] has been synthesized and demonstrated as efficient sensitizer in dye-sensitized solar cells. A mesoporous titania film stained with **JJ-12** exhibits a remarkable incident monochromatic photon-to-current conversion efficiency of 82%. Under standard AM 1.5 sunlight, the solar cell using a liquid-based electrolyte consisting of 0.6 M 1,2-dimethyl-3-propylimidazolium iodide (DMPII), 0.05 M I_2, 0.1 M LiI, and 0.5 M *tert*-butylpyridine in acetonitrile exhibits a short-circuit photocurrent density of 16.47 mA/cm^2, an open-circuit voltage of 0.71 V, and a fill factor of 0.71, corresponding to an overall conversion efficiency of 8.34 %.

1. Introduction

Dye-sensitized solar cells (DSSCs) have been extensively studied as a novel sunlight-to-electricity conversion system [1–5]. The working principle of the dye-sensitized solar cell is the following. Upon photoexcitation, the dye molecules inject an electron into the conduction band of TiO_2, leaving the dye in its oxidized state (D+, also referred to as dye cation). The dye is restored to its ground state by electron transfer from the redox pair. The regeneration of the sensitizer by iodide intercepts the recombination of the conduction band electron with the oxidized dye. The I_3^- ions formed by oxidation of I^- diffuse to the cathode where the regenerative cycle is completed by electron transfer to reduce I_3^- to I^-. DSSCs consist of a dye-sensitized TiO_2 electrode, a Pt-sputtered counter electrode, and a redox couple. In these cells, the sensitizer is one of the key components for high-power conversion efficiencies. Polypyridyl ruthenium sensitizers such as *cis*-dithiocyanato-bis(4,4′-dicarboxy-2,2′-bipyridine)ruthenium (II) (**N719**) have shown to be excellent dyes in DSSCs, and their photoconversion efficiency is more than 10% under air mass 1.5 sunlight [6]. The main drawback of this sensitizer is the lack of absorption in the red region of the visible spectrum. An important goal on ruthenium dyes has been the development of new ruthenium dyes having a wide and red-shifted MLCT band [7–9]. Numerous attempts have been made to molecularly engineer ruthenium sensitizers to broaden the absorption band and increase the molar absorption coefficient. One of the successful approaches is to replace one of the 4,4′-dicarboxylic acid-2,2′-bipyridine (dcbpy) anchoring ligands in **N3** with a highly conjugated ancillary ligand. Several groups have successfully developed efficient ruthenium sensitizers by introducing extended conjugation units on the bipyridyl ligand such as thiophene [10–14] and alkoxybenzene [15–17] derivatives. Another approach is to synthesize

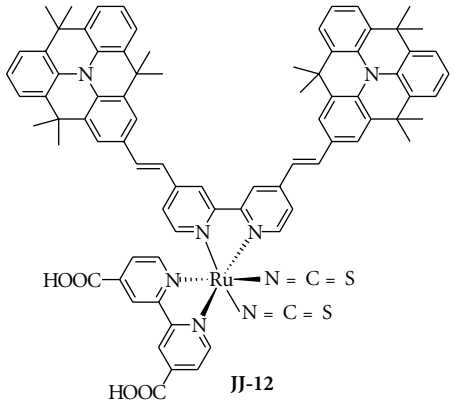

Figure 1: Molecular structure of **JJ-12**.

efficient ruthenium sensitizers through a systematic tuning of the LUMO and HOMO energy levels of the ruthenium polypyridyl complexes by introducing a ligand with a low-lying π^* molecular orbital or by destabilizing the metal t_{2g} orbital with a strong donor ligand [18]. Thus, the systematic designs of efficient ruthenium sensitizers to enhance the absorption coefficient and red shift the MLCT band by increasing the conjugation length of the ancillary ligands such as a styryl-substituted bipyridine and using strong σ-donating power of the amine are well documented strategies. As even small structural modifications of sensitizers result in significant changes in redox energies and the threshold wavelength, the ruthenium sensitizer, **JJ-12**, is molecularly engineered in a way to have a red-shift and high absorption coefficient of MLCT band. Here, we report the synthesis of a novel ruthenium sensitizer containing benzo[1,9]-quinolizino(acridin-2-yl)vinyl-2,2′-bipyridine and its excellent photovoltaic performances in DSSCs (Figure 1).

2. Experimental Section

2.1. NMR Spectra, UV-Vis Spectra, and Emission Spectra Measurement. All of the reactions were carried out under an argon atmosphere. ^{1}H and ^{13}C NMR spectra were recorded on a Varian Mercury 300 spectrometer. UV-vis spectra were recorded in a 1 cm path length quartz cell on a Cary 5 spectrophotometer. Emission spectra were recorded on a Spex Fluorolog 112 using a 90° optical geometry. The emitted light was detected with a Hamamatsu R928 photomultiplier operated in single-photon counting mode.

2.2. Electrochemical Impedance Spectra (EIS) and I-V Curve Spectra Measurement. Electrochemical impedance spectra (EIS) of DSSCs were measured with an impedance analyzer (VersaSTAT 3, AMETEK) connected to a potentiostat under illumination conditions at room temperature. The spectra were scanned in a frequency range from 10^{-1} Hz to 10^5 Hz and AC amplitude 10 mV at room temperature.

Photoelectrochemical data were measured using a 1000 W xenon light source (Oriel, 91193) that was focused to give 1000 W/m^2, the equivalent of one sun at air mass (AM) 1.5, at the surface of the test cell. The light intensity was adjusted with an Si solar cell that was doubled-checked with an NREL-calibrated Si solar cell (PV Measurement Inc.). The applied potential and measured cell current were measured using a Keithley model 2400 digital source meter. The current-voltage characteristics of the cell under these conditions were determined by biasing the cell externally and measuring the generated photocurrent. This process was fully automated using WaveMetrics software.

2.3. Dye-Sensitized Solar Cell Fabrication. Fluorine-doped tin oxide (FTO) glass plates (Pilkington TEC Glass-TEC 8, Solar 2.3 mm thickness) were cleaned in a detergent solution using an ultrasonic bath for 30 min and then rinsed with water and ethanol. Then, the plates were immersed in 40 mM $TiCl_4$ (aqueous) at 70°C for 30 min and washed with water and ethanol. A transparent nanocrystalline layer was prepared on the FTO glass plates by using a doctor blade printing TiO_2 paste (Solaronix, Ti-Nanoxide T/SP), which was then dried for 2 h at 25°C. The TiO_2 electrodes were gradually heated under an air flow at 325°C for 5 min, at 375°C for 5 min, at 450°C for 15 min, and at 500°C for 15 min. The thickness of the transparent layer was measured by using an Alpha-Step 250 surface profilometer (Tencor Instruments, San Jose, CA, USA). A Paste containing 400 nm sized anatase particles (CCIC. PST-400C) was deposited by means of doctor blade printing to obtain the scattering layer, and then dried and heated under same condition which was applied for TiO_2 (Solaronix, Ti-Nanoxide T/SP) paste described above. The resulting film was composed of a 10 μm thick transparent layer and a 4 μm thick scattering layer. The TiO_2 electrodes were treated again with $TiCl_4$ at 70°C for 30 min and sintered at 500°C for 30 min. Then, they were immersed in **JJ-12** (0.3 mM in ethanol) solutions and kept at room temperature for 24 h. FTO plates for the counter electrodes were cleaned in an ultrasonic bath in H_2O, Acetone, and 0.1 M aqueous HCl, subsequently. The counter electrodes were prepared by placing a drop of an H_2PtCl_6 solution (2 mg Pt in 1 mL ethanol) on an FTO plate and heating it (at 400°C) for 15 min. The dye adsorbed TiO_2 electrodes, and the Pt counter electrodes were assembled into a sealed sandwich-type cell by heating at 80°C using a hot-melt ionomer film (Surlyn) as a spacer between the electrodes. A drop of the electrolyte consisting of 0.6 M 1,2-dimethyl-3-propylimidazolium iodide (DMPII), 0.05 M I_2, 0.1 M LiI, and 0.5 M *tert*-butylpyridine in acetonitrile was placed in the drilled hole of the counter electrode and was driven into the cell via vacuum backfilling. Finally, the hole was sealed using additional surlyn and a cover glass (0.1 mm thickness).

2.4. Typical Synthesis Procedures and Analytical Data. **4,4′-bis((E)-2-(4,4,8,8,12,12-hexamethyl-8,12-dihydro-4H-benzo[1,9]quinolizino[3,4,5,6,7-defg]acridin-2-yl)vinyl)-2,2′-bipyridine** (**7**): 4,4,8,8,12,12-hexamethyl-8,12-dihydro-4H-benzo[1,9]quinolizino[3,4,5,6,7-defg]acridine-2-carbaldehyde (130 mg, 0.33 mmol), tetraethyl[2,2′-bipyridine]-4,4′-diylbis(methylene) bis(phosphonate) (80 mg, 0.17 mmol)

and potassium *tert*-butoxide (55 mg, 0.50 mmol) were dissolved in tetrahydrofuran (50 mL), and the mixture was stirred for 0.5 h. After the solvent was removed under reduced pressure, H_2O (50 mL) and methylene chloride (50 mL) were added. The organic layer was separated and dried in $MgSO_4$. The solvent was removed under reduced pressure. The pure product **7** was obtained by column chromatography on silica gel (methylene chloride:hexane = 1 : 1, R_f = 0.3). Yield: 90%. ^{1}H NMR ($CDCl_3$): 8.73 (d, 2H, J = 5.1 Hz), 8.65 (s, 2H), 7.63 (s, 4H), 7.57 (d, 2H, J = 16.2 Hz), 7.44 (m, 12H), 7.18 (m, 4H), 1.71 (s, 24H), 1.67 (s, 12H). ^{13}C NMR ($CDCl_3$): 156.5, 149.5, 146.3, 133.4, 132.8, 131.5, 130.6, 130.2, 130.1, 129.9, 123.9, 123.5, 123.3, 122.4, 120.9, 118.1, 35.6, 33.0. Anal. calcd. for $C_{68}H_{62}N_4$: C, 87.33; H, 6.68. Found: C, 87.30; H, 6.71.

JJ-12 *Complex*. A mixture 4,4′-bis((E)-2-(4,4,8,8,12,12-hexamethyl-8,12-dihydro-4H-benzo[1,9]quinolizino[3,4,5,-6,7-defg]acridin-2-yl)vinyl)-2,2′-bipyridine (130 mg, 0.14 mmol) and a dichloro(*p*-cymene)ruthenium (II) dimer (43 mg, 0.07 mmol) in argon-degassed DMF (15 mL) was stirred at 70°C for 4 h under reduced light. Subsequently, 4,4′-dicarboxylic-2,2′-bipyridine (34 mg, 0.14 mmol) was added into the flask, and the reaction mixture was stirred at 160°C for 4 h. At last, an excess of NH_4NCS (105 mg, 1.40 mmol) was added to the resulting dark solution, and the reaction continued for another 4 h at 140°C. Then the reaction mixture was cooled down to room temperature, and the solvent was removed under vacuum. Water was added to get the precipitate. The precipitate was filtered out, washed with water, and dried under vacuum. The resulting solid was dissolved in methanol containing 2,2 equivalent of tetrabutylammonium hydroxide to confer solubility by deprotonating the carboxylic group and purified on a Sephadex LH-20 column with methanol as eluent. The collected main band was concentrated, and the solution pH was lowered to 5.1 using 0.02 M nitric acid. The precipitate was collected on a sintered glass crucible by suction filtration and dried in air. Yield: 60%. ^{1}H NMR (CD_3OD): 9.35–8.90 (m, 6H), 8.23 (s, 1H), 8.08–7.18 (m, 24H), 6.86 (s, 1H), 1.61 (m, 24H), 1.33 (m, 12H), 0.87 (m, 9H). Anal. calcd. for $C_{82}H_{70}N_8O_4RuS_2$: C, 70.52; H, 5.05. Found: C, 70.63; H, 5.01

3. Results and Discussion

The synthetic route for the preparation of **JJ-12** is depicted in Scheme 1. First, trimethyl 2,2′,2′′-nitrilotribenzoate **3** was prepared by the Ullmann coupling reaction [19] of methyl 2-aminobenzoate **1** and methyl 2-iodobenzoate **2** and compound **6** was synthesized through methylation, cyclization and formylation from compound **3**. 2-Bromo-4,4′-bis((E)-2-(4,4,8,8,12,12-hexamethyl-8,12-dihydro-4H-benzo[1,9]quinolizino[3,4,5,6,7-defg]acridin-2-yl)vinyl)-2,2′-bipyridine **7** was prepared from the reaction of 4,4,8,8,12,12-hexamethyl-8,12-dihydro-4H-benzo[1,9]quinolizino[3,4,5,6,7-defg]acridine-2-carbaldehyde **6** and tetraethyl[2,2′-bipyridine]-4,4′-diylbis(methylene))bis(phosphonate) using the Horner-Emmons-Wadsworth reaction [20].

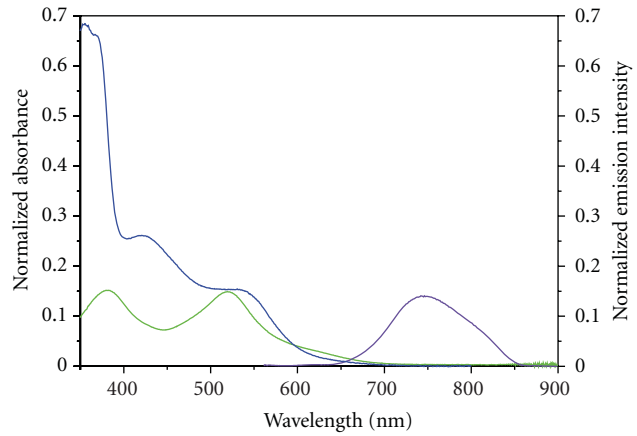

(a)

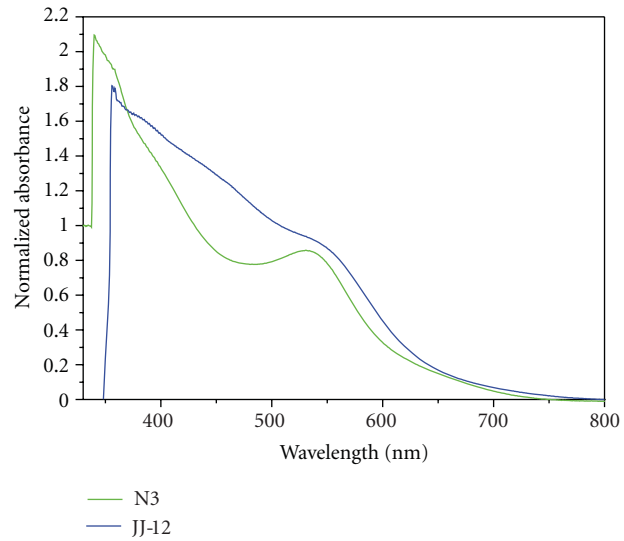

(b)

Figure 2: Absorption and emission spectra (a) of **JJ-12** (blue line) and **N3** (green line) in EtOH, and absorption spectra (b) of **JJ-12** (blue line) and **N3** (green line) adsorbed on TiO_2 film.

The one-pot synthetic procedure developed for heteroleptic polypyridyl ruthenium sensitizers was adapted for the preparation of new **JJ-12** [21, 22]. The analytical and spectroscopic data of novel sensitizer are consistent with the formulated structure.

Figure 2 shows the ultraviolet-visible spectra of **JJ-12**, together with the **N3** absorption spectrum as a reference. The polypyridyl complexes of **JJ-12** show very broad and intense absorption peaks throughout the whole absorption region. The UV-vis spectrum of **JJ-12** displays two absorption bands at 420 and 531 nm in the visible region, which are characteristic of the metal-to-ligand charge transfer (MLCT) bands [23, 24]. The low-energy MLCT band of **JJ-12** at 531 nm is 11 nm red shifted relative to that of **N3**. The red shift of **JJ-12** sensitizer is attributable to the increase of π-conjugation in an ancillary ligand and donor ability of

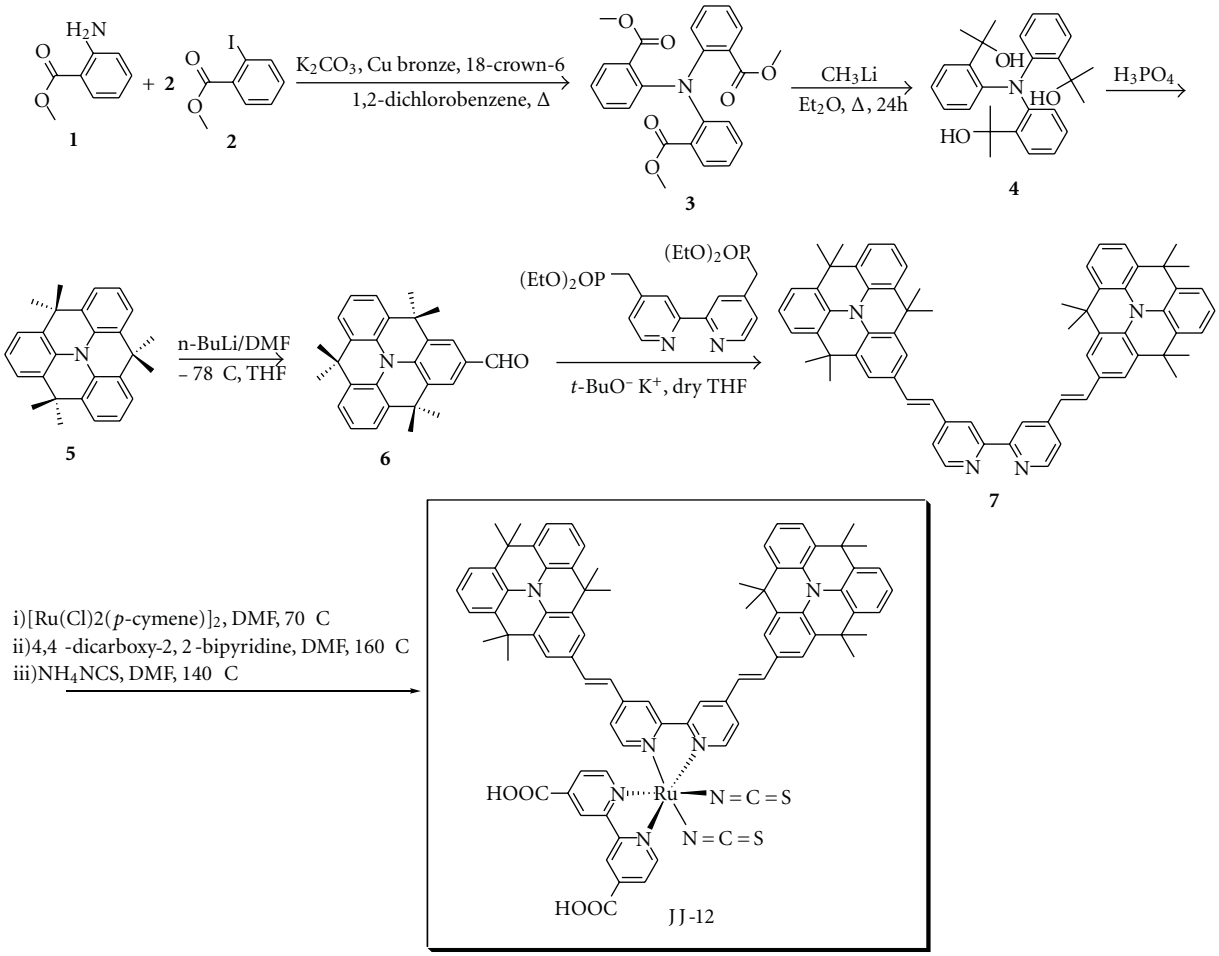

Scheme 1: Schematic diagram for the synthesis of sensitizers **JJ-12**.

benzo[1,9]quinolizinoacridine. The low-energy MLCT band at 531 nm of **JJ-12** exhibits a molar extinction coefficient of $15.4 \times 10^3\,\mathrm{M}^{-1}\,\mathrm{cm}^{-1}$, which is higher than that of the **N3** dye ($14.4 \times 10^3\,\mathrm{M}^{-1}\,\mathrm{cm}^{-1}$). Adsorption of **JJ-12** onto a TiO_2 electrode was observed to broaden the absorption band and to red shift the absorption threshold up to 770 nm, ensuring a good light-harvesting efficiency (Figure 2(b)). Such broadening and red shift have been observed in many ruthenium sensitizers on TiO_2 electrodes [25, 26].

We also observed that the **JJ-12** exhibited strong luminescence maxima at 740–755 nm when they were excited with their MLCT absorption bands at 298 K in an air-equilibrated ethanol solution.

The electrochemical properties of the novel sensitizer **JJ-12** were studied by cyclic voltammetry in CH_3CN with 0.1 M tetrabutylammonium hexafluorophosphate using TiO_2 film with adsorbed dyes as the working electrode. The oxidation potential of **JJ-12** adsorbed on TiO_2 film shows a quasi-reversible couple at 0.92 V versus NHE (Table 1). The value may be compared to 1.12 V versus NHE measured for **N3**. The 0.20 V cathodic shift of the **JJ-12** oxidation potential compared to that of **N3** is attributable to the influence of the electron-rich fused triphenylamine donor ring. The oxidation potential of **JJ-12** sensitizer is energetically favorable for iodide oxidation [27]. The reduction potentials of **JJ-12** dye calculated from the oxidation potentials and the $E_{0\text{-}0}$ determined from the intersection of absorption and emission spectra are −0.96 V for **JJ-12** versus NHE [28]. The value is much more negative than the conduction band level of TiO_2 at approximately −0.5 V versus NHE, ensuring the thermodynamic driving force for charge injection [29, 30].

Figure 3 shows the incident monochromatic photon-to-current conversion efficiency (IPCE) using 0.6 M 1,2-dimethyl-3-propylimidazolium iodide (DMPII), 0.05 M I_2, 0.1 M LiI, and 0.5 M *tert*-butylpyridine in acetonitrile. The cell was fabricated using a double layer of 10 μm thick TiO_2 (20 nm nanoparticles) and 4 μm thick scattering TiO_2 (400 nm nanoparticles). The incident photon-to-current conversion efficiency (IPCE) of **JJ-12** exceeds 70% in a broad spectral range from 440 to 630 nm, reaching a maximum 82% at 520 nm. The band tails off toward 800 nm, contributing to the broad spectral light harvesting that is characteristic of polypyridyl ruthenium dyes [31–33]. For reference, **N3** dye affords a maximum IPCE of 75% at 520 nm under the

Table 1: Optical, oxidation, and DSSC performance parameters of dyes.

Dye	λ_{abs}[a]/nm (ε/M^{-1} cm^{-1})	E_{ox}[b]/V	$E_{0\text{-}0}$[c]/V	E_{LUMO}[d]/V	J_{sc} (mA cm^{-2})	V_{oc} (V)	FF	η[e] (%)
JJ-12	531 (15,430); 420 (24,430)	0.92	1.88	−0.96	16.47	0.71	0.71	8.34
N3	520 (14,400); 380 (14,682)				14.52	0.72	0.69	7.23

[a]Absorption spectra was measured in ethanol solution. [b]Oxidation potential of dyes on TiO_2 were measured in CH_3CN with 0.1 M $(n\text{-}C_4H_9)_4NPF_6$ with a scan rate of 50 mVs^{-1} (*versus* NHE). [c]$E_{0\text{-}0}$ was determined from intersection of absorption and emission spectra in ethanol. [d]E_{LUMO} was calculated by E_{ox}-$E_{0\text{-}0}$. [e]Performances of DSSCs were measured with 0.18 cm^2 working area. Electrolyte: 0.6 M DMPII, 0.05 M I_2, 0.1 M LiI, and *tert*-butylpyridine in acetonitrile.

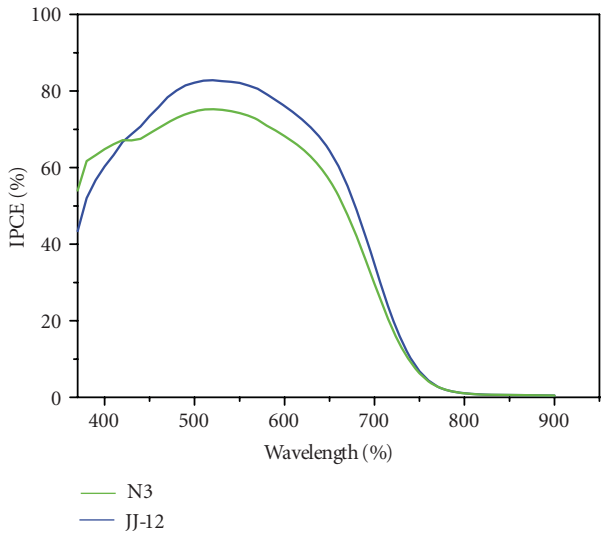

Figure 3: IPCE of **JJ-12** (blue line) and **N3** (green line).

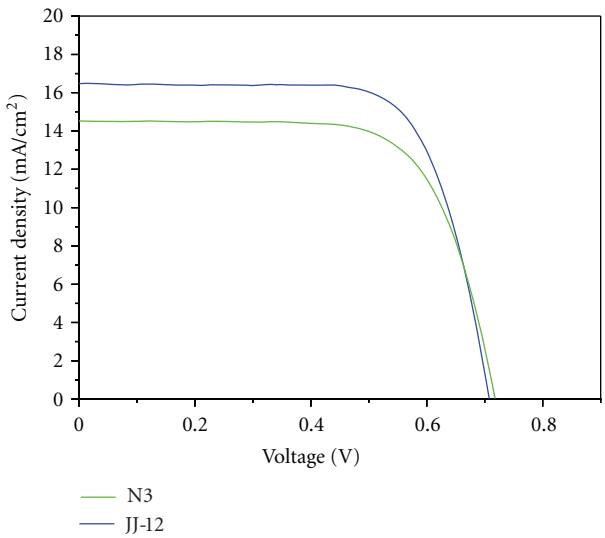

Figure 4: J- V curve of **JJ-12** (blue line) and **N3** (green line).

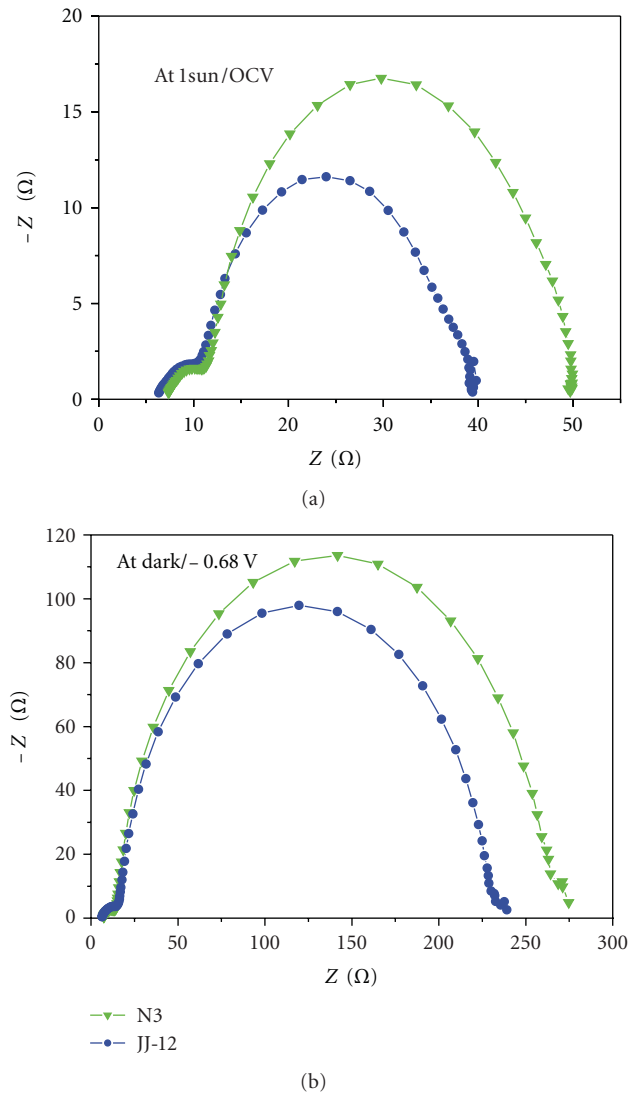

Figure 5: Electrochemical impedance spectra measured under the illumination (1 sun) and in the dark for the cells with different dye adsorption conditions (i.e., **JJ-12** (blue), **N3** (green)).

same condition. The **JJ-12** sensitizer's IPCE spectrum is more enhanced in 420–740 nm range compared to that of **N3** as a result of extended π-conjugation of fused triphenylamine ring, which is consistent with the absorption spectrum of **JJ-12**.

The J- V curve for the devices based on **JJ-12** is shown and compared with that of **N3** in Figure 4. Under standard global AM1.5 solar condition, the **JJ-12** sensitized cell gave a short-circuit photocurrent density (J_{sc}) of 16.47 mAcm^{-2}, an open-circuit voltage (V_{oc}) of 0.71 V, and a fill factor of 0.71, corresponding to an overall conversion efficiencies η of 8.34%. The photovoltaic performance of the **JJ-12** and **N3** sensitized cells is presented in Table 1. Under the same condition, the **N3** sensitized cell gave a J_{sc} of 14.52 mAcm^{-2},

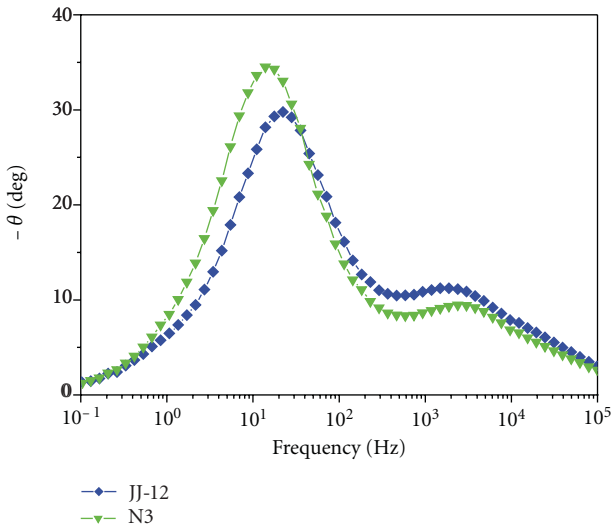

Figure 6: Electrochemical impedance spectra of **JJ-12** and **N3**-sensitized cells in the form of a bode phase plot(Measured under open-circuit conditions and AM 1.5 simulated sunlight illumination (100 mWcm^{-2}).

V_{oc} of 0.72 V, and a fill factor of 0.69, corresponding to η of 7.23%.

The ac impedances of the cells were measured under the illumination conditions. Figure 5(a) shows the ac impedance spectra measured under open-circuit conditions and under illumination of 100 mWcm^{-2}. The radius of the intermediate-frequency semicircle in the Nyquist plot decreased in the order of **N3** (34.55 Ω) > **JJ-12** (22.50 Ω), indicating the improved electron generation and transport. This result is in good agreement with that of short-circuit photocurrent trend shown in Table 1. Figure 5(b) shows the ac impedance spectrum measured under dark condition. In the dark under forward bias (−0.68 V), the semicircle in intermediate frequency regime demonstrates the dark reaction impedance caused by the electron transport from the conduction band of TiO_2 to I_3^- ions in electrolyte. The increased radius of the semicircle in intermediate frequency regime implies a reduced electron recombination rate at the dyed TiO_2/electrolyte interface. In dark, the radius of the intermediate-frequency semicircle showed the increasing order of **JJ-12** (214.70 Ω) < **N3** (243.90 Ω), in accord with the trends of the V_{oc} value in Table 1.

The electron lifetime can be estimated from the following relationship. $\tau_c = 1/\omega_{max} = 1/2\pi f_{max}$; f_{max} is the maximum frequency of the intermediate frequencies peak [34]. The results are displayed in the form of a bode-phase plot, as shown in Figure 6. The f_{max} values of **JJ-12** and **N3** are 22.63 Hz and 13.81 Hz, respectively. The τ_c values show a significant gap among the dyes, resulting in the increasing order of **N3** > **JJ-12**. The different τ_c values might be caused by the different molecular structure of the dyes. The low value of τ_c in **JJ-12** compared to those of **N3** may be due to the defects of the **JJ-12** monolayer on the TiO_2 electrodes. The results of the electron lifetime are well consistent with those of the V_{oc} in Table 1.

4. Conclusions

In conclusion, a novel ruthenium bipyridyl sensitizer incorporating highly conjugated benzo[1,9]quinolizino(acridin-2-yl)vinyl units has been synthesized and characterized. A solar-cell device based on the sensitizer **JJ-12** in conjunction with a volatile electrolyte yielded an overall conversion efficiency of 8.34%. The efficient performance of **JJ-12** is attributed to its high absorption extinction coefficient of MLCT band and extended absorption in the visible region. We believe that the development of highly efficient ruthenium sensitizers is possible through meticulous molecular engineering.

Acknowledgment

This work was supported by the Electronics and Telecommunications Research Institute (ETRI).

References

[1] B. O'Regan and M. Grätzel, "A low-cost, high-efficiency solar cell based on dye-sensitized colloidal TiO_2 films," *Nature*, vol. 353, no. 6346, pp. 737–740, 1991.

[2] K. Hara, H. Sugihara, Y. Tachibana et al., "Dye-sensitized nanocrystalline TiO_2 solar cells based on ruthenium(II) phenanthroline complex photosensitizers," *Langmuir*, vol. 17, no. 19, pp. 5992–5999, 2001.

[3] T. Horiuchi, H. Miura, K. Sumioka, and S. Uchida, "High efficiency of dye-sensitized solar cells based on metal-free indoline dyes," *Journal of the American Chemical Society*, vol. 126, no. 39, pp. 12218–12219, 2004.

[4] S. A. Haque, S. Handa, K. Peter, E. Palomares, M. Thelakkat, and J. R. Durrant, "Supermolecular control of charge transfer in dye-sensitized nanocrystalline TiO_2 films: towards a quantitative structure-function relationship," *Angewandte Chemie—International Edition*, vol. 44, no. 35, pp. 5740–5744, 2005.

[5] D. Kuang, P. Walter, F. Nüesch et al., "Co-sensitization of organic dyes for efficient ionic liquid electrolyte-based dye-sensitized solar cells," *Langmuir*, vol. 23, no. 22, pp. 10906–10909, 2007.

[6] M. K. Nazeeruddin, F. D. Angelis, S. Fantacci et al., "Combined experimental and DFT-TDDFT computational study of photoelectrochemical cell ruthenium sensitizers," *Journal of the American Chemical Society*, vol. 127, no. 48, pp. 16835–16847, 2005.

[7] T. Renouard, R. A. Fallahpour, M. K. Nazeeruddin et al., "Novel ruthenium sensitizers containing functionalized hybrid tetradentate ligands: synthesis, characterization, and INDO/S analysis," *Inorganic Chemistry*, vol. 41, no. 2, pp. 367–378, 2002.

[8] M. K. Nazeeruddin, P. Péchy, T. Renouard et al., "Engineering of efficient panchromatic sensitizers for nanocrystalline TiO_2-based solar cells," *Journal of the American Chemical Society*, vol. 123, no. 8, pp. 1613–1624, 2001.

[9] K. Chen, Y. H. Hong, Y. Chi, W. H. Liu, B. S. Chen, and P. T. Chou, "Strategic design and synthesis of novel tridentate bipyridine pyrazolate coupled Ru(ii) complexes to achieve superior solar conversion efficiency," *Journal of Materials Chemistry*, vol. 19, no. 30, pp. 5329–5335, 2009.

[10] K. J. Jiang, N. Masaki, J. B. Xia, S. Noda, and S. Yanagida, "A novel ruthenium sensitizer with a hydrophobic 2-thiophen-2-yl-vinyl- conjugated bipyridyl ligand for effective dye sensitized TiO_2 solar cells," *Chemical Communications*, no. 23, pp. 2460–2462, 2006.

[11] C. Y. Chen, S. J. Wu, C. G. Wu, J. G. Chen, and K. C. Ho, "A ruthenium complex with superhigh light-harvesting capacity for dye-sensitized solar cells," *Angewandte Chemie—International Edition*, vol. 45, no. 35, pp. 5822–5825, 2006.

[12] C. Y. Chen, S. J. Wu, J. Y. Li, C. G. Wu, J. G. Chen, and K. C. Ho, "A new route to enhance the light-harvesting capability of ruthenium complexes for dye-sensitized solar cells," *Advanced Materials*, vol. 19, no. 22, pp. 3888–3891, 2007.

[13] Y. Cao, Y. Bai, Q. Yu et al., "Dye-sensitized solar cells with a high absorptivity ruthenium sensitizer featuring a 2-(hexylthio)thiophene conjugated bipyridine," *Journal of Physical Chemistry C*, vol. 113, no. 15, pp. 6290–6297, 2009.

[14] F. Gao, Y. Wang, D. Shi et al., "Enhance the optical absorptivity of nanocrystalline TiO_2 film with high molar extinction coefficient ruthenium sensitizers for high performance dye-sensitized solar cells," *Journal of the American Chemical Society*, vol. 130, no. 32, pp. 10720–10728, 2008.

[15] P. Wang, C. Klein, R. Humphry-Baker, S. M. Zakeeruddin, and M. Grätzel, "A high molar extinction coefficient sensitizer for stable dye-sensitized solar cells," *Journal of the American Chemical Society*, vol. 127, no. 3, pp. 808–809, 2005.

[16] D. Kuang, C. Klein, S. Ito et al., "High-Efficiency and stable mesoscopic dye-sensitized solar cells based on a high molar extinction coefficient ruthenium sensitizer and nonvolatile electrolyte," *Advanced Materials*, vol. 19, no. 8, pp. 1133–1137, 2007.

[17] P. Wang, S. M. Zakeeruddin, J. E. Moser et al., "Stable new sensitizer with improved light harvesting for nanocrystalline dye-sensitized solar cells," *Advanced Materials*, vol. 16, no. 20, pp. 1806–1811, 2004.

[18] P. A. Anderson, G. F. Strouse, J. A. Treadway, F. R. Keene, and T. J. Meyer, "Black MLCT absorbers," *Inorganic Chemistry*, vol. 33, no. 18, pp. 3863–3864, 1994.

[19] R. J. Bushby, D. R. McGill, K. M. Ng, and N. Taylor, "p-Doped high spin polymers," *Journal of Materials Chemistry*, vol. 7, no. 12, pp. 2343–2354, 1997.

[20] C. Zhang, A. W. Harper, and L. R. Dalton, "Formylation of diethyl 2-thienylmethylphosphonate for one-pot synthesis of aminothienostilbene-carboxaldehyde," *Synthetic Communications*, vol. 31, no. 9, pp. 1361–1365, 2001.

[21] C. Lee, J. H. Yum, H. Choi et al., "Phenomenally high molar extinction coefficient sensitizer with "donor-acceptor" ligands for dye-sensitized solar cell applications," *Inorganic Chemistry*, vol. 47, no. 7, pp. 2267–2273, 2008.

[22] S. R. Jang, C. Lee, H. Choi et al., "Oligophenylenevinylene-functionalized Ru(II)-bipyridine sensitizers for efficient dye-sensitized nanocrystalline TiO_2 solar cells," *Chemistry of Materials*, vol. 18, no. 23, pp. 5604–5608, 2006.

[23] T. Bessho, E. Yoneda, J. H. Yum et al., "New paradigm in molecular engineering of sensitizers for solar cell applications," *Journal of the American Chemical Society*, vol. 131, no. 16, pp. 5930–5934, 2009.

[24] F. Matar, T. H. Ghaddar, K. Walley, T. DosSantos, J. R. Durrant, and B. O'Regan, "A new ruthenium polypyridyl dye, TG6, whose performance in dye-sensitized solar cells is surprisingly close to that of N719, the 'dye to beat' for 17 years," *Journal of Materials Chemistry*, vol. 18, no. 36, pp. 4246–4253, 2008.

[25] K. S. Chen, W. H. Liu, Y. H. Wang et al., "New family of ruthenium-dye-sensitized nanocrystalline TiO_2 solar cells with a high solar-energy-conversion efficiency," *Advanced Functional Materials*, vol. 17, no. 15, pp. 2964–2974, 2007.

[26] F. Gao, Y. Wang, J. Zhang et al., "A new heteroleptic ruthenium sensitizer enhances the absorptivity of mesoporous titania film for a high efficiency dye-sensitized solar cell," *Chemical Communications*, no. 23, pp. 2635–2637, 2008.

[27] M. K. Nazeeruddin, A. Kay, I. Rodicio et al., "Conversion of light to electricity by cis-X2bis(2,2′-bipyridyl-4,4′-dicarboxylate)ruthenium(II) charge-transfer sensitizers ($X = Cl^-$, Br^-, I^-, CN^-, and SCN^-) on nanocrystalline TiO_2 electrodes," *Journal of the American Chemical Society*, vol. 115, no. 14, pp. 6382–6390, 1993.

[28] X. Li, K. Hou, X. Duan, F. Li, and C. Huang, "Ruthenium(II) complex based on 4,4′-di(*p*-methylphenyl)-2,2′- bipyridine: synthesis and photoelectrochemical properties," *Inorganic Chemistry Communications*, vol. 9, no. 4, pp. 394–396, 2006.

[29] A. M. Bond, G. B. Deacon, J. Howitt, D. R. MacFarlane, L. Spiccia, and G. Wolfbauer, "Voltammetric determination of the reversible redox potential for the oxidation of the highly surface active polypyridyl ruthenium photovoltaic sensitizer cis-$Ru(II)(dcbpy)_2(NCS)_2$," *Journal of the Electrochemical Society*, vol. 146, no. 2, pp. 648–656, 1999.

[30] P. Wang, S. M. Zakeeruddin, J. E. Moser, and M. Grätzel, "A new ionic liquid electrolyte enhances the conversion efficiency of dye-sensitized solar cells," *Journal of Physical Chemistry B*, vol. 107, no. 48, pp. 13280–13285, 2003.

[31] C. Y. Chen, J. G. Chen, S. J. Wu, J. Y. Li, C. G. Wu, and K. C. Ho, "Multifunctionalized ruthenium-based supersensitizers for highly efficient dye-sensitized solar cells," *Angewandte Chemie—International Edition*, vol. 47, no. 38, pp. 7342–7345, 2008.

[32] A. Islam, F. A. Chowdhury, Y. Chiba et al., "Synthesis and characterization of new efficient tricarboxyterpyridyl (β-diketonato) ruthenium(II) sensitizers and their applications in dye-sensitized solar cells," *Chemistry of Materials*, vol. 18, no. 22, pp. 5178–5185, 2006.

[33] D. Kuang, C. Klein, S. Ito et al., "High molar extinction coefficient ion-coordinating ruthenium sensitizer for efficient and stable mesoscopic dye-sensitized solar cells," *Advanced Functional Materials*, vol. 17, no. 1, pp. 154–160, 2007.

[34] R. Kern, R. Sastrawan, J. Ferber, R. Stangl, and J. Luther, "Modeling and interpretation of electrical impedance spectra of dye solar cells operated under open-circuit conditions," *Electrochimica Acta*, vol. 47, no. 26, pp. 4213–4225, 2002.

Hindawi Publishing Corporation
International Journal of Photoenergy
Volume 2012, Article ID 768368, 6 pages
doi:10.1155/2012/768368

Review Article

Thin Film Photovoltaics: Markets and Industry

Arnulf Jäger-Waldau

Renewable Energy Unit, Joint Research Centre, European Commission, Via E. Fermi 2749, 21027 Ispra (VA), Italy

Correspondence should be addressed to Arnulf Jäger-Waldau, arnulf.jaeger-waldau@ec.europa.eu

Received 5 December 2011; Accepted 21 December 2011

Academic Editor: Bhushan Sopori

Since 2000, total PV production increased almost by two orders of magnitude, with a compound annual growth rate of over 52%. The most rapid growth in annual cell and module production over the last five years could be observed in Asia, where China and Taiwan together now account for about 60% of worldwide production. Between 2005 and 2009, thin film production capacity and volume increased more than the overall industry but did not keep up in 2010 and 2011 due to the rapid price decline for solar modules. Prices for photovoltaic electricity generation systems have more than halved over the last five years making the technology affordable to an ever-increasing number of customers worldwide. With worldwide over 60 GW cumulative installed photovoltaic electricity generation capacity installed in November 2011, photovoltaics still is a small contributor to the electricity supply, and another 10 to 15 years of sustained and aggressive growth will be required for photovoltaic solar electricity to become one of the main providers of electricity. To achieve this, a continuous improvement of the current solar cell technologies will be necessary.

1. Introduction

Photovoltaics has enjoyed extraordinary growth during the last decade with overall growth rates above 50% per annum, indicating that further increase of production facilities is an attractive investment. The last World Energy Outlook released by the International Energy Agency (IEA) in November 2011 indicates that more and more renewable energy and in particular solar energy will be needed and used in the coming decades to ensure a stable and secure energy supply as well as limit the effects of energy-induced climate change [1].

On the one hand the IEA stressed an urgent need to accelerate actions to tackle climate changes as 80% of the total energy-related CO_2 emissions allowed under the 450 ppm scenario for 2035 are already "locked in" by the existing capital stock (power plants, buildings, factories, etc.), but on the other, the IEA only forecasts an increase of non-hydrorenewables in power generation from 3% in 2009 to 15% in 2035, which is far below the renewable energy potential.

Due to the current financial and economic constraints, the introduction of renewable energy sources and photovoltaic electricity generation systems is often depicted as a too expensive energy option. This is a short-sighted view as it does not take into account that all those renewable energy generation technologies that do not require fuels, for example, solar, wind, and so forth, reduce the price volatility risk and enhance the predictability of power generation cost.

There are several studies that examine the difficult issue of quantifying the effect of the inclusion of RES in an energy portfolio and the reduction in the portfolio energy price. This is in addition to the employment benefits and the economic benefits of avoided fuel costs and external costs (GHG), money which could be spent within the economy and used for local wealth creation [7].

Production data for the global cell production in 2010 is about 24 GW (Figure 1), which is about the double compared to 2009. (Solar cell production capacities mean (i) in the case of wafer silicon-based solar cells only the cells; (ii) in the case of thin films, the complete integrated module; (iii) only those companies that actually produce the active circuit (solar cell) are counted; (iv) companies that purchase these circuits and make cells are not counted.) For 2011 a further increase to about 30 GW is expected. The significant uncertainty in the data for 2011 is due to the very competitive market environment, as well as the fact that some companies

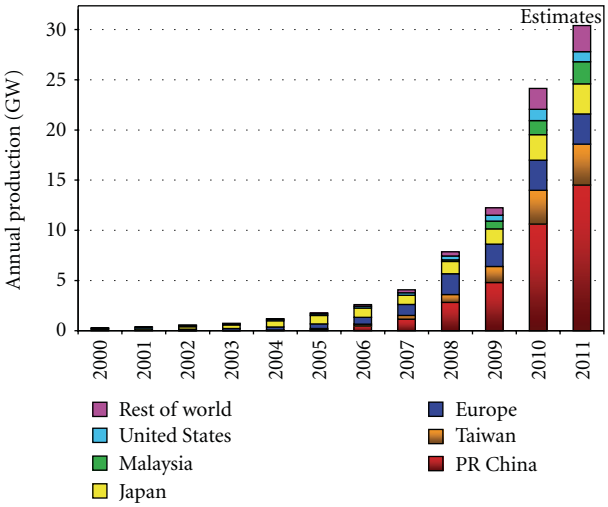

Figure 1: Worldwide PV production from 2000 to 2011. (data source: PV News [2], Photon International [3], and own analysis).

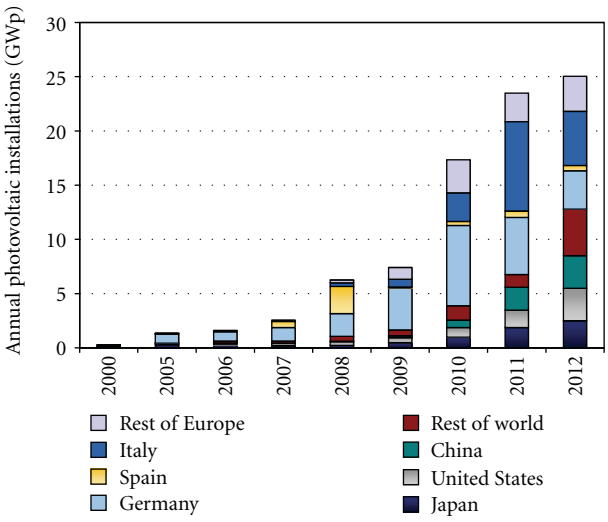

Figure 2: Annual photovoltaic installations from 2000 to 2012. 2011 and 2012 are still estimates. (data source: Bank Sarasin [4], EPIA [5], EurObserv'ER [6], and own analysis).

report shipment figures, others report sales, and again others report production figures. The continuation of the difficult economic situation worldwide as well as a fierce competition and a production capacity that is more than twice the actual market led to a decreased willingness to report confidential company data. The previous tight silicon supply situation reversed due to massive production expansions as well as the economic situation. This led to a price decrease on the spot market from the 2008 peak of around 500 \$/kg to below 30 \$/kg at the end of 2011.

More than 80% of the current production uses wafer-based crystalline silicon technology. A major advantage of this technology is that complete production lines can be bought, installed, and up and producing within a relatively short time frame. This predictable production start-up scenario constitutes a low-risk placement with calculable return on investments. However, the temporary shortage in silicon feedstock and the market entry of companies offering turn-key production lines for thin film solar cells led to a massive expansion of investments into thin film capacities between 2005 and 2010.

Since 2000, total PV production increased by two orders of magnitude, with a compound annual growth rate (CAGR) of 53%. The most rapid growth in annual production over the last five years could be observed in Asia, where China and Taiwan together now account for more than 60% of world-wide production.

The change of the market from a supply-restricted to a demand-driven market and the resulting overcapacity for solar modules have resulted in a dramatic price reduction of PV systems of more than 50% over the last four years. Average prices for grid-connected PV systems were reported with 2,540 \$/kWp (1,880 €/kWp) for residential and 2,350 \$/kWp (1,740 €/kWp) for commercial systems at the beginning of December 2011 [8].

2. Markets

Market predictions for the 2011 PV market vary between 21.9 GW and 24 GW with a consensus value in the 23 GW range (Figure 2). For 2012 analyst expectations vary between 20.5 GW and 27 GW. Despite these moderate growth forecasts, massive capacity increases are still ongoing or announced, and if all of them are realised, the world-wide production capacity for solar cells will exceed 65 GW at the end of 2011 and 85 GW at the end of 2012. This indicates that even with the optimistic market growth expectations, the planned capacity increases are way above the market growth. The consequences are either low utilisation rates or the build-up of high inventories resulting in a continued price pressure in an oversupplied market. Such a development will accelerate the consolidation of the photovoltaics industry and spur more mergers and acquisitions.

With a cumulative installed capacity of over 46 GW, the European Union is leading in PV installations with a little more than 70% of the total worldwide 63 GW of solar photovoltaic electricity generation capacity at the end of 2011 (Figure 3).

In 2012, the European market share of new installations is expected to drop from about 70% to 50% due to the rapid growing markets in Asia and North America. This development reflects the fact that the rapid cost reduction during the last few years is opening more and more markets worldwide, easing the dependency of the PV industry from a few very strong markets.

Asia and Pacific Region. The Asia and Pacific region shows an increasing trend in photovoltaic electricity system installations. There are a number of reasons for this development, ranging from declining system prices, heightened awareness, favourable policies, and the sustained use of solar power for rural electrification projects. Countries such as Australia, China, India, Indonesia, Japan, Malaysia, Repuplic of Korea, Taiwan, Thailand, The Philippines and Vietnam show a very positive upward trend, thanks to increasing governmental

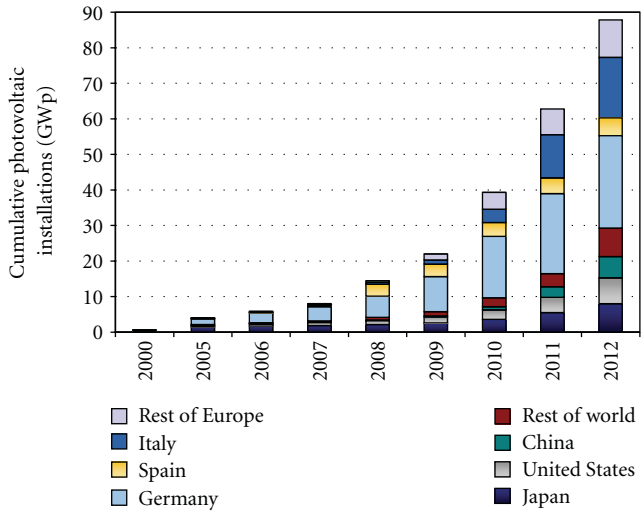

Figure 3: Cumulative photovoltaic installations from 2000 to 2012. 2011 and 2012 are still estimates. (data source: Bank Sarasin [4], EPIA [5], EurObserv'ER [6] and own analysis).

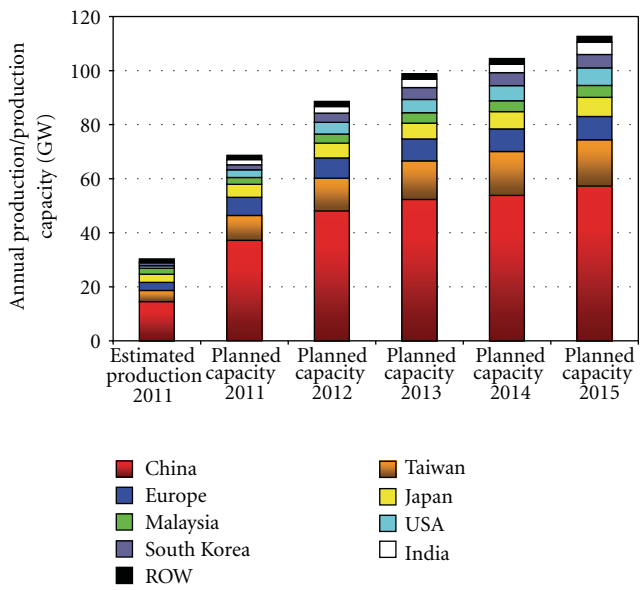

Figure 4: Actual and planned PV production capacities.

commitment towards the promotion of solar energy and the creation of sustainable cities.

The introduction or expansion of feed-in tariffs is expected to be an additional big stimulant for on-grid solar PV system installations for both distributed and centralised solar power plants in countries such as Australia, Japan, Malaysia, Thailand, Taiwan, and Republic of Korea.

In 2010 about 2.5 GW of new PV electricity generation systems was installed in the region. The largest market was Japan with 990 MW followed by China with 560 MW and Australia with 380 MW. For 2011 a market increase to about 5 GW is expected, driven by the major market growth in China (2 GW), India, Japan, Malaysia, and Thailand. Market expectations for the region range between 7 and 8 GW in 2012.

The Asian Development Bank (ADB) launched an Asian Solar Energy Initiative (ASEI) in 2010, which should lead to the installation of 3 GW of solar power by 2012 [9]. In their report, ADB states: "*Overall, ASEI aims to create a virtuous cycle of solar energy investments in the region, toward achieving grid parity, so that ADB developing member countries optimally benefit from this clean, inexhaustible energy resource.*"

European Union. Market conditions for photovoltaics differ substantially from country to country. This is due to different energy policies and public support programmes for renewable energies and especially photovoltaics, as well as the varying grades of liberalisation of domestic electricity markets. After a tenfold increase of solar photovoltaic electricity generation capacity between 2001 and 2008, the newly installed capacity more than quadrupled in the last three years to exceed 46 GW cumulative installed capacity at the end of 2011 [10, 11]. For 2012 market expectations vary between 11 and 13 GW of new installations.

The legal framework for the overall increase of renewable energy sources was set with the Directive 2009/28/EC, and in their National Renewable Energy Action Plans (NREAPs), 26 Member States have set specific photovoltaic solar energy targets, adding up to 84.5 GW in 2020. However, since the submission of the NREAPs in 2010 a number of positive signs have emerged for PV. In Italy, the 4th *Conto Energia* was enacted in the first half of 2011 and it limits the support for PV installations until 2017 or 23 GW whatever is reached earlier. In August 2011 Greece announced the "*Helios*" project, which aims to install up to 10 GW of PV electricity systems on public land by 2020. These developments indicate that the targets set in the NREAPs should be seen as the guaranteed minimum and not the overall goal.

In 2011 Italy overtook Germany as the biggest market with an expected new connected capacity of 8.2 GW versus 5.2 GW, respectively. The market growth in these two countries is directly correlated to the introduction of the Renewable Energy Sources Act or "*Erneuerbare Energien Gesetz*" (EEG) in Germany in 2000 and the "*Conto Energia*" in Italy in 2005.

North America. In 2010, Canada more than tripled its cumulative installed PV capacity to about 420 MW, with 300 MW new installed systems. For 2011 a further increase of the market from 350 to 400 MW is estimated. This development is driven by the introduction of a feed-in tariff in the province of Ontario in 2009.

With close to 900 MW of new installed PV capacity, the USA reached a cumulative PV capacity of 2.5 GW at the end of 2010. Utility PV installations more than tripled compared to 2009 and reached 242 MW in 2010. The top ten states—California, New Jersey, Nevada, Arizona, Colorado, Pennsylvania, New Mexico, Florida, North Carolina, and Texas accounted for 85% of the US grid-connected PV market [12]. For 2011 an increase of the US market to 1.6 GW is estimated.

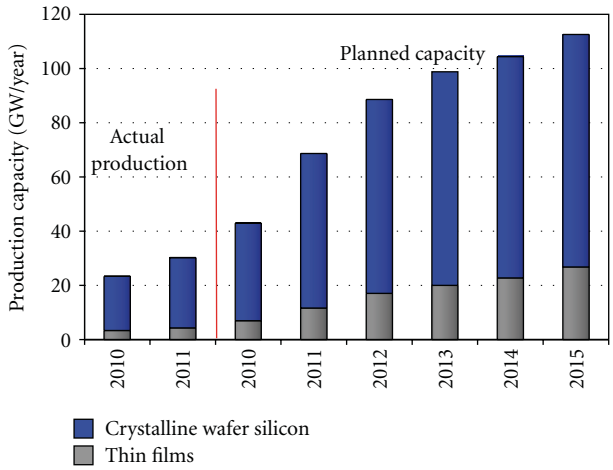

Figure 5: Actual and planned PV production capacities of thin film and crystalline silicon-based solar modules.

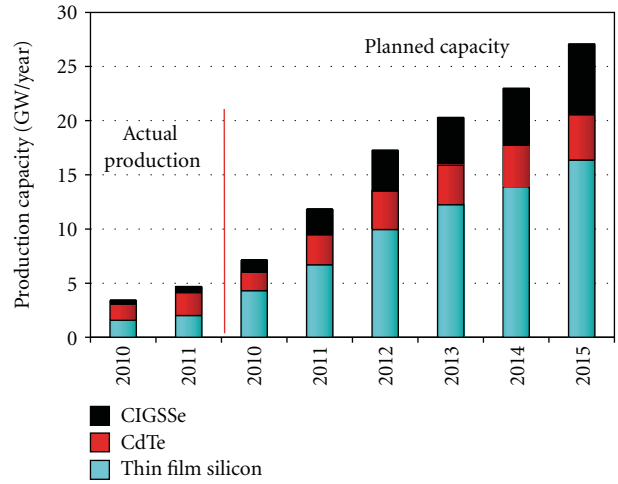

Figure 6: Actual production and planned capacities of the different thin film technologies.

PV projects with Power Purchase Agreements (PPAs), with a total capacity of 6.1 GW, are already under contract and to be completed by 2014 [13]. If one adds that 10.5 GW of projects, which are already publicly announced, but PPAs have yet to be signed, this makes the total "pipeline" more than 16.6 GW.

Many state and federal policies and programmes exist and one of the most comprehensive databases about the different support schemes in the USA is maintained by the Solar Centre of the State University of North Carolina. The Database of State Incentives for Renewable Energy (DSIRE) is a comprehensive source of information on state, local, utility, and selected federal incentives that promote renewable energy. All the different support schemes are described therein and it is highly recommended to visit the DSIRE website (http://www.dsireusa.org/) and the corresponding interactive tables and maps for details.

The 2012 market expectations for Canada and the USA together vary between 3.5 and 5 GW.

3. Thin Film Photovoltaic Industry

Thin film photovoltaics was always an integral part of the industry. Back in 1994 about 80 companies with a total production capacity of 130 MW existed worldwide and their activities ranged from research to production of solar cells. About half of them were actually manufacturing and other 29 companies were involved in module production only. Out of the solar cell companies, 41 companies used crystalline silicon (72 MW capacity), 2 ribbon silicon (1 MW capacity), 19 amorphous silicon (46 MW capacity), 3 CdTe (11 MW capacity), 5 CIS (research only), and 10 companies other concepts like III–V concentrator cells or spherical cells.

Since then the world wide production capacity of solar cells has increased about 500 times exceeding 68 GW in 2011 with thin films accounting for 11.5 GW or 17%.

The reported future production capacities are based on a survey of more than 300 companies worldwide with a cut-off date at the beginning of December 2011. Despite the fact that a significant number of players delayed or cancelled their expansion plans and some companies had to seize operations due to bankruptcy, the number of new entrants into the field, notably large semiconductor or energy related companies overcompensated this. The announced production capacities increased again in 2011. It is important to note that production capacities are often announced, taking into account different operation models such as number of shifts and operating hours per year. In addition the announcements of the increase in production capacity do not always specify when the capacity will be fully ramped up and operational. This method has of course the setback that (a) not all companies announce their capacity increases in advance and (b) that in times of financial tightening, the announcements of the scale back of expansion plans are often delayed in order not to upset financial markets. Therefore, the capacity figures just give a trend but do not represent final numbers.

If all these ambitious plans can be realised by 2015, China will have about 50.8% of the world-wide production capacity of 112 GW, followed by Taiwan (15.2%), Europe (7.6%), and Japan (6.3%) (Figure 4).

In 2005 production of thin film solar cells reached for the first time more than 100 MW per annum. The first 100 MW thin-film factories became operational in 2007, followed by the first 1 GW factory in 2010. Between 2005 and 2010, the Compound Annual Growth Rate (CAGR) of thin-film solar cell production was above the overall industry, driven by the temporary shortage in silicon feedstock and the market entry of companies offering turnkey production lines for thin-film solar cells. Despite the fact that in production capacity terms, the market share of thin films is still increasing, the pace has slowed down considerably because the vast majority of new production capacity announcements over the last two years were for wafer-based silicon technologies.

In 2011, more than 200 companies were involved in thin-film solar cell activities, ranging from basic R&D activities to major manufacturing activities and over 150 of them

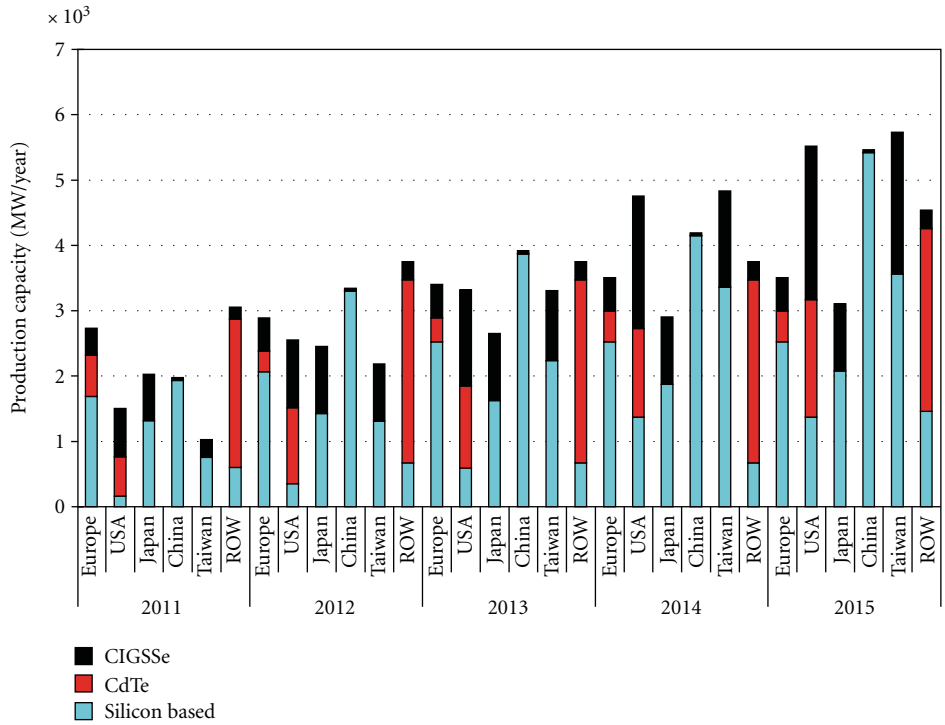

Figure 7: Projected thin film PV production capacities. Regional distribution of the different technologies.

have announced the start or increase of production. If all expansion plans are realised in time, thin-film production capacity could be around 17 GW, or 19% of the total 88 GW, in 2012 and about 27 GW, or 24%, in 2015 of a total of 112 GW (Figure 5).

In August 2007, when the first survey was presented at the 22nd EUPVSEC in Milano, it was found that in 2006 just 21 companies had produced thin film solar modules, which were available in the market with quantities above 1 MW. Since then the number has more than tripled to 65. However, the production quantities are in general still quite small. Out of the over 120 companies, with announced production plans, about 40% produced 10 MW or more and only 5% produced more than 100 MW in 2011.

More than 70 companies are silicon based and use either amorphous silicon or an amorphous/microcrystalline silicon structure (Figure 6). Thirty-six companies announced using $Cu(In,Ga)(Se,S)_2$ as absorber material for their thin-film solar modules, whereas nine companies use CdTe and eight companies go for dye and other materials.

Despite the fact that the majority of companies use thin film silicon structure, the dominating thin film technology in the market in 2011 is CdTe with about 2.1 GW followed by thin film silicon with 2 GW and CIGSSe with 0.6 GW. In terms of projected capacity increases, thin film silicon is leading followed by CIGSSe and CdTe.

The technology as well as the company distribution varies significantly from region to region (Figure 7).

This regional distribution reflects on the one hand the scientific knowledge base concerning the different thin film technologies and also the investment options and availability of human resources. This last issue is a very crucial one for the future development of photovoltaics and thin film photovoltaics in particular. All these new thin film factories will need not only qualified operators and process engineers but also scientists with a profound knowledge of the respective materials in order to improve the guaranteed start-up processes and secure the competitiveness of the companies for the years to come. Compared to the silicon wafer-based PV technology, the different thin film technologies still have a significant number of fundamental material problems to solve in order to unlock the full efficiency and cost saving potential of the different technologies.

The change of the market from a supply-restricted to a demand-driven market and the build-up overcapacity for solar modules have resulted in a dramatic price reduction of more than 50% over the last three years. Sepecifically companies in their start-up and expansion phase, with limited financial resources and restricted access to capital, are struggling in the current market environment. This situation is believed to continue for at least the next few years and put further pressure on the reduction of the average selling prices (ASP). The recent financial crisis added pressure as it resulted in higher government bond yields, and ASPs have to decline even faster than previously expected to allow for higher project internal rate of returns (IRRs). On the other hand, the rapidly declining module and system prices open new markets, which offer the perspectives for further growth of the industry—at least for those companies with the capability to expand and reduce their costs at the same pace.

4. Conclusion

The increase of conventional energy prices has increased the investment attention for renewable energies and in particular photovoltaics significantly. Since 2006 the investments and growth in thin film photovoltaics have surpassed the already high growth rates of the whole photovoltaics industry but have recently slowed due to technology and financial reasons.

Thin film solar cells still offer the possibility of reducing the manufacturing costs considerably; however, considering the increasing maturity of wafer-based production technologies, observed learning curves, and recent cost reductions, newcomers have to enter the game at already very competitive levels. In addition, the entry ticket, that is, factory size for thin film manufacturers into the market, has increased from a 20 MW factory in 2006 to a minimum of 100 MW in 2011 and is still growing with the increasing market volume.

Thin film technologies still need a lot of research over a wide range of issues, ranging from improvement of the understanding of basic material properties to advanced production technologies and the possible market perspectives. To tackle these problems, a long-term vision for photovoltaics and long-term research are needed.

However, there is no "winning technology" and a viable variety of technology options have to be ensured. To focus on any single technology option now could be a road block in the future. Public research funding structures should take into account that different technologies are at different development stages and need different kind of support measures.

In order to realise high production volumes for PV we must now look towards already available high-throughput, high-yield production technologies analysing if and how they can be utilised for PV in the future. This is especially important for thin film solar cell materials, that have only a limited backing by other industries, such as that provided by the microelectronic industry, in the development of production technologies for silicon solar cells. In addition, there are a number of research issues common to all thin film technologies which have to be solved. No single solar cell technology can neither satisfy the world-wide demand nor all the different wishes consumers have for the appearance or performance of PV systems.

Disclaimer

The opinion given in this paper is based on the current information available to the author and does not reflect the opinion of the European Commission.

References

[1] International Energy Agency, *World Energy Outlook 2011*, International Energy Agency, Paris, France, 2011.

[2] PV News, *Greentech Media*, 2011.

[3] *Photon International*, March 2011.

[4] M. Fawer and B. Magyar, *Solarwirtschaft: Hartes Marktumfeld—Kampf um die Spitzenplätze*, Bank Sarasin, 2011.

[5] European Photovoltaic Industry Association, *Global Market Outlook for Photovoltaics Until 2015*, European Photovoltaic Industry Association, 2011.

[6] "Photovoltaic energy barometer, systèmes solaires," *le Journal du Photovoltaique*, no. 5, 2011.

[7] S. Awerbuch, "The true cost of fossil-fired electricity in the EU: a CAPM-based approach," *Power Economics*, January 2003.

[8] PVinsights.com, *Solar PV Grid-Tie System Weekly Prices*, December 2011.

[9] Asian Development Bank, *Asia Solar Energy Initiative: A Primer*, Asian Development Bank, 2011.

[10] German Federal Network Agency (Bundesnetzagentur), EEG Data, November 2011.

[11] Gestore Servici Energetici, Il contatore fotovoltaico, November 2011.

[12] Solar Energy Industry Association (SEIA), *U.S. Solar Market Insight, US Solar Industry Year in Review*, Solar Energy Industry Association (SEIA), 2010.

[13] *The US PV Market in 2011—Whitepaper*, Greentech Media Inc., Enfinity America Corporation, 2011.

Hindawi Publishing Corporation
International Journal of Photoenergy
Volume 2012, Article ID 697653, 6 pages
doi:10.1155/2012/697653

Research Article

Gas Nozzle Effect on the Deposition of Polysilicon by Monosilane Siemens Reactor

Seung Oh Kang, Uk June Lee, Seung Hyun Kim, Ho Jung You, Kun Park, Sung Eun Park, and Jong Hoon Park

Technical R&D Center, Semi-Materials Co., Ltd., Youngcheon, Gyeongbuk 770-803, Republic of Korea

Correspondence should be addressed to Jong Hoon Park, jhpark@semimaterials.com

Received 31 August 2011; Accepted 15 December 2011

Academic Editor: Bhushan Sopori

Deposition of polysilicon (poly-Si) was tried to increase productivity of poly-Si by using two different types of gas nozzle in a monosilane Bell-jar Siemens (MS-Siemens) reactor. In a mass production of poly-Si, deposition rate and energy consumption are very important factors because they are main performance indicators of Siemens reactor and they are directly related with the production cost of poly-Si. Type A and B nozzles were used for investigating gas nozzle effect on the deposition of poly-Si in a MS-Siemens reactor. Nozzle design was analyzed by computation cluid dynamics (CFD). Deposition rate and energy consumption of poly-Si were increased when the type B nozzle was used. The highest deposition rate was 1 mm/h, and the lowest energy consumption was 72 kWh · kg^{-1} in this study.

1. Introduction

Poly-Si is widely used as a raw material in the semiconductor and photovoltaic industry. Generally, most of poly-Si produced by Siemens reactor are chemical vapor deposition (CVD) systems with mixed gas of monosilane (SiH_4, MS) or trichlorosilane ($SiHCl_3$, TCS) and hydrogen (H_2). High purity silicon slim rods are installed in a Siemens reactor, and they are heated by an electric current flowing through them during deposition process. Poly-Si is deposited by thermal decomposition of silanes in a hydrogen environment in a Siemens reactor. Between two types of poly-Si production system, TCS-Siemens reactor is preferred than MS-Siemens reactor because TCS-Siemens is safe and inexpensive process for poly-Si production than MS-Siemens reactor. Therefore, almost 77% of the poly-Si produced worldwide is currently obtained from TCS-Siemens reactor.

As the price of MS gas decreases, poly-Si production by MS-Siemens reactor was realized as an attractive method for commercialization because low decomposition temperature and high decomposition rate of MS gas have an advantage for lowering the unit cost of Poly-Si production.

The reaction in the Siemens reactor at the specific temperature, the gases undergo the following reactions:

$$\begin{aligned} SiH_4\ g &\longrightarrow Si\ (s) + 2H_2\ g \\ SiHCl_3\ g + H_2\ g &\longrightarrow Si\ (s) + 3HCl\ g \end{aligned} \quad (1)$$

The decomposition temperature of MS is 300–500°C [1], and, at this temperature, the kinetic energy of the individual silicon atoms is too low to form crystalline structures [2]. MS-Siemens reactors are typically operated at temperatures in the range 800–900°C [3]. On the other hand, the decomposition temperature of TCS is about 350–400°C [4]. TCS-Siemens reactors are typically operated at higher temperatures than MS-Siemens reactors because amorphous structures might cause chlorine encapsulations [5]. These chlorine encapsulations would cause defects and degrade the quality of the poly-Si. Therefore, typical temperature range for TCS-Siemens reactor is around 1050–1100°C much higher than MS-Siemens reactor [6, 7].

Gas flow control is important to increase the productivity of MS and TCS-Siemens reactor because the poly-Si production is produced by CVD method.

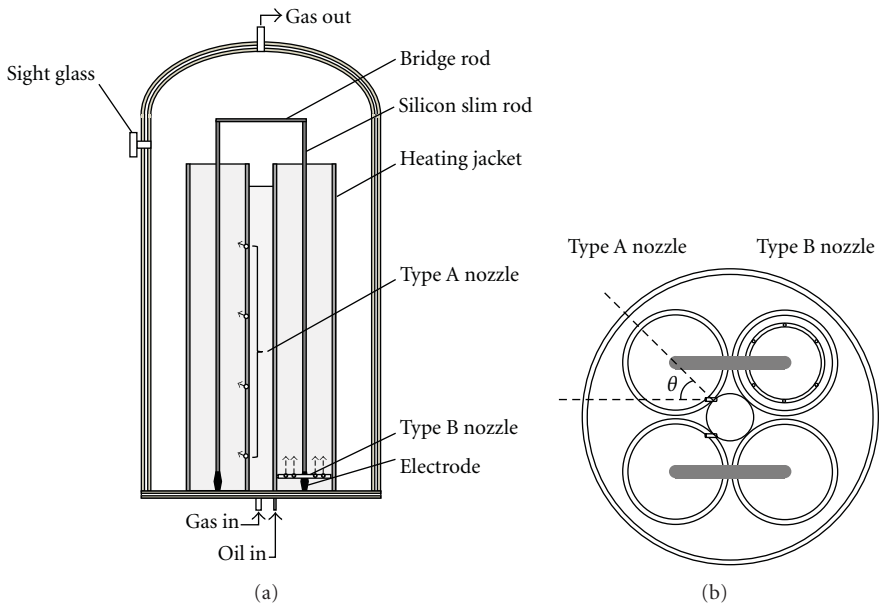

Figure 1: Schematic diagram of MS-Siemens reactor.

In this study, poly-Si was deposited by MS-Siemens reactor and the gas flow control was tried with two different types of nozzle system. The analysis of mass, heat, flow, momentum, concentration of source gas, and so forth in the inner space of reactor were accomplished by computational fluid dynamics (CFD). It is not easy to confirm the phenomena of heat and flow in the reactor because heat and flow in the inner space of reactor could be changed with the structure, shape, position of nozzle, the flow pattern, and temperature distribution of fluid. The analysis of heat and flow is necessary to understand the deposition behavior of poly-Si in a Siemens reactor. Optimum design of nozzle is suggested for high productivity and economic poly-Si production process through the comparison of simulation and experimental results.

2. Experimental

Deposition of poly-Si was performed in a Siemens reactor using SiH_4 + H_2 system. MS-Siemens reactor is consisted of chamber, nozzle, gas supply system, exhaust system, base plate, electrode, heating jacket, and so forth as shown in Figure 1. 4 highly pure silicon slim rods (9N) with thickness of 7 mm and length of 2100 mm were used as a substrate. 2 slim rods were connected by a bridge silicon rod. The reactor was equipped with heating jacket around silicon slim rods for preheating of slim rod before applying an electric current and cooling of system temperature during deposition process.

Two different types of nozzle are used in this study called as type A and B. The type A is composed of 4 orifices, and they were vertically distributed with constant interval. Each nozzle was set at an angle of 45 degree to the slim rod. The type B was a ring type, consisted of 6 orifices, which sprayed diluted gas from bottom to up at the height of 100 mm.

Experiment was performed with the MS concentration of 4%, deposition time of 55 hours, silicon slim rod surface temperature of 850°C, and reactor pressure of 3.5 kgf·cm^{-2}.

To understand the behavior of gas flow in the reactor, the commercial CFD software was used. The credibility of CFD analysis has been acquired and recognized through the researches for the transport phenomena of mass, heat, and momentum in the various geometries that have been performed for a long time. The ANSYS FLUENT 12.1 is used as a simulation program to analyze the transport phenomena of fluid and describe the geometry of reactors. According to the geometry of reactor, turbulent and vortex flow could occur and other turbulent and vortex flow could be formed by the momentum, energy, concentration, and so forth. Therefore, it is difficult to calculate the heat and flow of gas mixture directly.

Thus, lots of variables and turbulent models are required to calculate the turbulent effect in the flow of fluid. The realizable k-epsilon turbulent model is applied to precisely analyze the phenomena about wall boundary layer and the turbulent effects for extensive range. To get the reliable results in the simulation, the modeling of reactor and operating conditions were employed with 3-dimensional geometry. 8,500,000 meshes and Intel Xeon CPU (2.67 GHz/2.66 GH) with 24 GB memory were used for calculation.

3. Results and Discussion

Experimental conditions and results are shown in Table 1. The type of nozzle was only variable parameter in this study, and the other experimental parameters such as initial rod size, rod temperature, reactor pressure, monosilane flow rate, and concentration were fixed. As deposition time increased, 7 mm of silicon rod was changed to 45.2 mm and 62.6 mm

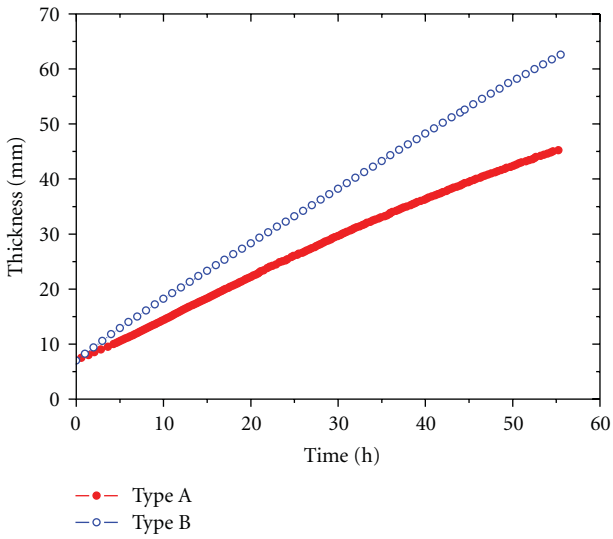

Figure 2: The deposition thickness change of silicon rod with deposition time.

Table 1: Experimental conditions and results.

Experimental data	Nozzle type A	Nozzle type B
Initial rod size (mm)	7 (square)∗2100(H)	7 (square)∗2100(H)
Rod temperature (°C)	850	850
Reactor pressure (kgf·cm^{-2})	3.5	3.5
SiH_4 flow rate (l·min^{-1})	5 to 40	5 to 40
SiH_4 concentration (%)	4	4
Run time (h)	55.3	55.5
Silicon deposition thickness (mm)	45.21	62.6
Deposited silicon (mm·h^{-1})	0.69	1
Energy consumption (kWh·kg^{-1})	111	72

and the amount of deposited poly-Si was 31,320 g and 60,750 g for type A and B nozzle, respectively. The changes of silicon rod thickness with increasing deposition time are shown in Figure 2. Deposition rates of poly-Si were calculated to 0.69 mm/h for type A nozzle and 1 mm/h for type B nozzle. The deposition rate of type B nozzle was larger than that of type A. In order to understand these phenomena, the simulations of each case were performed.

The simulation about the heat and flow phenomena in the reactors and deposition rate on the slim rod were conducted to explain the experimental results.

The simulation results in Figure 3 show that type B nozzle has a larger concentration of MS gas on the 10 mm position from silicon rod surface than type A. The deposition rate of poly-Si on silicon slim rod surface of type B is also larger than that of type A, and this result matches with experimental result. High deposition rate of type B nozzle is caused by the high MS concentration on the silicon slim rod. MS gas distribution is more clarified in Figure 4. As mentioned above, the type A nozzle is composed with 4 vertically arranged orifices that make the circulation flows around the slim rod. Circulation gas stream of type A uniformly distributes the MS gas in a reactor. Therefore, the deposition rate of type A was relatively lower than that of type B.

On the other hand orifice of type B nozzle was distributed around silicon slim rod. Thus, the stream of gas mixture could be formed around slim rod, and the higher MS concentration of type B increased the deposition rate.

The velocity of gas mixture in an inner wall of heating jacket is shown in Figure 5. In case of type A, strong circulating flow formed inner wall of heating jacket because gas mixture of SiH_4 and H_2 was emitted from vertically located 4 orifices of nozzle between silicon slim rod and heating jacket. Emitted gas mixture flow upward due to silicon slim rod was being heated. Therefore, gas stream could be vortex flow as shown in Figure 5.

Gas stream of type B nozzle could be vertically formed around silicon slim rod because gas mixture was emitted to upward from the bottom of silicon slim rod. In this reason, fast deposition of poly-Si was possible.

Figure 6 shows the thickness variation of 4 poly-Si rod according to the height. The thickness of poly-Si varies with deposition position. The highest thickness of poly-Si deposited with type A nozzle was measured at the center of poly-Si rod. It is certain that the vortex gas stream of type A makes nonuniform deposition of poly-Si.

In case of nozzle B, poly-Si was uniformly deposited in whole position because gas stream was formed around silicon slim rod. The average deposition thickness was 62.5 mm, and deposition rate was 1 mm/h.

Energy consumption is very important parameter for poly-Si production because the power consumption has a larger fraction about 25% for poly-Si production in a mass production system.

The overall value of energy consumption in this study is shown in Figure 7. 3,490 kWh for type A and 4,381 kWh for type B of electrical power were consumed, respectively. It could be converted to quantitative value such as energy consumption per unit weight of poly-Si, and it was 111 kWh·kg^{-1} and 72 kWh·kg^{-1} for type A and B, respectively. It seems that the energy consumption is closely related deposition rate. High deposition rate of type B has low energy consumption, and low deposition rate of type A has high energy consumption.

4. Conclusions

Deposition of poly-Si was conducted in a MS-Siemens CVD reactor using SiH_4 + H_2 system. To understand the importance of nozzle design, deposition of poly-Si was conducted two different type of nozzle (A and B). Type A was composed of vertically arranged 4 orifices, and type B was composed of circularly distributed 6 orifices.

Through experiment, it was realized that the type B nozzle is better than type A for poly-Si deposition. Type B

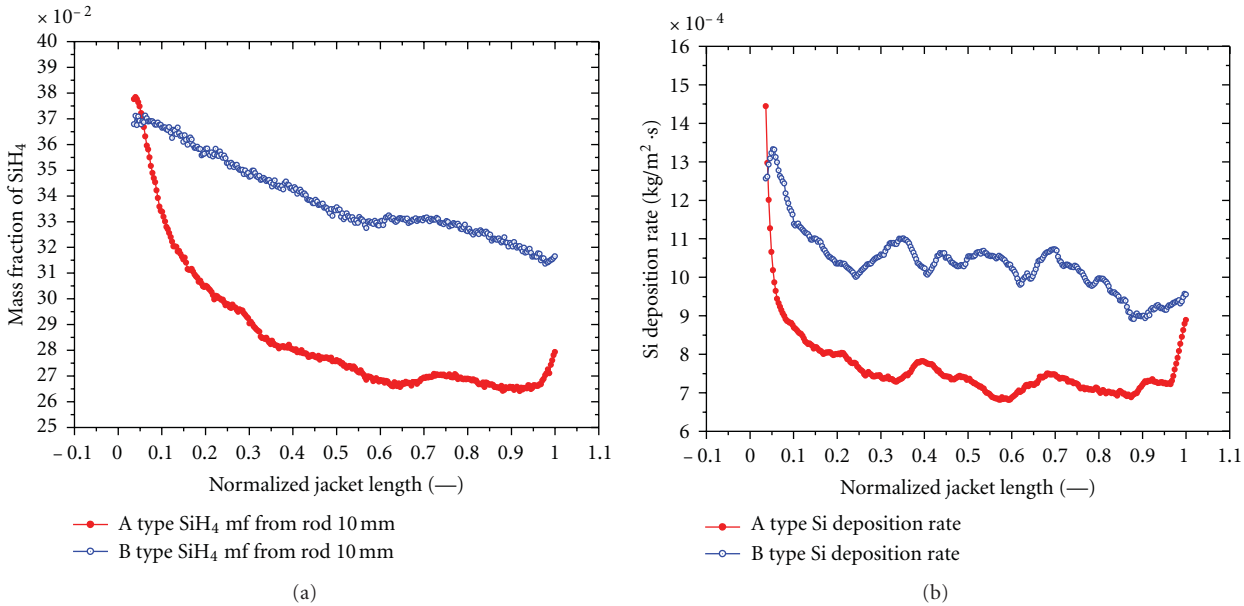

Figure 3: Simulation analysis of (a) SiH_4 mass fraction and (b) silicon deposition rate between type A and B nozzle.

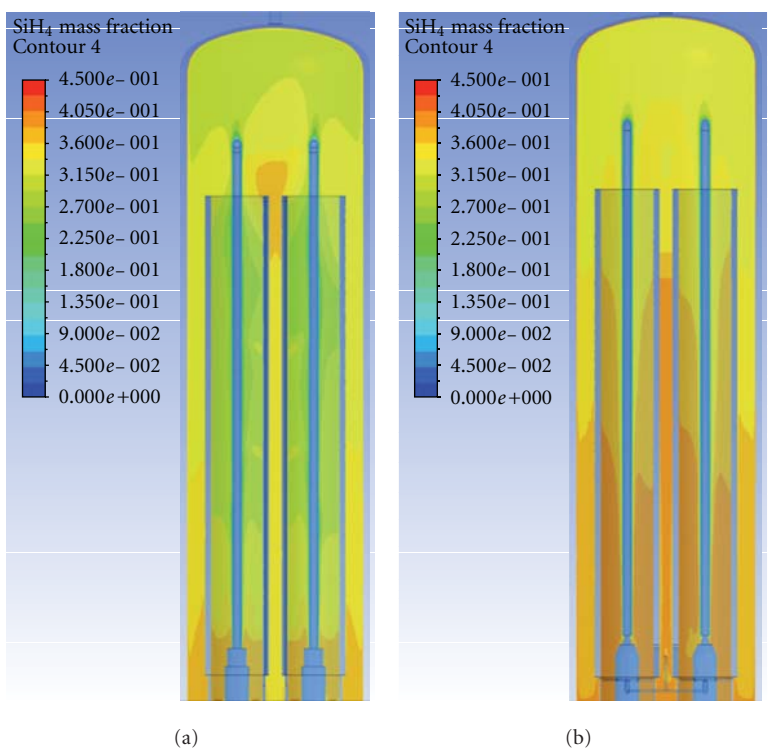

Figure 4: Simulation analysis of SiH_4 mass fraction between nozzle (a) type A and (b) B.

nozzle has high deposition rate, uniform deposition, and low energy consumption.

The highest deposition rate in this study was 1 mm/h, and lowest energy consumption for production of unit weight of poly-Si was 72 $kWh \cdot kg^{-1}$.

CFD analysis was performed to understand the experimental results. In the case of type A, the vortex flow was formed in the reactor which makes nonuniform deposition of poly-Si and low SiH_4 concentration around silicon slim rod.

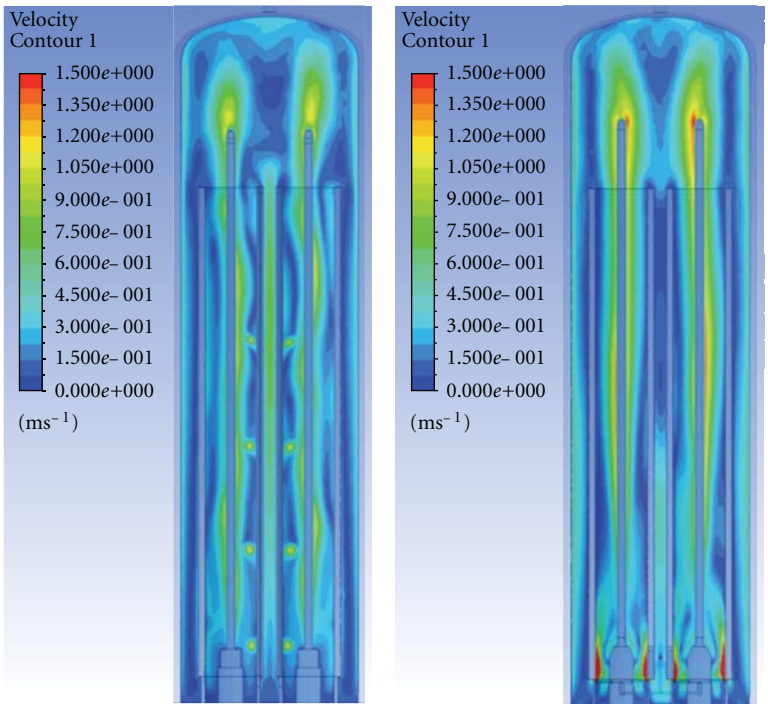

(a) (b)

Figure 5: Simulation analysis results of fluid velocity between nozzle (a) type A and (b) B.

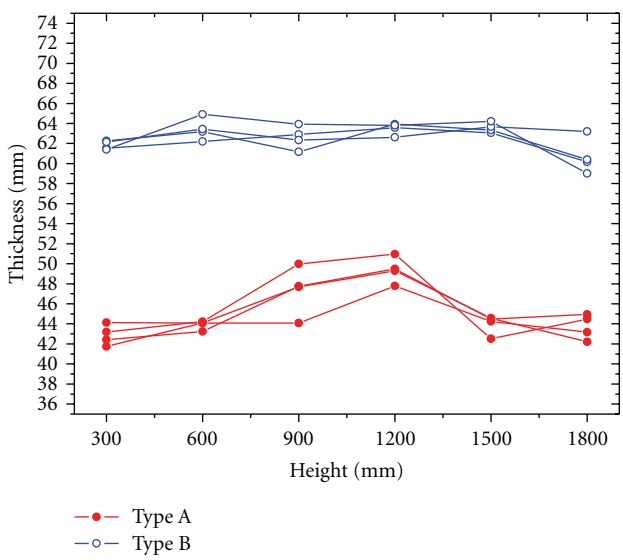

Figure 6: Thickness variation of 4 poly-Si rod along the height.

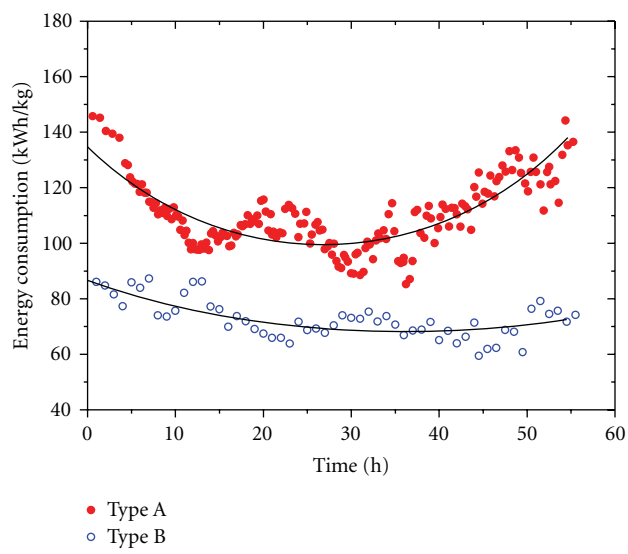

Figure 7: Power consumption throughout the deposition process.

On the other hand, in case of type B nozzle, high concentration of source gas was supplied on the silicon slim rod because gas mixture of $SiH_4 + H_2$ flows along the slim rod.

The experimental results with type B nozzle in this study such as 1 mm/h of deposition rate and 72 $kWh \cdot kg^{-1}$ could be adapted as mass production system for lowering the unit production cost.

Acknowledgments

This research was financially supported by the Ministry of Knowledge Economy (MKE), Korea Institute for Advancement of Technology (KIAT), and Daegyeong Leading Industry Office through the Leading Industry Development for Economic Region.

References

[1] A. K. Praturi, R. Lutwack, and G. Hsu, *Chemical Vapor Deposition of Silicon from silane Pyrolysis*, JPL Publication, 1977.

[2] W. A. P. Claassen and J. Bloem, "The nucleation of CVD silicon on SiO_2 and Si_3N_4 substrates," *Journal of the Electrochemical Society*, vol. 127, no. 1, pp. 194–202, 1980.

[3] W. C. Breneman, R. N. Flagella, J. M. Gaston, and D. W. Hagan, "Improved process for the production of ultra high purity polycrystalline silicon," patent EP0294908, 1988.

[4] S. M. Load, "Machine for production of granular silicon," patent US 6827786, 2004.

[5] W. O. Filtvedt, M. Javidi, A. Holt et al., "Development of fluidized bed reactors for silicon production," *Solar Energy Materials and Solar Cells*, vol. 94, no. 12, pp. 1980–1995, 2010.

[6] M. A. Rodgers, "Process for manufacturing pure polycrystalline silicon," patent US 4170667, 1979.

[7] F. Kőppl, H. Hamster, R. Griesshammer, and H. Lorenz, "Process for the deposition of pure semiconductor material," patent US 4179530, 1979.

Hindawi Publishing Corporation
International Journal of Photoenergy
Volume 2012, Article ID 549382, 5 pages
doi:10.1155/2012/549382

Research Article

$Cd_{1-x}Zn_xS$ Thin Films with Low Zn Content Prepared by Chemical Bath Deposition

Caijuan Tian, Jingjing Gao, Wei Li, Lianghuan Feng, Jingquan Zhang, and Lili Wu

College of Materials Science and Engineering, Sichuan University, Chengdu 610064, China

Correspondence should be addressed to Wei Li, waylee2000@sohu.com

Received 16 November 2011; Accepted 27 December 2011

Academic Editor: Bhushan Sopori

Chemical bath deposition (CBD) was used for the growth of $Cd_{1-x}Zn_xS$ thin films with low Zn content. The influence of preparation conditions, such as pH, temperature, and concentration, on film properties was investigated. The chemical growth mechanism of $Cd_{1-x}Zn_xS$ thin films was analyzed, and optimized growth conditions for the thin films were established. The fill factor and short-circuit current were improved while $Cd_{1-x}Zn_xS$ was used to replace CdS as the window layer in CdTe solar cells.

1. Introduction

The highest conversion efficiency of CdS/CdTe thin film solar cells till now is 16.7% [1]. However, the band gap of CdS is not high enough so that the short wavelength photons are easy to be absorbed. The band gap of $Cd_{1-x}Zn_xS$ varies in the range of 2.42 to 3.6 eV as zinc content increases [2]. While $Cd_{1-x}Zn_xS$ is used to replace CdS as a window layer, not only the absorption of the window layer will be reduced, but also the short-circuit current of the $Cd_{1-x}Zn_xS$/CdTe thin film solar cells will be increased [3]. It is worth noting that two issues exist in the CdTe solar cells. One is the lattice parameter varying linearly with zinc content in the compound and thus resulting in a large lattice mismatch between $Cd_{1-x}Zn_xS$ and CdTe. The other is the electrical resistivity increasing dramatically by the increase of zinc content [4]. Therefore, $Cd_{1-x}Zn_xS$ at low Zn content is an ideal alternative material for CdTe thin film solar cells as the window layer.

Many ways, such as vacuum evaporation [4], chemical bath deposition [3, 5, 6] and, SILAR [7], have been used to prepare $Cd_{1-x}Zn_xS$ thin films. Among these techniques, CBD presents many advantages: inexpensive, simple equipment, low temperature (<100°C), and large-area deposition. So it is well suited for the manufacture of photovoltaic devices [3, 5]. Because the solubility products of CdS ($K_{sp} = 10^{-28}$) and ZnS ($K_{sp} = 10^{-23.8}$) are different by several orders of magnitude, the complexing agent is essential for codeposition of CdS and ZnS. In this work, NH_3 was used as the complexing agent to prepare $Cd_{1-x}Zn_xS$ thin films at low Zn content. The influence of growth conditions on the properties of $Cd_{1-x}Zn_xS$ was investigated to understand the deposition process and thus to improve the characteristics of the films. Subsequently $Cd_{1-x}Zn_xS$ thin films were used as the window layer for the CdTe solar cells.

2. Experimental Details

In the CBD process, $Cd_{1-x}Zn_xS$ thin films are prepared by slow release of S^{2-} and effective control of free Zn^{2+} and Cd^{2+} ions in the solution. The main chemical reactions happened in the solution can be described as follows:

$$(1-x)Cd(NH_3)_4{}^{2+} + xZn(NH_3)_4{}^{2+} + SC(NH_2)_2 + 2OH^- \longrightarrow Cd_{1-x}Zn_xS + CH_2N_2 + 2H_2O + 4NH_3 \quad (1)$$

In this work, a certain a mount of $ZnCl_2$, $CdCl_2$, and NH_4Cl were dissolved in 200 mL DI water at room temperature. When the solution was heated to 60°C, a solution of ammonia was added to the solution and stirred for 5 min. Here the ammonia combines Cd^{2+} and Zn^{2+} to form the complex $Cd(NH_3)_4^{2+}$ and $Zn(NH_3)_4^{2+}$ which can constantly release Cd^{2+} and Zn^{2+}. Then clean glass substrates or TCO-coated ones were placed vertically in the reaction

bath. Finally, a certain a mount of thiourea was added to the solution, which slowly releases S^{2-} as a sulfur source. The rotating speed of the agitator during the deposition process was 30 r/min. The depositions were performed with $CdCl_2$, $ZnCl_2$, and $SC(NH_2)_2$ concentrations varying from 0.001 to 0.06 mol/L, ammonia concentrations in the range of 0.072 to 0.179 mol/L, and pH values between 8.5 and 10.5 to obtain the optimum growth conditions of the $Cd_{1-x}Zn_xS$ thin films. The values of pH were controlled by adding NH_4Cl to form a buffer solution with the desired pH. After a deposition of 1.5 hour, the substrates were released from the solution. One side was cleaned by HCl for testing convenience and then the substrates were deterged by DI water to remove the contaminant ions.

CdTe solar cells with a $Cd_{1-x}Zn_xS$ layer (~180 nm) were fabricated for indicating the application of $Cd_{1-x}Zn_xS$ thin films. CdTe films followed by the deposition of $Cd_{1-x}Zn_xS$ thin films were prepared by the close-spaced sublimation (CSS) technique. After CSS deposition of CdTe with thickness of 8 μm, the samples were treated in $CdCl_2$ vapor at 380°C for 30 min. Then they were etched with Br-Methanol and rinsed in DI water and blown dry in N_2. The back contact layer was formed by applying Sb_2Te_3 to the etched CdTe surface and heat treating it in N_2 at 300°C [8]. Finally, Au was used to complete the fabrication of CdTe solar cells. For reference purpose, CdTe solar cells with a CdS layer (~180 nm) were also fabricated.

The composition of the $Cd_{1-x}Zn_xS$ thin films was determined by X-ray fluorescence (XRF) measurements. The structural properties of the films were studied by X-ray diffraction (XRD). Measurement of the optical transmittance was made over the wavelength range 300~900 nm with a data interval of 1 nm. Scanning electron microscopy (SEM) was performed to investigate the surface morphology of the films. Electrical resistivity along the lateral direction was measured by depositing Al-stripes on the $Cd_{1-x}Zn_xS$ thin films and performing two-point probe measurements. The resulting PV devices were characterized using the light $J-V$ measurement under simulated AM 1.5 illumination (i.e., 100 mW/cm^2) with standard current-voltage measurement equipments.

3. Results and Discussions

3.1. Structural Properties. Figure 1 shows XRD patterns of $Cd_{1-x}Zn_xS$ thin films prepared at different pH values. It is found that the $Cd_{1-x}Zn_xS$ thin films are hexagonal with a preferential orientation along the (002) plane in the alkaline environment. When the pH value is 8.5, only a single strong $Cd_{1-x}Zn_xS$ (002) peak can be detected. However, as the pH value increases, the intensity of the $Cd_{1-x}Zn_xS$ (002) peak decreases and peaks of ZnS and ZnO also emerge in these patterns. This is probably caused by the excessive ammonia which leads to the reactions of $Zn(NH_3)_4^{2+}$ and OH^-, and that may be responsible for the accentuation of ZnO peak when the pH value increases to 9.5. When the pH value reaches up to 10.0, on the contrary, all the peaks are weakened.

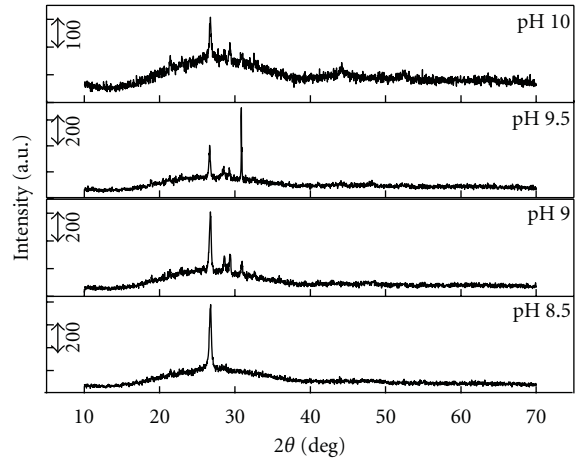

Figure 1: XRD patterns of $Cd_{1-x}Zn_xS$ thin films prepared at different pH values.

We investigate XRD patterns (not shown there) of $Cd_{1-x}Zn_xS$ thin films prepared at different temperatures. As the bath temperature increases from 60°C to 90°C, the intensity of $Cd_{1-x}Zn_xS$ (002) firstly becomes strong and then weakens. Also, peaks other than $Cd_{1-x}Zn_xS$ cannot be detected in the thin films deposited at 70°C. Therefore, the optimal bath temperature to preparing $Cd_{1-x}Zn_xS$ thin films by CBD is 70°C.

As the buffering agent, NH_4Cl also affects the hydrolytic equilibrium of NH_4^+; therefore, it could balance the concentration of NH_3 to control the reaction rate. If no buffering agent is expected in the reactions, the deposition rate would be too fast at the beginning; however, it would be saturated quickly, and this is harmful to fabricate $Cd_{1-x}Zn_xS$ thin films with good quality. A suitable concentration of NH_4Cl enables the linear increase of deposition rate of $Cd_{1-x}Zn_xS$ thin films with the time, and that will be beneficial to deposit $Cd_{1-x}Zn_xS$ thin films [9]. When the concentration of NH_4Cl is 0.04 mol/L, the intensity of $Cd_{1-x}Zn_xS$ (002) peak is stronger than that of the concentrations of 0.03 and 0.05 mol/L. What is more, no obvious peak of $Cd_{1-x}Zn_xS$ (002) could be observed from the XRD patterns when the concentration of NH_4Cl changes to 0.025 mol/L or 0.055 mol/L. This is due to the insufficient buffering of NH_3 when the concentration of NH_4Cl is too low.

Usually, two mechanisms, homogeneous particles formation and heterogeneous surface reaction, are available when thiourea reacts with $CdCl_2$ and $ZnCl_2$. On the one hand, $[Cd(NH_3)_4]^{2+}$ and $[Zn(NH_3)_4]^{2+}$ combine with OH^- to form complexing ions. These ions are absorbed on the surface of the substrate, and then they react with thiourea to form metastable complex. Subsequently, the metastable complex decomposes to form a new $Cd_{1-x}Zn_xS$ surface. Therefore, the surface of $Cd_{1-x}Zn_xS$ thin films is compact and homogeneous (see Figure 2). On the other hand, the S^{2-} released from thiourea through hydrolysis reaction combines with free Cd^{2+} and Zn^{2+} ions to generate $Cd_{1-x}Zn_xS$ particles [10, 11]. These particles deposit on the surface of the substrate, which results in a rough and porous surface.

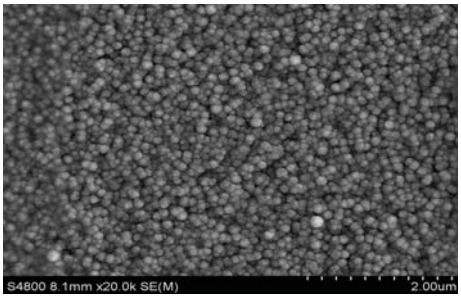

Figure 2: SEM Image of $Cd_{1-x}Zn_xS$ thin films prepared by CBD.

By carefully controlling the bath concentration of thiourea, the reaction can be driven mainly as the heterogeneous mechanism. Hence, the structural properties of $Cd_{1-x}Zn_xS$ thin films will be different. When the concentration of thiourea increases from 0.02 to 0.03 mol/L, the intensity of $Cd_{1-x}Zn_xS$ (002) peak is strengthened; however, as the concentration increases more, the peak height reduces lower and can hardly be differentiated from the background in XRD patterns.

Upon the previous analysis, it is found that the pH value, temperature, the bath concentration of NH_4Cl, or thiourea greatly affect the deposition of $Cd_{1-x}Zn_xS$ thin films. As far as good crystallinity films are concerned, the standard conditions for growth of $Cd_{1-x}Zn_xS$ thin films are $[ZnCl_2]$ = 0.001 mol/L, $[CdCl_2]$ = 0.005 mol/L, $[NH_4Cl]$ = 0.04 mol/L, $[SC(NH_2)_2]$ = 0.03 mol/L, T = 70°C, and pH 8.5. In addition, we deposited $Cd_{1-x}Zn_xS$ thin films under these conditions and then annealed at 350°C in N_2 atmosphere. The XRD patterns of as-deposited and annealed $Cd_{1-x}Zn_xS$ thin films are shown in Figure 3. The diffraction peak positions do not change dramatically after annealing, but the average grain sizes of the films change from 17.5 to 32.8 nm according to Scherrer's equation.

3.2. Compositional Properties. The X-ray fluorescence analysis using the fundamental parameter (FP) method was used to determine the composition of the $Cd_{1-x}Zn_xS$ films. Figure 4 gives the evolution of Zn content with the preparation conditions, that is, pH value, and the concentration of thiourea. It is found that, when the pH value increases, Zn content decreases, and the same situation is found when the temperature rises. Similarly, we varied the thiourea concentration, while the rest of the variables were maintained under the standard conditions. The Zinc content reaches up to 20 at% by increasing the thiourea concentration and then decreases. This is ascribed to the different solubility products of CdS and ZnS and the different stability constants for the cadmium and zinc precursors. For the standard conditions, $Cd_{1-x}Zn_xS$ films at x ∼20 at% were obtained.

3.3. Electrical Properties. Figure 5 shows the plots of conductivity versus temperature for $Cd_{1-x}Zn_xS$ thin films. The conductivity of $Cd_{1-x}Zn_xS$ thin films prepared at pH values varied from 8.5 to 9.5 increases monotonically as the temperature increases. The increase of σ with temperature

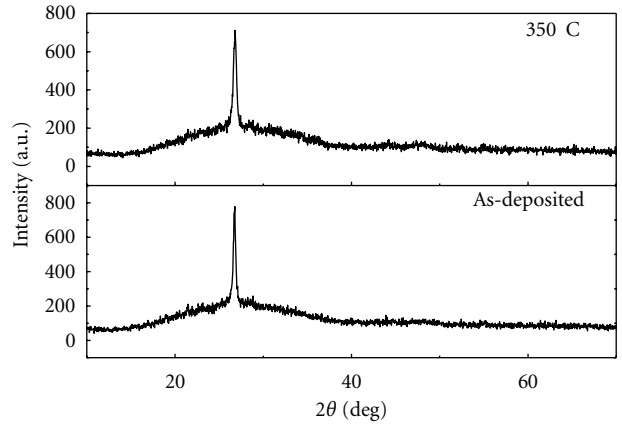

Figure 3: XRD patterns of $Cd_{1-x}Zn_xS$ prepared under the optimum conditions before and after annealing.

is ascribed to the growth of large grains, which increases the electron mean free path and reduces the scattering effect. However, for thin films prepared at pH 10, an abnormal behavior occurred in the range of 39–110°C. This phenomenon is also observed in CdS thin films [12, 13]. The relationship between σ and T can be described as

$$\sigma = \sigma_0 \exp\ -\frac{E_a}{kT}\ , \tag{2}$$

where σ_0 is constant, k is the Boltzmann constant, and E_a is activation energy. The values of E_a for thin films except for pH 10 are listed in Table 1. The thin films prepared at pH from 8.5 to 9.5 indicate three linear regions. The first at lower temperatures may be ascribed to the transitions from the impurity levels in the band gap to the bottom of the conduction band or the top of the valence band. The second is attributed to electron or hole transitions to the conduction or valence band. The third at higher temperatures is due to the electron transitions through the extended states in the conduction band [14].

3.4. Optical Properties. Considering the potential application of $Cd_{1-x}Zn_xS$ thin film as the window layer in CdTe thin film solar cells, it is necessary to investigate the influence of preparation conditions on the optical properties of $Cd_{1-x}Zn_xS$ thin films. We varied one of the standard conditions while maintained other rest of variables. Figure 6 shows the transmittance of the $Cd_{1-x}Zn_xS$ thin films prepared at different pH values. An extended spectral response for all the thin films at short wavelengths is noted. One can also see that the transmittance of the $Cd_{1-x}Zn_xS$ thin films is higher than 60% when the wavelength is longer than 500 nm, in which the transmittance increases as the pH value decreases. For thin films prepared at pH 8.5 and 9.0, it is much higher than that of the other pH values. The same situation is found while varying the temperature, the concentration of NH_4Cl and thiourea. It seems that pH 8.5 or 9.0 is the optimum pH value. Using the Tauc equation, the band gap of $Cd_{1-x}Zn_xS$ thin films is calculated by extrapolating the linear part of the curve to the $\alpha h\nu$ axis, and the interception is the value of E_g.

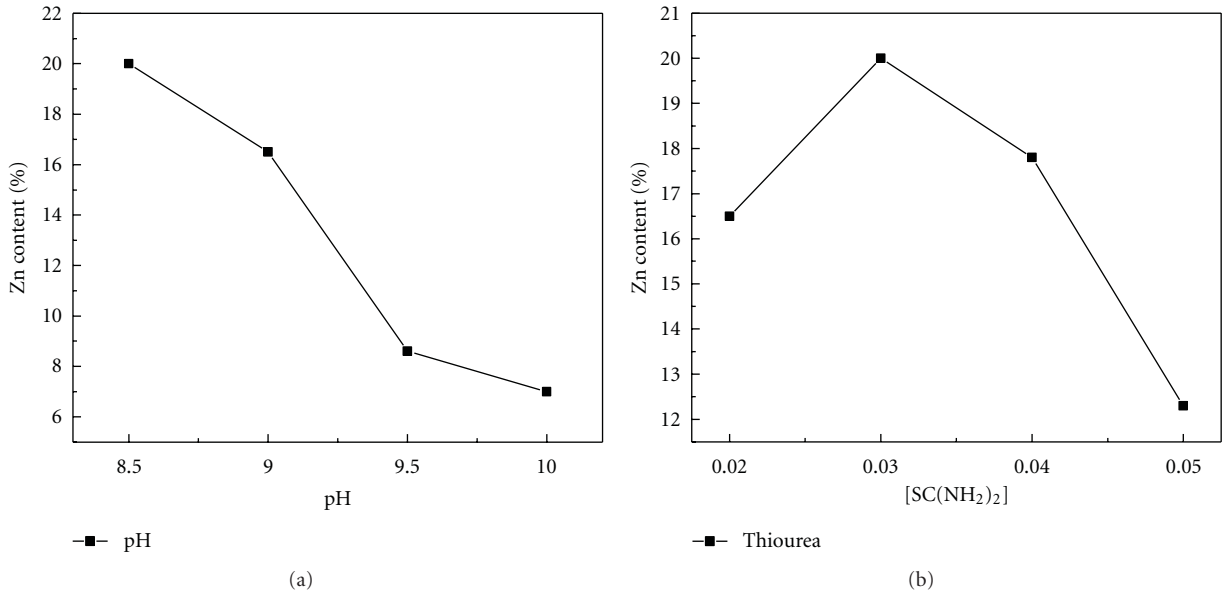

Figure 4: Plots of Zn content versus different deposition conditions of $Cd_{1-x}Zn_xS$ thin films.

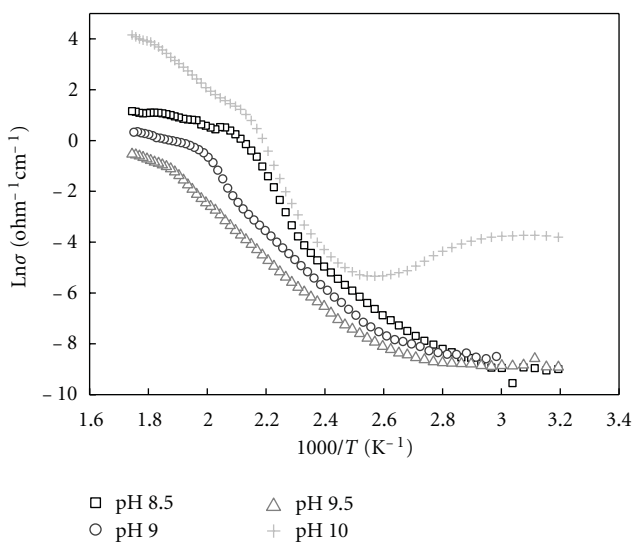

Figure 5: Variation of $\ln\sigma$ versus 1000/T for $Cd_{1-x}Zn_xS$ prepared at different pH values.

From Figure 6, for thin films prepared at pH 9.5 and 10.0, they exhibit two absorption edges. The value of E_g can be calculated in the short wavelength regions to be about 3.6 eV. As evidenced by the XRD observations (see Section 3.1), we attribute it to the formation of ZnS or ZnO. The value of E_g for thin films prepared at pH 8.5 and 9.0 is about 2.56 eV, which is larger than that of CdS (~2.4 eV). That means $Cd_{1-x}Zn_xS$ thin films prepared on these conditions may be better than CdS as the window layer of CdTe thin film solar cells.

From the properties of $Cd_{1-x}Zn_xS$ thin films at low Zn content, we find that the standard conditions are the optimum ones for thin film deposition in fact.

Table 1: The values of activation energies for $Cd_{1-x}Zn_xS$ prepared at different pH values.

pH	E_{a1} (eV)	E_{a2} (eV)	E_{a3} (eV)
8.5	0.57	1.67	0.24
9	0.22	1.01	0.29
9.5	0.13	0.86	0.43

3.5. Device Performance. CdTe thin film solar cells with the $Cd_{1-x}Zn_xS$ window layer were fabricated based on the previous analysis. Table 2 shows the electrical parameters, for example, open circuit V_{oc}, short-circuit current density J_{sc}, fill factor FF, and conversion efficiency η for CdTe thin film solar cells with a $Cd_{1-x}Zn_xS$ or CdS widow layer. It is found that open circuit voltage changes very little, but the short circuit current for CdTe thin film solar cells with a $Cd_{1-x}Zn_xS$ layer is higher than those with a CdS layer.

4. Conclusions

$Cd_{1-x}Zn_xS$ thin films in the range of $x \leq 20$ at% were prepared by CBD. Under the optimum preparation conditions, the thin films were found to be hexagonal, which show highly preferential orientation. And the value of activation energies attributed to electron or hole transitions to the conduction or valence band is about 1.67 eV. The optical properties also show that the given preparation conditions are proper to deposit $Cd_{1-x}Zn_xS$ thin films with high transmittance in both long and short wavelength ranges. $Cd_{1-x}Zn_xS$ is used to replace CdS as the window layer; the fill factor and short-circuit current were improved, which means $Cd_{1-x}Zn_xS$ thin films are more suitable for the window layer in CdTe solar cells.

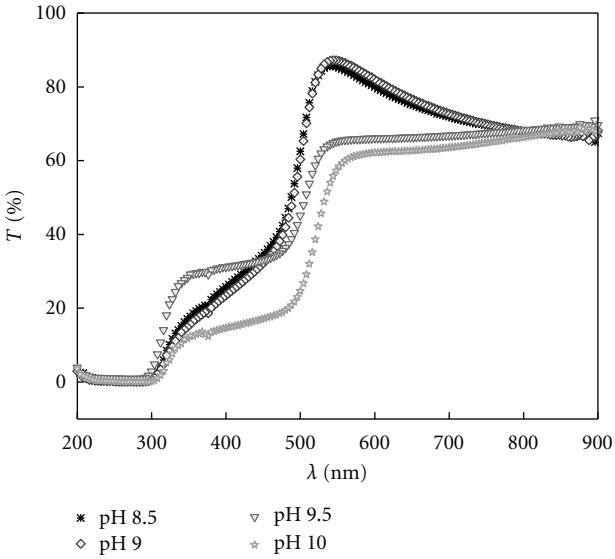

Figure 6: Transmittance curves of $Cd_{1-x}Zn_xS$ thin films prepared at different pH values.

Table 2: Parameters for CdTe thin film solar cells.

Window layer	V_{oc} (mV)	J_{sc} (mA/cm^2)	FF	η
$Cd_{1-x}Zn_xS$	691	22.1	58.5%	8.9%
CdS	681	19.7	53.2%	7.1%

Acknowledgments

Financial support from National Basic Research Program of China (Grant no. 2011CBA007008), National Natural Science Foundation of China (Grant no. 61076058), and the Science and Technology Program of Sichuan Province, China, (Grant no. 2008GZ0027) is gratefully acknowledged.

References

[1] M. A. Green, K. Emery, Y. Hishikawa, and W. Warta, "Solar cell efficiency tables (version 37)," *Progress in Photovoltaics*, vol. 19, no. 1, pp. 84–92, 2011.

[2] T. D. Dzhafarov, F. Ongul, and I. Karabay, "Formation of CdZnS thin films by Zn diffusion," *Journal of Physics D*, vol. 39, no. 15, pp. 3221–3225, 2006.

[3] T. Yamaguchi, Y. Yamamoto, T. Tanaka, Y. Demizu, and A. Yoshida, "(Cd,Zn)S thin films prepared by chemical bath deposition for photovoltaic devices," *Thin Solid Films*, vol. 281-282, no. 1-2, pp. 375–378, 1996.

[4] L. C. Burton and T. L. Hench, "$Zn_xCd_{1-x}S$ films for use in heterojunction solar cells," *Applied Physics Letters*, vol. 29, no. 9, pp. 612–614, 1976.

[5] J. Zhou, X. Wu, G. Teeter et al., "CBD-$Cd_{1-x}Zn_xS$ thin films and their application in CdTe solar cells," *Physica Status Solidi (B)*, vol. 241, no. 3, pp. 775–778, 2004.

[6] N. Gaewdang and T. Gaewdang, "Investigations on chemically deposited $Cd_{1-x}Zn_xS$ thin films with low Zn content," *Materials Letters*, vol. 59, no. 28, pp. 3577–3584, 2005.

[7] M. P. Valkonen, T. Kanniainen, S. Lindroos, M. Leskelä, and E. Rauhala, "Growth of ZnS, CdS and multilayer ZnS/CdS thin films by SILAR technique," *Applied Surface Science*, vol. 115, no. 4, pp. 386–392, 1997.

[8] S. Hu, Z. Zhu, W. Li et al., "Band diagrams and performance of CdTe solar cells with a Sb_2Te_3 back contact buffer layer," *AIP Advances*, vol. 1, no. 4, Article ID 042152, 2011.

[9] I. O. Oladeji and L. Chow, "Synthesis and processing of CdS/ZnS multilayer films for solar cell application," *Thin Solid Films*, vol. 474, no. 1-2, pp. 77–83, 2005.

[10] Y. J. Chang, C. L. Munsee, G. S. Herman et al., "Growth, characterization and application of CdS thin films deposited by chemical bath deposition," *Surface and Interface Analysis*, vol. 37, no. 4, pp. 398–405, 2005.

[11] M. Kostoglou, N. Andritsos, and A. J. Karabelas, "Modeling thin film CdS development in a chemical bath deposition process," *Industrial and Engineering Chemistry Research*, vol. 39, no. 9, pp. 3272–3283, 2000.

[12] R. Lozada-Morales, M. Rubín-Falfán, O. Zelaya-Angel, and R. Ramírez-Bon, "Characterization of cubic CdS thin films annealed in vacuum," *Journal of Physics and Chemistry of Solids*, vol. 59, no. 9, pp. 1393–1398, 1998.

[13] H. Xie, C. Tian, W. Li et al., "Preparation of p-type CdS thin films and in situ dark conductivity in vacuum deposited CdS : Cu films," *Applied Surface Science*, vol. 257, no. 5, pp. 1623–1627, 2010.

[14] S. K. J. Al -Ani, M. N. Makadsi, I. K. Al -Shakarchi, and C. A. Hogarth, "Preparation, and structural, optical and electrical properties of the $CdTe_{1-x}S_x$ system," *Journal of Materials Science*, vol. 28, no. 1, pp. 251–258, 1993.

Hindawi Publishing Corporation
International Journal of Photoenergy
Volume 2012, Article ID 614320, 4 pages
doi:10.1155/2012/614320

Research Article

Effects of Controlling the AZO Thin Film's Optical Band Gap on AZO/MEH-PPV Devices with Buffer Layer

Jaehyoung Park,[1,2] Ki-Chang Jung,[1] Ari Lee,[1] Hyojung Bae,[1] Daehwa Mun,[1] Jun-Seok Ha,[1] Young-Bu Mun,[3] E. M. Han,[1] and Hang-Ju Ko[2]

[1] *Department of Advanced Chemicals and Engineering, Chonnam National University, Gwangju 500-757, Republic of Korea*
[2] *Photovoltaic and Optoelectronic Device Center, Korea Photonics Technology Institute, Gwangju 500-460, Republic of Korea*
[3] *THELEDS Co., Gwangju 506-253, Republic of Korea*

Correspondence should be addressed to Jun-Seok Ha, jsha@jnu.ac.kr

Received 31 August 2011; Accepted 27 December 2011

Academic Editor: Bhushan Sopori

Organic/inorganic hybrid solar cells were fabricated incorporating aluminum-doped zinc oxide (AZO) thin films of varying optical band gap in AZO/poly(2-methoxy-5-(2′-ethyl-hexyloxy)-*p*-phenylene vinylene) structures. The band gaps were controlled by varying the flow rates of Ar and O_2 used to deposit the AZO. Devices with CdS buffer layer were also fabricated for improved efficiency. The effects of AZO optical band gap were assessed by testing the *I*–*V* characteristics of devices with structures of glass/ITO/AZO/MEH-PPV/Ag under AM1.5 illumination (100 mW/cm^2). Efficiency was improved about 30 times by decreasing the AZO optical band gap, except in devices deposited without oxygen. A power conversion efficiency of 0.102% was obtained with the incorporation of a CdS buffer layer.

1. Introduction

Organic/inorganic hybrid solar cells are promising for their low manufacturing costs, facile processing, and applicability in flexible devices. They incorporate organic polymers such as MEH-PPV and poly(3-hexylthiophene) (P3HT) that act as light absorbers and electron donors. Efficient separation of charge carriers from their place of generation in the light absorption layers depends on the electron properties of the inorganic material and the morphology of its interface with the polymer [1, 2]. Therefore various inorganic semiconductors have been tested to improve efficiency; examples include cadmium selenide (CdSe) nanorods [3] and nanoparticles [4], cadmium sulfide (CdS) nanorods [5] and nanowires [6], ZnO thin film [7] and nanorods [8–10], and TiO_2 nanoparticles [11]. Controlling the optical band gap of inorganic materials through the use of Al-doped zinc oxide (AZO) is also promising as these stable thin films have high electron mobility and affinity. ZnO/P3HT devices' efficiencies have been doubled upon the incorporation of a nanocrystalline CdS buffer layer that introduces a cascading energy band gap structure between the ZnO and P3HT [12].

This work reports improvement of PV performance by controlling the optical band gap of AZO in AZO/poly [2-methoxy-5-(2′-ethyl-hexyloxy)-*p*-phenylene vinylene] (MEH-PPV) devices. Furthermore, we introduced CdS thin-film buffer layer between AZO and MEH-PPV for improved efficiency.

2. Experimental Methods

Soda lime glass substrates were sequentially cleaned ultrasonically in acetone, isopropyl alcohol, and deionized water and dried in nitrogen gas. An indium tin oxide (ITO) transparent conductive oxide layer was deposited on each substrate by DC magnetron sputtering through a patterned shadow mask. The patterned ITO glass was annealed for 15 minutes by RTA under nitrogen and oxygen. The sheet resistance of the ITO conductive oxide was 30 Ω/□, measured by four-point probe. 3 wt.% AZO targets were formed from

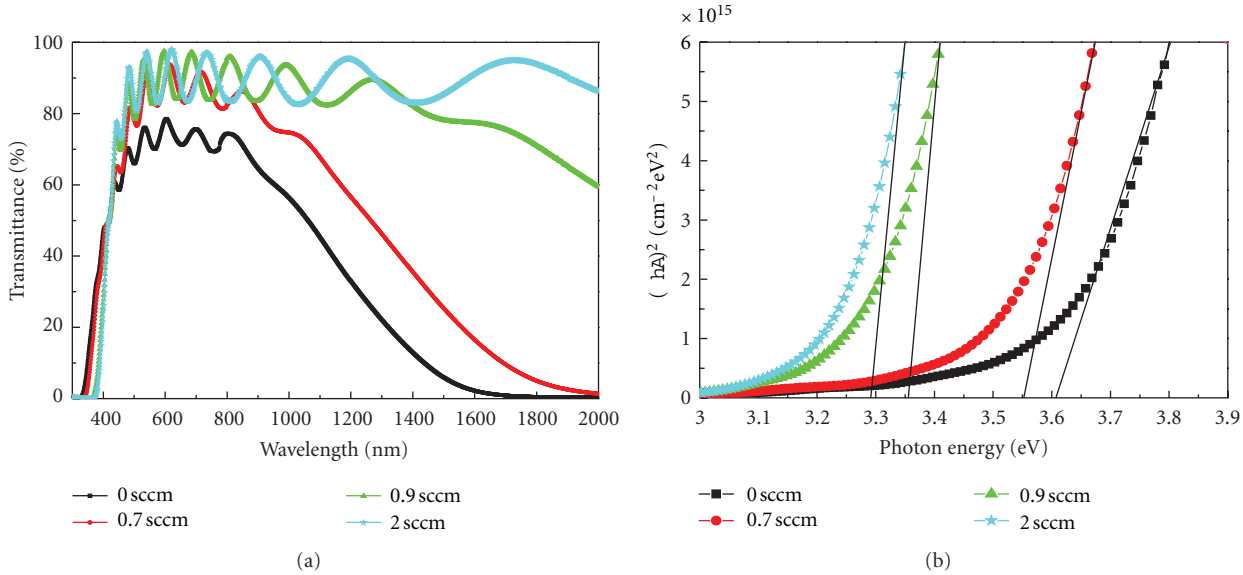

Figure 1: (a) Transmittance spectra of AZO thin films with various optical band gaps. (b) Evaluation of the AZO thin films' $(\alpha h\nu)^2$ versus h curves.

high-purity ZnO (99.99%) and $Al(OH)_3$ (99.99%) powders. The AZO thin films' optical band gaps were controlled by varying the O_2 and Ar gas mixture used during the RF magnetron sputtering. Ratios of the flow rates of argon and oxygen of 15 : 0, 14.3 : 0.7, 14.1 : 0.9, and 13 : 2 were used. CdS layers were deposited on the AZO thin films by RF magnetron sputtering under an Ar gas flow of 25 sccm. 10 mg MEH-PPV polymer in 1 mL chloroform was then spin-coated as a thin film over the inorganic film. Ag anodes were deposited by electron beam evaporation under vacuum at below 4×10^{-8} Pa.

Scanning electron microscopy (SEM) was performed on a Hitachi S-4700 scanning electron microscope. Transmittance and absorption spectra were measured on a Cary 500 scan UV-Vis-NIR spectrophotometer. Photoluminescence spectra were recorded at room temperature under 325 nm He-Cd laser excitation. Energy conversion efficiencies were measured under 100 mW/cm^2 illumination from an AM1.5 solar simulator.

3. Results and Discussions

Transmittances were measured between 300 nm and 2000 nm to assess the AZO samples' optical band gaps (Figure 1). In direct band gap semiconductors, intrinsic absorbance occurs near the band edge. Absorption coefficients were calculated using Lambert's law. The AZO thin films' optical band gaps were estimated by extrapolating the linear portions of plots $(\alpha h\ )^2$ versus h using the relation $\alpha h\ = A(h\ - E_g)^{1/2}$, where T is the transmittance, t is the film's thickness, α is the absorption coefficient, h is the photon energy, A is a constant, and E_g is the direct optical band gap [13]. Optical band gaps of the AZO films deposited at argon and oxygen ratios of 15 : 0, 14.3 : 0.7, 14.1 : 0.9, and 13 : 2 were calculated to be 3.29, 3.35 3.54, and 3.61 eV, respectively. The optical band gap increased as the O_2 partial pressure during deposition decreased due to Al ions being substituted into the ZnO lattice [14]. The AZO thin film showed an optical band gap of 3.29 eV, similar to that of intrinsic ZnO. PV performances of the AZO thin films in devices with MEH-PPV generally increased as the AZO's optical band gap decreased, except in devices deposited without oxygen (Table 1). Sheet resistance, from Hall measurements, decreased from $1.08 \times 10^6\ \Omega/\square$ to 69.18 $\Omega/\square$ as the optical band gap of the AZO increased. Concurrently, bulk carrier concentration increased from -1.45×10^{19}/cm^3 to -6.73×10^{20}/cm^3. Devices deposited without oxygen showed good charge collection because of low sheet resistance and high carrier concentration. As the AZO's optical band gap decreased, the electron barrier between the lowest unoccupied molecular orbital (LUMO) levels of MEH-PPV and AZO decreased [15].

Absorbances of the devices' layers were calculated from transmittance spectra; the PL spectrum of MEH-PPV was also measured (Figure 2). The optical absorption of MEH-PPV film peaked at 500 nm, showing an edge at 590 nm in the visible region. CdS thin film began to absorb slowly from around 550 nm to 490 nm. The optical absorptions of AZO and intrinsic ZnO thin film were in the UV region. The PL spectrum of MEH-PPV thin film shows that photoinduced charge transfer occurred in the MEH-PPV thin film [16].

Previous insignificant PV performances have been attributed to the great electron barrier between the LUMO levels of MEH-PPV and AZO [15], and the movement of electrons to the cathode from charge carrier separation may have been limited. CdS thin films were used as buffer layers between the MEH-PPV and AZO. CdS thin film started to absorb slowly from around 550 nm to 490 nm (Figure 2). The optical band gap of CdS thin film was 2.2 eV. The CdS layer, with an optical band gap of 2.2 eV, created a cascading

Table 1: Average PV performances of various AZO thin films in devices with MEH-PPV.

Sample	O_2 flow rate (sccm)	Ar flow rate (sccm)	optical band gap (eV)	J_{sc} (mA/cm^2)	V_{oc} (V)	FF (%)	PCE (%)
1	0	15	3.61	0.371	0.16	25.54	0.019
2	0.7	14.3	3.54	0.147	0.012	23.12	0.001
3	0.9	14.1	3.35	0.234	0.116	24.36	0.008
4	2	13	3.29	0.321	0.264	28.19	0.03

Table 2: Average PV performances of AZO/CdS/MEH-PPV and AZO/MEH-PPV devices.

Sample	J_{sc} (mA/cm^2)	V_{oc} (V)	FF (%)	PCE (%)
AZO/MEH-PPV	0.321	0.264	28.19	0.03
Device with buffer layer	0.497	0.478	31.96	0.102

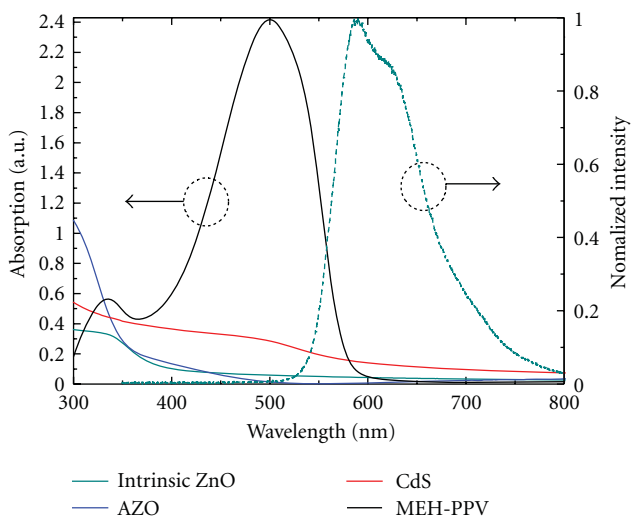

Figure 2: Absorption spectra of intrinsic ZnO, AZO, CdS, and MEH-PPV thin film (left). PL spectrum of MEH-PPV thin film (right).

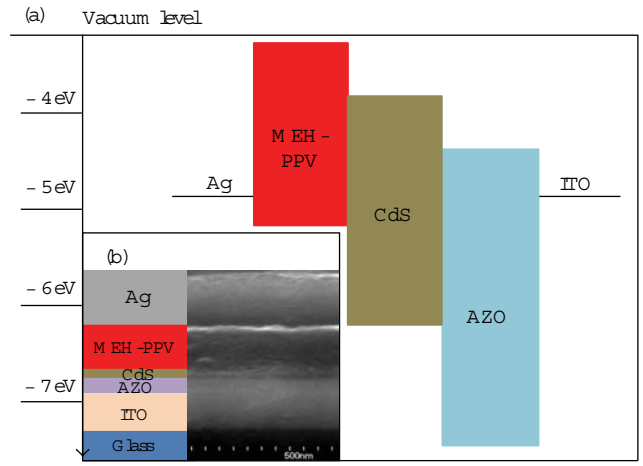

Figure 3: (a) An energy band diagram. (b) The AZO/CdS/MEH-PPV device and its cross-section SEM image.

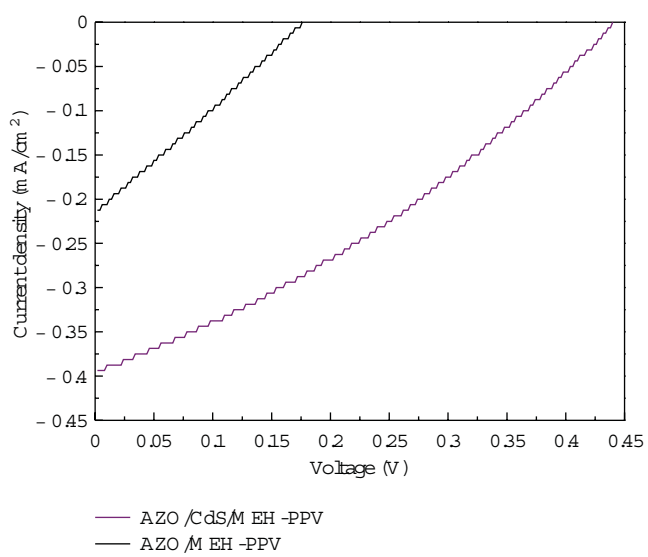

Figure 4: *I–V* characteristics of AZO/CdS/MEH-PPV and AZO/MEH-PPV devices.

energy band gap structure between the AZO and MEH-PPV (Figure 3(a)) in the device structure that was characterized by SEM (Figure 3(b)).

The *I–V* behaviors of AZO/MEH-PPV bilayers were compared with AZO/CdS/MEH-PPV devices (Figure 4 and Table 2). AZO layers of 3.29 eV optical band gap were used as they resulted in the highest energy conversion efficiency (Table 1). V_{oc} and J_{sc} were doubled in the device with a CdS buffer layer under simulated AM1.5 illumination (Figure 4). These results were attributed to the cascading energy band gap structure of the CdS between AZO and MEH-PPV. This CdS layer could be photoexcited to produce additional photocurrent to improve energy efficiency, similar to in the AZO and MEH-PPV layers [9].

4. Conclusions

The PV efficiency of MEH-PPV/AZO hybrids could be increased by controlling the optical band gap of the AZO thin film. Addition of a CdS buffer layer also significantly improved PV efficiency. These results demonstrate that controlling the optical band gap of ZnO and hybrid organic/inorganic solar cells with buffer layers can provide promising improvements to hybrid PV technologies.

Acknowledgments

This research was financially supported by the Ministry of Education, Science Technology (MEST) and the National Research Foundation of Korea through the Human Resource Training Project for Regional Innovation.

References

[1] S. D. Oosterhout, M. M. Wienk, S. S. van Bavel et al., "The effect of three-dimensional morphology on the efficiency of hybrid polymer solar cells," *Nature Materials*, vol. 8, no. 10, pp. 818–824, 2009.

[2] S. D. Oosterhout, L. J. Koster, S. S. van Bavel et al., "Controlling the morphology and efficiency of hybrid ZnO:polythiophene solar cells via side chain functionalization," *Advanced Energy Materials*, vol. 1, no. 1, pp. 90–96, 2011.

[3] W. U. Huynh, J. J. Dittmer, and A. P. Alivisatos, "Hybrid nanorod-polymer solar cells," *Science*, vol. 295, no. 5564, pp. 2425–2427, 2002.

[4] A. M. Peiro, P. Ravirajan, K. Govender et al., "Hybrid polymer/metal oxide solar cells based on ZnO columnar structures," *Journal of Materials Chemistry*, vol. 14, p. 1087, 2004.

[5] D. C. Olson, J. Piris, R. T. Collins, S. E. Shaheen, and D. S. Ginley, "Hybrid photovoltaic devices of polymer and ZnO nanofiber composites," *Thin Solid Films*, vol. 496, no. 1, pp. 26–29, 2006.

[6] S. H. Choi, H. Song, I. K. Park et al., "Synthesis of size-controlled CdSe quantum dots and characterization of CdSe-conjugated polymer blends for hybrid solar cells," *Journal of Photochemistry and Photobiology A*, vol. 179, no. 1-2, pp. 135–141, 2006.

[7] L. Wang, Y. Liu, X. Jiang, D. Qin, and Y. Cao, "Enhancement of photovoltaic characteristics using a suitable solvent in hybrid polymer/multiarmed CdS nanorods solar cells," *Journal of Physical Chemistry C*, vol. 111, no. 26, pp. 9538–9542, 2007.

[8] T. Yang, W. Cai, D. Qin et al., "Solution-processed zinc oxide thin film as a buffer layer for polymer solar cells with an inverted device structure," *Journal of Physical Chemistry C*, vol. 114, no. 14, pp. 6849–6853, 2010.

[9] D. Bi, F. Wu, M. Wang et al., "Device performance correlated with structural properties of vertically aligned nanorod arrays in polymer/ZnO solar cells," *Journal of Physical Chemistry C*, vol. 114, no. 32, pp. 13846–13852, 2010.

[10] M. Wang and X. Wang, "P3HT/ZnO bulk-heterojunction solar cell sensitized by a perylene derivative," *Solar Energy Materials and Solar Cells*, vol. 92, no. 7, pp. 766–771, 2008.

[11] T.-W. Zeng, Y. Y. Lin, H. H. Lo et al., "A large interconnecting network within hybrid MEH-PPV/TiO_2 nanorod photovoltaic devices," *Nanotechnology*, vol. 17, no. 21, p. 5387, 2006.

[12] E. D. Spoerke, M. T. Lloyd, E. M. McCready, D. C. Olson, Y.-J. Lee, and J. W. P. Hsu, "Improved performance of poly(3-hexylthiophene)/zinc oxide hybrid photovoltaics modified with interfacial nanocrystalline cadmium sulfide," *Applied Physics Letters*, vol. 95, no. 21, Article ID 213506, 2009.

[13] K. Kuriyama, T. Kato, and T. Tanaka, "Optical band gap of the filled tetrahedral semiconductor LiZnN," *Physical Review B*, vol. 49, no. 7, pp. 4511–4513, 1994.

[14] K. A. Jeon, J. H. Kim, W. Y. Shim, W. Y. Lee, M. H. Jung, and S. Y. Lee, "Magnetic and optical properties of $Zn_{1-x}Mn_xO$ thin films prepared by pulsed laser deposition," *Journal of Crystal Growth*, vol. 287, no. 1, pp. 66–69, 2006.

[15] P. P. Boix, J. Ajuria, G. Garcia-Belmonte et al., "Letter dynamics of bulk polymer heterostructure/electrolyte devices," *The Journal of Physical Chemistry Letters*, vol. 1, no. 22, pp. 3277–3282, 2010.

[16] H. J. Chen, L. Wang, and W. Y. Chiu, "Effects of annealing treatment on the properties of MEH-PPV/titania hybrids prepared via in situ sol-gel reaction," *European Polymer Journal*, vol. 43, no. 11, pp. 4750–4761, 2007.

Hindawi Publishing Corporation
International Journal of Photoenergy
Volume 2012, Article ID 748383, 5 pages
doi:10.1155/2012/748383

Review Article

Zinc-Based Semiconductors/Polymer Thin Films Junction for Photovoltaic Application

Souad Al-bat'hi, K. A. Buhari, and M. I. Latiff

Department of Manufacturing and Materials Engineering, Faculty of Engineering, International Islamic University Malaysia, Jalan Gombak, 53100 Kuala Lumpur, Malaysia

Correspondence should be addressed to Souad Al-bat'hi, su3ad@iium.edu.my

Received 16 August 2011; Accepted 21 December 2011

Academic Editor: Bhushan Sopori

Thin films of ZnO and ZnTe semiconductors were deposited on ITO conducting glass substrates by sputtering and electrodeposition techniques, respectively. On the other hand, thin films of ion conducting solid polymer electrolyte were prepared by solution cast technique. The polymer is a blend of 50 wt% polyethylene oxide and 50 wt% chitosan. To provide redox couple (I^-/I^{3-}), the polymer was complexed with ammonium iodide NH_4I with addition of few crystals of iodine I_2. Ammonium iodide NH_4I was added to the solution in different amounts (wt%) weight ratios to supply the charge carriers for the polymer electrolytes. The highest ionic conductivity of the polymer electrolyte was 1.18×10^{-5} S cm^{-1} at room temperature. Structural and optical properties of the semiconductor thin films were characterized by X-ray diffractometer and UV-Vis spectrophotometer. The XRD shows crystalline structures for both ZnO and ZnTe thin films. The UV-Vis shows direct energy gaps E_{ZnO} of 3.1 eV and E_{ZnTe} of 2.2 eV. The polymer film was sandwiched between the ZnO and ZnTe semiconductors to form ITO/ZnO/polymer/ZnTe/ITO double-junction photovoltaic cell, and the photovoltaic properties were studied. The highest open-circuit voltage V_{oc}, short-circuit current density J_{sc}, and fill factor FF of the fabricated cells are 0.5 V, 55 μA cm^{-2}, and 27%, respectively.

1. Introduction

The search for clean energy as an alternative to conventional energy sources is rapidly increasing in the recent past. Photovoltaic cells can be a promising candidate. Silicon has been the material of choice for photovoltaic designers because it is inexpensive and relatively well understood—and, of course, because it has properties that make it appropriate for photovoltaic applications [1, 2]. Recent advances in photovoltaic technology, however, have made other materials in combination attractive for the design of solar cells. Designers layer semiconductor materials with differing bandgap energies to result in higher conversion efficiencies. Although silicon can be used as one of these layers [3], alloys combining Group II elements with Group VI elements are enticing choices because of the wide range of bandgap energies they offer the designers [4]. The photovoltaic designer must maximize power by optimizing the tradeoffs between current and voltage. To maximize current, it is desirable to capture as many photons from the spectrum of solar radiation as possible. A small bandgap may then be selected so that even photons with lower radiation energies can excite electrons into the conduction band. However, the small bandgap results in a lower photovoltage. Additionally, the photons with higher energies will have much of their energy wasted as heat, instead of conversion into electrical energy. Alternatively, the designer can choose a higher bandgap, but then will not capture any photon energy less than that bandgap, resulting in a lower photocurrent and, in turn, reducing the output current of the device. Multijunction cells use a combination of semiconductor materials to more efficiently capture a larger range of photon energies. They do so without sacrificing photovoltage or creating losses of heat to the degree of single-junction cells.

Multiple layer solar cells consist of semiconductors with decreasing bandgaps. The top layers are designed to absorb higher-energy photons while transmitting lower-energy photons that are absorbed by lower layers of the cell [5].

Decades of research on single-junction thin film solar cells led to an efficiency of 19.2% [6]. Higher efficiencies

could be achieved by using stacked (multijunction)/tandem solar cell structures [7].

Employing wide and small bandgap semiconductors in a tandem solar cell reduces the energy losses inherent to single-junction cells. The wide bandgap subcell lowers the thermalization losses associated with absorption of high-energy photons in a small bandgap cell, and on the other hand the small bandgap subcell absorbs the low-energy photons for which a wide bandgap cell is not sensitive. Hence in a tandem solar cell the photon energy can be better preserved. Recently semiconducting organic molecules and polymers are being considered for tandem solar cells, resulting in power conversion efficiencies over 5% [8]. Multijunction solar cells have attracted many investigators in recent years. The last 2 decades have seen large improvements in III–V compound multijunction (MJ) solar cells. InGaP/InGaAs/Ge monolithic cascade 3-junction cells with newly recorded efficiency of 31.7% at AM 1.5 (1-sun) were achieved on Ge substrates [9]. III–V compound multijunction (MJ)/(tandem) solar cells have the potential for achieving high conversion efficiencies of over 50% and are promising for space and terrestrial applications [10]. Tandem junctions consisting of an amorphous silicon (a-Si:H) top cell and a microcrystalline silicon (μc-Si:H) bottom cell are of particular interest since by this concept stable solar energy conversion efficiencies of cells and modules well above 10% have been achieved [11].

This paper describes our recent progress in a zinc-based PV research. Alloys of Group II and Group VI elements as well as other related compounds that lend themselves well to the design of double-junction cells have been employed. Zinc oxide (ZnO) thin film is one of the typical transparent conducting oxides with a large bandgap of 3.36 eV suitable to the application for such hybrid photovoltaic devices [12]. The other semiconductor material used is zinc telluride (ZnTe) thin film. As it is a potentially low-cost semiconductor for switching devices and multijunction solar cells with a bandgap 2.26 eV [13]. Results on the performance of ITO/ZnO/PEO/ZnTe/ITO double-junction photovoltaic cells have been reported.

2. Experimental

2.1. Preparation of Semiconductor Thin Films. ZnO thin films were deposited on ITO conducting glass substrates, by radio frequency (rf) magnetron sputtering technique (MUE-ECO, ULVAC, Inc.) by using 5.06-cm-diameter ZnO target with 99.99% purity. The distance from the target to the substrate was 9.5 cm and the base pressure was 1×10^{-4} Pa [14, 15] whereas samples of ZnTe were prepared by electrodeposition technique [16]. The general approach of experimental and characterization details were described in an earlier work [17] and will not be repeated here. However, if excess of elemental chalcogenide is unavoidable in the ZnTe films, heat treatment allows its elimination.

2.2. X-Ray Diffraction. Structure and crystallography study of deposited ZnTe and ZnO thin films were examined by X-ray diffractometer (Shimadzu 6000), with operating voltage and current of 40 kV and 30 mA, respectively. The X-ray wavelength is 1.54 Å that proved the crystalline phase formation of cubic ZnTe and hexagonal wurtzite ZnO structures.

2.3. UV-Vis Characterization. For the determination of the energy gap of ZnTe and ZnO samples, the best method is to study the absorption edge through the measurement of the absorption spectra by using UV-Vis spectrophotometer (Lambda 35) with scan speed of 240 nm/min that confirms energy bandgap of ~2.3 eV and 3.36 eV, respectively.

2.4. Preparation of Electrolyte. The electrolyte films were prepared by the solution cast technique. 0.25 g of PEO, polyethylene oxide (Aldrich), and 0.25 g chitosan (FLUKA) were dissolved in 1% acetic acid solution. Differing amounts of ammonium iodide (NH_4I), according to the weight percentage ratio required, were added to the different solutions containing the same amount of PEO and chitosan (Table 1). The solutions were continuously stirred until complete dissolution of the salt. To get the redox couple, I^-/I^{3-} some iodine (I_2) crystals were added to each of the solutions containing different amounts of NH_4I and mixed thoroughly. The solutions were then cast in different Petri dishes and left to dry to form films.

2.5. Impedance Measurements. The nearly dry films were removed from the Petri dishes, cut to the required size, and the impedance were measured using the HIOKI 3531-01 LCR Hi-Tester. Measurements were carried out over the frequency range from 50 Hz to 1 MHz. The conductivity σ of the electrolyte films were calculated from the following equation:

$$\sigma = \frac{t}{R_b A}, \tag{1}$$

where t is thickness of the polymer film and A is the electrolyte-electrode contact area and R_b is the bulk resistance. The bulk resistance value (R_b) was obtained from the plot (Figure 1) of negative imaginary impedance versus real impedance.

2.6. Device Assembly. Photovoltaic double-junction cells were constructed and assembled using an ITO/ZnO window electrode and ITO/ZnTe counter electrode. The polymer electrolyte film with the highest room temperature conductivity was sandwiched between the two electrodes as shown in Figure 2. The photovoltaic properties of cells configuration ITO/ZnO/Polymer/ZnTe/ITO were studied. Current density-voltage (J-V) characteristics for the determination of open circuit voltage, V_{oc} and short-circuit current density; J_{sc} was carried out under dark and illuminated conditions. The effective area of the cell exposed to the light was 0.07 cm^2. The fill factor (FF) can be calculated from the following equation:

$$\mathrm{FF} = \frac{J_{max} V_{max}}{J_{sc} V_{oc}}. \tag{2}$$

J_{sc} is the short-circuit current density (μA cm^{-2}), V_{oc} is the open-circuit voltage (mV), and J_{max} (μA cm^{-2}) and V_{max} (mV) are the maximum current density and maximum

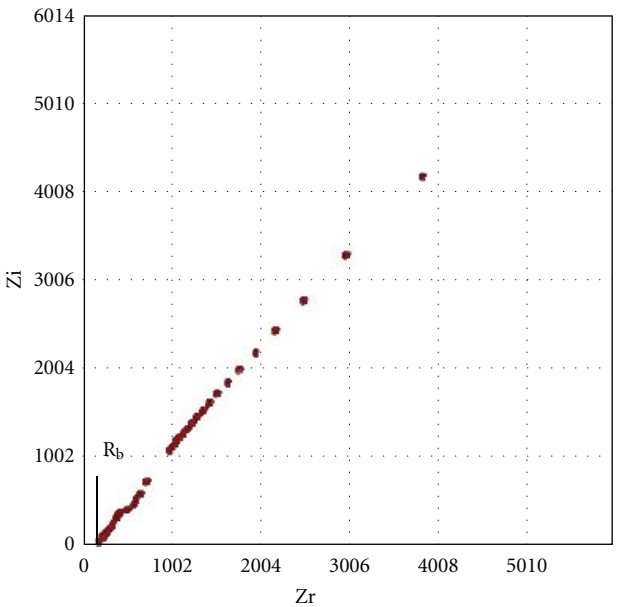

Figure 1: The Cole-Cole plot showing bulk resistance R_b of sample containing 45% ammonium iodide.

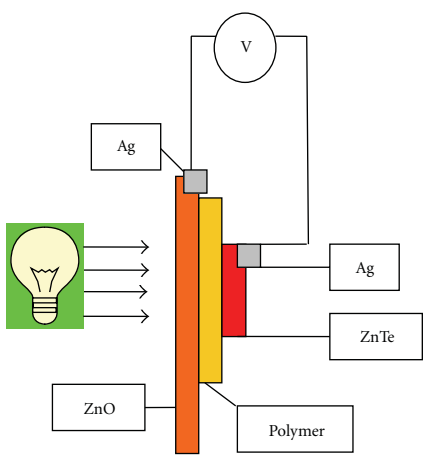

Figure 2: ZnO/polymer/ZnTe junction.

voltage in the J-V curve, respectively, at the point of the maximum power output.

In this work a neon lamp was used for photoillumination. Alnama et al. [18] observed optogalvanic (OG) transitions corresponding to near-UV region between 380 and 420 nm. The OG technique is a powerful spectroscopic tool that complements absorption spectroscopy. Zhu et al. [19] have reported 351 OG transitions in neon between 337 and 598 nm, and 223 of these OG transitions are associated with neon transition. Reddy and Venkateswarlu [20] recorded about 300 transitions in the OG spectrum of neon in the visible wavelength region, 410–670 nm. Thakur and Narayanan [21] observed two photon transitions from the metastable 3s state to higher ns and nd states of neon between 500 and 548 nm. These results show that the neon spectrum extends from the UV region and covers the visible range as well. Since the energy gap of ZnO and ZnTe films are ~3.3 eV and 2.2 eV, respectively, corresponding to a wavelength of 376 nm to 565 nm, the neon lamp can therefore be used to illuminate the fabricated cells. The wavelength above 565 nm corresponding to the energy gap of ZnTe will be transmitted and will not be absorbed by the electrons in the semiconductors. The photons with energy greater than the energy gap can produce electron-hole pairs but the excess energy can be lost as heat.

Table 1: The electrolyte, composition and its conductivity at room temperature.

Chitosan (g)	PEO (g)	NH_4I Wt. %	NH_4I (g)	σ (S cm^{-1})
0.25	0.25	0	0.000	$(5.17 \pm 1.7) \times 10^{-10}$
0.25	0.25	5	0.026	$(1.59 \pm 3.5) \times 10^{-10}$
0.25	0.25	10	0.055	$(2.35 \pm 0.9) \times 10^{-10}$
0.25	0.25	15	0.088	$(8.52 \pm 2.4) \times 10^{-9}$
0.25	0.25	20	0.125	$(1.84 \pm 0.5) \times 10^{-8}$
0.25	0.25	25	0.166	$(1.84 \pm 0.6) \times 10^{-8}$
0.25	0.25	30	0.214	$(9.21 \pm 2.6) \times 10^{-8}$
0.25	0.25	35	0.269	$(2.25 \pm 1.3) \times 10^{-7}$
0.25	0.25	40	0.333	$(9.5 \pm 1.6) \times 10^{-7}$
0.25	0.25	45	0.409	$(1.18 \pm 0.7) \times 10^{-5}$*
0.25	0.25	50	0.500	$(9.83 \pm 5.7) \times 10^{-6}$

*: referring to the highest conductivity at room temperature.

3. Results and Discussion

3.1. Electrolyte Conductivity. The different compositions of the electrolyte prepared in this study with their room temperature conductivity are given in Table 1 that shows the highest conducting sample, prepared by using 0.25 g PEO, 0.25 g chitosan, and 0.409 g NH_4I. Although the conductivity is not satisfactorily high enough, this sample was used to make the semiconductor/polymer/semiconductor double-junction. Figure 1 shows Cole-Cole plot for the highest conducting sample at room temperature. The initial increase in conductivity is attributed to an increase in the number of mobile ions. However, the conductivity is then decreased due to the formation of neutral ion pairs, as a result of ion association. The intercept of the plot with the real impedance axis represents the electrolyte bulk resistance R_b. It is observed that the value of R_b is decreasing for different compositions of the electrolyte prepared at room temperature, which lead to higher ionic conductivity, based on (1) in Section 2.5.

3.2. X-Ray Diffractogram. Figure 3 shows XRD pattern for ZnO thin film prepared at room temperature. The diffractogram exhibits peaks at $2\theta = 30.5°$ and $34.7°$. ZnO peaks are characteristic of the hexagonal form [22].

3.3. UV-Vis Spectrophotometry. To study the absorption edge through the measurement of the absorption spectra, we need to grow the ZnO samples onto an optically transparent

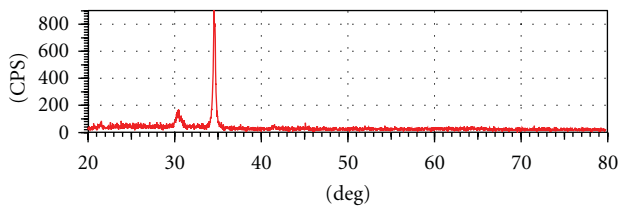

Figure 3: X-ray diffraction spectra of as-deposited ZnO films obtained at room temperature.

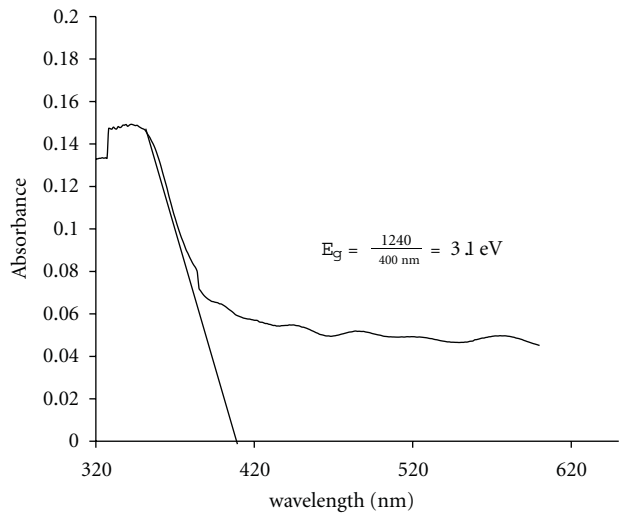

Figure 4: The absorption spectrum of ZnO thin film.

substrate, in the region of our interest. The best candidate is ITO coated glass, which is transparent in a spectral region that includes the visible wavelengths and extended to 320 nm in the ultraviolet. The energy gap value of the ZnO on ITO/glass is less than the expected room temperature energy gap reported for ZnO (E_g = 3.4-3.3 eV) [23, 24].

Figure 4 shows the result of the optical absorption spectrum of ZnO thin film sputtered on ITO/glass substrate. The extrapolation intersects with the wavelength axis at λ = 400 nm presenting the corresponding energy gap (E_g = 3.1 eV.) of ZnO thin film on ITO/glass at room temperature not far from the 3.4-3.3 eV reported by [23]. This result shows that the prepared film is suitable for use for photovoltaic cell applications as window materials.

3.4. Device Fabrication and Characterization. For device fabrication, the polymer electrolyte film with the highest room temperature conductivity was sandwiched between the ZnO and ZnTe semiconductors as shown in Figure 2.

The highest short-circuit current density; J_{sc}, open-circuit voltage V_{oc} and the fill factor FF obtained from the cell with configuration ITO/ZnO/Polymer/ZnTe/ITO are 55 μA cm^{-2}, 0.5 V, and 27% respectively. The *J-V* characteristics of the ZnO/polymer/ZnTe cells in the dark and under white light are shown in Figure 5. In the dark, the system operates as a diode, since it shows a diode-like characteristic and Schottky-type behavior. Under illumination the system operates as a solar cell.

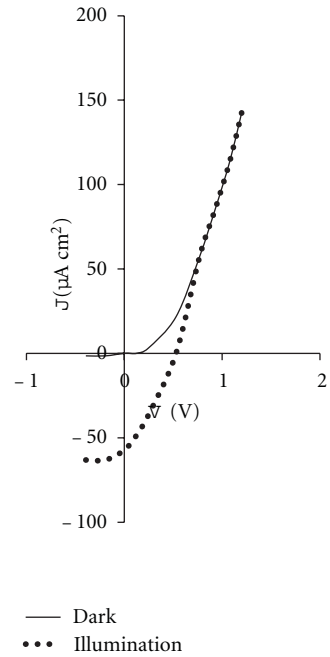

Figure 5: *J-V* Characteristic of ZnO/polymer/ZnTe in the dark and under illumination.

Excess iodine in the polymer electrolyte initiates I^-/I^{3-} redox couple. During preparation of the electrolyte film, the NH_4I salt dissociates into NH_4^+ and I^-.

Upon illumination, electrons in the valence band of ZnO semiconductor are exited into the conduction band due to absorption of photons energy. These electrons will flow to the counter electrode ZnTe through the external circuit. The less energetic photons that are not absorbed in the ZnO layer will penetrate the polymer electrolyte to the counter electrode ZnTe where it can be absorbed and free electrons will be released. Within the electrolyte a triiodide ion formed from interaction between a monoiodide ion and an iodine molecule:

$$I^- + I_2 \longrightarrow I^{3-}. \tag{3}$$

At the interface between electrolyte and ZnTe counter-electrode, triiodide ion is reduced by an electron to a monoiodine ion and an iodine atom:

$$I^{3-} + e^- \longrightarrow 2I^- + \frac{1}{2}I_2. \tag{4}$$

At the interface between electrolyte and ZnO electrode, the monoiodine ion releases the electron back to ZnO semiconductor by oxidation as shown below and the cycle continues:

$$I^- \longrightarrow \frac{1}{2}I_2 + e^-. \tag{5}$$

4. Conclusions

Double-junction photovoltaic cells of structure ITO/ZnO/PEO-chitosan/ZnTe/ITO were fabricated by using different

techniques. Sputtering for ZnO fabrication, electrodeposition for ZnTe, and solution cast technique for solid-state polymer electrolyte. Structural and optical characterization of ZnO and ZnTe exhibits hexagonal and cubic structures, respectively, and energy gap of 3.1 and 2.2 eV, respectively. Electrical characterization of the polymer electrolyte has shown highest conductivity of $1.18 \times 10^{-5}\,\mathrm{S\,cm^{-1}}$. Device performance has been measured in the dark and under illumination. We have shown that PEO-chitosan blend can host the redox I^-/I^{3-} couple for the operation of double-junction photovoltaic cells. The performance of the semiconductor/polymer electrolyte/semiconductor double-junction solar cell can still be improved by improving the electrolyte conductivity. The highest short-circuit current density; J_{sc}, open-circuit voltage V_{oc} and the fill factor FF obtained from the cell with configuration ITO/ZnO/polymer/ZnTe/ITO are $55\,\mu\mathrm{A\,cm^{-2}}$, 0.5 V and 27%, respectively. The low output current can be attributed to the low conductivity of the electrolyte.

References

[1] V. Badescu, "Simple optimization procedure for silicon-based solar cell interconnection in a series-parallel PV module," *Energy Conversion and Management*, vol. 47, no. 9-10, pp. 1146–1158, 2006.

[2] R. K. Ahrenkiel, "Recombination processes and lifetime measurements in silicon photovoltaics," *Solar Energy Materials and Solar Cells*, vol. 76, no. 3, pp. 243–256, 2003.

[3] X. Deng, "Study of triple-junction amorphous silicon alloy solar cells," *AIP Conference Proceedings*, vol. 462, pp. 297–302, 1998.

[4] T. Skotheim, "A tandem photovoltaic cell using a thin-film polymer electrolyte," *Applied Physics Letters*, vol. 38, no. 9, pp. 712–714, 1981.

[5] W. A. Daoud and M. L. Turner, "Effect of interfacial properties and film thickness on device performance of bilayer TiO_2-poly(1,4-phenylenevinylene) solar cells prepared by spin coating," *Reactive and Functional Polymers*, vol. 66, no. 1, pp. 13–20, 2006.

[6] K. Ramanathan, M. A. Contreras, C. L. Perkins et al., "Properties of 19.2% efficiency ZnO/CdS/$CuInGaSe_2$ thin-film solar cells," *Progress in Photovoltaics: Research and Applications*, vol. 11, no. 4, pp. 225–230, 2003.

[7] H. S. Ullal, K. Zweibel, and B. Von Roedern, "Polycrystalline thin film photovoltaics: research, development, and technologies," in *Proceedings of the 29th IEEE Photovoltaic Specialists Conference*, pp. 472–477, New Orleans, La, USA, May 2002.

[8] T. Ameri, G. Dennler, C. Lungenschmied, and C. J. Brabec, "Organic tandem solar cells: a review," *Energy & Environmental Science*, vol. 2, no. 4, pp. 347–363, 2009.

[9] M. Yamaguchi, "III-V compound multi-junction solar cells: present and future," *Solar Energy Materials and Solar Cells*, vol. 75, no. 1-2, pp. 261–269, 2003.

[10] M. Yamaguchi, T. Takamoto, and K. Araki, "Super high-efficiency multi-junction and concentrator solar cells," *Solar Energy Materials and Solar Cells*, vol. 90, no. 18-19, pp. 3068–3077, 2006.

[11] J. Meier and S. Dubail, in *Proceedings of the 1st World Conference onPhotovoltaic Energy Conversion*, p. 409, Vienna, Austria, 1994.

[12] M. S. White, D. C. Olson, S. E. Shaheen, N. Kopidakis, and D. S. Ginley, "Inverted bulk-heterojunction organic photovoltaic device using a solution-derived ZnO underlayer," *Applied Physics Letters*, vol. 89, no. 14, Article ID 143517, 2006.

[13] B. M. Basol and V. K. Kapur, "Preparation of ZnTe thin films using a simple two-stage process," *Thin Solid Films*, vol. 165, no. 1, pp. 237–241, 1988.

[14] S. J. Lim, S. Kwon, and H. Kim, "ZnO thin films prepared by atomic layer deposition and rf sputtering as an active layer for thin film transistor," *Thin Solid Films*, vol. 516, no. 7, pp. 1523–1528, 2008.

[15] H. S. Yoon, K. S. Lee, T. S. Lee et al., "Properties of fluorine doped ZnO thin films deposited by magnetron sputtering," *Solar Energy Materials and Solar Cells*, vol. 92, no. 11, pp. 1366–1372, 2008.

[16] M. Neumann-Spallart and C. Königstein, "Electrodeposition of zinc telluride," *Thin Solid Films*, vol. 265, no. 1-2, pp. 33–39, 1995.

[17] S. A. Mohamad, W. J. Basirun, Z. A. Ibrahim, A. K. Arof, and M. Ebadi, "Structure and optical characterization of electrodeposited zinc selenide thin films," in *Proceedings of the International Conference on Advances in Materials and Processing Technology (AMPT '09)*, Kuala Lumpur, Malaysia, October 2009.

[18] K. Alnama, J. H. Fillion, and D. Gauyacq, "Rydberg transitions in neon observed by optogalvanic effect in the 830–870 and 380–420 nm regions," *Journal of Quantitative Spectroscopy and Radiative Transfer*, vol. 105, no. 1, pp. 139–147, 2007.

[19] X. Zhu, A. H. Nur, and P. Misra, "Laser optogalvanic wavelength calibration with a commercial hollow cathode iron-neon discharge lamp," *Journal of Quantitative Spectroscopy and Radiative Transfer*, vol. 52, no. 2, pp. 167–177, 1994.

[20] B. R. Reddy and P. Venkateswarlu, "Optogalvanic effect in neon hollow cathode discharge," *Optics Communications*, vol. 85, no. 5-6, pp. 491–499, 1991.

[21] S. N. Thakur and K. Narayanan, "Rydberg series in the visible two-photon optogalvanic spectrum of neon," *Optics Communications*, vol. 94, no. 1–3, pp. 59–65, 1992.

[22] S. Sanchez, C. Lucas, G. S. Picard, M. R. Bermejo, and Y. Castrillejo, "Molten salt route for ZnSe high-temperature electrosynthesis," *Thin Solid Films*, vol. 361, pp. 107–112, 2000.

[23] J. S. Tawale, K. K. Dey, R. Pasricha, K. N. Sood, and A. K. Srivastava, "Synthesis and characterization of ZnO tetrapods for optical and antibacterial applications," *Thin Solid Films*, vol. 519, no. 3, pp. 1244–1247, 2010.

[24] M. Purica, E. Budianu, E. Rusu, M. Danila, and R. Gavrila, "Optical and structural investigation of ZnO thin films prepared by chemical vapor deposition (CVD)," *Thin Solid Films*, vol. 403-404, pp. 485–488, 2002.

Hindawi Publishing Corporation
International Journal of Photoenergy
Volume 2012, Article ID 391213, 7 pages
doi:10.1155/2012/391213

Research Article

A New Approach for Optimal Sizing of Standalone Photovoltaic Systems

Tamer Khatib,[1] Azah Mohamed,[1] K. Sopian,[2] and M. Mahmoud[3]

[1] *Department of Electrical, Electronic & System Engineering, Faculty of Engineering & Built Environment, National University of Malaysia, Selangor, 43600 Bangi, Malaysia*
[2] *Solar Energy Research Institute, National University of Malaysia, Selangor, 43600 Bangi, Malaysia*
[3] *Department of Electrical Engineering, Engineering Faculty, An-Najah National University, Nablus 97300, Palestine*

Correspondence should be addressed to Tamer Khatib, tamer_khat@hotmail.com

Received 16 August 2011; Accepted 16 November 2011

Academic Editor: Peter Rupnowski

This paper presents a new method for determining the optimal sizing of standalone photovoltaic (PV) system in terms of optimal sizing of PV array and battery storage. A standalone PV system energy flow is first analysed, and the MATLAB fitting tool is used to fit the resultant sizing curves in order to derive general formulas for optimal sizing of PV array and battery. In deriving the formulas for optimal sizing of PV array and battery, the data considered are based on five sites in Malaysia, which are Kuala Lumpur, Johor Bharu, Ipoh, Kuching, and Alor Setar. Based on the results of the designed example for a PV system installed in Kuala Lumpur, the proposed method gives satisfactory optimal sizing results.

1. Introduction

Based on the fact that PV systems are clean, environment friendly, and secure energy sources, PV system installation has played an important role worldwide. However, the drawback of PV system is the high capital cost compared with conventional energy sources. Currently, many research works are carried out focusing on optimization of PV systems so that the number of PV modules, capacity of storage battery, capacity of inverter, and PV array tilt angle can be optimally selected. PV system size and performance strongly depend on metrological variables such as solar energy and ambient temperature, and therefore, to optimize a PV system, extensive studies related to the metrological variables have to be done [1].

The research works related to PV system size optimization can be found in [2–14]. In [2], the probabilistic approach is used to optimize PV systems by considering a probability function which is expressed as the probability of losing load in terms of storage battery, PV array energy output, and load demand. Therefore, the determination of optimum storage battery is done based on the reliability of the PV system, and the optimum PV system array size is calculated using the worst month method. In [3], an optimum design for PV systems in Sudan is developed based on a clear sky model for global solar prediction in Sudan. The optimization of PV panel tilt angle was done based on Jordan and Liu model for solar energy incident on a tilt surface. However, to optimize the array and storage sizes, it is assumed that the stored energy in a storage battery is equal to the difference between the load power and PV array generated power. In Europe, optimization of PV system is done for three sites in which optimization considers sizing curves derivation and minimum storage requirement [4]. To avoid any load interruption, the PV array size is designed based on the worst monthly average of solar energy. As for finding the minimum storage requirement, the same method used in plotting sizing curves is used, and the minimum storage requirement is calculated for each year of the used historical data. In [5], a PV system model is developed to optimize its size based on a well-defined solar energy potential and load. The developed model contains models for PV array, storage battery, and charge regulator. However, the optimization considers the combined minimum cost with minimum loss of load probability. In [6], optimization of PV systems in Algeria is implemented by dividing the regions into four zones using the sky clearness index. The optimization of PV systems is based on loss of load probability calculated

using the daily solar energy. After calculating the loss of load probability values, sizing curves for 12 sites in Algeria have been generated using a simulation program.

Optimization of PV systems in Greece has been done based on zero load rejection condition which investigates that the desired PV system is always able to supply load without any cutoffs [7]. The simulation program called as the "PHOTOV-III" is used to set the number of PV modules and capacity of battery based on load demand. In the simulation, the number of PV modules is fixed while the battery capacity value is kept changing based on load demand until zero load rejection. After that, the number of PV module is increased, and the simulation is repeated. The simulation generates sizing curves based on zero load rejection condition. In [8], optimization of PV systems in Delhi is done using the loss of power probability. A defined load and daily solar energy has been used to calculate the loss of power probability. Then sizing curve is generated based on the calculated loss of power probability. The number of PV modules and battery capacity are also evaluated based on the minimum cost. An analytical method for sizing of PV systems based on the concept of loss of load probability is also developed [9]. The method considers the standard deviation of loss of load probability and another two new parameters: annual number of system failures and standard deviation of annual number of failures. The optimization of PV array tilt angle is also done so as to maximize the collected yield. In [10], optimization of standalone PV systems in Iran is presented using the available daily global solar radiation determined from cloud cover. Here, the optimization of PV system considers the optimum tilt angle for the solar panels in Iran. After finding the optimum tilt angle, the size of PV system for a specific load demand is calculated using the worst month method. Optimization of PV systems in Spain and North America has been presented in [11, 12] by using a regression model for calculating PV array capacity. This model is represented by a linear equation in terms of mean yearly of global solar energy, minimum value of monthly global solar energy, minimum value of monthly clearness index, and the variability of monthly daily solar energy. The variability of monthly daily solar energy is defined as the difference between mean yearly of global solar energy and minimum value of monthly global solar energy divided by the mean yearly of global solar energy. To validate the accuracy of the developed model, the output results of the model are compared with the method for generating sizing curves [11, 12]. In [13], an optimization method for PV system based on observed time series of solar radiation has been presented. Here, the sizing curve is constructed based on the three climate zones in UK, and a curve-fitting method considering an exponential function is applied so as to define the optimum sizes of PV array and battery storage.

Optimal sizing of a standalone PV system in Kuala Lumpur, Malaysia has been presented in [14]. The optimization method considers three steps in which the first step involves estimation of PV array output based on one-year solar energy records. It is assumed that the output energy of a PV array is a function of peak sun shine hours, ambient temperature, and wire and dust losses. The second step is estimating the daily status of the battery storage which is done based on the previous amount of the stored energy, PV array output energy, load energy demand, battery's efficiency, and inverter's efficiency. In the third step, the loss of load probability is defined, and then the system cost is formulated in terms of the cost of PV array, batteries, and other components. However, the system cost equation is partially derived and has to be solved graphically. Thence, the plotted graph contains two lines; one represents the loss of load probability while the other line results from the partial derivate of the system cost equation. The tangent of these two lines gives the optimum size of PV. However, this method [14] has several disadvantages, such that, the sizing curve has to be constructed for each particular load, uses graphical solution rather than a precise formula to calculate the optimum PV size, and determines optimal PV sizing for Kuala Lumpur region only and do not consider other regions in Malaysia. To overcome these limitations, the proposed research attempts to derive optimization formulas for a standalone PV system that can be applied for the whole of Malaysia. These formulas are useful for calculating the optimum PV array and battery storage capacity based on the desired loss of load probability without having to use graphical solution. This work uses the long term solar energy data (1975–2004) provided by the Solar Energy Research Institute (SERI), Universiti Kebangsaan Malaysia (UKM).

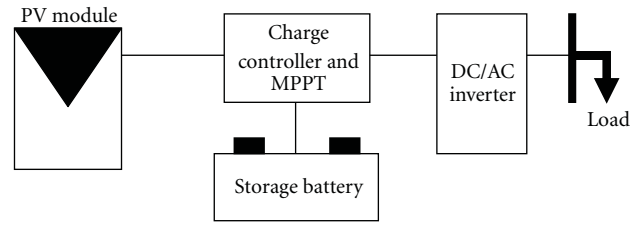

Figure 1: Typical PV system components.

2. Energy Flow Analysis for a Standalone PV System

Figure 1 shows a typical PV system consisting of a PV module/array, power conditioner such as charge controller or maximum power point tracking controller, storage batteries, inverter, and load.

In general, PV array collects energy from the sun and converts it to DC current. The DC current flows through a power conditioner to supply load through an inverter. The daily output or energy produced by a PV module/array is given by

$$E_{\mathrm{PV}} = A_{\mathrm{PV}} * E_{\mathrm{sun}} * \boldsymbol{\eta}_{\mathbf{PV}} \quad \boldsymbol{\eta}_{\mathbf{inv}} \quad \boldsymbol{\eta}_{\mathbf{wire}}, \tag{1}$$

where Apv is the area of the PV module/array and E_{sun} is daily solar irradiation. η_{PV}, η_{inv}, and η_{wire} are efficiencies of PV module, inverter, and wires, respectively.

The energy at the front end of a PV system or at the load side is given by

$$\text{Energy difference} = \sum_{i=1}^{366} (E_{\text{PV}} - E_L), \tag{2}$$

where E_L is the load energy demand.

The result of (2) is that it may be either positive ($E_{\text{PV}} > E_L$) or negative ($E_{\text{PV}} < E_L$). If energy difference is positive then there is an excess in energy (EE), while if it is negative then there will be an energy deficit (ED). The excess energy is stored in batteries in order to be used in case of energy deficit. Meanwhile, energy deficit can be defined as the disability of the PV array to provide power to the load at a specific time. The annual energy amount supposed to be stored in the storage battery is given by

$$E_B = \text{Energy excess} - \text{Energy deficit}\ \boldsymbol{\eta}_{\textbf{charge}}, \tag{3}$$

where $\boldsymbol{\eta}_{\textbf{charge}}$ is the charging efficiency of a storage battery.

Using (3), the expected daily storage battery capacity, C_B, can be calculated as follows:

$$C_B = \frac{E_B}{366}. \tag{4}$$

3. Proposed Optimization Method

In designing PV systems, it is important to know the power supply availability. 100% availability of a power supply means that the power supply is able to cover load demand in a year without any interruptions. On the other hand, 0.0% availability of a power supply means that the power supply is not able to cover load demand in a year at all. This means that high PV systems availability leads to high-reliability and vice versa. However, high-reliability PV systems incur high initial cost, and, therefore, it is not feasible to design PV systems with very high availability rates. The availability of a PV system is expressed in a statistical value which is the loss of load probability (LLP). LLP is the ratio of annual energy deficits to annual load demand, and it is given by

$$\text{LLP} = \frac{\sum_{i=1}^{366} \text{Energy deficits}_i}{\sum_{j=1}^{366} \text{Energy demand}_j}. \tag{5}$$

To generalize the proposed optimization, the following parameters are defined for PV array and battery storage sizing as follows:

$$C_A = \frac{C_{\text{PV}}}{L}, \qquad C_s = \frac{C_B}{L}, \tag{6}$$

where C_B, C_{PV}, and L are battery capacity at specific load, PV array capacity at specific load, and load, respectively.

Considering that the relation between C_A and LLP is exponential while the relation between C_A and C_S is linear [2–14], the following formulas are derived for optimum values of C_A and C_S

$$\text{optimum } C_A = c_1 e^{C_2 \text{LLP}} + c_3 e^{C_4 \text{LLP}}, \qquad \text{optimum } C_s = c_5 + c_6 C_A. \tag{7}$$

Figure 2 shows the proposed optimization algorithm in which the optimization process starts with defining some constants and initials such as load demand, PV efficiency, inverter efficiency, wire efficiency, and charging efficiency. Then a series of daily solar irradiation for the targeted site is obtained. This series must be calculated based on long historical data in order to achieve an accurate PV system size. However, after defining the load demand (Wh/day), a range of PV array area must be set. Each value of PV array area will generate different values of output energy using (1). From each PV array area value, C_A is then calculated. Subsequently, the energy difference is calculated using (2). During the calculation of energy difference, arrays of EE and ED values will be constructed. At specific PV array area, LLP, C_s, and C_A are calculated and stored in arrays. This loop will be repeated till the max range of PV array area is reached. Finally, plots of LLP versus C_A and C_s versus C_A are constructed, and from these plots, curve-fitting equations are derived using the MATLAB fitting toolbox so as to derive C_A as a function of LLP and C_s as a function of C_A as described in (7).

4. Results and Analysis

The proposed method for optimizing PV systems has been applied for five sites in Malaysia, namely, Kuala Lumpur, Johor Bharu, Ipoh, Kuching, and Alor Setar. The long solar energy term data between the year 1975 to 2005 for these sites have been used for this purpose. Figure 3 shows the plots of C_A versus LLP for the five sites while Figure 4 shows the relation between C_s versus C_A.

The MATLAB fitting toolbox is used to fit the curves which are plotted in Figures 3 and 4. Table 1 shows the coefficients of (7) for the chosen sites.

4.1. Case Study Based on Malaysian Weather Profile. The optimal sizing of PV system which considers the capacities of PV array and battery storage using the proposed method is compared to the method in [14] as both methods are applicable for PV systems installed in Malaysia. Using the data for daily load demand (2.215 kWh/day), loss of load probability (0.01), and location coordinate (Kuala Lumpur), the method in [14] obtained the optimum PV array and battery storage sizes of 720 Wp and 135 Ah, respectively, with a LLP of 0.01. Similar data of daily load demand (2.215 kWh/day), loss of load probability (0.01), and location coordinate (Kuala Lumpur) are also used to determine the optimal sizing of PV system using the proposed method. Using the coefficient values for Kuala Lumpur as shown in Table 1, the calculated optimum C_A and C_S are 2.02 and 0.793, respectively. This means that the optimum ratings for the PV array and battery storage of the proposed method are 725 Wp and 146 Ah, respectively. It is noted that the

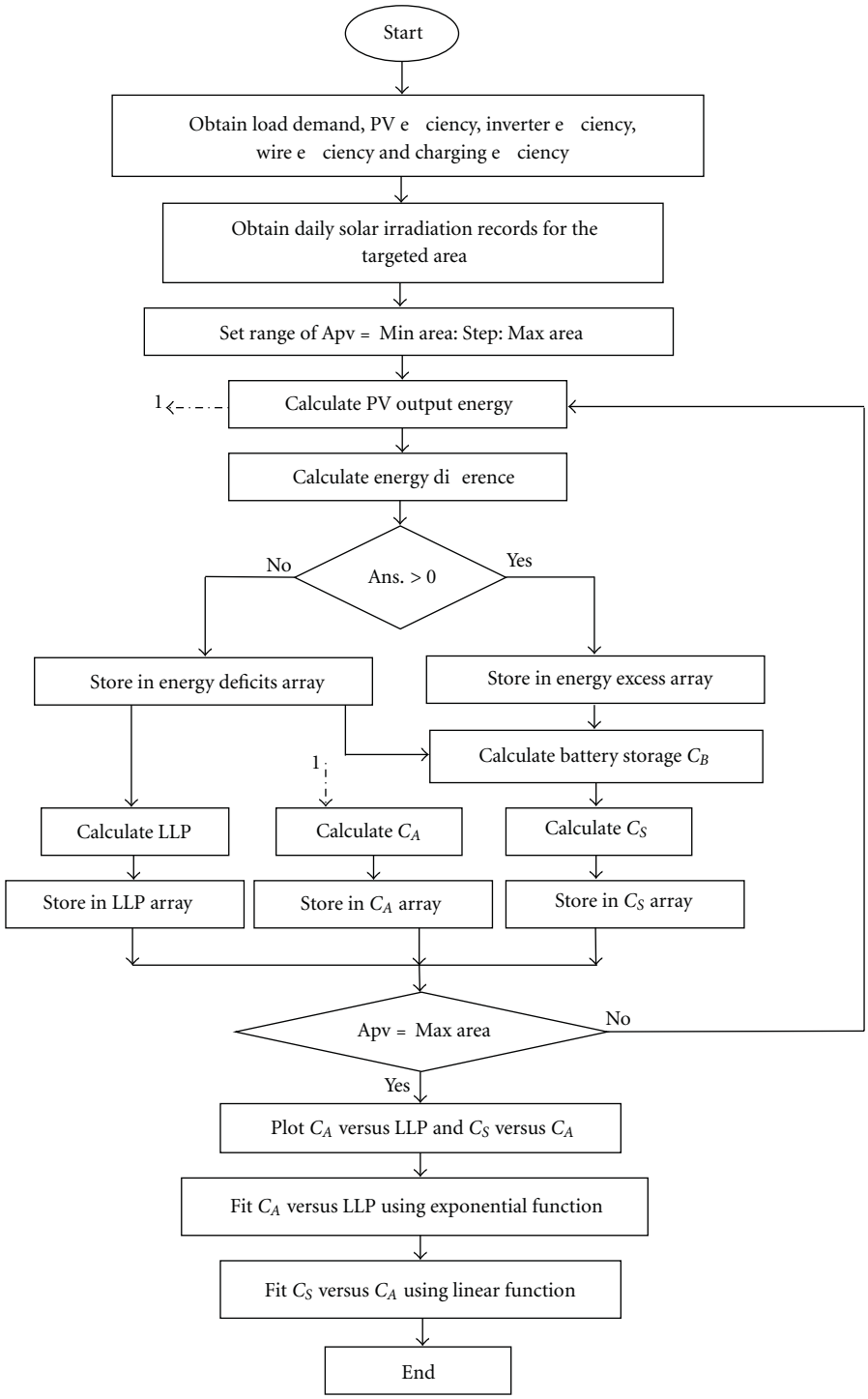

Figure 2: Proposed optimization algorithm.

optimum ratings for the PV array and battery storage of the proposed method and the method in [14] are comparable except that the optimum battery storage capacity is slightly higher than that in [14]. The difference in this value is due to different solar energy data used in which in [14] only one year (1999) solar energy data is used while in the proposed method, long term solar energy data (1975–2005) have been used.

The proposed method is considered to be better than the method in [14] due to several reasons; firstly, the method in [14] deals with data for Kuala Lumpur only while the proposed method deals with five main sites in Malaysia. Secondly, the proposed method provides two simple formulas to find the optimum size of a PV system while the method in [14] is based on plotting sizing curves and then search for the minimum cost using the first derivative of system's cost

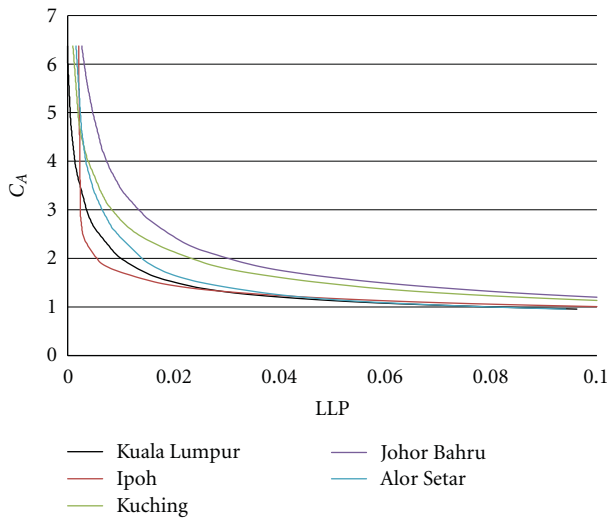

Figure 3: Optimum PV array sizes at different LLPs.

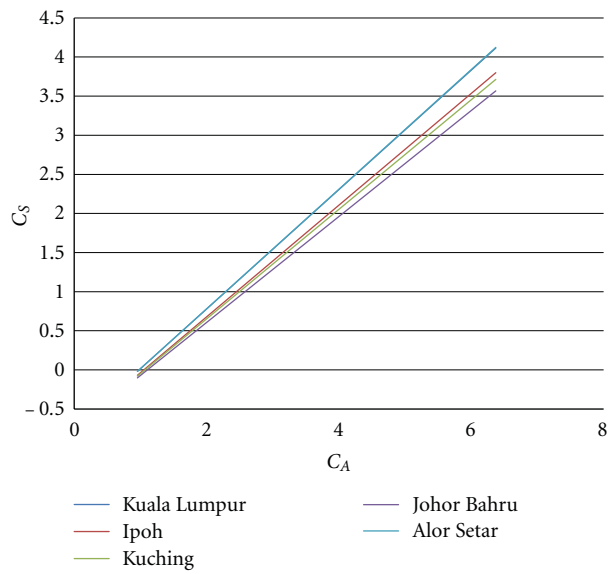

Figure 4: Optimum battery storage sizes (C_s) at different PV array sizes (C_A).

Table 1: Coefficients C1–C6 of (7) after curve fitting.

	C1	C2	C3	C4	C5	C6
Kuala Lumpur	2.355	−140	1.529	−5.938	0.7637	−0.75
Johor Bharu	4.117	−120	2.433	−8.310	0.6776	−0.75
Ipoh	1.151	−142	1.509	−4.858	0.7140	−0.75
Kuching	3.182	−167	2.426	−9.817	0.7000	− 0.75
Alor Setar	3.613	−142	1.667	−7.051	0.7648	−0.75
Average	2.884	−142	1.913	−7.195	0.7240	−0.75

equation. Thirdly, the proposed method is valid for all loads, while the method in [14] deals with each load as an individual case. In [14], to determine the optimum PV system size for a specific load, a sizing curve based on the provided

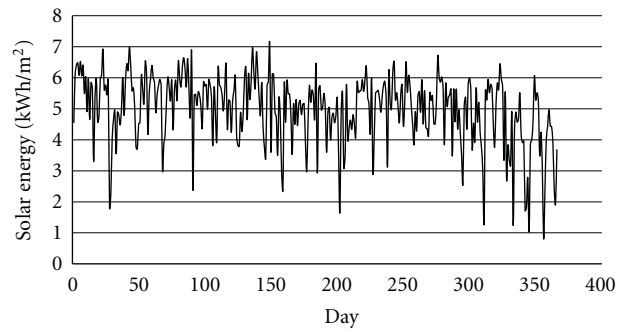

Figure 5: Daily solar energy for Kuala Lumpur.

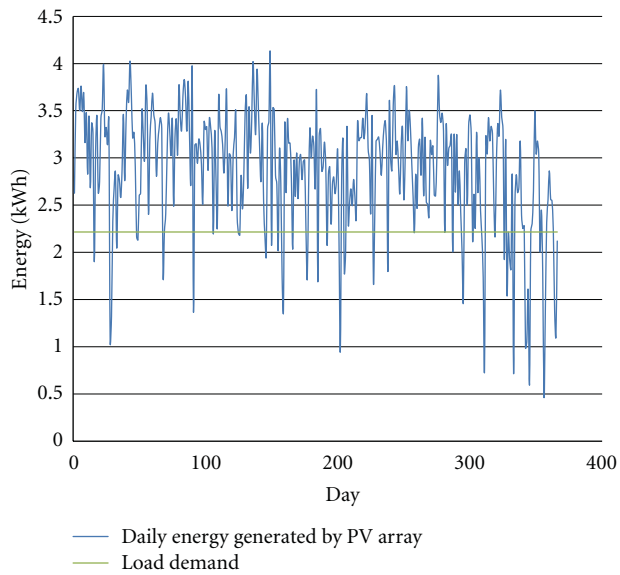

Figure 6: Generated energy by the designed PV array.

load should be plotted. That's to say, the method in [14] needs to perform simulation for each specific load, while the optimum size of PV system by the proposed method can be easily determined by using the two simple equations of (7).

4.2. Designed PV System Analysis. The designed PV system is based on the optimum ratings for the PV array and battery storage of the proposed method which are 725 Wp and 146 Ah, respectively, and the average daily solar energy data for Kuala Lumpur as shown in Figure 5. The annual average solar energy is 4.9 kWh/m^2 with December having the worst solar energy average, while May has the best solar energy average in one year. The energy produced by the designed PV array is then calculated with respect to the load, and the energy is plotted as shown in Figure 6. The average energy generated by the designed PV array is 2.9 kWh. This energy is supposed to cover the load demand while the excess energy is stored in the battery. In the case of fully charged batteries, the excess energy will be dumped using a dumping load. Figure 7 shows the energy balance of the system in which negative energy indicates that the battery is used to supply the load,

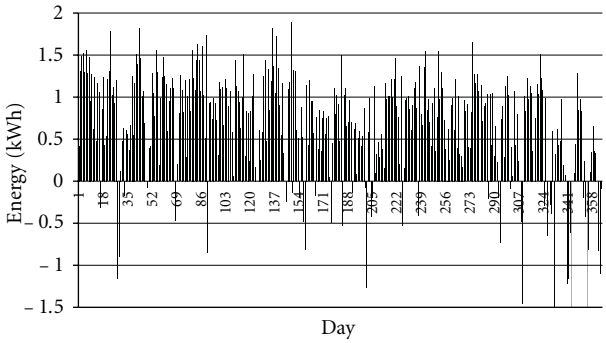

Figure 7: Energy balance for designed PV system.

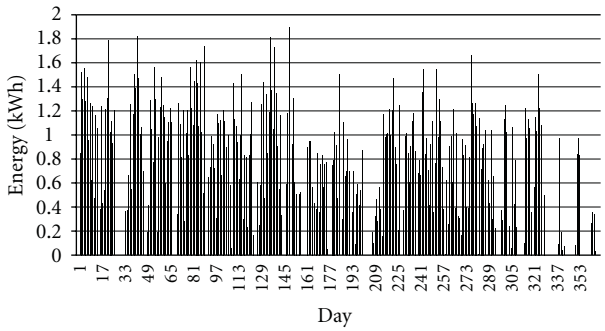

Figure 8: Dumped energy for the designed PV system.

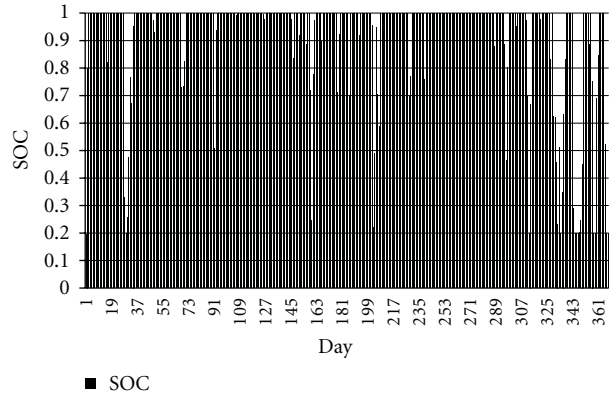

Figure 9: Battery storage SOC for the designed PV system.

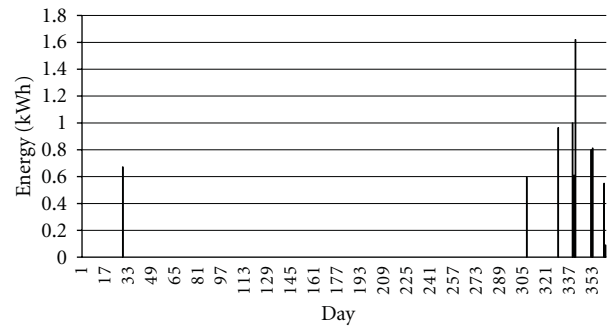

Figure 10: Loss of load days for the designed PV system.

while the positive net energy indicates that this energy has to be stored in the battery or dumped.

Figure 8 shows the net energy which needs to be dumped. The daily average of dumped energy is 0.67 kWh while the sum of the dumped energy per year is 244 kWh. Dumping this daily energy of 0.67 kWh may be considered feasible than storing it in a battery considering that the stored energy in a battery with 80% charging efficiency is 0.54 kWh/day. The cost of dumped energy per year based on kWh unit price is 65$ per year. Installing battery storage to save this amount of energy may cost more than dumping since the price of Ah/12 V of battery storage is about 2.5–3.5 $, and furthermore battery storage needs changing every 4 to 5 years. Therefore, the most appropriate solution to the problem of net energy is to add a load which does not require a stable energy demand. A suitable load for this purpose is a water pump which is used for pumping domestic water in which the amount of pumped water depends on the excess energy.

Figure 9 shows the state of charge (SOC) of the battery storage for a year (1–366 days). The SOC value of 1.0 indicates that the battery is not used while SOC value is less than 1.0 means that the battery is used. From the figure, the battery supplies power to the load for 79 days which is about 22% of the days in a year. From the 79 days, the battery reaches its allowable minimum SOC (0.2) twelve times, while SOC value greater than 0.6 is about 62% of the 79 days. When the SOC reaches a value of 0.2, some load will be lost, and this is the loss of load days as shown in Figure 10. The figure shows the percentage of covered load demand during loss of load days. During a year, the load is lost for 10 days which means 2.7% of a year. However, most of load loss incidences happen in December and November. Form the figure, in most load loss days, 60% of load demand is covered, and the loss of load probability is 0.95%.

5. Conclusion

A new method for optimal sizing of a standalone PV system has been presented. The capacity of PV array is optimally selected based on the desired loss of load probability, while the battery storage size is selected based on the optimum PV array capacity. The proposed method has been used to optimize PV systems at five sites in Malaysia. However, to ensure the validity of the proposed method, a designed example of a previous work is selected as a benchmark. The proposed method gives very close values to the taken benchmark method, but the proposed method is better than the benchmark method because of its simplicity and wide validity.

References

[1] T. Khatib, "A review of designing, installing and evaluating standalone photovoltaic power systems," *Journal of Applied Sciences*, vol. 10, no. 13, pp. 1212–1228, 2010.

[2] P. Arun, R. Banerjee, and S. Bandyopadhyay, "Optimum sizing of photovoltaic battery systems incorporating uncertainty through design space approach," *Solar Energy*, vol. 83, no. 7, pp. 1013–1025, 2009.

[3] O. E. Elsheikh Ibrahim, "Sizing stand-alone photovoltaic systems for various locations in Sudan," *Applied Energy*, vol. 52, no. 2-3, pp. 133–140, 1995.
[4] A. Fragaki and T. Markvart, "Stand-alone PV system design: results using a new sizing approach," *Renewable Energy*, vol. 33, no. 1, pp. 162–167, 2008.
[5] G. B. Shrestha and L. Goel, "A study on optimal sizing of stand-alone photovoltaic stations," *IEEE Transactions on Energy Conversion*, vol. 13, no. 4, pp. 373–378, 1998.
[6] A. Hadj Arab, B. Ait Driss, R. Amimeur, and E. Lorenzo, "Photovoltaic systems sizing for Algeria," *Solar Energy*, vol. 54, no. 2, pp. 99–104, 1995.
[7] J. K. Kaldellis, "Optimum technoeconomic energy autonomous photovoltaic solution for remote consumers throughout Greece," *Energy Conversion and Management*, vol. 45, no. 17, pp. 2745–2760, 2004.
[8] N. D. Kaushika, N. K. Gautam, and K. Kaushik, "Simulation model for sizing of stand-alone solar PV system with interconnected array," *Solar Energy Materials and Solar Cells*, vol. 85, no. 4, pp. 499–519, 2005.
[9] R. Posadillo and R. López Luque, "Approaches for developing a sizing method for stand-alone PV systems with variable demand," *Renewable Energy*, vol. 33, no. 5, pp. 1037–1048, 2008.
[10] J. Samimi, E. A. Soleimani, and M. S. Zabihi, "Optimal sizing of photovoltaic systems in varied climates," *Solar Energy*, vol. 60, no. 2, pp. 97–107, 1997.
[11] M. Sidrach-de-Cardona and L. M. López, "A simple model for sizing stand alone photovoltaic systems," *Solar Energy Materials and Solar Cells*, vol. 55, no. 3, pp. 199–214, 1998.
[12] M. Sidrach-de-Cardona and L. Mora López, "A general multivariate qualitative model for sizing stand-alone photovoltaic systems," *Solar Energy Materials and Solar Cells*, vol. 59, no. 3, pp. 185–197, 1999.
[13] T. Markvart, A. Fragaki, and J. N. Ross, "PV system sizing using observed time series of solar radiation," *Solar Energy*, vol. 80, no. 1, pp. 46–50, 2006.
[14] W. X. Shen, "Optimally sizing of solar array and battery in a standalone photovoltaic system in Malaysia," *Renewable Energy*, vol. 34, no. 1, pp. 348–352, 2009.

Hindawi Publishing Corporation
International Journal of Photoenergy
Volume 2012, Article ID 171432, 8 pages
doi:10.1155/2012/171432

Research Article

Electrochemical Deposition of $Cu_xSn_yS_zO$ Thin Films and Their Application for Heterojunction Solar Cells

Yuki Nakashima and Masaya Ichimura

Department of Engineering Physics, Electronics and Mechanics, Nagoya Institute of Technology, Gokiso, Showa, Nagoya 466-8555, Japan

Correspondence should be addressed to Masaya Ichimura, ichimura.masaya@nitech.ac.jp

Received 11 July 2011; Accepted 26 November 2011

Academic Editor: Peter Rupnowski

$Cu_xSn_yS_zO$ (CTSO) thin films were deposited from an aqueous solution containing $CuSO_4$, $SnSO_4$, and $Na_2S_2O_3$ by electrochemical techniques. The deposited films were characterized by Auger electron spectroscopy, X-ray diffraction, and optical transmission spectroscopy. The photoelectrochemical measurement showed that the films have p-type conduction and photosensitivity. ZnO/CTSO heterojunction solar cells were fabricated. Rectification properties were observed, and the cell showed an efficiency of 4.9×10^{-3}% under AM1.5 illumination.

1. Introduction

For heterojunction solar cells, compound semiconductors composed of cheap and nontoxic elements are strongly desired. For an absorption layer, CdTe and $CuInSe_2$ are popular but their constituent elements are toxic (Cd, Se) or not abundant (Te, In, Se). Cu_xO (x = 1,2) and SnS are considered as promising because of their suitable band gap and p-type conduction. In addition, their constituent elements are all nontoxic and abundant. There are several reports on solar cells based on Cu_xO [1–4] and SnS [5–10]. Their thin films have been deposited by various techniques, such as evaporation, spray pyrolysis, chemical techniques, and sulfurization or oxidation of metal, and the highest efficiency reported so far is about 1.3% for both the materials [1, 7]. Recently, Cu_2ZnSnS_4 was successfully applied for the absorber layer [11, 12], which has evoked interest for new multinary compounds and alloys with a narrow band gap and p-type conduction.

In this paper, we deposit a quaternary alloy $Cu_xSn_yS_zO$ (CTSO) and apply it for solar cells for the first time. CTSO can be considered as a mixture of Cu_xO and SnS, and we may be able to tune its properties by controlling the composition values x, y, and z. Thus CTSO will be potentially advantageous for absorption layers of heterojunction solar cells. To deposit CTSO films, we adopted electrochemical techniques. Electrochemical deposition (ECD) is a low-cost, simple technique, and suitable for large-scale deposition. It has been successfully used to deposit various semiconductors including Cu_xO [13–15] and SnS [16–18]. As a partner of CTSO in the heterojunction (the window or buffer layer), we selected ZnO. ECD of ZnO was well established [19, 20], and successful fabrication of ZnO/Cu_2O [21–23] and ZnO/SnS [24] solar cells by the electrochemical techniques has been reported. Therefore, ECD fabrication of ZnO/CTSO heterojunction solar cells is worth attempting. To discuss their solar cell characteristics, we evaluate the band offset at the ZnO/CTSO heterojunction using X-ray photoelectron spectroscopy (XPS).

2. Experimental Procedure

2.1. Film Deposition and Characterizations. For the $Cu_xSn_yS_zO$ deposition, we used an aqueous solution containing $CuSO_4$, $SnSO_4$, and $Na_2S_2O_3$. $CuSO_4$ concentration was set 10 mM and $Na_2S_2O_3$ concentration 100 mM, and $SnSO_4$ concentration was varied. pH was about 3 (unadjusted), and the solution amount is 50 mL. In an acidic

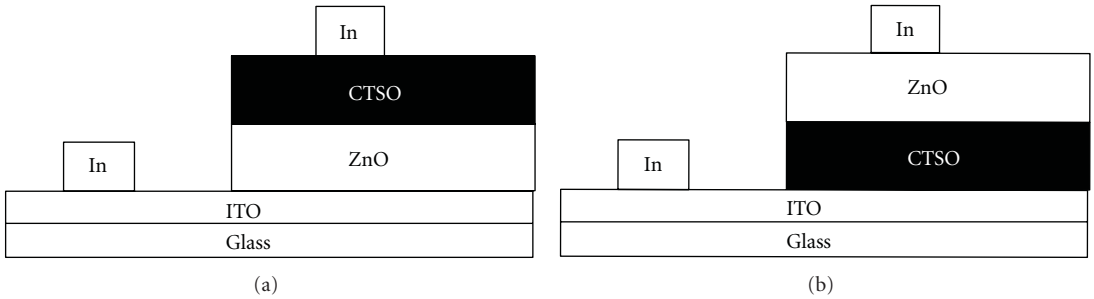

Figure 1: Schematic illustrations of (a) the CTSO/ZnO superstrate heterostructure and (b) the ZnO/CTSO substrate heterostructure. For the substrate structure (b), the light should be incident on the ZnO side through a transparent electrode. However, since the metal electrode was deposited on ZnO, the light was incident on the substrate side in the measurement.

solution, $S_2O_3{}^{2-}$ ions are expected to release S atoms by the following reaction [25]:

$$2H^+ + S_2O_3{}^{2-} = S + H_2SO_3. \quad (1)$$

The deposition solution was hazy because of sulfur colloids formed by the above reaction. A three-electrode cell was used with a saturated calomel electrode (SCE) as the reference electrode, an indium-tin-oxide (ITO)-coated glass sheet as the working electrode, and a platinum sheet as the counter electrode. The deposition potential is determined by cyclic voltametry (CV). By CV, we study the current response of the electrochemical system under the application of a triangular potential sweep. The cathodic scan is from 0 to −1.5 V versus SCE, and the anodic scan is from −1.5 to +0.5 V versus SCE with a scan rate of 20 mV/s. The compositional analysis was carried out by Auger electron spectroscopy (AES) using the model JEOL JAMP 7800 Auger microprobe at probe voltage 10 kV and current 2×10^{-8} A. An argon-ion sputtering with an acceleration voltage of 3 kV and a current of 20 mA was used to sputter the film surface. The x, y, and z values were calculated using standard Cu_2S, SnS, CuO, and SnO_2 compounds. Profile meter Accretech Surfcom-1400D was used to measure the thickness of the film. The surface morphology of the film was analyzed by scanning electron microscope (SEM, Hitachi S-2000S), keeping the acceleration voltage at 10 kV. The X-ray diffraction (XRD) measurement was carried out with the RIGAKU RINT-2000 diffractometer using Cu Kα_1 radiation. Furthermore, the photoconductivity of the film was examined by means of the photoelectrochemical (PEC) measurements. The PEC measurement was carried out using the same three-electrode cell as that used for the deposition. The deposited film was used as the working electrode, and a solution containing 100 mM $Na_2S_2O_3$ was used for the electrolyte. The backside of the sample was illuminated by pulsed light coming from an Xe lamp. The incident light was turned off and on mechanically every five seconds by putting and removing a barrier between the lamp and the sample, respectively [16, 17, 26]. The potential applied to the working electrode was scanned linearly first in the cathodic potential range (from 0 to −1 V versus SCE) and then the anodic potential range (from 0 to +1 V versus SCE).

2.2. Heterostructure Fabrication and Characterization. For any heterostructure solar cell, one can consider two different geometries, that is, superstrate and substrate structures. Thus we attempted to fabricate both the types of cells shown in Figure 1. Indium metal electrodes were deposited by thermal evaporation. The electrode size is 1 mm^2 and the distance between electrodes is 1 mm. ZnO was also deposited by the electrochemical technique. For the ZnO deposition, we used a solution containing 100 mM zinc nitrate [19]. The deposition temperature was 313 K. The deposition potential was a two-step pulse with $E_1 = -1.3$ V versus SCE, $E_2 = -0.6$ V versus SCE, and each pulse duration was 10 s. The deposition time was 3 min. For the photovoltaic characterization, current-voltage (I-V) characteristics were measured in the dark and under illumination. An Xe lamp with an AM1.5 radiation filter was used as the light source, and its radiation power was about 100 mW/cm^2. The glass side of the sample was illuminated for all the samples. For the substrate structure cell, the ZnO side should in fact be irradiated. However, we are not able to deposit transparent electrode but only a metal electrode on ZnO. Thus, since the ZnO side surface is shielded by the metal electrode, the substrate side was illuminated.

The band offset was evaluated using XPS PHI-5000 (ULVAC-PHI). The XPS spectra were measured using the Al Kα line as an X-ray source. We adopted the core-level spectroscopy technique [27]: we first measured the valence band maximum (VBM) with respect to the metal 3d or 4d level for the individual layer, and then measured the core level difference at the heterointerface by removing the upper layer by Ar-ion sputtering.

3. Results and Discussion

3.1. CTSO Films Deposition. We varied concentration of $SnSO_4$ from 3 to 30 mM as shown in Table 1. Figure 2 shows CV results for the solutions of condition 1 (3 mM $SnSO_4$) and condition 5 (30 mM $SnSO_4$). In the negative scans, reduction current peaks appeared, and we adopted the deposition potential around the reduction peak potential.

First, we attempted deposition using DC bias in all the solution conditions, keeping the deposition time 30 min. We obtained thin films except for the 30 mM $SnSO_4$ condition,

Table 1: Deposition conditions and the corresponding film thickness and composition. $CuSO_4$ concentration was 10 mM and $Na_2S_2O_3$ concentration 100 mM. Data in the parentheses are for the film fabricated by 5 min deposition. All other data are for the 30-min-deposited films. The deposition potential of condition 5 is a two-step pulse potential with $E_1 = -1.3$ V versus SCE, $E_2 = -0.6$ V versus SCE, and each pulse duration was 10 s.

	$SnSO_4$ [mM]	Deposition potential [V versus SCE]	Thickness [μm]	Cu : Sn : S : O
Condition 1	3	−0.80	0.50 (0.15)	1.7 : 0.084 : 0.13 : 1.0 (2.5 : 0.47 : 0.52 : 1.0)
Condition 2	6	−0.82	0.30	2.1 : 0.50 : 0.60 : 1.0
Condition 3	9	−0.85	0.35	2.1 : 0.49 : 0.79 : 1.0
Condition 4	12	−0.87	0.30	2.6 : 0.71 : 0.90 : 1.0
Condition 5	30	two-step pulse	2.5	0.97 : 0.68 : 1.3 : 1.0

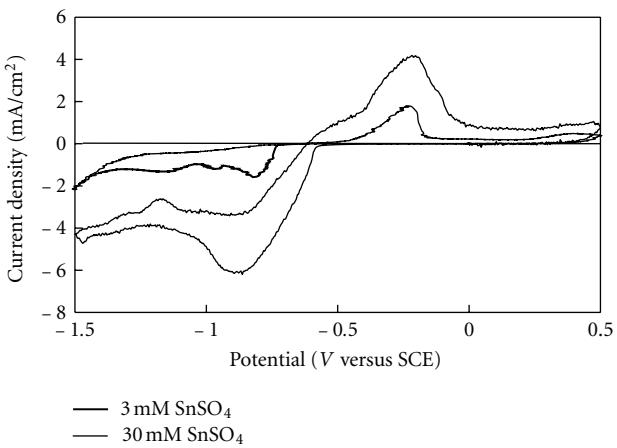

Figure 2: Cyclic voltametry results for the solutions containing 3 mM and 30 mM $SnSO_4$.

where the adhesion was so poor that a film was not formed on the substrate. Thus, we applied a two-step pulse potential with $E_1 = -1.3$ V versus SCE, $E_2 = -0.6$ V versus SCE, and pulse duration of 10 s (condition 5). The effects of the pulse biasing with such a long pulse duration were discussed in our previous paper for SnS deposition [18]. During the "off" period, poorly deposited parts are thought to dissolve, resulting in better surface morphology. The pulse biasing in fact improved adhesion for condition 5, but the surface morphology was not improved sufficiently, as shown below. In preparatory experiments, we found that the pulse biasing is not effective for improving morphology of Cu_xS films. Thus we did not try the pulse-biasing deposition for the Cu-rich conditions (conditions 1–4).

Table 1 also shows the thickness and composition of the films. From the table, we can see that as the $SnSO_4$ concentration was increased, both Sn and S contents were increased. The oxygen content is larger than or comparable to the sulfur content. The source of the oxygen in the films would be dissolved oxygen in the solution since we did not purge oxygen before the deposition.

Figure 3 shows the SEM images of the films deposited under condition 1 (Figure 3(a)) and condition 5 (Figure 3(b)). The film deposited under condition 1 seems more compact than that deposited under condition 5, and the growth seems to be dendritic for deposition under condition 5. In our previous work, we deposited SnS using 30 mM $SnSO_4$ and 100 mM $Na_2S_2O_3$ as in condition 5 [18]. Films deposited using DC potential were porous, but those deposited using a pulse bias were much more compact. However, in the present case, the film deposited using a pulse bias (condition 5) is porous as shown in Figure 3(b), and therefore the pulse biasing is not so effective to improve the morphology in case of CTSO.

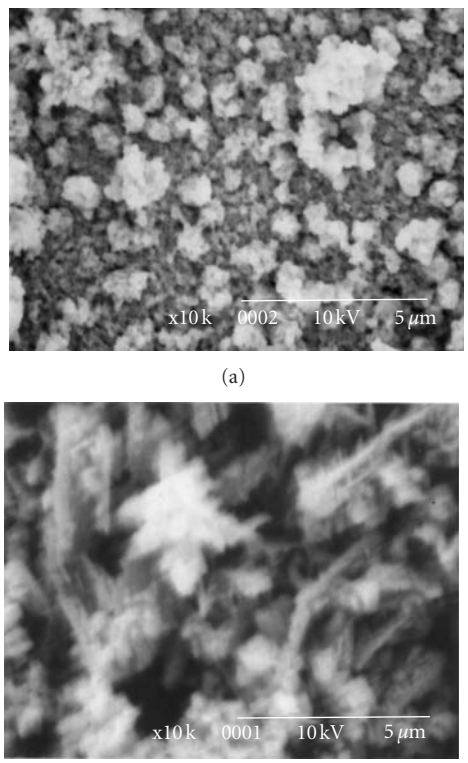

Figure 3: SEM images of the films deposited under condition 1 (a) and condition 5 (b). The former one is denser than the latter.

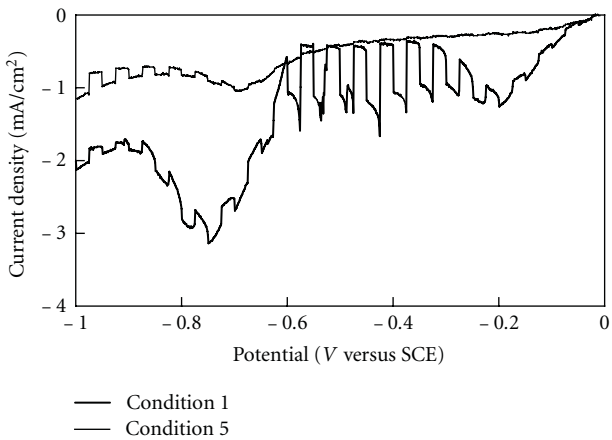

Figure 4: Results of the PEC measurement for the films deposited under condition 1 and condition 5. The step-form variation in the current is due to the turning on/off of the illumination. The observed photocurrent is negative for both the samples.

To investigate the photosensitivity of the deposited films, we performed the PEC measurement. Figure 4 shows the results of the PEC measurement for condition 1 and condition 5. The current was not changed by illumination for the anodic scan, and thus only the results for the cathodic scan are shown in the figure. During the cathodic scan, the current was changed due to the light chopping. When the junction of the semiconductor-electrolyte is illuminated, photogenerated electrons/holes are separated in the space charge region. The photogenerated minority carriers arrive at the interface of the semiconductor-electrolyte to participate in the electrochemical reaction at the film/electrolyte interface. The current becomes more negative under the light illumination during the cathodic scan. This implies that the minority carriers generated here are electrons. Thus, the deposited films are p-type. The photocurrent for the film deposited under condition 1 is bigger than those for the other condition films. Therefore, we adopt condition 1 for fabrication of the solar cells. The poor photoresponse of the film deposited under condition 5 would partly be due to the porous nature of the film (see Figure 3).

The color of the deposition solution changed with time because of spontaneous chemical reactions. To investigate dependence of film properties on deposition time, we changed deposition time from 30 to 5 min. The composition and thickness of the film obtained by 5 min deposition under condition 1 were shown in the parentheses in Table 1. It can be seen that Sn and S contents are larger for the shorter deposition time. The average deposition rate is also larger for the initial 5 min (0.03 μm/min) than for the 30 min deposition (0.017 μm/min). We may consider that Sn and S reacted in the solution to form SnS colloidal particles, resulting in decrease in Sn and S contents in the film and also decrease in deposition rate for a longer deposition time.

The XRD spectra of the films deposited under condition 1 are shown in Figure 5 with the spectrum for the ITO glass substrate. The observed peaks are all attributed to the ITO substrate for the 5 min deposition sample, whereas a broad peak appears near $2\theta = 43^\circ$ for the 30 min deposition sample. We could not identify the broad peak since its 2θ value does not correspond to those of the dominant peaks of related binary compounds (SnS_x, Cu_xO, x = 1 or 2). Since SnS and Cu_2O films deposited by ECD exhibited clear diffraction peaks [18, 21], the absence of clear diffraction peaks indicates that the CTSO films are amorphous or nanocrystalline and do not include those separate binary phases.

For estimating the band gap, we measured the optical transmission of CTSO. Figure 6 shows the optical transmission of the CTSO film deposited under condition 1 with a deposition time of 5 min. The transmission is low in the whole range obviously because of scattering due to the rough surface morphology (Figure 3). A clear absorption edge did not appear, which will be due to amorphous or nanocrystalline nature of the film revealed by XRD (Figure 5). For the direct-band optical absorption, the absorption coefficient α is given by

$$\alpha = \frac{k\left(h \quad - E_g\right)^{1/2}}{h}, \tag{2}$$

where k is a constant, E_g the band gap, and h the photon energy. Figure 7 shows h versus $(\alpha h \quad)^2$ plot. There is no clear straight-line portion in the plot, and α begins to increase gradually around 1 eV and then more steeply around 1.5 eV. Thus, the band gap would be in a range between 1 and 1.5 eV.

3.2. Heterojunction Solar Cells. We attempted to fabricate the superstrate and substrate heterojunctions with ZnO as a window layer and CTSO as an absorption layer. In case of the superstrate heterojunction, we found that the underlying ZnO layer was dissolved during the subsequent CTSO deposition. The same problem was also reported for the SnS deposition on ZnO [24]. Recently, a buffering method was proposed to prevent dissolution of ZnO during deposition of Cu_2O on it [28]. A suitable amount of ZnO is dissolved into the Cu_2O deposition solution, and then stability of ZnO can be improved. This method is effective for alkaline solutions because the solubility of $HZnO_2^-$, the product of ZnO dissolution, is relatively low. In the present case, pH of the CTSO deposition solution is about 3, and the solubility of Zn^{2+}, the product of ZnO dissolution in acidic solutions, is quite high. Thus the ZnO dissolution could not be prevented by the buffering technique. Therefore, we actually fabricated the substrate heterojunction only. Figure 8 shows the dark I-V characteristics for the substrate heterojunction with the 30-min-deposited CTSO layer. The rectification property appeared, but we did not find any photovoltaic effects.

In the substrate structure, the light is incident on the CTSO (absorption layer) side, and thus the light is attenuated before reaching the pn junction region. This would be the main reason why the photocurrent was not observed for the 30-min-deposited CTSO layer, and thus we reduced the CTSO film thickness. Figure 9 shows the dark and illuminated I-V characteristics for the substrate heterojunction with the 5-min-deposited CTSO layer. We

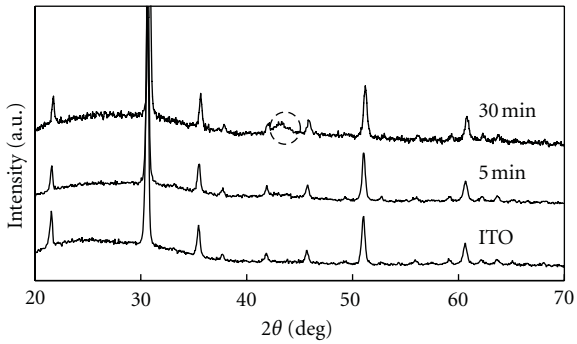

Figure 5: XRD spectra for the CTSO films deposited under condition 1 with different deposition time (5 min and 30 min). A broad peak near $2\theta = 43^\circ$ observed for the 30 min deposition sample (the circle in the figure) can be attributed to the CTSO film, and all other peaks are due to ITO.

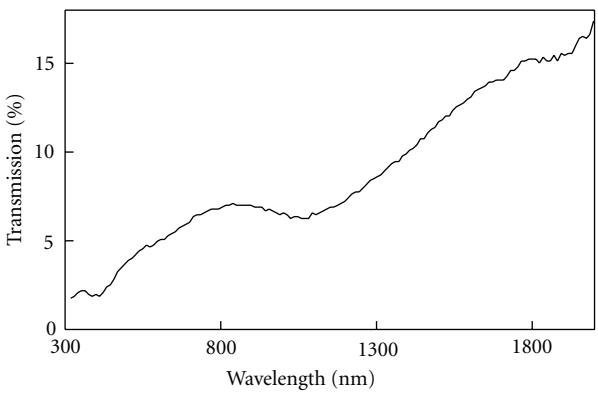

Figure 6: Optical transmission of the CTSO film deposited under condition 1 for 5 min.

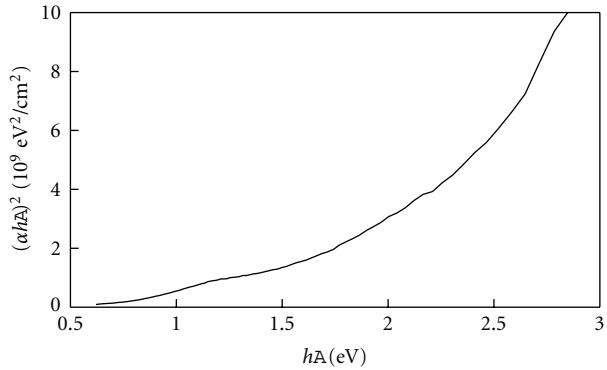

Figure 7: Plot of the absorption coefficient for band gap estimation of the CTSO film deposited under condition 1.

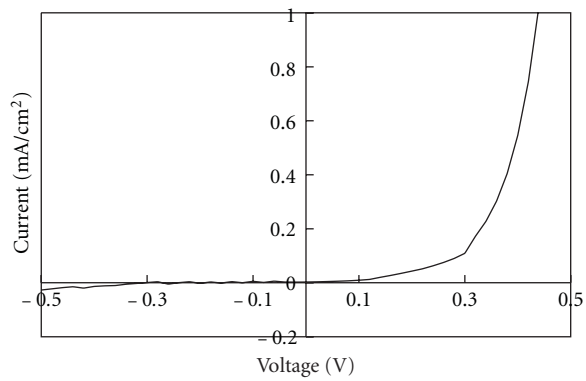

Figure 8: Dark I-V characteristic for the substrate heterojunction with the 30-min-deposited CTSO film (condition 1).

confirmed rectification and photovoltaic effects. The conversion efficiency of the best cell was 4.9×10^{-3}% with V_{oc} of 0.165 V, I_{sc} of 0.1 mA/cm^2, and FF of 0.30. The efficiency is significantly lower than those of SnS- and Cu_2O-based solar cells, for which efficiency values larger than 1% were reported [1, 7]. It should be noted that while those previously reported cells were all superstrate-structure cells, the cell fabricated in this work is of the substrate structure as noted above. Thus the observed poor photovoltaic properties will be mainly due to the cell structure (substrate structure). Another possible reason for the poor properties could be poor crystallinity of CTSO. Since there are no sharp diffraction peaks in the XRD spectra shown in Figure 5, the CTSO films are considered to be amorphous or nanocrystalline. Then the carrier diffusion length will be very short. On the other hand, clear diffraction peaks are observed for ECD SnS and Cu_2O, as mentioned above, and thus the diffusion length may be longer in them than in CTSO. To improve the performance, annealing may be effective and will be attempted in a future study. Properties of the heterointerface are another important factor and thus will be discussed in the next subsection.

3.3. Band O sets. For the ZnO/CTSO cells, we confirmed photovoltaic effects, but the short-circuit current was small. The band offset at the interface is one of the most influential parameters for the efficiency of the heterojunction solar cells. Thus, to discuss the observed solar cell properties, the XPS technique was used to determine the band offset of the prepared junction. For the ZnO/CTSO structure, the valence-band offset ΔE_v is given by the equation

$$\Delta E_v = \Delta E^{\text{CTSO}}_{\text{VBM-Sn}} - \Delta E^{\text{ZnO}}_{\text{VBM-Zn}} - \Delta E_{\text{Zn-Sn}}, \tag{3}$$

where $\Delta E^{\text{CTSO}}_{\text{VBM-Sn}}$ is the energy separation between the valence-band maximum (VBM) and the Sn4d core level for CTSO, $\Delta E^{\text{ZnO}}_{\text{VBM-Zn}}$ the separation between VBM and the Zn3d core level for ZnO, $\Delta E_{\text{Zn-Sn}}$ the energy difference across the interface between the Sn4d core level in the CTSO side, and the Zn3d core level in the ZnO side of the junction. Figure 10 shows the XPS spectra of CTSO (deposited under condition 1) and ZnO. The VBM positions were deduced by linear extrapolation of the leading edge of the expanded spectra, as shown in Figure 10(b), and the first and second terms of (3) were obtained as follows:

$$\begin{aligned} \Delta E^{\text{CTSO}}_{\text{VBM-Sn}} &= 25.25\,\text{eV}, \\ \Delta E^{\text{ZnO}}_{\text{VBM-Zn}} &= 8.1\,\text{eV}. \end{aligned} \tag{4}$$

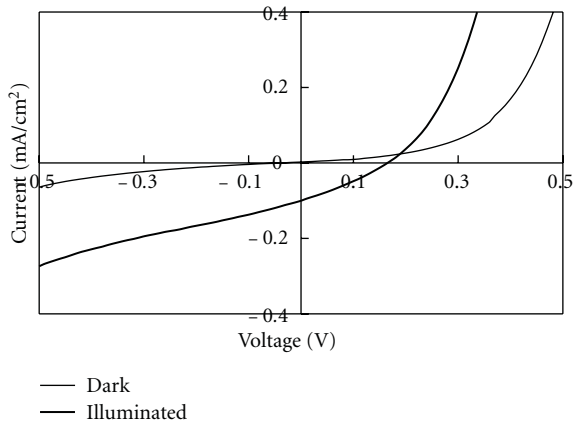

Figure 9: Dark and illuminated I-V characteristics for the substrate heterojunction with the 5-min-deposited CTSO film (condition 1).

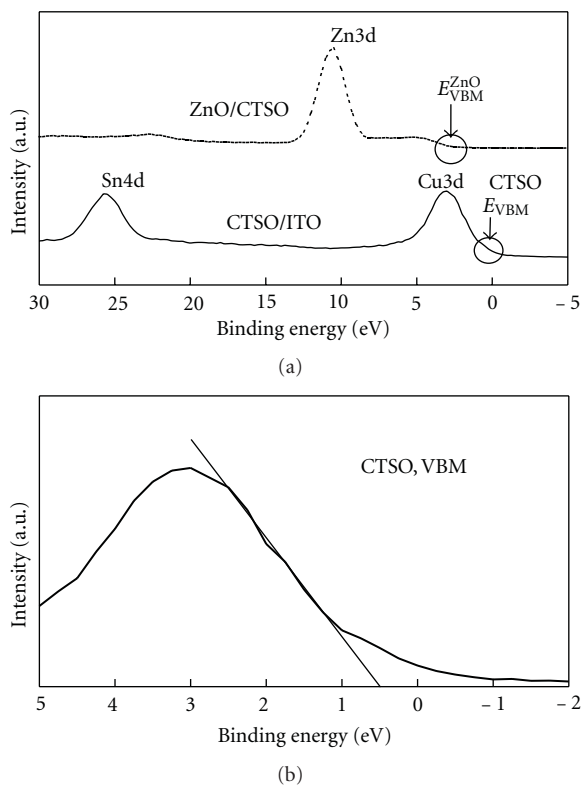

Figure 10: (a) XPS spectra for the ZnO and CTSO films. The CTSO film was deposited under condition 1. (b) expanded spectrum near VBM for CTSO. The straight line in (b) is the linear extrapolation of the leading edge, and the intercept on the energy axis corresponds to the VBM position.

Figure 11 shows the XPS spectra for the interface between CTSO and ZnO. The three spectra were taken with different sputtering time to determine the position of each peak. From this result, we estimated

$$\Delta E_{\text{Zn-Sn}} = 15.25\,\text{eV}. \tag{5}$$

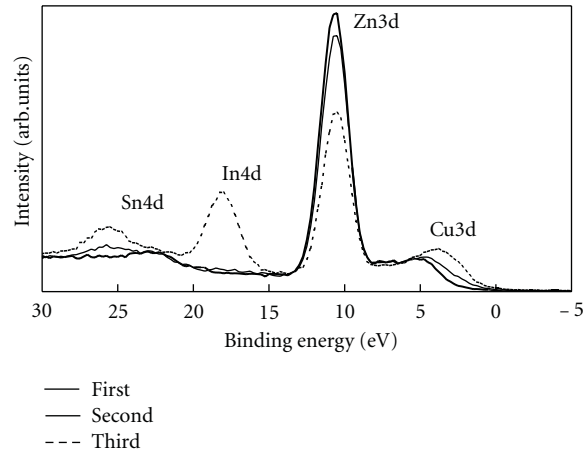

Figure 11: XPS spectra of Sn4d and Zn3d core levels near the ZnO/CTSO interface taken with three different sputtering times.

On the basis of (3), we calculated ΔE_v as 1.9 eV. The conduction-band offset ΔE_c was calculated using the band gap of each material as

$$\Delta E_c = \left(E_g^{\text{ZnO}} - E_g^{\text{CTSO}}\right) - \Delta E_v. \tag{6}$$

The band gap of ZnO is 3.4 eV. As described above, we were not able to accurately evaluate the band gap of CTSO from the optical transmission measurement, and E_g^{CTSO} was only roughly estimated to be in a range of 1 to 1.5 eV. Figure 12 shows the schematic of the band alignment estimated from the XPS results. Considering the ambiguity of the band gap value, the band edges of CTSO were indicated by the thick lines with a width corresponding to 0.25 eV. As shown in the figure, even if we consider the uncertainty of the band gap of CTSO, we may conclude that the conduction band offset will be small. In that case, we can expect that the short circuit current will be relatively large since there is only a low barrier for the electron flow. However, the ZnO/CTSO cell showed a small short circuit current. As discussed in the previous section, the cell geometry (substrate structure) and the short diffusion length of carriers in CTSO may be the reason of the low efficiency. Another possible reason is that ZnO and CTSO were mixed at the heterojunction interface, to form an interface layer which hinders the electron flow. As shown in Figure 11, the transition of composition from ZnO to CTSO is not sharp, that is, the Zn signal is still significant even after the Cu and Sn signals appear. This may be partly due to the roughness of the surface/interface and partly due to the atomic mixing at the interface. Thus, heterostructures with other materials than ZnO also need to be investigated.

4. Conclusion

Using the electrochemical techniques, $Cu_xSn_yS_zO$ (CTSO) thin films have been deposited from an aqueous solution containing $CuSO_4$, $SnSO_4$, and $Na_2S_2O_3$. The $CuSO_4$ and $Na_2S_2O_3$ concentrations were fixed at 10 mM and 100 mM, respectively, while the $SnSO_4$ concentration was varied. The

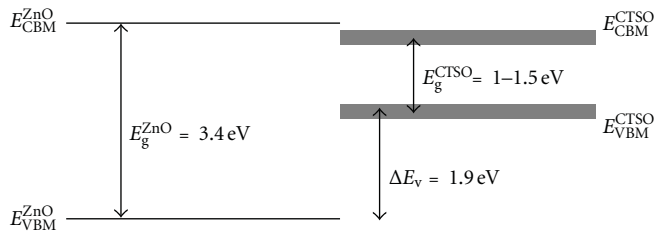

Figure 12: Band diagram of the ZnO/CTSO heterojunction deduced form the XPS results.

deposited films showed clear p-type conduction and photosensitivity. The film deposited with the solution containing 10 mM $CuSO_4$, 3 mM $SnSO_4$, and 100 mM $Na_2S_2O_3$ has a band gap of 1.0–1.5 eV and seems to be nanocrystalline or amorphous according to the XRD results. The film was used for fabricating ZnO/CTSO heterojunctions. Rectification properties were observed, and the best cell showed an efficiency of 4.9×10^{-3}% under AM1.5 illumination.

Acknowledgments

The authors would like to thank Drs. M. Kato, A. M. Abdel Haleem, and S. Chowdhury for their useful discussion and Mr. Moriguchi for his technical assistance in the XPS measurement.

References

[1] A. Mittiga, E. Salza, F. Sarto, M. Tucci, and R. Vasanthi, "Heterojunction solar cell with 2% efficiency based on a Cu_2O substrate," *Applied Physics Letters*, vol. 88, no. 16, Article ID 163502, 2006.

[2] K. Akimoto, S. Ishizuka, M. Yanagita, Y. Nawa, G. K. Paul, and T. Sakurai, "Thin film deposition of Cu_2O and application for solar cells," *Solar Energy*, vol. 80, no. 6, pp. 715–722, 2006.

[3] H. Tanaka, T. Shimakawa, T. Miyata, H. Sato, and T. Minami, "Electrical and optical properties of TCO-Cu_2O heterojunction devices," *Thin Solid Films*, vol. 469-470, pp. 80–85, 2004.

[4] L. Papadimitriou, N. A. Economou, and D. Trivich, "Heterojunction solar cells on cuprous oxide," *Solar Cells*, vol. 3, no. 1, pp. 73–80, 1981.

[5] M. Gunasekaran and M. Ichimura, "Photovoltaic cells based on pulsed electrochemically deposited SnS and photochemically deposited CdS and $Cd_{1-x}Zn_xS$," *Solar Energy Materials and Solar Cells*, vol. 91, no. 9, pp. 774–778, 2007.

[6] H. Noguchi, A. Setiyadi, H. Tanamura, T. Nagatomo, and O. Omoto, "Characterization of vacuum-evaporated tin sulfide film for solar cell materials," *Solar Energy Materials and Solar Cells*, vol. 35, no. C, pp. 325–331, 1994.

[7] K. T. Ramakrishna Reddy, N. Koteswara Reddy, and R. W. Miles, "Photovoltaic properties of SnS based solar cells," *Solar Energy Materials and Solar Cells*, vol. 90, no. 18-19, pp. 3041–3046, 2006.

[8] D. Avellaneda, M. T. S. Nair, and P. K. Nair, "Photovoltaic structures using chemically deposited tin sulfide thin films," *Thin Solid Films*, vol. 517, no. 7, pp. 2500–2502, 2009.

[9] M. Ristov, G. Sinadinovski, M. Mitreski, and M. Ristova, "Photovoltaic cells based on chemically deposited p-type SnS," *Solar Energy Materials and Solar Cells*, vol. 69, no. 1, pp. 17–24, 2001.

[10] M. Sugiyama, K. Miyauchi, T. Minemura, and H. Nakanishi, "Sulfurization growth of SnS films and fabrication of CdS/SnS heterojunction for solar cells," *Japanese Journal of Applied Physics*, vol. 47, no. 12, pp. 8723–8725, 2008.

[11] H. Katagiri, K. Jimbo, S. Yamada et al., "Enhanced conversion efficiencies of Cu_2ZnSnS_4-based thin film solar cells by using preferential etching technique," *Applied Physics Express*, vol. 1, no. 4, Article ID 041201, 2008.

[12] K. Wang, O. Gunawan, T. Todorov et al., "Thermally evaporated Cu_2 $ZnSnS_4$ solar cells," *Applied Physics Letters*, vol. 97, no. 14, Article ID 143508, 2010.

[13] T. D. Golden, M. G. Shumsky, Y. Zhou, R. A. VanderWerf, R. A. Van Leeuwen, and J. A. Switzer, "Electrochemical deposition of copper(I) oxide films," *Chemistry of Materials*, vol. 8, no. 10, pp. 2499–2504, 1996.

[14] K. Nakaoka, J. Ueyama, and K. Ogura, "Photoelectrochemical behavior of electrodeposited CuO and Cu_2O thin films on conducting substrates," *Journal of the Electrochemical Society*, vol. 151, no. 10, pp. C661–C665, 2004.

[15] J. Lee and Y. Tak, "Electrochemical deposition of a single phase of pure Cu_2O films by current modulation methods," *Electrochemical and Solid-State Letters*, vol. 3, no. 2, pp. 69–72, 2000.

[16] K. Mishra, K. Rajeshwar, A. Weiss et al., "Electrodeposition and characterization of SnS thin films," *Journal of the Electrochemical Society*, vol. 136, no. 7, pp. 1915–1923, 1989.

[17] Z. Zainal, M. Z. Hussein, and A. Ghazali, "Cathodic electrodeposition of SnS thin films from aqueous solution," *Solar Energy Materials and Solar Cells*, vol. 40, no. 4, pp. 347–357, 1996.

[18] K. Omoto, N. Fathy, and M. Ichimura, "Deposition of SnS_xO_y films by electrochemical deposition using three-step pulse and their characterization," *Japanese Journal of Applied Physics*, vol. 45, no. 3A, pp. 1500–1505, 2006.

[19] M. Izaki and T. Omi, "Characterization of transparent zinc oxide films prepared by electrochemical reaction," *Journal of the Electrochemical Society*, vol. 144, no. 6, pp. 1949–1952, 1997.

[20] S. Peulon and D. Lincot, "Mechanistic study of cathodic electrodeposition of zinc oxide and zinc hydroxychloride films from oxygenated aqueous zinc chloride solutions," *Journal of the Electrochemical Society*, vol. 145, no. 3, pp. 864–874, 1998.

[21] M. Izaki, T. Shinagawa, K. T. Mizuno, Y. Ida, M. Inaba, and A. Tasaka, "Electrochemically constructed p-Cu_2O/n-ZnO heterojunction diode for photovoltaic device," *Journal of Physics D: Applied Physics*, vol. 40, no. 11, article 010, pp. 3326–3329, 2007.

[22] J. Katayama, K. Ito, M. Matsuoka, and J. Tamaki, "Performance of Cu_2O/ZnO solar cell prepared by two-step electrodeposition," *Journal of Applied Electrochemistry*, vol. 34, no. 7, pp. 687–692, 2004.

[23] S. S. Jeong, A. Mittiga, E. Salza, A. Masci, and S. Passerini, "Electrodeposited ZnO/Cu_2O heterojunction solar cells," *Electrochimica Acta*, vol. 53, no. 5, pp. 2226–2231, 2008.

[24] M. Ichimura and H. Takagi, "Electrodeposited ZnO/SnS heterostructures for solar cell application," *Japanese Journal of Applied Physics*, vol. 47, no. 10, pp. 7845–7847, 2008.

[25] E. Fatas, R. Duo, P. Herrasti, F. Arjona, and E. Garcia-Camarero, "Electrochemical deposition of cds thin films on Mo and Al substrates," *Journal of the Electrochemical Society*, vol. 131, no. 10, pp. 2243–2246, 1984.

[26] K. L. Hardee and A. J. Bard, "Semiconductor electrodes. x. photoelectrochemical behavior of several polycrystalline metal oxide electrodes in aqueous solutions," *Journal of the Electrochemical Society*, vol. 124, no. 2, pp. 215–224, 1977.

[27] A. J. Nelson, C. R. Schwerdtfeger, S. H. Wei et al., "Theoretical and experimental studies of the ZnSe/$CuInSe_2$ heterojunction band offset," *Applied Physics Letters*, vol. 62, no. 20, pp. 2557–2559, 1993.

[28] K. P. Musselman, A. Marin, A. Wisnet, C. Scheu, J. L. MacManus-Driscoll, and L. Schmidt-Mende, "A novel buffering technique for aqueous processing of zinc oxide nanostructures and interfaces, and corresponding improvement of electrodeposited ZnO-Cu_2O photovoltaics," *Advanced Functional Materials*, vol. 21, no. 3, pp. 573–582, 2011.

Hindawi Publishing Corporation
International Journal of Photoenergy
Volume 2012, Article ID 709581, 6 pages
doi:10.1155/2012/709581

Research Article

Dye-Sensitized Solar Cells Using Mesocarbon Microbead-Based Counter Electrodes

Chien-Te Hsieh, Bing-Hao Yang, and Wei-Yu Chen

Department of Chemical Engineering and Materials Science, Yuan Ze Fuel Cell Center, Yuan Ze University, Taoyuan 320, Taiwan

Correspondence should be addressed to Chien-Te Hsieh, cthsieh@saturn.yzu.edu.tw

Received 30 May 2011; Accepted 26 November 2011

Academic Editor: Peter Rupnowski

The dye-sensitized solar cells (DSCs) equipped with mesocarbon microbead (MCMB)-based counter electrodes were explored to examine their cell performance. Three types of nanosized additives including platinum, carbon nanotubes (CNTs), and carbon black (CB) are well dispersed and coated over microscaled MCMB powders. In the design of the counter electrodes, the MCMB graphite offers an excellent medium that allows charge transfer from the ITO substrate to the dye molecule. The active materials such as Pt, CNT, and nanosize CB act as an active site provider for the redox reaction. Among these counter electrodes, the DSCs fabricated with CB electrode exhibit the highest power conversion efficiency. This improved efficiency can be attributed to the fact that the CB nanoparticles not only offer a large number of catalytic sites but also low charge transfer resistance, facilitating a rapid reaction kinetics. Such design of carbon counter electrode has been confirmed to be a promising candidate for replacing Pt electrodes.

1. Introduction

Dye-sensitized solar cell (DSC) is one of the representative organic solar cells, resembling a photosynthesis process in nature [1]. Up to now, DSC has drawn considerable attention due to its low-cost production, environmentally benign material, and facile fabrication, compared with Si-based solar cell [2–5]. A DSC is a typical electrochemical system, consisting of a wide bend gap semiconductor photoanode, a dye, an electrolyte, and a counter electrode [6]. It is generally recognized that nanocrystalline TiO_2 is one of the suitable materials for the photoanode of DSCs. This is attributed to the fact that its edge of conduction band allows the electron injection from the excited state of dye. The function of counter electrode is to reduce I_3^- to I^- in electrolyte by electron transferred from photoanode. Platinum coated on indium- or fluorine-coated tin oxide (ITO or FTO) conducting glass often serves as counter electrode in DSCs because the Pt counter electrode displays high electric conductivity and high electrochemical catalytic activity for triiodide reduction [7, 8]. However, the Pt film can be decomposed to PtI_4 compound by I_3^-/I^- electrolyte during the DSC operation, reducing the performance, long-term durability, and commercial success of DSCs. Additionally, to reduce the usage amount of noble Pt, seeking one cheap candidate to replace costly Pt is still a challenge.

More recently, early reports have pointed out that carbonaceous counter electrodes show a potential feasibility to replace Pt-based electrodes. Several carbon candidates including activated carbon paste [8], carbon nanotubes (CNTs)-based paste [6, 9, 10], Pt-loaded carbon black [11, 12], and nanoscaled carbon powder [13, 14] have been proven to show the catalytic capability for reduction of I_3^- ions. However, a better understanding is required to optimize the cell performance using different carbon counter electrodes. In this paper, spherical mesocarbon microbead (MCMB) graphite has been selected as a matrix electrode material due to its good electric conductivity, stability, and easy coating. Actually, MCMB powders with microscaled size have been extensively used as anode materials in Li-ion battery. To improve the cell performance, three types of additives, Pt nanoparticles, CNTs, and carbon black (CB)

nanoparticles, were well dispersed over MCMB graphite surface. The DSCs fabricated with different counter electrodes were examined using their incident photon to current efficiency (IPCE) spectra and photocurrent-voltage curves for comparison. This study aims to shed some lights on (i) how the carbon-based counter electrodes affect the performance of DSCs and (ii) the possibility of carbon counter electrodes to replace Pt electrodes in this photovoltaic device.

2. Experimental

Commercial MCMB (Osaka Gas Co., Japan) graphite powders, having an average size of 10 μm, were used as matrix. The MCMB sample was initially dispersed into ethylene glycol, forming carbon slurry. The CNTs employed in this study were prepared by a catalytic chemical vapor deposition. The vapor growth of CNTs was carried out in a horizontal furnace at 850°C, using Ni nanoparticles and ethylene as catalyst and carbon precursor, respectively. The other additive, conductive CB (Super P, Taiwan Maxwave Co., Ltd.) was one of commonly used conducting materials for electrode preparation in Li-ion battery. The fabrication process of the carbon black was based on partial oil oxidation of carbochemical and petrochemical raw materials. The CB powder with a mean size of 20–50 nm displayed high conductivity and purity (>99.5%). The CNT and CB samples were poured into the MCMB slurry and then dispersed in an ultrasonic bath for 0.5 hr, respectively. The weight ratio of MCMB to the carbon additive (i.e., CNT and CB) was set at 90 : 10. After filtration, the carbon composites were placed in a vacuum oven, and the composites were then heated at 105°C over night to evaporate ethylene glycol, thus giving dry carbon composite powders.

The procedure for the formation of counter electrode can be descried as follows. Each carbon composite was added into a solution of poly vinylidenefluoride (PVdF) in N-methyl pyrrolidinone (NMP), and the mixture was then mixed at ambient temperature to form an electrode slurry. The PVdF was a binder to adhere the interface between particle-particle and particle-substrate. The mixtures were blended by a 3-D mixer using zirconia balls for 3 hr to prepare uniform slurries. All electrodes were prepared by coating the slurry on ITO glass with a spin coater. To obtain the uniform coating, the coating process consists of two steps: (i) the spinning speed of the first-stage coating process was set at 500 rpm for 5 sec, and then (ii) the second-stage speed was raised to 3000 rpm and maintained for 10 sec. Then, the electrodes were heated to 120°C to evaporate the solvent, NMP, in a vacuum oven overnight. The electrode layers, consisted of 90 wt.% carbon composite and 10 wt.% PVdF binder, were adjusted to have a thickness of 5–20 μm. The two kinds of carbon counter electrodes, CNTs and CB attached to MCMB powders, are designated to C2 and C3 electrodes, respectively. For comparison, Pt nanoparticles were well dispersed over pure MCMB counter electrode by using plasma sputtering. The Pt loading to the whole active material was set at 5 wt%. The Pt-coated MCMB counter electrode was designated to C1 electrode. The schematic diagrams for different counter electrodes are illustrated in Figure 1. Table 1 lists these carbon electrodes with various compositions. The morphology of electrode materials was observed by using field-emission scanning electron spectroscope (FE-SEM, JEOL JSM-5600). The crystalline structures of the carbon samples were characterized by X-ray diffraction (XRD, Shimadzu Labx XRD-6000) spectroscopy and Raman spectroscopy (Renishaw Micro-Raman spectrometer).

The photoanode used here was composed of TiO_2 powder (P25, Degussa), glacial acetic acid, ethylene cellulose, carbowax, and Triton X-100. A screen printer was applied to coat the TiO_2 layer on the ITO substrate with sheet resistance of 10 /square. The treated ITO glass was dried at 80°C for 8 hr and then sintered at 450°C for 1 hr, forming the TiO_2 photoelectrodes. The electrolyte composition was composed of lithium iodide (0.5 M), iodine (0.05 M), 4-tert-butylpyridine (0.5 M), and 1-methyl-3-propylimidazolium iodide (0.6 M) in 3-methoxypropionitrile. To ensure the dye adsorption, each photoanode was immersed in 0.3 mM N719/ethanol solution (Solaronix) overnight. The sandwichtype DSCs having an active area of 0.49 cm^2 were used to compare their cell performance. The I-V curves of DSCs were examined by an Keithley meter under Oriel solar simulator illumination (AM 1.5, 100 mW/cm^2). The light intensity of the illumination source was calibrated by using a standard silicon photodiode.

3. Results and Discussion

The crystallographic structure of the carbon samples is observed by XRD analysis. Typical XRD patterns of C1, C2, and C3 electrode materials are depicted in Figure 2. The XRD pattern of fresh MCMB was also showed for comparison. The XRD pattern of fresh MCMB shows a diffraction peak (002) centered at *ca.* $2\theta = 26.1°$, originated from the crystalline nature of graphite. Basically, the interlayer distance, d_{002}, is close to 0.335 nm for highly oriented graphite carbon [15]. The d_{002} value of fresh MCMB is approximately 0.337 nm according to the calculation of Bragg's equation. It can be seen that the addition of Pt, CNTs, and CB do not significantly alter the XRD intensity of graphite. The C1 pattern displays several representative Pt peaks after the Pt sputtering on MCMB spheres. Both XRD patterns of C2 and C3 carbon composites almost show typical peaks regarding the crystalline graphite at fixed positions, implying that the MCMB matrix still maintains a highly sp^2 crystalline structure.

To inspect the influence of additive, Raman spectroscopy is an appropriate technique to analyze the graphite degree of carbon materials. Figure 3 shows the Raman spectra of C1, C2, and C3 electrode materials. The Raman spectrum of fresh MCMB is also used to compare with other three spectra. It is known that the Raman band at 1580 cm^{-1} is assigned to the stacking of the graphite hexagon network plane (G band), whereas the band at 1350 cm^{-1} can be attributed amorphous carbon or deformation vibrations of a hexagonal ring (D band) [16]. The I_D/I_G intensity ratio has an order as follows: C1 (0.31) > C2 (0.26) > C3 (0.14). Excepting for C3 sample, original MCMB has a lower I_D/I_G

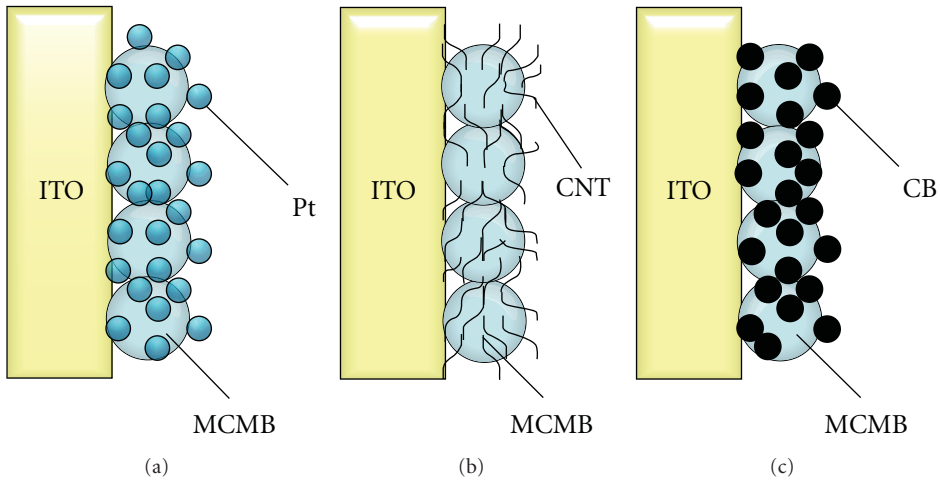

Figure 1: Schematic diagrams of (a) Pt, (b) CNTs, and (c) CB coated on MCMB powders.

Table 1: Parameters for solar cells based on different carbon counter electrodes.

Electrode	Composition (wt%)	I_{SC} (mA cm^{-2})	V_{OC} (V)	FF	η (%)
C1	C : Pt (95 : 5)	7.45	0.69	0.62	3.17
C2	C : CNT (90 : 10)	7.68	0.74	0.52	2.96
C3	C : Super P (90 : 10)	7.19	0.72	0.69	3.55

ratio of 0.18 than C1 and C2 samples. As to C1 sample, this increase of I_D/I_G ratio is presumably due to two reasons: (i) Pt deposits occupy some coverage of crystalline graphite, and (ii) graphite surface may be partially destroyed during the sputtering process. For C2 sample, this raising I_D/I_G ratio can be attributed to the fact that few imperfect defects or surface oxides are attached to the sidewall or both ends of CNTs, inducing the disorder degree in the carbon composites.

Figures 4(a), 4(b), and 4(c) shows top-view FE-SEM images of C1, C2, and C3 carbon counter electrodes at the same magnification, respectively. As shown in Figures 4(a) and 4(d), Pt deposits are well dispersed and coated over the surface of graphite. The inset of this figure clearly reflects that as-deposited Pt has an average size of 5–10 nm and a narrow particle size distribution. As for C2 sample, a large number of CNTs cover the graphite surface, forming a nanomicro junction hybrid. The CNTs possess an average diameter of 50–80 nm and a length of several micrometers. The one-dimensional CNTs are coiled tube shape, indicating that some carbon atoms randomly stack and thus form some imperfections on the sidewall of nanotubes, which has been demonstrated elsewhere [16, 17]. The FE-SEM image of C3 sample shows a large amount of CB nanoparticles attached to graphite powders. The size of the particulates ranges from 20 to 50 nm. These particulates seem like nanosized tips that cover the graphite matrix.

The IPCE spectra for the DSCs fabricated with various carbon-based counter electrodes are illustrated in Figure 5. The spectra apparently reveal that the DSCs typically display a similar distribution but different photon to current efficiencies within the wavelength region of 300–800 nm. The maximum IPCE takes place at approximately 530 nm for all DSCs, indicating the nature of the N719 dye. It is found that C2 counter electrode exhibits the highest IPCE response than other two electrodes in the whole region of wavelength. This can be presumably due to the amount of dye adsorption. The porosity of the carbon composites can be determined by physisorption of nitrogen at -196°C. The Brunauer-Emmett-Teller (BET) surface areas have an order as follows: C2 (50.6 m^2/g) > C3 (12.6 m^2/g) > C1 (4.5 m^2/g) $\approx$ original MCMB (2.1 m^2/g). This finding demonstrates that the CNT additive offers more surface area accessible for the organic adsorption, raising the dye capacity per unit area of electrode. Basically, original graphite powder is a nonporous solid media after high-temperature graphitization. As for the two carbons, an increase of BET surface area may be due to (i) nanosized particles and (ii) nanovoids or nanocavities from the particle aggregation. However, it is worth noting that the IPCE intensity is not proportional to the BET surface area. This discovers two crucial messages: (i) the dye affinities to carbon and to platinum are different, and (ii) the inner surface of CNTs cannot be completely wetted by dye molecule, thus inducing the low surface accessibility.

Figure 6 shows the typical photocurrent-voltage curves of DSCs fabricated with various carbon electrodes. The performance curves reflect different photovoltaic behaviors, originated from the effect of counter electrodes. To evaluate the cell performance, the power conversion efficiency (η) of

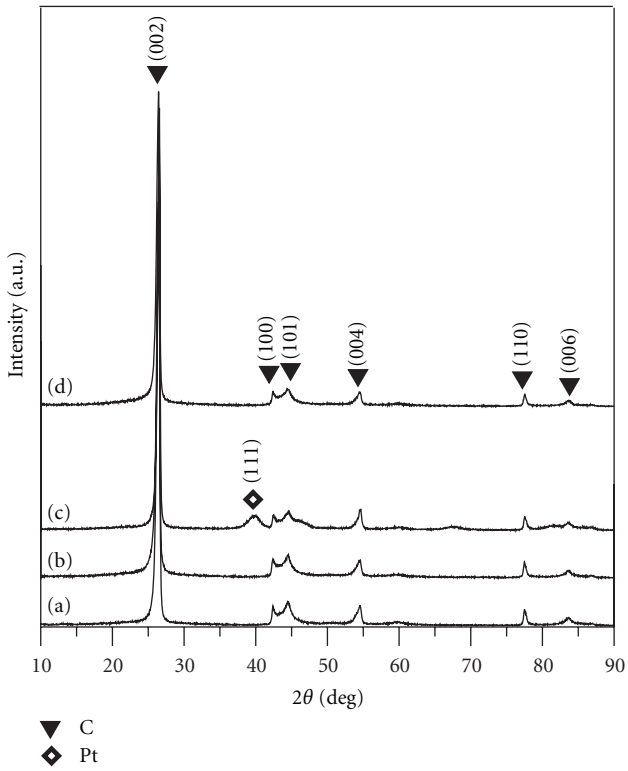

Figure 2: Typical XRD pattern of different carbon counter electrodes: (a) MCMB, (b) C1, (c) C2, and (d) C3.

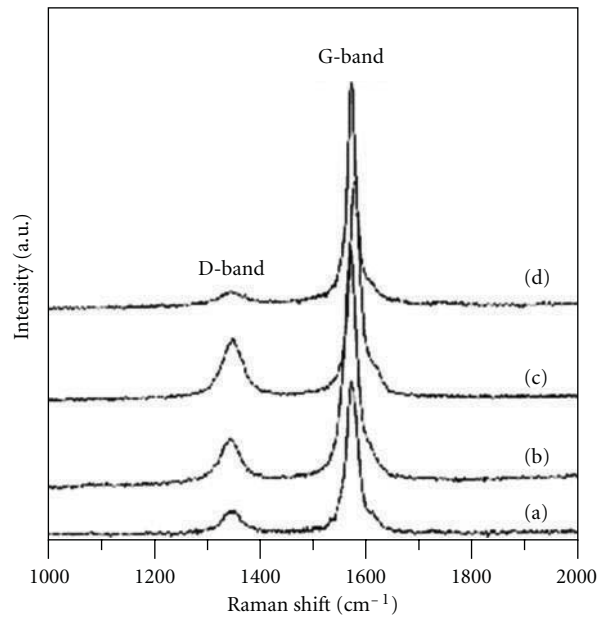

Figure 3: Raman spectra of different carbon counter electrodes: (a) MCMB, (b) C1, (c) C2, and (d) C3.

the DSC can be calculated by

$$\eta(\%) = \frac{V_{OC} I_{SC} FF}{P_{in} A} \times 100, \quad (1)$$

where I_{SC} is short-circuit current, V_{OC} is open-circuit voltage, FF is fill factor, A is active area of photoelectrode, and P_{in} is incident light power (100 mW/cm^2 in this study). The FF value is obtained from

$$FF = \frac{V_m I_m}{V_{OC} I_{SC}}, \quad (2)$$

where V_m and I_m are voltage and photocurrent at maximum output power point, respectively. Table 1 summarizes the cell performance with different counter electrodes, according to the calculations from (1) and (2). All DSCs exhibit a fairly high FF value (>0.69 V) but quietly different other performance factors. This difference among these counter electrodes is significantly related to the redox reaction on the design of counter electrodes.

The mechanism on the counter electrodes consists of three steps: (i) ionic diffusion, (ii) catalytic I^-/I_3^- reaction, and (iii) charge transfer at interface between counter electrode and electrolyte. The reduction reaction on the surface of counter electrode can be written as $I_3^- + 2e^- \rightarrow 3I^-$, whereas the oxidation of iodide occurs on the dye molecule [7, 10]. Accordingly, the charge-transfer reactions at the interfaces of electrolyte/counter electrode and electrolyte/dye molecule are so crucial to influence the efficiency of counter electrodes. Basically, the reduction reaction (i.e., I^-/I_3^-) would take place at catalytic sites on the carbon electrodes [11]. These active sites usually locate on some defects of sidewalls or edges of carbon crystals. Thus, the number of defect sites on the carbon electrodes acts an important role in affecting the power performance of DSCs. Since the MCMB powder exhibits highly oriented crystal (see Figures 2 and 3), thus there are a less number of defect sites for the catalytic reaction. However, the microsized graphite offers an excellent medium that allows charge transfer from the ITO substrate to the dye molecule. The active materials such as Pt, CNT, and nanosize CB act as an active site provider for the redox reaction, as illustrated in Figure 1.

As shown in Table 1, the η value for all DSCs displays an order as follows: C3 (3.55%) > C1 (3.17%) > C2 (2.96%). This result demonstrates that both CNTs and CB are capable of generating a number of catalytic sites for the redox reaction, similar to Pt deposits. In comparison, the DSC equipped with CB counter electrode (C3 electrode) has the greatest η and FF values. It is of interest that as shown in Figure 6, C2 electrode represents the highest IPCE response but the lowest power conversion. This can be presumably due to a large amount of dye adsorbed on interior or surface structure of CNTs. However, only low surface coverage of dye adsorbed can be utilized owing to less number of catalytic sits and longer pathway of electron transportation through one-dimensional pathway, comparing with zero-dimensional CB nanoparticles. However, these CB particles not only offer a large number of catalytic dots but also short charge-transfer path, thus inducing fast redox kinetics. On the basis of the cell performance, three designs of counter electrodes show a commercial feasibility to replace expansive Pt film counter

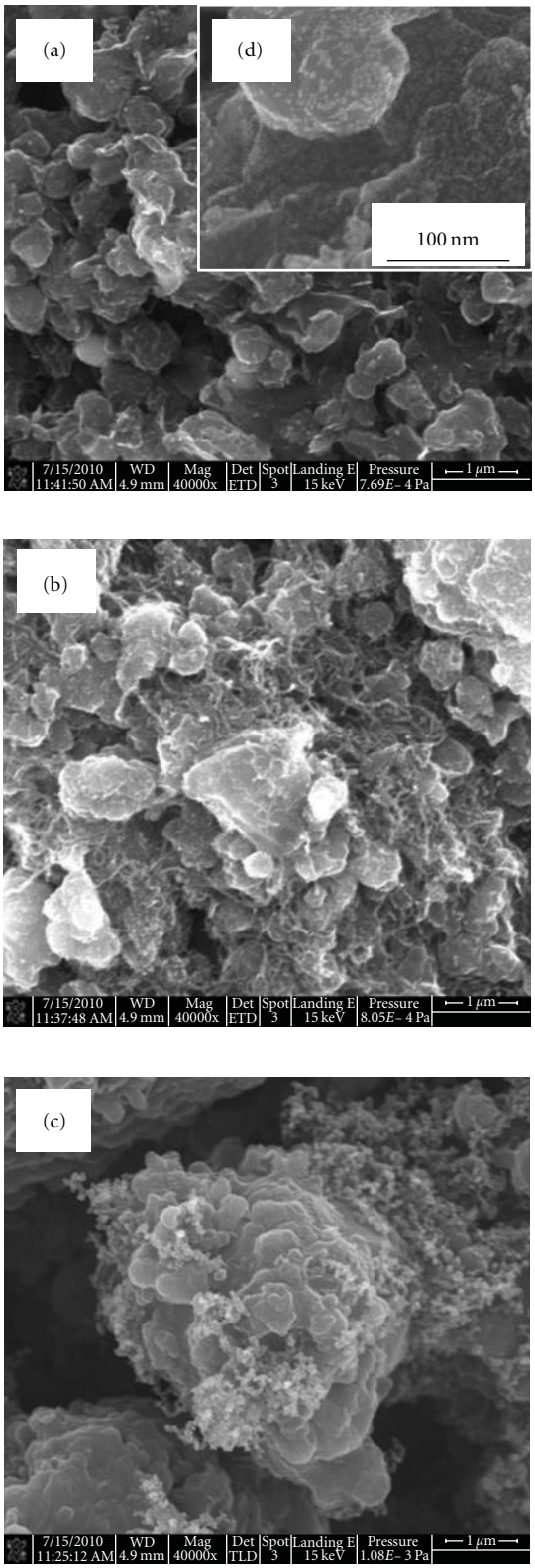

Figure 4: SEM images for (a) Pt, (b) CNTs, and (c) CB coated on MCMB powders. (d) The FE-SEM shows the dispersion of Pt nanoparticles over MCMB surface.

electrodes in DSC devices. However, to improve the power conversion of DSCs, an optimal factor combination such as loading of active carbon materials and dispersion degree still requires a significant investigation.

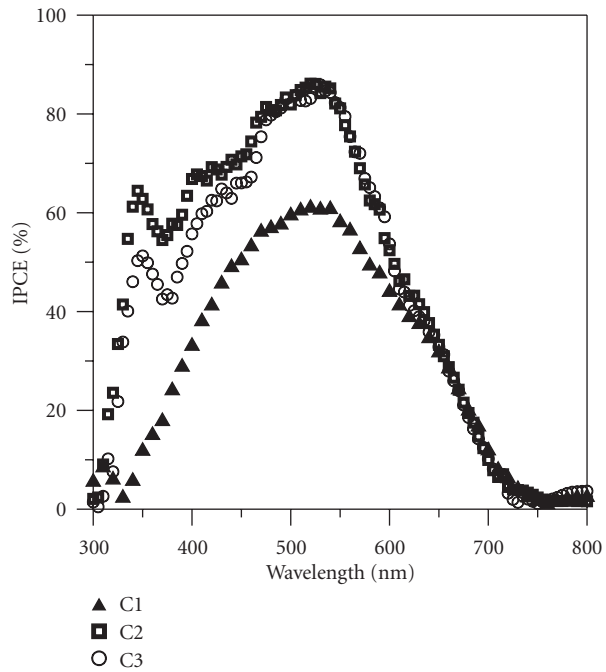

Figure 5: IPCE spectra for the DSCs fabricated with different counter electrodes.

4. Conclusions

We have investigated the performance of DSCs fabricated with different MCMB-based counter electrodes, including Pt, CNT, and CB additives. The three types of nanosized materials were well dispersed over the graphite matrix, inducing an increased porosity for the dye adsorption. The MCMB offered an excellent charge transfer medium between active material and ITO substrate, whereas the attached Pt deposits, CNTs, and CB nanopowders provided a number of catalytic sites for the I^-/I_3^- reduction. The DSC using the CNT counter electrode displayed the improved IPCE response but the lower power conversion efficiency, comparing with the other two DSCs. This can be attributed to two explanations: (i) the dye affinities to carbon and to platinum are different, and (ii) the inner surface of CNTs cannot be completely wetted by dye molecule, thus inducing the low surface accessibility. For comparison, the CB decoration over MCMB not only generated a large number of catalytic sites but also rapid reaction kinetics, thus leading a higher power conversion. On the basis of the above results, such design of carbon counter electrode has been proven to be an attractive candidate for replacing Pt counter electrode in the DSCs.

Acknowledgment

The authors are very grateful for the financial support from the National Science Council of the Republic of China under

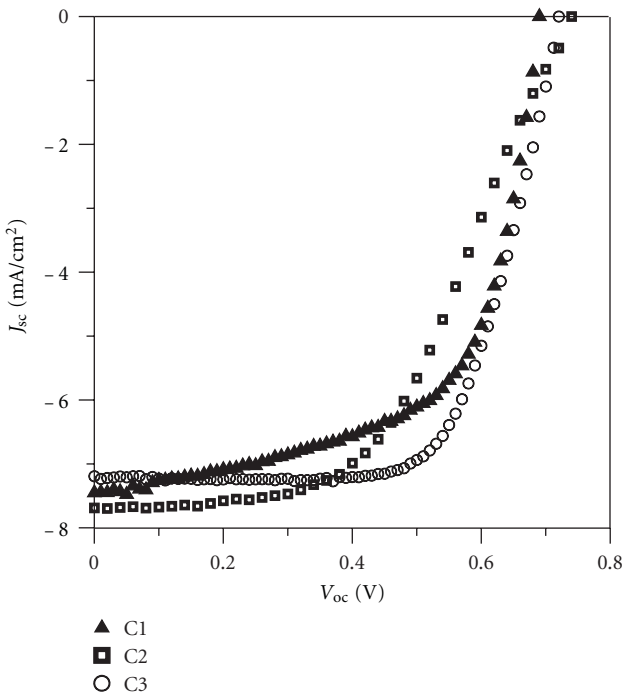

Figure 6: Photocurrent-voltage curves for the DSCs fabricated with different counter electrodes.

the Contracts NSC 100-2120-M-155-001 and NSC 100-2221-E-155-031.

References

[1] H. Choi, H. Kim, S. Hwang, W. Choi, and M. Jeon, "Dye-sensitized solar cells using graphene-based carbon nano composite as counter electrode," *Solar Energy Materials and Solar Cells*, vol. 95, no. 1, pp. 323–325, 2011.

[2] N. Yang, J. Zhai, D. Wang, Y. Chen, and L. Jiang, "Two-dimensional graphene bridges enhanced photoinduced charge transport in dye-sensitized solar cells," *ACS Nano*, vol. 4, no. 2, pp. 887–894, 2010.

[3] W. J. Lee, E. Ramasamy, D. Y. Lee, and J. S. Song, "Performance variation of carbon counter electrode based dye-sensitized solar cell," *Solar Energy Materials and Solar Cells*, vol. 92, no. 7, pp. 814–818, 2008.

[4] W. J. Lee, E. Ramasamy, D. Y. Lee, and J. S. Song, "Efficient dye-sensitized solar cells with catalytic multiwall carbon nanotube counter electrodes," *ACS Applied Materials & Interfaces*, vol. 1, no. 6, pp. 1145–1149, 2009.

[5] J. Han, H. Kim, D. Y. Kim, S. M. Jo, and S. Y. Jang, "Water-soluble polyelectrolyte-grafted multiwalled carbon nanotube thin films for efficient counter electrode of dye-sensitized solar cells," *ACS Nano*, vol. 4, no. 6, pp. 3503–3509, 2010.

[6] J. G. Nam, Y. J. Park, B. S. Kim, and J. S. Lee, "Enhancement of the efficiency of dye-sensitized solar cell by utilizing carbon nanotube counter electrode," *Scripta Materialia*, vol. 62, no. 3, pp. 148–150, 2010.

[7] W. Hong, Y. Xu, G. Lu, C. Li, and G. Shi, "Transparent graphene/PEDOT-PSS composite films as counter electrodes of dye-sensitized solar cells," *Electrochemistry Communications*, vol. 10, no. 10, pp. 1555–1558, 2008.

[8] J. Chen, K. Li, Y. Luo et al., "A flexible carbon counter electrode for dye-sensitized solar cells," *Carbon*, vol. 47, no. 11, pp. 2704–2708, 2009.

[9] H. J. Choi, J. E. Shin, G. W. Lee, N. G. Park, K. Kim, and S. C. Hong, "Effect of surface modification of multi-walled carbon nanotubes on the fabrication and performance of carbon nanotube based counter electrodes for dye-sensitized solar cells," *Current Applied Physics*, vol. 10, no. 2, pp. S165–S167, 2010.

[10] M. Y. Yen, C. Y. Yen, S. H. Liao et al., "A novel carbon-based nanocomposite plate as a counter electrode for dye-sensitized solar cells," *Composites Science and Technology*, vol. 69, no. 13, pp. 2193–2197, 2009.

[11] P. Li, J. Wu, J. Lin, M. Huang, Y. Huang, and Q. Li, "High-performance and low platinum loading Pt/Carbon black counter electrode for dye-sensitized solar cells," *Solar Energy*, vol. 83, no. 6, pp. 845–849, 2009.

[12] H. Han, U. Bach, Y. B. Cheng, R. A. Caruso, and C. MacRae, "A design for monolithic all-solid-state dye-sensitized solar cells with a platinized carbon counterelectrode," *Applied Physics Letters*, vol. 94, no. 10, Article ID 103102, pp. 1–3, 2009.

[13] W. J. Lee, E. Ramasamy, D. Y. Lee, and J. S. Song, "Grid type dye-sensitized solar cell module with carbon counter electrode," *Journal of Photochemistry and Photobiology A*, vol. 194, no. 1, pp. 27–30, 2008.

[14] S. Lee, W. Seok Choi, and B. Hong, "A comparative study of dye-sensitized solar cells added carbon nanotubes to electrolyte and counter electrodes," *Solar Energy Materials and Solar Cells*, vol. 94, no. 4, pp. 680–685, 2010.

[15] Q. M. Gong, Z. Li, Y. Wang, B. Wu, Z. Zhang, and J. Liang, "The effect of high-temperature annealing on the structure and electrical properties of well-aligned carbon nanotubes," *Materials Research Bulletin*, vol. 42, no. 3, pp. 474–481, 2007.

[16] C. T. Hsieh, Y. T. Lin, W. Y. Chen, and J. L. Wei, "Parameter setting on growth of carbon nanotubes over transition metal/alumina catalysts in a fluidized bed reactor," *Powder Technology*, vol. 192, no. 1, pp. 16–22, 2009.

[17] C. T. Hsieh, Y. T. Lin, J. Y. Lin, and J. L. Wei, "Synthesis of carbon nanotubes over Ni- and Co-supported $CaCO_3$ catalysts using catalytic chemical vapor deposition," *Materials Chemistry and Physics*, vol. 114, no. 2-3, pp. 702–708, 2009.